Jacob Kleiman
Masahito Tagawa
Yugo Kimoto *Editors*

Protection of Materials and Structures From the Space Environment

Springer

Astrophysics and Space Science Proceedings
Volume 32

Protection of Materials and Structures From the Space Environment

Editors

Jacob Kleiman
Masahito Tagawa
Yugo Kimoto

Springer

Editors
Jacob Kleiman
Integrity Testing Laboratory Inc.
Markham
Ontario
Canada

Masahito Tagawa
Graduate School of Engineering
Kobe University
Kobe
Japan

Yugo Kimoto
Japanese Aerospace Exploration Agency
Ibaraki
Japan

Preface

The collection of papers in this book was presented at the tenth meeting of the International Conference on Protection of Materials and Structures from Space Environment (ICPMSE-10J) held in Okinawa, Japan, in June 2011.

The year 2011 marked a remarkable achievement for ICPMSE: its tenth meeting. Since the first meeting in 1992, the conference has grown steadily, attracting a large number of engineers, scientists, researchers, and managers from industrial companies, scientific institutions, and government agencies in Canada, USA, Asia, and Europe, thus becoming a truly international event.

The most recent ICPMSE meeting, originally scheduled for 2010, was postponed to 2011. This was because Japanese scientists from JAXA and other organizations wanted to join ITL in organizing the meeting and even offered to conduct it in Japan.

It seemed for a moment that the devastation caused by the nuclear accident at Fukushima, which was triggered by an earthquake and tsunami off the Pacific coast of the Tohoku region of Japan on March 11, 2011, would put in jeopardy the IPCMSE-10J meeting. However, there were practically no withdrawals or cancellations in participation due to these tragic events. The organizing committee is very thankful to all participants who decided to attend the meeting despite the situation in the North-East region of Japan.

The year 2011 was very special to the space community worldwide, since it marked the 50th anniversary of Yuri Gagarin's spaceflight. Gagarin, popularly called "The Columbus of the Cosmos," was the first human being to journey into outer space, when his Vostok spacecraft completed an orbit of the Earth on April 12, 1961. Half a century ago, Gagarin's spaceflight kicked off the era of human space travel. Since then, humans have established a solid presence in space through manned space stations, travel to the Moon, and future plans of space colonization.

In addition to the ISS that is fully functional, with astronauts and cosmonauts servicing it and using it for scientific and commercial activities, space laboratories like China's Tiangong 1 are being planned to be launched.

The year 2011 was also remarkable in that it marked the end of the US space shuttle era, with NASA officially setting a date of June 28 for the launch of the last

space shuttle Atlantis, after which the Atlantis and NASA's two other orbiters, Discovery and Endeavour, will retire for good.

New countries with ambitious space exploration programs that include launching satellites to orbit the Moon, landing on the Moon, and building space stations are joining the world space community. Mars exploration programs are also getting wider support and are gaining momentum. A common denominator for all activities of mankind in space is the safety of astronauts and cosmonauts and the reliability of the structures that operate in conditions of space environment. The influence of the space environment on materials and structures will remain, therefore, a timely topic for years to come. Questions about thermal stability, resistance to radiation, resistance to combined effects of various space factors, etc. will continue to accumulate with the development of new materials and protective coatings.

The goals of the ICPMSE meeting are, therefore, as in the past years, to facilitate exchanges between members of the various engineering disciplines involved in the development of space materials, including aspects such as environmental hazards of LEO, GEO, and Deep Space; ground-based qualification; and in-flight experiments and lessons learned from operational vehicles. To reflect on all such developments, the program of the meeting, in addition to the traditional topics of protection of materials and structures from atomic oxygen, VUV, and particle irradiation and thermal effects includes also such topics as micrometeoroids, space weather, and relevant protection issues for travel to Moon, Mars, and other planets as well as Deep Space exploration.

As a result of a very enthusiastic response to the first call for papers, over 100 contributions covering a wide range of topics on environmental issues were submitted with over 60 of them being published in these proceedings.

<div style="text-align: right">

Jacob Kleiman
Masahito Tagawa
Yugo Kimoto

</div>

Organization

The Tenth International Conference on Protection of Materials and Structures from Space Environment

ICPMSE-10J
June 12–June 17, 2011
Bankoku-Shinryokan, Okinawa, Japan
General Chairperson: Kleiman, J. (ITL/Univ. Toronto, Canada)
Chairpersons: Kimoto, Y. (JAXA, Japan) and Tagawa, M. (Kobe Univ., Japan)

International Organizing Committee

Banks, B. A. (Alphaport, USA)
Briet R. (CNES, France)
Cho, M. (KIT, Japan)
de Groh, K. K. (NASA, USA)
Edwards, D. L. (NASA, USA)
Grossman, E. (SOREQ, Israel)
Kimoto, Y. (JAXA, Japan)
Minton, T. K. (Montana State Univ., USA)
Nikanpour, D. (CSA, Canada)
Novikov, L. S. (Moscow State Univ., Russia)
Russel, J. F. (ONERA, France)
Tykhy, V. (Design Bureau Yuzhnoe, Ukraine)
van Eesbeek, M. (ESTEC, The Netherlands)
Yang, D. (Harbin Inst. Tech., China)

International Program Committee

Daly, M. (York University, Canada)
Feng, W. (Beijing Institute of Satellite, China)
Finkenor, M. (NASA, USA)
Golden, J. (Boeing, USA)
Grigorievsky, A. V. (JSC Kompozit, Russia)
Ishizawa, J. (JAXA, Japan)
Kim, D. W. (Seoul National Univ., Korea)
Semprimoschnig, C. (ESTEC, The Netherlands)

National Executive Committee

Tagawa, M. (Kobe Univ., Japan, Chair)
Iwata, M. (KIT, Japan)
Matsumoto, K. (JAXA, Japan)
Miyake, H. (Tokyo City Univ., Japan)
Miyazaki, E. (JAXA, Japan)
Shimamura, H. (JAXA, Japan)
Tachikawa, S. (JAXA/ISAS, Japan)
Watanabe, R. (Tokyo City Univ., Japan)
Yokota, K. (Kobe Univ., Japan)
Toyama, D. (JTB Western Corp., Japan)
Miyagi, T. (OCVB, Japan)
Yamashiro, A. (OCVB, Japan)

Session Moderators

Opening Session A
Moderators: Jacob Kleiman, Yugo Kimoto, Masahito Tagawa

Session B1: Space Environmental Effects on Materials and Structures in LEO/GEO Environment (AO/VUV, Radiation, etc.)
Moderators: Bruce A. Banks, Eitan Grossman

Session B2: Space Environmental Effects on Materials and Structures in LEO/GEO Environment (AO/VUV, Radiation, etc.)
Moderators: Kim K. deGroh, Yugo Kimoto

Session C: Space Environmental Effects on Materials and Structures in GEO, MEO and Interplanetary Environments (electrons, protons)
Moderators: Hiroaki Miyake, Minoru Iwata

Session C2: Space Environmental Effects on Materials and Structures in GEO, MEO and Interplanetary Environments (electrons, protons)
Moderators: A. V. Grigorevskiy, Masahito Tagawa

Session C3: Space Environmental Effects on Materials and Structures in GEO, MEO and Interplanetary Environments (electrons, protons)
Moderators: Christopher Semprimoschnig, Eiji Miyazaki

Session D: Outgassing, debris, contamination, micrometeoroids
Moderators: Stéphanie Remaury, Jun-ichiro Ishizawa

Session E: Fundamental Interactions between Space Environment and Materials
Moderators: Timothy K. Minton, Sharon K. R. Miller

Session F1: Synthesis and Modification of Materials and Surfaces for Protection in Space, Material Properties
Moderators: Christian Durin, Hiroyuki Shimamura

Session F2: Synthesis and Modification of Materials and Surfaces for Protection in Space, Material Properties
Moderators: Irina Gouzman, Dea-won Kim

Session G Space tribology materials
Moderators: Rikio Watanabe, Koji Matsumoto

Poster Session
Moderators: Rikio Watanabe, Kumiko Yokota

Group picture of the participants of the ICPMSE-10J. Bankoku-Shinryokan, Okinawa, Japan, – June 15, 2011

Acknowledgments

Contents

Protection of Materials and Structures from Space Environment – ICPMSE Proceedings Series: How Did It All Start?

Jacob Kleiman

Abstract A historical overview of the first ten meetings of the International Conference for Protection of Materials from Space Environment (ICPMSE) is presented. Through the published documents and pictures from personal archives the rich history of the meeting is illustrated. The collaborative links with ESA, CNES, ONERA and JAXA are described that helped to make the ICPMSE series of meeting a truly International event. The review is based on published ICPMSE proceedings as well as on personal archives of Prof. J. Kleiman who initiated the meeting in 1991.

Keywords ICPMSE • ISMSE • CNES • ONERA • JAXA • Kobe University • CSA

The year was 1989. It was the year when the Long Duration Exposure Facility (LDEF) satellite [1] was brought back to Earth from almost a 5-year stay in low Earth orbit (LEO). A number of successful LDEF meetings in USA followed, where the results from exposure of numerous materials to LEO orbit environment were discussed. The UTIAS materials scientific team led by Prof. Tennyson, who was one of the principal investigators on the UTIAS LDEF Material's experiment, participated in the LDEF community meetings. Working closely with the space materials group at the UTIAS, Dr. Kleiman, then a Research Scientist with the R&D Group of 3M Canada and an Adjunct Professor at the UTIAS, soon realized that the North American space environment community, when the LDEF meetings were stopped, is lacking a meeting place where the latest developments in new materials, their behavior in LEO and other space environments, the results from ground based experiments and from flights can be shared and discussed. And that is how the first ICPMSE meeting was initiated in 1991.

J. Kleiman (✉)
Integrity Testing Laboratory Inc, Markham, ON, Canada
e-mail: jkleiman@itlinc.com
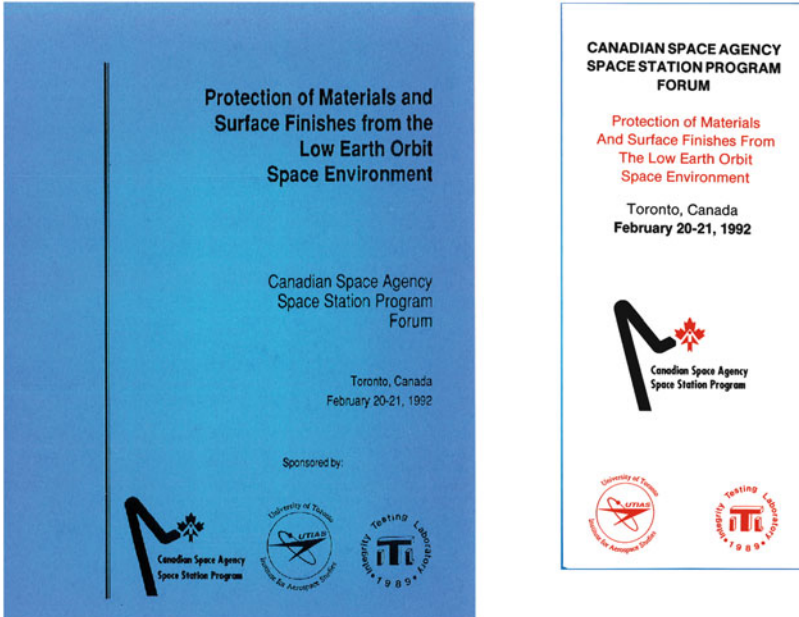
Fig. 1 The front page of the proceedings and the announcement brochure of the first meeting ICPMSE-1 in Toronto, Canada, 20–21 February, 1992

Fig. 2 Mementos from the ICPMSE-1 meeting. (**a**) Lunch arranged at the STEAR Program final projects exhibition; (**b**) participants of the ICPMSE-1; (**c**) Gary Pippin and Jacob Kleiman during the question period; (**d**) Prof. R. Tennyson explains the UTIAS LDEF experiment (seen on the table in front of him)
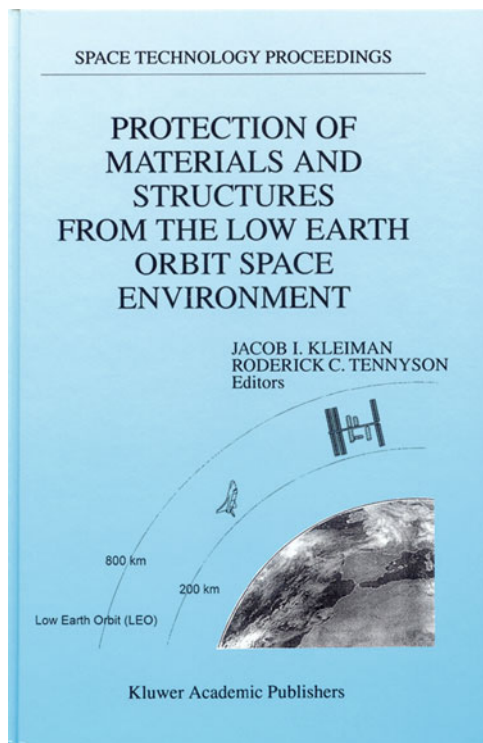
Fig. 3 The front page of the proceedings of the ICPMSE – 3: Toronto, Canada, 25–26 April, 1996, [2]

Fig. 4 Mementos from the ICPMSE-3 meeting. (**a**) A group of participants from Russia, Israel, USA and Netherlands on a coffee break; (**b**) participants of the Ukrainian delegation at ICPMSE-3 with Canadian hosts; (**c**) round table panel of speakers after one of the sessions; (**d**) even lunches were used for discussions

Fig. 5 The front page of
the proceedings of the
ICPMSE – 4: Toronto,
Canada, 23–24 April,
1998, [3]
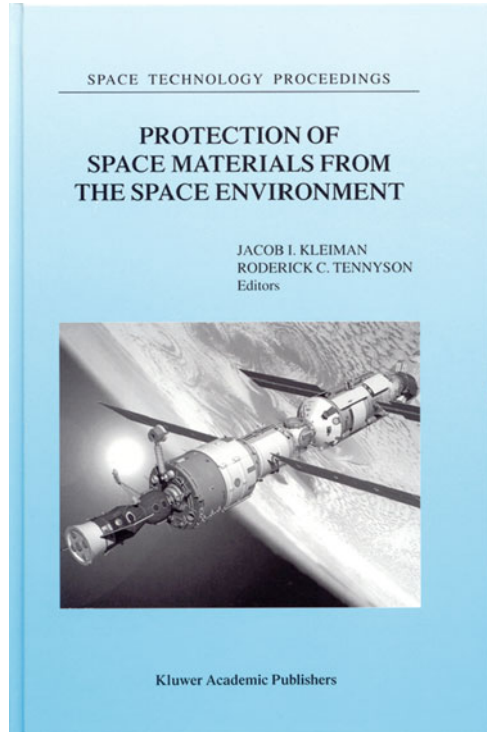
Another, very instrumental factor in the initiation of the ICPMSE series of
conferences was the Canadian Space Agency's Strategic Technologies for Auto-
mation and Robotics (STEAR) Program. Through the STEAR Program, CSA
promoted the advancement of strategic space technologies, including those
contributing to the longevity of materials and structures in the space environment.
As part of this effort, a program on development of new protective coatings was
conducted during the period 1991–1995. The first ICPMSE meeting was devoted
largely to the results of this STEAR program.

With years, however, the meeting became a focal gathering point in North
America for scientists, researchers, managers, students and academicians to discuss
the latest developments in the area of interaction of materials and structures with the
harsh space environment. Initially, the ICPMSE meetings were focused, mainly, on
the effects of the low Earth orbit environment on materials. But with time it became
clear that there is an intimate relationship between the various space environment
factors and gradually, the scope of the meetings widened, including also the GEO
and other environments. Also, following the worldwide space community plans for
the colonization of the Moon and Mars, it was decided to add to the topics of the
ICPMSE meetings the planetary and the interplanetary environments.

Fig. 6 The front page of the proceedings of ICPMSE – 5: Arcachon, France, 5–9 June, 2000, [4]

Very soon, from being a North American event, the ICPMSE meetings became a truly international event, attracting scientists from Europe, Asia and other parts of the world.

Being a biannual event, the ICPMSE meeting coincided in the year 2000 with another international meeting, the International Symposium on Materials in a Space Environment (ISMSE) that was organized since 1979 in Europe by CNES, ONERA and ESA every 3 years. A mutual decision was made by the ICPMSE and ISMSE organizers to conduct in such "coinciding" years both meetings jointly in Europe. First such joined meeting was conducted in the year 2000 in
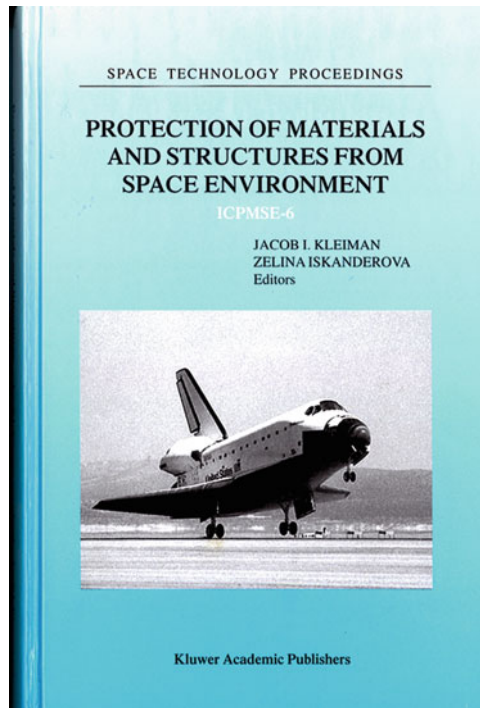
Fig. 7 The front page of the proceedings of ICPMSE – 6: Toronto, Canada, May 10–13, 2004, [5]

Fig. 8 Mementos from the ICPMSE-6 meeting. (**a**) Members of the Russian delegation on a after-conference trip to Niagara Falls with ITL hosts; (**b**) conference dinner – a not to miss event at the meetings; (**c**) participants of the ICPMSE-6; (**d**) Bruce Banks delivers a talk at a session chaired by Tim Minton

Fig. 9 Special edition of JSR with selected papers from the ICPMSE-6 meeting, [6]

Arcachon (ICPMSE-5/ISMSE-8) (Fig. 6), [4]. The next such meeting was in 2006 in Collioure, France (ICPMSE-8/ISMSE-10) (Fig. 11), [8].

Starting from the third ICPMSE meeting in 1998, Dr. Kleiman initiated the publishing of the Proceedings of the meetings as peer reviewed hard-cover books with such reputable publishing houses as Kluwer, Springer and the American Institute of Physics.

In addition to such publications, the papers presented at the ICPMSE meetings were repeatedly published in special editions of such peer-reviewed journals as Journal of Spacecraft and Rockets (Fig. 9) [6] and in High Performance Polymers [11].

With many countries joining the space community and actively contributing to the space environmental studies, it was the next logical step to extend the organizational effort of the ICPMSE meetings to other organizations and countries. Since Japan became one of the major players in the area of exploration of the effects of the space environment on materials it was logical to bring the ICPMSE meeting to Japan.

Fig. 10 The front page of the proceedings of the ICPMSE – 7: Toronto, Canada, May 10–13, 2004, [7]
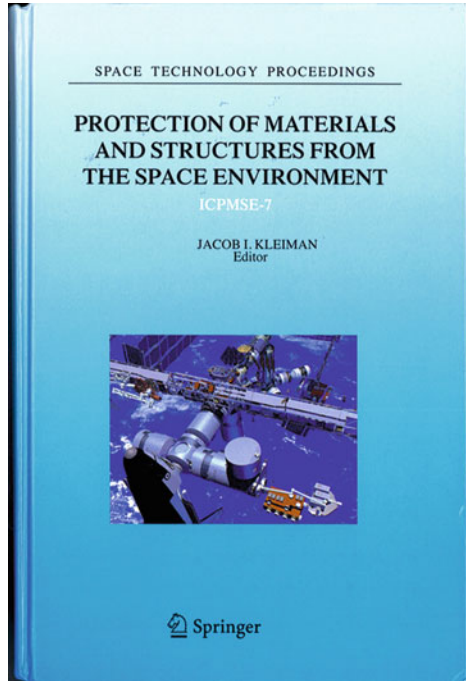
Fig. 11 The front page of the CD with the proceedings of ICPMSE – 8: Collioure, France, 19–23 June, 2006, [8]
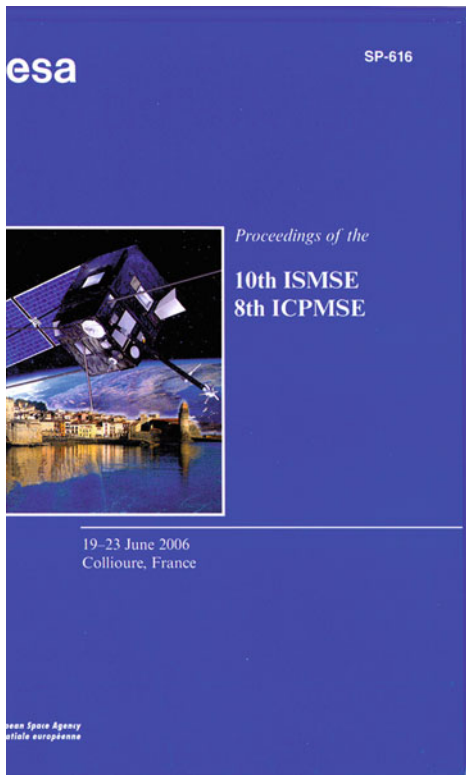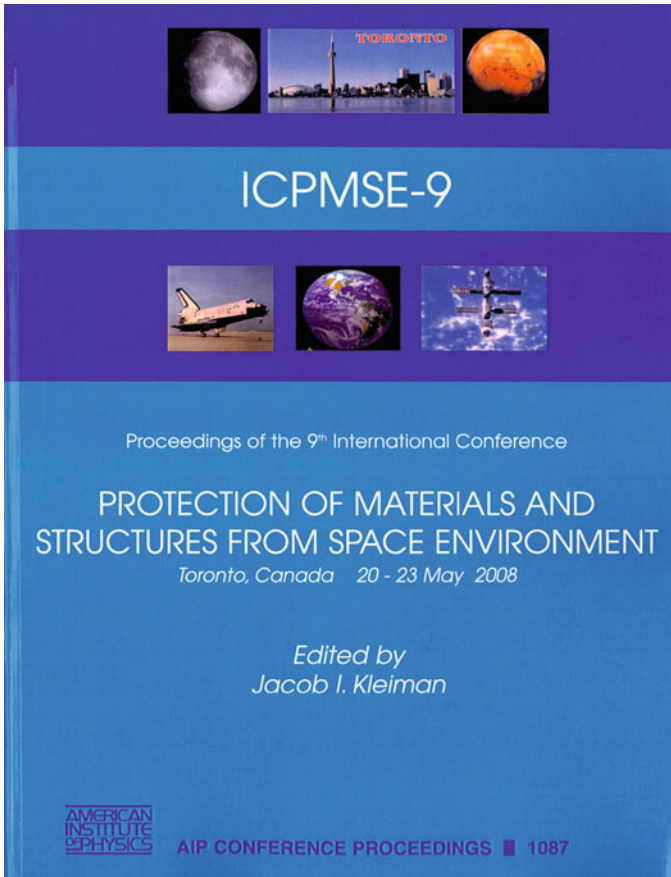
Fig. 12 The front page of the proceedings ICPMSE – 9: Toronto, Canada, May 20–23, 2008, [9]

And for these reasons, the jubilee tenth ICPMSE meeting will be organized jointly between Canada and Japan and will take place between 12 and 17 June, 2011 in Okinawa, Japan.

The presented snapshots from a number of ICPMSE meetings (Figs. 2, 4, 8, 13) attest to the true international spirit and very friendly atmosphere that accompanied all meetings.

Fig. 13 Mementos from the ICPMSE-9 meeting. (**a**) Participants of the ICPMSE-9; (**b**) conference dinner – as usual, a not to miss event at the meetings; (**c**) and of course nothing can come close to a real Russian dance; (**d**) members of the USA delegation with J. Kleiman; (**e**) Canadian hosts proved that not only in France you can catch a glimpse of a real Can-Can dance; (**f**) members of the Korean delegation at lunch

References

1. http://en.wikipedia.org/wiki/Long_Duration_Exposure_Facility)
2. Kleiman JI, Tennyson RC (eds) (1999) Protection of materials and structures from the low Earth orbit space environment. In: Proceedings of the ICPMSE-3, third international conference, Toronto, 25–26 Apr 1996. Space technology proceedings, vol 2, Kluwer, ISBN 0-7923-5540-7
3. Kleiman JI, Tennyson RC (eds) (2001) Protection of space materials from the space environment. In: Proceedings of the ICPMSE-4, fourth international conference, Toronto, 23–24 Apr 1998. Space technology proceedings, vol 4, Kluwer, ISBN 0-7923-6981-5
4. CNES (2000) Protection of space materials and structures from the LEO space environment. In: Werling E, CNES and Kleiman J, ITL Inc. (eds) Proceedings of the ICPMSE-5, fifth

international conference held in conjunction with the 8th international symposium on "Materials in a Space Environment", Arcachon, 5–9 Jun 2000. Available on CD only

5. Kleiman JI, Iskanderova Z (eds) (2003) Protection of materials and structures from space environment. In: Proceedings of the ICPMSE-6, sixth international conference, Toronto, 1–3 May 2002. Space technology proceedings, vol 5, Kluwer, ISBN 1-4020-1690-5

6. Special issue of the J Spacecraft Rockets that was prepared and published in 2004 by special editor David Edwards and invited editor Jacob Kleiman containing a selection of papers from the sixth international conference, ICPMSE-6 that took place in Toronto, 1–3 May 2002

7. Kleiman JI (ed) (2006) Protection of materials and structures from the space environment. In: Proceedings of the ICPMSE-7, seventh international conference, Toronto, 10–13 May 2004. Space technology proceedings, vol 6, Springer, ISBN-10 1-4020-4281-7 (HB)

8. European Space Agency (2006) Protection of materials and structures from the space environment. In: Dinguirard M (ed) Proceedings of the ICPMSE-8, eighth international conference held in conjunction with the 10th international symposium on "Materials in a Space Environment", Collioure, Publication SP-616, 19–23 Jun 2006. Available on CD only

9. Kleiman JI (ed) (2009) Protection of materials and structures from space environment. In: Proceedings of the 9th international conference, ICPMSE-9, Toronto, 20–20 May 2008. Published by AIP conference proceedings 1087, ISBN 978-0-7354-0619-3

10. Kleiman JI, Personal Archives

11. Special Issue of High Performance Polymers of papers from a Joint Conference Materials for Space Applications: Arcachon, France, June 5–9, 2000, vol 13, ed. John W. Connell, IOP Publ., 2001, 165 pages

Analyses of Hubble Space Telescope Aluminized-Teflon Insulation Retrieved After 19 Years of Space Exposure

Kim K. de Groh, Deborah L. Waters, Jelila S. Mohammed, Bruce A. Perry, and Bruce A. Banks

Abstract Since its launch in April 1990, the Hubble Space Telescope (HST) has made many important observations from its vantage point in low Earth orbit (LEO). However, as seen during five servicing missions, the outer layer of multilayer insulation (MLI) has become successively more embrittled and has cracked in many areas. In May 2009, during the 5th servicing mission (called SM4), two MLI blankets were replaced with new insulation pieces and the space-exposed MLI blankets were retrieved for degradation analyses by teams at NASA Glenn Research Center (GRC) and NASA Goddard Space Flight Center (GSFC). The MLI blankets were from Equipment Bay 8, which received direct sunlight, and Equipment Bay 5, which received grazing sunlight. Each blanket contained a range of unique regions based on environmental exposure and/or physical appearance. The retrieved MLI blanket's aluminized-Teflon® fluorinated ethylene propylene (Al-FEP) outer layers have been analyzed for changes in optical, physical, and mechanical properties, along with space induced chemical and morphological changes. When compared to pristine material, the analyses have shown how the Al-FEP was severely affected by the space environment. This paper reviews tensile properties, solar absorptance, thermal emittance, x-ray photoelectron spectroscopy (XPS) data and atomic oxygen erosion values of the retrieved HST blankets after 19 years of space exposure.

K.K. de Groh (✉) • D.L. Waters
NASA Glenn Research Center, Cleveland, OH 44135, USA
e-mail: kim.k.degroh@nasa.gov

J.S. Mohammed
NASA Goddard Space Flight Center, Greenbelt, MD 20771, USA

B.A. Perry
Ohio Aerospace Institute, Brook Park, OH 44142, USA

B.A. Banks
Alphaport at NASA Glenn Research Center, Cleveland, OH 44135, USA

1   Introduction

The HST was launched on April 25, 1990 into LEO as the first mission of NASA's Great Observatories program. It is a telescope capable of performing observations in the near-ultraviolet, visible and near-infrared wavelengths. The HST was designed to be serviced on-orbit to upgrade scientific capabilities. Five servicing missions (SM) have taken place, with the last mission occurring in May 2009 after 19 years in space. During servicing mission 2 (SM2), in February 1997, severe cracking of the 5 mil Al-FEP outer layer of the multilayer insulation (MLI) blankets was observed on the light shield (LS), forward shell and equipment bays of the telescope [1, 2]. Patches of 2 mil thick (50.8 μm) Al-FEP were placed over the worst cracks in MLI on Equipment Bays 8 and 10 (two patches were attached to each bay).

   In May 2009 during the fifth servicing mission (called SM4), two degraded MLI blankets that were originally installed on the telescope were replaced with new insulation pieces, called New Outer Blanket Layers (NOBLs), and the space exposed MLI blankets were brought back for analysis by teams at NASA Glenn Research Center and NASA Goddard Space Flight Center. No other spacecraft material has been retrieved and analyzed after having this length of space exposure. The two blankets retrieved during SM4 included Equipment Bay 8 MLI, which received direct sunlight, and Equipment Bay 5 MLI, which received grazing sunlight. Also retrieved were remnants of the two patches that were placed over cracked areas on Bay 8 during SM2. The retrieved MLI blankets' Al-FEP outer layers were found to be highly degraded and have been analyzed for changes in optical, physical, and mechanical properties, along with space induced chemical and morphological changes and heat induced changes. This paper reviews the tensile properties, solar absorptance, thermal emittance, XPS data and atomic oxygen erosion values of the retrieved HST blankets after 19 years of space exposure.

2   Materials and Environmental Exposure

2.1   HST SM4 Bay 5 and Bay 8 MLI

The Bay 5 and 8 MLI blankets originally installed on HST (exposed to space for 19.1 years), and 2 mil Al-FEP patches installed on Bay 8 on February 18, 1997 during SM2 (exposed to space for 12.2 years) were retrieved by astronauts on May 18, 2009 during SM4. As can be seen in the illustration in Fig. 1, Bay 8 is located 15° from the +V3 solar facing axis, and therefore is almost directly facing the sun. Bay 5 faces towards the +V2 solar array drive arm direction, and at 75° from the +V3 direction, receives grazing sunlight. The environmental effects that cause
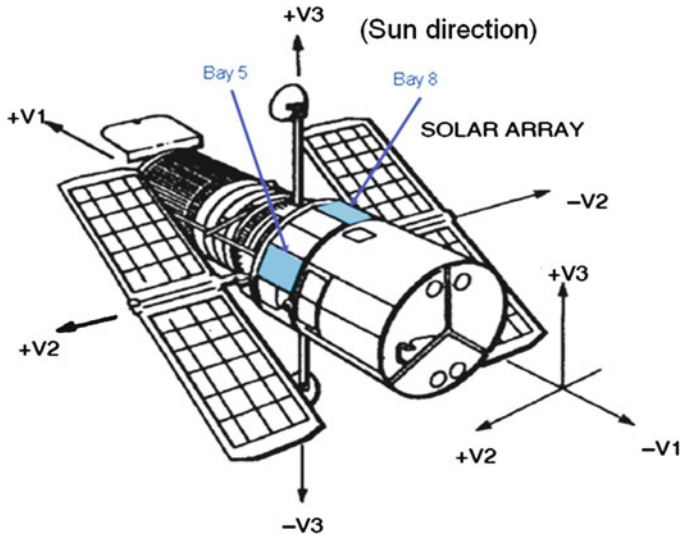
Fig. 1 Locations and orientations of Bays 5 and 8 on HST (+V3 is the solar facing axis)

degradation of the MLI are primarily temperature cycling, solar radiation, particle radiation, and atomic oxygen.

2.2 Environmental Exposure

The sun exposure on each bay was determined by the science pointing profile of HST. The attitude profile between 1/1/00 and SM4 was analyzed to determine the "typical" attitude of HST. The results were then extrapolated to provide estimates of the sun exposure since launch. Equivalent hours of sun exposure (ESH) of the telescope from deployment to SM4 are estimated as 111,000 h, based on time in orbit, average time exposed to the sun per orbit, and length of each orbit. Based on the attitude profile from 2000 and SM4, and extrapolating over mission life, Bay 5 was exposed to ~24,300 ESH and the unpatched and patched areas of the Bay 8 MLI were exposed to ~89,300 ESH and ~30,300 ESH, respectively.

The HST underwent an estimated 110,000 thermal cycles overall, from deployment to SM4. The range of temperatures seen by Bay 5 and Bay 8 vary greatly, because they are dependent on HST attitude and environmental heating variables. Thermal Desktop was used to model the Bay 5 and Bay 8 MLI and simulate the general thermal cycling behavior. Bay 5 MLI temperatures were estimated to range from $-175\ °C$ to $0\ °C$ and the Bay 8 temperatures were estimated to range from $-175\ °C$ to $40\ °C$, for the attitude and orbit configurations modeled.

The X-ray fluence for solar facing surfaces was computed to be 641.1 J/m^2 between 1–8 Å and 43.1 J/m^2 between 0.5 and 4 Å. Data for x-ray fluence is based on x-ray flux data from the Geosynchronous Operational Environmental Satellites

(GOES) for the time period of launch (1990) through SM2 (February 1997) [3]. For SM2 through SM4, the x-ray fluence was estimated assuming an average 11-year solar cycle [3].

Electron and proton fluence from solar wind particles trapped in Earth's magnetic field have been calculated from deployment until December 9, 1999 using NASA's proton and electron models, AP-8 and AE-8, respectively [3]. The data for SM4 were extrapolated from these prior data, and indicated the Bay 5 and Bay 8 MLI received an electrons fluence of 5.6×10^{13} particles/cm^2 for electrons >40 keV, and a proton fluence of 5.4×10^{10} particles/cm^2 for protons >40 keV.

The atomic oxygen fluence was computed for the duration of the HST mission over the period of time from deployment to SM4. This was accomplished by adding: (1) the prediction over the period of time from deployment to SM1 as predicted by SAIC's version 5.0 Environmental Work Bench, which uses MSIS-86 atmospheric model, to (2) a prediction based on orbital and atmospheric data from NASA Goddard for SM1 to SM4. The parameters used in the SM1 to SM4 fluence calculation included altitude, atmospheric density, and orbital velocity corrected for the Earth's atmosphere co-rotation. Based on these calculations the total ram fluence was 2.61×10^{21} atoms/cm^2. If the surfaces of Bay 8 are 15° from solar facing, then the fluence would be ~25.8 % of the ram fluence or ~6.73×10^{20} atoms/cm^2. But, as the surfaces are solar facing but randomly tipped (always with Bay 8 somewhat towards the sun), then the fluence is decreased an additional factor of $2/\pi$ resulting in the probable fluence of ~4.28×10^{20} atoms/cm^2. Because the Bay 5 faces towards the +V2 direction and is 75° off the solar facing axis, the fluence was estimated as ~28.0 % of the ram fluence, or 7.30×10^{20} atoms/cm^2. As the surfaces are randomly tipped, the fluence would be decreased by $2/\pi$ resulting in a probable fluence of ~4.65×10^{20} atoms/cm^2.

3 Experimental Procedures

A DDL Inc. Model 200Q Electromechanical Test System was used to determine the load-displacement data from which elongation to failure (percent elongation) and ultimate tensile strength (UTS) were determined. The tensile samples were sectioned to the specifications defined in American Society for Testing and Materials (ASTM) Standard D-638 for Type V tensile specimens [4]. Care was taken to avoid cracks and impact sites. The initial grip distance was set at 25.4 mm and the test speed was 12.7 mm/min.

Solar absorptance and thermal emittance measurements were taken at both GSFC and GRC. Both as-retrieved and heat-treated samples were measured at GRC. Initially, heat treatment was planned to be conducted at two temperatures: 120 °C and 200 °C (the highest temperature reached for very tightly curled insulation [2, 5]). But, finally, only the effect of moderate on-orbit heating (120 °C) was evaluated. Heating was conducted for 96 hours as prior data indicates a minimum of 72 h is necessary to heating effects to be stabilized [6].

Cary 5000 spectrophotometers equipped with Spectralon integrating spheres were used to measure total reflectance from 250 to 2,500 nm at an 8° angle of incidence at both GSFC and GRC. Absorptivity data were integrated with respect to the air mass zero solar spectrum to obtain solar absorptance. Samples at GRC were measured with an Al spacer backed by a single layer of sample of the quilted Al/Kapton/Al inner film (Region 8.15) replicating the on-orbit configuration.

Emissivity measurements were obtained at GSFC using a Gier-Dünkle DB-100 InfraRed Reflectometer following the ASTM E408-71 standard test method. The normal emittance (ε_n) of the surface was measured from 5 to 40 μm while at room temperature. Three measurements were taken for each sample, with the exception of Bay 8 Region 3, which was highly delaminated, hence only one measurement was taken. Emissivity measurements were obtained at GRC using a Surface Optics Corporation Model SOC 400 T Reflectometer. The SOC 400 T measures the directional reflectance of surfaces over a large spectral range, 2–25 μm, to obtain the directional thermal emittance over a large temperature range. Automatic integration of reflectivity data in the infrared with respect to blackbody curves is used to calculate total emittance for a selectable temperature range. Data were obtained at 293, 313 and 393 K. The samples were placed in the sample holder face-down with an aluminum spacer and were backed by a sample of the quilted Al/Kapton/Al MLI inner layer.

Samples for thickness measurements were mounted in epoxy, and then SiC paper and diamond slurry were used to polish the cross sections. Thickness measurements were taken at three locations along each sample's cross-section, using a scanning electron microscope (SEM).

Atomic oxygen erosion yield (Ey) of the HST samples (cm^3/atom) was calculated in two separate ways, by mass loss and by thickness loss measurements. The mass of 12.7 mm diameter circular samples were measured using a Mettler M3 balance and compared to the mass of pristine material to determine mass loss. The mass loss was divided by the sample area (1.366 cm^2), density and the atomic oxygen fluence to determine Ey. Erosion yield determined by thickness loss was computed by dividing the thickness loss in cm by the atomic oxygen fluence.

Samples were analyzed for elemental composition using a M-Probe X-Ray Photoelectron Spectrometer. Three locations on samples from various regions were run using a general survey scan, with a spot size of 800 μm, to determine atomic percent composition.

4   Results and Discussion

To retrieve the MLI blankets, astronaut John Grunsfeld unpeeled each blanket from its Velcro secured border, then folded the blankets and placed them into EVA storage bags. Although great care was taken in retrieval planning and execution, the retrieval process did cause cracking at fold seams, introducing handling cracks that were not present on-orbit prior to retrieval.
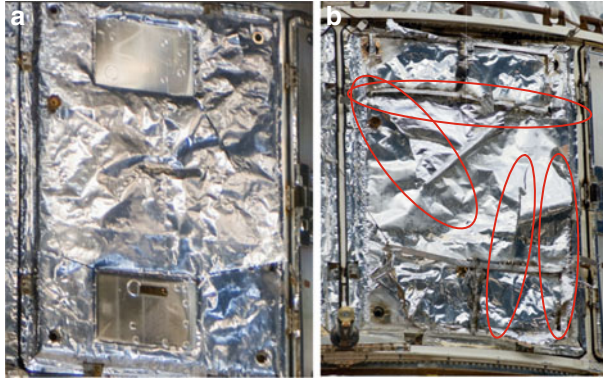
Fig. 2 On-orbit photos of Equipment Bays 5 and 8 just prior to retrieval during SM4: (**a**) Bay 5, and (**b**) Bay 8 (composite photo of two on-orbit images) with large cracks *circled*

The Bay 5 and Bay 8 MLI blankets are shown in the on-orbit photos taken during SM4 in Fig. 2a, b, respectively. As can be seen, the Bay 5 MLI has several large cracks extending from the two rectangular radiator areas. The Bay 8 MLI also has several very large cracks, and one side of the largest crack on Bay 8 curled up into a cone-like roll, as seen in Fig. 2b. Also, the Bay 8 patches were seen to be highly degraded with the majority of the Al-FEP completely gone. Upon post-retrieval visual inspection, the Bay 8 MLI appeared significantly more degraded than the Bay 5 MLI, as the Bay 8 MLI was broken into many pieces after removing it from the EVA bag, unfolding it and laying it flat again. In fact, the Bay 8 Al-FEP outer layer needed to be reassembled post-flight like a puzzle.

4.1 Exposure Regions

The retrieved Bay 5 and Bay 8 MLI blankets contained a range of unique regions which were identified based on environmental exposure and/or physical appearance and given assigned numbers. For example, the Bay 8 MLI that was not covered by patch material and was exposed to the space environment for the full 19.1 years had areas with three distinct appearances: shiny areas, hazy-white areas and areas where the Al was delaminated. These regions were defined as Regions 8.1, 8.2 and 8.3, respectively. Also, as mentioned, one of the Bay 8 outer layer Al-FEP cracked areas (not covered by patch material) curled up into a cone-like roll. In the curled region, the backside Al was exposed to the space environment, therefore this material heated to a higher temperature on-orbit than the nominal space-facing FEP because of the low emittance of the aluminized surface. This "curled" area was divided into two regions: a tightly curled region (8.7) and a loosely curled region (8.8), as those two regions may have heated differently on-orbit. Some areas of the patches installed during SM2 eventually degraded exposing the underlying MLI to the space environment once again as observed during SM3B and SM4. Therefore, the

Table 1 HST SM4 Bay 5 and Bay 8 region definitions

HST material Bay region	Description
Pristine (P)	Pristine 5 mil Al-FEP
5.1	Nominal/shiny
5.4	Nominal/Al-delaminated
8.1	Nominal/shiny
8.2	Nominal/white hazy
8.3	Nominal/Al-delaminated
8.7	Cone/tight curl
8.8	Cone/loose curl
8.11	Patched SM2-SM4
8.13	Patched SM2-SM3B
8.15	Protected inner layer (Al/Kapton/Al)

MLI under the patched areas are divided into two regions: region patched during SM2 and exposed by SM3B (SM2-SM3B, patched 5.1 years, called 8.13), and region patched during SM2 and still covered at SM4 (SM2-SM4, patched 12.2 years, called 8.11).

A total of 10 different regions were identified on Bay 5 (R1 – R10), and 15 different regions were identified on Bay 8 (R1 – R15) and 4 regions identified on the retrieved Patches (R16–19). The regions selected for testing are defined in Table 1. During sectioning of samples from the blankets, care was taken to avoid any cracks or imperfections in the samples which would affect the tests.

The delaminated regions of Bays 5 and 8 appear very different, and were likely caused by different factors. Bay 5 delaminated samples have a checkerboard-like pattern of delaminated areas on a surface that has predominately retained its Al backing. Bending these samples indicated that there is no tendency for more Al to flake off. In contrast, Bay 8 delaminated samples have small patches of Al sprinkled throughout a mostly delaminated surface and additional Al separates from the FEP on handling the samples.

4.2   Tensile Properties

The average UTS and percent elongation at failure of the HST and pristine Al-FEP are shown in Fig. 3a, b, respectively. Because of the degree of embrittlement of the HST samples, many broke while being punched out or handled prior to testing. Others were tested but failed at pre-existing cracks, causing a premature break. Data from premature breaks were not included in the average. Five samples from region 8.7 were tested, and all broke prematurely, thus no data are reported.

All HST material was extremely embrittled. Elongation at failure was reduced from 255 % for pristine material to 8.5 % for Bay 5 nominal/shiny material and to1.4 % for Bay 8 nominal/shiny material. The Bay 8 Al-FEP, which had a significantly higher solar exposure and on-orbit thermal cycling temperature, was found to fracture very easily with handling, like thin brittle glass. All regions also
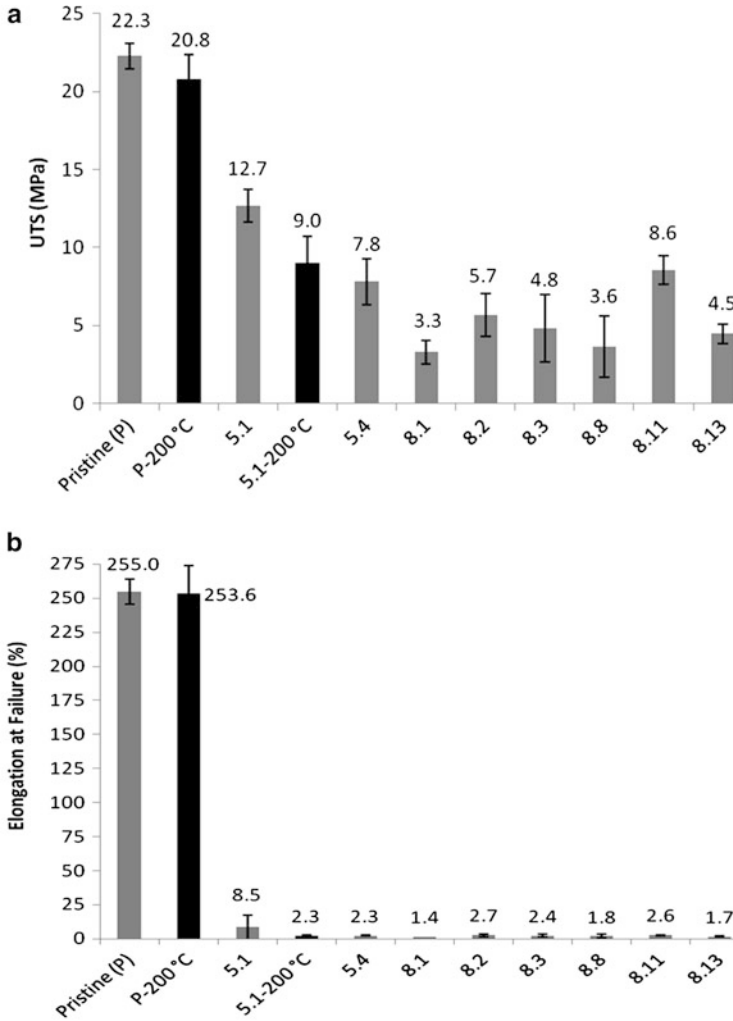
Fig. 3 Tensile properties of pristine and HST Al-FEP: (**a**) average UTS, and (**b**) average elongation at failure

experienced large decreases in UTS, from 22.3 MPa for pristine Al-FEP to 12.7 MPa and 3.3 MPa for Bay 5 and Bay 8 nominal/shiny material, respectively. Although the standard deviation is large compared to some of the absolute values, both the UTS and the elongation at failure appears to correlate with the amount of solar exposure a sample received. For example, the solar facing Bay 8 material is more embrittled than the solar grazing Bay 5 material, and the elongation at failure of Bay 8 material is proportional to the amount of time that it was patched.

Heating pristine Al-FEP marginally decreased its strength, and had no effect on elongation. The Bay 8 MLI was too embrittled to conduct studies to assess the
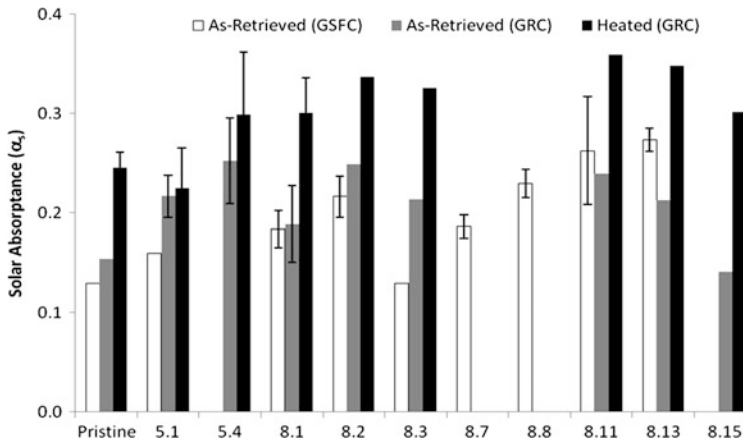
Fig. 4 As-retrieved and 120 °C (96 h) heated solar absorptance values

effect of heating, but heating Bay 5 Region 1 material at 120 °C for 96 h further reduced both the elongation and strength of the samples. This supports the mechanism proposed for degradation in which solar radiation and solar heating play synergistic roles.

4.3 Optical and Thermal Properties

The as-retrieved and 120 °C-heated solar absorptance values obtained at GSFC and GRC are shown in Fig. 4. It should be noted that the pristine Al-FEP absorptance obtained at GRC (0.15) was slightly higher than the value obtained at GSFC (0.13). This is attributed to calibration differences between the two instruments; hence comparisons should only be made between data taken on the same instrument. As-retrieved samples from both GSFC and GRC experienced an increase in solar absorptance, compared to pristine Al-FEP, with the exception of Bay 8 Region 3 (delaminated region), which was measured at GSFC without the inner layer. The GSFC absorptance of Bay 5 was slightly higher (0.16) than pristine Al-FEP (0.13), while Bay 8 had a wide range of absorptance values, with the greatest absorptance for Bay 8 Region 13 (0.27). This is the region that was patched between SM2 and SM3B, and then exposed again to space. The data trends for absorptance changes are consistent for both GSFC and GRC, with the Bay 8 hazy-white region (Region 2) and the patched regions (Regions 11 and 13) having the greatest increases in solar absorptance.

As stated previously, the GRC samples were measured with a piece of the inner layer embossed Al/Kapton/Al to best replicate the optical properties in space. As might be expected, the reflectance of the inner layer was found to have the biggest impact on the solar absorptance of the delaminated regions (5.4 and 8.3), increasing the absorptance significantly as compared to the GSFC data without the inner layer.
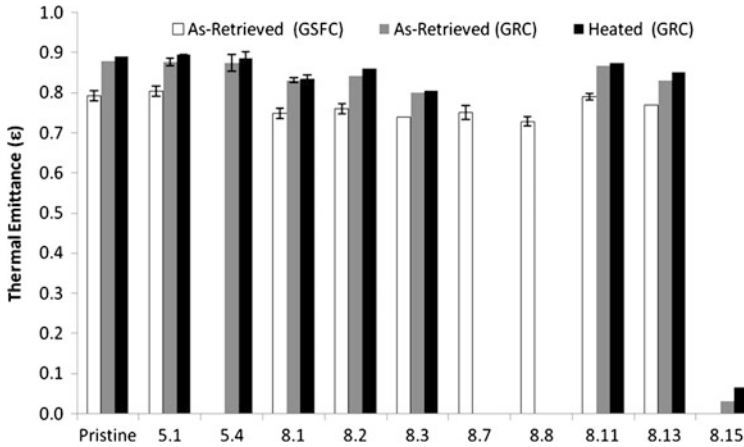
Fig. 5 As-retrieved and heated emittance values

Heating was found to increase the solar absorptance of the pristine Al-FEP by 0.09. The Bay 8 Al-FEP experienced similar increases due to heating (0.09–0.11), with the regions that were covered by patches increasing even more (0.12–0.14). Although the Bay 5 thermal cycled to a lower maximum temperature on-orbit (0 °C) than Bay 8 (40 °C), the Bay 5 Al-FEP experienced very small increases in absorptance with heating as well. The reason for this is currently unknown.

The as-retrieved and heated thermal emittance values obtained at GSFC and GRC are plotted in Fig. 5. The GSFC thermal emittance values were found to decrease for all samples except Bay 5 region 1 and Bay 8 region 11 (the region patched between SM2 and SM4). Emittance loss is typically associated with thickness loss of FEP, but for Bay 8 regions 7 and 8, samples may have experienced additional emittance change due to excessive heating on-orbit or possibly from contamination. For example, if the emittance of silicone is lower than FEP then a thick enough layer of silicone contamination could decrease the emittance of the FEP. Similar to the GSFC emittance values, the GRC emittance was found to decrease for all samples except Bay 5 Region 1 (also Bay 5 Region 4) and Bay 8 region 11, the region patched between SM2 and SM4. Heating had little impact on the emittance values of the retrieved HST MLI.

4.4   X-Ray Photoelectron Spectroscopy (XPS)

The XPS analyses for pristine Al-FEP and regions 5.1, 8.1, 8.2 and 8.11 are provided in Table 2. As expected, the pristine Al-FEP is comprised of C (33.4 %) and F (66.7 %). The Bay 8 nominal regions (1 and 2) were similar with an increase in C ($\approx$39 %), a decrease in F ($\approx$51 %) and the presence of O ($\approx$6 %), N ($\approx$2 %) and Si (0.4–1.2 %). Bay 8 Region 11, which was patched from SM2-SM4 had a high concentration of C, possibly due to contamination from the Velcro patch.

Table 2 XPS results for atomic percent composition

HST SM4 material Bay region	Atomic %					F/C ratio
	C	N	O	F	Si	
Pristine	33.27	0.00	0.00	66.73	0.00	2.01
5.1	19.44	1.12	36.36	22.56	20.52	1.16
8.1	39.19	2.31	6.35	50.87	1.29	1.30
8.2	39.50	2.12	5.43	52.55	0.41	1.33
8.11	59.41	4.10	18.70	15.14	2.65	0.25

Table 3 Atomic oxygen erosion yield comparison

HST material Bay region	Description	Mass loss Ey (cm^3/atom)	Average thickness (cm)	Thickness loss[a] Ey (cm^3/atom)	Ratio of Ey(TL)/ Ey(ML)
8.1	Shiny	1.17E-23	0.00722	1.37E-23	1.17
8.2	White hazy	8.22E-24	0.00886	9.84E-24	1.20
8.3	Al-delaminated	1.12E-23	0.00769	1.29E-23	1.15
5.1	Shiny	1.27E-24	0.01241	1.43E-24	1.12
P	Pristine	–	0.01308	–	–

[a]Based on 130.1 μm original thickness

Surprisingly, Bay 5 was found to have a significant amount of Si contamination with the presence of 20 % Si and 36 % O. The back of the solar arrays are coated with DC 93–500 silicone and because Bay 5 faces towards the +V2 solar array direction, the DC 93–500 is most likely the source of contamination. As only one area of Bay 5 was tested, additional tests could determine if silicone contamination is wide spread or localized on the blanket. This would be good to determine, particularly as silicone contamination could impact Ey values along with optical and thermal results.

In a study by de Groh et al. [7], samples sectioned from Al-FEP circular thermal shields covering the bi-stem booms on the second set of HST solar arrays (retrieved after 8.25 years of space exposure) were examined with scanning electron micros-copy for surface morphology and with energy dispersive spectroscopy (EDS) for surface chemistry. Pristine Al-FEP and solar-facing and anti-solar-facing thermal shield surfaces did not have any evidence of contamination, with only C and F peaks observed. However, a crazed surface texture was observed on one of the solar-grazing samples. The EDS data indicated the crazed texture is due to silicone contamination. Hence, the Bay 5 silicone contamination is consistent with contam-ination found on the solar-grazing surface of the retrieved solar array thermal shields, which is probably caused by contamination from the DC 93–500 silicone coating on the anti-solar side of the solar arrays.

4.5 Atomic Oxygen Erosion Yield (Ey)

Atomic oxygen Ey values determined through mass loss for the probable AO fluence are provided in Table 3. Because the AO fluence for Bay 8 Regions 7, 8,

11 and 13 were not computed, Ey values were not determined for these regions. The Ey value of the HST SM4 Bay 8 nominal shiny FEP (Ey = 1.37×10^{-23} cm^3/atom) was found to be an order of magnitude greater than for the Bay 5 nominal shiny FEP (Ey = 1.43×10^{-24} cm^3/atom). This is attributed to the significantly higher dose of solar radiation, combined with the higher on-orbit temperature, for the solar facing blanket. These data provide evidence that solar exposure plays a significant role in the AO erosion of FEP.

Table 3 also provides the average Al-FEP thickness, Ey values calculated based on thickness loss and the ratio of thickness loss Ey to mass loss Ey. The two Ey methods gave consistent results, with thickness loss Ey ~16 % higher than mass loss Ey. The reason for this difference is not known.

The Ey values of the HST SM4 FEP were found to be orders of magnitude greater than those determined from shuttle flight experiments such as the Evaluation of Oxygen Interaction with Materials III, reported from 5.0×10^{-26} cm^3/atom [8] to 1.8×10^{-25} cm^3/atom [9], the Long Duration Exposure Facility, determined to be 3.37×10^{-25} cm^3/atom for ram facing surfaces [10] and Materials International Space Station Experiments 2 (MISSE 2), determined to be 2.00×10^{-25} cm^3/atom for ram facing surfaces [11]. Again, this is thought to be attributed to the effects caused by the significantly higher solar exposure of the HST materials.

5 Summary and Conclusions

Two MLI blankets retrieved from the HST during SM4 after 19.1 years in space have been analyzed for space-induced mechanical, optical and thermal properties. In addition, atomic oxygen Ey values were determined. The blankets experienced different solar exposures and thermal cycling temperature ranges, due to their positions on the telescope and each had regions with differing types of damage.

The mechanical properties of the blanket's Al-FEP outer-layers were extremely degraded. The Bay 8 Al-FEP, which had a significantly higher solar exposure and on-orbit thermal cycling temperature, was more embrittled than the solar-grazing Bay 5 insulation, and was found to fracture like thin brittle glass. Areas on Bay 8 which had been protected by a patch for a period of time on-orbit were slightly less embrittled than areas which had been exposed for all 19.1 years. However, even the least brittle samples still had only 3 % of the elongation at failure of pristine materials. Heating pristine Al-FEP marginally decreased its strength, and had no effect on elongation. The Bay 8 MLI was too embrittled to conduct studies to assess the effect of heating, but heating Bay 5 Region 1 material reduced both the elongation and strength of the samples. The results of these tests support the proposed model for on-orbit degradation of Al-FEP, in which radiation causes chain scission of the polymers, and thermal heating to high temperature extremes causes the Al-FEP to become much more embrittled.

All space exposed samples experienced an increase in solar absorptance, as compared to pristine Al-FEP, with the exception of Bay 8 Region 3, which is the

region where the Al has delaminated from the FEP. The greatest increase in absorptance occurred in the patched areas, likely due to contamination from the patches. The thermal emittance values were found to decrease for all samples except Bay 5 Region 1 and Bay 8 region 11, the region patched between SM2 and SM4.

The Ey value of the HST SM4 Bay 8 nominal shiny FEP (1.37×10^{-23} cm³/atom) was found to be an order of magnitude greater than for the Bay 5 nominal shiny FEP (1.43×10^{-24} cm³/atom). This is attributed to the significantly higher dose of solar radiation, combined with the higher on-orbit temperature, for the solar facing blanket. The silicone contamination on Bay 5 may have decreased the Ey somewhat, but further studies are needed to assess this. The Ey values of the HST SM4 FEP were found to be orders of magnitude greater than those determined from prior flight missions, such as shuttle experiments (0.5 to 1.8×10^{-25} cm³/atom), LDEF (3.37×10^{-25} cm³/atom) and MISSE 2 experiments (2.00×10^{-25} cm³/atom). These results support the belief that the effects of solar exposure play a significant role in the AO erosion of FEP.

References

1. Hansen PA, Townsend JA, Yoshikawa Y, Castro DJ, Triolo JJ, Peters WC (1998) Degradation of Hubble Space Telescope metallized Teflon® FEP Thermal Control Materials. SAMPE Int Symp 43:570
2. Townsend JA, Hansen PA, Dever JA, de Groh KK, Banks BA, Wang L, He C (1999) Hubble Space Telescope Metalized Teflon FEP Thermal Control Materials: On-Orbit Degradation and Post-Retrieval Analysis. High Perform Polym 11:81–99
3. Dever JA, de Groh KK, Banks BA, Townsend JA, Barth JL, Thomson S, Gregory T, Savage W (2000) Environmental Exposure Conditions for Teflon® Fluorinated Ethylene Propylene on the Hubble Space Telescope. High Perform Polym 12:125–139
4. American Society for Testing and Materials ASTM D 638-95 (1995) Standard test method for tensile properties of plastics. ASTM, West Conshohocken, PA
5. de Groh KK, Martin M (2004) Thermal Contributions to the Degradation of Ground Laboratory and Space-irradiated Teflon®. J Spacecraft Rockets 41(3):366–372
6. de Groh KK, Gaier JR, Hall RL, Espe MP, Cato DR, Sutter JK, Scheiman DA (2000) Insights into the Damage Mechanism of Teflon® FEP from the Hubble Space Telescope. High Perform Polym 12:83–104
7. de Groh KK, Finlay KA, Snyder A (2008) Degradation of Hubble Space Telescope Aluminized-Teflon Bi-Stem Thermal Shields. High Perform Polym 20:410–428
8. Koontz SL, Leger LJ, Visentine JT, Hunton DE, Cross JB, Hakes CL (1995) EOIM-III Mass Spectrometry and Polymer Chemistry: STS 46, July-August 1992. J Spacecraft Rockets 32(3):483–495

9. Rutledge SK, Banks BA, Cales M (1994) A comparison of atomic oxygen erosion yields of carbon and selected polymers exposed in ground based facilities and in low earth orbit, AIAA 94–2628; also NASA TM 1006622

10. Banks BA (1997) The Use of Fluoropolymers in Space Applications. In: Schiers J (ed) in Modern Fluoropolymers: High Performance Polymers for Diverse Applications. John Wiley & Sons, Ltd

11. de Groh KK, Banks BA, McCarthy CE, Rucker RN, Roberts LM, Berger LA (2008) MISSE 2 PEACE Polymers Atomic Oxygen Erosion Experiment on the International Space Station. High Perform Polym 20:388–409

Effect of Solar Exposure on the Atomic Oxygen Erosion of Hubble Space Telescope Aluminized-Teflon Thermal Shields

Aobo Guo, Claire C. Ashmead, Kim K. de Groh, and Edward A. Sechkar

Abstract When exposed to low Earth orbit (LEO) environment, external space-craft materials degrade due to radiation, thermal cycling, micrometeoroid and debris impacts, and interaction with atomic oxygen (AO). Collisions between AO and spacecraft can result in oxidation of external spacecraft surface materials, which can lead to erosion and severe structural and/or optical properties deterioration. It is therefore essential to understand the AO erosion yield (Ey), the volume loss per incident oxygen atom (cm^3/atom) of polymers to assure durability of spacecraft materials. The objective of this study was to determine whether solar radiation exposure can increase the rate of AO erosion of polymers in LEO. The material studied was a section of aluminized-Teflon® fluorinated ethylene propyl-ene (Al-FEP) thermal shield exposed to space on the Hubble Space Telescope (HST) for 8.25 years. Retrieved samples were sectioned from the circular thermal shield and exposed to ground laboratory thermal energy AO. The results indicate that the average Ey of the solar facing HST Al-FEP was 1.9×10^{-24} cm^3/atom, while the average Ey of the anti-solar HST Al-FEP was 1.5×10^{-24} cm^3/atom. The Ey of the pristine samples was 1.6 to 1.7×10^{-24} cm^3/atom. These results indicate that solar exposure affects the post-flight erosion rate of FEP in a plasma asher. Therefore, it likely affects the erosion rate while in LEO.

Keywords Hubble Space Telescope • Low Earth orbit • Teflon embrittlement

A. Guo • C.C. Ashmead
Hathaway Brown School, Shaker Heights, OH 44122, USA

K.K. de Groh (✉)
NASA Glenn Research Center, Cleveland, OH 44135, USA
e-mail: kim.k.degroh@nasa.gov

E.A. Sechkar
ASRC Aerospace Corp at NASA Glenn, Cleveland, OH 44135, USA

1   Introduction

When exposed to low Earth orbit (LEO), external spacecraft materials can degrade as a result of radiation, thermal cycling, micrometeoroid and debris impacts, and interaction with atomic oxygen (AO). AO is the most predominant chemical species in LEO, formed when ultraviolet (UV) radiation at wavelengths below 0.243 μm causes diatomic oxygen to photodissociate [1]. The average impact energy of AO at International Space Station (ISS) altitudes ($\approx$400 km above the Earth) and at spacecraft orbital speeds of $\approx$7.7 km/s is approximately 4.5 eV [2]. Collisions of spacecraft with the residual AO can result in oxidation of the external spacecraft surfaces. Oxidation of susceptible materials, such as polymers, can result in fragmentation of the polymer chains and formation of volatile material, causing erosion and resulting in severe structural and/or optical properties deterioration. Atomic oxygen erosion of polymeric components, such as thermal control films and solar array blankets, can be a serious threat to spacecraft performance and durability. It is, therefore, essential to understand the AO erosion yield (Ey), the volume loss per incident oxygen atom (cm^3/atom) of polymers to have knowledge of materials durability relevant to spacecraft applications [2]. Aside from AO, UV radiation can also cause significant alteration to polymeric surfaces, posing additional problems for spacecraft. Absorption of a photon of UV radiation by an organic molecule raises the molecule to an excited state, potentially stimulating bond dissociation and formation of free radicals that can cause further scission and crosslinking [3]. Because the solar facing sides of the thermal shields are hotter than the anti-solar sides, there can be increased mobility of the free radicals allowing them to react more readily thus causing more polymer chain damage that probably manifests itself as a reduction in elongation to failure. If sufficient ultraviolet radiation fluence is accumulated, the degradation could end up causing the chopped polymer segments to be small enough to evaporate thus impacting optical and emittance properties. It can also cause degradation of mechanical properties, discoloration, and altered electrical properties [4]. Other forms of solar exposure, such as charged particle radiation, x-rays from solar flares, and heating and thermal cycling, are additional environmental threats that can degrade spacecraft materials. The issue of whether solar radiation can increase the rate of AO erosion, hence the AO erosion yield, is of debate in the space community. This research addresses the AO erosion of a commonly used spacecraft thermal control material, aluminized-Teflon fluorinated ethylene propylene (Al-FEP), specifically whether solar radiation exposure increases the rate of AO erosion. This study is unique in that it utilizes Al-FEP that has been exposed to the space environment for 8.25 years on the Hubble Space Telescope, material that was then retrieved by astronauts during a servicing mission and brought back to Earth.

Shortly after the Hubble Space Telescope (HST) was deployed into LEO on April 25, 1990, the metal bi-stem booms supporting the solar arrays (SA-I) were discovered to be rapidly contracting and expanding as the telescope orbited in and out of the Earth's shadow, causing a thermal-induced jitter [5]. In response to this problem, the European Space Agency (ESA) built new HST solar arrays (SA-II) with bi-stem
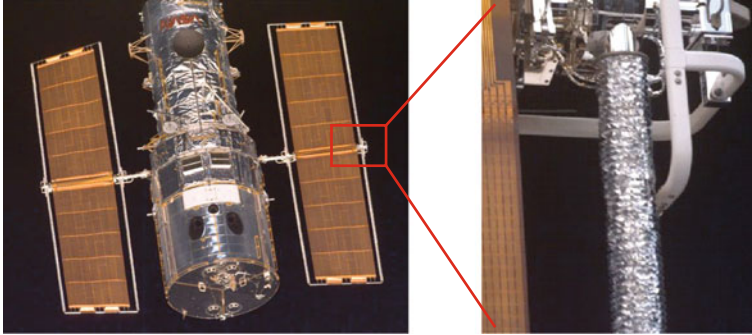
Fig. 1 Hubble Space Telescope with SA-II photographed in March 2002 during SM3B with a close-up photograph of a section of BSTS [5]

thermal shields (BSTS) comprised of 2 mil (0.051 mm) Al-FEP rings fused together into circular bellows shape (with the FEP layer facing space) for thermal insulation [5]. Astronauts replaced the original arrays with the BSTS containing arrays during servicing mission 1 (SM1) in December 1991. Figure 1 shows the HST with SA-II and a close-up image of a section of BSTS. During the fourth servicing mission (SM3B) in March 2002 after experiencing 8.25 years of space exposure the SA-II were replaced with a third set of arrays (SA-III) and the SA-II was brought back to Earth. ESA provided a section of retrieved BSTS to NASA Glenn Research Center so that environmental durability studies of the Al-FEP could be conducted.

Because the thermal shields were wrapped around the solar array bi-stems and hence had solar, anti-solar, and solar-grazing surfaces, the objective of this experiment was to characterize the AO Ey of retrieved HST BSTS Al-FEP with respect to solar angle to see if the Ey varied with solar exposure. The solar-facing surfaces were found to be extremely embrittled with through-thickness cracks, while the anti-solar-facing side was very ductile, like pristine material [5]. It was therefore theorized that solar-facing Al-FEP would have a greater erosion yield, due to additional damage to the material induced from the solar radiation and/or heating caused by solar exposure. For this study 24 samples were sectioned from a single weld of the retrieved HST BSTS Al-FEP, and Ey values versus solar angle were determined using a RF plasma asher.

2 Materials and Experimental Procedures

2.1 Materials

The BSTS consisted of welded-together FEP rings whose backsides were coated with approximately 1,000-Å thick vapor-deposited aluminum and whose inner and

outer diameters (when laid flat) were 6 cm and 10 cm, respectively. Using an X-acto knife, the ESA-supplied 20 weld section was separated into 20 welds (Welds 1–20) by cutting through the inner fused region. Each weld consisted of two pieces of Al-FEP seamed at the top; these were then separated and consistently labeled either side A or side B. Both sides of Weld 15 were used for conducting this study (Side B in Test 1 and Side A in Test 2, as indicated in the Experimental Procedures section below).

For the purposes of this experiment, the direct solar-facing surface is defined as being 0° and the anti-solar-facing surface as 180°, with solar-grazing surfaces as 90° and 270°. Researchers who examined the retrieved solar array and sectioned the BSTS 20-weld section stated that the most damaged (cracked) region of the BSTS was solar-facing on-orbit (Van Eesbeek M (2004) personal communication, ESA). However, the exact position and thus the specific angle of the BSTS sample that was directly solar-facing was not known. Therefore, the 0° position was chosen to be the center of the most obviously damaged region. Pristine Al-FEP samples (2 mil thick) obtained from Sheldahl and pristine BSTS samples fabricated at the same time as the HST BSTS for pre-flight environmental durability testing [6] were also tested to provide control Ey values. Kapton H was used as an exposure reference because of its well-characterized in-space erosion yield (3.0×10^{-24} cm^3/atom) [7].

2.2   Space Environmental Exposure

The estimated environmental exposure conditions for the SA-II BSTS Al-FEP, installed during SM1 and retrieved during SM3B, are given in Table 1 [5]. Details on the computation of number of thermal cycles, equivalent sun hours (ESH), albedo solar exposure, x-ray fluence, electron and proton fluence, AO ram fluence, and thermal modeling are described by de Groh et al. [5]. The ESH, X-ray fluence and AO fluence were adjusted for weld geometry with surfaces 23.5° from sun incidence [5].

AO ram fluences were modeled based on the Mass Spectrometer Incoherent Scatter Model 86 (MSIS-86) [8]. The AO fluences for solar-facing and anti-solar facing surfaces were determined by multiplying the ram fluence by 0.2528 and 0.3167, respectively [9], and then were further adjusted by a factor of 0.399 (cosine 66.5°) from the ram fluence value due to the weld geometry [5].

3   Experimental Procedures

3.1   Samples

For Test 1, sixteen samples were sectioned from HST BSTS Weld 15 Side B at approximately every 20–30°. Eight samples (mostly solar grazing and anti-solar)

Table 1 Environmental exposure conditions for HST BSTS surfaces

Exposure		SM1 to SM3B (SA-II)
Shuttle missions		STS-61 and STS-109
Mission dates		Dec. 1993 and March 2002
Exposure duration (years)		8.25
Thermal cycles (#)		45,100
Temperature range (°C)		Anti-solar: -140 and solar: $+43$
ESH, solar-facing: direct/Albedo/total		~19,600/~500/~20,000
ESH, anti-solar (albedo only)		~6,200
X-ray fluence: 1–8 Å/0.5–4 Å (J/m^2)		63.8/4
Electron fluence (#/cm^2), >40 keV		2.08×10^{13}
Proton fluence (#/cm^2), >40 keV		2.55×10^{10}
AO fluence (atoms/cm^2)	Ram	1.2×10^{21}
	Solar	1.2×10^{20}
	Anti-solar	1.5×10^{20}
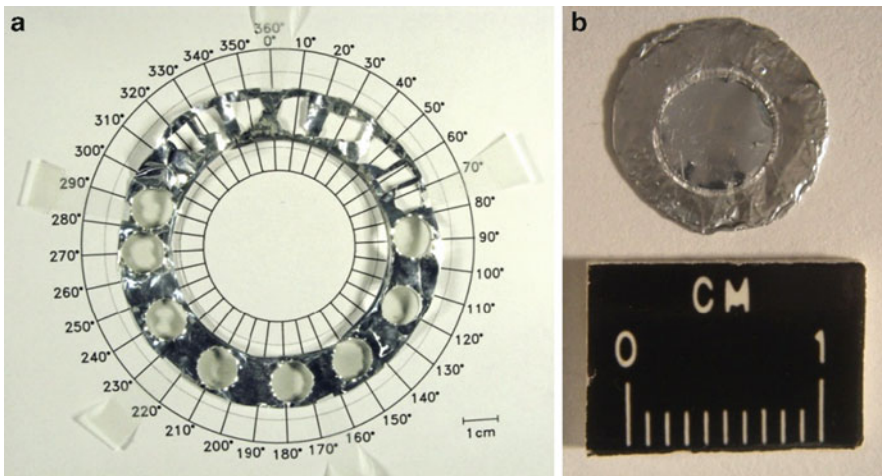
Fig. 2 (**a**) Weld 15 side B after sectioning of 16 test samples at specified angles, and (**b**) an irregularly shaped sample from Weld 15 side A in its Al holder

were sectioned using a 1.1 cm diameter circular punch. Eight solar-facing samples were cut by hand using an X-acto knife to avoid cracks. Figure 2a shows the location where each of the samples was sectioned from Weld 15 Side B. Samples were then exposed to thermal energy AO in a Structure Probe, Inc. Plasma Prep II asher for Ey determination versus on-orbit solar angle. Multiple exposure tests were conducted to evaluate effects of Ey versus AO fluence. Seven of the irregularly shaped hand-cut samples were fragile and so were placed in small aluminum holders with circular apertures to provide support during handling and exposure, as well as to provide smaller exposure windows to AO than the sample holder (described below) provides, shown in Fig. 2b below. The individual aluminum

holders created to mount the irregularly shaped samples were exposed to AO prior to use to remove any organic coating that could contaminate the samples and contribute to erroneous results pertaining to mass loss.

For Test 2, eight samples were sectioned from the solar side of Weld 15 Side A. Five of the samples were obtained using a 1.1 cm diameter circular punch and three of the samples were cut by hand using an X-acto knife. Once again, the three irregularly shaped samples were placed in pre-AO exposed individual aluminum holders. Samples in the individual Al holders in both tests were left in the holders during the entire test duration and were weighed while in the holders. Three 1.1 cm-diameter pristine BSTS samples, three 1.1 cm diameter pristine Al-FEP samples, and two 2.54 cm diameter Kapton H samples were also sectioned using circular punches. Samples obtained between 270° clockwise to 90° are considered "solar-facing" samples while those obtained between 90° clockwise to 270° are termed "anti-solar," corresponding with the Sample Angle Template shown in Fig. 2a. Samples at 90° and 270° are referred to as "solar-grazing". It should be noted that the angles of samples sectioned from Side A match those of the Side B samples, since samples at a particular angle (such as 60°) were facing the same direction on the telescope.

3.2 Mass Measurements

The erosion yield values obtained for this experiment were determined based on mass loss. Due to the hygroscopic nature of Kapton H polyimide, all Kapton H samples were either dehydrated for at least 48 h prior to measuring their masses (as in the case of the Kapton flux test) or prioritized to be immediately weighed once taken out of the asher (as in the case of the Kapton witness sample in each test exposure).

A test was conducted to compare the dehydrated weight of Al-FEP to non-dehydrated weight. Al-FEP sample weights were found to not vary significantly when dehydrated, therefore the Al-FEP samples were not dehydrated prior to sample weighing. All sample weights were obtained using a Mettler Balance with a sensitivity of ± 1 µg.

3.3 Ground-Laboratory RF Plasma Asher Exposure

The samples were exposed to AO in a Structure Probe, Inc. Plasma Prep II asher, which generates a plasma by exciting the ambient air with 100 W of continuous RF power at 13.56 MHz. The operation pressure was between 0.5 and 1.0×10^2 mTorr. The samples were exposed to AO while being held in a metal sample holder with a large central opening for a Kapton fluence witness sample (2.54 cm diameter) and with 22 smaller sample openings (1.1 cm diameter). Figure 3 shows the sample holder loaded with Kapton samples for a flux test (described below) along with sample position descriptions noted (A-Y).
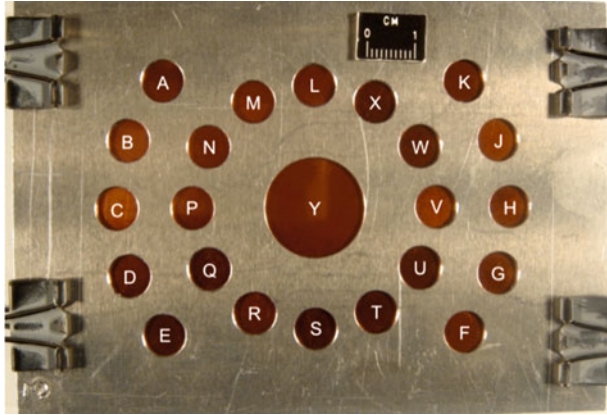
Fig. 3 Sample holder with 23 Kapton H samples and position identifications

Each test included six individual AO exposures, so that the effect of fluence on Ey could be determined. The same sample was always placed in the same position for each incremental exposure. Aside from protecting the edges and backs of the samples from the AO plasma and keeping the samples from curling during exposure, the holder also provided a well-defined exposure area necessary for further calculations. The holder was always placed in the same position in the asher in an effort to ensure the same flux (f, atoms/(cm²s)) for each sample position.

The 2.54 cm diameter Kapton H fluence witness sample was placed in position Y in the metal holder for every test in order to determine the AO effective fluence (F, atoms/cm²). The fluence of each sample in every exposure needed to be calculated to compute erosion yield, and finding individual sample fluences is discussed in the Flux Tests section below. As stated previously, Kapton H is used as a fluence reference because of its well-characterized in-space erosion yield in LEO. The equation to compute the exposure fluence in the asher is provided in (1).

$$F = \frac{\Delta M_K}{A_K \rho_K E_K} \tag{1}$$

where

F = *plasma asher effective AO fluence (atoms/cm²)*
ΔM_K = *mass loss of Kapton H witness sample (g)*
A_K = *exposed surface area of Kapton H witness sample (cm²)*
ρ_K = *density of Kapton H (1.4273 g/cm³)* [5]
E_K = *erosion yield of Kapton H (3.00 × 10⁻²⁴ cm³/atom)* [7]

As mentioned, two tests were conducted, each with samples from a different Weld Side: Test 1 included Side B samples and Test 2 included Side A samples. For each test, the samples were exposed to six different individual AO exposures and

their Ey were determined. Exposures 1 and 2 were 3.5 h each, exposure 3 was 7 h, exposure 4 was 14 h, and exposures 5 and 6 were 28 h each, for a total exposure of 84 h per test. The fluence values of Test 1 ranged from $\approx 1.5 \times 10^{19}$ atoms/cm^2 for Exposure 1 to a cumulative fluence of $\approx 1.3 \times 10^{21}$ atoms/cm^2 (depending on position). The fluence values of Test 2 ranged from $\approx 1.9 \times 10^{19}$ atoms/cm^2 for Exposure 1 to a cumulative fluence of $\approx 1.4 \times 10^{21}$ atoms/cm^2.

3.4　Flux Tests

The AO fluence of the individual test samples was calculated because flux can vary with position in the asher. A Kapton H flux test was conducted to determine the effective flux of each of the 23 positions, with a Kapton H witness sample in each position of the sample holder. Since the fluence of a Kapton H sample can be determined using (1), and because flux is simply fluence divided by time in seconds, the effective flux for each position was determined based on mass loss of each individual Kapton H sample. Twenty-two k constants, one corresponding to each of the 22 positions in the holder, were then calculated, compensating for the position-based flux variation relative to the central 2.54 cm diameter Kapton H witness sample ($k = 1$). The k constants were then used to calculate the precise flux and fluence each sample was exposed to in every test. The k constants were based on the positional flux relative to the Kapton H sample flux in position Y, as shown in (2):

$$f_n = k_n \times f_k \qquad (2)$$

where

f_n = flux of the sample in position n (atoms/cm^{2}s)
n = sample holder position
k_n = constant, a fraction of the fluence of a sample in position n relative to the
　　fluence of the Kapton H in position Y (k_n = 1 for Kapton H)
f_k = flux of Kapton H witness sample

Two separate flux tests were conducted and the resulting k values for each sample position were averaged. In order to calculate the fluence each sample was exposed to during each individual test, the effective fluence was determined for the Kapton H witness sample in position Y and then multiplied by the average k factor for each position to obtain the fluence for each sample position.

3.5　Exposure Area Measurements

The exposure area of each sample opening in the metal holder was calculated by taking diameter measurements in three orientations using Fowler & NSK Max-Cal

Fig. 4 Photograph of HST-BSTS 30° sample (position N) prior to the first exposure showing the AutoCAD trace line used for surface area calculation
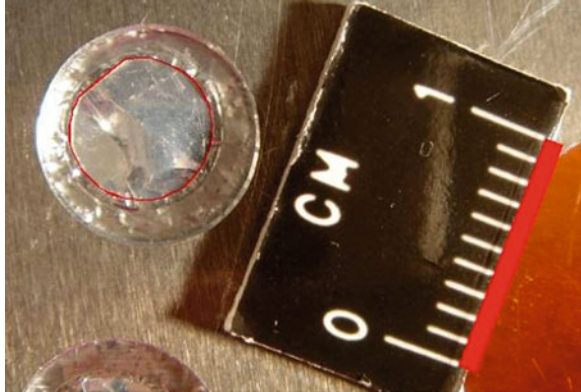
electronic digital calipers and averaging the values. For the irregularly shaped samples, the exposed surface area was found by tracing the exposed perimeter of the samples (from photographs of the samples taken with a scale bar) using AutoCAD, a computer aided design software program. An example of this technique can be seen in Fig. 4, where the perimeter of the surface area is outlined in red.

3.6 Erosion Yield Calculation

Once mass loss, fluence, density, and exposure area values were obtained, the erosion yield (E_y) was calculated using (3):

$$E_y = \frac{\Delta M_S}{(A_S \rho_S F)} \tag{3}$$

where

$\Delta M_S = $ mass loss of sample (g)
$A_S = $ exposed surface area of sample exposed to atomic oxygen (cm^2)
$\rho_S = $ density of sample (g/cm^3)
$F = $ plasma asher Kapton H effective AO fluence ($atoms/cm^2$)

3.7 Photo-Documentation

Close-up photographs were taken of the irregularly shaped samples before and after each exposure using a Canon digital camera mounted on a Landcamera stand so that surface area measurements could be obtained using AutoCAD.

4 Results and Discussion

The solar-facing side of the BSTS was found to be extremely embrittled with numerous through-thickness cracks and pieces of insulation material missing in some places. Visually, the anti-solar side of Weld 15 did not appear to be degraded. These observations are consistent with mechanical property degradation studies conducted by de Groh et al. [5] on other Welds from the 20-Weld section provided by ESA.

4.1 Material Degradation

Figure 5a, b provide photographs of solar facing HST BSTS sample 299° (position M) from Test 2 wrapped in its Al holder in the sample holder prior to AO exposure and after the fifth AO exposure, respectively. This sample provides an example of a sample that was excessively degraded after the fifth exposure. The pre-exposure surface area was 0.153 cm^2, while the surface area after Exposure 5 was 0.141 cm^2. The blue ovals in the images highlight a distinguishing feature in the small Al holder, while the excess erosion can be seen in Fig. 5b in the upper left section of the sample where a piece of material is missing.

   Although both the pristine samples (pristine Al-FEP and pristine BSTS) and the anti-solar-facing samples became hazy-white with AO exposure, none of these samples were found to be excessively degraded after the full AO exposure. Some of the solar-facing samples that were excessively eroded, such as HST BSTS sample 10°, appear to have warped and/or curled during exposure.

   This warping would lead to the post-exposure photographs misrepresenting their surface area, resulting in their true surface areas differing from the ones computed. As this would introduce error into the Ey values, it was concluded that the cumulative Ey values should not include these higher fluence exposures.

4.2 Fluence and Erosion Yield Values

Seven of the samples in Test 1 were found to be excessively degraded after the sixth exposure and three of the samples in Test 2 were found to be excessively degraded after the fifth exposure. Therefore the cumulative Ey for the Test 1 samples are based on data from Exposures 1–5, and the cumulative Ey for the Test 2 samples are based on data from Exposures 1–4. It should be noted that in a couple of the individual exposures, there were a few surprisingly low mass loss values. In these situations (BSTS sample 65° in Test 1, BSTS sample 299° in Test 2, and Pristine Al-FEP [Position C in Test 1]) the fluences for those individual test exposures were not included when computing the cumulative Ey values. The Polar Plot shown in
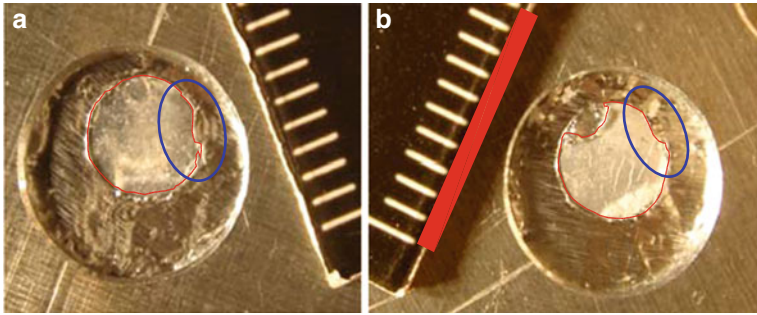
Fig. 5 HST BSTS sample 299° (position M) from Test 2 in small Al holder in sample holder: (**a**) prior to AO exposure, and (**b**) after the fifth AO exposure
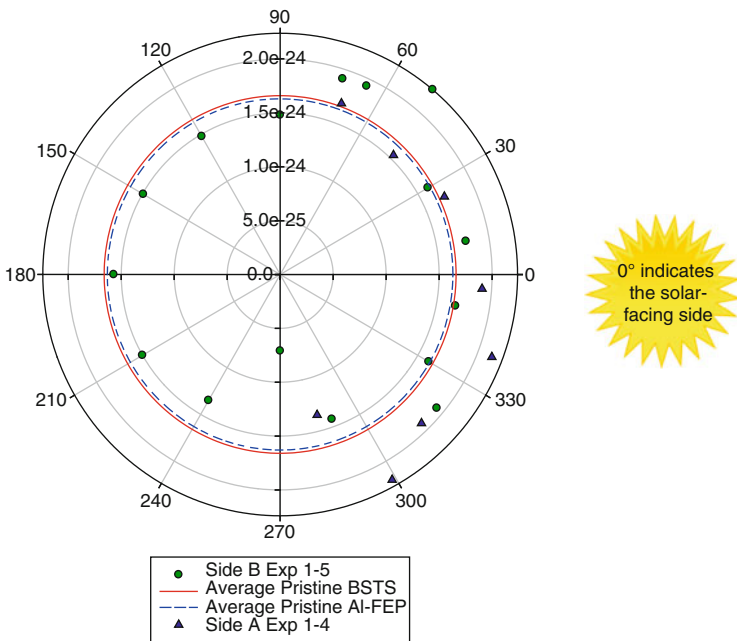
Fig. 6 Polar Plot of E_y versus solar angle for pristine and HST BSTS samples

Fig. 6 shows E_y versus solar angle for the HST BSTS samples, along with average E_y values for the pristine Al-FEP samples and pristine HST BSTS samples (represented as dashed and solid lines, respectively).

As can be seen in Fig. 6, the asher E_y values of the anti-solar samples are slightly lower (average E_y of 1.48×10^{-24} cm^3/atom) than the average E_y values for the pristine BSTS and pristine Al-FEP, which were found to be 1.66×10^{-24} cm^3/atom and 1.63×10^{-24} cm^3/atom, respectively. Although there is a fair amount of scatter in the E_y of the solar-facing samples, the majority of solar-facing E_y values are
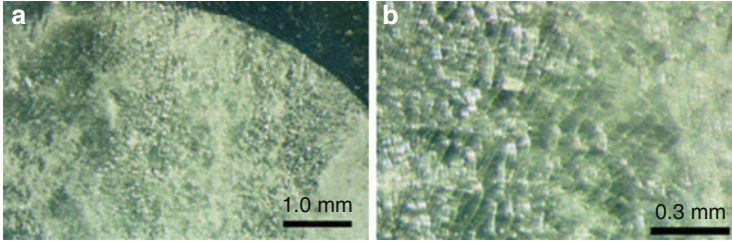
Fig. 7 Solar-grazing Sample 270°: (**a**) both the exposed and protected (*upper right*) areas of the sample can be seen, and (**b**) close-up showing the crazed surface

higher than those for the anti-solar or pristine samples. The average Ey for side B of the solar facing HST BSTS sample was calculated as 1.79×10^{-24} cm^3/atom, and side A was 1.94×10^{-24} cm^3/atom. The average Ey for the solar facing HST BSTS sample was computed to be 1.86×10^{-24} cm^3/atom, and the anti-solar side was calculated as 1.48×10^{-24} cm^3/atom (Test 1 exposures 1–5 and Test 2 exposures 1–4). There was a 26 % difference between HST BSTS Average Solar and Average Anti-Solar Ey.

Another observation that can be made from Fig. 6 is that the Ey of samples centered around the 270° solar-grazing angle (samples 270°, 290°, 285° and 240°) are lower than all the other Ey values. This is particularly true for the HST BSTS 270° sample, which had an Ey of only 7.10×10^{-25} cm^3/atom, only half the Ey of the HST BSTS solar-grazing sample 90° of 1.48×10^{-24} cm^3/atom. After examining the HST BSTS 270° sample under the microscope, it was observed that this sample has a patchy appearance and contains some crazed areas, as shown in Fig. 7. Therefore, it appears that this sample may contain a layer of contamination. The orientation of the sample was such that silicone contamination from the silicone on the anti-solar side of the array could be possible.

In a study by de Groh [5] pristine, solar-facing, anti-solar-facing and solar-grazing BSTS samples were examined with scanning electron microscopy for surface morphology and with energy dispersive spectroscopy (EDS) for surface chemistry. The pristine, solar-facing and anti-solar-facing surfaces did not have any evidence of contamination, with only C and F peaks observed [5]. However, a crazed surface texture was observed on one of the solar-grazing samples [5]. The EDS data indicate the crazed texture is due to silicone contamination [5]. The back surfaces of the solar arrays were coated with DC 93–500 silicone, so it appears that the solar-grazing surface facing the array received silicone contamination from the solar arrays, which impacted the asher Ey values in this test. If the anti-solar samples also received very small amounts of contamination on-orbit (perhaps below the detection limit of EDS), this would explain the slightly lower Ey values of the anti-solar samples compared with those of the pristine samples.

It should be noted that the erosion yield of Teflon FEP in a plasma asher can be substantially higher than the erosion yield in LEO. For example, the erosion yield of FEP determined after 4 years of space exposure on the ISS as part of the Materials

International Space Station Experiment 2 (MISSE 2) was found to be 2.00×10^{-25} cm^3/atom [10], which is an order of magnitude lower than the Ey determined in this study using a plasma asher. It should also be noted that de Groh et al. [11] have shown a correlation of increased erosion yield with increased ESH for Teflon FEP from numerous spaceflight experiments [11].

In summary, the average Ey values of the solar-facing HST BSTS samples were found to be 26 % higher than the Ey of the anti-solar-facing samples, and 12–15 % higher than pristine BSTS or Al-FEP samples, respectively. These results indicate that solar exposure affects the post-flight erosion rate of FEP in a plasma asher. Therefore, it likely affects the erosion rate while in LEO. It is important that spacecraft engineers consider the enhanced erosion of Teflon FEP on solar-facing surfaces when designing durable spacecraft components.

5 Summary

To determine whether solar exposure affects the rate of atomic oxygen erosion of Al-FEP, a very commonly used spacecraft thermal control material, ground-laboratory AO experiments have been performed on space exposed FEP. The material studied was a section of Al-FEP thermal shield exposed to space on the HST for 8.25 years. In these investigations, samples were sectioned from the circular thermal shield and exposed to AO in an air-operated radio-frequency plasma asher for Ey determination versus on-orbit solar angle. The Ey values of 24 HST BSTS samples were determined in a series of two separate tests, with the Ey values compared relative to Kapton H in an asher. Along with pristine BSTS and Al-FEP samples, the Ey values of the HST samples were determined for six different exposure tests. Cumulative Ey were calculated, though, because error had to be taken into account; the most accurate data excluded the last exposure for Test 1 and the last two exposures for Test 2. The average Ey of the solar facing HST Al-FEP was found to be 1.9×10^{-24} cm^3/atom, while the average Ey of the anti-solar HST Al-FEP was 1.5×10^{-24} cm^3/atom. The Ey of the pristine samples was 1.6 to 1.7×10^{-24} cm^3/atom. These results indicate that radiation and solar exposure affects the post-flight erosion rate of FEP in a plasma asher. Therefore, it likely affects the erosion rate while in LEO.

In addition, it was determined that one of the solar-grazing surfaces (270°) was contaminated on-orbit with silicone contamination, likely the surface facing the solar arrays, which impacted the erosion yield of samples in that orientation. Last, the erosion yield versus fluence comparisons show that the rate of erosion of all samples is greater at the surface of the sample, and that solar-facing samples in particular have higher rates of erosion than other samples for fluences below $\approx 5.0 \times 10^{20}$ atoms/cm^2. By using this fluence and the solar facing erosion yield determined in this study, it appears that solar radiation reacted with the FEP to a depth of ≈ 9 μm.

References

1. Dickerson RE, Gray HB, Haight GP (1979) Chemical principles, 3rd edn. Benjamin Cummings, Menlo Park, p 457
2. Banks BA, Miller SK, de Groh KK (2004) Low earth orbital atomic oxygen Interactions with materials. AIAA-2004-5638; also NASA/TM-2004-213223
3. Dever JA (1991) Low earth orbital atomic oxygen and ultraviolet radiation effects on polymers. NASA technical memorandum-103711
4. Dever JA, Banks BA, de Groh KK, Miller SK (2005) Degradation of spacecraft materials. In: Myer K (ed) Handbook of environmental degradation of materials. William Andrew, Norwich, pp 465–501
5. de Groh KK, Finlay KA, Snyder A (2008) Degradation of hubble space telescope aluminized-teflon bi-stem thermal shields. High Perform Polym 20:410–428
6. Dever JA, de Groh KK (2002) Vacuum ultraviolet radiation and atomic oxygen durability evaluation of HST Bi-Stem thermal shield materials. NASA TM-2002-211364
7. Banks BA (1997) The use of fluoropolymers in space applications, Ch. 4. In: Modern fluoropolymers: high performance polymers for diverse applications. Wiley, Chichester
8. Hedin AE (1987) MSIS-86 thermospheric model. J Geophys Res 92:4649–4662
9. Rockwell International Corporation (1990) Rocketdyne Division, Seal Beach, CA, USA, Specification RC 1800 review C, p18
10. de Groh KK, Banks BA, McCarthy CE, Rucker RN, Roberts LM, Berger LA (2008) MISSE 2 PEACE Polymers Atomic Oxygen Erosion Experiment on the International Space Station. High Perform Polym 20:388–409
11. de Groh KK, Banks BA, Guo A, Ashmead CC, Mitchell GG, Yi GT (2010) MISSE 6 polymers atomic oxygen erosion data. Presented at the 2010 NSMM, Scottsdale, 28 Jun–1 Jul 2010

Post-flight Analysis of Materials Exposed on the Spectrometer Sub-unit of MEDET (18 Months On-Board ISS)

Virginie Rejsek-Riba, Sabine Soonckindt, Sophie Duzellier, S. Remaury, C. Durin, J.M. Desmarres, A. Tighe, M. Van Eesbeek, C. Lobascio, and M. Nebiolo

Abstract A variety of materials were exposed to the Low Earth Orbit (LEO) environment, mainly Ultraviolet Radiation and Atomic Oxygen, through The Material Exposure and Degradation Experiment (MEDET). The degradations of polymeric films with and without atomic oxygen protection coating, quartz with and without thermal control coating, and solar cell cover glass adhesives, were studied in flight and post-flight. Yellowing for AO protected polymeric films and silicone resins due to UV exposure and the decrease of thicknesses for other samples like polymeric films due to AO erosion have been highlighted. Thermo-optical properties have been determined and the surface morphology classified as cone-like due to surface erosion or containing microcracks in silicone layers.

Keywords Low Earth Orbit • Ultraviolet • Atomic oxygen • Thermo-optical degradation • Material degradations

V. Rejsek-Riba (✉) • S. Soonckindt • S. Duzellier
ONERA – The French Aerospace Lab, 2 Av. Belin, Toulouse F-31055, France
e-mail: virginie.rejsek-riba@onera.fr

S. Remaury • C. Durin • J.M. Desmarres
CNES, 18 Av. Belin, Toulouse F-31401, France

A. Tighe • M. Van Eesbeek
ESA-ESTEC, Keplerlaan 1, Noordwijk NL-2200, AG, Netherlands

C. Lobascio • M. Nebiolo
Thales Alenia Space Italia SpA, Strada Antica di Collegno 253, Torino I-10146, Italy

1   Introduction

The Material Exposure and Degradation ExperimenT (MEDET) is an active experiment that was exposed to the Low Earth Orbit (LEO) environment for 18 months on board ISS/Columbus, from February 2008 to September 2009. It combines seven sub-experiments devoted to the measure of the radiative space environment mainly Ultraviolet (UV) and Atomic Oxygen (AO) and its associated effects on materials. Therefore, it allows for real time characterization of the ISS local environment and materials degradation.

MEDET experiments are mostly oriented in RAM on the ISS orbit (91% of mission time in RAM). The Spectrometer sub-unit of MEDET surveys the optical properties of 20 different materials candidates used for space applications. Samples included different polymeric films with and without atomic oxygen protection coating, quartz with and without thermal control coating, and solar cell cover glass adhesives. The Spectrometer experiments collected data on UV-Visible (UV-V) and Visible-Near Infrared (V-NIR) transmission spectra.

Our previous work [1, 2] focused on the flight results of Spectrometer from preliminary analysis and qualitative observation of the degradation modes expected for such a mission namely: yellowing for AO protected polymeric films and silicone resins due to UV exposure and the decrease of thicknesses for other samples like polymeric films due to AO erosion.

This paper reports on the post-flight characterizations of the Spectrometer samples and physico-chemical data. The correlation with the degradation phenomena is discussed.

2   Experimental Procedure

2.1   *Spectrometer*

The optical spectral transmission of the samples are measured by a system composed of quartz optical fibers, two miniature spectrometer modules (200–1,000 nm) and illumination sensors (IS) (Fig. 1, left). The materials samples are placed on a rotating wheel, containing 24 positions and the sun is used as the light source for the spectra acquisition (Fig. 1, right) [2].

The measurements are allowed when the light is detected by the IS within a $\pm 40°$ acceptance angle considering a threshold value. Sun light passing through the sample is collected by a quartz diffuser. Halves of the collected light are transmitted to an UV-Visible (200–700 nm) and Visible-near IR (V-NIR) spectrometers (400–1,000 nm).

Each of these miniature spectrometer modules (standard laboratory Zeiss MMS devices) consists of a grating, optics and a charge-coupled device (CCD) detector. To ensure redundancy, two sets UV-V and V-NIR spectrometers are used, and both are operated simultaneously allowing each sample to be measured twice at each wheel rotation.
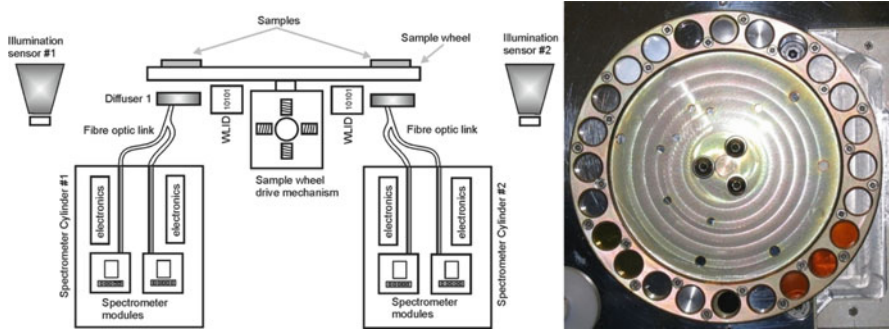
Fig. 1 Schematic of the spectrometer sub-unit (*left*), flight wheel with samples (*right*)

2.2 Flight Samples

Table 1 lists the flight samples that included different polymeric films, quartz, thermal control coatings and cover glass adhesives.

Polyimide films studied, Kapton® HN (75 µm), Upilex® 25 S (25 µm) and Upilex® 75RN (75 µm), are considered as reference materials for this orbit.

Mapatox K and 41B are atomic oxygen resistant coatings based on polysiloxane. They are deposited on Kapton® HN, samples represent respectively a thickness of 95 and 120 µm for Mapatox K and 41B. Preliminary AO ground data [3] have shown that Mapatox K is resistant to UV and AO degradation and hence potentially the best protective coating for Kapton.

Thermal control coatings are deposited on suprasil (2 mm). The FSR1 and 2 are the same materials but from two different lots. The FSRC is identical to FSR but coated with a transparent and conductive layer. The RSR is similar to FSR with a different percentage of long chains of polydimethylsiloxane.

KF01C01 is a multi-layered polymeric film with the following composition: Polyethylene – Polyolefin adhesive with flame retardant – Polyamide – EVOH – Polyamide – Polyolefin adhesive with flame retardant – Polyethylene (nearly same composition for Covex).

VLM3301 is a co-extruded Polyurethane and Polyester film. Both having a thickness of 120 µm, they have been developed for use by the packaging industry, with potential application as bladder for space inflatable systems, due to their low permeability features. Because of their known inability to withstand direct space exposure, their application is typically under protective layers of other materials, such as beta cloth and Kevlar.

The PEN sample (Polyethylene Naphtalate) is 2 µm thick and therefore mounted between two PGO (synthetic quartz glass).

2.3 Mission Environment and Parameters

During the mission, spectra for each material were acquired once or twice per day (triggered by an illumination threshold) from initiation of the mission i.e. for

Table 1 List of materials for flight samples

Flexible and rigid thermal control coatings	Flexible solar reflector (FSR), rigid solar reflector (RSR)
Reference for coatings	Suprasil, PGO
Cover glass adhesives	RTV-S690 and S695, DC-93500
Thermal control foils	Kapton® HN, Upilex® 25 S, Upilex® 75RN
AO protection coatings	Kapton® HN + Mapatox K or 41B
(Multilayer) polymeric films (inflatable structures)	KF01C01, VLM3301, Covex, PEN

18 months in LEO exposure, except for some small data gaps due to power outages at MEDET/EUTEF levels.

Atomic oxygen fluence has been measured on-board MEDET with carbon coated Quartz Crystal Micro-balances (QCM) sensors [4] and estimated as $3.11*10^{21}$ atom/cm^2 for the entire mission (RAM AO-facing tray for 18 months). This figure is consistent with ONERA calculation ($2.29*10^{21}$ atom/cm^2 [5]).

Table 2 summarizes all environmental parameters of the mission.

3   Post-Flight Analysis of Samples

3.1   *Measurements and characterization techniques*

A large set of measurements have been performed after return of the experiment. The analysis campaign is still on-going therefore, in this paper, only part of the data is presented.

Firstly, the samples have been submitted to visual inspection (optical microscopy). The mass and thermo-optical properties (reflectance and transmission spectra) have been measured as well.

The UV-Vis-IR measurement system of ONERA is composed of a Perkin Elmer Lambda 900 spectrophotometer connected to a specular transmission accessory and an integrating sphere in air. The calibration was performed using a Spectralon SRS-99-010 standard. The transmission spectra in the range 250–2,500 nm were acquired at intervals of 1 nm, with the lamp change at 319.2 nm.

The FT-IR measurement system is composed of a Bruker Nicolet 800 FTIR spectrophotometer connected to an integrating gold sphere. All measurements were performed in air. Transmission and reflectance spectra in the range 3–20 µm are performed with a central sample holder. FT-IR-ATR measurements were performed with the same Bruker spectrophotometer to an ATR (Attenuated Total Reflectance) accessory equipped with a reflection diamond cell. Using the FT-IR-ATR cell very thin samples can be evaluated because the penetration depth of the evanescent wave is typically ~1.0 µm.

A number of other parameters were also measured at CNES, including thickness (by mechanical probe), surface roughness (by profilometry) and other surface

Table 2 Mission parameters

Duration (h)	10,272
Thermal cycles	6,800
Pressure	$5*10^{-6}$ to 10^{-7} mbar
RAM position	91 % of the whole mission
Illumination (ESH)	3,800
AO fluence (atom/cm^2)	Kapton erosion: $1.71*10^{21}$ QCM carbon : $3.11*10^{21}$
	Calculation: $2.29*10^{21}$

features using standard laboratory equipment like SEM, AFM, confocal imaging/spectral interferometry (Fogale ZoomSurf 3D).

A Sartorius ME36S balance with an accuracy of $1*10^{-6}$ g has been used for weight measurements.

3.2 Polymeric films

The Kapton® HN material is widely used as a reference sample for estimating AO fluence or degradation. For this sample, the main degradation expected is a decrease of the thickness and the presence of rough eroded surface characterized by a cone-like morphology as demonstrated by K. de Groh for MISSE2 samples [6] and many other researchers.

The change in the feature of the UV-Visible spectra during the flight with a shift of the UV cut off towards smaller wavelengths and an increase of the overall transmission intensity confirmed the loss of thickness [2]. The ground analysis also confirmed the expected degradation mechanisms as illustrated in Figs. 2 and 3.

Moreover, the transmission measured on the flight sample is zero as the Kapton sample is no longer transparent. The cone-like features of the eroded surface as disclosed in Fig. 3 indicate a directional erosion of the surface and the thickness of the flight sample being eroded down to 24 μm ±20 % (or at 20 μm using a probe).

The elemental analysis of the surface by EDX shows no difference whether performed at the top or bottom of the cones. The bright contrast particles have been analyzed and identified as phosphorus and calcium. Kapton HN contains a slip additive based on dicalcium phosphate. This explains the origin of such contamination.

The Kapton samples coated with MAPATOX show a very good resistance against AO (no erosion). However, (micro) cracks of the coatings indicate some damage due to the environment.

As shown in Fig. 4, the features of these cracks are very different for MAPATOX K and 41B. This difference is also observed with the transmission spectra (Fig. 5).

Profilometry measurements could be performed on small areas of the samples (the coating is transparent) showing that the cracks could potentially reach the
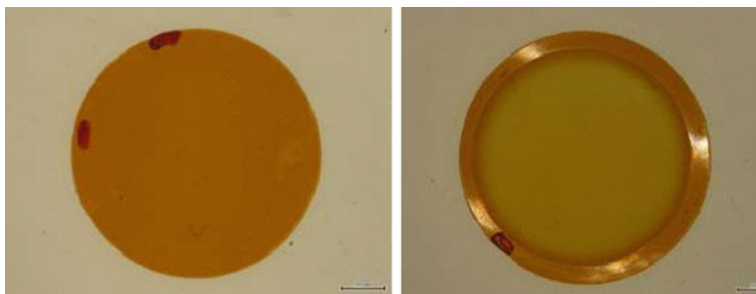
Fig. 2 Pictures of the Kapton® HN sample before (*left*)/after flight (*right*). One can notice the whitening effect due to the surface state (the sample from transparent has become diffusing)
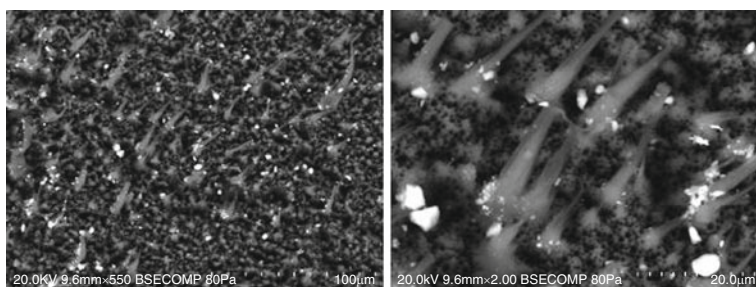
Fig. 3 SEM photographs of the Kapton® HN sample (*tilted*)
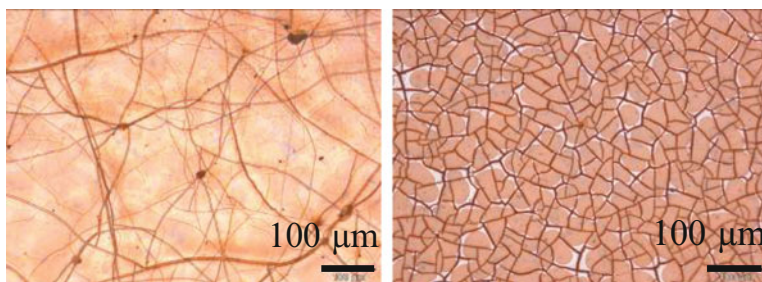
Fig. 4 SEM photographs of flight samples of Kapton® HN coated with MAPATOX 41B (*left*) and MAPATOX K (*right*)

substrate when coated with MAPATOX K. However, this point should be confirmed with a microsection measurement (the cracks observed on the MEDET MLI, also coated with Mapatox K, were found to be 4–5 μm deep) Fig. 6.

Considering the (large) dimensions of the MAPATOX K cracks, it is assumed that mechanical and thermal constraints are at the origin of such damages. On the transmission spectra of these samples, one can observe a decrease of the overall intensity for all wavelengths (modification of the surface state) and the absence of shifting of the UV cut off (no yellowing).

Fig. 5 Specular transmission spectra for the Kapton HN coated with MAPATOX K (*left*) and 41B (*right*)
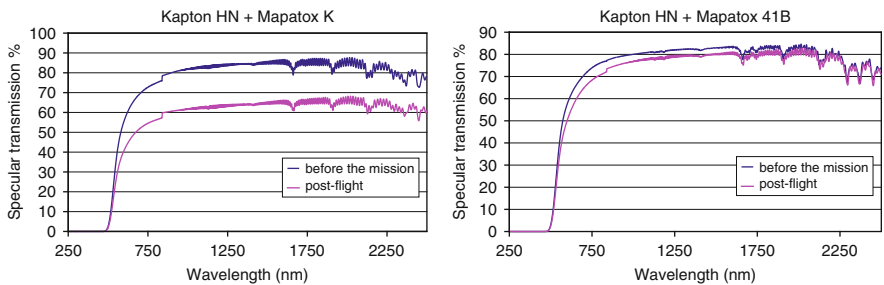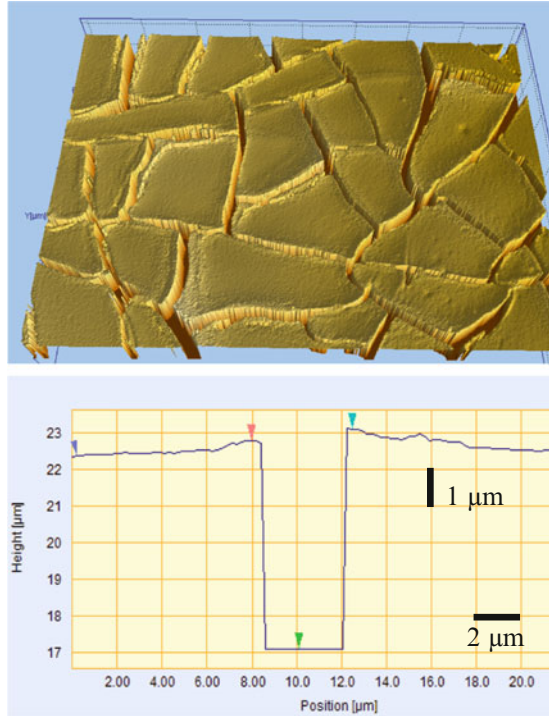
Fig. 6 Profilometry 3D (*left*) and 1D (*right*) of the Kapton®HN with MAPATOX K sample. The flat bottom in the 1D profile means that the instrument reached a saturation in this direction and that the cracks here are deeper than the 8 μm maximum reached. The width of the crack is 3–4 μm

The FT-IR spectra present absorption peaks from the Kapton and the coating. The differences observed on spare and flight samples (around 1,000 cm^{-1}) can be correlated to the formation of Si-O links (silicon oxide layer) (Fig. 7).

Regarding the Upilex 75RN, the flight sample was subjected to AO erosion with a clear whitening of the sample and a final thickness estimated at 20 μm (probe measurements). The 25 μm thick Upilex sample has been completely eroded by AO in 11 months.
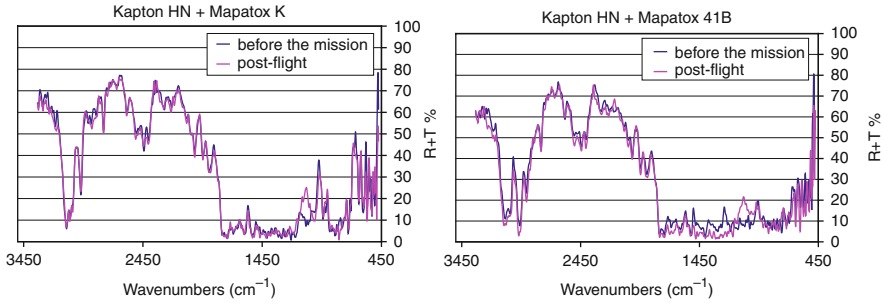
Fig. 7 FT-IR spectra of Kapton + Mapatox K (*left*), 41B (*right*)

The erosion is non uniform with an edging effect (Fig. 8, difference of color at masked sample junction). SEM shows cone-like morphology uniform over the sample (central) area, but much denser than for previous polymers, and with some non eroded zones ("protected" by contamination particles at the top, Fig. 9b). The cones orientation indicates unidirectional erosion. Silicon, oxygen and carbon are detected at the top and bottom of the cones with EDX.

With the reduced thickness of the samples because of the AO erosion, the FT-IR peaks are better defined for flight samples. Therefore the absence of great change in FT-IR on spare and flight samples allows qualitative conclusion about AO erosion of samples (see Fig. 10).

The Kapton HN and Upilex 75RN sample initial thicknesses were identical (75 μm) and both materials have similar chemical composition (polyimide). At the end, the degree of degradation is different and Kapton seems much more eroded than Upilex which contradicts the thickness data (probe). As 35 μm were estimated using weighting approach, it is believed that the probe measure (only 20 μm) provides a false estimate (due to the squeezing of the cones presence).

3.3 Thermal Coatings (Silicon Based)

The FSR1, FSR2 and RSR flight samples show similar degradation patterns with micro cracks (two patterns and different depths) and slight yellowing effects (Fig. 11). The RSR sample exhibits much tighter cracks patterns due to the difference in the proportion of short/long polydimethylsiloxane chains.

The main pattern crosses the whole coating layer (several μm deep) which tends to flake off. The daughter pattern presents narrow cracks of few hundreds of nm (Fig. 12 right).

It is assumed that mechanical and thermal constraints contribute also this degradation.

The FSRC sample rather exhibits a folded aspect creating a bumpy surface (amplitudes in the 0.5–1.5 μm range) but no micro cracks (Fig. 13).

Fig. 8 Upilex 75RN spare and flight samples (optical microscopy)
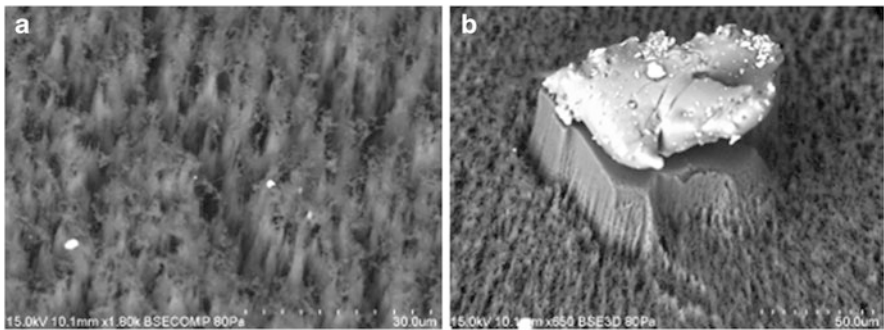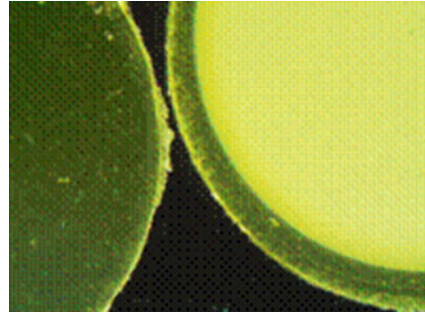
Fig. 9 SEM images of Upilex 75RN with cone-like morphology (**a** and **b**)
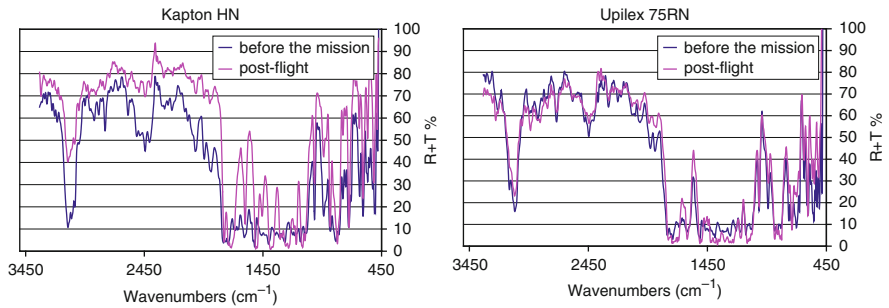
Fig. 10 Kapton HN (*left*) and Upilex 75RN (*right*) FTIR spectra

The specular transmission spectra measured before and after the flight also confirm this difference (Fig. 14).

For the FSR1 material, one can observe a decrease of the spectra intensity for all wavelengths (modification of the surface state, much lower for FSRC) and a shift of the cut off (yellowing, no shift for FSRC). The FT-IR spectra (Fig. 15) also reveal the formation of Si-O links (silicon oxide layer). As previously, no or little change is observed for the FSRC.
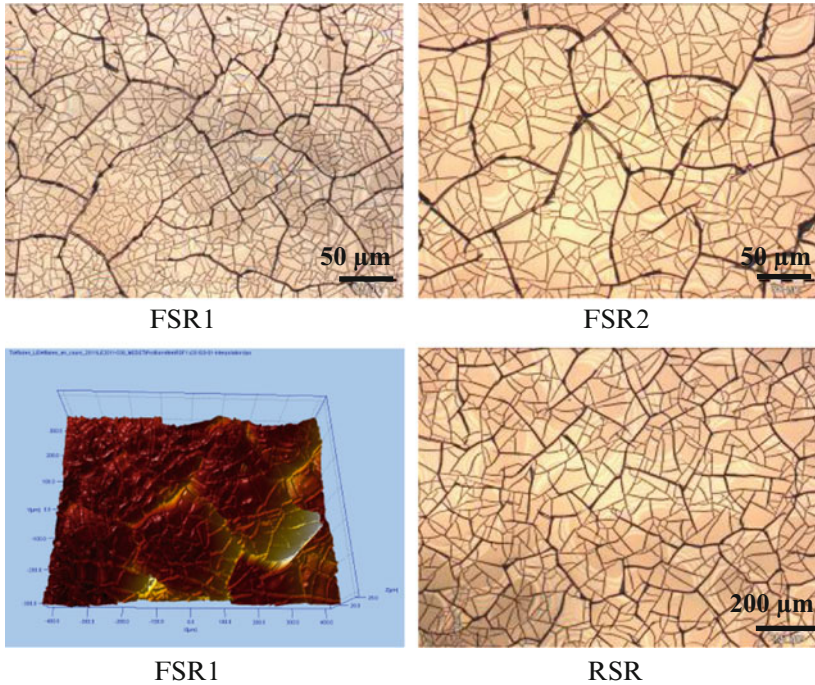
Fig. 11 Optical views of the solar reflectors flight samples and a 3D profilometry analysis image of FSR1 (*lower left picture*)

3.4 Multilayer Polymeric Films

These samples are multilayer structures. The degradations observed regard the synergy of AO erosion and UV effect (yellowing) (Fig. 16).

The final thicknesses of the samples are 45, 53 and 55 μm respectively for the KF01C1 (originally 120 μm), VLM3301 (originally 120 μm) and Covex (originally 140 μm) showing the strong erosion of these materials.

For the KF01C01 and Covex samples, the presence of two strips of darker color seems indicating the erosion is not homogeneous over the area of the sample (edging effect).

SEM shows cone-like morphology uniform over the sample area, with white residue at the top. The cones orientation indicates directional erosion (Fig. 17). Silicon, Oxygen and Carbon are detected with EDX at the top of these cones, Carbon and Oxygen at the bottom.

The VLM3301 exhibits uniform erosion with no edging effect. The SEM inspection also shows cone-like morphology over the whole sample area, with again white residue at the top (Silicon, Oxygen and Carbon are detected at the
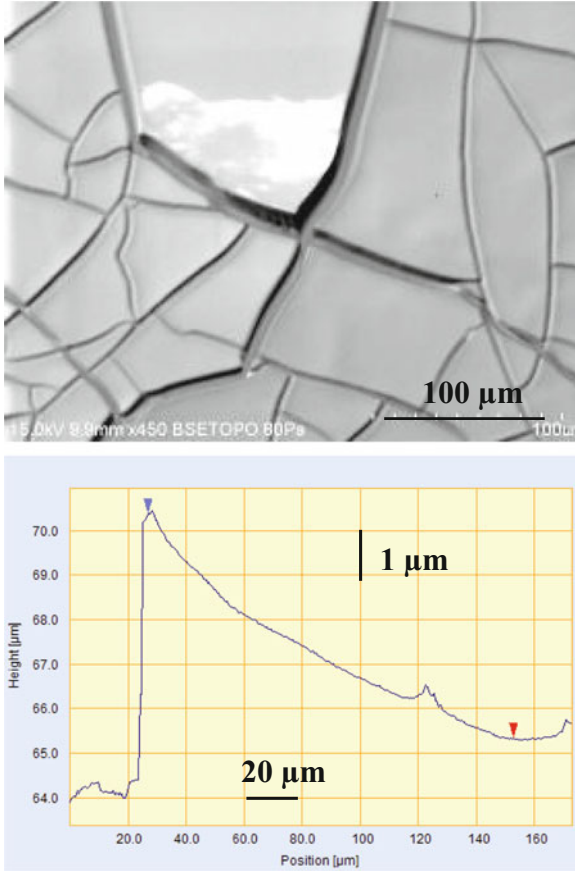
Fig. 12 SEM image of the RSR sample showing the extend of observed cracking (sample *tilted*, *left*), 1D profilometry analysis across one of the cracks (*right*)

top of these cones, Carbon and Oxygen at the bottom). The cones orientation indicates directional erosion.

The FT-IR spectra measurement does not bring new elements about the new created links at the origin of the yellowing (saturation of the signal due to the thickness of the stacking).

3.5 Summary of Thermo-Optical Properties Results

Table 3 summarizes the alpha and epsilon parameters data as measured on spare and flight samples after return.
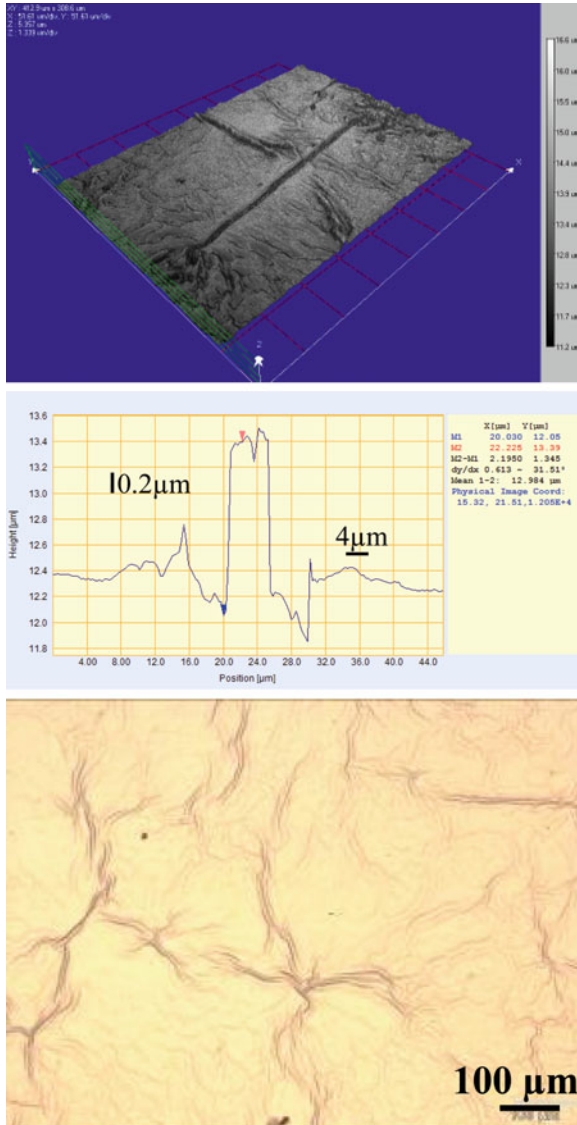
Fig. 13 Optical picture (*left*), 3D (*middle*) and 1D profilometry (*right*) of the FSRC flight sample

4 Correlation with Flight Measurements

A large set of raw UV-Visible spectra for each material were recorded during the flight. A very extensive amount of work was performed for sorting the raw data based on the illumination sensors measurements and open position spectra [2].
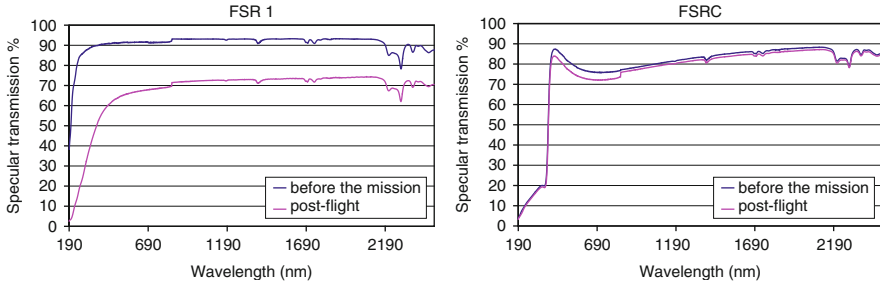
Fig. 14 Specular transmission spectra for the FSR1 (*left*) and FSRC (*right*) samples
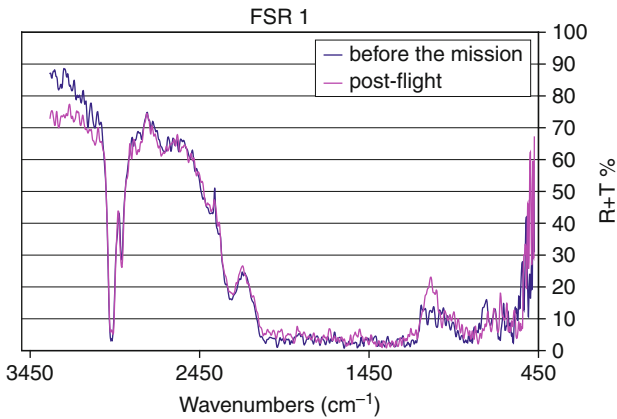
Fig. 15 FT-IR spectrum for the FSR1 showing the Si-O peak at 1,000 cm^{-1}
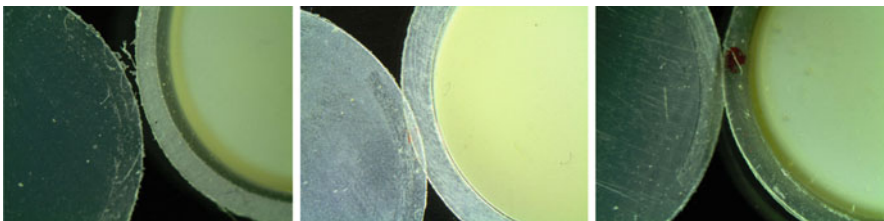
Fig. 16 Comparison of spare and flight samples for the KF01C01 (*left*), VLM3301 (*middle*) and Covex (*right*) (optical microscopy)

And yet comparisons are not straightforward as even for a given illumination level, light incidence for the measurements varies from one acquisition to the next and during a single acquisition cycle (the wheel complete rotation takes 12 min).
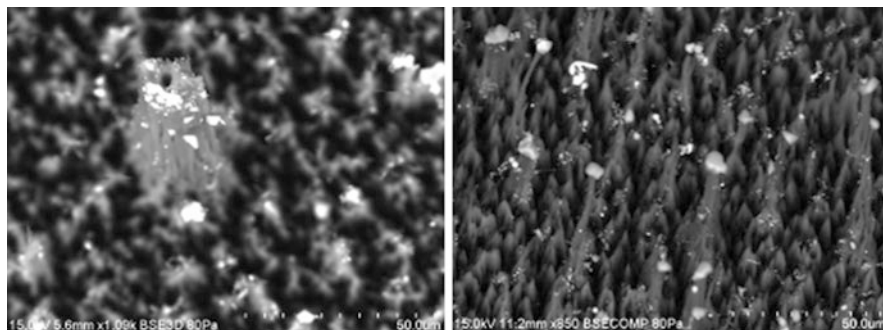
Fig. 17 SEM photographs of the KF01C01 sample (*tilted*)

Table 3 Emissivity data ($\varepsilon_{IR} = \pm 0.005$) and absorptance data ($\alpha_s = \pm 0.002$)

Sample	ε_{IR} before	ε_{IR} after	$\Delta\varepsilon_{IR}$	α_s before	α_s after	$\Delta\alpha s$
Upilex 75RN	0.822	0.835	+0.013	0.260	0.266	+0.006
Kapton HN	0.740	0.568	−0.172	0.303	0.276	−0.027
Kapton HN + Mapatox K	0.821	0.825	+0.004	0.306	0.332	+0.026
Kapton HN + Mapatox 41B	0.839	0.858	+0.019	0.322	0.335	+0.013
PGO	0.810	0.841	+0.031	0.000	0.000	0.000
Quartz	0.904	0.892	−0.012	0.001	0.004	+0.003
FSR1	0.900	0.885	−0.015	0.002	0.067	+0.065
FSR2	0.893	0.889	−0.004	0.000	0.068	+0.068
RSR	0.838	0.807	−0.031	0.001	0.068	+0.067
FSRC	0.910	0.898	−0.012	0.051	0.054	+0.003
PEN between 2 PGO (1 mm)	0.708	0.369	−0.339	0.019	0.139	+0.120
KF01C01	0.883	0.851	−0.032	0.024	0.113	+0.089
VLM3301	0.799	0.28	−0.519	0.063	0.175	+0.112
Covex	0.823	0.827	+0.004	0.032	0.097	+0.065

Nevertheless, the analysis of flight spectra allowed to reach conclusions for several samples about their degradation modes i.e. the erosion of the polymeric films (the variation of the flight spectra intensity demonstrated the reduction of the thickness or the change in the surface state of eroded samples), the resistance of Mapatox K and 41B for AO erosion, the yellowing of the thermal coatings (shifting of the UV cut off).

5 Conclusions

The following table provided a summary of degradation mechanisms for each family of samples on-board the MEDET spectrometer.

Table 4 Correlation material and mode of degradation

Material type	Degradation: main contributor
Thermal control foils: Kapton® HN, Upilex® 25 S, Upilex® 75RN	AO erosion + UV
AO protection coatings: Kapton® HN + Mapatox K or 41B	UV + thermal constraints
Flexible and rigid thermal control coatings: FSR and RSR	AO erosion + UV + thermal constraints
(Multilayer) polymeric film for inflatable structures: KF01C01, VLM3301, Covex	AO erosion + UV

The results are consistent with what was expected before the flight (describe in the literature). The quantitative evaluation of resistance or degradation is here not straightforward due to the uncertainty on some parameters inputs as ATOX fluence for instance (Table 4).

References

1. Rejsek-Riba V et al (2009) Material Exposure and Degradation ExperimenT on-board international space station: preliminary results of materials degradation on the spectrometer sub-unit. In: Proceedings of the 11th ISMSE, Aix en Provence
2. Rejsek-Riba V et al (2011) Spectrometer results of material exposure and degradation experiment on-board international space station. J Spacecraft Rockets 48:38
3. Remaury S, Guillaumon JC, Nabarra P (2002) Behavior of thermal control coatings under atomic oxygen and ultraviolet radiation. Space Technol Proc ICPMSE 5:193–201
4. Tighe AP, Iwanosky B, Van Eesbeek M, Duzellier S, Dinguirard M, Falguere D, Pons C, Inguimbert V, Rejsek V, Durin C, Mandeville JC, Gabriel S, Goulty D, Roberts G (2009) Overview of results from the materials exposure and degradation experiment (MEDET) after 18 months in orbit on the ISS. In: Proceedings of the 11th ISMSE, Aix en Provence
5. Crepel M (2009) Traitement des données Spectrometer et triage selon les critères de validité en vol. Etude et interprétation en temps réel de l'évolution des propriétés évoluant en orbite basse, training report ONERA Sept 2009, Aix en Provence
6. De Groh KK, Banks BA (2009) MISSE 2 PEACE polymers erosion morphology studies. In: Proceedings of the 11th ISMSE, Aix en Provence

Polymer Strain Experiment on MISSE 6

Deborah L. Waters, Kim K. de Groh, Bruce A. Banks, and Edward A. Sechkar

Abstract Experiments have been conducted in low Earth orbit (LEO) on the Long Duration Exposure Facility (LDEF) and the Materials International Space Station Experiment 2 (MISSE 2) that involved slightly stretched polymers held at their perimeters. In several instances, tearing occurred at the polymers' perimeters. A possible cause for such material failure may be polymer shrinkage as a result of LEO exposure, causing the stress level to gradually increase until the polymers tear. The potential for tearing may be increased by radiation induced surface embrittlement of the polymer. An active experiment, called the Polymer Strain Experiment (PSE), was designed and installed on MISSE 6B to measure the strain in 6 one-end free standing polymers as a function of time. It was thought that radiation or other environmental factors may possibly induce shrinkage in some polymers developing a tensile stress when held in place. Post-flight testing was conducted on the six flight samples including dehydration shrinkage, thermal vacuum strain, scanning electron microscopy and mandrel bend testing.

Keywords MISSE • Polymer Strain • Radiation induced embrittlement

D.L. Waters (✉) • K.K. de Groh
NASA Glenn Research Center, Cleveland, OH 44135, USA
e-mail: Deborah.L.Waters@nasa.gov

B.A. Banks
Alphaport Inc., NASA Glenn Research Center, Cleveland, OH 44135, USA
e-mail: Bruce.A.Banks@nasa.gov

E.A. Sechkar
ASRC Aerospace Corporation, Cleveland, OH 44135, USA
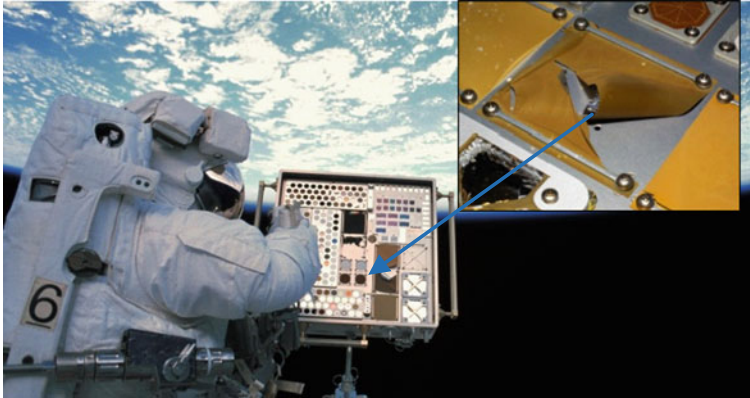
Fig. 1 Photo of MISSE 1 (*tray 1*) taken during expedition 6 on January 15, 2003 after 17 months of space exposure. Insert image: post-flight photograph of sample J3 (C-TOR-LM) taken at NASA Langley Research Center showing excessive shrinking and curling of the polymer

1 Introduction

Figure 1 provides an example of a cracked and strained electrically conductive polymer C-TOR-LM (AO-resistant polybenzimidazole) flown on MISSE 1. A possible cause for such material failure may be that the polymers shrink as a result of their LEO exposure causing the stress level to gradually increase until the polymers tear. The cracking and curling phenomenon was observed in- space in the aluminized-Teflon FEP multilayer insulation covering the Hubble Space Telescope (HST). On HST, the length of cracks induced in the Teflon insulation has been observed to be on the order of meters, as shown in Fig. 2. The cracking of FEP on HST has been attributed to radiation induced embrittlement that is further enhanced with thermal exposure [1]. Curling of cracked insulation through environmentally induced surface strain of the Teflon has allowed the underlying components to be directly exposed to the space environment; hence in those areas the insulation is no longer functioning properly for thermal control.

2 Polymer Strain Experiment

To better understand on-orbit environmentally induced shrinkage, or strain, an active experiment, called the Polymer Strain Experiment (PSE), was designed and flown on MISSE 6B to measure the strain in 6 one-end free standing polymers as a function of time. The objective of the MISSE 6 PSE was to measure radiation and thermal exposure-induced strain in thin film polymers as a function of exposure time in LEO. The experiment was flown on the wake side of MISSE 6B, which received radiation exposure and limited atomic oxygen exposure.

Fig. 2 Large radiation-induced cracks with curling of the multilayer insulation on HST as observed during Servicing Mission 2, after 6.8 years in space [2]
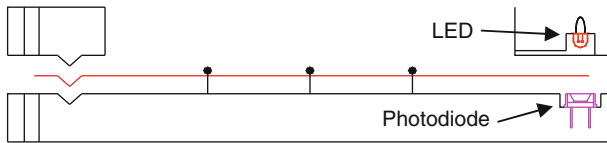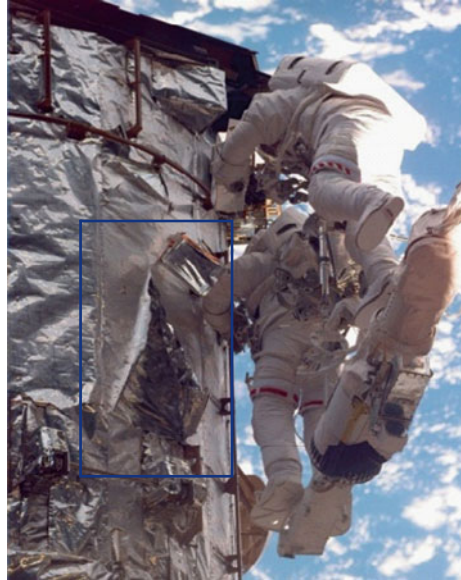
Fig. 3 Schematic cross-section drawing of PSE

In the PSE, six long thin opaque rectangular polymer film samples were positioned such that one end of the polymer sample was held securely in place, while the other end was left unattached and hence free to move as the polymer shrinks or expands. The free end was positioned inside one end of the hardware that contained a small light emitting diode (LED) and a photodiode, placed above and below the free end of the sample, respectively, as shown in Fig. 3. Figure 4 shows the calibration plot of the photodiode short circuit current as a function of displacement of the free end of the polymers. There is a linear portion of the curve that was planned for use to convert changes in short circuit current to displacement and ultimately strain by knowing the length of the sample. As the polymer sample shrinks (or expands) due to environmentally induced interactions, the photodiode short circuit current changes in proportion to the strain of the sample. Small gauge wires were positioned over the polymer film samples to keep the samples from curling on-orbit. Table 1 lists the thin film samples along with their mission relevance. The polymers tested included: Kapton HN polyimide with a back-surface coating of vacuum deposited aluminum (VDA) (sample 5), Kapton XC (sample 2), VDA coated polyimide CP1 (sample 3), Teflon fluorinated ethylene propylene (FEP) with a back surface coating of VDA (sample 4), Si/Kapton
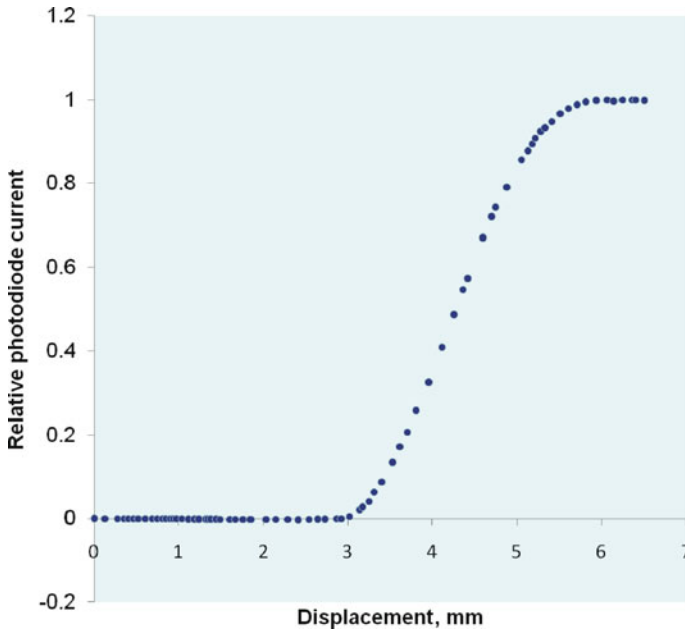
Fig. 4 PSE calibration curve for experiment

Table 1 MISSE 6B PSE samples

Sample #	Material	Mission relevance
1	Si/2 mil Kapton E/VDA/Inconel/ VDA	James Webb Space Telescope sunshield candidate
2	1 mil Kapton XC	James Webb Space Telescope wiring insulation material
3	VDA/1 mil CP1	Solar sail material
4	2 mil FEP/VDA	Common thermal control material
5	1 mil Kapton HN/VDA	Common thermal control material
6	2 mil FEP/carbon coating	Elevated temperature thermal control material

E/VDA/Inconel/VDA (sample 1) and Teflon FEP/carbon paint (sample 6). A pre-flight photograph of the PSE is provided in Fig. 5.

3 Materials International Space Station Experiment 6

MISSE 6 was delivered to ISS during the STS-123 mission, and both 6A and 6B were placed outside of the Columbus Module on March 22, 2008 in a ram/wake orientation. Figure 6 is a photo showing the location of MISSE 6A and 6B on the
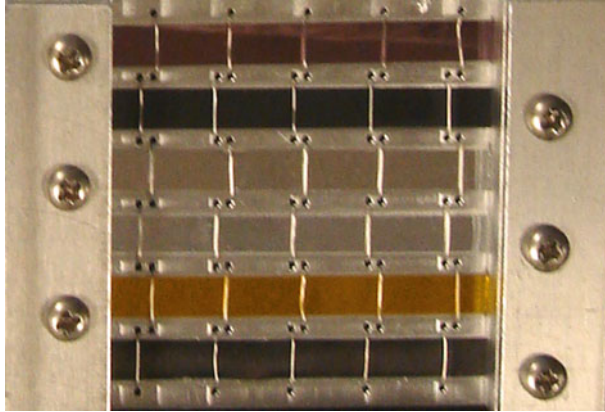
Fig. 5 Photo of pre-flight PSE MISSE 6
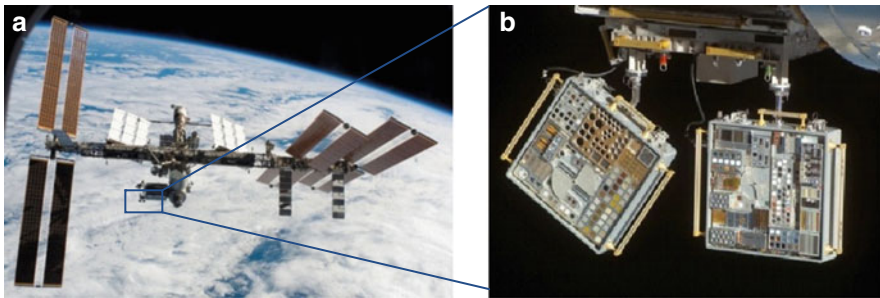
Fig. 6 Photographs of MISSE 6A and 6B: (**a**) location on the ISS Columbus module and (**b**) close-up image of the ram surfaces of 6A (*left*) and 6B (*right*)

Columbus module, and includes a close-up image of the ram surfaces of both Passive Experiment Containers (PECs) [3]. These images were taken during the STS-123 mission. MISSE 6A and 6B were retrieved on September 1, 2009 during the STS-128 mission after 1.45 years of space exposure. MISSE 6A and 6B includes both passive and active experiments with over 1,200 samples. It was powered by ISS (120 V), and the active experiment data were stored on battery powered data loggers for post-flight downloading and analysis [4].

Figure 7 provides an on-orbit photograph of the ram side of the MISSE 6B tray just prior to retrieval during STS-128. Because of ISS maneuvers during the MISSE 6 mission, the wake side of MISSE 6 was exposed to the ram direction for limited durations, and hence received atomic oxygen exposure. The atomic oxygen fluence for the wake side of MISSE 6B was determined based on mass loss of a Kapton HN witness sample, assuming a LEO erosion yield of 2.8×10^{-24} cm^3/atom [5], and was found to be 1.2×10^{20} atoms/cm^2 [6]. The Boeing ISS Thermal Analysis Group estimated the solar exposure for the wake side of MISSE 6 to be 1,950 equivalent sun hours (ESH). This value was determined based on modeling the
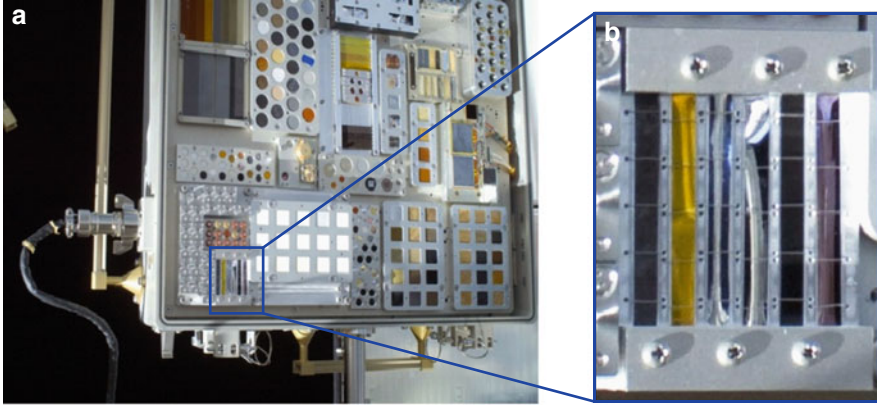
Fig. 7 On-orbit photograph of the wake side of MISSE 6B just prior to retrieval during the STS-128 mission: (**a**) portion of the MISSE 6B tray, and (**b**) blown-up image of the Polymer Strain Experiment with reflections shown in the center two samples (samples not warped or broken)

solar exposure to the surface of the Columbus module near the location of MISSE 6 using the Boeing Integrated ISS TRASYS model and included albedo effects (Pippin HG (2010) Boeing, personal communication). The temperature sensors on the MISSE 6B UV wake side showed a range of $-50\,°C$ to $150\,°C$. The radiation dose levels measured by NASA Langley were considered to be low in comparison to most of the other MISSE missions due to ISS shielding the experiments [7].

4   Calculations for Strain Testing

Strain is defined as the change in length when compared to the original length. The percent strain is reported in thermal vacuum strain testing and shown in (1).

$$\%\varepsilon = (\Delta L / L) \times 100 \tag{1}$$

For dehydration shrinkage studies the percent strain could be calculated by utilizing the calibration curve in Fig. 4, the length of the exposed polymer and the change in short circuit current after being normalized as shown in (2).

$$\%\varepsilon = (\Delta L / L) \times 100 = (1/mL)\big(I_1/I_{1Ref} - I_2/I_{2Ref}\big) \times 100 \tag{2}$$

Where:

m = Slope of the linear portion of the relative current vs. length calibration plot (0.497/mm)

I_2/I_{2Ref} = Normalized photodiode output current of polymer in air

I_1/I_{1Ref} = Normalized photodiode output current of polymer in vacuum

ΔL = Change in length of the polymer as a result of dehydration
L = Exposed length of the polymer (47.2 mm)

Using the values above, (3) becomes:

$$\%\varepsilon = (0.0426) \times \left(I_1/I_{1Ref} - I_2/I_{2Ref} \right) \times 100 \tag{3}$$

For mandrel bend testing, (4) is used:

$$\%\varepsilon = (\Delta L/L) \times 100 = (\pi R - \pi(R - t/2))/(\pi(r + t/2)) \times 100$$
$$= t/(D + t) \times 100 \tag{4}$$

Where:

D = 2r = mandrel diameter
t = thickness of polymer
R = mandrel radius + thickness of polymer

5 Experimental Procedure

5.1 Dehydration Shrinkage Studies

Before the samples were removed from the flight sample holder, the samples were dehydrated at approximately 50 mTorr in a vacuum desiccator equipped with wired connectors connected to a power supply and a current meter. This allowed the LEDs the ability to be turned-on and the photodiodes to sense the short circuit current for each sample. The samples were first tested in air with one sample removed (FEP/VDA) as a fully unobstructed illumination control. The samples were dehydrated for over 48 h before testing. The test was repeated after 48 h of rehydration with a different material used as a control case (VDA/CP1). The second control case was necessary to allow testing of all six materials because the FEP/VDA sample was initially removed. The samples were then dehydrated for 48 h and the readings were taken again.

5.2 Thermal Vacuum Strain Testing

After the dehydration shrinkage studies, the flight samples were removed from the sample holder and the individual samples were sectioned for various tests. The samples were marked for identification and length measurements. The samples length was measured in air between two glass microscope slides using an Olympus optical microscope with a Boeckeler Instruments Microcode II digital stage electronic caliper. The samples were all horizontally leveled and each measured five times to minimize standard deviations. All samples were placed in a vacuum oven (VWR Scientific Inc.) at 125 °C for 24 h. After vacuum heating, the samples were

removed and were allowed to rehydrate for 48 h prior to length measurement. Once measured this process was repeated for the six samples at 140 °C, 155 °C, 170 °C, 185 °C and 200 °C. The back-up samples were also measured before and after the 125 °C heating.

5.3   Scanning Electron Microscopy

After dehydration shrinkage testing, a small section of the flight sample was cut for scanning electron microscopy. A JEOL JSM-6390 LV Scanning Electron Microscope (SEM) was used to observe both the flight samples as well as the back-up samples for the sake of comparison. The samples were all coated with a thin layer of gold prior to imaging to reduce charging of the polymer materials.

5.4   Mandrel Bend Testing

Figure 8a shows a drawing of the mandrel bend testing technique. This test will allow the percent strain to induce surface cracking to be determined by use of subsequently smaller mandrels under low tension. The flight sample, shown in yellow in Fig. 8a, was placed on a compliant platform, shown in red, with the space exposed side face down. Decreasing sizes of mandrels, shown in blue, are gently pushed onto the sample back in a spring-loaded apparatus, shown in Fig. 8b. The sample was held in place for 5 s with each mandrel. After every mandrel was used, the exposed surface was observed using an Olympus optical microscope for strain-induced surface cracks.
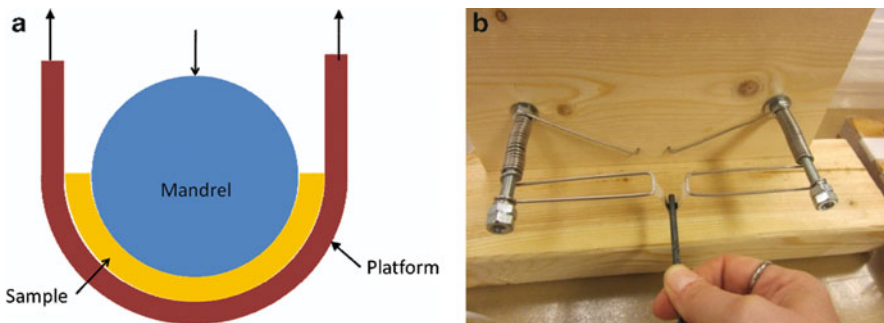
Fig. 8   (**a**) Mandrel bend-test diagram. (**b**) Spring-loaded bend-test apparatus

6   Results and Discussion

Figure 9 provides a post-flight photograph of the Polymer Strain Experiment. Unfortunately, it was discovered after the experiment was retrieved that the 15 V power supply was not connected to the experiment, and therefore the electronics did

Fig. 9 Post-flight photograph
of the MISSE 6B PSE
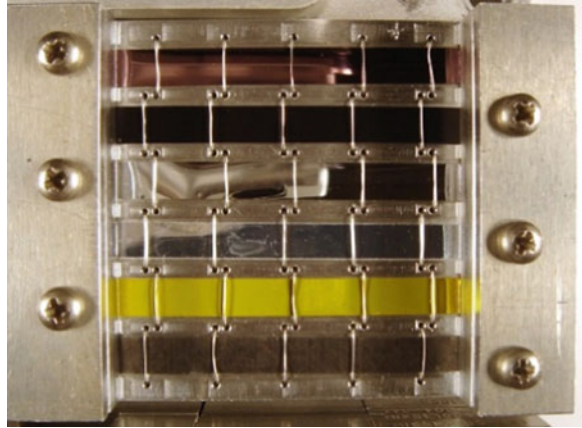
not power up or record any data. Therefore, in an effort to obtain meaningful data
from the experiment, the flight samples were observed and tested in other ways
post-retrieval.

6.1 Dehydration Shrinkage Data

The dehydration shrinkage testing yielded inconsistent data. It was noted that the
photodiode was very sensitive to movement and that the reference photodiode short
circuit current varied by up to two orders of magnitude from one sample location to
another. This caused the dehydration shrinkage to vary considerably from one test
to another. It may have been that the active area of the photodiode was too small to
receive photodiode illumination to accommodate small misalignments due to launch
vibration or ground testing. Any bumping of the dehydration chamber changed the
results of the testing. Future experiments would benefit from having a large area of
photodiode sensing and an independent reference for the unobstructed illumination.

6.2 Thermal Vacuum Testing

After 24 h at 125 °C, all of the flight samples appeared to have gained length with
the exception of the FEP/VDA sample. Most of the flight samples appear to have
very low percent strains with the exception of the FEP/VDA sample for the
continuation of increased temperatures as shown in Fig. 10. The standard deviations
ranged from 0.4 to 2.3 for this data set. Figure 11 shows data taken at 125 °C for
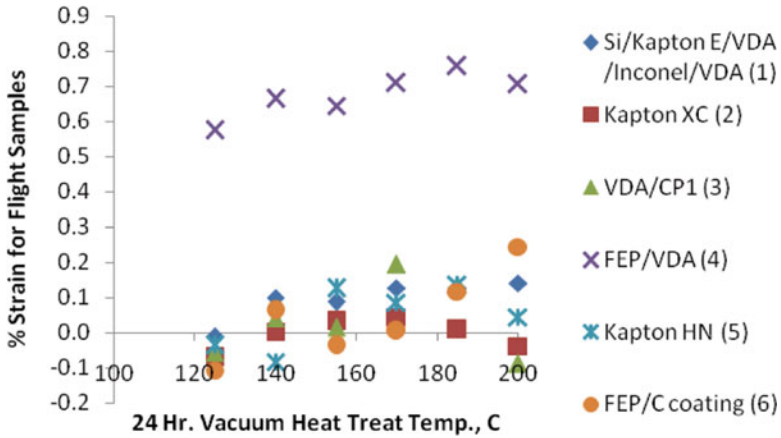
Fig. 10 Percent strain for thermal vacuum testing flight samples
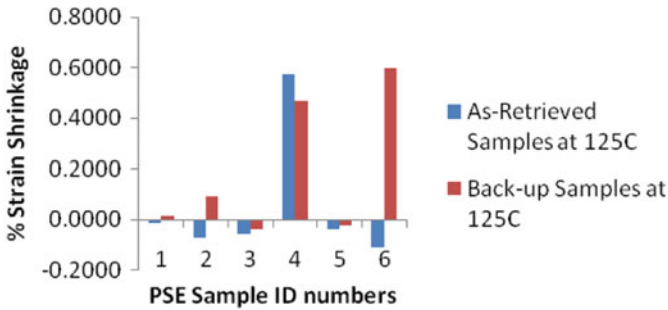
Fig. 11 Percent strain shrinkage at 125 C for flight samples and back-up samples
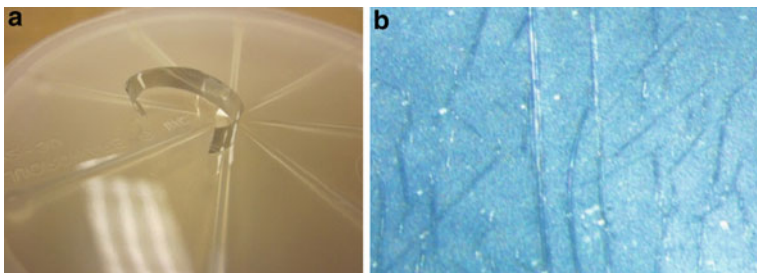
Fig. 12 (**a**) FEP/VDA flight sample curling after 170 °C, but was completely flat after 200 °C. (**b**) Cracking on FEP/VDA space exposed surface after 200 °C

both the flight samples compared to the back-up samples, which were also measured. The FEP/VDA back-up sample was fairly consistent with the flight sample, although the back-up FEP/C coating sample showed a large percent strain

while the flight sample showed a lengthening at 125 °C. Figure 10 shows that the FEP/C coating flight sample does continue to show a positive percent strain as the temperature is increased. Figure 12a shows the FEP/VDA sample curling after 24 h at 170 °C. The VDA side is on the convex side, indicating more shrinkage of the FEP space exposed surface relative to the less radiation damaged bottom surface. Figure 12b shows cracking on the surface of the FEP/VDA sample after the 200 °C heating. Thus, it appears that both pristine and radiation exposed FEP has a significant shrinkage strain upon heating and that the shrinkage of the space exposed material is not uniform throughout the thickness. This tendency to curl indicates that if an FEP/VDA blanket is held flat by its perimeter that a tensile stress will build up on the space exposed surface until cracks are initiated. Once the cracks become large, then the FEP/VDA torn pieces will tend to roll up exposing the underlying materials to increased temperatures due to a lack of emissive surfaces as has occurred on the HST light shield [1].

6.3   Scanning Electron Microscopy

All of the flight samples were observed and compared to pristine material. Figure 13 shows pristine and flight Si/Kapton E/VDA/Inconel/VDA. The surface on the flight sample showed only protective coating defect sites or impact sites with atomic oxygen texture where the Kapton was exposed. Figure 14 shows pristine and flight Kapton XC. The flight black Kapton shows the difference in surface texture that may be a result of the differences in erosion yield between the low erosion yield of the black carbon pigment and the higher erosion yield of Kapton. Figure 15 shows pristine and flight VDA/CP1. Surface defects or impact sites are visible on the flight sample. FEP/VDA, both pristine and flight are shown in Fig. 16. Impact sites
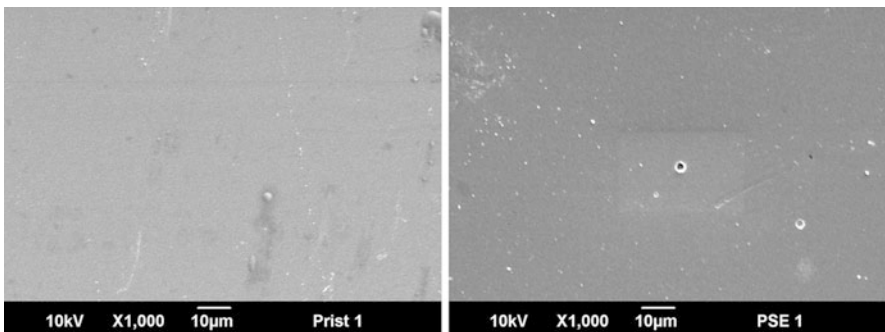
Fig. 13 Pristine (*left*) and flight (*right*) Si/Kapton E/VDA/Inconel/VDA
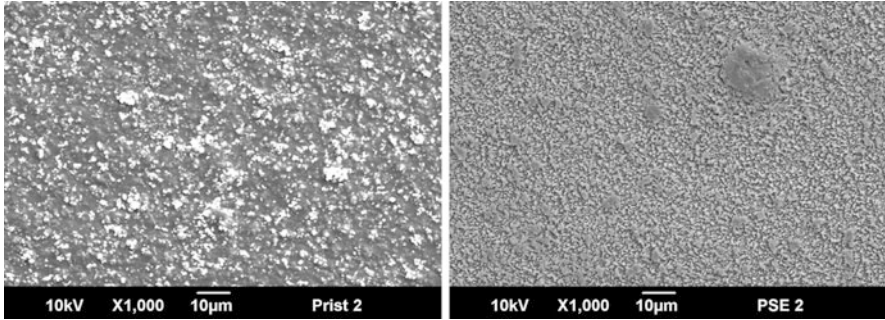
Fig. 14 Pristine (*left*) and flight (*right*) Kapton XC
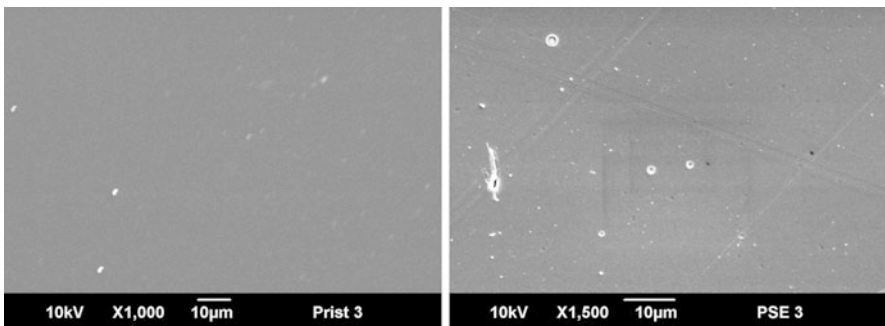
Fig. 15 Pristine (*left*) and flight (*right*) VDA/CP1
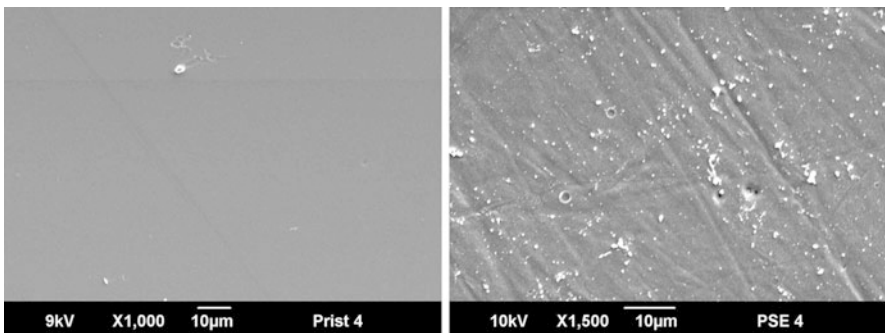
Fig. 16 Pristine (*left*) and flight (*right*) FEP/VDA

and/or debris on the surface are visible. Figure 17 shows Kapton HN pristine vs. flight showing the gradual development of texture for the flight sample. The Kapton also had surface defects or possible micrometeoroid/debris impact sites. The FEP with carbon backing coating shows possible defects and/or impact sites
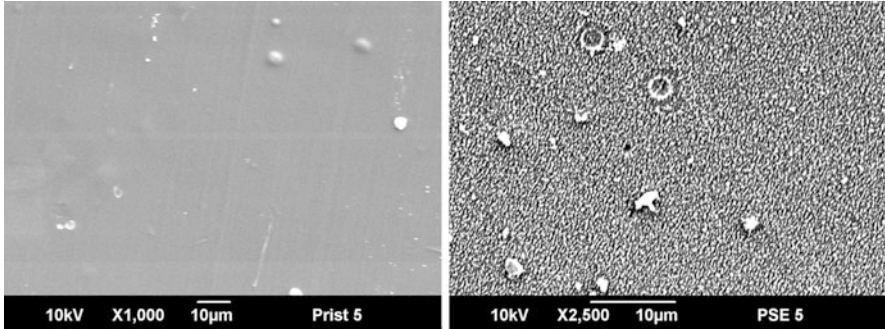
Fig. 17 Pristine (*left*) and flight (*right*) Kapton HN
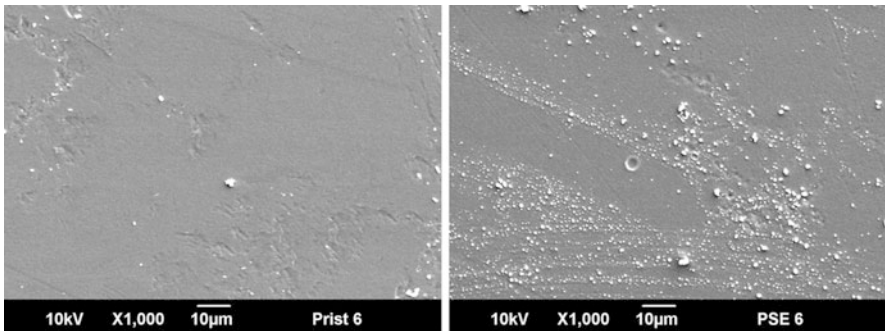
Fig. 18 Pristine (*left*) and flight (*right*) FEP/C coating

but with little surface texturing as would be expected because of its low erosion yield in Fig. 18.

6.4 Mandrel Bend Testing

Table 2 shows each of the as-retrieved flight samples that were mandrel bend tested. The percent strain for the samples with cracking is also given in the table. Three of the samples, Kapton XC, Kapton HN and FEP/C coating showed no evidence of cracking down to a mandrel size of 0.518 mm. The Si/Kapton E/VDA/Inconel/VDA sample showed only cracks in the Si coating visible down to the Kapton E bulk material, shown in Fig. 19. Figures 20 and 21 show both the VDA/CP1 and FEP/VDA samples with visible scratches or potential cracks from the testing. Although the cracking was clearly evident in the region of the bending, the cracks were surprisingly not always parallel to the bent axis. Cracking is a concern for large polymer blankets that are constrained around their perimeter and must survive thermal cycling.

Table 2 Percent strain from mandrel bend testing

Sample	Thickness	% Strain
Si/Kapton E/VDA/Inconel/VDA	2 mil	3.86
Kapton XC	1 mil	None
VDA/CP1	1 mil	1.04
FEP/VDA	2 mil	7.24
Kapton HN	1 mil	None
FEP/C coating	2 mil	None
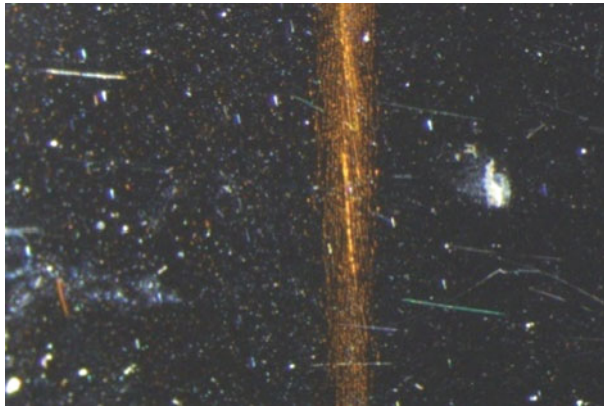
Fig. 19 Si/Kapton E/VDA/Inconel/VDA after bend testing -Si coating cracked from testing
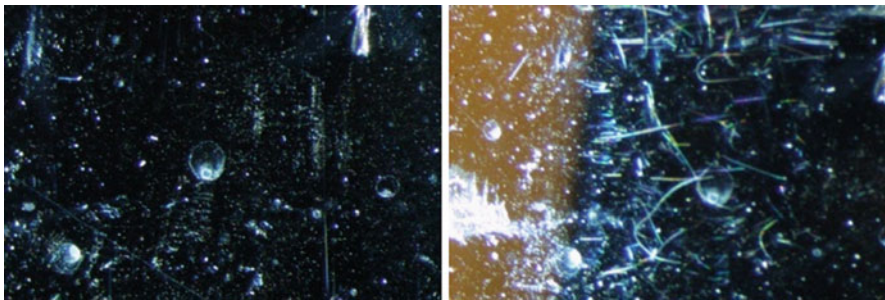
Fig. 20 VDA/CP1 before (*left*) and after (*right*) bend testing showing mandrel bend induced scratches or cracks
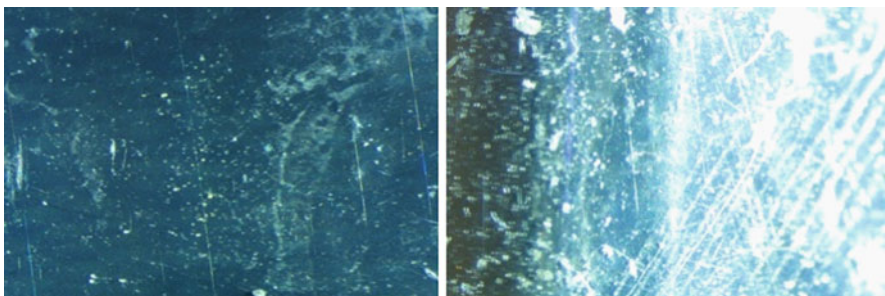
Fig. 21 FEP/VDA before (*left*) and after (*right*) bend testing showing cross-hatched pattern, possible cracking

7 Conclusions

It was discovered after the experiment was retrieved that the 15 V power supply powering the experiment was not connected. However, post flight analysis was conducted to assess shrinkage as a result of vacuum heating as well as cracking as a function of temperature from 125 °C to 200 °C. It appears that the FEP/VDA for both pristine and space exposed materials have significant shrinkage. The FEP/VDA that was space exposed indicates that the shrinkage of the exposed surface was greater than the non-exposed surface especially after heating to 170 °C. Restraining such materials to a flat configuration may cause cracking and tearing of blankets when the tensile stress accumulates with continued space radiation exposure. Si/Kapton E/ VDA/Inconel/VDA, VDA/CP1 and FEP/VDA indicated surface cracking as a result of space exposure. Such cracking is a concern for large blankets that are tightly constrained around their perimeter and must survive thermal cycling. In order to get a better understanding for the individual environmental components contributions to cracking, similar testing with pristine materials should be done and compared to flight data, where the samples have had synergistic radiation, dehydration and thermal cycling in the space environment.

References

1. de Groh KK, Banks BA, Dever JA, Hodermarsky JC (2004) Ground-based durability projection of ePTFE on ISS based on Hubble Space Telescope degradation data. High Perform Polym 16:319–337
2. Townsend JA, Hansen PA, Dever JA, de Groh KK, Banks BA, Wang L, He C (1999) Hubble Space Telescope metalized Teflon® FEP thermal control materials: on-orbit degradation and post-retrieval analysis. High Perform Polym 11:81–99
3. de Groh KK, Banks BA, Dever JA, Jaworske DJ, Miller SK, Sechkar EA, Panko SR (2008) NASA Glenn Research Center's Materials International Space Station Experiments (MISSE 1–7). In: Proceedings of the international symposium on "SM/MPAC&SEED Experiment," Tsukuba, 10–11 Mar 2008, JAXA-SP-08-015E, Mar 2009, pp 91–119; also NASA TM-2008-215482, Dec 2008
4. de Groh KK (2010) Materials spaceflight experiments. In: Blockley R, Shyy W (eds) Encyclopedia of aerospace engineering. Wiley, Chichester, pp 2535–2552
5. de Groh KK, Banks BA, McCarthy CE, Rucker RN, Roberts LM, Berger LA (2008) MISSE 2 PEACE polymers atomic oxygen erosion experiment on the international space station. High Perform Polym 20:388–409
6. Finckenor MM, Golden JL, Kravchenko M, O'Rourke MJE (2010) Analysis of international space station vehicle materials on MISSE 6. Presented at the 2010 national space and missile materials symposium (NSMMS), Scottsdale, 28 Jun–1 Jul 2010
7. Pippin HG, Wert JL, Will WE (2010) MISSE 6 post-flight examination, disassembly and analysis results. Report submitted to the Air Force Office of Scientific Research, Contract FA9550-09-C-0206, 21 Dec 2010

Passive Space Environment Effect Measurement on JEM/MPAC&SEED

Yugo Kimoto, Junichiro Ishizawa, and Hiroyuki Shimamura

Abstract A space materials exposure experiment was conducted on the exterior of the International Space Station (ISS) using the Micro-Particles Capturer and Space Environment Exposure Device (MPAC&SEED) of the Japan Aerospace Exploration Agency (JAXA). The MPAC&SEED experiments were aboard both the Russian Service Module (SM/MPAC&SEED) and the exposed Facility of the Japanese Experiment Module, KIBO Exposed Facility (JEM/MPAC&SEED). The JEM/MPAC&SEED was attached to the Space Environment Data Acquisition Equipment-Attached Payload (SEDA-AP).

The MPAC&SEED experiment included samples to monitor the fluence of AO, UV, the total dose of space radiation and the maximum temperature. In this paper, the results of the analyses of the space environment effects on the JEM/MPAC&SEED monitoring samples are described.

Keywords Atomic oxygen • JEM/MPAC&SEED • Space environment • Space radiation • TID • Ultraviolet

1 Introduction

The effects of the space environment on materials are very severe and complex and depend upon the orbit in which the spacecraft is placed. In particular, in the orbit in which the International Space Station (ISS) is operated, interaction with both high-energy particles in space and the dominant neutral gas, atomic oxygen (AO), causes performance problems. Space debris, comprising man-made objects in orbit around the Earth that no longer serve any useful purpose, are also a hazard causing concern. Spacecraft surfaces are exposed to the full strength of solar UV radiation.

Y. Kimoto (✉) • J. Ishizawa • H. Shimamura

Japan Aerospace Exploration Agency, Tsukuba, Ibaraki 305-8505, Japan

e-mail: kimoto.yugo@jaxa.jp

In addition, the surface degradation associated with contamination can adversely affect optical performance. The space environment and data on its effects are thus crucial for spacecraft design. In a space materials exposure experiment, the materials are exposed in space, retrieved back to Earth and analyzed. The information from the flight samples provides an understanding of the actual space environment effects on materials. During its 5 years and 9 months in Low Earth Orbit (LEO), NASA's Long Duration Exposure Facility (LDEF) provided information on the micrometeoroid or orbital debris environment based on the impacts on its samples [1]. The Material International Space Station Experiment (MISSE) series has been examined and exposed on the exterior of the ISS [1]. ESA's Materials Exposure and Degradation Experiment (MEDET) on the ISS has been implemented [1]. The National Space Development Agency of Japan (NASDA), the forerunner of JAXA, implemented the space materials exposure experiment on the STS-85/ Evaluation of Space Environment and Effects on Materials (ESEM) mission in 1997, and on the Exposed Facility Flyer Unit (EFFU) of the Space Flyer Unit (SFU) in 1996 [1, 2].

The Micro-Particles Capturer (MPAC) and Space Environment Exposure Device (SEED) are the Japanese space materials exposure experiments on the ISS. MPAC is a micrometeoroid capture experiment, while SEED is a passive experiment designed to expose materials. There are two MPAC and SEED projects. One is for the Japanese Experiment Module Exposed Facility (JEM/EF) on the ISS, and the other is for the Service Module (SM) on the ISS [1–3]. The MPAC and SEED on the JEM/EF (hereafter JEM/MPAC&SEED) are one of the sets of instruments comprising the Space Environment Data Acquisition equipment – Attached Payload (SEDA-AP) [4]. A JEM/MPAC&SEED experiment was launched on the Space Shuttle flight 127 (2J/A mission) on 15 July, 2009 and was exposed to the space environment attached to the Space Environment Data Acquisition Equipment-Attached Payload (SEDA-AP), which is on the KIBO Exposed Facility (EF) and mounted on the Experiment Logistics Module-Exposed Section (ELM-ES). SEDA-AP with JEM/MPAC&SEED was transferred to the EFU#9 of EF on 23 July, 2009, whereupon exposure to space commenced. SEDA-AP consists of seven sensors that measure neutrons, plasma, heavy ions, high-energy light particles, atomic oxygen, cosmic dust, and their effects. The orbital position of SEDA-AP on the ISS and JEM/MPAC&SEED is shown in Fig. 1.

On 9 April, 2010, the JEM/MPAC&SEED samples were retrieved by extravehicular activity (EVA) and intra-vehicular activity (IVA) after 259 days (8.5 months) of in-orbit exposure. JEM/MPAC&SEED samples arrived on the ground in the Kennedy Space Center (KSC) on the Space Shuttle flight 131 (19A mission) and were moved to Japan. A primary check was performed in KSC, before transport to Japan.

A front view of the JEM/MPAC&SEED hardware is shown in Fig. 2. The MPAC has two functions; capturing space debris and micrometeoroids of 0.001–0.1 mm in diameter and measuring their flux in orbit. Silica-aerogel is
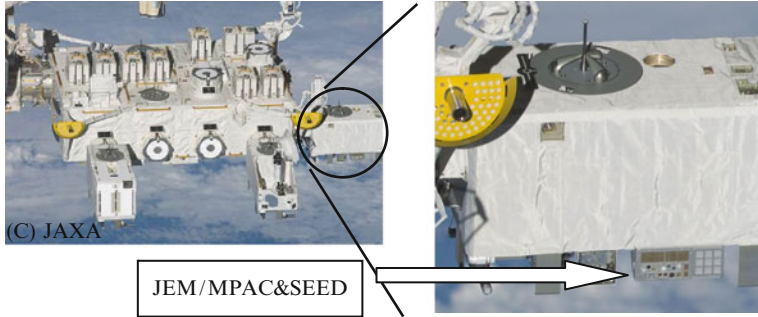
Fig. 1 Orbital position of SEDA-AP and JEM/MPAC&SEED. *Left panel*: location of SEDA-AP on the KIBO Exposed Facility of the ISS, and *right panel*: location of JEM/MPAC&SEED on SEDA-AP

☐ (dashed) Sample Unit 1: Silica-aerogel for MPAC
☐ Sample Unit 2: Gold plate for MPAC and SEED materials
☐ Sample Unit 3: SEED materials
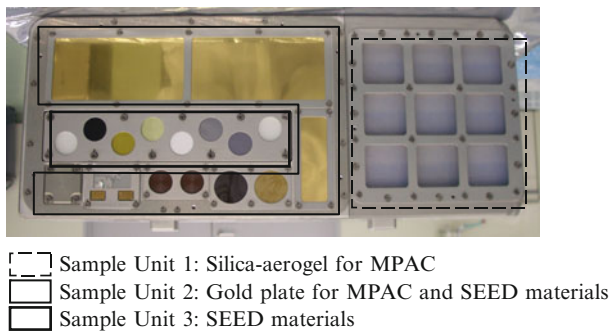
Fig. 2 Photographs of JEM/MPAC&SEED

used for MPAC on Sample Unit 1 to capture micro-particles with minimum damage, while gold plate is used for MPAC on Sample Unit 2 to investigate the flux of impacts on the same. The SEED has holders to expose nine material samples (25.4 mm (1 in.) dia. and 32.3 mm (1.27 in.) dia.) and space environment monitoring samples on Sample Units 2 and 3. A material list of SEED samples, including space environment monitoring samples, is shown in Table 1. The black paint and Thermo Label were not exposed to space.

The JEM/MPAC&SEED was a passive experiment that used neither a power source nor communication; hence no in-situ information was telemetered from space. Samples to monitor AO, UV fluence, total dose of space radiation, and temperature were situated on board as "space environment monitoring samples". In this study, the results of analyses of the effects of space on the space environment monitoring samples have been investigated.

Table 1 SEED material list

SEED samples	SEED space environment monitoring samples
Solid lubricants/MoS$_2$ on Ti-6Al-4V	UV monitor/ITO coated DUS601 (Urethane Sheet)
White paint/NOVA 500 ASTRO WHITE	Dosimeter 1/RADFET
Black paint/NOVA 500 ASTRO BLACK	Dosimeter 2/alanine dosimeter
Ge-coated black Kapton	Dosimeter 3/TLD
Black Kapton	AO monitor/Vespel
Polysiloxane-block-polyimide film "BSF-30"	Temperature/thermo label
Modified polyimide film/siloxane coated PI	–
ITO coated UPILEX-25S	
UPILEX-125S	

2　Space Environment Monitoring Samples

2.1　UV Fluence Monitoring

For our UV fluence monitoring, we used a DUS601 (Urethane Sheet) covered with ITO to protect against AO erosion. The same type of sample was also used in the past mission (SM/MPAC&SEED) [5]. Solar-absorption (αs) data, along with the calibration data were acquired in the Xe-resonance lamp-irradiation test to evaluate the UV fluence. We arranged the samples on gel sheets in a vacuum chamber to prevent increased temperature because of the Xe lamp that contains an infrared wavelength region. Two polyurethane sheets are attached.

2.2　Space-Radiation Effect: Total Ionizing Dose (TID)

We used three types of dosimeters to evaluate the effect of space radiation: Thermo-Luminescent Dosimeter (TLD), alanine dosimeter, and Radiation-Sensitive Field-Effect Transistor (RADFET). The same types of samples were also used in the past mission (SM/MPAC&SEED) [5]. The TLD was also used on the ESEM mission 1. A TLD is a small device that is used to evaluate radiation exposure by measuring the amount of visible light emitted by a crystal when heated in the detector. The amount of emitted light depends on the ionizing irradiation exposure. We arranged six TLDs behind a 4.5-mm-thick aluminum shield on both the ram and wake sides of a sample tray.

An alanine dosimeter is a solid device consisting mainly of alanine and polystyrene, the radical density of which increases in proportion to the dose of radiation received. The relative density of the radical is measured using Electron Spin Resonance (ESR). Two alanine dosimeters were arranged behind a 0.15-mm aluminum shield with silver coated FEP on a sample tray.

A RADFET is a specially designed P-channel metal oxide semiconductor (PMOS) transistor with a thick gate oxide, which is optimized for increased radiation sensitivity [6, 7]. The RADFET is suitable for real-time space dosimetry missions in terms of cost, weight, and low power consumption variables. The RADFETs used in MPAC&SEED were 400 nm implanted gate-oxide devices, manufactured by the Tyndall National Institute of Ireland. We arranged two RADFETs on a sample tray. This RADFET had a 0.8-mm-thick equivalent aluminum lid.

3 AO Monitoring

Vespel (SP-1) was selected for AO monitoring. Vespel is made from aromatic polyimide powder. Kapton-100H was selected as the AO monitoring sample on the ESEM mission 1. Vespel (t = 500 μm) is thicker than Kapton-100H (t = 25 μm). If we were to extend the exposure period of MPAC&SEED on the JEM mission, the AO would completely erode the Kapton-100H; therefore, we selected Vespel due to its larger thickness [6]. Ground AO irradiation testing was conducted to calibrate the atomic-oxygen fluence. We conducted irradiation tests at JAXA's Combined Space Effects Test Facility, which is equipped with PSI's FAST AO source, a deuterium UV-ray source, and an electron-beam source [8].

Figure 3 illustrates the dependence of mass loss from Vespel and its dependence on the AO fluence. The efficiency of mass losses on the linear part is equal to Re = 2.92×10^{-24}[cm^3/atoms]. Using this relationship between AO fluence and mass loss, AO fluence acting on the test specimen in orbit is derived as follows.

$$AOFluence[atoms/cm^2] = \frac{\Delta W}{\text{Re} \bullet \rho \bullet A} \tag{1}$$

In that equation, density ρ. [= 1.43 g/cm^3], exposed surface A [= 3.14 cm^2] and ΔW is mass loss [g].

The effect of UV on Vespel that is an AO monitoring sample was also verified in a series of experiments. In the first series, the samples were AO irradiated at 3×10^{21}[atoms/cm^2], followed by UV irradiation at 100 [ESD]. In the second series, the samples were UV irradiated at 100 [ESD] followed by AO irradiation at 3×10^{21} [atoms/cm^2]. Figure 4 shows both irradiation test results with the data from Fig. 3 also added. As can be seen from Fig. 4, the Re was not affected by the ultraviolet rays.
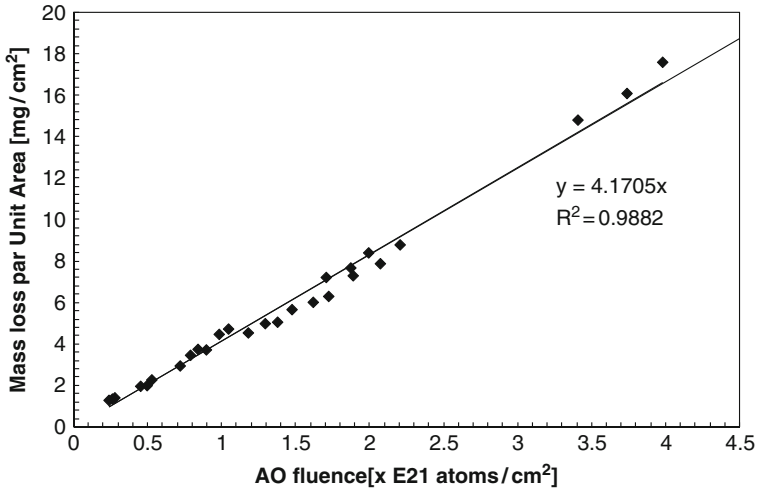
Fig. 3 Mass loss from Vespel by AO exposure. The x-axis represents AO fluence; the y-axis, the mass difference from the initial value, which is divided by the density and exposed surface area
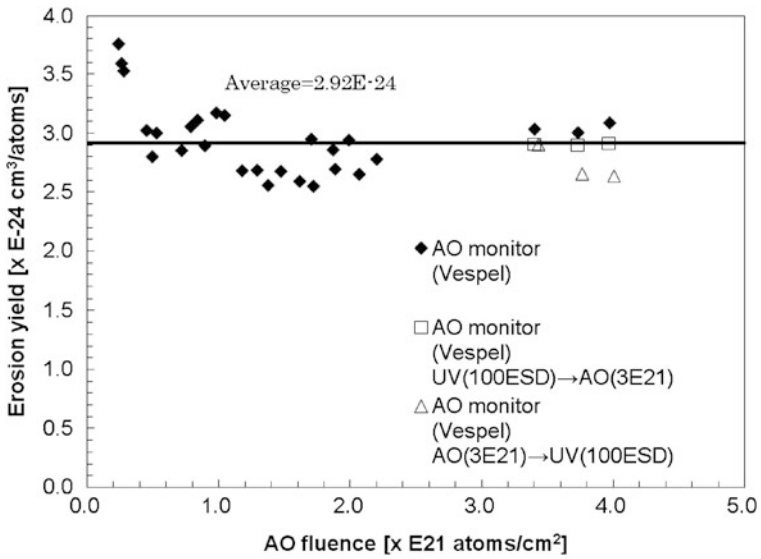
Fig. 4 Erosion yield (Re) from AO exposure. The x-axis represents AO fluence; the y-axis, erosion yield (Re)

3.1 Maximum Temperature

For temperature monitoring, four thermolabels are attached inside/on a sample tray [5]. Each thermolabel can measure only the maximum temperature.
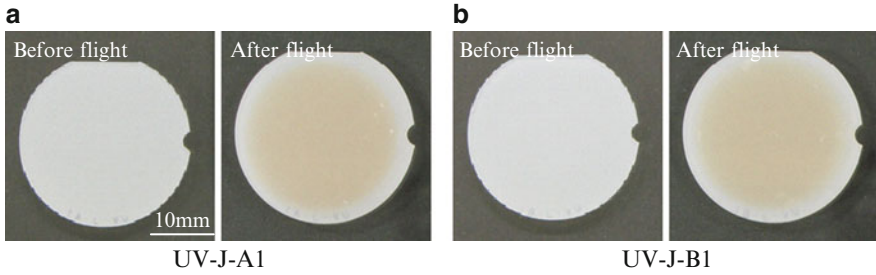
Fig. 5 Surface changes of two UV monitoring samples both before and after exposure to space
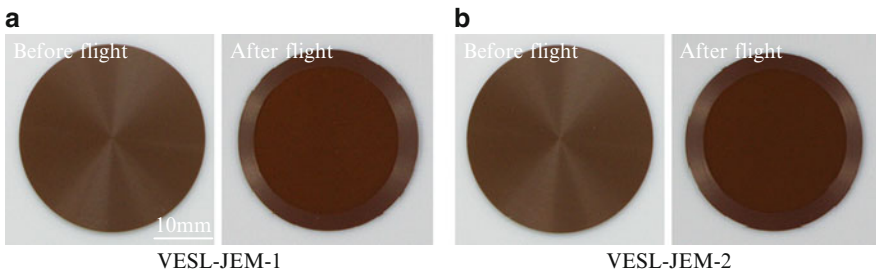
Fig. 6 Surface changes of two AO monitoring samples both before and after exposure to space

4 Results and Discussion

4.1 Retrieved UV and AO Monitoring Samples

Figure 5 displays two UV monitoring samples both before and after exposure to space. The top surfaces of the UV monitoring samples are changed from milky–white to brown. Figure 6 displays two AO monitoring samples both before and after exposure to space. The shiny appearance of the top surfaces changes to mat, while the rim side that was masked by the holder remaining unchanged.

4.2 Deriving the Space Environment Factor Values from Monitoring Samples

Table 2 presents the derived results of both the monitoring samples and space environment models. The first-retrieved SM/MPAC&SEED monitoring sample data (labeled as #1) on the RAM side are also shown. The exposure duration of SM/MPAC&SEED#1 was 315 days (10 months) [5].

Table 2 Derivation space environment factors

		JEM/MPAC&SEED		SM/MPAC&SEED#1 (RAM)	
		Monitoring sample	Model	Monitoring sample	Model
UV [ESD]		<30	56.85	18.1	73.8
TID [Gy] (Al shield thickness)	Alanine (0.15 mm)	5	5.27×10^1	1.95	6.76×10^1
	RADFET (0.8 mm)	0.16	3.29	4.40×10^{-1}	4.08
	TLD (4.5 mm)	0.10	4.25×10^{-2}	1.46×10^{-3}	2.03×10^{-1}
AO [atoms/cm^2]		5.91×10^{20}	1.40×10^{21}	2.04×10^{20}	2.85×10^{21}
Maximum temperature [°C]		<50[a] <50[b]	–	–	–

[a]At a depth of approximately 5 mm in Sample Unit 3
[b]At a depth of approximately 5 mm in Sample Unit 2

The orbital and altitude flight information of the ISS during this experiment period was analyzed. The average flight altitude was 343 km; the inclination was 51.6°. We compared flight data and data from the space-environment model for the UV, TID and AO in the Space Environment and Effects System (SEES) [9] from 23 July, 2009 to 9 April, 2010. We used the F10.7 and Ap index data available from NOAA Space Weather Data and Products [10] for neutral gas estimation and considered the flight-direction change, shape of the ISS structure and shadow of the Earth in our calculations.

As for UV fluence, the monitoring sample output was 1/2 the model output when UV fluence was 30 [ESD]. The UV fluence of JEM/MPAC&SEED was 1.7 times greater than that of SM/MPAC&SEED#1. The reason for discrepancy between the JEM/MPAC&SEED and model was the uncertainty of the UV model in SEES, while the reasons for the low numbers of SM/MPAC&SEED#1 UV fluence compared to JEM/MPAC&SEED were the view factors from SM/MPAC&SEED and the contamination effect [4].

TID from models is overestimated except for shield thickness equal to 4.5 mm. One of the reasons for discrepancies between the flight data and model calculation is the difference of electron and proton fluxes within a certain energy range [11, 12]. Renewal of space radiation models and continuous monitoring is required.

AO fluence, which is derived from the AO monitoring sample, is 40 % less than the model output, while the AO fluence of JEM/MPAC&SEED is three times greater than SM/MPAC&SEED#1. The reason for discrepancy between JEM/MPAC&SEED and the model is also the uncertainty of the AO (neutral gas) model in SEES. In addition, the reasons for the low numbers of SM/MPAC&SEED#1 AO fluence compared to JEM/MPAC&SEED are the view factors from SM/MPAC&SEED and the contamination effect [5]. The exposure period of SM/MPAC&SEED#1 from 2001 to 2002 coincided with the solar maximum and the solar activity was so high that it could

affect AO (neutral gas) fluence for model calculation. Moreover, the AO monitoring sample of JEM/MPAC&SEED may also have been affected by contamination.

The effects of these derived space environment factors must be verified from the perspectives of SEED sample analysis and their ground evaluation tests.

Moreover, it is necessary to measure and analyze the space environment and data on its effects continuously and in the long term to establish more reliable conclusions. In this mission, SEDA-AP had an active space environment monitor space radiation (Standard Dose monitor: DOM) and AO fluence (Atomic Oxygen Monitor : AOM)[12]. Namely, both passive and active space radiation and AO fluence data were acquired during JEM/MPAC&SEED exposure to space [13, 14]. This space environment measurement sensor data onboard SEDA-AP will be used for this analysis in future.

5 Conclusions

8.5 months space-exposed JEM/MPAC&SEED were retrieved successfully and all samples were analyzed. Using the space environment monitoring samples, UV fluence, total ionized dose i.e. TID and AO fluence information data were acquired. The space environment data obtained in this experiment, the modeling data and the data from previous SM/MPAC&SEED#1 were compared. The space environment and data on its effects must be continuously measured and analyzed on a more long-term basis in order to establish more reliable conclusions. This space environment measurement sensor data onboard SEDA-AP will be used for this analysis in future.

References

1. Edwards DL, Tighe AP, van Eesbeek M, Kimoto Y, de Groh KK (2010) Overview of the Natural Space Environment and ESA, JAXA, and NASA Materials. Flight Experiments MRS Bull 35:25
2. Suzuki M, Shimamura H, Imagawa K (2008) In: Proceedings of the international symposium on Japan's Materials Space Exposure Experiments "SM/PAC & SEED Experiment", JAXA-SP-08-015E, International Congress Center EPOCHAL TSUKUBA, Tsukuba, Ibaraki, Japan
3. Kimoto Y, Ichikawa S, Miyazaki E, Matsumoto K, Ishizawa J, Shimamura H, Yamanaka R, Suzuki M (2009) Proceedings of the 9th international conference on protection of materials and structures from space environment, Toronto, 20–23 May 2008, Kleiman J (ed), AIP conference proceedings 1087, Melville, p 207
4. Koga K, Goka T, Matsumoto H, Koshiishi H, Kimoto Y, Kanamori T, Kamakura C, Ito M, Endo M (2001) COSPAR Colloquium Series, vol 14. Pergamon Press, Amsterdam, p 365
5. Kimoto Y, Yano K, Ishizawa J, Miyazaki E, Yamagata I (2009) Passive Space-Environment-Effect Measurement on the International Space Station. J Spacecraft Rockets 46:22

6. Kimoto Y, Koshiishi H, Matsumoto H, Goka T (2003) Total Dose Orbital Data by Dosimeter Onboard Tsubasa (MDS-1) Satellite. IEEE Trans Nucl Sci 50(6):2301
7. Kimoto Y, Satoh Y, Tachihara H (2009) Small Total dose Measurement System for SDS-1, Acta Astronaut 65(9–10):1446
8. Shimamura H, Baba S, Miyazaki E (2011) JAXA-RM-10-013 (in Japanese)
9. http://sees.tksc.jaxa.jp
10. http://www.swpc.noaa.gov/Data/index.html
11. Goka T, Matsumoto H, Koshiishi H, Lui H, Kimoto Y, Matsuda S, Imaizumi M, Kawakita S, Anzawa O, Aoyama K, Tanioka Y, Ichikawa S, Sasada T, Yamakawa S (2002) Space Environment and Effect Measurements from the MDS-1 (Tsubasa) Satellite, In: Proceedings of the 23rd ISTS, Matsue, 26 May–2 Jun 2002 AGNI Publishers, Tokyo, p 1747
12. Koga K, Matsumoto H, Koshiishi H, Liu H, Goka T (2002) New results from space environment measurements on the Tsubasa (MDS-1) Satellite, In: Proceedings of the 5th international workshop on radiation effects on semiconductor devices for space application, Takasaki, p 17
13. Matsumoto H, Koshiishi H, Goka T, Kimoto Y, Green BD, Galica GE, Nakamura T, Abe T, Badono S, Murata S, Sullivan JD (2001) IEEE Trans Nucl Sci 48(6):2043
14. Galica GE, Green BD, Joshi PB, Nakamura T, Abe T, Kobayashi M, Matsumoto H, Koshiishi H, Goka T, Kimoto Y (2006) Atomic Oxygen Monitor Based on Carbon Actinometers, Proc. of the 10th International Symposium on "Materials in a Space Environment" (ISMSE) and 8th International Space Conference on "Protection of Materials and Structures from the Space Environment" (ICPMSE). (SP-616, September 2006)

Attenuation of Scattered Thermal Energy Atomic Oxygen

Bruce A. Banks, Katelyn T. Seroka, Jason B. McPhate, and Sharon K. Miller

Abstract The attenuation of scattered thermal energy atomic oxygen is relevant to the potential damage that can occur within a spacecraft which sweeps through atomic oxygen in low Earth orbit (LEO). Although there can be significant oxidation and resulting degradation of polymers and some metals on the external surfaces of spacecraft, there are often openings on a spacecraft such as telescope apertures, vents, and microwave cavities that can allow atomic oxygen to enter and scatter internally to the spacecraft. Atomic oxygen that enters a spacecraft can thermally accommodate and scatter to ultimately react or recombine on surfaces. The atomic oxygen that does enter a spacecraft can be scavenged by use of high erosion yield polymers to reduce its reaction on critical surfaces and materials. Polyoxymethylene and polyethylene can be used as effective atomic oxygen scavenging polymers.

Keywords Atomic oxygen • Erosion yield • Low Earth orbit • Scattered • Thermal energy

1 Introduction

Spacecraft in low Earth orbit (LEO) sweep through atomic oxygen resulting in hyperthermal (~4.5 eV) atomic oxygen attack on ram facing surfaces. Although there can be significant oxidation and resulting degradation of polymers and some

B.A. Banks (✉) • K.T. Seroka
Alphaport Inc., NASA Glenn Research Center, Cleveland, OH 44135, USA
e-mail: Bruce.A.Banks@nasa.gov

J.B. McPhate
Space Sciences Laboratory, University of California, 7 Gauss Way, Berkeley, CA 94720-7450, USA

S.K. Miller
NASA Glenn Research Center, Cleveland, OH 44135, USA

metals on the external surfaces of spacecraft, there can also be damage to materials and sensitive surfaces within a spacecraft if the atomic oxygen is allowed to enter. Atomic oxygen can enter spacecraft through openings such as telescope apertures, vents, and microwave cavities. The atomic oxygen that does enter will either react with organic or other reactive surfaces, reassociate to become chemically inactive diatomic oxygen, or lose its hyperthermal energy as it scatters off multiple surfaces and becomes thermally accommodated atomic oxygen [1–3]. This thermally accommodated atomic oxygen is still fully capable of reacting with materials even though its reaction probability is greatly reduced compared to hyperthermal atomic oxygen. Sensitive optical filters, optical sensors that operate on photoelectric effect principals, or microwave cavities can be compromised by the presence of a fluence of thermal energy atomic oxygen.

The objective of this investigation is to compare the degree to which scattered thermal energy atomic oxygen is attenuated by the material it scatters from. This is relevant to considerations of what materials may be best to have within a spacecraft to scavenge the atomic oxygen and to reduce its damage to sensitive materials and surfaces.

2   Apparatus and Procedure

The experiments were conducted in radio frequency plasma ashers operating on air [4]. Kapton H polyimide witness samples were used to measure the flux of atomic oxygen inside and outside of scattering chambers. Drawings and photos of the three types of scattering chambers used include: an open-ended chamber (Fig. 1), a cylindrical Faraday cage chamber (Fig. 2), and two rectangular Faraday cage chambers (Fig. 3). In the first two scattering chamber configurations, the walls were lined with various test materials to assess the impact of the material's interaction with atomic oxygen. The atomic oxygen Kapton H effective flux within the scattering chambers were measured by means of mass loss of the Kapton H witness sample at the bottom of the chambers. Kapton H effective flux in a thermal energy plasma asher is the hyperthermal flux in LEO that produces the same rate of erosion of Kapton H. A comparison of flux inside-to-outside scattering chambers was made by placing 2.54 cm diameter by 0.0127 cm thick Kapton H witness samples inside and outside the chambers and comparing weight loss per area. Outside the scattering chambers 1.905 cm diameter Kapton H witness samples were used to measure the ratio of inside-to-outside effective flux. The open-ended chamber typically used 0.05 mm thick sample materials to line the cylinders that were 5.65 cm long by 2.61 cm inside diameter. The Faraday cage chamber used the same set of materials but was 1.56 cm long by 2.61 cm inside diameter.

The rectangular Faraday cages were used to assess the impact of various size inner lid openings on the mass loss of a Kapton H sample inside the cage as well as the fractional area of Kapton within the Faraday cage.
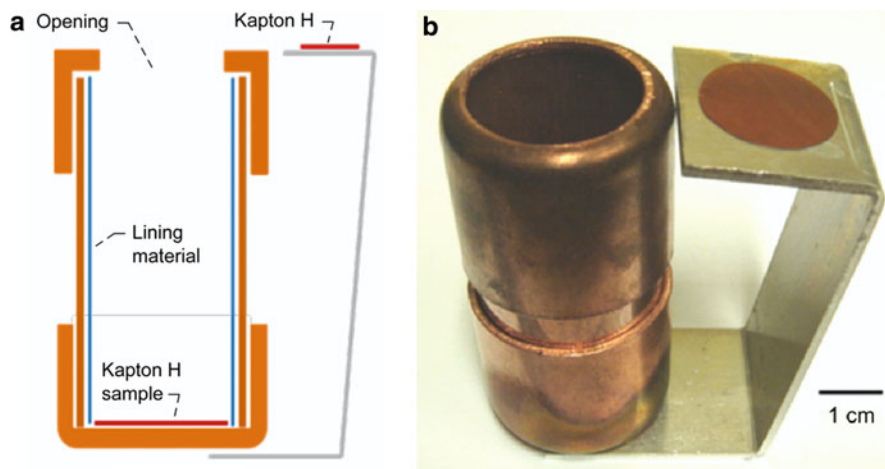
Fig. 1 Open-ended scattering chamber configuration used which allowed oxygen atoms, ions, electrons, and UV radiation to enter and interact with the chamber wall and Kapton at the bottom. (**a**) Section view (not to scale). (**b**) Photo
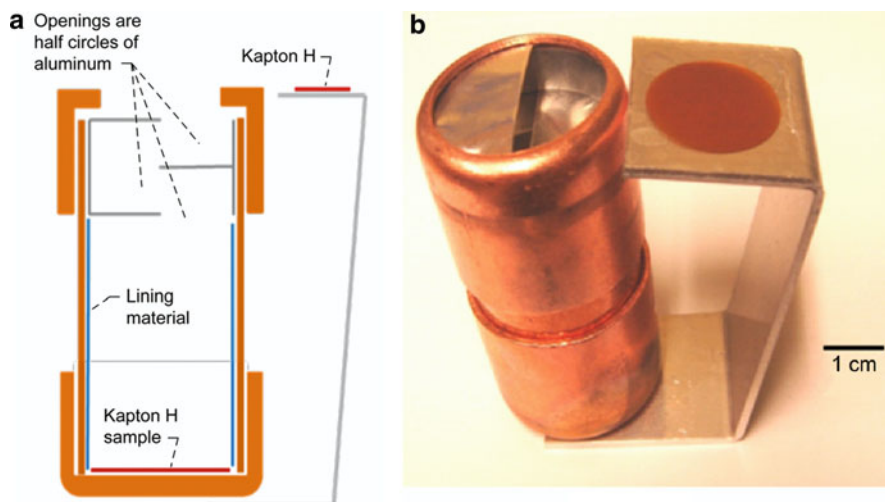
Fig. 2 Cylindrical Faraday cage chamber configuration with three aluminum half-circles that prevent the line of sight of to entrance of oxygen atoms, ions, and electrons into the chamber. (**a**) Section view (not to scale) (**b**) Photo

The open-ended chamber (Fig. 1) allowed a greater flux of atomic oxygen, ions, electrons and UV radiation to enter the scattering chamber than the Faraday cage chamber (Fig. 2). The Faraday cage chamber prevented line of sight entrance of atomic oxygen, ions or electrons. To accomplish this, the Faraday cage utilized three aluminum half-circles as shown in Fig. 2.
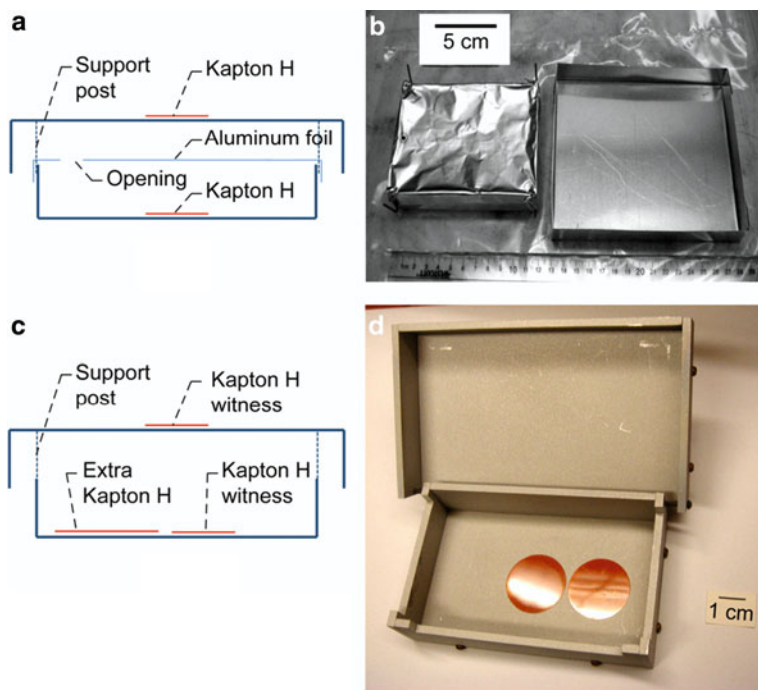
Fig. 3 Two rectangular Faraday cages made of aluminum. (**a**) Section view (not to scale) showing an all-aluminum chamber with a lid supported by four wire posts and separate inner chamber covered by aluminum foil. (**b**) Photo of cage (a). (**c**) Section view (not to scale) of a two part Faraday cage. (**d**) Photo of cage (c)

The outer lid of the Faraday cage in Fig 3a and b measured approximately 15.2 by 11.4 by 2.1 cm high. This lid is shown upside down on the right side of Fig. 3b and fit over the inner chamber which is shown on the left side of Fig. 3b. The inner chamber measured approximately 11.7 by 7.5 by 2.5 cm high and had four wires attached to it to hold the lid 0.7 cm above the chamber. A representative opening into the Faraday cage shown in Fig. 3a and b can be seen as the small hole through the aluminum foil on the left side of the chamber. This opening was varied in size and in some cases two openings were used. The Faraday cage shown in Fig. 3c and d was a simple hinged overlapping box that allowed covering the inner surface with varying amounts of Kapton to assess the attenuation of atomic oxygen due to fractional coverage of Kapton. The lids of both Faraday cages overlapped the lower chambers shown in Fig. 3 thus preventing line of sight of plasma into the cages. Samples of 2.54 cm diameter Kapton H were placed on top of the lid and inside the chamber to assess the inside-to-outside mass loss ratio.

The Kapton H witness samples were vacuum dehydrated for at least 48 h prior to all weight loss measurements in accordance with ASTM-E 2089–00, "Standard Practices for Ground Laboratory Atomic Oxygen Interaction Evaluation of Materials for Space Applications" [4]. The mass of the Kapton H witness samples

was measured by averaging three mass measurements made within 5 min after removal from vacuum desiccation using a 10 μg sensitivity Sartorius balance.

To assess the effects of various materials on the attenuation of the thermal energy atomic oxygen flux in the scattering chambers, linings of various metals, metal oxides, polymers, and graphite were used on the vertical sides of the chambers. The ratio of Kapton H effective flux, inside-to-outside, was measured by comparing the Kapton mass loss and correcting for area differences (in the case of open-ended and cylindrical Faraday cages). As can be seen by the Figs. 1, 2, and 3, the geometries of the scattering chambers were sufficiently different that direct comparison of atomic oxygen attenuation for any specific material cannot be made between the types of chambers. However, relative comparison of the differences from material to material can be made in terms of which sidewall causes the greatest attenuation in atomic oxygen for each configuration. The sidewall materials chosen for evaluation were: aluminum, copper, 300 series stainless steel, gold, silicon dioxide coated Kapton H, flexible graphite made from pure, natural graphite flake (GRAFOIL), polyethylene, fluorinated propylene ethylene (FEP) Teflon, polyoxymethylene (POM), and chlorotrifluoroethylene (CTFE).

Thermal energy isotropic atomic oxygen behaves as a reactive gas where its partial pressure in a chamber determines the erosion rate of the polymer inside the chamber. The difference between the erosion rate inside the chamber and outside the chamber is influenced by the entry aperture area and the atomic oxygen partial pressure losses due to reaction with the wall and recombination within the chamber.

3   Results and Discussion

The flux in the asher was ~5×10^{15} atoms/(cm^2 s) and the durations of exposures were typically ~24 to 68 h. Thus, the fluence exposed to the outside Kapton H samples was at least ~3.4×10^{20} atoms/(cm^2).

The ratio of effective flux outside-to-inside for the open-ended scattering chamber is shown in Fig. 4. As can be seen, in general, the chamber lining materials that do not react with atomic oxygen tend to cause less attenuation of the atomic oxygen thus allowing a higher ratio of mass loss inside the scattering to outside the chambers. Copper reacts with atomic oxygen to form a non-protecting brown Cu_2O copper oxide [5] that was found to spall from smooth copper surfaces. Thus, the copper lining of the open scattering chamber tended to reduce the amount of atomic oxygen mass loss. To prevent copper oxide from spalling, the copper surfaces were roughened by cross scratching the surface with rough sandpaper.

The results of the Faraday cage scattering chamber are shown in Fig. 5. Although the geometries are quite different between the open and the Faraday scattering chambers, a comparison of ranking between materials indicates only minor differences in atomic oxygen attenuation. Again as in the open scattering chamber case, the chamber lining materials that do not react with atomic oxygen tend to prevent atomic oxygen attenuation. This leads to higher mass loss of the Kapton
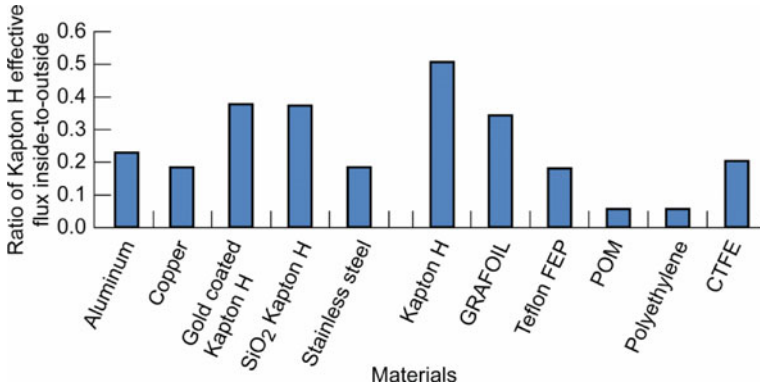
Fig. 4 Ratio of Kapton H mass loss inside-to-outside for the open-ended scattering chambers that are lined with various materials
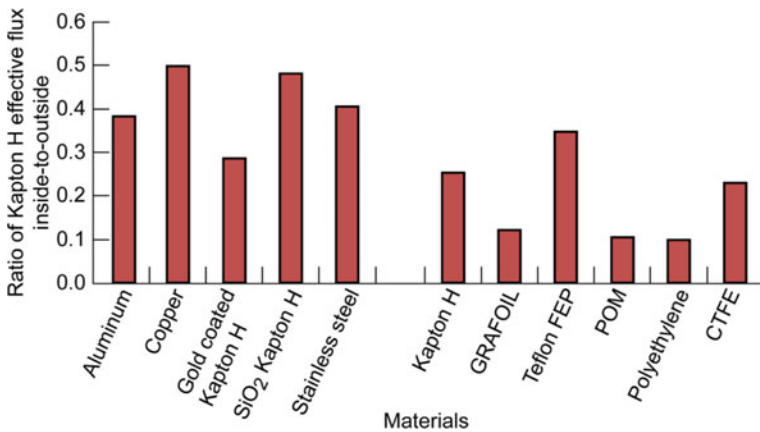
Fig. 5 Ratio of Kapton H effective flux inside-to-outside for Faraday cage scattering chambers that are lined with various materials

inside relative to outside the chambers. However, the best polymers, of those tested, to have in the Faraday cage to attenuate atomic oxygen are POM and polyethylene. Graphite from GRAFOIL is thought to be too friable to be safely used inside spacecraft.

It is also interesting to compare the amount of attenuation in atomic oxygen flux inside the Faraday cage as a function of the erosion yield measured in an asher environment. This was done assuming that the erosion yield for Kapton H is 3×10^{-24} cm^3/atom [6, 7]. Figure 6 is a plot of ratio of Kapton H effective flux inside a Faraday cage to outside the Faraday cage for various cage-lining materials as a function of the effective atomic oxygen erosion yield in an asher environment. As can be seen, in general, those materials that have a high erosion yield in the thermal energy plasma environment tend to cause less erosion of the Kapton H

Fig. 6 Ratio of Kapton H effective flux inside-to-outside of a Faraday cage as a function of asher measured erosion yield
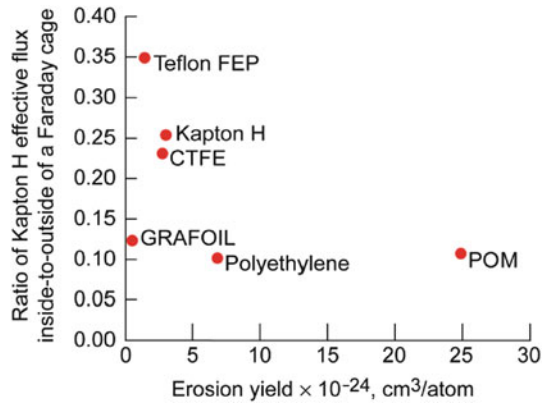
witness samples within the Faraday cages. This is probably due to a reduction in the atomic oxygen density in the Faraday cage caused by greater reaction with the sidewall materials. It is interesting to see the effect of the atomic oxygen entry area into the Faraday cage upon the erosion rate within the cage. The number density of atomic oxygen within a Faraday cage is dependent on flux impinging upon the cage, the area for the atomic oxygen entrance into the cage, and the losses within the cage. The losses include reaction and recombination with the wall materials and Kapton H sample at the base of the cage. Thus, the greater the area and erosion yield of materials that react with atomic oxygen, the more scavenging of atomic oxygen will occur. This will reduce the mass loss of Kapton H within the chamber relative to outside the chamber. If there is relatively little reaction with the walls of the chamber then the flux inside the chamber will be close to that outside the chamber.

Only when the aperture into the chamber is sufficiently small will the losses within the chamber become significant enough to start showing reductions in polymer erosion relative to outside the chamber. Figure 7 compares the ratio of mass loss inside-to-outside Faraday cages as a function of the fractional area of the entrance aperture into the inside chamber plotted on a semi-log format.

The data appears to have a simple power law dependence upon aperture area ratio. The ratio of mass loss of Kapton H inside-to-outside the Faraday cage is related to the ratio of aperture area to maximum inner lid area raised to the 0.268 power (shown as the curve fit line in Fig. 8). This results in a correlation coefficient of 0.95. The reason the ratio of mass loss inside-to-outside is not one for an inner lid fractional area of one is because there is also attenuation of the flux as the atomic oxygen travels between the outer lid and the outside of the inner lid. As can be seen from Fig. 8, an aperture of only 0.1 % of the inner lid area still produces a flux within the chamber that is ~10 % of that outside the Faraday cage. This implies that a small aperture on a spacecraft, which is oriented in the ram direction, has the potential to react a significant fraction of the ram fluence within the spacecraft.
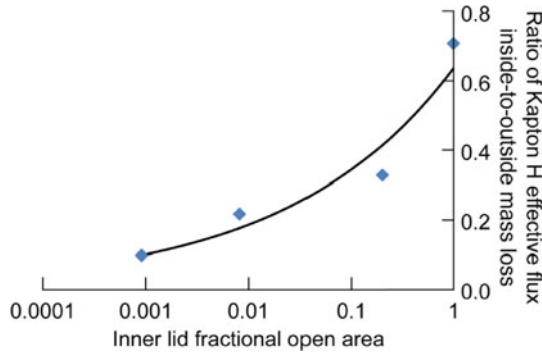
Fig. 7 Ratio of Kapton H effective flux inside-to-outside the Faraday cages as a function of the ratio of inner lid aperture to total inner lid area
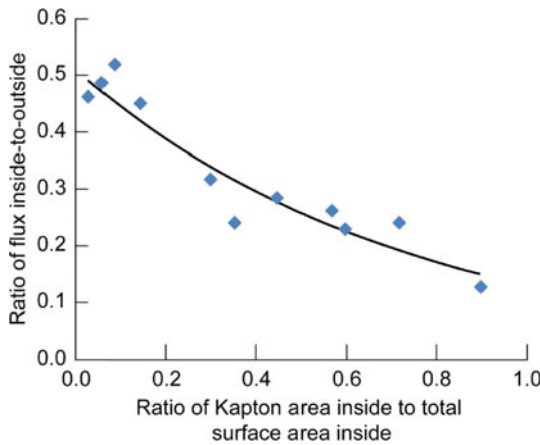
Fig. 8 Attenuation of atomic oxygen flux within a Faraday cage due the scavenging effect of varying amounts of Kapton H within the cage

Even though the atomic oxygen becomes thermally accommodated resulting in low reaction probabilities [3], it can bounce around until it reacts with an organic or reactive surface. This can be overcome by using sacrificial polymers within the spacecraft to scavenge the atomic oxygen that scatters within it.

The resulting attenuation of atomic oxygen flux within a Faraday cage, due the scavenging effect of varying amounts of Kapton H within the cage, is shown in Fig. 8 for the Faraday cage shown in Fig. 3c and d. This figure shows the dependence of the ratio of inside flux to outside flux upon the fraction of surface area inside the Faraday cage that is covered with Kapton H. The profile reasonably matches (a correlation coefficient of 0.9) and exponential dependence upon fractional coverage with Kapton. The results indicate that to reduce the flux by almost a factor of 5 within the cage, the Kapton fractional area coverage needs to be at least 90 %. Thus, for effective scavenging of trapped atomic oxygen it is important to use a significant area coverage of polymers that have high reaction probabilities.

4 Summary

A ground laboratory investigation was conducted to assess the erosion rate of atomic oxygen that enters cavities in an effort to simulate telescope, vents, or microwave openings on spacecraft in low Earth orbit. To accomplish this, tests were conducted in RF plasma ashers to measure the ratio of mass loss of Kapton H polyimide placed inside and outside of three types of scattering chambers: an open-ended chamber which allowed a flux of atomic oxygen, ions, electrons and UV radiation to enter, a cylindrical Faraday cage chamber in which atomic oxygen could enter but very little ion, electron, or UV radiation, and a larger rectangular Faraday cage chamber was used to assess the effect of the atomic oxygen entry area into the Faraday cage upon the erosion rate within the cage.

The results of the investigation indicate that even small openings which allow ram atomic oxygen to enter a spacecraft can cause considerable reaction within the spacecraft to sensitive surfaces. This is in spite of the fact that the atomic oxygen thermally accommodates to have low reaction probabilities. The use of polymers within a spacecraft can contribute to scavenging of the atomic oxygen thus significantly reducing its flux. Tests were conducted on five metals or metal oxides, five polymers and graphite to assess their ability to reduce atomic oxygen flux within spacecraft. The results of the testing indicate that metals or metal oxides that do not react with atomic oxygen do little to reduce the flux of atomic oxygen within the spacecraft. However, copper which does not form a protective oxide and does react with atomic oxygen and reduces atomic oxygen flux. Polymers that have low atomic oxygen erosion yields tend not to scavenge atomic oxygen, whereas polymers that have high atomic oxygen erosion yields tend to scavenge atomic oxygen. Thus, use of atomic oxygen scavenging polymers that have high atomic oxygen erosion yields are recommended to minimize atomic oxygen attack within spacecraft that have openings to the low Earth orbital environment.

References

1. Banks BA, de Groh KK, Miller SK (2004) Low Earth orbital atomic oxygen interactions with spacecraft materials, NASA/TM—2004-213400 and paper presented at the Fall 2004 meeting of the Materials Research Society, Boston, 29 Nov–3 Dec 2004
2. Banks BA, Miller SK, de Groh K (2004) Low Earth orbital atomic oxygen interactions with materials. Paper presented at the second international energy conversion engineering conference sponsored by the American Institute of Aeronautics and Astronautics, AIAA–2004–5638, NASA/TM—2004-213223, Providence, Rhode Island, 16–19 Aug 2004
3. Banks B, Miller S, de Groh K, Demko R (2003) Scattered atomic oxygen effects on spacecraft materials, NASA/TM—2003-212484, Jun 2003 and Proceedings of the 9th international symposium on materials in a space environment, Noordwijk, 16–20 Jun 2003, ESA SP-540, Sept 2003
4. ASTM E 2089–00 (2000) Standard practices for ground laboratory atomic oxygen interaction evaluation of materials for space applications

5. Silverman E (1995) Space environmental effects on spacecraft LEO materials selection guide. NASA contractor report 4661, section 6.2.2
6. de Groh KK, Banks BA, McCarthy CE, Rucker RN, Roberts LM, Berger LA (2008) MISSE 2 PEACE polymers atomic oxygen erosion experiment on the international space station. J High Perform Polym 20(4/5):388–409
7. Stambler AH, Inoshita KE, Roberts LM, Barbagallo CE, de Groh KK, Banks BA (2009) Ground-laboratory to in-space atomic oxygen correlation for the PEACE polymers. In: Kleiman J (ed) Proceedings of the 9th international conference on protection of materials and structures from space environment, Toronto, 20–23 May 2008. AIP conference proceedings, 1087, Melville

Optical and Scanning Electron Microscopy of the Materials International Space Station Experiment (MISSE) Spacecraft Silicone Experiment

Ching-cheh Hung, Kim K. de Groh, and Bruce A. Banks

Abstract Under a microscope, atomic oxygen (AO) exposed silicone surfaces are crazed and seen as "islands" separated by numerous crack lines, much analogous to mud-tile cracks. This research compared the degree of AO degradation of silicones by analyzing microscopic images of samples exposed to low Earth orbit (LEO) AO as part of the Spacecraft Silicone Experiment. The experiment consisted of eight silicone samples exposed to different AO fluence levels (ranged from 1.46 to 8.43×10^{21} atoms/cm^2) during two Materials International Space Station Experiment (MISSE) missions. Image analysis software was used to analyze optical microscopic images. The fraction of sample surface area occupied by crack lines was obtained and used to characterize silicone degradation and the resulted loss of specular transmittance. SEM images from the eight samples exposed to different AO fluences suggest a sequence of surface shrinkage, stress, and crack, followed by re-distribution of stress and shrinking rate on the sample surface. Energy dispersive spectra (EDS) indicated that after long AO exposure, silicone samples will eventually have a SiO$_2$ surface layer with some trapped CO and CO$_2$.

Keywords Silicone • Microscope • Atomic oxygen degradation • MISSE

1 Introduction

In LEO, the AO environment causes silicones to shrink at the surface as the AO exposed surface converts to a glassy brittle silicate layer, which then cracks due to shrinkage giving the surface a crazed, or mud-tile cracked, appearance [1]. Because

C.-c. Hung (✉) • K.K. de Groh
National Aeronautics and Space Administration, Glenn Research Center,
Cleveland, OH, USA
e-mail: ching-cheh.hung-1@nasa.gov

B.A. Banks
Alphaport, Inc., Cleveland, OH, USA

silicone is a commonly used pliable spacecraft material used for applications, such as the use of DC 93-500 to bond cover glasses to solar cells for the ISS photovoltaic array blankets, characterization of its degradation during space exposure is essential for this material to be used properly.

Because AO exposure typically does not cause silicones to lose mass, its AO degradation is better characterized by other changes that can be more accurately measured than mass loss (which is used for the majority of other hydrocarbon based materials) [2]. This study was accomplished by measuring surface cracks in silicone samples exposed to LEO AO on the exterior of the International Space Station as part of the Spacecraft Silicones Experiment flown on both Materials International Space Station Experiment 2 and 4 (MISSE 2 and 4) [3].

The degree of AO degradation of silicones was characterized and compared by analyzing optical microscope images of these samples. This Experiment consisted of eight DC 93-500 silicone samples exposed to eight different AO fluence levels (ranged from 1.46 to 8.43 $\times$ 10^{21} atoms/cm^2).

The most obvious effect observed for silicones during AO environment exposure are changes in surface morphology. Under optical microscopy, all space exposed silicone surfaces contain "islands" separated by numerous crack lines after they have been exposed to relatively low AO fluence exposures. Surface morphology changes, however, have not been used in the past to characterize silicone degradation during AO exposure. This is because of the difficulty in developing a standard method that can quickly, accurately and quantitatively analyze changes in surface morphology. The problem of using numbers to characterize changes in pictures, however, is greatly alleviated due to the recent advancement of imaging analysis computer software. In this study, images from an optical microscope were analyzed using commercially available software to determine the average area of "islands", the density of crack lines, and the percent of total area that is occupied by the crack lines. Relationships between these morphological parameters and the AO fluences were then examined and discussed. A scanning electron microscope (SEM) was used to analyze smaller features of the samples exposed to the LEO environment over several different fluence levels. Development of individual cracks as a function of fluence was examined. In addition, energy dispersive spectrum (EDS) was used to semi-quantitatively analyze the relative concentrations of silicon, oxygen and carbon. Results of the SEM investigation were used to infer the kinetics of atomic oxygen-silicone reactions.

2 Methods

2.1 Silicone Samples and LEO Exposure

Eight DC 93-500 samples were exposed to LEO ram exposure during two different MISSE missions (MISSE 2 and 4) such that each sample received a different

Table 1 MISSE 1 and 2 mission and space exposure summary

MISSE PEC	1 and 2	3 and 4
Launch mission	STS-105	STS-121
Date placed outside ISS	8/16/2001	8/3/2006
Location on ISS	PEC 1: high pressure gas tank	PEC 3: high pressure gas tank
	PEC 2: quest airlock	PEC 4: quest airlock
Orientation	Ram and Wake	Ram and Wake
Retrieval mission	STS-114	STS-118
Date retrieved from ISS	7/30/2005	8/18/2007
LEO exposure duration	3.95 years	1 year

AO fluence level. Four samples were exposed during each of the MISSE missions. Three of the four samples in each mission were covered with different thickness layers of Kapton H film in order for each of the samples in the same mission to receive a different AO fluence, as the AO needs to erode through the cover-laying Kapton before attacking the underlying silicone. The samples were 0.025 cm (10 mil) thick and were placed on 0.16 cm (1/16 in.) thick fused silica slides to keep the samples from bending and hence inducing cracking in the glassy oxidized layer [3]. The sample space exposures are summarized in Table 1. The sunlight and temperature history and the detailed results of previous studies of these samples are summarized elsewhere [3–5].

2.2 Optical Microscopy

The stereomicroscope used in this study was a MZ 16 by Leica Microsystems. Images of the samples are taken by a digital color camera (TRV3.3 by MicroPublisher). The camera is controlled by computer software (Image Pro Plus by Media Cybernetics), which acquire, process, analyze and measure the images from the camera. Image analysis used in this study is described in details in the following section.

The Leica Microsystems camera receives white light reflected from the sample surface. Since the crack region is less transparent and more reflective than the rest of the sample surface, the image obtained from the camera shows a network of white crack lines and black "island" areas. Figure 1a is an example of an optical microscope image This picture is from the MISSE sample exposed to the highest AO fluence (sample 2-E5-1, which did not contain a Kapton H cover and received an AO fluence of 8.43×10^{21} atoms/cm^2 during the MISSE 2 mission). In this report, all the optical microscope images were taken from an 1,110 μm × 830 μm area at the center of the sample surface. This is equivalent to 100× magnification.

The parameters to characterize the optical microscope images obtained from the image analysis software include: (1) the average area of islands, (2) the fraction of sample surface area that is occupied by crack lines, and (3) the total length of crack

Fig. 1 Optical micrograph of silicone DC93-500 exposed to 8.43 E21 fluence atomic oxygen in lower Erath orbit during MISSE 2 mission. (**a**) Original picture. (**b**) Convert original picture into *black* crack and *white* non-crack area. (**c**) Convert all cracks into *thin lines*

lines per unit area of the sample surface. These parameters were obtained using image analysis software. Details of this process are described below using Fig. 1 as the illustrating example.

The original picture (Fig. 1a) was at first modified by removing the shades of grey, so that the region occupied by crack lines became 100% white and the rest of the areas became 100% black. The black and white in this picture was then inverted to give Fig. 1b, which can be used by the software to calculate individual and total white (island) areas. The black thick lines (crack lines) in Fig. 1b were then reduced to thin lines by the software to result in Fig. 1c, from which the perimeter of individual areas as well as sum of perimeters of all areas in the picture can be calculated by the software.

The total length of the crack lines in the picture were then calculated as half of the sum of perimeters of all areas in the picture. Individual, total and average island areas were also calculated from Fig. 1c.

2.3 Scanning Electron Microscopy

A Hitachi S-3100 was used to take 350× pictures. A Hitachi S-4700II was used to take 1000× and higher magnification. The surfaces of samples were then individually coated with thin layers of 40% Pd-60% Au. Morphologies of all AO exposed silicone surfaces were examined. Pictures of every sample were taken at three different magnifications: 350×, 1000× and 5000×. From these images, the kinetics of shrink-crack interaction could be examined. EDS spectra of all AO exposed silicone surfaces, and a pristine sample surface, were also obtained and analyzed. All spectra were taken with the same instrument settings of 6KV and 10 μA. From each spectrum, the ratios of C to Si peak height and O to Si peak height were measured and calculated. The peak height ratios of AO exposed samples were then compared to those of the pristine sample. From these results, a semi-quantitative analysis can be made to measure the changes of the chemical composition of silicone resulting from AO exposure over a long period of time.

Table 2 Morphological parameters of silicone samples exposed to different AO fluencies during MISSE 2 and 4 missions

Fluence $\times E^{21}$	Total crack length in 1 mm^2 of sample (mm)	Crack/sample surface area ratio	Average Island area (μm^2)	Approx. crack width (μm)
8.43	52	0.56	979	11
8.18	59	0.53	696	9
8.01	46	0.45	1,191	10
7.75	48	0.49	1,146	10
2.14	42	0.38	1,234	9
1.89	41	0.35	1,472	9
1.72	27	0.25	3,089	9

3   Results and Discussions

3.1   Optical Microscopy

'It was observed that the silicone sample with the lowest AO fluence (sample 4-E22-5) has a large amount of debris material on it, seen primarily as white spots and clusters. These are residual fragments of the Kapton H cover layer placed on top of the silicone for the purpose of adjusting AO exposure of the under-laying silicone to a lower level. Since the residue resulted in strong interference during image analysis, optical microscope data obtained from this sample were not further examined.

The three different characterization parameters (the average area of islands, the fraction of sample surface area that is occupied by crack lines, and the total length of crack lines per unit area of the sample surface) for the samples that were degraded by AO exposure to seven different fluence levels are summarized in Table 2. Since average crack widths can be estimated from crack length and crack area described above, they were calculated and also shown in Table 2. Figure 2 contains plots and corresponding trend lines of these morphological parameters plotted against the AO fluence.

Figure 3 is a plot of crack length per area vs crack area per total area. It shows that crack area increases almost linearly with crack length, indicating that crack width does not change much. Newly formed cracks continue to have the same width as the old ones until the fluence reaches a very high level. This suggests that crack propagation is mostly either by growth of new cracks or by lengthening of the old cracks, until the island areas become thick, glassy, and small.

As described previously, the image of AO exposed silicone samples obtained from reflected light shows white crack lines and black "island" areas. This illustrates that the island areas transmit light, and the crack areas are more reflective.

A consequence of the growth of crack area would therefore be a loss of specular transmittance with fluence. This would be a problem for Fresnel concentrators made of DC 93-500, or similar behaving silicones, which could represent large
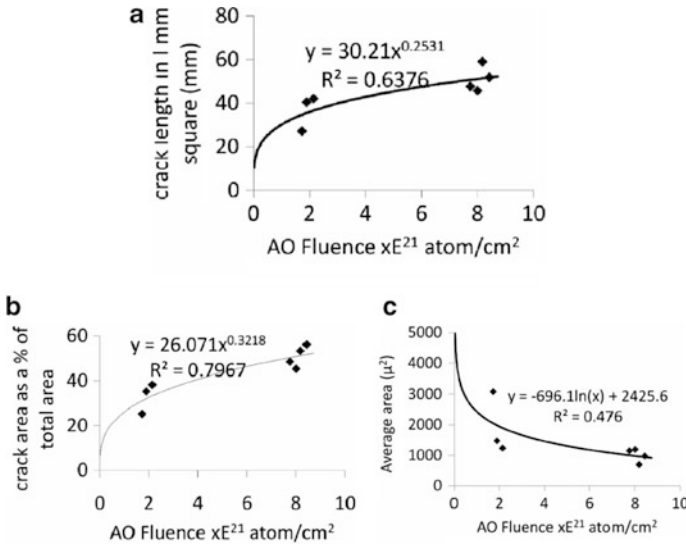
Fig. 2 Plots and the trend lines of morphological parameters as a function of the fluence. (**a**) Total length of cracks in mm within 1 mm^2 of atomic oxygen exposed silicone samples. (**b**) Crack area as a % of area of atomic oxygen exposed silicone samples. (**c**) Average island area
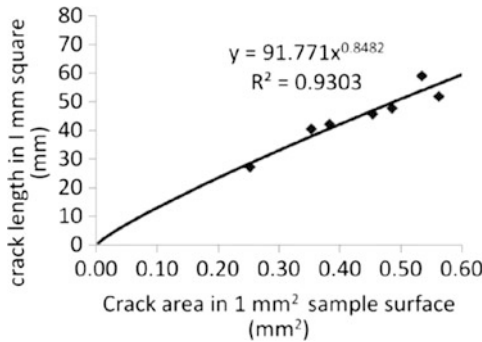
Fig. 3 Crack surface area increases almost linearly with crack length, indicating the crack width does not change much during the entire time of atomic oxygen exposure

losses for concentrator based photovoltaic systems. Light can be specularly transmitted through the islands that are free of cracks, however, the bottom of cracks are not parallel to the pristine surface of the DC 93-500 and thus cause the light passing through them to be diffusely scattered. Assuming the specular transmittance (1) is zero at the crack area and (2) does not change due to AO exposure at the island area, then the % of specular transmittance loss would be the same as the % of crack area, or the y axis of Fig. 2b. From this point of view crack area as a % of total surface area seems to be a more relevant parameter to characterize the transmittance loss due to AO exposure.

Fig. 4 Island area as a % of area of atomic oxygen exposed silicone samples
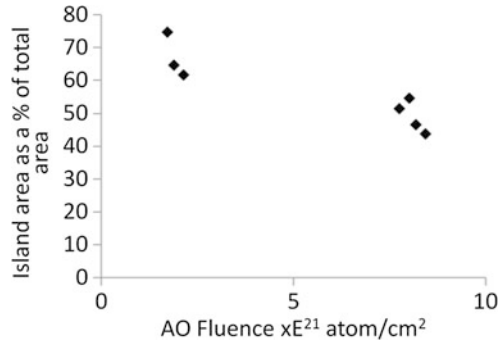
For the AO fluence level studied (1.72 to 8.43 $\times$ 10^{21} atom/cm^2), adding island area as percent of total area to crack area as percent of total area (Fig. 2b) would result in 100 %. Therefore, for the plot of percent island area (y) vs fluence (X), the data fitting (Fig. 4) would be

$$y = 100 - (26.071X^{0.3218}) \qquad\qquad X \geqslant 1.72$$

$$y = 100 - (26.071)1.720^{0.3218}(X/1.72) \qquad X \leqslant 1.72$$

The first equation is from data fitting number in Fig. 2b. The second equation assumes a linear relation at a fluence level from zero to 1.72 $\times$ 10^{21} atom/cm^2, the lowest fluence examined in this research.

The above empirical equation suggests the specular transmittance loss would be proportional to AO fluence when the fluence is low, and proportional to one third power (i.e.,$X^{0.3218}$) of the AO fluence when the fluence is high.

3.2 Scanning Electron Microscopy

The representative SEM images of silicone samples exposed to different AO fluencies are presented in Fig. 5a to d. It can be seen that at lower AO exposure levels (Fig. 5a and b), the cracks are relatively simple and can be understood as the result of shrinkage of a thin layer of silicone surface due to silicone-AO reactions.

It can also be seen that new crack lines split old crack lines, and some old crack lines seem to stop cracking after some time, as many new crack lines become wider and deeper than the old crack lines. This data suggests that the oldest and first cracks, which are narrow, occur on surfaces that are under only small tensile stress. After the event of a crack, there will be a re-distribution of stress and tensile stress parallel to the crack becomes reduced. However, in directions approximately perpendicular to the initial cracks, stress builds up to accumulate to greater than that at the time of the initial cracks. This causes the newest cracks to open wider and
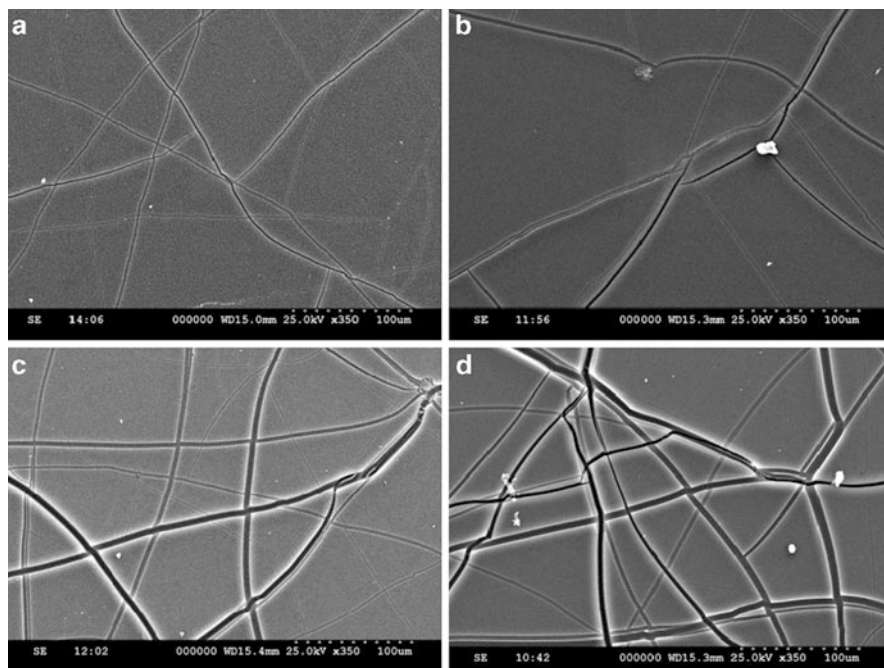
Fig. 5 SEM pictures of silicone exposed to different level of AO fluences (**a**) 1.72×10^{21} atom/cm^2 (**b**) 2.14×10^{21} atom/cm^2 (**c**) 7.75×10^{21} atom/cm^2 (**d**) 8.43×10^{21} atom/cm^2

deeper than the initial cracks. In general, the process continues to cause the newest branch cracks to be wider and deeper than older cracks. Consequently, some of the old crack lines diminish their cracking because the stress on them decreases. The more mud tiled the surface becomes, the deeper the thickness of silicone oxidation, which grows slower with fluence because the atomic oxygen has a more difficult time migrating deep to unoxidized silicone. Although the surface gradually becomes very cracked, the islands remain well adhered because their base is a gradual transition to unoxidized silicone.

It would only be for very thin silicone membranes where oxidation could occur through the full thickness causing the silicone to be significantly converted to silica that the mud tiles could break apart. This may be a durability threat for silicone Fresnel lenses, inflatable structures, or silicone coatings in low Earth orbit.

The results give a complex overall picture of the morphology change of silicone surfaces during silicone-AO reactions. Shrinkage causes stress. Thin AO exposed silicone is brittle. After long AO exposure, the part of the surface that has not yet cracked develops a thick glassy layer, which is structurally stronger than a newly formed very thin oxide layer. Shrinkage and stress of thin AO exposed layers cause cracks. Cracks then cause sudden surface movements, which cause stress on the surface to re-distribute, which results in a new shrink rate on the surface and new crack rate at the crack lines. The activity of cracking increases for some crack lines,
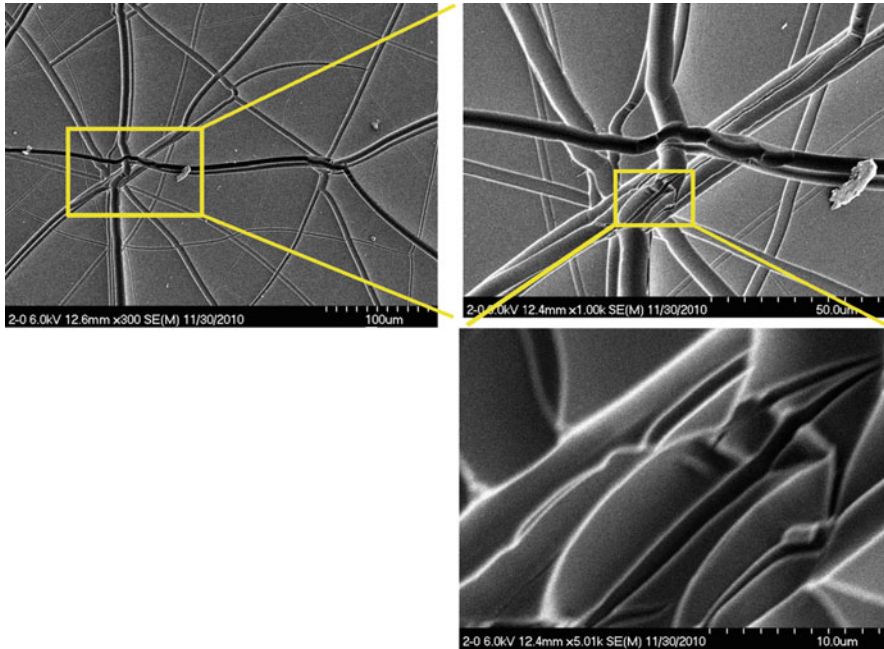
Fig. 6 An illustration of the complex surface morphology after repeated shrink, crack and stress redistribution (AO fluence $= 8.43 \times 10^{21}$ atom/cm^2)

Table 3 Calculated values of the semi-quantitative atomic C/Si and O/Si concentration of the AO exposed sample relative to the pristine sample	AO fluence		
	$\times 10^{21}$ atom/cm^2	(O/Si)/(O/Si)$_p$	(C/Si)/(C/Si)$_p$
	1.46	1.52	0.32
	1.72	1.73	0.28
	1.89	1.65	0.35
	2.14	1.95	0.34
	7.75	2.58	0.16
	8.01	2.47	0.21
	8.18	2.06	0.17
	8.43	2.50	0.22

but diminishes for some others. Above all of these, the AO continues to react with the entire silicone surface, most likely at a higher rate at the stressed crack lines because those are places where some interior silicone is newly exposed to AO. The result is the newly formed thin oxide layer which is more inclined to crack under stress.

Figure 6a to c are pictures of the complex crack morphology from the highest AO fluence exposed sample in this research (fluence $= 8.43 \times 10^{21}$ atom/cm^2)

The semi-quantitative atomic C/Si and O/Si concentrations of the flight samples relative to the pristine sample were calculated and are shown in Table 3. The carbon

content decreased relatively quickly at the beginning when the fluence level was lower than the MISSE 4 value, but leveled to 20% of the pristine value at the MISSE 2's fluence. The oxygen content appears to increase at a slower rate.

Assuming the pristine DC93-500 has a C/Si and O/Si values of 2 and 1, respectively, Table 3 would suggest the highest AO fluence exposed silicone has C/Si and O/Si values of about 0.44 and 2.50, respectively. From these numbers, it is theorized that the AO exposed silicone will eventually become SiO_2 with a mixture of CO and CO_2 trapped inside.

4 Conclusions

Eight DC 93-500 samples exposed to eight different AO fluence levels (ranged from 1.46 to 8.43×10^{21} atoms/cm^2) during two different MISSE missions (MISSE 2 and 4) were examined using optical microscopy, scanning electron microscopy and energy dispersive spectroscopy. From image analysis software, (1) the average area of islands was found to range from 1,000 to 3,100 μm^2; (2) the total length of crack lines per unit area of the sample surface was found to range from 27 to 59 mm crack length per mm^2 of sample surface;(3) the fraction of sample surface area that is occupied by crack lines was found to range from 25 to 56% for the fluence levels tested; and (4) average crack width can be estimated from crack length and crack area described above, and was calculated to be about 10 μm.

The fraction of sample surface area that is occupied by crack lines is believed to be the most useful morphological parameter in characterizing the degree of silicone degradation caused by AO exposure.

The series of SEM images from the eight MISSE flight samples exposed to different AO fluences suggest a complex sequence of surface stress due to shrinkage, cracking, and then re-distribution of stress and shrinking on the sample surface. The data suggests that the oldest cracks, which are narrow, occur on surfaces that are under only small tensile stress. After a "crack event" there is a re-distribution of stress and the tensile stress parallel to the crack becomes reduced. However, in directions approximately perpendicular to the initial cracks, stress builds, which causes the newest cracks to be wider and deeper than the initial cracks. The energy dispersive spectra (EDS) indicated that upon AO exposure, carbon content quickly decreased to 32% of the pristine value for the least exposed sample in this set of experiments (1.46×10^{21} atoms/cm^2), but leveled to 20% of the pristine value for the most exposed sample in this set of experiments (8.43×10^{21} atoms/cm^2). The oxygen content appears to increase at a slower rate. The least and most AO exposed samples were, respectively, 52% and 150% above the pristine values. The highest AO fluence exposed flight sample appears to have a surface layer which contains SiO_2 with perhaps some CO and CO_2 trapped in the SiO_2 layer.

References

1. de Groh KK, McCollum TA (1995) Low Earth orbit durability of protected silicone for refractive photovoltaic concentrator arrays. J Spacecraft Rockets 32(1):103–109
2. Hung C-c, Cantrell G (1994) Reaction and protection of electrical wire insulators in atomic-oxygen environments, NASA TM 106767
3. de Groh K, Banks B, Dever J, Jaworske D, Miller S, Sechkar E, Panko S (2008) NASA Glenn Research Center's Materials International Space Station Experiments (MISSE 1-7), NASA TM-2008-215482
4. Pippin G (2008) Summary status of MISSE-1 and MISSE-2 experiments and details of estimated environmental exposures for MISSE-1 and MISSE-2. Final report Air Force contract 02-S470-011-C1
5. Pippin G (2008) Summary status of MISSE-3 and MISSE-4 experiments and details of estimated environmental exposures for MISSE-3 and MISSE-4. Final report Universal Technology Corporation contract 07-S568-030-C1-R1 (Government prime contract FA8650-050D-5807)

The Effect of Tensile Stress on the Erosion of Polyimide in an Atomic Oxygen Environment

Ronen Verker, Dan Hassin, Nurit Atar, and Eitan Grossman

Abstract Polyimide (PI) films, used as thermal blankets for satellites, are exposed to AO irradiation and subjected to hypervelocity debris impacts. Ground based experiments showed that due to these impacts, residual tensile stresses are formed in the PI causing accelerated erosion in an AO environment. However, fundamental research in regard to stress related AO erosion effect is missing.

The objective of this work is to study the erosion mechanism of Kapton (commercial PI) films which are subjected to tensile stresses in an environment simulating AO exposure. The combined effect of the tensile stresses' magnitude and direction on Kapton films erosion while exposed to AO environment are studied in terms of changes in surface morphology.

The results reveal that the Kapton's surface morphology is affected by the stress intensity and by its applied direction relative to the polymer chains direction. At low AO fluencies, without applied stress, a classical carpet-like morphology was attained. Under combined effect of stress and AO irradiation, an ordered surface was formed almost orthogonal to the direction of the applied stress.

Keywords LEO • Polyimide • Birefringence • Atomic oxygen • Stress • Erosion

1 Introduction

Most of the satellites launched nowadays are being sent into low Earth orbit (LEO) altitudes, ranging from 200 to 800 km. The External surface of most of these satellites is made of Kapton, a commercial version of polyimide (PI). The degrading for polymers environment in LEO includes atomic oxygen (AO), ultraviolet (UV) and ionizing radiation, ultrahigh vacuum (UHV), thermal cycling, micrometeoroids

R. Verker (✉) • D. Hassin • N. Atar • E. Grossman
Space Environment Department, Soreq NRC, Yavne 81800, Israel
e-mail: rverker@soreq.gov.il

and orbital debris [1, 2]. Due to separate, combined or synergistic interactions with these space hazards, polymers in particular suffer a relatively rapid erosion, chemical and structural modification, and surface roughening [3, 4].

AO, produced by the photo-dissociation of molecular oxygen in the upper atmosphere, is the main constituent of the residual atmosphere in LEO [5]. AO is considered as one of the most serious hazards to spacecraft external materials. Although the oxygen atoms have low density ($\sim 1 \times 10^8$ atoms/cm^3) and low energy (~ 0.1 eV), their collision with the external surfaces of spacecraft, orbiting at a velocity of 8 km/s, results in impacts equivalent to an energy of ~ 5 eV and flux of 10^{14}–10^{15} O-atoms/(cm^2 s) [6].

Hypervelocity debris at LEO altitudes contain, mainly, man-made constituents [6, 7]. Typical velocities of debris particles range from a few kilometers per second up to 16 km/s, making these hypervelocity particles a threat to spacecraft [8, 9]. Ground based experiments showed that due to these impacts, residual tensile stresses are formed in PI causing accelerated erosion in an AO environment [10].

Shimamura et al., [11] exposed stressed PI films both in LEO and in ground-based simulation systems. The samples were stressed to a maximum of 7 MPa, which is in the elastic region of PI stress-strain curve and exhibits only a small percentage of the yield stress of PI [12]. The combined effect of stress and AO irradiation did not affect the PI mechanical properties [11].

In a previous work by Verker et al., [13] PI was locally stressed and exposed to a simulated AO environment. As a result of this exposure the PI roughness increased. The increased roughness is a result of a combined effect of stress and AO attack [13]. However, during these previous experiments the amount and direction of the applied stress was not well controlled.

The objective of this work is to perform a mechanochemical study in regard to the erosion mechanism of PI films. Mechanochemistry is associated with the mechanical activation of covalent bonds [14]. The PI films were subjected to a controlled amount and lateral angle (relative to the polymer principal orientation direction) of the tensile stresses in an environment simulating AO exposure. The separate and combined effects of the tensile stresses' magnitude on the PI erosion are studied in terms of changes in the surface morphology.

2 Experimental

The material studied in this work is commercial 25 μm-thick Kapton-HN film (DuPont, Inc.). The Kapton samples were die cut into dogbone-shaped specimens with a constant width of 4 mm in the gauge region. Kapton is a semicrystalline polymer characterized by anisotropic mechanical and optical properties. The film's anisotropy is attributed to a higher degree of orientation formed as a result of the machine's drawing direction during the manufacturing process. Due to this orientation the Kapton film has a diversity of about 30 % in its ultimate tensile stress, while stress is applied parallel or perpendicular to its principal orientation direction [15].

The experimental work was performed using a small mechanical system specially designed for combined stress and AO irradiation experiments and fitted to operate in a small vacuum chamber of 70 mm in diameter. This mechanical system allows for controlled formation of tensile stresses in thin Kapton films while being subjected to an environment simulating AO exposure. The system was designed to apply a maximum stress of 200 MPa, above the Kapton's ultimate tensile strength point.

A conventional RF-plasma reactor (15 W, 13.56 MHz, Model PDC-3XG from Harrick), operating at 300 mTorr of dry air, was used to simulate the effect of AO in LEO. The mechanical system was stressed to the desired value and was put inside the plasma system for AO irradiation. In order to perform a quasi-iso-stress test and to decrease creeping effects, the mechanical system was re-stressed every 24 h to its original value and the area of the irradiated sample was re-measured. Using this setup stress -AO erosion tests were performed under stresses varying from 0 to 120 MPa.

In order to measure the AO equivalent flux a reference Kapton sample was attached next to the stressed sample. The reference sample was not subjected to any stresses during the irradiation and its mass loss was measured at the end of each test.

Since Kapton is characterized by anisotropic mechanical properties, its principle orientation direction must be identified. The stress-AO irradiation experiments must take into consideration the angle between the material's principle orientation direction and the direction of the stress which is applied on the sample.

The Kapton's anisotropy is expressed not only by mechanical characteristics but also by an optical anisotropy known as birefringence. Namely, the Kapton film is characterized by two unequal indices of refraction (n_1, n_2) along two principle optical axes. This optical phenomenon was used to determine the principle mechanical orientation of the Kapton. The optical axes were measured by a polarimetry method and the mechanical orientation direction was identified correspondingly.

Birefringence causes the light traveling along one axis to experience a different refractive index than light travelling along the other axis. It is possible to refer light polarized at any other direction as a combination of its projections on the two optical axes. The measurement presented in this work is based on the fact that when a linearly polarized light beam enters an optically anisotropic sample, the birefringence of the sample produces a relative phase shift between the two polarization components related to the different optical axes. This phase shift along the pathlength inside the sample causes a change in the polarization orientation, or optical retardation, which can be measured [16]. Schematic representation of the optical measuring system is shown in Fig. 1.

The system is composed of a light source, two polarizers, a sample and an optical detector. The optical measurements were performed using a green laser (532 nm wavelength, output power 16 mW from Photo Suwetch Inc.). Polarization of the laser beam was achieved using a polarizing beamsplitter cube from Thorlabs. The sample was mounted between two parallel polarizers on a manual rotating frame characterized by 10° rotation intervals. A laser power meter was used as an optical power-meter (Model Nova from Ophir).

Fig. 1 Schematics of the
system for measurement of
optical retardation and optical
principle axes used for
measuring PI films
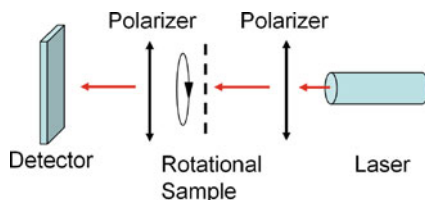
The basic principle of the measurement is as follow: When polarized light
(according to the direction of the first polarizer) enters the anisotropic sample the
direction of the polarization is changed. Since the polarizers are parallel, the second
polarizer attenuates any polarized light in a direction different from the original
polarization. According to the change in the power of the light at the exit of the
second polarizer during rotation of the sample the directions of the principle optical
axes can be indicated.

The surface morphology of the samples was studied using an Atomic Force
Microscope (AFM, Nanoscope IV MultiMode from Veeco). Power Spectral Density
(PSD) analysis of the AFM results was performed using the NanoScope 7 software
package by Digital Instruments/Veeco.

3   Results and Discussion

A 25 μm-thick Kapton sample was located on a rotatable frame between the two
parallel polarizers using the optical measuring system described in Fig. 1. The
dependence of the laser power at the exit of the second polarizer on the rotation
angle is shown in Fig. 2a, where 0° is defined as the direction transverse to the
machine's rolling direction.

Maximum power was obtained when there was no change in the direction of
polarization, i.e., the polarization of the entering light lay on one of the optical axes.
Maximal power was obtained at 25° and 115° rotation angles. This indicates that
the two optical axes are transverse one to another and lay 25° and 115° from the
machine's transverse direction. Minimum power was obtained when there was
maximum change in the direction of polarization, i.e., the polarization of the
entering light lay between the optical axes (45° from each optical axis).

One can notice that the power at 115° is lower than the power at 25°. The
difference between the two maximal power spots is derived from the ability to
polarization of the Kapton sample itself. This indicates that the direction of the
oriented microstructure is along the 115° optical axes. According to these
measurements the principal orientation direction, which is the material's mechani-
cally strong direction, is 115° from the machine's transverse direction. Previous
work showed that high strength and stiffness and low ultimate elongation were
found along the principal orientation direction in the same type of Kapton films.
Low strength and stiffness and high ultimate elongation were found transverse to
the principal orientation direction [15].
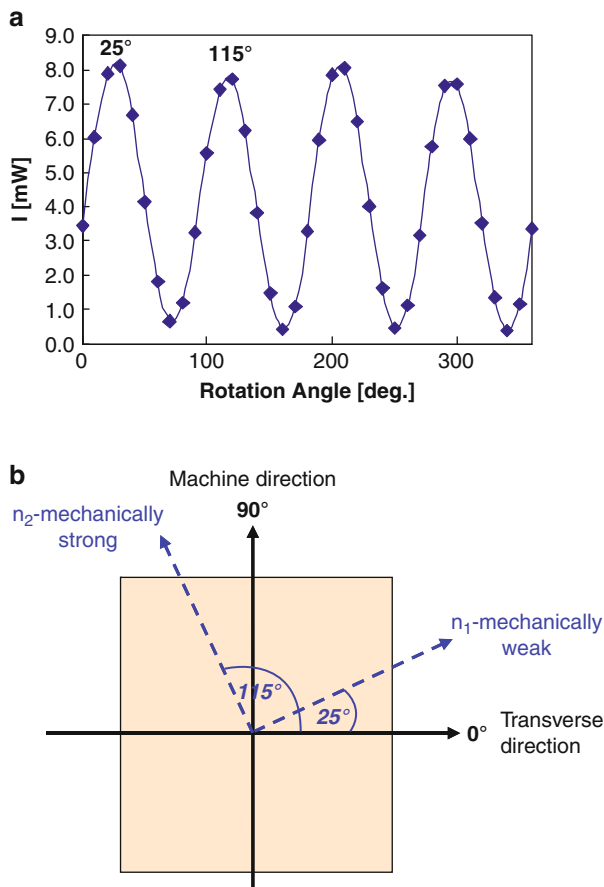
Fig. 2 Dependence of the polarized light optical transmittance intensity of a 25 μm-thick Kapton sample on its rotation angle (**a**). Polar plot of the Kapton sample (**b**), showing the machine and transverse directions (*black solid arrows*) and the principle axes of the refractive indexes (*blue dashed lines*), taken from Fig. 2a

Figure 2b presents a polar plot sketched according to measurements presented in Fig. 2a of the 25 μm-thick Kapton sample showing (black solid arrows) the production machine direction (at 90°) and its transverse direction (at 0°). The plot also shows (blue dashed line arrows) the principle orientation direction (denoted as n_2) at 115° and its transverse direction (denoted as n_1) at 25°. The results that are presented hereafter were all performed by applying stress parallel to the Kapton's principle orientation direction (115°) that is the mechanically strong direction.

During this work two sets of experiments were performed. In the first set that was defined as a reference set of experiments, only stresses were applied in the n_2 direction while the samples were under vacuum conditions, but without AO irradiation. In the second set, the combined effect on the Kapton's surface morphology of stresses, applied in the n_2 direction, and AO irradiation was examined.
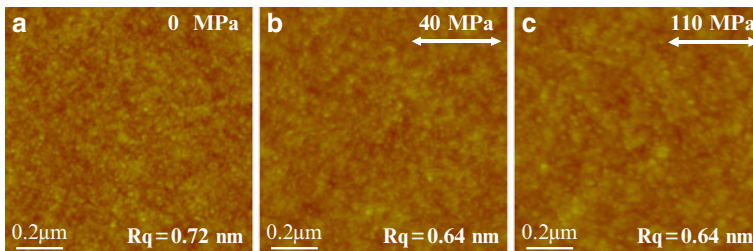
Fig. 3 AFM images of unstressed 25 μm-thick Kapton sample (**a**), and samples subjected to stresses of 40 MPa (**b**) and 110 MPa (**c**) in the 115° (n_2) direction for 90 h in low vacuum environment. Z-scale 25 nm
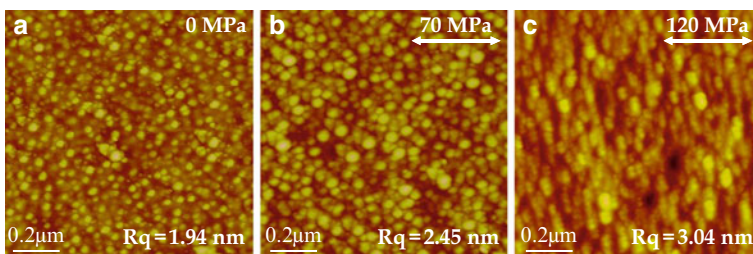
Fig. 4 AFM images of 25 μm-thick Kapton samples exposed to an AO fluence of 1.8×10^{19} AO/cm^2 while subjected to stresses of 0 MPa (**a**) 70 MPa (**b**) and 120 MPa (**c**) in the 115° (n_2) direction for 90 h. Z-scale 25 nm

Figure 3 shows the results of AFM images from the reference set of experiments of unstressed 25 μm-thick Kapton sample (a) and samples subjected to stresses of 40 MPa (b) and 110 MPa (c) in the n_2 direction for 90 h in low vacuum environment of the plasma chamber. A period of 90 h is a typical AO exposure time. The lateral angle of the applied stress relative to the image layout is denoted by arrows. The results presented in Fig. 3 show that stress alone does not have any significant effect on the morphology of the Kapton either at low stresses of 40 MPa which are in the elastic region of the Kapton's stress-strain curve or at 110 MPa which is in the plastic region of the Kapton's stress-strain curve [12]. No significant difference was obtained for the Root Mean Square (RMS) surface roughness, R_q, as a result of the exposure of the samples to various amounts of stresses under vacuum conditions.

Figure 4 shows AFM images from the combined stress-AO irradiation effect set of tests of 25 μm-thick Kapton samples. These samples were exposed to an AO fluence of 1.8×10^{19} AO/cm^2 while subjected to stresses of 0 MPa (a) 70 MPa (b) and 120 MPa (c) in the n_2 direction for 90 h. The lateral angle of the applied stress relative to the image layout is denoted by arrows.

Figure 4a shows the surface morphology of a reference sample which was exposed to AO irradiation alone. The surface morphology of this sample is characterized as carpet-like, which is typical to erosion of Kapton by AO [17]. Figure 4b shows the surface morphology of a sample which was exposed to AO irradiation while being
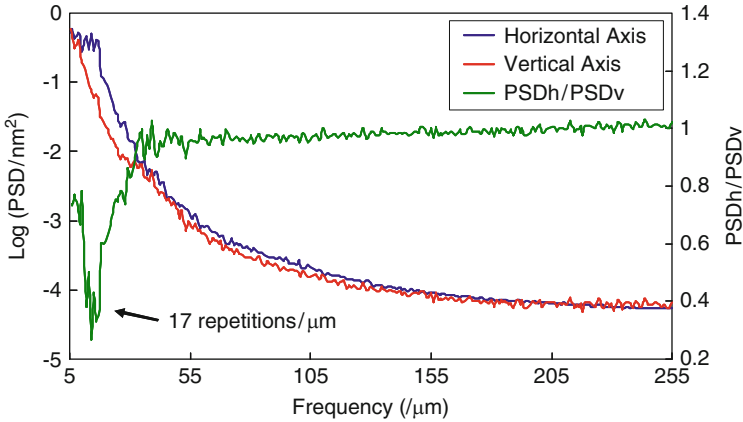
Fig. 5 PSD image analysis measurements of Fig. 4c AFM image

under a stress of 70 MPa which is in the elastic region of the Kapton's stress-strain curve [12]. The surface morphology of this sample has also carpet-like morphology but the effect of stress on the morphology can be noticed by the larger grains formed as a result of the combined effect compared to the reference unstressed sample. While the reference sample's grains (Fig. 4a) have a typical diameter of about 30 nm, the 70 MPa stressed sample's grains (Fig. 4b) have a diameter of about 45 nm. This difference can also be noticed by the RMS values: 1.94 nm for the reference sample and 2.45 nm for the 70 MPa stressed AO irradiated sample.

Figure 4c shows the surface morphology of a sample which was exposed to AO irradiation while being under a stress of 120 MPa which is in the plastic region of the Kapton's stress-strain curve [12]. The surface of this sample does not show carpet-like morphology but is rather totally different compared to the previous surfaces. The influence of the combined effect of stress and AO irradiation on the morphology in this case is prominent, characterized by an oriented morphology, almost orthogonal to the direction of the applied stress. This morphology repeated itself in several experiments. The RMS value of this sample was the largest compared to the previous two, 3.04 nm.

The cause to this new morphology can be attributed to two reasons: (1) selective faster AO erosion of amorphous regions and exposure of a crystalline structure which already exists underneath the Kapton's surface or (2) formation of a large scale crystalline structure as a result of the strains the Kapton experience while under stress and AO irradiation.

Figure 5 shows the PSD plots of the AFM result of Fig. 4c both horizontally (parallel to the stress direction) and vertically (orthogonal to the stress direction). Also given in Fig. 5 is the quotient of the horizontal PSD (PSDh) by the vertical PSD (PSDv) at any given frequency. The PSD function provides a graphic representation of the amplitude of a surface's roughness as a function of the spatial frequency of features present on the roughness. It reveals periodic surface features and determines how such features are distributed and how frequent they appear.

One of the biggest advantages of the PSD function is its ability to estimate the anisotropy of surfaces [18].

The PSD plot in the vertical direction (red line) decays exponentially as the frequency increases. The PSD plot in the horizontal direction (blue line) shows a shoulder at a frequency of 17 repetitions/μm. The difference between the horizontal PSD plot and the vertical PSD plot demonstrates the anisotropy of the surface as a result of the combined effect of AO irradiation and stress. This anisotropy is even more pronounced as the horizontal PSD is divided by the vertical PSD (green line), showing again a peak at a frequency of 17 repetitions/μm. This frequency correlates to features 60 nm wide which are repeatedly present in the sample horizontal direction, which is the stress direction. These 60 nm wide features can easily be seen in Fig. 4c as elongated features with varying length of 100–300 nm.

Ojeda et al. studied the morphology of the Pyromellitic dianhydrideoxydianiline (PMDA-ODA) PI crystals. This material has the same molecular structure as Kapton. According to their work, close examination of particular crystal showed that it consisted of independent bundles of lamellae. These bundles had an average width of about 250 nm. Between the lamellar structures amorphous regions were present. Generally, the thickness at the outer perimeter of PMDA-ODA lamellar crystals ranged from 5 to 15 nm, and the length of these lamellar crystals ranging in size from 0.5 to 5 μm [19].

It is therefore suggested that the elongated features apparent in Fig. 4c are associated with these bundles of lamellar structures. The appearance of the elongated features may be associated with the stresses that were applied orthogonally. The stresses caused the lamellar structures to separate, allowing AO to penetrate and erode more easily the amorphous regions between the crystalline areas.

Factor et al. studied PMDA-ODA PI structure using grazing incidence X-ray scattering of thin films. They show that PMDA-ODA PI has different amounts of crystallinity at the surface and in the bulk. According to their work the surface layer of the PI thin film had higher crystallinity than the bulk of the material [20].

4   Summary and Conclusions

The effect of applied tensile stress on the erosion of Kapton under AO irradiation was studied. The stress was applied along the Kapton film principle mechanical axis which was found to be different then it's principle rolled manufacturing axis. The application of stress was performed by a mechanical system specially designed to operated in an AO environment.

The results reveal that the Kapton's surface morphology is affected by the stress intensity and its direction relative to the polymer chains direction. At low AO fluencies, without applied stress, a classical carpet-like morphology was attained. Under combined effect of stress and AO irradiation, an ordered surface was formed almost orthogonal to the direction of the applied stress. The appearance of the ordered features may be associated with the stresses that were applied orthogonally.

The stresses caused the Kapton's lamellar structures to separate, allowing AO to penetrate and erode more easily the amorphous regions between the crystalline areas.

References

1. Tribble AC (2003) The space environment: implementation for spacecraft design, Princeton, NJ: Princeton University Press, p 82
2. Silverman EM (1995) Space environmental effects on spacecraft e LEO material selection guide. NASA contractor report no. 4661. NASA Langley Research Center, Langley
3. Grossman E, Gouzman I (2003) Space environment effects on polymers in low Earth orbit. Nucl Instrum Meth B 208:48–57
4. Grossman E, Gouzman I, Viel-Inguimbert V, Dinguirard M (2003) Modification of a 5-eV atomic-oxygen laser detonation source. J Spacecraft Rockets 40:110–113
5. Minton TK, Garton DJ (2001) Dynamics of atomic-oxygen-induced polymer degradation in low Earth orbit. In: Advanced series in physical chemistry: chemical dynamics in extreme environments. World Scientific, Singapore, pp 420–489
6. Hastings D, Garrett H (1996) Spacecraft-environment interactions. Cambridge University Press, Cambridge
7. Tennyson RC, Shortliffe G (1997) MOD impact damage on composite materials in space. In: Proceedings of the 7th international symposium on materials in space environment, Toulouse, France, vol 399, pp 485–492
8. Meshishnek MJ (1995) Overview of the space debris environment. Aerospace report TR-95 (5231)-3, pp 1–28
9. Schonberg WP (2010) Protecting Earth-orbiting spacecraft against micro-meteoroid/orbital debris impact damage using composite structural systems and materials: an overview. Adv Space Res 45:709–720
10. Verker R, Grossman E, Gouzman I, Eliaz N (2008) POSS-polyimide nanocomposite films: simulated hypervelocity space debris and atomic oxygen effects. High Perform Polym 20:475–491
11. Shimamura H, Nakamura T (2010) Investigation of degradation mechanisms in mechanical properties of polyimide films exposed to a low earth orbit environment. Polym Degrad Stab 95:21–33
12. Du-Pont, Technical bulletin (2008)
13. Verker R, Grossman E, Gouzman I, Eliaz N (2007) Residual stress effect on degradation of polyimide under simulated hypervelocity space debris and atomic oxygen. Polymer 48:19
14. Beyer MK, Clausen-Schaumann H (2005) Mechanochemistry: the mechanical activation of covalent bonds. Chem Rev 105:2921–2948
15. Blumentritt BF (1978) Anisotropy and dimensional stability of polyimide films. Polym Eng Sci 18:1216–1219
16. Saleh BEA, Teich MC (2007) Fundamentals of photonics, 2nd edn. Hoboken, New-Jersey, USA
17. Zhao XH, Shen ZG, Xing YS, Ma SL (2001) A study of the reaction characteristics and mechanism of Kapton in a plasma-type ground-based atomic oxygen effects simulation facility. J Phys D Appl Phys 34:2308–2314
18. Sawant PD, Sabri YM, Ippolito SJ, Bansal V, Bhargava SK (2009) In-depth nano-scale analysis of complex interactions of Hg with gold nanostructures using AFM-based power spectrum density method. Phys Chem Chem Phys 11:2374–2378
19. Ojeda JR, Martin DC (1993) High-resolution microscopy of PMDA-ODA poly(imide) single-crystals. Macromolecules 26:6557–6565
20. Factor BJ, Russell TP, Toney MF (1993) Grazing-incidence x-ray-scattering studies of thin-films of an aromatic polyimide. Macromolecules 26:2847–2859

Critical Evaluation of Testing Results for Russian and Western Space Materials in Ground-Based Simulator Facilities and in Space Experiments

Z. Iskanderova, J. Kleiman, V. Issoupov, S.F. Naumov[†], S.P. Sokolova, A.O. Kurilenok, L.S. Novikov, V.N. Chernik, A.V. Grigorevskiy, and L.V. Kiseleva

Abstract A critical evaluation of space flight experiments and ground-based testing results in LEO simulating facilities for Russian space materials and their functional US and European space materials counterparts, as well as predictive performance evaluation are presented and discussed. Results of long-term GEO imitating ground-based testing are presented also for selected advanced thermal control materials.

In a number of Russian, Western and collaborative space materials experiments samples were installed on the external surfaces of the Space Station MIR and, for the last decade, on Russian or US segments of the International Space Station in removable cassettes for long-term exposure and brought back to Earth.

In ground-based testing, various acceptable LEO-imitating conditions have been explored. Oxygen plasma testing has been used efficiently as a screening testing tool. Fast atomic oxygen testing conducted in collaborative projects at various facilities in US and Canada at FAO fluencies 10^{19}–10^{21} at/cm^2, accompanied by UV irradiation are compared with results on selected materials that were tested in a hyper-thermal O-plasma beam source at the Institute of Nuclear Physics of Moscow State University, Russia.

Mass loss, change of thermal optical properties, morphology evolution and surface resistivity changes have been all analyzed using advanced analytical techniques. The influence of some aspects of space materials design and testing on the prediction and evaluation of functional performance and durability in space is discussed.

Z. Iskanderova (✉) • J. Kleiman • V. Issoupov
Integrity Testing Laboratory Inc, 80 Esna Park Dr, Markham, ON, Canada L3R 2R7
e-mail: ziskanderova@itlinc.com

S.F. Naumov[†] • S.P. Sokolova • A.O. Kurilenok
RSC Energia, Lenina str., 4a, Korolev, Moscow region 141070, Russia

L.S. Novikov • V.N. Chernik
Skobeltsyn Institute of Nuclear Physics Moscow State University, Moscow 119992, Russia

A.V. Grigorevskiy • L.V. Kiseleva
JSC "Kompozit", Korolev, Moscow region, Russia

1 Introduction

The research studies of space environments and their registration, development of reliable space environmental models, simulation of space environments and their interaction with materials in various testing facilities have been performed in US, Europe, and USSR/Russia since the start of the space era in the mid-sixties. Since experiments on materials' testing in open space started, a very large amount of data has been collected in various experiments conducted by Russian, USA and European scientists.

Almost immediately after the data on behavior of materials in LEO and GEO accumulated, various attempts at building predictive models describing the interaction of different space environment factors with materials started to appear.

This paper is an attempt of a critical evaluation of space flight experiments and ground-based testing results in LEO simulating facilities for Russian space materials and their functional US and European space materials counterparts. Some results on predictive performance evaluation of polymeric and carbon-based materials are also presented and discussed in this paper.

2 Russian, Western and Collaborative Space-Flight Material Experiments

Russian Space Corporation (RSC) "Energia" has been evaluating materials performance in open space experiments since 1969 [1–3]. Materials were flown on the external surfaces of the SALYUT and MIR Orbital Space Stations (OSS), as well as for the last decade on the International Space Station (ISS) Russian Segment "ZVEZDA". The tests of new materials exposure in detachable cassettes started in 1977 on the outside of the Salyut-7 Orbital Station. Cassettes 4 FM-110 with material samples were installed on the outer surface, underwent exposure from 100 to 672 days and then returned to the ground. About 70 various samples of materials were tested. The tests were performed with the purpose to confirm space life time for thermal control coatings, films, composite materials and multi layer insulation (MLI) used in thermal control systems. During Salyut-7 tests, existing and newly developed thermal control materials and coatings were tested in-flight, functional performance of the selected materials was confirmed, and materials for spacecraft external surfaces with active lifetime of ~10 years and more in LEO were selected. Historically, Russian space scientists have been always on a forefront of spaceflight materials testing, using, after Soyuz and Salyut, the MIR Space Station.

The National Aeronautics and Space Administration (NASA) and European Space Agency (ESA) have also conducted through a number of years a variety of Space Environment Effects on Materials (SEEM) flight experiments. An outstanding example of US long-term space materials experiment was the Long Duration Exposure Facility (LDEF), which spent almost 60 months (1984–1990) in LEO. It consisted of a variety of space materials experiments, including the Canadian one prepared by University of Toronto Institute for Aerospace Studies (UTIAS) [4]. LDEF studies accumulated a wealth of data regarding long-term durability and performance for all types of Western external space materials, many of them with implication to future spacecraft design [5, 6], and led, for instance, to development of some prediction abilities of materials durability in space [7]. Collaborative Russian-Western space flight materials experiments have been also a very reach source of information on space materials interaction with space environment, including ARAGATZ (potential space contaminations analysis), MEEP, MEDET, PIE, POSA1, POSA2, etc, to mention a few, all of them extending the knowledge of materials real performance in space.

During the last decade of the twentieth century 10 cassettes containing more than 600 various material samples were placed on the outer surface of MIR Space Station. Testing times varied from 309 to 1,638 days (see, for example, Fig. 1 and Table 1). As mentioned above, most experiments have been done using Removable Cassette Containers (RCC), denoted as CKK in Russian (Fig. 1). The cassettes were placed and photographed on the outer surfaces during the Cosmonauts or Astronauts Extra Vehicle Activities (EVA), and brought back the same way after space exposures. Inflight LEO experiments provided the unique opportunity for post-flight materials investigation and allowed characterizing their long-term durability and performance in open space at various space conditions, such as the level of solar activity, etc..

Similar experiments were continued at the International Space Station (ISS) by NASA starting from August 10, 2001, as a series of ongoing Materials on International Space Station Experiments (MISSE) [8].

ITL was actively involved in analyzing samples flown on LDEF by the UTIAS team. ITL also had an opportunity to participate in a few MISSE experiments, namely, the MISSE-1(4 years in flight) and MISSE-3 (1.5 years in flight) [9]. Presently, ITL is participating in a collaborative Russian-Canadian space experiment in which a number of samples are exposed in a multiyear open space exposure on the Russian Module "ZVEZDA" at ISS (launched in November 16, 2010).

Practically, all classes of materials and coatings developed and used in the space industry were tested in Russian, US, and collaborative Russian-European or Russian-US-European space flight experiments (with JAXA also joining in such studies in the last years [10]). They included thermal control paints – organic, silicate and silicone paints, as well as anodized coatings, to serve as solar reflectors, solar absorbers, total reflectors and total absorbers. Polymer films and multi-layers, textiles for optical applications and vacuum isolation, carbon- and glass- fiber reinforced plastic (CFRP and GFRP) composites, and a variety of protective and thermal control coatings have been also tested in such space flight experiments.

Fig. 1 Example of CKK layout for in-flight space materials experiments on the Russian module of the international space station [2]

CKK N 2, 4-CM

CKK N 1, 3, 5-CM
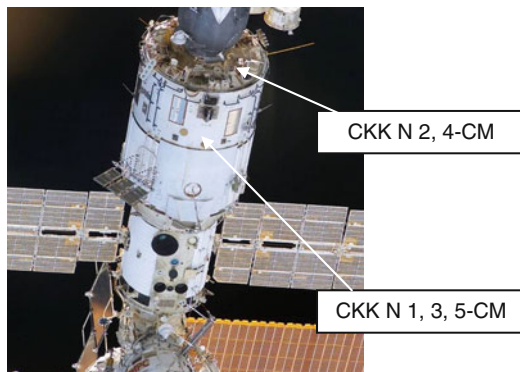
Table 1 Examples of space exposure experiments with removable cassette containers (CKK) at the service module (CM) and docking compartment (CO) at the Russian module of ISS [3]

Name of cassette	Installation date	Dismounting date	Exposure, days	Number of samples	Location
CKK #1-SM	25.01.02	27.02.04	756	84	CM
CKK #2-SM	25.01.02	03.09.04	958	84	CM
CKK #3-SM	27.02.04	19.08.05	539	84	CM
CKK #4-SM	03.09.04	In flight	–	84	CM
CKK #5-SM	19.08.05	22.02.07	554	60	CM
CKK #9-SM	22.02.07	In flight	–	66	CM
CKK #1-CO	25.01.02	27.02.04	756	72	CO1
CKK #2-CO	27.02.04	In flight	–	81	CO1

For example, mass loss results for the most representative high performance space polymer films – polyimides and per-fluorinated polymers [2] are presented in Fig. 2, and solar absorptance data for a Russian space-approved silicate paint with zinc oxide pigments is presented in Fig. 3.

It can be seen from Fig. 2, that per-fluorinated polymers demonstrated better stability under space environment influence, when compared to poly-imides. However, the difference appeared to be not as strong as it was indicated many times by NASA results [4]. The reason is still not clear, but in many cases similar discrepancies may be attributed to the influence of contaminations accumulated on material samples in open space [3, 4].

The behavior of the in-flight materials at the MIR OSS discovered the problem of the station external surfaces' contamination by outgassing products from the organic materials (MLI components, cables, casings of the devices, glues, rubber, composite materials, etc.), as well as from propellant combustion remaining products of the propulsion systems. These contamination products have been deposited onto the surfaces as contamination films, the presence of which have been confirmed later in numerous studies. Those films have been causing additional degradation of thermal optical characteristics of the spacecraft external surface materials. That is why during ISS design and development specific emphasis was
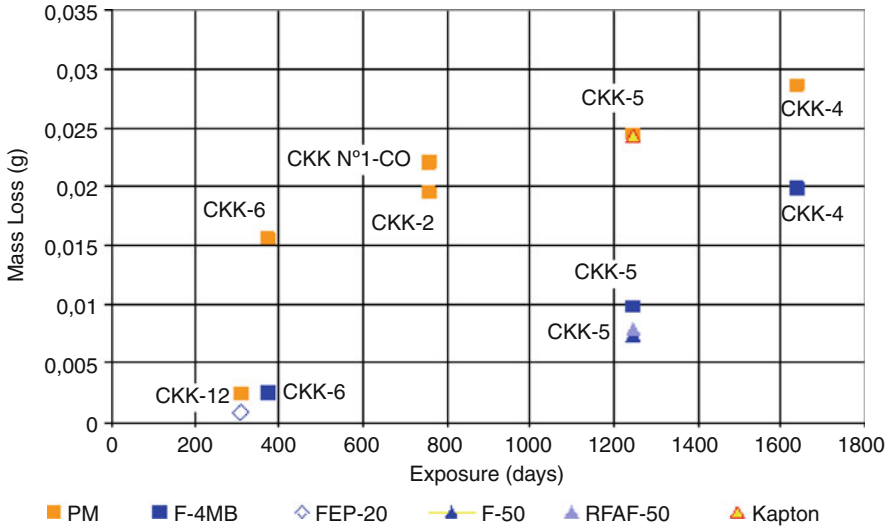
Fig. 2 Mass loss in fluoro-plastic and polyimide films during Russian space flight materials testing experiments [2]
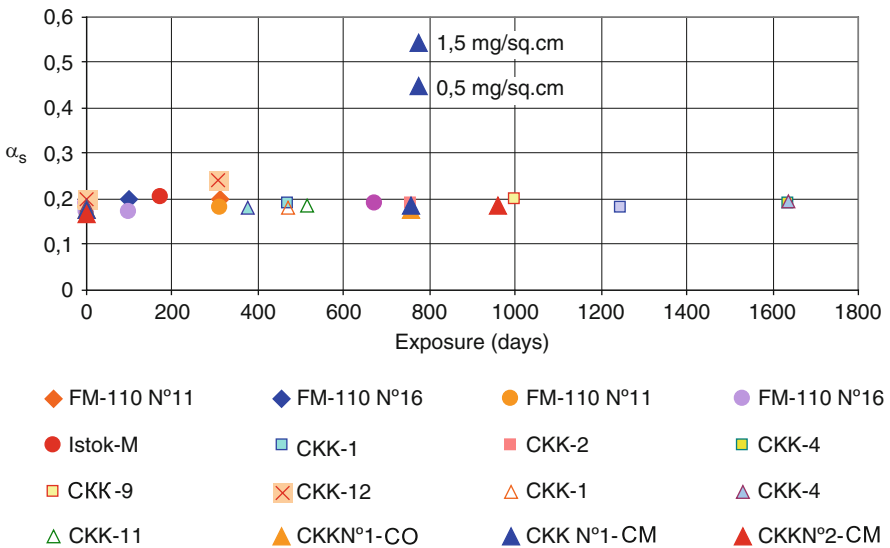
Fig. 3 Summary of the flight test results for Russian thermal control silicate paint with zinc oxide pigments [2]

made on providing cleanliness of the ISS modules and external surfaces. It is worth saying also that the contamination problems can be resolved only in space experiments, since on the ground it is not possible to create proper test conditions in the ground-based testing facilities.

It is known for many years and was confirmed recently by MISSE results that the silicate paints, with so called "liquid glass" silicate binders, while being fragile and hard to handle, are very resistant to atomic oxygen, the most aggressive factor of LEO space environment for organic materials. Therefore silicate thermal control paints could be expected to keep the thermal optical characteristics practically unchanged in long-term LEO spaceflights.

The summary of results for Russian silicate thermal control paint, presented in Fig. 3, represents an impressive example of this type of performance. However, in particular experiments some contaminations (the amounts are indicated near the triangles in the upper portion of the figure) still appeared on the painted surface.

3 Oxygen Plasma Beam Facility and Space Materials Testing at SINP-MSU

For over 50 years a valuable input in the field of space environment imitation and testing has been made, among others, by the team of Skobeltsin Institute of Nuclear Physics (SINP) at Moscow State University (MSU), Russia.

Thus, Professor S N. Vernov with his colleagues at SINP have been studying cosmic rays since mid-thirties of the twentieth century, discovering the Outer Earth Radiation Belt in 1958, independently of J. Van Allen [11]. The extensive studies and results in this area of research for more than half of a century have been published in a 2-volume monograph "Models of Cosmos"[1], dedicated to the 50-th Anniversary of the flight of the first Sputnik. The majority of the ground-based LEO space environment simulation and materials testing have been done at SINP in oxygen plasma beam facility, primarily designed as a spinoff in development of advanced Magnetic Hydrodynamic Engines [12]. Experiments in this plasma accelerator have been done with an oxygen plasma beam (OPB) consisting of ions, atoms and molecules of oxygen with mean atom energy of 20–40 eV and flux density mostly around 2.5–$3.5 \cdot 10^{16}$ cm^{-2} s^{-1}. Due to the dissociation of fast molecules and neutralization of the ions upon collisions with the surface, the atoms and ions with mean velocity in the mentioned above range impacted on the material. The fluence was considered to be equivalent to that of a 5 eV AO beam that initiates the same Kapton HN mass loss. The AO equivalent fluence was evaluated using the Kapton HN witness film mass loss in an assumption of the erosion yield $Y = 4.4 \cdot 10^{-24}$ g/atom, i.e. in accordance with the standard technique of AO fluence determination in ground based facilities [13].

During the testing, the changes in weight and thickness in the samples were measured, the visual appearance regarding surface morphology development was evaluated, and reflection spectra in the range 0.2–2.5 μm were registered. The results of effective erosion yield measurements for a number of common space materials when exposed to OPB with average energy E ~ 30 eV, presented as a ratio to Kapton HN erosion yield at the same oxygen energy E ~ 30 eV, are given in the last column of Table 2. Similar ratios for the same materials erosion yields at

Table 2 Relative effective erosion yields of main space materials at the exposure to 5 eV FAO beams and to oxygen plasma beam source

Material	Ym/Yk @ E = 5 eV	Ym/Yk @ E = 30 eV
Polyimide (Kapton HN)	1	1
Mylar PET	1–1,1	1,07
LDPE	>0,8	0,93
Pyrolytic graphite	0,23	0,23
Polyvinyl fluoride (Tedlar)	1,02–1,12	1,11
Polystyrene	0,91	0,94
PMMA	>1,8	2,5
Epoxy resin	0,57	0,59
Carbon/epoxy composite	0,41–0,36	0,38
Polyamide 6 (Nylon)	0,91	0,93
Aromatic polyamide (Kevlar)	0,21	0,2

E = 5 eV, collected from space flights and from the experiments with 5 eV FAO beams are presented in the first column.

As can be seen, the ratios in both columns are quite close for majority of the presented materials. These results may be considered as strong evidence that the predictive correlation between the chemical-structural composition of hydrocarbon polymers (and carbon) and their erosion yields in LEO, introduced in [7] and based on space data at E = 5 eV, is working effectively for an extended FAO energy range! It was used later for predictions of expected space results in [14] and confirmed by recent results of MISSE/PEASE polymers experiment [15, 16].

Some details and consideration have been specified in [16] in order to consider in the AO erosion mass loss the contribution from possible inorganic additives often being present in industrial polymers that are fully erosion resistant, or in case if some "char" left from an eroded sample. Taking into account these considerations, the MISSE/PEACE polymers space erosion results have shown even better coefficient of regression, then in Fig. 4. These results provide additional strong evidence of the fundamental nature of the processes considered in the original "gamma-correlation" development [7] that was used in [14] and in other cases. Another predictive correlation, also presented in [14], may be useful for expected LEO resistance estimate on polymeric materials of complicated or unknown chemical composition, since it is based on the experimental quantitative "flammability" characteristic – Oxygen Index.

The observed erosion effects are strongly pronounced when the FAO energy is lower then the threshold for dynamic sputtering. In an attempt to understand better and explain this phenomena, ITL scientists conducted a review of the worldwide experimental data for energy dependence of carbon erosion yield by oxygen in a wide energy range, from a few eV and up to 10^4 eV. A unique set of data has been collected and compiled by Z. Iskanderova in 1995 in the course of the project on influence of content and structure of hydrocarbon polymers on erosion by atomic oxygen [7]. The compilation of the collected data presented as a graph (see Fig. 5) in comparison with computer simulation results of physical sputtering from the "Sputtering Data", W. Eckstein et al. 1993 [17] were later published in [18].
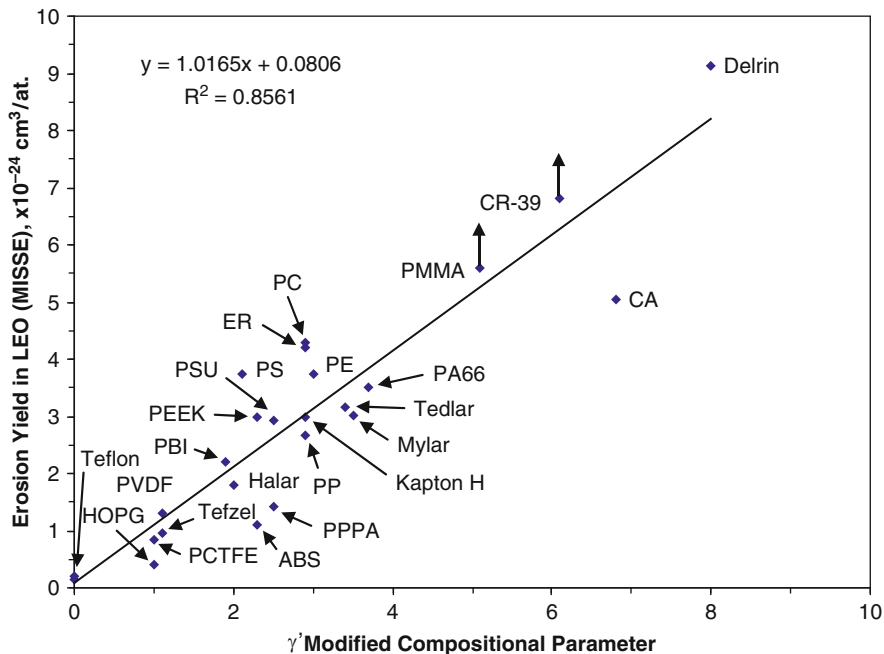
Fig. 4 MISSE/PEACE space experiment erosion yield results of [15, 16] for a variety of hydrocarbon and fluorinated polymers, presented versus the modified parameter γ'mod (see also [7])
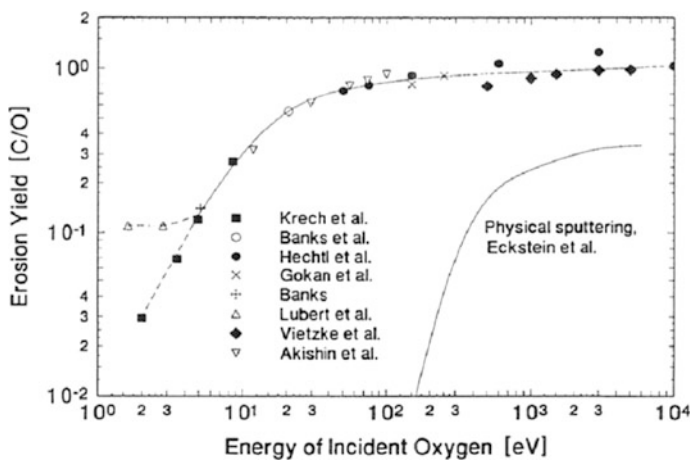

Fig. 5 Energy dependence of the total erosion/etching yield for carbon by oxygen (*left* side curve collection of data) and physical sputtering yield (*right*-side curve) (Eckstein et al. [17]) due to energetic oxygen impact on graphite at room temperature [18]

As can be seen from Fig. 5, for oxygen etching of graphite, for oxygen energies E ~ 120–150 eV, i.e. below the physical or dynamic sputtering threshold, the erosion/etching yield Y has a strong energy dependence, and at higher energy values almost levels up at Y ~ 1 [C/O].

Energy dependence of erosion yield by atomic oxygen for Kapton HN was presented by D. Ferguson based on compilation of experimental data available up to year 1984, in approximately the same energy range [19]. Later on, a detailed experimental data collection and compilation for Kapton HN in a lower energy range up to E ~ 40 eV, i.e. for hyper-thermal energy oxygen species, was performed by V. N. Chernik [20]. For both carbon and Kapton HN the hyper-thermal oxygen erosion yield shows a power-like energy dependence when still in the sub-threshold energy range regarding dynamic sputtering.

However, in the OPB, as well as in many other FAO testing facilities, erosion of fluorocarbon polymers and, specifically, per-fluorinated polymers was drastically increased in comparison to erosion in LEO. Other evidence of these effects have been seen also in [15], where some hydrocarbon and fluorinated polymers have been exposed to oxygen ion beam with an average energy E ~ 70 eV. Sputtering results did show already some "scattering" around the "gamma-correlation", and significantly higher erosion rates have been measured for fluorinated polymers, with the highest values measured for per-fluorinated Teflon. This fact was also indicated in other studies, where etching or erosion rates have been drastically different for fluorinated, and, specifically, per-fluorinated polymers in space flights and in testing facilities. It was identified, that those materials are having quite a strong energy dependence and sharp "chemical sputtering" thresholds of their oxygen erosion or etching [21].

A comprehensive overview and analysis of all available experimental data for a number of polymer-based materials in a wide energy range, including threshold values and etching rate energy dependence when using reactive neutral beams for industrial etching of some photo-resists in advanced microelectronic processing, in comparison with space materials results, have been started already [22].

It should be mentioned, that the use of the OPB facility is not straightforward when evaluating qualitatively the expected LEO space durability of new, previously untested materials, multilayer structures, as well as thin vacuum deposited protective coatings that may have pinholes, mini-crack, and other structural defects. Strong undercutting phenomena in such defects can be expected to accelerate significantly the erosion processes due to multiple scattering of more energetic O ions and atoms (E ~ 20–40 eV) then in LEO environment.

Another point that always needs to be considered is to use discretely the differences or ratios in mass loss in estimates of expected durability in LEO environment for two different materials (or materials with and without coatings). In some cases just using the ratio of mass loss $\Delta m_1/\Delta m_2$ under oxygen beam exposure is not enough (!). Such an approach is appropriate, for instance, for pure polymers, when the mass loss Δm is growing mostly in a linear fashion during exposure time. At the same time, the ratio of $\Delta m_1/\Delta m_2$ alone can not help in the evaluation of comparative durability or erosion resistance for many other advanced materials. This is especially true when dealing with composite materials where the

mass loss, at least for one of them, happens to be non-linear in regard of exposure time, or AO fluence, and finally levels up, indicating surface conversion to fully protective surface structures, as, for example, for many surface modified space materials [23, 24] or some silicone paints [25, 26].

4   LEO Imitation Testing Results at ITL and in Collaboration: 1988–2011

Starting from 1988, ITL Inc in Canada was actively involved in evaluation of main Western space materials after ground-based and in-flight testing, performing materials characterization and surface analysis. Later this approach was expanded to include development and application of different surface modification technologies for protection of space materials, space durability prediction and evaluation. An International Program, in collaboration with NASA, ESA and Russian space material scientists, was started that included comparative testing and performance evaluation of a large number of space materials. A few examples of results from a recent extended study and testing of almost 60 Russian and Western flight-proven advanced space materials [26] are highlighted here.

The major objective of this study was a comparative evaluation of the impact of simulated LEO space environment on a variety of Russian space materials an their US and European counterparts and the comparison of the results from three different LEO simulation facilities involved in this study and to other LEO simulation facilities results, where possible [26].

Russian flight-proven space materials included: space polymer films: Polyimide (PI) film (PM-1EU), Back-and both-sides aluminized PI films (PM-1EU-OA, PM-1EU-DA), PET Polymer film (PET-A), Non-Metalized films multi-layer (NIIKAM-DPL), per-fluorinated Teflon polymer film (F-4 MB), metalized film multi-layer (SOT-1 S-100): Thermal Control Paints: Acrylic paints-Charge-dissipative (EKOM-1, EKOM-2), and Conductive (EKOM-1P), and non-conductive (AK-512), Silicone paints – Non-conductive (KO-5191, 40-1-28), Silicate paint – Non-conductive (TRSO-TsM); Fabrics (ITO-coated RAM-1, ITO-coated RAM-2, Arimide fabrics 5359-87, 56420, 5365-89, and TSON-SOT M).

Western space materials included, among others, Kapton HN and Kapton H, both pristine and aluminized; ITO coated back-metalized Kapton samples from Sheldahl Corp., Teflon-FEP, Ag/Teflon-FEP (Sheldahl Corp.), Z306, Z302, A276 (Lord Corp.); MAP conductive and non-conductive thermal-control paints: SG121FD, PN, PNC, PCBE, PSB, etc. Examples of the results for Russian and some Western thermal control paints, exposed to indicated FAO fluencies, are presented in Table 3, and for selected Russian and Western thin films, including the ITO-coated in Table 4.

The results (Table 3) show less mass loss, i.e. better erosion resistance of EKOM paints, in comparison with US paints (and after silylation surface treatment at ITL

Table 3 Mass change under FAO exposure for some Russian and western (functional counterparts) thermal control paints [26]

Material	FAO Fluence $\times$ 10^{20} at/cm^2	Mass (g)		Mass change (mg)	Erosion results (μg/cm^2)
		Before FAO	After FAO		
EKOM-1, white	7.22	3.38245	3.38119	−1.26	−178.3
EKOM-1P grey	9.96	3.49427	3.49335	−0.92	−130.2
EKOM-2- black	7.61	3.32738	3.32525	−2.13	−301.5
A276:Z306, grey	5.53	42.08252	42.07120	−11.32	−786.1
Z302,black	5.25	7.45808	7.44878	−9.30	−492.8
AK512b, black	1.9	1.69888	1.69655	−2.33	−329.8
TRSO-TsM, white	1.9	2.99754	2.98753	−10.01	−1416.8[a]
PN -black	1.86	0.71763	0.71764	0.01	1.4
PNC- black	1.86	0.72675	0.72674	−0.01	−1.4
PCBE- white	1.86	1.49589	1.49627	0.38	54.8
SG121FD-white	1.86	1.53108	1.53167	0.59	85.1
A276	1.86	0.19004	0.18835	−1.69	−243.9

[a]The high mass loss of this silicate paint can be explained by desorption of bound water from the water-bound silicate binder

Table 4 Mass change of some Russian and western (functional counterparts) space materials (AO fluence 7.5×10^{19} at/cm^2 [26])

Material	Mass before FAO (g)	Mass after FAO (g)	Mass change (mg)	Erosion results (μg/cm^2)
ITO/RAM-1	0.05020	0.05019	−0.01	−1.57
ITO/RAM-2	0.06692	0.06691	−0.01	−1.57
ITO/Kapton 100 HN	0.02316	0.02321	0.05	7.85
ITO/Kapton 300 HN	0.07005	0.06998	−0.07	−10.99
PM-1EU-DA	0.01157	0.01156	−0.01	−1.57
PM-1EU[a]	0.09378	0.09319	−0.59	−92.60
Kapton 100 HN[a]	0.02131	0.02086	−0.45	−70.63
Teflon FEP	0.10229	0.09870	−3.59	−563.44
F-4 MB (Russian Teflon)	0.10000	0.09583	−4.17	−662.79

[a]Kapton 100 HN and Russian polyimide PM-1EU, 20 μm, have been included as reference materials

full surface stabilization and protection of EKOM paints was achieved [27]). Almost no mass loss (sometimes mass gain) can be seen for MAP thermal control silicone paints, supporting the expectations of their self-protective behavior under AO in space by surface conversion to protective silicon oxides.

It can be seen in Table 4 that the Indium-Tin-Oxide (ITO) coatings mass loss and (based on additional SIMS analysis) the protective ability of quite brittle ITO is sensitive to the type of substrate. For metallized films, double-side aluminized Russian polyimide is almost fully stable under FAO, both back-aluminized Kapton 100HN and Russian polyimide have close erosion yields, with Teflon FEP and Russian Teflon having also very close erosion rate values. Both Teflons have high

erosion rate under FAO, as may have been expected, considering their different erosion yields in space and under FAO, discussed above.

5 Major Classes of Space Materials and Effects in LEO Space and LEO Imitating Environments

To summarize the results of multi-year LEO environment exposure space materials experiments and LEO environment imitating ground based testing, space materials can be naturally divided into classes, with space environment effects specific for particular class:

- *Polymer films, carbon – graphite and organic paints:*
  - Surface erosion occurs, regardless of the supplying sources and places of manufacturing, affecting, to different extent, the thermal optical and, where appropriate, electrical properties.

- *Metalized (front-side and both-sides) space polymer films*:
  - Russian and Western – showed stable behavior, indicating well developed metallization processes of thin space polymer films by Russian and Western technologies.

- *Black, white (and gray) thermal control conducting and non-conducting paints*:
  - AO, UV and temperature range sensitive binders and
  - AO or radiation sensitive (pigments), long-term durability partially depends on the volume amount of pigments, and preparation technology.

- *Silicone paints*:
  - Surface stabilization and self-protection due to oxygen uptake and oxides-based surface conversion (may show *mass increase under AO due to the final balance of some volatiles release and oxygen uptake – not to mix-up with contaminations!*)
  - Russian charge-dissipative or conductive EKOM paints maintain their performance and charge dissipative properties at comparatively long-term imitated LEO expose, and two of them in long-term imitating GEO exposure (see next chapter).
  - These features favor them for both GEO and LEO, with some possible surface modifications added values performed at ITL, to be used for the LEO long-term missions.

- *Silicate paints*:
  - Brittle due to "liquid glass" binders (!),
  - Significant mass loss under FAO exposure, regardless of the paint manufacturers, that is caused by the loss of bound water by the silicate, or "liquid glass", water-borne binders.

- *Oxide-based and other ceramic protective coatings*;
- *They are* highly sensitive to the materials to be coated and to coating manufacturing/deposition technology
- *Some Technological Aspects*:

  – Quality of substrates' surfaces and deposition technology advancement are both very important, the final quality depending on the substrate's roughness, degree of pin-halls, cracks, interfaces bonding strength, etc.

- Indium Tin Oxide (ITO) thin film coatings – are brittle and prone to damage;
- Durability depends on quality of the substrate surface and deposition method, i.e. ITO coatings deposited on smooth polymer films allow extending their lifetime in LEO with good protection and charge dissipation. ITO coatings on rough 3D surfaces such as space textiles show diminished performance and lifespan.

6 Ground-Based GEO Simulation: Facility and Space Materials Testing

Some materials from the mentioned above program and advanced, newly developed space paints to be used in GEO, have been tested also at Radiation Testing Facility ("Komposit", Russia), that combines the protons, electrons, and Sun imitating UV sources, to simulate the influence of separate and combined GEO environmental factors [28, 29]. This facility allows to do space materials testing and evaluation under separate or combined GEO space environmental factors, evaluating the critical ones for expected GEO space durability and thermal optical functional properties sensitivity. This Radiation Testing Facility can provide electron and proton irradiation in an energy range 10–50 keV, solar imitating radiation up to 10 Solar Exposure Equivalents (SEE), at temperature range $\pm 150\,^{\circ}$C and vacuum as low as 10^{-5} Pa.

Results of three Russian EKOM paints that were tested in this facility simulating a long-term GEO exposure [27, 28] are presented in Fig. 6. It can be seen, that both silver-grey EKOM-1P and black EKOM-2 can be fully certified for long-term GEO flights applications, but the white EKOM-1 is very sensitive to space radiation.

A significant amount of efforts have been made during an extended research studies with the goal to develop a silicate white paint for long-term GEO application, with most significant success being recently the new Li-silicate white paint development and testing [28]. Irradiation of various white paints was performed at $E_p = 20\,$keV, $E_e = 40\,$keV, $j_p = 4{\cdot}10^{11}\,$cm^{-2}s^{-1}, $j_e = 2{\cdot}10^{12}\,$cm^{-2}s^{-1}, $T = 45\,^{\circ}$C and under UV irradiation with acceleration factor ranging between 2 and 3. Proton exposure with fluence up to $(6–7){\cdot}10^{16}\,$cm^{-2} corresponds to an average of 15 years in real GEO environment. The testing results for a number of samples of these paints, together with other Russian thermal control white paints, are presented in Fig. 7. These results very clear and impressively illustrate the better performance of this new development.
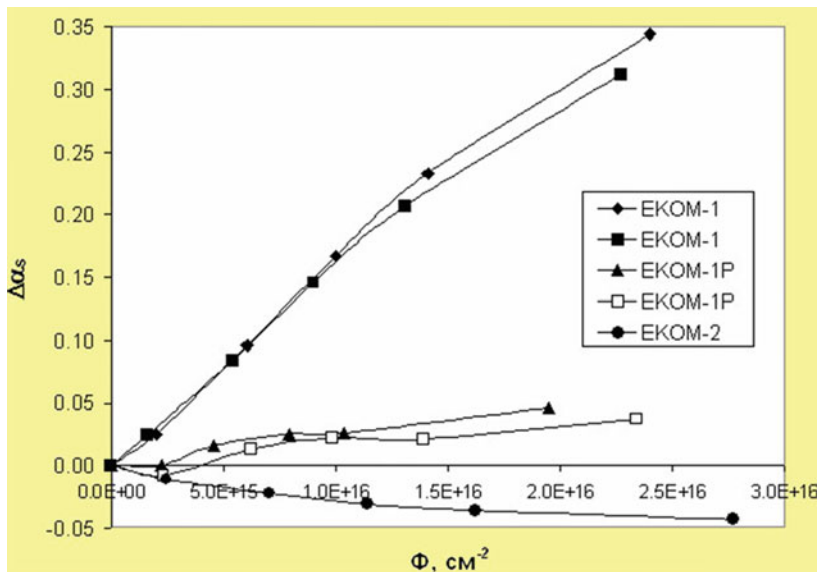
Fig. 6 Ground-based simulated GEO radiation testing of Russian conductive thermal control EKOM paints with simultaneous proton, electron and solar exposure [27, 28]
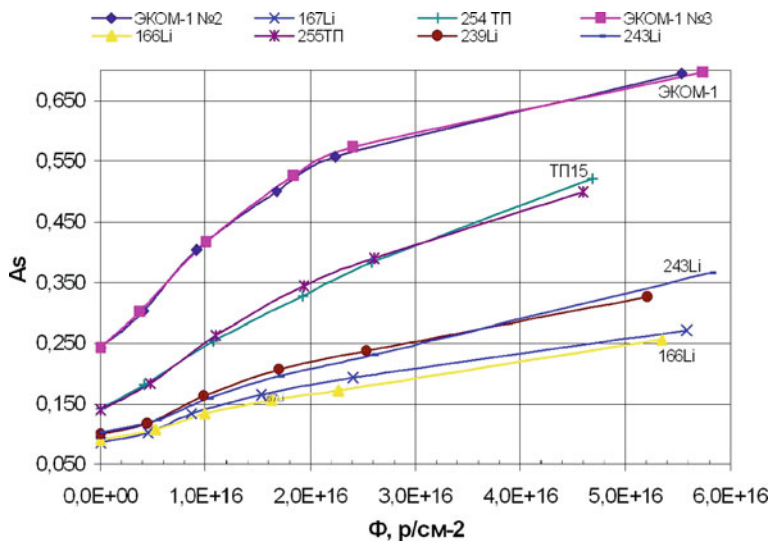
Fig. 7 Change of Solar Absorptance (As) versus the proton irradiation fluence (up to ~10 years equivalence of GEO exposure) at simultaneous proton, electron and UV irradiation for Russian white thermal control paints [29]

It is important to mention that this is a conductive paint with specific volume resistance $\rho_v \leq 10^5$ $\Omega \cdot$m. At the same time, these innovative paints demonstrated full compliance with the adhesion and outgasing standards of modern space materials.

7   Conclusions

An attempt was made to perform and present a comparison and critical evaluation of selected long-term Russian, USA, European, and joint space flight experiments, and ground-based testing results in LEO simulating facilities for Russian space materials and their US and European space materials functional counterparts.

Space materials of various classed had been tested in space flights in extended, long-term exposures to real LEO space environment. They have been mounted in cassettes and put at external locations at the earlier Russian Space Stations, or have been mounted on the surfaces of special satellites like the Long Duration Exposure Facility (LDEF, USA).

Similar experiments are continued now at ISS by the International ISS Team as MISSE experiments (USA), materials experiments at Russian "Zvezda" ("Star") and Japanese and European material experiments. In all these experiments the influence of samples location, mission longevity, space contamination and other facators should always be taken intoacocunt when comparing the results.

Some relevant aspects of accelerated testing in various ground-based LEO simulating facilities are raised and discussed in this paper, including the conditions and results from SINP (MSU, Russia) Atomic Oxygen Beam Facility, few USA FAO facilities and an advanced Canadian LEO simulation facility, as well as results of work in collaboration.

Predictive tools, developed for evaluation of expected space materials durability, considerations regarding energy dependence of erosion rates in space and LEO simulators for specific materials, space durability and long-term testing results for various classes of space materials are highlighted and evaluated in comparison. Some ground-based experimental testing results and new successful developments of Russian scientists are also presented for external space materials in GEO environment.

References

1. Panasyuk V, Novikov LS (eds) (2007) Model Kosmosa (Space model), vol 2, 8-th edn. University "Book House", Moscow (in Russian)
2. Naumov SF, Borisov VA, Gorodetskiy AA, Sokolova SP, Gerasimova TI, Kurilenok AO (2007) Interaction of external spacecraft materials and coatings with space environment: space flight experiments, ibid; Tribble A. C., Lukins R., Watts E., Borisov V.A., Demidov S.A., Deniusenko V.A., Gorodetsky A. A., Grishin V.K., Naumov S.F., Sergeev V.K., Sokolova S. P. (January-February 1996), United States and Russian thermal control coating results in low Earth orbit, Journal of Spacecraft and Rockets, v. 33, No1
3. Naumov SF, Borisov VA, Gorodetsky AA, Sokolova SP, Gerasimova TI, Kurilyonok AO, Novikov LS (2008) Study of materials and coatings on the spacecraft surfaces in the Salyut, MIR and ISS orbital stations: 1990–2008. In: Kleiman J (ed) Proceedings of the 9th international conference on protection of materials and structures from space environment, Toronto, 20–23 May 2008. Published by AIP conference proceedings 1087, pp 30–47

4. Tennyson RC, Mabson GE, Morison WD, Kleiman J (1991) LDEF mission update: composites in space. Adv Mater Processes 139(5):33–36
5. Silverman EM (1995) Space environmental effects on spacecraft: LEO materials selection guide, V.1 and V.2. NASA, Hampton
6. Tribble AC (2003) The space environment: implications for spacecraft design (revised and expanded edition). Princeton University Press, Princeton
7. Iskanderova ZA, Kleiman JI, Gudimenko Yu, Tennyson RC (1995) Influence of content and structure of hydrocarbon polymers on erosion by atomic oxygen. J Spacecr Rocket 35:878
8. MISSE Experiments: http://en.wikipedia.org/wiki/Materials_International_Space_Station_Experiment
9. Iskanderova ZA, Kleiman JI, Tennyson RC (2008) Pristine and surface-modified polymers in LEO: MISSE results versus predictive models and ground-based testing. In: Proceedings of 9th ICPMSE, Toronto, 20–23 May 2008, pp 300–311
10. Matsumoto K (ed) (2009) Proceedings of international symposium on SM/MPAC&SEED experiment. Japan Aerospace Exploration Agency, Tsukuba, 10–11 March 2008
11. Vernov N, Chudakov AE, Logachev UI, Gorchakov EB, Vakulov PV (1958) Outer radiation belt of the Earth, Diploma of Discovery #23, Priority of June 1958, State Committee for Inventions and Discoveries in the former Soviet Union
12. Kubarev V, Chernik VN (1995) Source of intensive oxygen plasma flows of low energy for technological applications. In: Proceedings of 24th international electric propulsion conference, vol 3. Moscow/Dnepropetrovsk, pp 1269–1277
13. ASTM-E-2089-00 (2000) Standard practices for ground laboratory atomic oxygen interaction evaluation of materials for space applications, vol 15.03
14. Kleiman J, Iskanderova Z, Banks BA, De Groh KK, Seckhar EA (2000) Predictions and measurements of the atomic oxygen erosion yield of polymers in low earth orbital flight. In: Proceedings of the 8th international symposium on materials in a space environment, Arcachon, 5–9 June 2000
15. Banks BA, Waters DL, Thorson SD, deGroh KK (2006) Comparison of atomic oxygen erosion yields of materials at various energy and impact angles, NASA/TM-2006-214363, Aug 2006
16. de Groh KK, Banks BA, McCarthy CE, Bucker RN, Roberts LM, Berger LA (2006) MISSE/PEACE polymers atomic oxygen erosion results, NASA/TM-2006-214482, Nov 2006; K.K. de Groh, B.A. Banks, C. McCarthy, L. Berger, L. Roberts and R. Rucker, "Analyses of the MISSE/Peace Polymers International Space Station Environmental Exposure Experiment", Proc. of the 10th Int. Symp. on Materials in a Space Environment and the 8th Int. Conf. of Protection of Materials and Structures in a Space Environment, Colliuore, France, 19–23 June, 2006
17. Eckstein W, Garcia-Rosales C, Roth J, Ottenberger W (1993) Sputtering data, Max-Plank-Institute fur Plasmaphysik report IPP9/82
18. Vietzke E, Haasz AA (1996) Chemical erosion. In: Hofer W, Roth J (eds) Physical processes of the interaction of fusion plasmas with solids. Academic, San Diego, p 135
19. Ferguson DC (1984) The energy dependence of surface morphology of Kapton degradation under atomic oxygen bombardment. In: Proceedings of 13th space simulation conference, Orlando, 8–11 Oct 1984
20. Chernik VN, Novikov LS, Akishin AI (2006) About adequacy of ground-based tests of polymers at higher atomic oxygen energy. In: Proceedings of the 10th ICPMSE, Collioure, June 2006, 20 eV–30 eV
21. Tagawa M, Yokota K, Kishida K, Okamoto A, Minton TK (2010) Energy dependence of hyper-thermal oxygen atom erosion of a fluorocarbon polymer: relevance to space environmental effects. ACS Appl Mater Interfaces 2(7):1866–1871
22. Iskanderova Z at al. A Comparative Overview of Etching Rates' Energy Dependence of a Wide Selection of Space Materials (in preparation)
23. Iskanderova Z, Kleiman I, Tennyson RC, Goudimenko Y, Cool G (1996) Surface modification of polymers and carbon-based materials by ion implantation and oxidative conversion. US Patent 5,683,757, Nov 1996

24. Gudimenko Y, Kleiman JI, Cool GR, Iskanderova ZA, Tennyson RC (1999) Modification of subsurface region of polymers and carbon-based materials. US Patent 5,948,484, 7 Sept 1999
25. Remaury S, Guillaumon JC, Nabarra P (2003) Behavior of thermal control coatings ender atomic oxygen and ultraviolet radiation. In: Kleiman JI, Iskanderova Z (eds) Protection of materials and structures from space environment. Kluwer, Dordrecht, p 193
26. Iskanderova Z, Kleiman J, Issoupov V, van Eesbeek M, Rhor T, Minton T (2009) Comparative testing, evaluation, and characterization of selected advanced flight-proven space materials. In: Proceedings of 11th international symposium on materials in a space environment (ISMSE), Aix-an-Provence, Sept 2009
27. Kleiman J, Gudimenko Y, Iskanderova Z, Grigorevsky AA, Finckenor M, Edwards D (2004) Simulated space environment exposure of surface-modified thermal control coatings. In: Proceedings of the 42nd aerospace sciences meeting, AIAA-2004-1258, Reno, Jan 2004
28. Grigorevsky AV, Galygin AN, Novikov LS, Khatipov SA, Walton JD (2009) Complex influence of space environment on optical properties of thermal control coatings. ISMSE-11, Aix-en-Provence
29. Grigorevsky AV, Kiseleva LV (2011) Complex investigations of new thermal control coatings, Present Proceedings

Accelerated Testing of Thermal Control Coatings Using Synchrotron Radiation and Evaluation of Materials Performance

H.R. Fischer, Yu. V. Butenko, C. Mooney, C. Semprimoschnig, M.H.W. Verkuijlen, E.R.H. van Eck, and T. Gerber

Abstract Accelerated testing of white thermal control coatings was performed using the high intensity UV radiation generated by a synchrotron and resulting in a substantial shortening of test times. The origin of coloration of metal oxides upon UV irradiation has been identified to be most likely a generation of oxygen vacancies connected with the appearance of colour centers in the crystal lattice.

Keywords Accelerated testing • White thermal control coatings • Synchrotron

1 Introduction

Current and planned missions especially those closer to the sun will face more severe and intense conditions, especially irradiation to IR, UV, X-rays etc. than known from the low Earth orbit (LEO) or geo-stationary orbit (GEO) environments. This means that new and advanced accelerated testing of the performance of materials must be evaluated to be able to predict more accurately the performance and the service-time of various materials.

H.R. Fischer (✉)
ESA-ESTEC, TEC-QT, Keplerlaan 1, 2200 AZ, Noordwijk, The Netherlands

TNO Materials Performance, De Rondom 1, 5612 AP, Eindhoven, The Netherlands
e-mail: hartmut.fischer@tno.nl

Y.V. Butenko • C. Mooney • C. Semprimoschnig
ESA-ESTEC, TEC-QT, Keplerlaan 1, 2200 AZ, Noordwijk, The Netherlands

M.H.W. Verkuijlen • E.R.H. van Eck
Radboud University, Nijmegen, The Netherlands

T. Gerber
SLS Villigen and PSI, Villigen, Switzerland

This applies also to white ceramic thermal insulating coatings e.g. such as those necessary for the BepiColombo mission. This is an especially challenging mission because Mercury's orbit is in close proximity to the Sun. It is evident that the intense solar irradiation at Mercury will cause very high temperatures at the surface of the spacecraft, challenging the functionality of all instrumentation during this mission. High temperature (in particular in combination with radiation) can lead to severe physicochemical degradation of materials e.g. surface roughness, reflectivity and absorptivity and consequently to a deterioration of the functional properties of materials. Normally, white, thermo-reflective paints are therefore applied to control the absorption of energy on exposed surfaces of spacecrafts [1]. However, these paints are usually based on non-absorbing ceramic material like ZnO, Zn_2TiO_4 or SiO_2 or Al_2O_3, embedded in a (polymer) binder. Such white paints are commonly successfully used for thermal control of spacecraft in LEO or GEO. At the Mercury orbit, there will be a much harsher environment with about 11 Solar constants in radiation and temperatures of the hottest exposed materials in the range of 450 °C with up to about 150,000 equivalent solar exposure hours for the most exposed materials.

Intrinsic ground based tests using the ESTEC Bake-out-Facility, BOF, (thermal cycling in vacuum) coupled with accelerated UV exposure showed intense colouration and/or degradation of the currently used thermal control paints. The underlying mechanism for the colouration is rather unclear; therefore additional investigations using also accelerated testing procedures were designed and performed.

Since synchrotron light sources provide an intense white beam of UV radiation, such sources are best suited for the accelerated testing of the performance of white thermal insulating coatings. Conventional light sources reach the same intensities only with difficulties; therefore accelerated testing is required, since no correction/repair of eventually damaged materials in space during a mission is possible.

The envisaged result is an indication and subsequently helps to develop an understanding of the mechanisms of UV initiated degradation for a better design of reliable thermal insulation materials in space.

2 Experimental Procedures

The ceramic coatings with a thickness of between 100 and 200 μm were manufactured using a plasma-spray coating process known already for some time in the manufacturing of thermal protective castings for airplane engine turbine plates [2]. The coatings were applied by DutchAero B.V (Eindhoven, Netherlands) and by Sulzer-Metco (Wohlen, Switzerland); the used ultra-pure ceramic powders (Al_2O_3 Starck, La_2O_3 and BN Aldrich and Y_2O_3 Sulzer) were annealed at 900 °C for 8 h. in air to remove residues of organic contamination and the substrates (glass, stainless steel, titanium alloy Ti6Al4V; 19×19 mm plates) were sandblasted before the application of the coating.

Accelerated testing and exposure was performed while placing the samples in an unfocussed white beam within the vacuum path for the exposure at the VUV
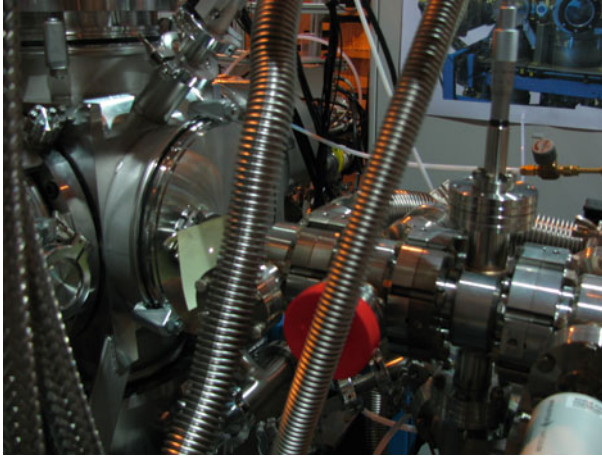
Fig. 1 Experimental set-up at VUV beamline, indicated is the location of the sample within the beam path and the size of the spot of the white beam using a fluorescent screen

beamline at the Swiss Light Source (SLS) in Villigen/Switzerland [3]. Although all synchrotron facilities can provide intense UV radiation required for accelerated testing, only a small number of experimental stations have indeed the option of using a white collimated UV beam and the placement of samples within the vacuum path. The beamline delivers radiation in the range of 5–30 eV photon energy with a photon flux of 10^{11}–10^{12} photons/s ($\times 10^{-4}$ bandwith) at a spot diameter of about 0.4 mm resulting in an integral energy density of VUV of about 5 kW/m². The experimental set-up chosen is shown in Fig. 1. The samples were mounted at the position of the monochromator exit slits. The monochromator was set to zero order, thus exposing the sample to the white beam.

For the purpose of this investigation on thermally stable white coatings, the following materials were tested: Al_2O_3, La_2O_3, Y_2O_3 and hexagonal BN as well as a Upilex R® polyimide film (UBE Industries) for reasons of calibration of the intensity of the SLS VUV beam.

The samples were exposed at different times spanning from 10 min to 16 h., the position between the different exposures was changed manually using a micrometer screw resulting in evenly well separated areas of exposure (see Fig. 2).

The beam damage to the material was determined by scanning over the spots (as shown in Fig. 2) and recording reflections spectra each 100 μm. Collected data were used to calculate ratio of reflection values of exposed and unexposed areas at a fixed wavelength. The optical characteristics (alpha/epsilon, IR absorption) were determined before and after UV irradiation following known procedures [4].

Additional exposure experiments were performed using the ESTEC TEC QTE, ESR facility set up for in-situ exposure of materials under vacuum during the recording of ESR spectra as described earlier. Finally, also another UV/VUV facility at ESTEC, the STAR, was used to expose plasma spray-coated samples in
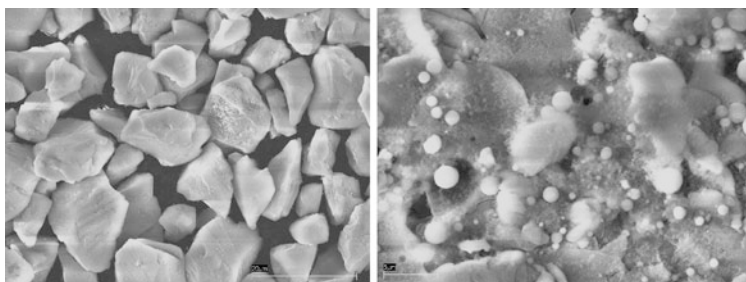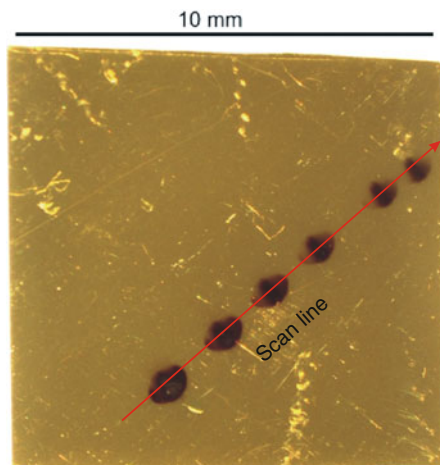
Fig. 3 SEM pictures of the ceramic Al_2O_3 powder used for the plasma-spray coating process (*left*) and of the resulting coating applied on Ti6Al4V (*right*)

a conventional way. Solid-state NMR experiments were performed at the national solid state NMR facility at the Radboud University to detect a change in metal coordination in the ceramics after exposure using a Varian 600 MHz/14.1 T spectrometer and a 2.5 mm double resonance MAS probe. ^{27}Al single pulse excitation (SPE) spectra were recorded using a short single pulse of 0.20 µs at an effective RF-field strength of 160 kHz and a sample spinning speed of 15 kHz. The ^{27}Al spectra were referenced to an aqueous solution of $Al(NO_3)_3$.

3   Results

The aim of this study was the creation of white and stable (in respect to UV–VIS, x-ray, IR irradiation) coatings for thermal management of a mission in close proximity to the sun. The applied plasma spray coating process resulted in mechanically stable, white and abrasion resistant ceramic coatings without using the currently applied wet-chemical processes or a polymeric binder (Fig. 3).

Fig. 4 Total solar reflectance of white ceramic coatings used
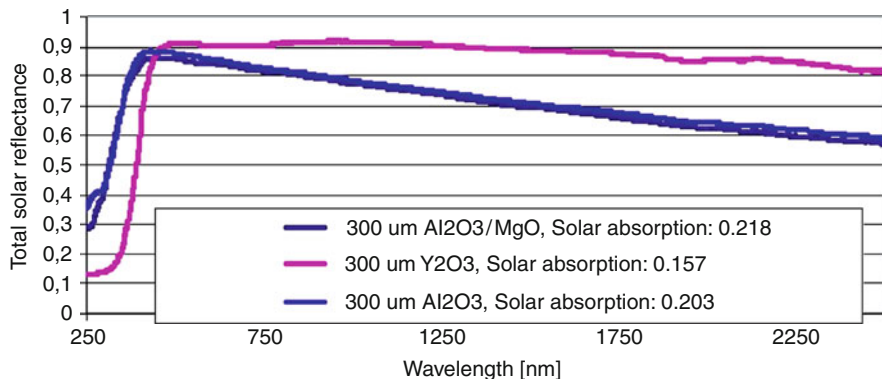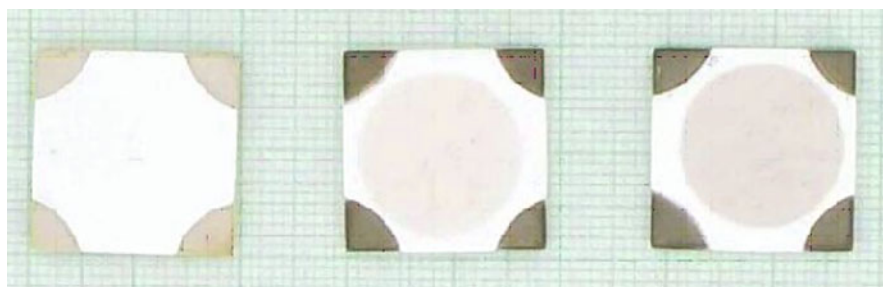

Fig. 5 Al_2O_3 coated samples at BOL, EOL 639 equivalent sun hours (esh) and EOL 1244 esh exposure (*left* to *right* respectively)

Among the thermodynamically most stable white ceramics are Mg-Al spinel, alumina, yttria and lanthanium oxide, having heats of formation: $MgAl_2O_4$: –2,299 kJ/mol, Al_2O_3: –1,676 kJ/mol; Y_2O_3: –1,920 kJ/mol and La_2O_3: –1,796 kJ/mol [5–8]. The coatings obtained show at the beginning of life (BOL, prior to exposure) good reflective properties (see Fig. 4).

However, despite their high stability, all these compounds show colouration after irradiation by VUV. A greyish-brownish colour is observed (see Fig. 5).

It was assumed that the origins of the colouration are metallic impurities, e.g. introduced by the plasma-spray process. This assumption was initiated by the observation of small metallic particles embedded in the plasma-sprayed coatings. The formation and source of such particles may possibly be due to the abrasion of parts of the plasma-spray apparatus being in contact with highly accelerated hard abrasive particles but could also have originated from the substrate as well. However, similar coatings deposited on glass as well as coatings derived from carefully selected ultra-pure ceramics showed the same colouration following irradiation. Hence, the colouration is not originated by impurities of the ceramics.
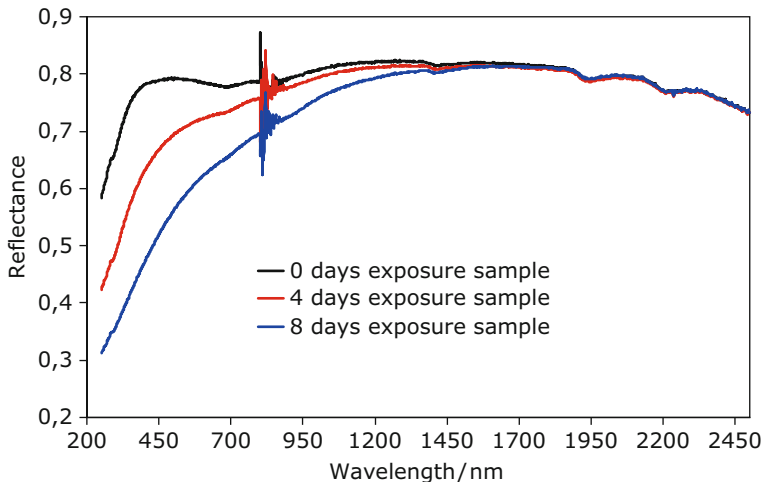
Fig. 6 Solar reflectance of Al_2O_3 coated samples at BOL, EOL 639 esh and EOL 1244 esh exposure
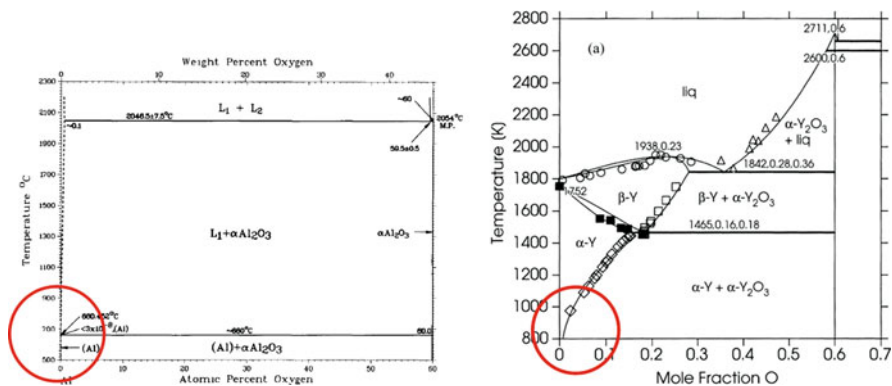
Fig. 7 Phase diagrams and areas of thermodynamic (in)stability of alumina and yttria [6, 7]

Measurements of the alpha/epsilon values of the exposed ceramic samples showed a gradual degradation of the reflectivity (see spectra in Fig. 6).

Also an irradiation of pure quartz-glass fibres fabrics resulted in a similar colouration effect. Although the ceramics should be stable under ambient conditions, the irradiation of (V)UV together with the application of vacuum may result in an abstraction of oxygen from the ceramics, resulting finally in oxygen vacancies in the lattice or the presence of metals. E.g. lanthanum [8] and also aluminum metals [6] are stable at extremely low oxygen partial pressures (see Fig. 7).

With the formation of oxygen vacancies resulting in hepta- or tetra- coordinated Al nuclei, these species should be detectable, e.g. in ^{27}Al-SS-NMR spectra (see Fig. 8). In extreme circumstances, metallic Al may also be formed. However, no

Fig. 8 ^{27}Al-SS-MAS-NMR spectra of virgin and UV irradiated Al_2O_3 powder

metallic Al is detectable (1,640 ppm) and also no hepta- or tetra-coordinated Al (30–40 ppm or 50–60 ppm) were found; the spectra of the alumina powder before and after irradiation are identical despite a clear visible colouration after irradiation [9]. This can only be explained by a very low concentration (< 1 %) of the colour centres below the detection limit of the NMR.

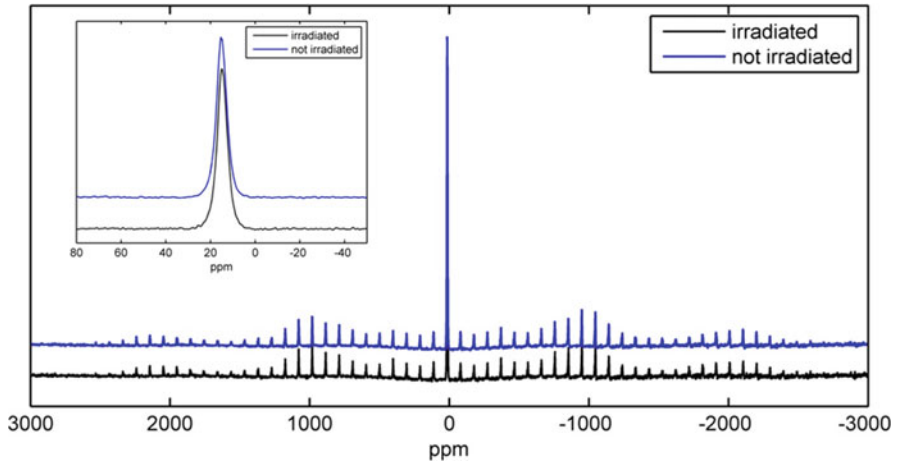A second source of the colouration could be a contamination by organic compounds (vacuum oil etc.) being nearly unavoidable. Such compounds are likely to degrade under the conditions of VUV/vacuum to graphite like structures and causing some colouration. In order to avoid such sources of contamination and to perform accelerated testing, the ultra-clean environment of a synchrotron experiment coupled with the high beam intensity and the high vacuum (~10^{-8} mbar) is ideal.

In order to quantify the damage by irradiation with the VUV synchrotron beam, a calibration of the intensity of the VUV beam was performed. For this, the spectra of the exposed areas of a sample which had been earlier tested within the ESTEC facilities with known flux intensities was measured and analysed. From this a development of the damage of a known white thermal control coating (MAP SG 121 FD), of Upilex R and of the ceramic coatings Al_2O_3 and BN on Ti6Al4V has been derived (Fig. 9).

Samples of the plasma spray coated ceramic materials irradiated under such circumstances show only small signs of colouration different to the white paint SG 121 FD. This material contains ZnO as pigment and a silicone binder, both are sensitive to UV irradiation. Silicones generate a brown-black colour in a radical driven degradation mechanism and ZnO develops colour centers connected with oxygen vacancies [10–12]. All materials show damage upon irradiation, with the exception of SG 121 FD, the amount of damage levels off at about 20,000–25,000 esh. The colouration of the alumina coating is very weak, possibly also due to a
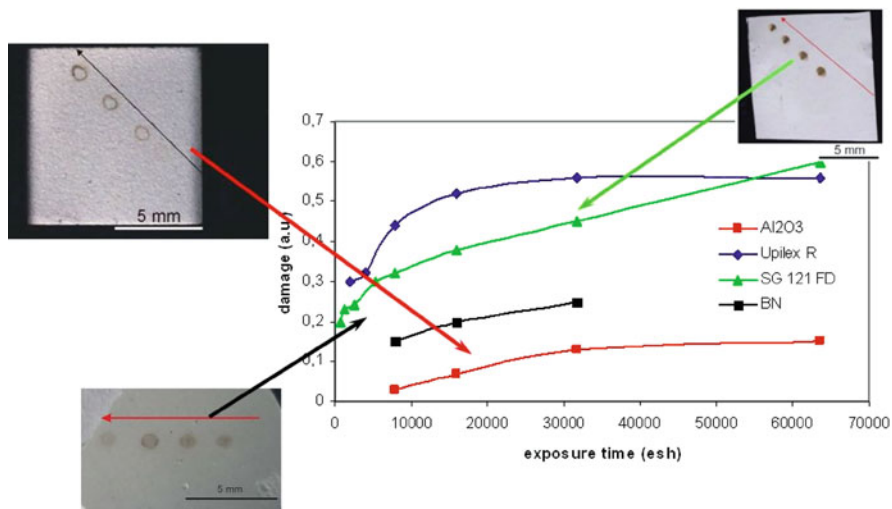
Fig. 9 Plot of the damage accumulation versus esh exposure of different white thermal control coatings (insets optical micrograph of the irradiated spots of the different materials)

residual part of x-rays present in the spectra of irradiation, causing a much harsher degradation of the ceramics.

The presence of x-rays is very likely since for example Y_2O_3 shows after 1 h irradiation by x-rays (Cu K_α) already a pink colour which vanishes after storage in air after approximately 1 week. Similarly, La_2O_3 shows also a light pink colouration after UV irradiation. All colourations disappear after annealing in air for about 8 h at 850–900 °C. All this hints to the formation of F (electrons trapped on an oxygen ion vacancy) and V (oxygen vacancy) centres, known to stabilize electron clouds and hence to contribute to colouration [13–15]. The formation and existence of F centres can be at least partially supported in the case of Y_2O_3 by the observation of (enhanced) fluorescence upon irradiation by UV.

Experiments to detect sources of colouration by ESR [16] were unsuccessful since the quartz-tubes develop also an ESR signal at g = 2.003 upon UV-irradiation which cannot be discriminated from a possible signal either developed from the F^+-centres or V^--centres of irradiated ceramics or from amorphous carbon species with unpaired spins/dangling bonds (π-defects) due to degradation of contaminations of organic nature [17]. All intensities of spin containing species follow a complex kinetic time law just like the evolution of colour centers in the sample vials. A healing of the F and V centers originated defects that can either be achieved by exposure and/or annealing in an oxygen containing environment Fig. 10.

The results show that an accelerated testing using synchrotron UV radiation is possible. Furthermore, the origin of colour changes in plasma-spray applied white ceramic coatings is most likely a generation of oxygen vacancies connected with the appearance of colour centers in the crystal lattice.
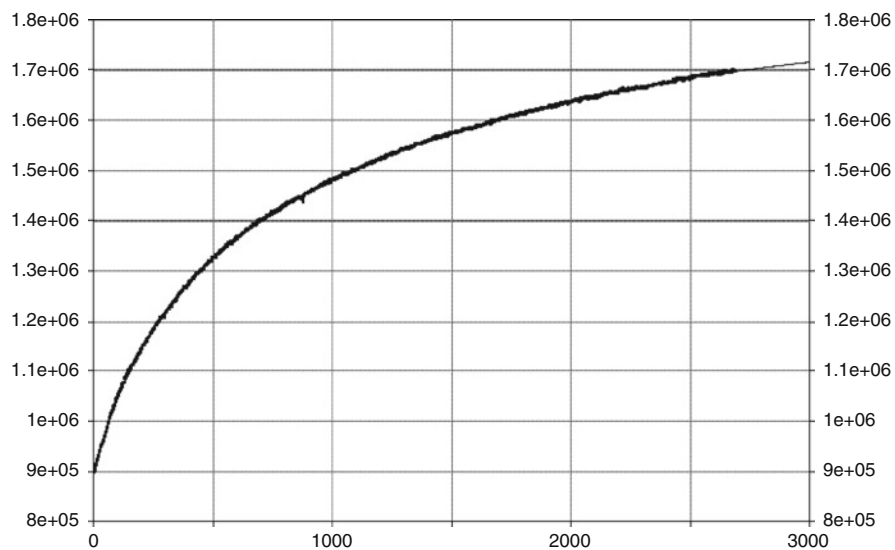
Fig. 10 The ESTEC ESR facility [16] and evolution of the intensity of the ESR signal at g = 2.003 originated from irradiation of Al$_2$O$_3$ powder baked out at 900 °C for 8 h. and irradiated in-situ in the ESR spectrometer

References

 1. Antonenko J (2003) Thermal control materials in mercury environment. In: Proceedings of the 9th ISMSE, Noordwijk, 169–177 (ESA SP-540 Sept. 2003)
 2. Herman H, Sampath S, McCune R (2000) Thermal spray: current status and future trends. MRS Bull 25:17–25
 3. Johnson M, Bodi A, Schulz L, Gerber T (2009) VUV beamline at the SLS for chemical dynamic studies. Nucl Instrum Methods Phys Res A 610:597–603
 4. Heltzel S, Semprimoschnig COA, van Eesbeek MRJ (2009) Environmental testing of thermal control materials at elevated temperature and intense ultraviolet radiation. J Spacecr Rocket 46:248
 5. Jung I-H, Decterov SA, Pelton AD (2004) Critical thermodynamic evaluation and optimization of the MgO-Al_2O_3 system. J Phase Equilib Diff 25:329–345
 6. Wriedt HA (1985) The Al-O-System. Bull Alloy Phase Diagr 6:548–553
 7. Djurovic D, Zinkevich M, Aldinger F (2007) Thermodynamic modeling of the yttrium – oxygen system. Comput Coupling Phase Diagr Thermochem 31:560–566
 8. Grundy AN, Hallstedt B, Gaukler LJ (2001) Thermodynamic assessment of the lanthanum-oxygen-system. J Phase Equilib 22:105–113
 9. Choi M, Matsunaga K, Oba F, Tanaka I (2009) ^{27}Al NMR chemical shifts in oxide crystals: a first-principles study. J Phys Chem C 113:3869–3873
10. Remaury S, Guillaumon J, Nabarra P (2004) Behaviour of thermal control coatings under atomic oxygen and ultraviolet radiation. Protection of materials and structures from space environment. Space Technol Proc 5:193–201
11. Tonon C, Duvignacq C, Teyssedre G, Dinguirard M (2001) Degradation of the optical properties of ZnO-based thermal control coatings in simulated space environment. J Phys D: Appl Phys 34:124–130
12. Marco J, Remaury S (2004) Evaluation of thermal control coatings degradation in simulated geo-space environment. High Perform Polymers 16:177–196
13. Kimura K, Kaneko J, Sharma S, Hong W, Itoh N (1999) Stimulated emission at 326 nm and ultrafast 100 ps lived luminescence component by ion irradiation of a-alumina. Phys Rev B 60:12626–12634
14. Guanglin H, Jie W (1993) ESR study on radiation grafting of Al_2O_3. Radiat Phys Chem 42:61–63
15. Museur L, Anglos D, Petitet JP, Michel J-P, Kanaev AV (2007) Photoluminescence of hexagonal boron nitride: effect of surface oxidation under UV-laser irradiation. J Luminescence 127:595–600
16. Hirayama Y, Obara M (2001) Ablation characteristics of cubic-boron nitride ceramic with femtosecond and picosecond laser pulses, J Appl Phys 90:6447; Rasmussen K, Grampp G, Eesbeek MV, Rohr T (2010) Thermal and UV degradation of polymer films studied in situ with ESR spectroscopy. ACS Appl Mater Interf 2:1879–1883
17. Gambino RJ, Thompson JA (1980) Spin resonance spectroscopy of amorphous carbon films. Solid State Commun 34:15–18

Effects of Secondary Electron Emission Yield of Polyimide Films on Atomic Oxygen Irradiation

Kumi Nitta, Eiji Miyazaki, Shinichiro Michizono, and Yoshio Saito

Abstract Secondary electron emission (SEE) from metal and insulating materials used for satellite thermal insulation or other such purposes was studied. The SEE yield measurement is very important for analyzing charge accumulation on satellite surfaces in a space environment because electron emission related to irradiated electrons influences the amount of surface charge. We considered degradation phenomena of spacecraft materials' surface caused by irradiation with atomic oxygen from two different sources. The SEE yields might change for a non-degraded sample. We measured the SEE yields for spacecraft material surfaces that were exposed to space environment factors. In preparation of exposed to space factors samples, they were irradiated by atomic oxygen (AO) to simulate degradation in a space environment. The samples were exposed to two different AO sources and three different fluencies, corresponding to different conditions of GEO orbit and time on orbit. This report is discussing the results for the polyimide films and the relationship between the SEE yields and sample degradation when irradiated by atomic oxygen. Furthermore, we consider the effect of different AO irradiation methods: the laser detonation method and the plasma asher method.

K. Nitta (✉) • E. Miyazaki
Aerospace Research and Development Directorate, Japan Aerospace Exploration Agency, 2-1-1 Sengen, Tsukuba 305-8505, Japan
e-mail: kumi.nitta@jaxa.jp

S. Michizono • Y. Saito
High-Energy Accelerator Research Organization (KEK), 1-1 Oho, Tsukuba 305-0801, Japan

Japan Aerospace Research and Development Directorate, Japan Aerospace Exploration Agency, Tsukuba, Japan

1 Introduction

A spacecraft electrical potential analysis tool that is available from the satellite design phase is necessary to support satellite operations [1].

Secondary electron emission (SEE) from materials produced by electrons and ions is an important parameter for analyzing the charging of satellites in space [2, 3]. However, the SEE yield is unknown for most materials used on the satellite surfaces. Furthermore, no one has reported radiation effects on the SEE yield.

This report presents the measurement results on polyimide films used as a reference material. Furthermore, we introduce the results of the SEE yield of the satellite materials to which we applied the degradation process to simulate the space environment, and we discuss the relationship between the SEE yield and the degradation of the samples irradiated with atomic oxygen. We used Beam Blanking Scanning Electron Microscopy (BBSEM) at an accelerating voltage of 600 eV–5 keV. This research is based on joint studies conducted by the Japan Aerospace Exploration Agency (JAXA) at the High-Energy Accelerator Research Organization (KEK).

2 Experimental Apparatus and Samples

2.1 SEE Measurement System Using BBSEM

We measured the SEE yield of cover glass by using BBSEM with a Faraday cup in order to observe secondary electrons at the High Energy Accelerators Research Organization (KEK) in Japan. The pulse-beam method was adopted for the measurement of SEE yield to avoid charging the surface of the insulator such as cover glass [4].

The pulse duration was 1 ms and the pulse current was 100 pA. Figure 1 illustrates the SEE measurement system. Primary electrons and secondary electrons are observed using a Faraday cup at +40 V. The SEE yield is calculated as the ratio of the primary electron current (Ip) to the secondary electron current (Is). Primary electrons are accelerated to above 0.6 keV.

3 Atomic Oxygen Beam Sources

We irradiated the polyimide films with atomic oxygen to investigate the influence of AO on the SEE yield. We used two AO-irradiation methods for the samples in this study. One is the laser detonation atomic oxygen beam source and the other is the plasma asher method. The Combined Space Effects Test Facility, located at JAXA's Tsukuba Space Center, has a vacuum chamber and three beam sources, i.e., Atomic Oxygen (AO), Electron Beam (EB) and Vacuum Ultraviolet radiation (VUV), generating a simulated space environment on the ground [5]. In the laser detonation atomic oxygen beam source the AO beam was generated by synchronized firing of a CO_2
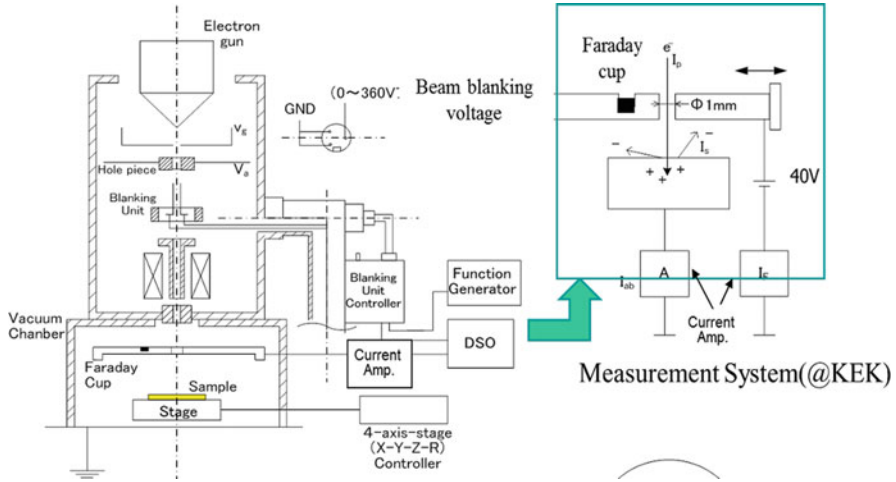
Fig. 1 Schematic diagram of SEE measurement system using BBSEM

laser (wavelength: 10.6 μm, output power: ~10 J/pulse) into a pulsed supersonic valve (PSV) nozzle that introduced oxygen gas. This method could simulate AO with the relative collisional energy of approximately 5 eV, as present in LEO. This type of source delivers high flux AO beam pulses Fig. 2.

In the case of the plasma asher method, the AO was generated by an ECR plasma source (Plasma Prep II: Physical Sciences Incorporated). This method does not simulate the collision energy and does not avoid the ultraviolet and high energy ion incident. However, it generates AO more easily than the laser detonation atomic oxygen beam source and avoids contamination from the materials of the fixture.

The fluence of AO was calculated to be 1E19, 1E20, and 5E20 atoms/cm^2 in this study. The fluence of AO corresponding to 5 years in a 900-km orbit is 1.1E20 atoms/cm^2. The fluence was enough to produce defects in the polyimide films. Figure 3 shows the experimental set-up for the plasma asher method.

4 Results and Discussion

Here we describe the measured SEE yield of the polyimide films. Figure 4 illustrates the dependency of the SEE yield of pristine polyimide films on the primary electron energy. We measured the SEE yield at the same electron energy five times; the plotted line connects the average values.

The secondary electron signal is like a saw wave. This is a representative wave of secondary electrons for insulators. The first primary incident electrons charge the sample surface. Subsequent primary electrons could not generate many secondary electrons from the charged sample. We found that the maximum SEE yield from the polyimide film is 1.1 when the primary electron energy is 600 eV. The SEE yields
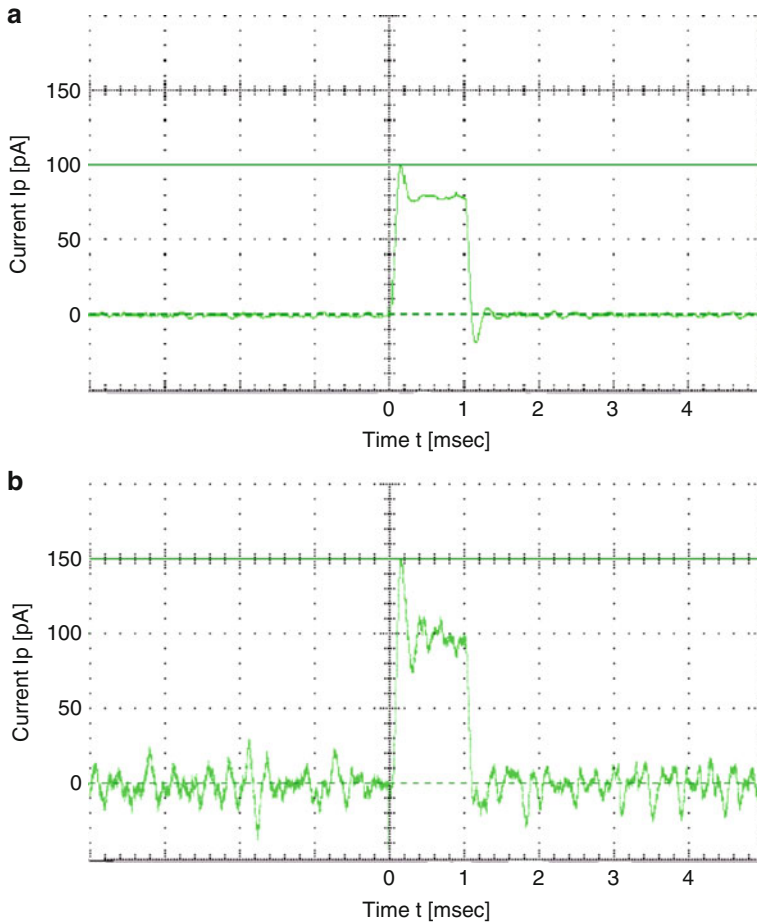
Fig. 2 Primary and secondary electron beam shapes. (**a**) Ip: primary current (Ip = 100 pA).
(**b**) Is: SEE current from polyimide film. The electron beam is accelerated to Ep = 700 eV
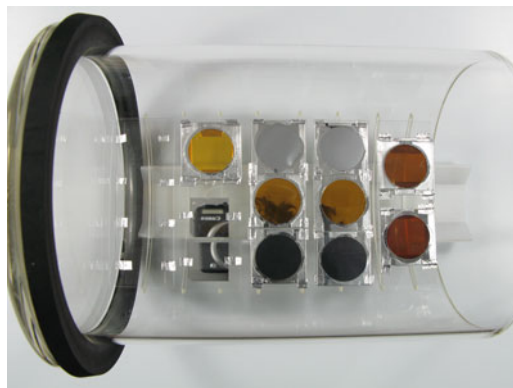
Fig. 3 Experimental set-up for the plasma asher method
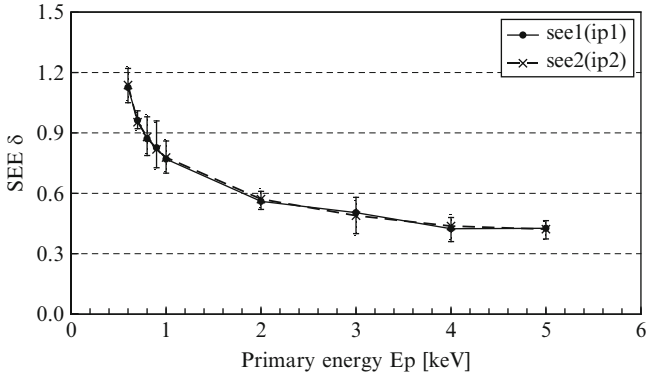
Fig. 4 Relation of the SEE yield of polyimide film to the primary electron energy
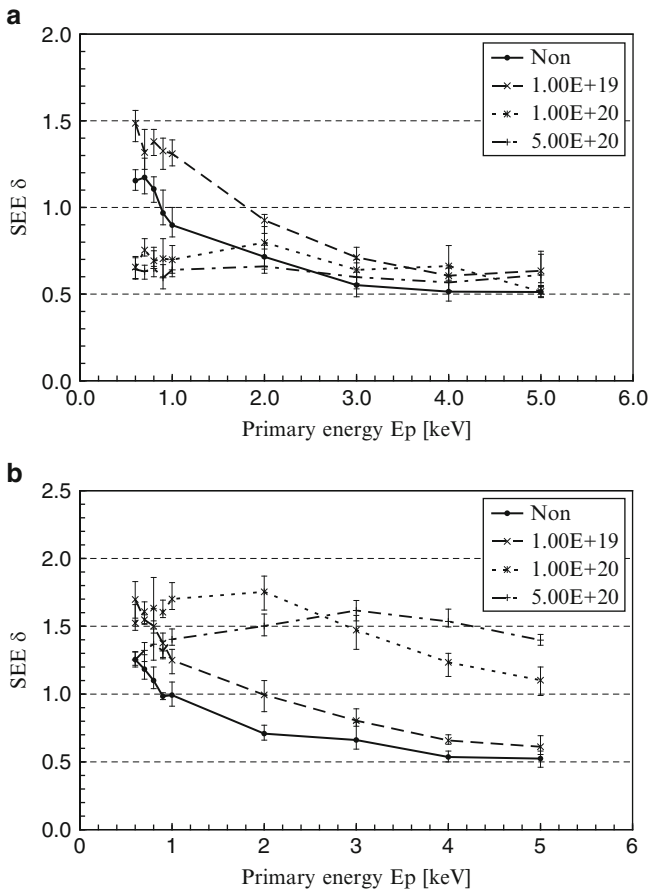
Fig. 5 SEE yields of the polyimide films after AO irradiation. (**b**), (**a**) Laser detonation method; plasma asher method
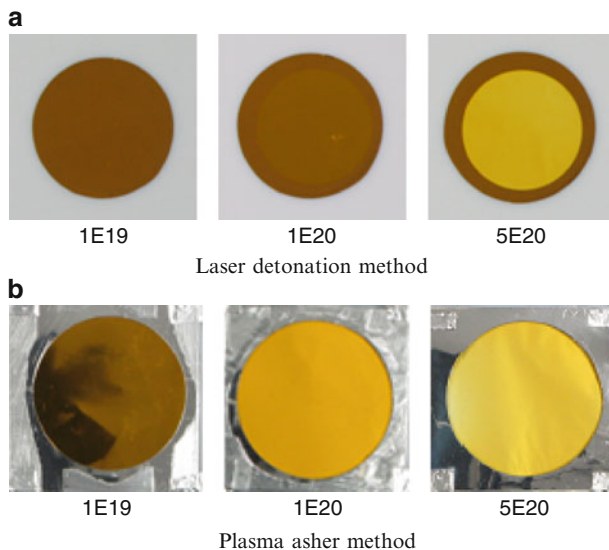
Fig. 6 Polyimide films after AO irradiation to different fluencies (as shown under each image). (**a**) Laser detonation method, (**b**) Plasma asher method
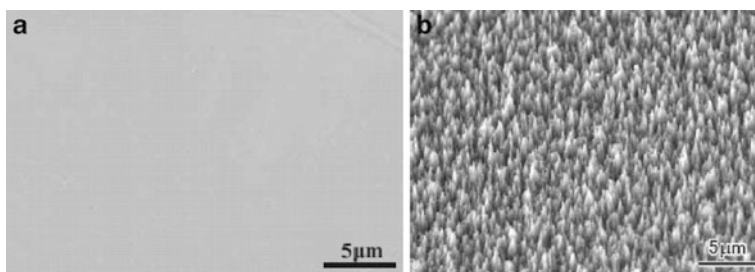
Fig. 7 SEM images of polyimide films [6]. (**a**) Non-irradiated polyimide film. (**b**) AO-irradiated sample at 3E19 atoms/cm^2

of polyimide films after AO irradiation are shown in Fig. 5a, b. We found that AO irradiation decreased the SEE yield of the polyimide films when using the laser detonation method.

It was found that the SEE yield of irradiated polyimide films was under one and that the higher the energy of the atomic oxygen the smaller the SEE yield. AO irradiation defects appeared on the surface of the polyimide films, creating a rough surface. On the other hand, we found that AO irradiation increased the SEE yield of the polyimide films when using the plasma asher method.

Figure 6 shows examples of polyimide films AO irradiated in both facilities to different fluencies. Figure 7 shows examples of SEM images of the non-irradiated and the AO-irradiated sample at 3E19 atoms/cm^2. Hence, the secondary electrons

on the surface that are generated by low-energy electrons seldom reach the polyimide film surface because the generated defects can disturb the secondary electrons on a high-energy irradiated surface. On the other hand, if the generated electron area increases and the area effects are stronger than the defect absorption, there are more secondary electrons generated compared with the non-irradiated sample. Consequently, we considered that the SEE yield of AO-irradiated polyimide films differs from non-irradiated polyimide films.

5   Conclusions

– We investigated the quantitative relation between SEE yield of polyimide films and irradiation fluence of AO from two different sources.
– We investigated the influence of AO in space on the SEE yield of polyimide films.
– The SEE yield of irradiated polyimide films was found to be less then 1 when using the laser detonation method. Moreover it was found that the higher the fluence of the atomic oxygen the smaller is the SEE yield.
– On the other hand, we found that AO irradiation increased the SEE yield of the polyimide films when using the plasma asher method.
– The secondary electrons on the surface that are generated by low-energy electrons seldom reach the polyimide film surface because the generated defects can disturb the secondary electrons.
– This result indicates that space plasma charges satellites change operation period.

These results are useful in satellite development.

References

1. Goka T (2005) JAXA space environment measurement: overview & plan. In: 9th spacecraft charging technology conference, Tsukuba, pp 30–35
2. Muranaka T, Hosoda S, Kim J-H, Hatta S, Ikeda K, Hamanaga T, Cho M, Usui H, Ueda HO, Koga K, Goka T (2008) Development of multi-utility spacecraft charging analysis tool (MUSCAT). IEEE Trans Plasma Sci 36(5):2336–2349, Part 2
3. Frezet M, Daly EJ, Granger JP, Hamelin JP (1984) Assessment of electrostatic charging of satellites in the geostationary environment. ESA J 13:89
4. Kawakita S, Imaizumi M, Takahashi M, Matsuda S, Michizono S, Saito Y (2002) Influence of high energy electrons and protons on secondary electron emission of over glasses for space solar cells, XXth ISDEIV

5. Miyazaki E, Shimamura H (2007) Current performance and issues of the combined space effects test facility, JAXA-RM-07-004
6. Shimamura H (2009) Effects of LEO environment on mechanical properties of polyimide films under tensile stress, JAXA-SP-08-015E, JAXA special publication: proceedings of international symposium on SM/MPAC & SEED experiment

The Effects of MEO Radiation Environment on Triple-Junction GaAs Solar Cells

Gao Xin, Yang Sheng-sheng, Wang Yun-fei, and Feng Zhan-zu

Abstract The effects of MEO (Altitude 20,000 km, Inclination 56°) radiation environment on the degradation of triple-junction GaAs cells (Manufactured in China) are investigated to provide the reference for solar array design. The results are presented on the performance degradation of triple-junction GaAs cells with various thicknesses of shielding silica coverglass in the MEO radiation environment, using the displacement damage dose methodology for analyzing and modeling. Degradation at different electron energies has been correlated with displacement damage dose. The maximum power of the cells without coverglass will be seriously degraded, reducing it to below 20% of the initial value by the accumulating proton dose at the end of a 1-year-mission. However, using a 100-μm-thick coveglass, the maximum power of the cells can be maintanined at 90% of the initial value. While a 100-μm-thick silica coverglass can practically block off the effects of protons on the GaAs cells in the MEO environment, its effect is not so pronounced for electrons. The use of the coverglass is of vital importance for shielding the damages by low energy protons in the MEO orbit.

Keywords Displacement damage dose • GaAs • Solar cell • MEO

1 Introduction

The space environment contains many different types of charged particles varying over a wide energy range, mainly including electrons, protons or their combinations. Exposure to the charged particles typically degrades the electrical performance of

G. Xin (✉) • Y. Sheng-sheng • W. Yun-fei • F. Zhan-zu
Science and Technology on Vacuum &Cryogenics Technology and Physics Laboratory,
Lanzhou Institute of Physics, Chinese Academy of Space Technology, Lanzhou 730000, China
e-mail: gaoxin510@163.com

semiconductor devices, especially less-shielded space solar cells that may result in the failure of a space mission. The present navigation satellite systems constructed by USA and Russia are flying at about 20,000 km altitude of the Medium Earth Orbit (MEO), and Chinese navigation system under construction will also be at similar orbits. Compared with the Geosynchronous Earth Orbit (GEO), these MEO orbits lie nearly in the center of the outer radiation belt of the Earth, a relatively more intense radiation situation. Therefore, an understanding of the radiation response of solar cells is extremely important for accurate prediction of the expected mission lifetime.

In order to predict the degradation of a particular electrical parameter of a solar cell, e.g., maximum power, open circuit voltage, or short circuit current in a space radiation environment, it is necessary to know how the parameter responds to different electron and proton energies, i.e., the energy dependence of the damage coefficients (DCs). Once the energy dependence of the DCs is known, predictions of the cell performance in space could be made for a given radiation environment. If the energy dependence of the DCs for a given parameter could be calculated it would reduce the number of experiments required and, hence, significantly reduce costs. The displacement damage dose (D_d) methodology, developed at the U.S. Naval Research Laboratory (NRL), addresses this issue by providing a means for predicting on-orbit cell performance from a minimum of ground-test data [1–5]. The principle of the methodology is the use of non-ionizing energy loss (NIEL) to calculate the energy dependence of the DCs.

In this paper, the results are presented about the performance degradation of triple-junction GaAs cells with various thicknesses of shielded silica coverglass in the MEO radiation environment, using the displacement damage dose methodology for analyzing and modeling.

2   Experimental Details

The GaAs cells used in this study consisted of 2 cm $\times$ 2 cm p-n type triple-junction InGaP$_2$/GaAs/Ge solar cells grown by Metal-Organic Chemical Vapor Deposition (MOCVD). The cells had no coverglass during irradiation. The cells were selected so that the beginning-of-life efficiency was almost identical for all of them. The irradiation experiments were performed at the ILU-6 electron radiation facility located in the Lanzhou Institute of Physics. The solar cells were irradiated at room temperature with 0.8, 1 and 2 MeV electrons. The solar cells were irradiated at a particular fluence level and immediately characterized after each irradiation. The temperature was monitored during the irradiation and was not higher than 30 °C throughout all sample irradiations. The beam dosimeter was calibrated with B3 films from GEX Corporation before each irradiation. Illuminated current-voltage measurements were performed under 1 sun, air mass zero (1 sun, AM0, 1367 W/m^2) conditions at 25 °C.

3   Results

3.1   *Calculation of NIEL*

NIEL is defined as part of energy lost per unit length by a particle moving in the material through Coulomb (elastic), nuclear elastic, and nuclear inelastic interactions thereby producing the initial displacement damage and excited phonons. This displacement damage creates defect energy levels in semiconductors that can act as trapping and recombination centers. It is the introduction of these defect levels that degrade the photovoltaic response of a solar cell through a reduction in the minority carrier diffusion length. The units of NIEL are typically MeV/cm or MeVcm^2/g. NIEL is a calculated quantity that takes into account the various interactions of an incident particle with a target atom/material. NIEL can be written as an integral over solid angle [6–8], i.e.

$$NIEL(E) = \frac{N_A}{A} \int_{\theta_{min}}^{\pi} \left[\frac{d\sigma(\theta,E)}{d\Omega} \right] T(\theta,E) L[T(\theta,E)] dT \qquad (1)$$

Where N_A is Avogadro's number, A is the atomic weight, and θmin is the scattering angle for which the recoil energy equals the threshold for atomic displacement. $d\sigma/d\Omega$ is the total differential cross section (elastic and inelastic) for atomic displacements. T is the recoil energy of the target atoms and L(T) is the so called partition factor which partitions the energy into ionizing and non ionizing events.

The Geant4 radiation transport toolkit is used as the basis of the simulation to calculate NIEL for electrons and protons in GaAs, and the results are shown in Fig. 1. The particle irradiation can induce damage not only in GaAs, but in InGaP$_2$ and Ge that also degrade the photovoltaic response of the triple-junction GaAs cells. However, in this paper, only the effect of irradiation in GaAs is considered, since the InGaP$_2$ and Ge sub-cell have better radiation-resistant performance than the GaAs sub-cell [9]. In fact, the majority of the degradation occurs due to diffusion length degradation in the GaAs sub-cell, and in all cases, this sub-cell becomes the current-limiting junction after irradiation.

4   Displacement Damage Dose Deposited

Solar cell response is typically characterized through the photovoltaic parameters (i.e., short circuit current (I_{sc}), open circuit voltage (V_{oc}), maximum power (P_{max}), and fill factor (FF)). The methodology of displacement damage dose (D_d) can simplify the performance evaluation since the displacement damage effects on the photovoltaic parameters for different particle energies can be correlated on the basis of D_d. The amount of non ionizing radiation dose deposited by the

Fig. 1 The calculated NIEL
of GaAs based on the Geant4
radiation transport toolkit
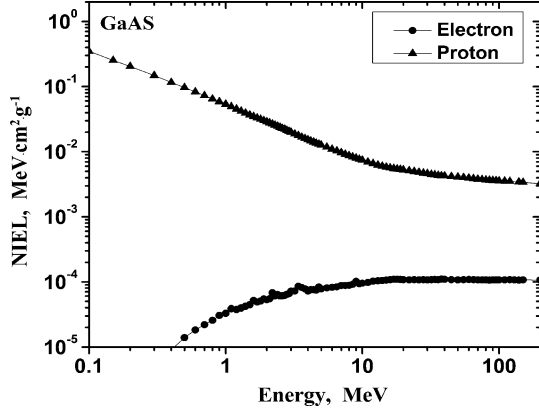
irradiating particle is referred to as displacement damage dose [10], which is
calculated by multiplying the particle fluence by the appropriate NIEL value for
the given irradiating particle, energy and target material, as shown in (2)

$$D_d = \Phi(E)S(E)\left[\frac{S(E)}{S(E_{ref})}\right]^{(n-1)} \tag{2}$$

Where $\Phi(E)$ is the fluence level for electrons, $S(E)$ is the NIEL value for
electrons incident on the target material, $S(E_{ref})$ is the NIEL for reference energy
electrons, and D_d is the resulting effective displacement damage dose. The refer-
ence energy for electron is usually taken as 1 MeV. The quantity in square brackets
accounts for a nonlinear dependence on NIEL. For any value of n other than unity,
the D_d represents an effective D_d for the given particle and reference energy (E_{ref}).
The available data [5, 11, 12] suggest that when the active region is primarily
composed of p-type material the electron DCs often follow a quadratic dependence
on NIEL ($n = 2$), whereas that for n-type material follows a linear dependence
($n = 1$), and for the most part, the DCs follow a power law dependence on NIEL
with an exponent varying between the value of one and two.

Figure 2 shows the data for the normalized maximum power (normalized to the
pre-irradiation values) measured on the triple-junction GaAs solar cells as a function
of electron fluence for three different electron energies indicated by the solid symbols.
For a given degradation level, the fluence level decreases for increasing electron
energy indicating that the higher energy electrons do relatively more damage.

If the normalized maximum power data are plotted as a function of effective 1 MeV
electron D_d given by (2), the data will collapse to a single characteristic curve, as
shown in Fig. 3. The photocurrent and photovoltage were also seen to fall on a single
curve (not shown here). In order to cause the data to collapse to a single curve, a
nonlinear least squares fitting of (2) is used to determine the best value of n. Since the
triple-junction cells degradation are primarily controlled by the response of the GaAs
sub-cell, the GaAs NIEL will be used to calculate Dd. The best correlation is obtained
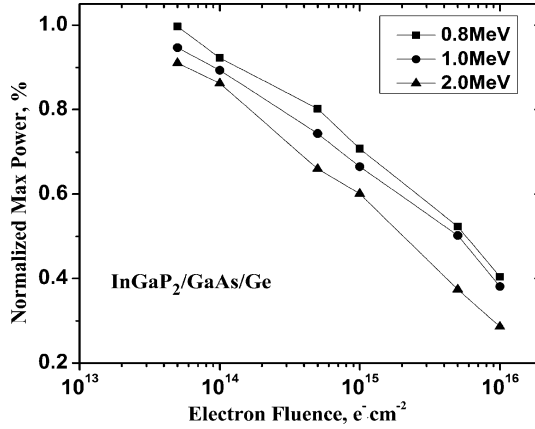
Fig. 2 Normalized maximum power as a function of electron fluence for 0.8, 1.0 and 2 MeV electrons on InGaP2/GaAs/Ge solar cells
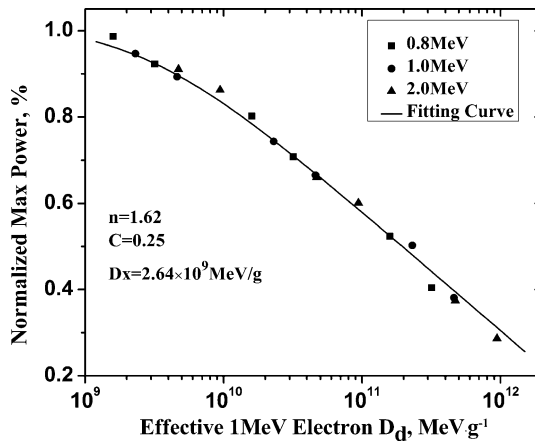
Fig. 3 Normalized maximum power as a function of the effective 1 MeV electron D_d. The solid symbols represent the experimental data and the solid line represents the fitting curve for the triple-junction cell

with $n = 1.62$, where E_{ref} is set to 1 MeV. This value of n suggests significant photoresponse from both the p-type emitter and n-type base regions.

For solar cells, the superposed degradation curves shown in Fig. 3 can be fitted using the semi empirical equation [13]

$$N(E) = 1 - C \log \left(1 + \frac{D_{eff}(E)}{D_x} \right) \qquad (3)$$

where, N(E) represents the normalized parameter of interest, $D_{eff}(E)$ is the effective dose given by (2), and C and D_x are fitting parameters to be determined. The solid line represents the characteristic curves generated using (3) for the cells. The fitting parameters are characteristic for this solar cell structure, and the best correlation is obtained with C = 0.25 and D_x = 2.64 × 10^9 MeV/g.

Once correlated in terms of D_d, the radiation data for a given particle fall on a single curve. The characteristic curve can be used to predict the cell response to irradiation by any particle energy or by a particle spectrum, and it can be seen that only a few experimental data are required to determine the characteristic parameters of the curve. On the contrary, if the normalized maximum power data are correlated with D_d (a product of $\Phi(E)$ and $S(E)$), not effective D_d in (2), in the many cases the data will not fall on a single curve, and in this case the data are dispersive. As can be induced by a nonlinear dependence of the DCs on NIEL [11, 12]. In the case of protons, the characteristic curve could be determined from measurements at a single energy, due to the value of n can be simply considered as unity. In the electron case, since the value of n can vary between one and two, it must be determined through experimental data. So generally electron data at two energies are required, except the DCs have a linear dependence on NIEL.

5 Effects of MEO Radiation Environment on the Solar Cells

In this section, we will calculate the total displacement damage dose deposited in the triple-junction GaAs solar cells from the radiation environments in MEO orbit (altitude 20,000 km, inclination 56 °).

Within the D_d methodology, analysis of electron effects in space begins with an analysis of the space radiation environment. The integral electron and proton spectra encountered in a MEO Earth orbit for a 1-year mission are shown in Fig. 4, an omni-directional spectrum based on AE8MAX and AP8MAX. Typically, the solar cell is shielded from this incident spectrum by the coverglass on the front and the solar array substrate in the rear. For the present example, only front side irradiation through the coverglass will be considered. To account for this shielding, the calculated slowed-down integral spectra for both 100 and 200 μm thickness of fused silica coverglass is also shown in Fig. 4, similarly an omni-directional spectrum based on Geant4 radiation transport toolkit. It can be seen that the proton spectrum of the MEO environment has been enormously attenuated by a silica coverglass, while it is not distinct for the case of the electron spectrum, due to the fact that electron can penetrate deeper in silica than proton does at the same energy.

The total effective dose deposited will be calculated as a function of fused silica coverglass thickness for the MEO radiation environment, according to (2). The results are shown in Table 1. It can be found that the D_{eff} deposited by electron before shielding can be slightly reduced from 4.09 × 10^9 MeV/g to 3.86 × 10^9 MeV/g, only about 5.6% by using a 200 μm-thick coverglass. However in the case of proton, the D_{eff} can be enormously lowered from
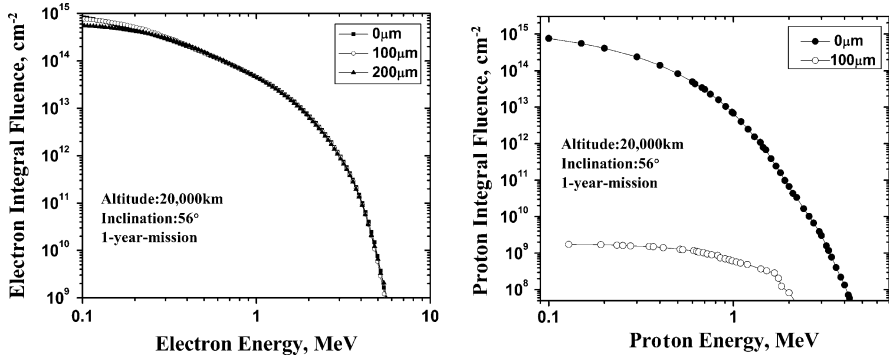
Fig. 4 The calculated electron (a-*left*) and proton (b-*right*) integral slowed-down spectra behind the various thicknesses of coverglass in MEO

Table 1 The calculated effective displacement damage dose (D_{eff}) from the MEO radiation environment behind different thicknesses of silica coverglass

Coverglass thickness, μm	Electron D_{eff}, MeV/g	Proton D_{eff}, MeV/g
0	4.09×10^9	8.83×10^{12}
100	4.04×10^9	8.71×10^7
200	3.86×10^9	–

8.83×10^{12} MeV/g to 8.71×10^7 MeV/g, a reduction about five orders of magnitude by a 100 μm-thick coverglass. The calculation results indicate that the D_d received by the unshielded solar cells will mainly come from a contribution by the proton radiation of the MEO environment; On the contrary, the electron radiation will dominate the D_d received by the shielded solar cells. The use of the coverglass is vitally important for shielding the damages by low energy proton. A further reduction in the D_{eff} can be achieved by increasing the coverglass thickness but would result in an increase of the overall weight of the solar array.

Using the characteristic curve in Fig. 3, the relation between effective D_d and coverglass thickness can be converted into that between normalized max power and coverglass thickness. The normalized max power of the cells will be seriously degraded if unshielded, theoretically being reduced to below 20% of the initial value by the accumulating proton dose at the end of a 1-year-mission. While in the case of using a 100-μm-thick coveglass, the normalized max power can be increased to 90% of the initial value.

6   Conclusions

In this paper, a comprehensive radiation damage analysis and modeling methodology for the triple-junction GaAs solar cells based on displacement damage dose (D_d) has been employed to predict the behavior of a home-made triple-junction

GaAs cell in MEO radiation environment. Degradation at different electron energies has been correlated with displacement damage dose (D_d). A 100-μm-thick silica coverglass can nearly block off the effects of proton on the cells in the MEO environment, but it is not effective for the case of electron on the cells. The max power of the cells without coverglass will be seriously degraded, mainly from the dose deposition of low energy proton; while in the case of the cells with coverglass, a notable improvement can be observed. The use of the coverglass is of vital importance for shielding the damages by low energy proton of the MEO environment. The methodology for the cell structure still needs to be validated through on-orbit data from space flight experiments.

References

1. Messenger SR, Burke EA, Xapsos MA, Summers GP, Walters RJ, Jun I, Jordan T (2003) NIEL for heavy ions: an analytical approach. IEEE Trans Nucl Sci. doi:10.1109/TNS.2003.820762
2. Jun I, Xapsos MA, Messenger SR, Burke EA, Walters RJ, Summers GP, Jordan T (2003) Proton nonionizing energy loss (NIEL) for device applications. IEEE Trans Nucl Sci. doi:10.1109/TNS.2003.820760
3. Walters RJ, Messenger SR, Cotal HL, Xapsos MA, Wojtczuk SJ, Serreze HB, Summers GP (1997) Radiation response of heteroepitaxial $n + p$ InP/Si solar cells. J Appl Phys. doi:10.1063/1.366024
4. Yamaguchi M, Takamoto T, Taylor SJ, Walters RJ, Summers GP, Flood DJ, Ohmori M (1997) Correlations for damage in diffused-junction InP solar cells induced by electron and proton irradiation. J Appl Phys. doi:10.1063/1.364449
5. Messenger SR, Jackson EM et al (1997) Structural changes in InP/Si solar cells following irradiation with protons to very high fluencies. J Appl Phys. doi:10.1063/1.370876
6. Burke EA (1986) Energy dependence of proton-induced displacement damage in silicon. IEEE Trans Nucl Sci. doi:10.1109/TNS.1986.4334592
7. Summers GP, Burke EA, Dale CJ, Wolicki EA, Marshall PW, Gehlhausen MA (1987) Correlation of particle-induced displacement damage in silicon. IEEE Trans Nucl Sci. doi:10.1109/TNS.1987.4337442
8. Burke EA, Campbell AB, Summers GP, Stapor WJ, Xapsos MA, Marshall PW, Zuleeg R (1987) Energy dependence of proton-induced displacement damage in gallium arsenide. IEEE Trans Nucl Sci. doi:10.1109/TNS.1987.4337456
9. Coral H, King R, Haddad M (2000) The effects of electron irradiation on triple-junction $Ga_{0.5}In_{0.5}P$/GaAs/Ge solar cells. In: Proceedings of IEEE 28th PVSC. IEEE Publ, New York
10. Messenger SR, Summers GP, Burke EA, Walters RJ, Xapsos MA (2001) Modeling solar cell degradation in space: a comparison of the NRL displacement damage dose and the JPL equivalent fluence approaches. Prog Photovoltaics Res Appl. doi:10.1002/pip. 357
11. Barde S, Ecoffet R, Costeraste J, Meygret A, Hugon X (2000) Displacement damage effects in InGaAs detectors: experimental results and semi-empirical model prediction. IEEE Trans Nucl Sci. doi:10.1109/23.903794
12. Warner JH, Messenger SR, Walters RJ, Summers GP (2005) Displacement damage correlation of proton and silicon ion radiation in GaAs. IEEE Trans Nucl Sci. doi:10.1109/TNS.2005.860737
13. Anspaugh BE (1996) GaAs solar cell radiation handbook. JPL, Kanpur

Interaction Mechanism of Soft X-rays with Irradiated Diamond-Like Carbon Films

Kazuhiro Kanda, Masahito Niibe, Kumiko Yokota, and Masahito Tagawa

Abstract The interaction mechanism of continuous soft X-rays with irradiated in vacuum diamond-like carbon (DLC) films, to simulate space environment conditions, was investigated using synchrotron radiation (SR). The thickness of the highly hydrogenated DLC film was found to decrease with increasing SR dose. The variation of local structure of DLC film was evaluated by measurements of the near edge X-ray absorption fine structure of carbon K-edge using SR. The characteristic peaks were observed in the spectrum of highly hydrogenated DLC film before irradiation, with these peaks disappearing from the spectrum after irradiation. These peaks are considered to be derived from the carbon bonding to hydrogen, which was desorbed by the soft X-ray irradiation. The $sp^2/(sp^2 + sp^3)$ ratio of DLC film was found to increase by the irradiation of soft X-ray.

Keywords Diamond-like carbon film • Near edge X-ray absorption fine structure • Soft X-ray • $sp^2/(sp^2 + sp^3)$ ratio • Synchrotron radiation

1 Introduction

Diamond-like carbon (DLC) films that have a number of excellent properties, such as hardness, low friction coefficient, and low surface energy, are used in various industrial fields. DLC films are used in many parts in spacecraft manufacturing. Their use as a lubrication material in space where oil cannot be used is especially attractive [1, 2]. The demands to the stability of materials used in spacecraft

K. Kanda (✉) • M. Niibe
Laboratory of Advanced Science and Technology for Industry, University of Hyogo,
Kamigori-cho, Hyogo 678-1205, Japan
e-mail: kanda@lasti.u-hyogo.ac.jp

K. Yokota • M. Tagawa
Graduate School of Engineering, Kobe University, Kobe 657-8501, Japan

manufacturing, due to the presence of such space environment factors as atomic oxygen, X-ray and vacuum are different from the demands to materials used in manufacturing on Earth.

DLC films are generally known to be durable against X-ray exposure. It was reported that DLC films withstood the exposure to synchrotron radiation (SR) in the soft X-ray region and in the absence of oxygen gas and were not etched [3]. With the DLC technology developing at an ever increasing pace in the last decade, various novel DLC film structures were developed with excellent properties. Recently irradiation of DLC film by soft X-rays in a vacuum has been reported to lead to desorption of hydrogen and an increase in the film density, hardness, and refractive index [4].

For safe use of DLC films in a space environment, it is imperative to know how different types of DLC films are affected by irradiation with soft X-rays and how the structure and material properties of DLC films change as a result of such irradiation. In a previous study we reported that irradiation of highly hydrogenated DLC films by soft X-rays caused desorption of hydrogen and a decrease in the film thickness [5]. However, the interaction mechanism of the DLC thin film with soft X-rays has not been sufficiently understood. Since the durability of DLC films against X-ray exposure is a necessary prerequisite for using DLC films in space safely, the information on the deterioration mechanism of DLC films caused by soft X-rays is undoubtedly important.

Near-edge X–ray absorption fine structure (NEXAFS) spectroscopy using synchrotron radiation was utilized as an efficient method to study the electronic and structural properties of thin films [6]. Quantitative data on the sp^2/sp^3 ratio, which is the ratio of the amount of sp^2 hybridized carbon atoms, $[sp^2]$, to that of sp^3 hybridized carbon atoms, $[sp^3]$ in the DLC film can be extracted from the NEXAFS spectrum with high sensitivity [7–9], because the isolated peak corresponding to the carbon $1s \rightarrow \pi^*$ resonance transition can be observed. In the present study, the changes in local structure of DLC films impaired by soft X-rays irradiation are discussed on the basis of measurement of the NEXAFS spectrum.

2   Experimental Apparatus

The SR irradiation of the DLC film was carried out at beamline 6 (BL06) of NewSUBARU synchrotron facility in the University of Hyogo. Details on the experimental apparatus at BL-6 are described in ref. [10]. For the irradiation experiment, the electron energy of the NewSUBARU ring was 1.0 GeV and the ring current was 220 mA on a top-up mode. The white radiation beam from a bending magnet was introduced at the sample stage via a pair of mirrors whose incident angle was 3°. The SR at the BL06 sample stage had a continuous spectrum from IR to soft X-rays, which are lower than 1 keV. The irradiated SR dose was represented by the product of the ring current and the exposure time. The base pressure in the reaction chamber was 1×10^{-6} Pa, and it was increased to 1×10^{-4} Pa during the SR exposure. After the SR exposure, the modified DLC films were kept at atmospheric conditions.

The NEXAFS measurement was carried out at the beamline 9A (BL09A) of NewSUBARU. The light source of BL09 is 11-m undulator. For the NEXAFS measurement, the electron energy of the NewSUBARU ring was 1.5 GeV and the ring current decayed from ≈ 300 mA. Details on the NEXAFS measurement procedure at BL09A are described in ref. [11]. The synchrotron radiation generated from 11-m undulator with 50 mm gap was dispersed using a varied-line-spacing plane grating of 1,200 lines/mm. Monochromatized SR light was irradiated at the sample at 54.7° (magic angle) with respect to surface normal of samples. Samples were mounted on a copper plate using carbon conductive tape in such a way that the carbon tape was completely covered by the sample and could not be seen from the surface. The electrons coming from the sample were detected in the total electron yield (TEY) mode. The intensity of the incident photon beams I_0 was measured by monitoring the photocurrent from a gold film. The absorption signal was given by the ratio between the out-coming electron intensity from the sample, I_s, and the intensity from the gold film, I_0. Absolute photon energy was obtained by aligning the π*(C = C) peak position of graphite to the literature value (285.38 eV) [12]. The uncertainty in the calibrated wavelength was estimated to be ±0.2 eV. The C K-edge NEXAFS spectra were measured in the energy range 275–335 eV. The energy resolution is estimated to be less than 0.5 eV FWHM.

The 200-nm thick DLC films were deposited on Si wafers by using the amplitude-modulated radio frequency plasma-enhanced chemical vapor deposition (RF PE-CVD) method [13]. Hydrogen content in this film was estimated at 50 % using a combination of Rutherford backscattering spectrometry (RBS) and elastic recoil detection analysis (ERDA) [5].

3 Results and Discussion

A variety of DLC films have been investigated using NEXAFS spectroscopy previously [7–9]. Figure 1 compares the carbon K-edge NEXAFS spectrum of a typical DLC film with that of graphite. In the NEXAFS spectrum of graphite, a pre-edge resonance at 285.4 eV is due to transitions from the C 1s orbital to the unoccupied π* orbital principally originating from sp^2 (C = C) sites. The sharp peaks located at 291.9 and 292.9 eV are assigned to 1s → σ* transitions. In the spectrum of typical DLC film, the amorphous nature of the films induces a spread of the σ* resonance and no recognizable structures can be identified. The broad band observed in the 288–310 eV range is assignable to the result of overlapping C1s → σ* transitions at the sp, sp2 and sp3 sites of the DLC film.

Figure 2 shows the C K-edge NEXAFS spectra of a RF PE-CVD DLC film before and after irradiation with a 300 mA·h dose of soft X-rays. As can be seen from Fig. 2, a number of peaks (marked with arrows) are present in the before irradiation NEXAFS spectrum. These peaks disappeared in the spectrum of the film after irradiation, with the NEXAFS spectrum resembling that of a typical DLC film. Since the RF PE-CVD DLC films contain large amounts of hydrogen, which is known to be desorbed by the irradiation with soft X-rays [5], the disappeared peaks in the spectra of irradiated DLC film can be associated with the carbon bonding to
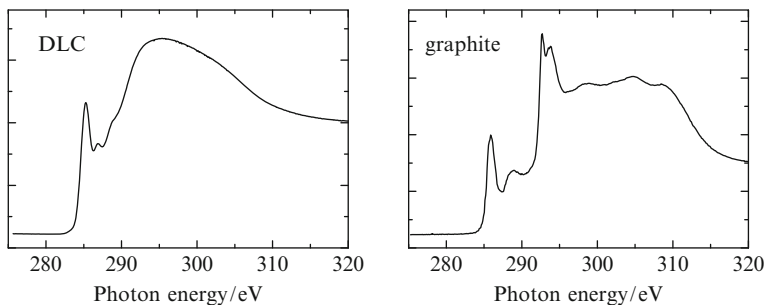
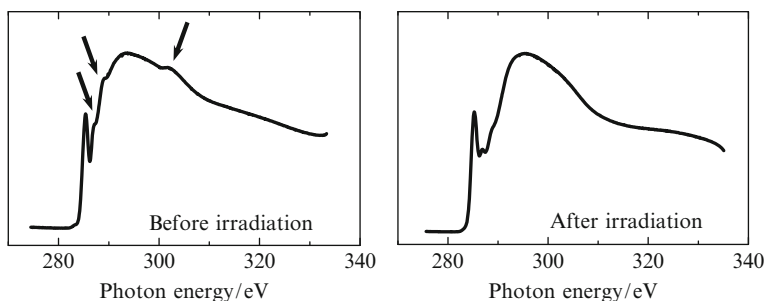**Fig.1** C K-edge NEXAFS spectrum of typical DLC film and graphite

Fig. 2 C K-edge NEXAFS spectrum of a RF PE-CVD DLC film before irradiation of soft X-rays and after irradiation with a 300 mA·h dose of soft X-rays. Arrows indicate specific peaks, which are not observed in the NEXAFS spectra of typical DLC films

hydrogen. The intensities of these peaks decreased with increasing of dose of soft X-rays, because hydrogen in the film was desorbed.

The peak intensity of the pre-edge resonance at 285.4 eV is considered as a good indication of sp^2 content. This resonance is not present in the spectrum of diamond, because diamond consists of carbon atoms, all in sp^3 (C–C) hybridization. The procedure for determination of sp^2 content from the NEXAFS measurements was established in the previous studies [7–9].

The amount of sp^2 hybridized carbon atoms can be extracted by normalizing the area under the peak of the resonance corresponding to $1s \rightarrow \pi^*$ transitions at 285.4 eV with the area under the broad peak in the DLC spectrum. The absolute $sp^2/(sp^2 + sp^3)$ ratio was determined by comparison with that from the NEXAFS spectrum of graphite. Figure 3 shows the dose dependence of the $sp^2/(sp^2 + sp^3)$ ratio of a RF PE-CVD DLC film determined from NEXAFS spectra. As shown in Fig. 3, the $sp^2/(sp^2 + sp^3)$ ratio of a RF PE-CVD DLC film in "as deposited" condition was ≈ 50 %. The $sp^2/(sp^2 + sp^3)$ ratio increased rapidly to ≈ 60 % by irradiation with a 300 mA·h dose of soft X-rays. In the dose region larger than 300 mA·h, the $sp^2/(sp^2 + sp^3)$ ratio remained almost unchanged at ≈ 60 % independently of the dose.

Fig. 3 SR dose dependence of $sp^2/(sp^2 + sp^3)$ ratio in the DLC film
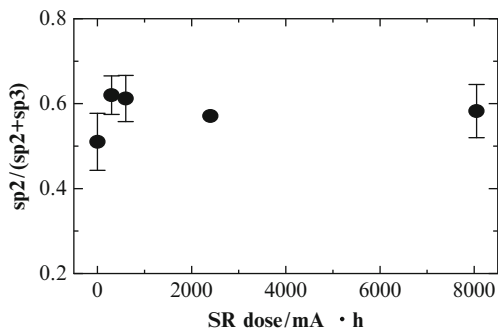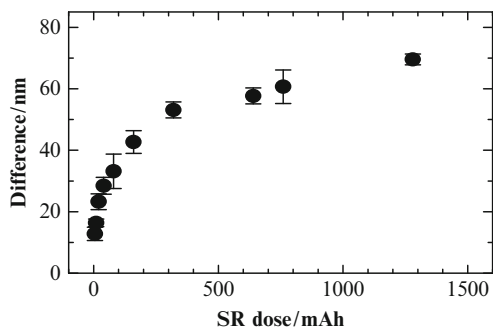

Fig. 4 DLC film thickness changes versus the irradiation SR dose. The difference in thickness between the area exposed to SR and shadowed by Au mask is plotted on the vertical scale

In the previous study, the film thickness of the highly hydrogenated DLC film was reported to decrease with increasing of SR dose in the range of 0 ~ 360 mA·h [5]. In the present study, the region of SR dose was extended to 1,280 mA·h. To measure the film thickness changes as a result of irradiation by soft X-rays, a DLC film was exposed to SR through an Au mesh, used as a mask. The difference in the thickness between the area exposed to SR and a shadowed by the Au mask was measured using a stylus profilometer (DEKTAK6M). Figure 4 shows the changes in this DLC film thickness difference versus the irradiation SR dose. As can be seen from Fig. 4, the thickness difference was found to increase steeply with SR dose in the region from 0 to 300 mA·h and increase slightly in the dose region larger than 300 mA·h. The coincidence in the dependence of the $sp^2/(sp^2 + sp^3)$ ratio in the film and the thickness difference on the SR dose indicates that the desorption of hydrogen from a DLC film by irradiation with soft X-rays causes a decrease in film thickness, which means increase in density, with the carbon atoms that lost the hydrogen forming $C = C$ bonding.

References

1. Donnet C, Fontaine J, Le Mogne T, Belin M, Héau C, Terrat JP, Vaux F, Pont G (1999) Diamond-like carbon-based functionally gradient coatings for space tribology. Surf Coating Technol 120–121:548–554, l
2. Donnet C, Erdemir A (eds) (2008) Tribology of diamond-like carbon. Springer, New York

3. Kyuragi H, Urisu T (1987) Synchrotron radiation-induced etching of a carbon film in an oxygen gas. Appl Phys Lett 50:1254–1256
4. Matsuura H, Ohkubo S, Oda K, Ushiro T (2007) Development of refractive-index modulation type difference optical element using a-C:H film. SEI Tech Rev 171:36–39, Japanese
5. Kanda K, Yokota K, Tagawa M, Tode M, Teraoka Y, Matsui S (2011) Effect on the soft X-rays on highly hydrogenated diamond-like carbon films. Jpn J Appl Phys 50:055801
6. Stöhr J (2003) NEXAFS spectroscopy. Springer, Berlin
7. Kanda K, Kitagawa T, Shimizugawa Y, Haruyama Y, Matsui S, Terasawa M, Tsubakino H, Yamada I, Gejo T, Kamada M (2002) Characterization of hard DLC films formed by Ar gas cluster ion beam-assisted fullerene deposition. Jpn J Appl Phys 41:4295–4298
8. Saikubo A, Kanda K, Niibe M, Matsui S (2006) Near-edge X-ray absorption fine-structure characterization of diamond-like carbon thin films formed by various method. N Diam Frontier Carbon Technol 16:235–244
9. Saikubo A, Yamada N, Kanda K, Matsui S, Suzuki T, Niihara K, Saitoh H (2008) Comprehensive classification of DLC films formed by various methods using NEXAFS measurement. Diamond Relat Mater 17:1743–1745
10. Kanda K, Ideta T, Haruyama Y, Ishigaki H, Matsui S (2003) Surface modification of fluorocarbon polymers by synchrotron radiation. Jpn J Appl Phys 42:3983–3985, Part1, No.6B
11. Niibe M, Mukai M, Miyamoto S, Shoji Y, Hashimoto S, Ando A, Tanaka T, Miyai M, Kitamura H (2004) Characterization of light radiated from 11m long undulator. AIP Conf Proc 705:576–579
12. Batson PE (1993) Carbon 1s near-edge-absorption fine structure in graphite. Phys Rev B 48:2608–2610
13. Nakahigashi T, Tanaka Y, Miyake K, Oohara H (2004) Properties of flexible DLC film deposited by amplitude-modulated RF P-CVD. Tribology Int 37:907–912

Degradation of Silicone Oils Exposed to Geostationary Environment Components: Ultraviolet Radiations and Electron Flux

H. Jochem, V. Rejsek-Riba, E. Maerten, A. Baceiredo, and S. Remaury

Abstract Degradation of polydimethylsiloxane and vinyl-terminated polydimethylsiloxane oils exposed to UV radiation or 1.25 MeV electron flux was investigated using EPR, GC Headspace, NMR, GPC and UV–vis-NIR spectroscopy. To examine the influence of synthetic method, these two oils were prepared by ring opening polymerization using either an inorganic initiator KOH or an organic catalyst N-Heterocyclic carbene. Under UV radiation, any chemical change is observed for polydimethylsiloxane, whereas vinyl-terminated polydimethylsiloxane presents a decrease of vinyl functions and an increase of chain length. Both polydimethylsiloxane and vinyl terminated polydimethylsiloxane demonstrated a degradation of thermo-optical properties, more significant for oils synthesized with organic catalyst. By improving oil purification, the degradation of thermo-optical properties can be reduced. Effects of electron flux are similar for each oil, thus independently of synthetic method and end functions. Electron flux generates important chemical damages initiated by homolytic chain scissions. Radical recombination produces gases (methane and ethane), new functions (Si-H) and bonds across silicone chains leading to a solid state material. Crosslinking of chains occurs by formation of $R\text{-}Si\text{-}(O)_3$ and $Si\text{-}CH_2\text{-}Si$ groups.

H. Jochem (✉)
ONERA - The French Aerospace Lab, F-31055 Toulouse, France

Université de Toulouse, UPS, LHFA, UMR 5069, 118 route de Narbonne,
F-31062 Toulouse cedex 4, France

CNES -French Aerospace Agency – 18 avenue Edouard Belin, F-31401 Toulouse cedex 9, France
e-mail: helene.jochem@onera.fr

V. Rejsek-Riba
ONERA - The French Aerospace Lab, F-31055 Toulouse, France

E. Maerten • A. Baceiredo
Université de Toulouse, UPS, LHFA, UMR 5069, 118 route de Narbonne,
F-31062 Toulouse cedex 4, France

S. Remaury
CNES -French Aerospace Agency – 18 avenue Edouard Belin, F-31401 Toulouse cedex 9, France

Silyl radicals are trapped in the polymer network and can be detected even 1 week after the end of irradiation.

1   Introduction

Due to their excellent properties such as good resistance to oxidation and UV radiation, wide operating temperature range, excellent insulating properties [1–3], silicone rubbers are used on spacecraft as thermal-control coatings or adhesives in solar cells. In GEO orbit, the spacecraft is exposed to space environment mainly characterized by vacuum, Ultra-Violet (UV) radiation and charged particles (electrons, protons). This aggressive environment causes degradation of materials. UV radiation is known to be responsible for thermo-optical degradations [4–7]. Besides, proton and electron fluxes generate important mechanical and surface properties damages [8–12]. In order to formulate better performing rubbers to increase spacecraft end of life, it is necessary to understand the space environment effects on the chemical structure of silicones. However due to the complexity of the formulated commercial resins, the determination of the degradation mechanisms is extremely difficult. The purpose of our project is, firstly, to develop experimental resins with a perfect control of the constituents, then, to study their degradation under GEO simulated environment in order to identify constituents responsible for the loss of thermo-optical and mechanical properties. We initiated our work with the study of silicone oils which are the main component of resins. They constitute a simplified system of resins and their liquid state allows carrying out a more important number of chemical analyses compared to a solid material. We have studied a silicone with a very simple structure: the polydimethylsiloxane (PDMS). To investigate the impact of functional end groups, we have also studied vinyl terminated polydimethylsiloxane used in formulation of resins. These two oils were synthesized by ring opening polymerization (ROP). To examine the influence of the synthetic method on degradation, ring opening polymerization was performed by using either an inorganic initiator potassium hydroxide KOH [13] or an organic catalyst N-Heterocyclic carbene (NHC) [14]. These silicones were exposed to UV radiation and electron flux independently to determine the effects of both irradiation factors on degradation.

2   Experimental Part

2.1   Materials

Polydimethylsiloxane (PDMS) and vinyl-terminated polydimethylsiloxane (vinyl-PDMS) with molecular weight of 50,000 g/mol were prepared by ring opening polymerization (ROP) of octamethyltetrasiloxane (D_4) (Fig. 1) using respectively
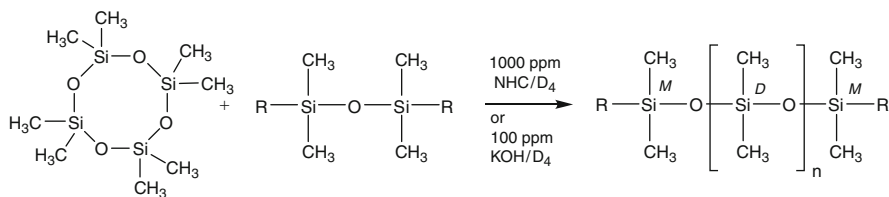
Fig. 1 PDMS (R = -CH$_3$) and Vinyl-PDMS (R = -CH = CH$_2$) syntheses by ROP of D$_4$
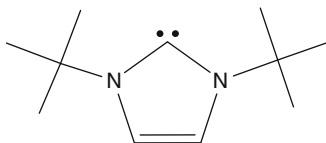

Fig. 2 N- heterocyclic carbène

N-Heterocyclic carbene (NHC) (Fig. 2) or potassium hydroxide (KOH) as organic catalyst or inorganic initiator. Hexamethyldisiloxane and divinyltetramethyl disiloxane were used as terminating agents for the synthesis of PDMS and vinyl-PDMS respectively. Ring opening polymerization of D$_4$ with KOH was performed at 150 °C during 15 hrs. Then, KOH was neutralized with CO$_2$ and the oils were filtered.

Oligomers and impurities were eliminated by heating at 150 °C under vacuum during several hours. Ring opening polymerization of D$_4$ with NHC was performed at 80 °C during 15 h. Then, NHC was degraded by heating at 160 °C during 30 min. Finally, oligomers and impurities were eliminated by heating at 150 °C under vacuum during several hours. After purification, the different oils were degassed under vacuum by repeating frozen/heating cycles and finally conditioned under nitrogen atmosphere in different quartz containers in order to remove all traces of oxygen which can be at the origin of curing.

3 Irradiation Facilities

Ultraviolet (UV) radiation was generated by a 1,000 W solar simulator (ORIEL) using ozone free Xenon arc lamp as the radiation source until 600 Equivalent Solar Hours (ESH) were achieved. (North/South faces of a GEO satellite receive 1,112 ESH per year).

Electron beam was supplied by a 2.7 MeV Van de Graaff accelerator connected to a vacuum vessel, GEODUR (ONERA facility). The electron energy was chosen at 1,250 keV and the irradiation current was fixed at 20 nA. The fluence was 10^{15} electron/cm^2 (corresponding to the dose received by the N/S faces per year).

4   Characterization Methods

Electronic Paramagnetic Resonance (EPR) spectra were recorded on an Elexys E500 BRUKER spectrometer at 115 K after irradiation.

The Headspace Gas Chromatography was performed with a Clarus 500 Gas Chromatograph/Mass Spectrometer from Perkin Elmer. Silicone oils were placed in an oven at 180 °C during 5 min and injected in BPX-5 column. Helium was used as gas vector.

^{1}H, ^{13}C and ^{29}Si liquid NMR spectra were recorded on a Brucker Avance 300 MHz. The ^{1}H, ^{13}C and ^{29}Si solid state NMR spectra were obtained on a Brucker Avance 400 MHz WB.

Gel Permeation Chromatography (GPC) was performed with a Waters linear styragel column and a refractive index detector (waters) with toluene as the eluent. PDMS standards were used for calibration.

Ultraviolet–visible-Near Infrared (UV–vis-NIR) spectroscopy was carried out using a Perkin Elmer Lambda 900 spectrometer. Specular transmission spectra were recorded in the wavelength range of 200–2,500 nm.

5   Degradation of Silicone Oils Under UV Radiation

5.1   Results and Discussion

Progressive yellowing of PDMS and vinyl-PDMS were observed during irradiation. Thermo-optical properties were measured by UV–vis-NIR spectroscopy. Spectra show a gradual decrease of transmission during irradiation and a shift of the cut off through the high wavelength, especially for the two oils synthesized with NHC (Figs. 3, 4, 5 and 6). At the end of irradiation at $\lambda = 400$ nm, the transmission is about to 63 % for oils synthesized with NHC compared to 80 % for those prepared with KOH. These results indicate that absorbent compounds are formed under UV radiations and this phenomenon is more significant for oils synthesized with NHC catalyst.

Then, NMR, GPC, EPR, GC headspace were used to characterize degradation of silicone structure and identify absorbent groups or species created during UV irradiations.

For PDMS oils synthesized with KOH or NHC, any change of the chemical structure can be detected by ^{1}H, ^{13}C, ^{29}Si NMR. GPC analysis showed similar molecular mass before and after irradiation. Furthermore, no volatiles were found by GC headspace and no radical could be detected by EPR. All these analyses did not allow us to identify the compounds responsible for thermo-optical properties degradation.

Contrary to PDMS oils, vinyl-PDMS oils evolved during the irradiation. The vinyl-PDMS synthesized with NHC became an elastic gum, and the one prepared
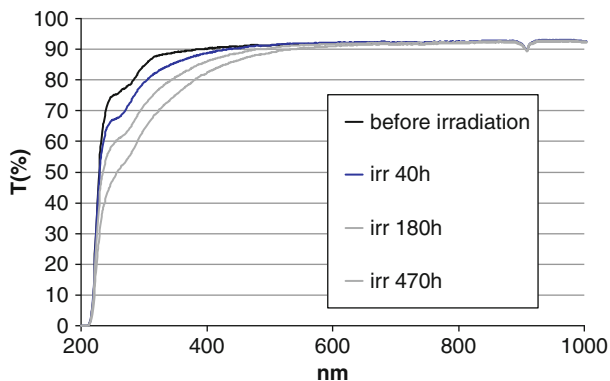
Fig. 3 Specular transmission spectra of PDMS/KOH in the wavelength range of 200–1,000 nm versus irradiation time
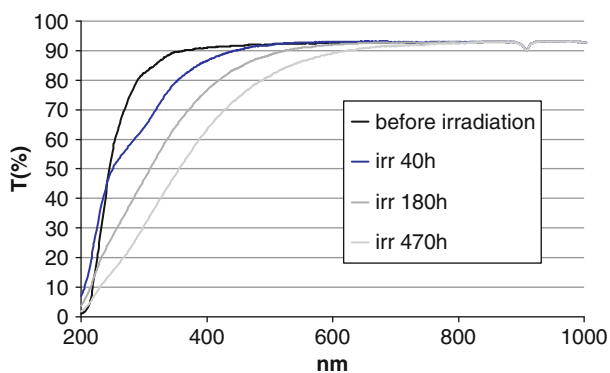

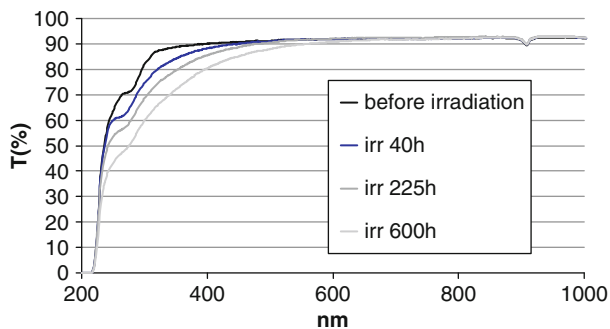**Fig. 4** Specular transmission spectra of PDMS/NHC in the wavelength range of 200–1,000 nm versus irradiation time

Fig. 5 Specular transmission spectra of vinyl-PDMS/KOH in the wavelength range of 200–1,000 nm versus irradiation time

Fig. 6 Specular transmission
spectra of vinyl-PDMS/NHC
in the wavelength range of
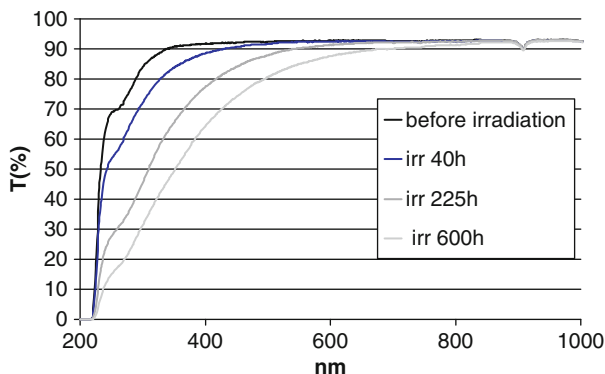200–1,000 nm versus
irradiation time

Table 1 Decrease of vinyl
functions during irradiation
time

Irradiation time (ESH)	Decrease of vinyl functions (%)	
	PDMS/NHC	PDMS/KOH
250	20	10
380	30	14
600	50	30

with KOH turned into a deformable gel. GPC was carried out on the soluble part of the two products. Results are similar for both oils and indicate the formation of two populations with different molecular mass. The major population presents a molecular mass of 100 000 g/mol and the minor one has a very high molecular mass, out of our column range (Mw > 400 000 g/mol). The chain length increase shows linear crosslinking between silicone chains.

The ^{1}H NMR spectra recorded during irradiation show a progressive decrease of the signal intensity of the vinyl end-groups (at 5–6 ppm) (Table 1).

At the end of irradiation, vinyl-PDMS/KOH presents a decrease of 30 % of vinyl groups. The phenomenon is more pronounced for vinyl-PDMS/NHC with a decrease of 50 %. As ageing is carried out by UV radiation, degradation should be initiated by a radical process [15]. However, none radical could be observed by EPR. Radicals are very reactive and recombine, probably instantaneously. Moreover, we expected to observe new bonds between PDMS chains, oligomers and gas production. Unfortunately no chemical change could be detected by ^{29}Si, ^{13}C and ^{1}H NMR or by GC headspace.

According to Israeli et al., direct photo-scission of the Si-Vinyl bond should not occur under UV irradiation. The radical process should occur via the initial addition of absorbent species to the unsaturated group [15]. UV spectroscopy shows the formation of absorbent species which could be responsible for the degradation of vinyl functions. The presence of a more important quantity of absorbent compounds in vinyl-PDMS oil prepared with NHC could explain the more significant decrease of vinyl functions compared to the one prepared with the inorganic initiator KOH.

Although vinyl-PDMS oils are transformed under UV radiation, the observed chemical changes can not explain the degradation of thermo-optical properties, and once again, the species responsible for the yellowing could not be characterized.

Fig. 7 Specular transmission spectra of purified vinyl-PDMS/KOH (*black*) in the wavelength range of 200–1,000 nm versus irradiation time compared to vinyl-PDMS/KOH (*gray*)
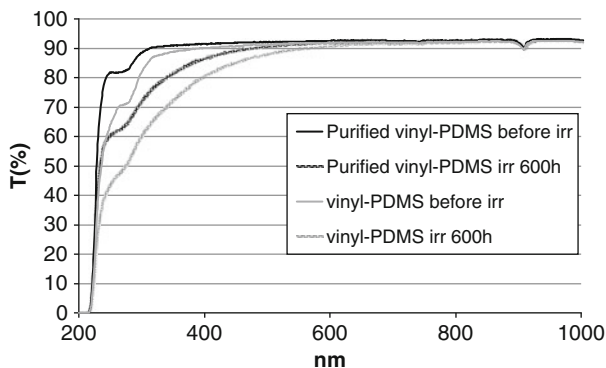
Both PDMS and vinyl-PDMS oils present a higher degradation of thermo-optical properties when synthesized with NHC. It must be mentioned that the amount of NHC used for oils synthesis is 10 times higher than KOH. Consequently, we suggested that residues of degraded catalyst are incompletely eliminated during treatment leading to the formation of absorbent species during UV radiation. For oils synthesized with KOH, we supposed that the degradation of thermo-optical properties could be due to the presence of impurities in starting reagents. To verify these hypotheses, a new study was carried out on highly purified vinyl-PDMS. Starting reagents, M_2Vi and D_4, were purified by distillation. Prolonged neutralization of catalyst and evaporation time were used to improve elimination of volatiles, impurities and the catalyst. Before irradiation, the highly purified vinyl-PDMS synthesized with KOH shows a much higher transmission in UV spectroscopy, especially for $\lambda < 350$ nm (Fig. 7). After irradiation, the transmission lost and the shift of the cut-off value towards higher wavelengths are similar for the two oils (about 20 % of transmission lost at 250 nm). It means that the quantity of absorbent species formed under UV is equivalent for the two oils. For vinyl-PDMS synthesized with NHC, before irradiation the two oils demonstrate the same UV curves. However, after irradiation, highly purified vinyl-PDMS exhibits a much higher transmission. This result shows that residual components coming from catalyst degradation are responsible for the major part of the degradation of thermo-optical properties and justify the need of an enhanced elimination of volatiles. Finally, even if transmission is generally improved with the two synthetic methods, apparition of absorbent species still occurs (Fig. 8).

6 Degradation of Silicone Oils Under electron Flux Irradiation

6.1 Results and Discussion

Results are similar for all oils independently of the functionalization or of the synthethis method. As it can be seen in Fig. 9, the starting oils became solid after irradiation. Because the samples were highly inhomogeneous after the irradiation,
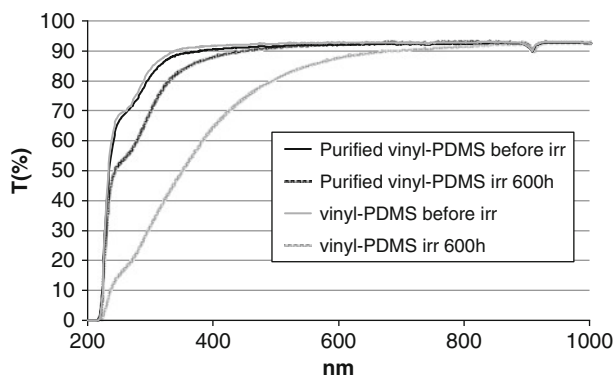
Fig. 8 Specular transmission spectra of purified vinyl-PDMS/NHC (*black*) in the wavelength range of 200–1,000 nm versus irradiation time compared to vinyl-PDMS/NHC (*gray*)

Fig. 9 Inhomogeneous PDMS/KOH after irradiation

thermo-optical transmission could not be measured by UV spectroscopy, however silicones appear colorless. Bubbles trapped in solid samples demonstrate gas production during irradiation. Methane and ethane were actually detected by GC headspace. Miller [16] and Dewhurst [17] have also observed these gases as well as molecular hydrogen that could not be detected by the mass spectrometer used in our project.
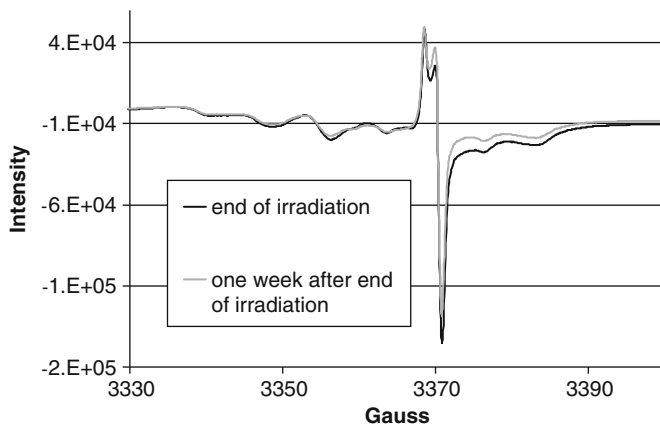
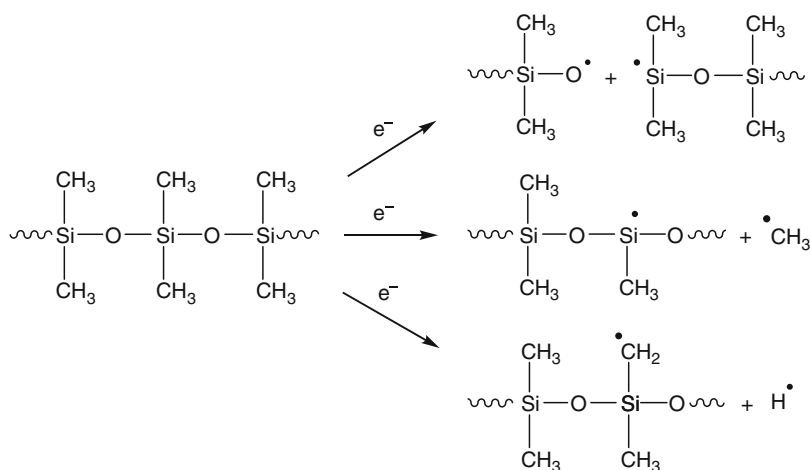**Fig. 10** EPR spectra after irradiation and 1 week after irradiation

Fig. 11 Scission of chains by radical process

^{29}Si solid state NMR spectra were recorded after irradiation and compared to spectra of initial oils. New peaks were observed at -29 ppm and -67 ppm. These signals can be attributed respectively to -Si-CH$_2$-Si- and R-Si(O)$_3$ functionalities [18] and indicate crosslinking of chains. A third peak at -32 ppm can be assigned to Si-H function.

Finally, EPR analysis was performed at 115 K immediately after the end of irradiation and 1 week later. Spectra show a singulet at 3,368 G (Fig. 10) attributed to silyl radicals [19, 20]. There is a peak superimposed to singulet at 3,370 G that is due to defects generated by electrons in EPR tube. One week after irradiation, the
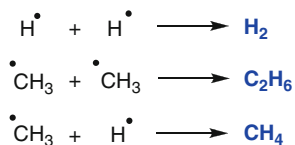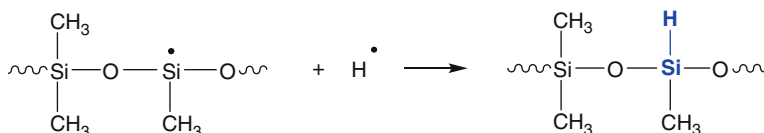
Fig. 12 Gas production

Fig. 13 Formation of Si-H function on silicone chain
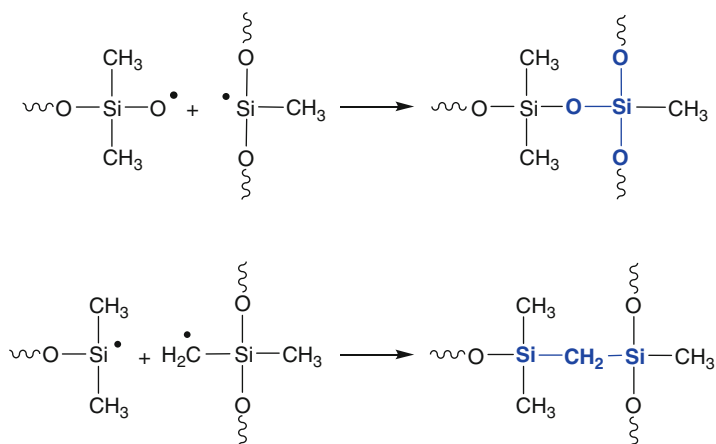
Fig. 14 Network formation via crosslinking of chains

signal is still present with a slightly decreased intensity. Radicals react very slowly probably because they are trapped in the silicone network.

Based on all these results, a mechanism of degradation can be proposed. Electrons of high energy cause the rupture of Si-O, Si-C and C-H bonds in silicone, leading to the formation of radicals (Fig. 11).

Radicals recombination generate gas production, methane, ethane and, possibly molecular hydrogen (Fig. 12), formation of new Si-H functionalities on silicone chains (Fig. 13), and crosslinking (Fig. 14). Crosslinking occurs along two paths leading to the formation of R-Si-$(O)_3$ and -Si-CH_2-Si- functionalities.

7   Conclusions

Irradiation by UV and electron fluxes leads to different type of silicone oil degradation. UV ageing of silicone oil is affected by the synthesis method used, and the end functions. Under UV irradiation any chemical change is observed for polydimethylsiloxane whereas vinyl-terminated polydimethylsiloxane exhibits an increased chain length. Both PDMS and vinyl-PDMS show degradation of thermo-optical properties, more significant for oils synthesized with organic catalyst. By purifying the starting reagents and eliminating the catalyst traces, the degradation of thermo-optical properties can be reduced. Irradiation by electrons generates scission of chains, leading to formation of radicals, production of methane and ethane, formation of new Si-H functions on silicone chains, and crosslinking of chains by creation of Si-CH$_2$-Si and Si-(O)$_3$ functionalities.

Currently, we are studying silicone resin degradation. Different parameters susceptible to impact on degradation are studied such as catalyst, additive or reinforced material. Degradations of silicone resins exposed to UV radiations, electron and proton fluxes independently are examined. Then synergistic effect of all these irradiations on silicone resin degradation will be investigated.

References

1. Noll W (1968) Chemistry and technology of silicones. Academic, New York
2. Biron M,(2007) Silicones ou siloxanes- structure et propriétés. Techniques de l'Ingénieur N 2280
3. De Buyl F (2001) Silicone sealants and structural adhesives. Int J Adhes Adhes 21:411–422
4. Grossman E, Gouzman I (2003) Space environment effects on polymers in low earth orbit. Nucl Instrum Methods Phys Res B 208:48–57
5. Dever JA, Banks BA, Yan L (2006) Vaccum ultraviolet radiation effects on DC 93.500 silicone film. Space Technol Proc 6:123–140
6. Marco J, Pons C (2002) UV and particles irradiations on thermal control coatings for simulated space environment final report
7. Marco J, Remaury S (2004) Evaluation of thermal control coatings degradation in simulated geo-space environment. High Perform Polymer 16:177–196
8. Marco J, Pons C (2006) Simulation of 1 year GEO orbit. Intermediate rapport
9. Zhang LX, He Sh Y, Xu Zh, Wei Q (2004) Damage effects and mechanisms of proton irradiation on methyl silicone rubber. Mater Chem Phys 83:255–259
10. Zhang L, Xu Zh, Wei Q, He Sh (2006) Effect of 200 keV proton irradiation on the properties of methyl silicone rubber. Radiat Phys Chem 75:350–355
11. Mingwei D, He Sh, Li R, Yang D (2006) Radiation effect of 150 keV protons on methyl silicone rubber reinforced with MQ silicone resin. Nucl Instrum Methods Phys Res B 248:31–36
12. Whang C (2006) Synergistic effect of protons and electrons on radiation damage of silicone rubber. J Spacecr Rocket 43(3):520–522
13. Grubb WT, Osthoff RC (1955) Kinetics of polymerization of a cyclic dimethylsiloxane. J Am Chem Soc 77(5):404–411
14. Rodriguez M, Marrot S, Kato T, Fleury E, Baceiredo A (2007) Catalytic activity of N-heterocyclic carbenes in ring opening polymerization of cyclic siloxanes. J Organomet Chem 692(4):705–708

15. Israeli Y, Phillipart JL, Cavezzan J, Lacoste J, Lemaire J (1992) Photo-oxidation of polydimethylsiloxane oils: II-effect of vinyl groups. Polym Degrad Stab 37:201–208
16. Miller A (1961) Radiation chemistry of polydimethylsiloxane. I. Crosslinking and gas yields. J Am Chem Soc 83:3519–3523
17. Dewhurst HA, St Pierre LE (1960) Radiation chemistry of hexamethylsiloxane a polydimethylsiloxane model. J Phys Chem 64(8):1063–1065
18. Hill DJT, Preston CML, Whittaker AK, Hunt S (2002) NMR study of the gamma radiolysis of poly(dimethylsiloxane) under vacuum at 303 K. Polymer 43:1051–1059
19. Siegel S, Judeikis H (1965) EPR study of the biphotonic nature of the solute sensitized photodecomposition of polydimethylsiloxane. J Chem Phys 43(2):343–351
20. Menhofer H, Heusinger H (1987) Radical formation in polydimethylsiloxanes and polydimethyldiphenylsiloxanes studied by the ESR spintrap technique. Radiat Phys Chem 29(4):243–251

Complex Investigations of New Black Thermal Control Coatings

A.V. Grigorevskiy, L.V. Kiseleva, and V.N. Strapolova

Abstract Complex investigations of new black thermal control coatings (TCCs) intended for spacecraft have been carried out. Changes of optical properties under combined exposure to space environment have been measured.

Abbreviations

As_o	Initial absorptance
Rs_o	Initial reflectance
ε	Emissivity
ρ_v	Specific volume resistance

1 Introduction

Space environment conditions affect greatly the service conditions of spacecraft that can vary to a great extent. This is determined by spacecraft orbits where they operate: low-Earth orbit, high-elliptical orbit passing through the Earth radiation belts, geostationary Earth orbit, interplanetary transfer orbit, etc. But whatever the orbit is, there exists solar electromagnetic radiation, vacuum, temperature changes and ionizing radiation, that produces in outer skin of a spacecraft absorbed doses from 10^2 to 10^9 rad annually.

A.V. Grigorevskiy (✉) • L.V. Kiseleva • V.N. Strapolova
JSC"Kompozit", 4, Pionerskaya str, Korolev, Moscow region 141070, Russia
e-mail: info@kompozit-mv.ru; grig19541@rambler.ru; test0650@rambler.ru

To maintain thermal balance of a spacecraft in service, its skin is covered with thermal control coatings with certain optical characteristics (A_s and ε) that change in operation conditions. In addition to standard process parameters like good spreading capacity, adhesion, etc. there are a number of other requirements imposed on external coatings of spacecraft with long-term lifetime:

– Stability of As and ε in operation conditions under exposure to damaging environmental factors and thermal cycling;
– Low outgassing level with $\Delta m/m \leq 1.0\%$ and content of volatile condensable material $\leq 0.1\%$;
– Low specific volume resistance ($\rho_v \leq 10^6 \ \Omega \times m$) for coatings of spacecraft that enter the Earth radiation belts.

2 Experimental Technique

To produce TCCs, radiation-resistant pigments and binders had to be chosen. For this purpose, samples of binders were prepared in form of films applied to substrates, 30 mm in diameter, made of AMg6 aluminum alloy and then cured at room temperature. Powders of black inorganic and organic pigment compounds were formed into tablets using a hydraulic press and a die made of a stainless steel with a polished surface to produce flat and smooth surfaces on the pressed tablets. Using the hydraulic press the pigment powder was compressed by the movable die until a solid tablet 3–4 mm in thickness was formed. Rated pressure required to form tablets from powder depends on hardness of pigment particles and varies within 12–15 MPa.

Using the " Cary 500" spectrophotometer, reflectance spectra in the wavelength range 0.2–2.5 µm have been measured for pigments, binders and TCCs before and after irradiation. Absorptance A_s was calculated using the reflectance spectra and data of extraterrestrial solar spectral density – $S(\lambda)$ [1].

The pigments and binders that demonstrated most radiation-resistant thermal optical properties were chosen according to their resistance to proton and electron radiation that cause the most severe deterioration of TCCs in highly-elliptical orbits and geostationary Earth orbits that is confirmed by numerous experimental data.

Proton irradiation of pigments and binders was performed using the UV-1/2 test facility [2]. the UV-1/2 was designed for studying physical-chemical properties of materials and coatings under separate and combined influence of space factors (vacuum as low as 10^{-5} Pa, electrons and protons with energies up to 50 keV, solar irradiation up to 10 see (solar exposure equivalent), temperature t $= \pm 150$ °C) and forecasting changes of their properties for long-term service.

Table 1 The characteristics of several black coatings

TCC	As_0	ε	ρ_v, Ohm $\times$ m
EKOM-2	0.95	$0.92 \div 0.95$	$\leq 7 \times 10^3$
AK-512 bl	0.90	0.90	$\leq 10^6$
Aeroglaze Z306	0.95	$0.89 \div 0.90$	$\geq 10^{10}$
PU1	0.96	0.88	–
PUK	0.97	0.91	$Rs < 5M\Omega/$

Basic enamel composition has been prepared based on chosen non-organic binders (liquid lithium or sodium glasses) and pigments. The pigment-binder ratio for these compositions was chosen between $6.0 \div 9.0$ for liquid glasses.

Enamel compositions were prepared using a porcelain ball grinder. Dispersion time for preparing homogeneous compositions was 1.5–2.0 h, depending on pigmentation level and on dispersivity and hardness of the pigments.

It was found that these pigments make possible to produce homogeneous dispersions. The enamels were applied on AMg6 aluminum alloy samples preliminary treated with sand paper and degreased with acetone.

3 Results and Discussion

The major components in TCCs are pigments and binders that define the radiation resistance of spacecraft coatings in service conditions. Usually, the initial optical characteristics of black TCC's, i.e. the absorptance As and the emissivity ε should be close to 1.

Table 1 shows the characteristics of several black coatings.

4 Study of black pigments

Optical properties of more than 15 black pigments in bulk form and in the form of tablets were studied. To prepare samples of pigments in bulk, samples of black TCC AK-512bl were used as substrates onto which the black pigment powder, nanoparticles or soot were applied. The FM-59M photometer measuring head was then put on top of the produced surface and the reflectance of the surface was measured. Table 2 provides the reflectance Rs values obtained from black pigments and nanoparticles in bulk form and from black pigments prepared as tablets. As one can see from Table 2, samples made from soot and/or ferric oxide pigments demonstrated maximum optical absorption.

However, when pigments are mixed with the binder, the optical properties of TCC deteriorate. As an example, one can take the heat-resistant black pigment that is used to prepare ECOM-2 TCC. If reflectance of the pigment is 1–2%, reflectance of TCC based on the pigment is 3–5%.

Table 2 Reflectance Rs values of black pigments and nanoparticles in bulk form and black pigments made as tablets

Pigment in bulk form	Rs_0	As_0	Pigment made as tablets	Rs_0	As_0
Nanoparticles Cu (40 nm)	0.038	0.962	Soot RuBtyp FW 171	0,007	0.993
Nanoparticles Ni (70 nm)	0.008	0.992	Soot Printex®75	0,013	0.987
Nanoparticles Cu (70 nm)	0.022	0.978	Pr_6O_{11}	0,144	0.856
Nanoparticles Fe (70 nm)	0.010	0.990	CuCr	0,056	0.944
Co	0.030	0.970	Fe_2O_3	0,015	0.985
Russian soot	0.008	0.992	Russian soot	0.016	0.984
Heat-resistant black pigment	0.013	0.987	Heat-resistant black pigment	0.030	0.970
Co_3O_4	0.023	0.977	Co_3O_4	0,052	0.948
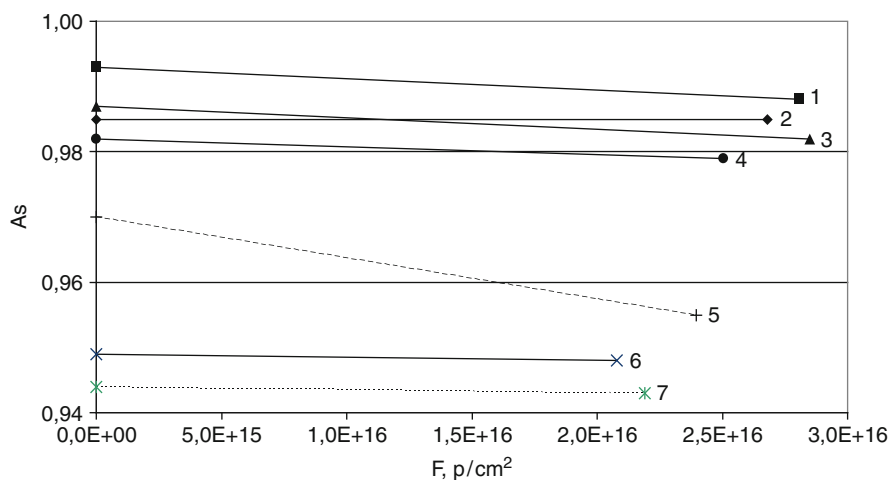
Fig. 1 Changes of optical properties (As) of different tableted black pigments after combined electron and proton radiation (*1* – soot RuBtyp FW 171, *2* – soot Printex®U, *3* – soot Printex®75, *4* – Russian soot, *5* – heat-resistant black pigment, *6* – Co_3O_4, *7* – CuCr)

After measuring the initial optical characteristics, the pigments were exposed to a combined proton and electron irradiation, with the energy of protons $Ep = 20$ keV and the energy of electrons $Ee = 40$ keV. The flux density of protons was kept at $\varphi_p = 3*10^{11}$ cm^{-2}s^{-1}, the flux density of electrons $\varphi_e = 2*10^{12}$ cm^{-2}s^{-1}. the experiments were conducted at a vacuum $P \leq 10^{-4}$ Pa and the temperature of the samples was kept at $T = 55 \pm 5$ °C.

Figure 1 shows the test results for black pigments. As can be seen from Fig. 1, the combined electron and proton radiation exerts insignificant influence on optical properties of the tested samples. A maximum change of absorptance As of 0.015 was found for the heat-resistant black pigment (line 5 in Fig. 1). The changes of absorptance values for other samples were below 0.005 that is within limits of spectrophotometer measurement error.

The optical reflectance spectra of pigment samples before the irradiation experiments are shown in Fig. 2.
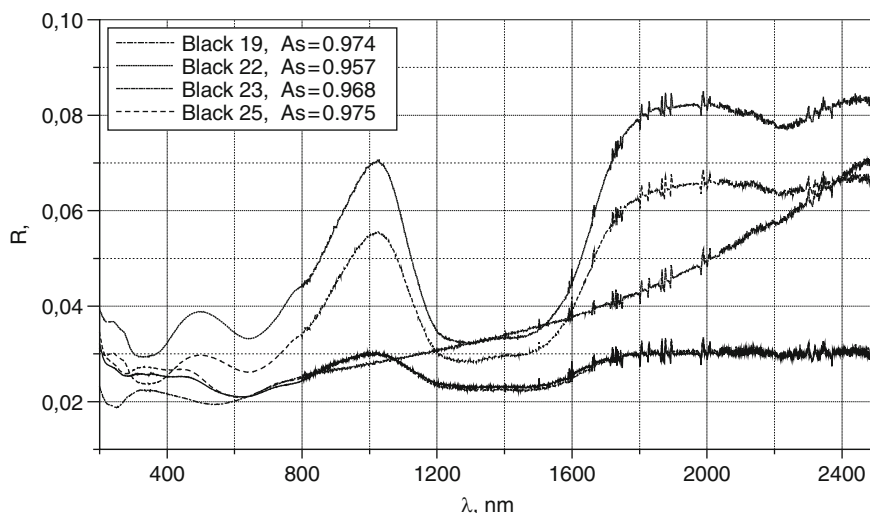
Fig. 2 Spectral dependences of reflectance for initial TCCs made from different black pigments

Table 3 Initial optical characteristics of TCCs made of black pigments and liquid glasses (sodium and lithium)

Composition of pigments	Rs_o	As_o	Binder
Co_3O_4	0.032	0.968	Lilg
Fe_3O_4 (magnetite)	0.049	0.951	Lilg
Magnetite, CO_3O_4, ultramarines, soot	0.030	0.970	Lilg
Magnetite, CO_3O_4, ultramarines, soot FW 17, matting additive, $LiSiF_6$	0.024	0.976	Lilg
Heat-resistant black pigment, carbonyl nickel, soot Printex 75, ultramarines	0.036	0.964	Lilg
Co_3O_4 , soot	0.026	0.974	Lilg
Co_3O_4	0.035	0.965	Lilg
magnetite, Co_3O_4, ultramarines, soot, matting additive	0.020	0.980	Lilg
magnetite + carbonyl nickel	0.055	0.945	Nalg
magnetite + Co_3O_4	0.038	0.962	Nalg
magnetite + carbonyl nickel + Co_3O_4 + soot	0.048	0.952	Nalg

Lilg liquid lithium glass, *Nalg* liquid sodium glass

5 Study of Black TCC

Tables 3 and 4 present initial optical characteristics of TCCs made of black pigments and liquid glasses (sodium and lithium). The optical characteristics of absorptance, As and emissivity, ε were measured using the spectrophotometer Cary 500, photometer FM-59M (with respect to reference sample of ECOM-2 having Rs = 3.8%) and thermo-radiometer TRM-I.

Table 4 Initial optical and electro physical characteristics of TCCs made of black pigments and liquid lithium glasses

Enamel composition	h, μm	Rs₀	ρ_v, Ohm × m
Nanoparticles of iron oxide	30	0,062	3,3
EKOM-2	140	0,049	5×10^5
Heat-resistant black pigment + soot	150	0,025	1.4×10^3
Co_3O_4	140	0,038	7×10^3
Co_3O_4	180	0,04	5.7×10^3
magnetite + Co_3O_4+ soot + ultramarines + matting additive + $LiSiF_6$	75	0,028	3.9×10^2
magnetite + Co_3O_4+ soot + ultramarines + matting additive + $LiSiF_6$	117	0,025	2×10^3

where *h* thickness

Table 5 Change of optical properties (As) of black TCCs based on liquid lithium glass after proton irradiation testing

TCC pigment	As₀	As_p	Fp, cm^{-2}	dAs
magnetite	0,048	0,088	1.8×10^{16}	−0,040
Co_3O_4	0,040	0,037	2.0×10^{16}	0,005
magnetite + carbonyl nickel	0,055	0,070	1.8×10^{16}	−0,015
magnetite + CO_3O_4	0,038	0,055	1.8×10^{16}	−0,017
magnetite + carbonyl nickel + Co_3O_4 + soot	0,048	0,065	1.8×10^{16}	−0,017

where As_p absorptance after proton radiation, *Fp* fluence of protons, *dAs* change of As
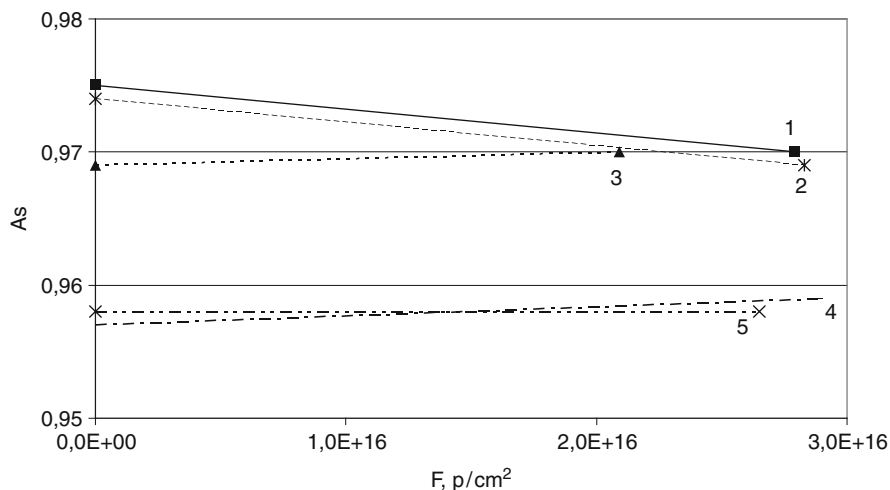

Fig. 3 Change of optical properties (As) of black TCCs based on liquid lithium glass after combined proton and electron irradiation (*1* – magnetite + cobalt oxide + soot + ultramarines + matting additive + lithium fluosilicate, *2* – heat-resistant black + ultramarines, *3* – magnetite, *4* – cobalt oxide, *5* – cobalt oxide + ultramarines)

Table 6 Change of optical properties (As) of black TCCs based on liquid lithium glass after combined proton and electron irradiation

№	TCC pigment	As_0	As_{p+e}
1	magnetite + CO_3O_4 + soot + ultramarines + matting additive + $LiSiF_6$	0,975	0,972
2	heat-resistant black pigment + ultramarines	0,974	0,969
3	Fe_3O_4	0,969	0,970
4	CO_3O_4	0,957	0,959
5	CO_3O_4 + ultramarines	0,958	0,958
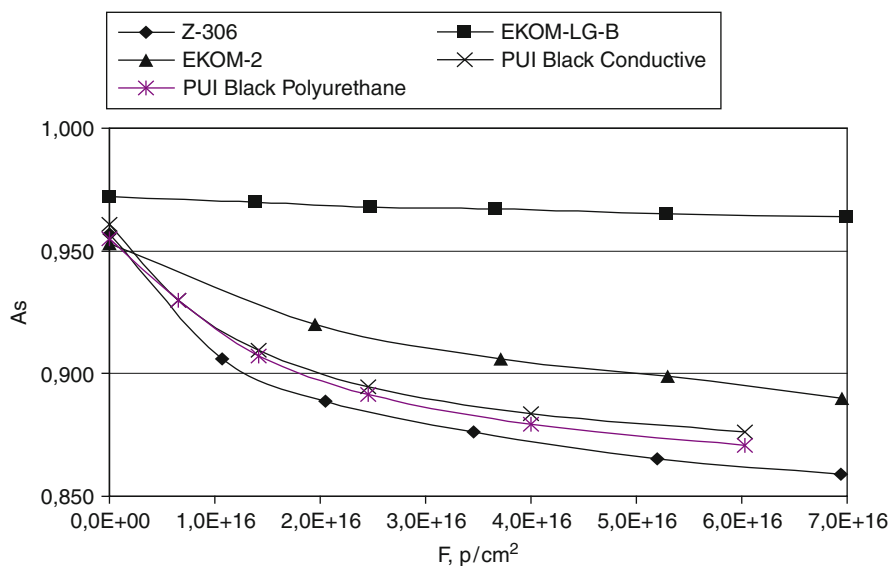
Fig. 4 Absorptance changes, As of black TCCs versus the combined irradiation fluence by protons and electrons

Table 4 gives also electro physical characteristics (specific volume resistance ρ_v) for a number of black TCCs.

To study the effects of ionizing radiation on changes of optical characteristics of black TCCs, they were irradiated in UV-1/2 system.

The irradiation of black TCCs based on liquid sodium glass was carried out at following conditions: proton energy – 20 keV, proton flux density – 10^{12} cm^{-2} s^1, pressure in vacuum chamber – 10^{-4} Pa (oil-free pumping), temperature of samples <30 °C. The test results for black TCCs based on liquid sodium glass are given in Table 5.

The irradiation of black TCCs based on liquid lithium glass was carried out at the following conditions: the proton energy – 20 keV, the electron energy – 30 keV, proton flux density – 10^{12} cm^{-2}·s^1, electron flux density – $2 \cdot 10^{12}$ cm^{-2} s^1, pressure in vacuum chamber – 10^{-4} Pa (oil-free pumping), temperature of samples <30 °C. The test results are presented in Fig. 3 and in Table 6.

Figure 4 shows changes of absorptance As of black TCCs as function of the combined irradiation flux by protons and electrons.

Irradiation of black TCCs with different binders was carried out as follows: proton energy – 20 keV, electron energy – 40 keV, proton flux density – 2.8 10^{11} cm^{-2} s^1, electron flux density – 2 10^{12} cm^{-2} s^1, pressure in vacuum chamber – 10^{-4} Pa (oil-free pumping), temperature of samples <30 °C.

Coating ECOM-LG-B is made on the basis of liquid lithium glass, ECOM-2 – on the basis of acrylic binder, other coatings - on the basis of polyuretanic binder. Considering that initial optical characteristics of all TCCs differ slightly, it is possible to draw a conclusion that change of absorptance for black TCCs under combined irradiation (protons + electrons) depends, first of all, on stability of binder that is used to prepare enamel.

6 Conclusions

To evaluate the changes of coating properties for long-term service in GEO the combined tests of TCC EKOM-LG-B were carried out:

– Outgassing tests;
– Thermal cycling test;
– Durability to combined effect of space environment (protons, electrons and UV solar radiation) with measurements of optical and electrical properties of coatings.

As a result of the conducted work, a black thermal control coating was developed with the following properties:

Absorptance, As	≥ 0.97
Emissivity, ε	≥ 0.93
Specific volume resistance, ρ_v, Ω*m	$\leq 10^5$
Mass, g/m^2	200
Adhesion: tearing failure stress (AMg6-type alloys) according to GOST 1476-69	40
According to GOST 15140, grade	2
Outgassing according to GOST R 50109:	
TML, %	≤ 1.0
CVCM, %	≤ 0.1
As (15 years in GEO) [3]	≥ 0.95

References

1. Space model (1983). Electromagnetic radiation of the Sun. In: acad. Vernov SN (ed), vol 1, ch. 5, MSU press, Moscow
2. Khassanchine RH, Kostyuk VI, Belyakov NA, Bajdaev DV (2006) On studying effect of combined action of damaging factors of space environment on outgassing process of non-metallic materials. Probl Atomic Sci Technol (1–2):44–48
3. Vasiliev V, Grigorevskiy A, Gordeev J (2002) Mathematical simulation methods in forecasting the change of integral and spectral optical characteristics of spacecraft external surface materials and coating. In: Kleiman JI, Iskanderova Z (eds) Protection of materials and structures from space environment, ICPMSE-6, sixth international conference, Kluwer, Toronto, pp 543–549, May 1-3, 2002

The Study of Simulated Space Radiation Environment Effect on Conductive Properties of ITO Thermal Control Materials

Feng Wei-Quan, Zhao Chun-Qing, Shen Zi-Cai, Ding Yi-Gang, Zhang Fan, Liu Yu-Ming, Zheng Hui-Qi, and Zhao Xue

Abstract In order to prevent detrimental effects of ESD caused by differential surface charging of spacecraft under space environments, an ITO transparent conductive coating is often deposited on the thermal control materials outside spacecraft. Since the ITO coating is exposed in space environment, the environment effects on electrical property of ITO coatings concern designers of spacecraft deeply. This paper introduces ground tests to simulate space radiation environmental effects on conductive property of ITO coating. Samples are made of ITO/OSR, ITO/Kapton/Al and ITO/FEP/Ag thermal control coatings. Simulated space radiation environment conditions are NUV of 500ESH, 40 keV electron of 2×10^{16} e/cm^2, 40 keV proton of 2.5×10^{15} p/cm^2. Conductive property is surface resistivity measured in-situ in vacuum. Test results proved that the surface resistivity for all ITO coatings have a sudden decrease in the beginning of environment test. The reasons for it may be the oxygen vacancies caused by vacuum and decayed RIC caused by radiation. Degradation in conductive properties caused by irradiation were found. ITO/FEP/Ag exhibits more degradation than other two kinds. The conductive property of ITO/kapton/Al is stable for vacuum irradiation. The analysis of SEM and XPS found more crackers and less Sn and In concentration after irradiation which may be the reason for conductive property degradation.

Keywords Space environment effects • Space environment • Surface charging • Electrical surface resistivity • Thermal control materials • In-situ measurement • Testing evaluation

F. Wei-Quan (✉) • Z. Chun-Qing • S. Zi-Cai • D. Yi-Gang • Z. Fan • L. Yu-Ming • Z. Hui-Qi • Z. Xue
Beijing Institute of Spacecraft Environment Engineering, Beijing 100094, China
e-mail: weiquan_feng@yahoo.com.cn

1 Introduction

ITO coating on thermal control materials is a good approach for eliminating surface charging. Indium tin oxide (ITO, or tin-doped indium oxide) is a solid solution of indium (III) oxide (In_2O_3) and tin(IV) oxide (SnO_2), typically 90% In_2O_3, 10% SnO_2 by weight [1]. It is transparent and colorless in thin layers. Indium tin oxide is one of the most widely used transparent conducting oxides because of its two chief properties, its electrical conductivity and optical transparency. ITO/Kapton/Al, ITO/FEP/Ag, and ITO/OSR are used for spacecraft outside thermal control materials [2]. Space environmental effects on ITO's surface resistivity are concerned since ITO coating is exposed directly to space radiation environment. Since ITO coating is very thin film, low energy electron and proton radiation were used for simulation. The low resistivity of ITO film is due to the large free carrier density. It is generally accepted that these free carriers are generated by two mechanisms: (1) Sn atom substitution of In atom and giving out one extra electron, (2) oxygen vacancies acting as two electron donors.

It was found in this investigation that three kinds of ITO coating's surface resistivity measured by in-situ method are decreased largely at beginning during irradiation. This may be due to the effects of oxygen vacancies and Radiation Induced Conductivity (RIC) caused by space environment. There are degradation of conductive property of ITO coatings under space radiation. ITO coatings on substrate of FEP/Ag are damaged more severely. Through SEM and XPS analysis, conductive degradation is due to crackers and element In and Sn decrease caused by space radiation. Conductive property of ITO/kapton/Al is very stable in space radiation environment. In-situ measurement of surface resistivity is very necessary for evaluating conductive properties of ITO coatings in space.

2 Experimental

2.1 ITO Test Specimens

There are three types of ITO test specimen which are ITO/OSR, ITO/Kapton/Al and ITO/FEP/Ag films. All of them are thermal control coatings for GEO spacecraft. Indium Tin Oxide is formed by substitutional doping of In_2O_3 with Sn which replaces the In^{3+} atoms from the cubic bixbyte structure of indium oxide. Sn thus forms an interstitial bond with oxygen as SnO_2. This valency state has relation with the ultimate conductivity of ITO. SnO_2 state means Sn^{4+} acts as a n-type donor releasing electrons to the conduction band. Both substitutional tin and oxygen vacancies of ITO contribute to the high conductivity.

For the undoped material of In_2O_3, Fermi level is located at mid bandgap of conduction band and valence band. Addition of Sn dopants results in the formation of donor states just below the conduction band. As the doping density is increased to some point, there are electron in conduction band. The free electron properties are

Fig. 1 ITO coated OSR
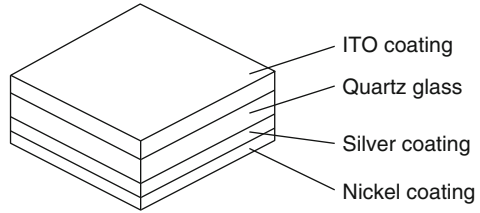
exhibited by the material when the density of electrons from the donor atoms exceeds certain value.

According to Ohm's law, the resistivity of ITO films is expressed as

$$\rho = 1/(q \, N\mu_H) \tag{1}$$

where, q is charge per carrier, N is carrier concentration N and μ_H is the Hall mobility.

Hall mobility is very low. The high conductivity of ITO films is said to be due to high carrier concentration rather than high Hall mobility.

ITO (Indium tin oxide) is one of the most widely used transparent conducting oxides because of its two chief properties, its electrical conductivity and optical transparency. Because of surface charging environment for GEO spacecrafts [3], the external thermal control coatings are required to be coated with ITO conductive film. Thin films of ITO are deposited on surfaces by sputter deposition techniques. The surface resistivity is about $10^4\Omega$/sq. which is enough to control space surface charging. ITO/OSR(Optical Solar Reflector), ITO/Kapton/Al and ITO/FEP/Ag are three external thermal control materials commonly used for spacecraft. ITO/OSR structure is shown in Fig. 1. The structures of ITO/Kapton/Al and ITO/FEP/Ag are similar to ITO/OSR. The ITO coating is open to space electron, proton and solar UV environments thus their environment conditions are very severe [4].

There are three samples for each type of ITO test specimen during irradiation test. The diameter of sample is 50 mm.

3 In-Situ Surface Resistivity Measurements [8, 9]

In order to measure surface resistance of ITO films during irradiation test a surface resistivity in-situ measuring device was designed as shown Fig. 2.

The measurement principle is according to ASTM-D257-99, as shown in Fig. 3. Surface resistivity of ITO coatings was investigated with a bi-ring electrode structure. Surface resistivity measurements were made with a Keithley 6517A instrument. The electrodes are made of copper foil with thickness of 0.2 mm. The diameter of the center electrodes E1 is 25 mm. The gap between the electrodes is 2 mm. The ring electrode E2 is 5 mm wide. The electrodes are affixed to the surfaces of the samples with a conductive adhesive. Two metal wires are attached to electrodes E1 and E2.

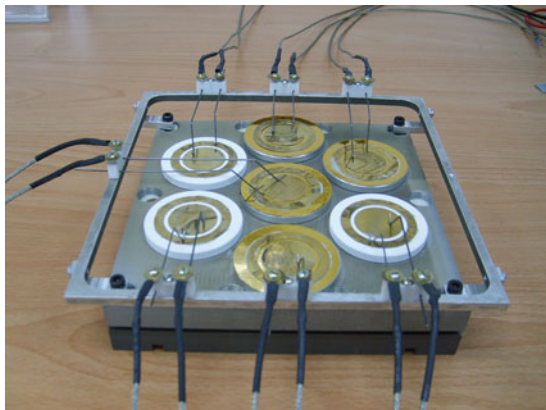Surface resistivity ρ_s was calculated using (2):

Fig. 2 Surface resistivity in-situ measurement set-up

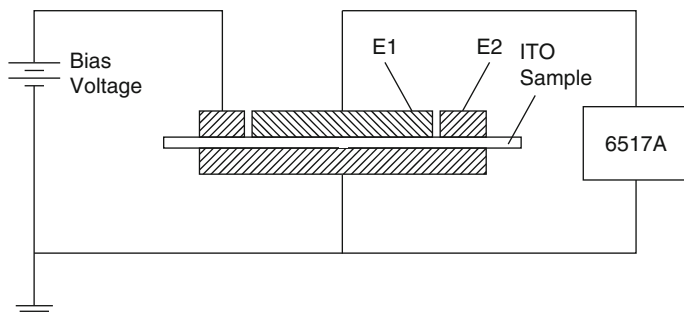**Fig. 3** Surface resistivity measurment principle

$$\rho_s = R_s \cdot \pi(d + g)/g \tag{2}$$

where,

R_s — Measuring resistance across gap,Ω;

ρ_s— Surface resistivity,Ω/sq;

g — gap distance,m;

d — Diameter of E1,m.

This in-situ measurement of surface resistivity was verified using a Keithley 8009 instrumetn at regular environment conditions in air.

4 Electron Irradiation

Electron irradiation test was performed on Combined Low Energy Irradiation Test Facility in Beijing Institute of Spacecraft Environment Engineering. This facility's capabilities include electrons with energies up to 120 keV and proton irradiation with energy up to 50 keV, solar electromagnetic radiation with intensity up to 6
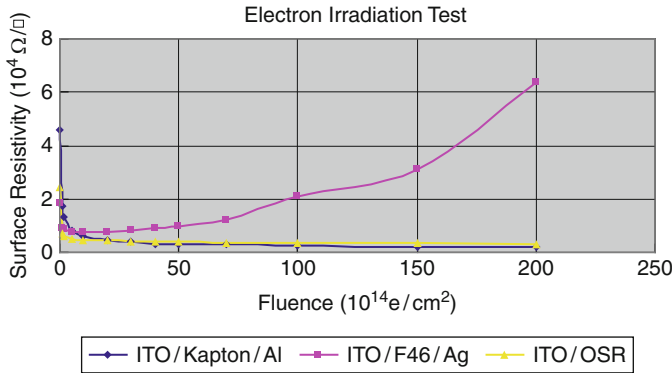
Fig. 4 Surface resistivity changes under electron irradiation

equivalent suns, vacuum up to 10^{-6} torr, and temperatures of sample less than 50 °C. The coating specimens were irradiated by an electron flux at the following conditions:

Electron energy: 40 keV;
Electron flux: 6.76 nA/cm^2;
Sample temperature during irradiation: about 20 °C
Testing chamber vaccum: 10^{-5} Torr or better
Electron fluence: 2×10^{16} e/cm^2

Specimens were placed on a cooled metal plate; the temperatures of specimens and plates were monitored by thermocouples during all experiments. The electron flux on each specimen was surveyed by Faraday cup placed in the electron beam. Surface resistivity changes are monitored during electron exposure intervals (Fig. 4). As shown in Fig. 4, in general, surface resistivity of three kinds of ITO specimens decreased sharply at the beginning and then increased very slowly for ITO/Kapton/Al and ITO/OSR and quickly for ITO/FEP/Ag. The conductive properties of ITO/FEP/Ag degraded more than other two kinds of ITO coatings.

ITO coatings, when exposed to ionizing radiation, undergo the formation of electron–hole pairs and consequently exhibit radiation-induced conductivity (RIC), largely increasing the conductive capability of ITO coatings used in ionizing environments. The sharp decrease of surface resistance at first is due to the RIC (Radiation Induced Conductivity) caused by electron irradiation. Electron irradiation increases charge carrier concentration inside the ITO coatings which plays a beneficial effect, increasing the conductive property. RIC is proportional to the electron dose rate. The long-time decay of RIC is determined by carrier recombination rate of the materials. At the same time, the vacuum condition increases oxygen vacancies concentration in ITO coatings which increase conductivity. After irradiation, when samples return to air condition, their surface resistivity increased.

The electron dose rate profile is calculated as shown in Fig. 5. Since ITO coating is very thin about 20 nm, the dose rate inside the ITO coatings is about 60 Gy/s. The density of ITO coating was assumed as 7 g/cm^3 for the calculation.
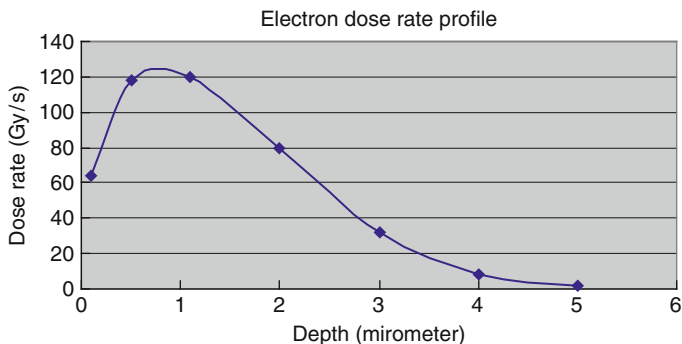
Electron dose rate profile

Fig. 5 Dose rate profile in sample for electron irradiation

5   Proton Irradiation

Proton irradiation test was performed on Combined Low Energy Irradiation Test Facility in Beijing Institute of Spacecraft Environment Engineering. The ITO coating specimens were irradiated by a proton flux at the following conditions:

Proton energy: 40 keV;
Proton flux: 0.8456 nA/cm^2;
Sample temperature during irradiation: about 20 °C
Testing chamber vaccum:10^{-4} Torr or better
Proton fluence: 2.5×10^{15}p/cm^2

The surface resistivity values, measured at intervals of proton irradiation as shown in Fig. 6, are quite different from the electron irradiation, i.e. in the beginning of irradiation, surface resistivity decreased slowly. Conductive property of ITO/OSR degraded more quickly than in two other kinds of ITO films.

The sudden decease of surface resistivity at first is also due to RIC caused by proton irradiation. RIC of the proton irradiation is less than that of the electron irradiation. The degradation of surface resistivity later for ITO/OSR means that it was damaged by irradiation. After irradiation, when samples return to air condition, their surface resistivity has increased. The proton dose rate profile is calculated as shown in Fig. 7. Since ITO coating is very thin about 20 nm, the dose rate inside the ITO coatings is about 7 Gy/s which is much less than that for electron irradiation.

6   Solar NUV Irradiation [6, 7]

Solar NUV irradiation test was performed on Combined Low Energy Irradiation Test Facility in Beijing Institute of Spacecraft Environment Engineering. The ITO coating specimens were irradiated by solar NUV at the following conditions:

NUV source: 1,000 W xenon lamp
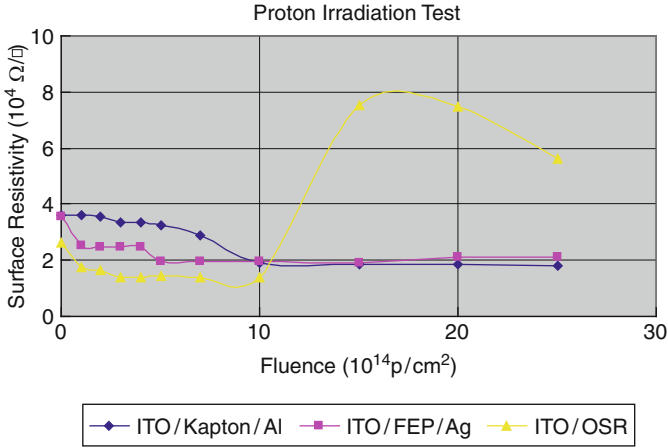Intensity at samples level: about 4 SC $\pm$ 10%;

Fig. 6 Surface resistivity changes under proton irradiation
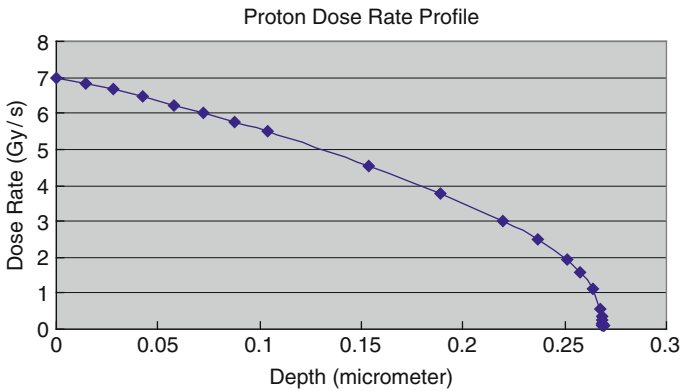

Fig. 7 Dose rate profile in sample for proton irradiation

Sample temperature during irradiation: about 30 °C
Testing chamber vaccum: 10^{-5} Torr or better
Total irradiation: 500 ESH

Surface resistivity is measured at interval of NUV irradiation as shown in Fig. 8. Surface resistivity of three kinds of ITO coatings suddenly decreased at the beginning to values that are much less than pristine values. This phenomenon is also due to the RIC caused by NUV irradiation. The degradation of surface resistivity later means that ITO coating was damaged by NUV irradiation. ITO/ FEP was damaged by NUV more than other two kinds of ITO samples. After irradiation, when samples return to air condition, their surface resistivity has increased. The intensity for NUV irradiation is 4SC (Solar Constant). One SC for all solar wavelength is 135.3 mW/cm^2 in which NUV occupies 7.4%. Thus one SC
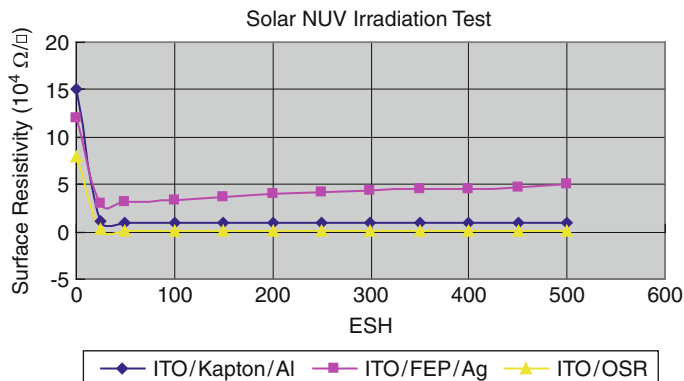
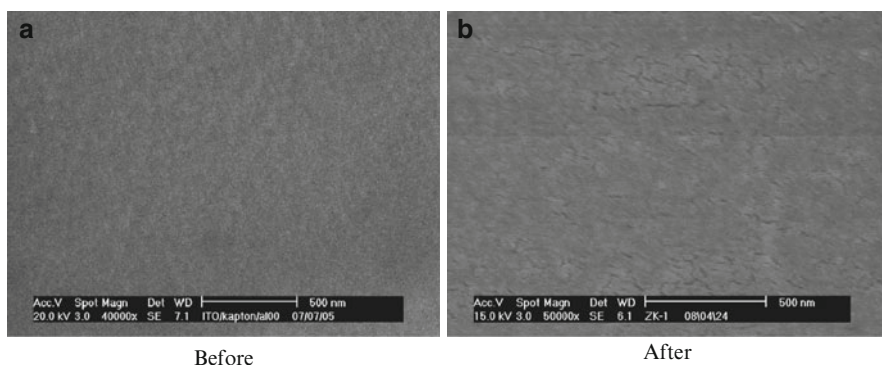**Fig. 8** Surface resistivity changes under solar NUV irradiation

Fig. 9 Surface Topography of ITO/Kapton/Al before and after electron irradiation

for NUV is 10 mW/cm^2. The dose rate for NUV irradiation on one square centimeter of ITO coating is about 40 mW.

7 Specimen Analysis

7.1 Scanning Electron Microscopy

Surface topography images of ITO samples, as analyzed with scanning electron microscopy (SEM) before and after electron/proton, UV irradiation are shown in Figs. 9, 10, and 11

There are small cracks after irradiation in the ITO/Kapton/Al sample as shown in Fig. 9. There are much more cracks after irradiation for ITO/FEP/Ag sample as shown in Figs. 10 and 11. ITO coating is difficult to adhere to FEP substrate.
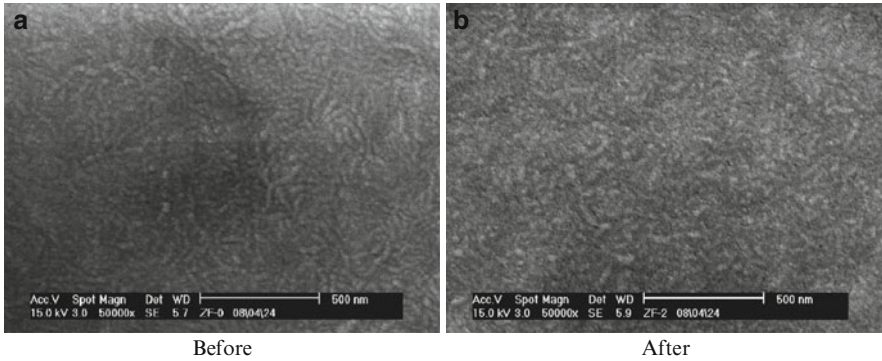
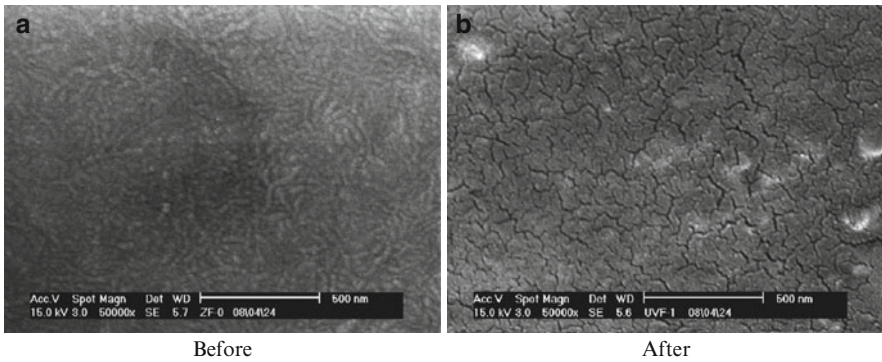Fig. 10 Surface topographies of ITO/FEP/Ag before and after proton irradiation

Fig. 11 Surface topography of ITO/FEP/Ag before and after UV irradiation

8 X-ray Photoelectron Spectroscopy [5]

X-ray photoelectron spectroscopy (XPS) is a semi-quantitative technique that provides information on the elemental composition in the upper layers of the materials. After irradiation, samples were taken out from the vacuum chamber instantly to performed XPS analysis. X-ray photoelectron spectroscopy (XPS) of ITO coating is used for measuring the elemental composition of the ITO coating before and after electron, proton and UV irradiation as shown in Tables 1, 2, 3, 4, 5, 6, and 7.

As can be seen from the XPS results, there is a general phenomenon for all samples, i.e. the concentrations of Sn and In decreased storngly. It means that ITO coatings are damaged by irradiation environment which is a factor to increase surface resistivity of ITO.

Table 1 Elemental composition of ITO/Kapton/Al before and after electron irradiation

Element composition (at. %)	C	N	O	In	Sn
Before irradiation	62.64	3.07	20.52	12.43	1.35
After	69.31	2.49	21.85	5.79	0.57

Table 2 Elemental composition of ITO/FEP/Ag before and after electron irradiation

Element composition (at. %)	C	O	F	In	Sn
Before	41.17	30.92	4.50	21.21	2.20
After	57.69	31.89	8.24	1.97	0.21

Table 3 Elemental composition of ITO/Kapton/Al before and after proton irradiation

Element composition (at .%)	C	N	O	In	Sn
Before irradiation	62.64	3.07	20.52	12.43	1.35
After irradiation	78.72	2.06	15.54	3.34	0.34

Table 4 Elemental composition of ITO/FEP/Ag before and after proton irradiation

Element composition (at. %)	C	O	F	In	Sn
Before irradiation	41.17	30.92	4.50	21.21	2.20
After irradiation	80.37	17.19	1.79	0.65	0.00

Table 5 Elemental composition of ITO/Kapton/Al before and after NUV irradiation

Element composition (at. %)	C	N	O	In	Sn
Before irradiation	62.64	3.07	20.52	12.43	1.35
After irradiation	70.61	1.48	22.04	5.16	0.71

Table 6 Elemental composition of ITO/F46/Ag before and after NUV irradiation

Element composition (at. %)	C	O	F	In	Sn
Before irradiation	41.17	30.92	4.50	21.21	2.20
After irradiation	70.89	14.69	5.50	7.10	0.82

Table 7 Elemental composition of ITO/OSR before and after NUV irradiation

Element composition (at. %)	C	O	Si	In	Sn
Before irradiation	54.97	26.88	8.01	9.17	0.97
After irradiation	57.29	25.15	7.46	9.03	1.07

9   Conclusions

The design principles of indium tin oxide film (ITO) are used on thermal control coatings to prevent electrostatic discharge for spacecraft surface charging. ITO/OSR, ITO/Kapton/Aland ITO/FEP/Ag are three main types of thermal control materials for spacecraft. Simulated space radiation environmental testing of these

ITO coatings using NUV, 40 keV electron and proton were performed. The dose rates for electron, proton and NUV were 50 Gy/s, 7 Gy/s and 40 mW/cm^2, respectively.

In-situ measurement of surface resistivity was used for evaluation. Scanning electron microscopy (SEM) and X-ray photoelectron spectroscopy (XPS) were used for analyzing ITO coating damage. Test results proved that the surface resistivity for all ITO coatings is decreasing sharply by 1–2 orders of magnitude in the beginning of vacuum irradiation tests. The reasons for such sudden decrease may be the oxygen vacancies increase and decayed RIC in ITO. Thus, the in-situ measurement and vacuum irradiation conditions are necessary for evaluation of ITO conductive ability for space applications.

The irradiation caused degradation of conductive properties for three kinds of ITO coatings. ITO/FEP/Ag exhibits stronger degradation than other two types. The reason for such behavior may be bad adhesion of ITO coating to FEP substrate. The conductive property of ITO/Kapton/Al is very stable for radiation environments. The SEM analysis found that extensive cracks are developing after irradiation tests. The XPS analysis confirmed a decrease in the concentration of Sn and In in the surface layers of the ITO coating after irradiation. These two damage-induced properties in the ITO coatings are detrimental for conductive properties of ITO coatings.

References

1. Chopra KL, Major S, Pandya DK (1983) Transparent conductors – A status review. Thin Solid Films 102:1–46
2. Zimcik DG, Wertheimer MR (1989) Evaluation of plasma deposited protective coatings for multipurpose space application. Surf Coat Technol 39(48):617–626
3. Purvis CK, Henry B, Garrett AC, Whittlesey N, Stevens J (1984) Design guidelines for assessing and controlling spacecraft charging effects. NASA technical paper, 2361
4. Finckenor MM, Kamenetzky RR, Vaughn JA, Mell R, Sims J, Thompson R, LeMaster P (1996) Investigation of space environmental effects on electrically conductive thermal control coatings at MSFC. In: 28th SAMPE international symposium technical conference. Long Beach, CA vol 28, pp 1080–1094
5. Fan JCC, John B (1977) X-ray photoemission spectroscopy studies of Sn doped indium oxide films. J Appl Phys 48:3524–3531
6. Zi-Cai SHEN, Chun-Qing ZHAO, Wei-Quan FENG et al (2009) Mechanism of degradation of the electrical properties of pellicular antistatic thermal control coatings under near ultraviolet irradiation. Spacecr Environ Eng 26(5):415–418
7. Zi-Cai SHEN, Chun-Qing ZHAO, Wei-Quan FENG et al (2008) Influence of near ultraviolet irradiation on the electrical property of OSR second surface mirror. Spacecr Environ Eng 25 (5):438–440
8. Chun-Qing Z, Wei-Quan F et al (2008) Study of in-situ measurement method of surface resistivity of thermal control coatings. Spacecr Environ Eng 4(2):410–415
9. Chun-Qing Z, Wei-Quan F et al (2008) Study of in-situ measurement method of surface resistivity of thermal control coatings. Spacecr Environ Eng 4(2):410–415

Computational Analysis of Mass Loss Rate of Polymeric Composites Under Electron Irradiation in Vacuum

R.H. Khasanshin, A.N. Timofeev, and A.N. Galygin

Abstract Problems concerning mass loss of polymeric composites in vacuum under electron radiation are considered. To describe this process a mathematical model in the form of a boundary-value task for set of partial equations with movable boundary of integration domain is proposed. The effect of irradiation on mass loss rate of polymeric composites accounting for changes in their properties was numerically analyzed.

1   Introduction

In accelerated tests, polymeric composites (PC) are irradiated by charged particles with intensities that are several orders greater than space radiation intensities. This is due to the fact that in tests that are usually conducted no longer than 24 h, material absorbs radiation dose equal to dose of 10–15 year service. For example, near-surface absorbed dose of ionizing radiations in PC with specific density $\rho = 1.5$ g/cm^3 is about 2×10^8 Gy [1] for 1-year service in GEO.

Polymeric composites are often used as thermal control coatings (TCC) that are subjected to maximum radiation exposure in service. It is known that irradiation of a PC is accompanied by intense gas formation but the evolution of volatile products (VP) from the material – vacuum interface is limited by diffusion. Well-developed surface morphology together with thin TCC films facilitates migration of radiolysis

R.H. Khasanshin (✉) • A.N. Timofeev • A.N. Galygin
OAO "Kompozit", 4, Pionerskaya str., 141070 Korolev, Moscow region, Russia
e-mail: rhkhas@mail.ru

products to free coating surface. In this case outgassing and destruction of material augment permeability of the film, accelerate migration processes and make them easier.

Despite the fact that characteristic thickness of TCC is about 100 μm, depth distribution of absorbed dose in material in service conditions is non-uniform. For instance, in GEO the absorbed dose below a thin layer of material with density 1.5×10^{-4} g/cm^2 decreases about 20 times [1]. Therefore, generation of radiolysis products, destruction of material and changes of its properties are non-uniform through depth. This should be considered in models describing TCC mass loss.

Experimental study of PC mass loss in vacuum under irradiation brought to light the necessity to take into consideration the radiation-induced sublimation of a number of non-metallic materials [2]. Dependence of characteristics of the process on type of radiation, energy and intensity was ascertained as well [3, 4]. Therefore, in this paper, the processes defining PC mass loss are analyzed based on the model accounting for the mobility of material-vacuum boundary.

2   Mathematical Model

Computational experiments are often used when a program is being prepared to test materials in space environment. As a rule, they consists in formulating basic principles managing the process under study, applying available mathematical model or developing a new one, appropriate to these principles, solving the mathematical problem and, at last, analyzing the obtained solutions.

In the model below it is postulated that irradiation of PC in vacuum is accompanied by:

- Radiolysis of organic components;
- Emission of forming and absorbed VP;
- Desorption of VP from free material surface;
- Chemical reactions;
- Radiation-induced destruction of potential outgassing products;
- Sublimation.

With these assumptions, finding the PC mass loss in vacuum under irradiation reduces to solution of a set of equations describing change of VP concentrations in material $C_i(x,t)$ ($i = 1, 2,\ldots, N$) due to the above-cited processes, as follows:

$$\frac{\partial C_i(x,t)}{\partial t} = \frac{\partial}{\partial x}\left(D_i(x,t)\frac{\partial C_i(x,t)}{\partial x}\right) - [\sum_{j=1}^{M}\sigma_{i \to j}^{rad} + \chi_i^{rad}(x)]C_i(x,t)+$$

$$+S_i^{rad}(x,t), \quad x \in (0, h - \upsilon t), \quad t>0, \qquad (1)$$

$$C_i(x,t)|_{t=0} = R_i = const, \qquad x \in [0, h] \qquad (2)$$

$$\left[D_i \frac{\partial C_i(x,t)}{\partial x} + [k_i + a_i^{rad} + \upsilon] C_i(x,t) \right]_{x=h-\upsilon t} = 0, \quad t > 0, \tag{3}$$

$$\left. \frac{\partial C_i(x,t)}{\partial x} \right|_{x=0} = 0, \quad t > 0, \tag{4}$$

where $\sigma_{i \to j}^{rad}$ – is the weighting coefficient of irradiation-induced decomposition of i-component through j-channel, s^{-1}; M – is the number of destruction channels of i-component; χ_i^{rad} – chemical reaction rates with involvement of i-component, s^{-1}; k_i – effective desorption coefficient of i–type VP, $\mu m \cdot s^{-1}$; $D_i(x,t)$ – effective diffusion coefficient of i–type VP, $\mu m^{-2} \cdot s^{-1}$; R_i – concentration of i–type VP in material before radiation, $rel.~units$; $S_i^{rad}(x,t)$ – i-type VP source function, $rel.~units \cdot s^{-1}$; a_i^{rad} – parameter defining influence of radiation on desorption kinetics of i–type VP, $\mu m \cdot s^{-1}$; υ – sublimation rate of material $\mu m \cdot s^{-1}$; h – thickness of PC, μm.

In (1), (2), (3), and (4) it is assumed that the material – vacuum boundary moves with a fixed velocity and material thickness changes as $\eta(t) = h - \upsilon t$.

For further convenience let us introduce generalized rate of first-order reactions taking place in material:

$$\beta_i(x) = \sum_{j=1}^{M} \sigma_{i \to j}^{rad} + \chi_i^{rad}(x) \tag{5}$$

Generally, $\upsilon = \upsilon(t)$, $k_i = k_i(t)$, $D_i = D_i(x,t)$ that is material-vacuum boundary propagation velocity, effective desorption and diffusion coefficients are functions of time. Such dependencies, for example, can be related with non-uniformity of filler depth distribution in PC and/or radiation-induced changes of its properties.

i-type VP source functions found using the Monte-Carlo method from calculations of distributions of absorbed doses of monochromatic electrons normally hitting PC flat plate target surface can be presented as:

$$S_i^{rad}(x) = A_i \exp[-B_i(x - C)^2] \tag{6}$$

where A_i, B_i and C – parameters depending on electron initial energy (E_0) and flux density (φ_e, $cm^{-2}~s^{-1}$) and on composition and thickness of material.

It is obvious that shape of function $S_i^{rad}(x)$ approximately follows the absorbed dose distribution. In general, the composition of a material can significantly alter under irradiation, therefore we should take into account time dependence of the source function.

An important feature of (1), (2), (3), and (4) is a movable material – vacuum boundary. To transform the integration range of this task into a range with fixed boundary, a new variable ξ was introduced

$$x = \xi \cdot \eta(t), \ \xi \in [0, 1] \tag{7}$$

and new designations stated: $u_i(\xi, t) = C_i(x, t), \tilde{D}_i(\xi, t) = D_i(x, t), \tilde{\beta}_i(\xi, t) = \beta_i(x),$ $k_i^{rad} = a_i^{rad} + k_i$. Then (1), (2), (3), and (4) can be written in new variables as follows:

$$\eta^2(t)\frac{\partial u_i(\xi, t)}{\partial t} = \xi\,\eta(t)\frac{d\eta(t)}{dt}\frac{\partial u_i(\xi, t)}{\partial \xi} + \frac{\partial}{\partial \xi}\left(\tilde{D}_i(\xi, t)\frac{\partial u_i(\xi, t)}{\partial \xi}\right) -$$
$$-\eta^2(t)\left[\tilde{\beta}_i u_i(\xi, t) + \tilde{S}_i(\xi, t)\right], \quad \xi \in (0, \eta(t)), \quad t>0, \qquad (8)$$

$$u_i(\xi, t)|_{t=0} = R_i, \qquad \xi \in [0, 1] \qquad (9)$$

$$\left[\tilde{D}_i(\xi, t)\frac{\partial u_i(\xi, t)}{\partial \xi} + \eta(t)\left(k_i^{rad}(t) - \frac{d\eta(t)}{dt}\right)u_i(\xi, t)\right]_{\xi=1} = 0, \qquad t>0, \qquad (10)$$

$$\left.\frac{\partial u_i(\xi, t)}{\partial \xi}\right|_{\xi=0} = 0, \qquad t>0. \qquad (11)$$

It should be noted that on the right side of (8) there is a member containing first-order derivative with respect to the variable ξ that is responsible for change of i–type VP concentration due to motion of computational domain.

Resulted from the conducted transformation is a set of differential equations (8), (9), (10), and (11) that is non-linear, but boundaries where spatial variable ξ changes are fixed.

Solution of (1), (2), (3), and (4) incorporates values of function $C_i(h-vt,t)$ – VP concentration in the near-surface layer of material. This value is used to find mass loss rate from unit surface:

$$\dot{M}_i(t) = m_i(k_i^{rad} + v)C_i(h - vt, t), \qquad (12)$$

where m_i–i-type molecule mass.

Total mass loss of material $M(t)$ from unit surface over the period t can be found from

$$M(t) = \sum_{i=1}^{N} M_i(t) = \sum_{i=1}^{N} m_i \int_{0}^{t} (k_i^{rad} + v)C_i(h - v\tau, \tau)d\tau. \qquad (13)$$

From now on, PC mass loss is considered as taking place at the cost of i-type VP, therefore the subscript i is not used.
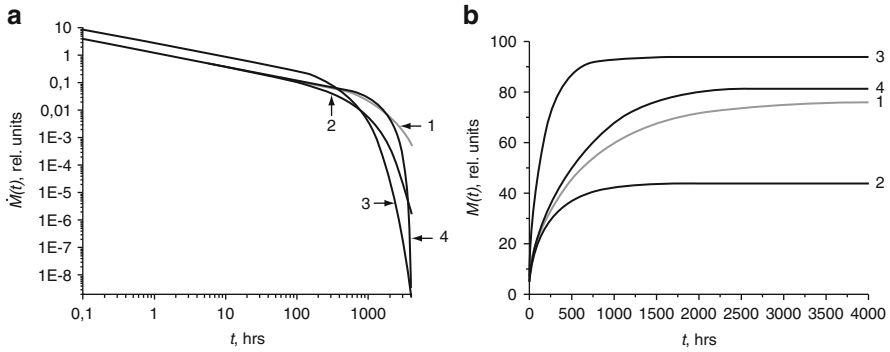
Fig. 1 Functions $\dot{M}(t)$ (**a**) and $M(t)$ (**b**) for following values of model parameters: 1–$D = 10^{-3}$, $\beta = 10^{-7}$, $\upsilon = 0$; 2–$D = 10^{-3}$, $\beta = 5 \times 10^{-7}$, $\upsilon = 0$; 3–$D = 5 \times 10^{-3}$, $\beta = 10^{-7}$, $\upsilon = 0$; 4–$D = 10^{-3}$, $\beta = 10^{-7}$, $\upsilon = 5 \times 10^{-6}$

3 Results of the Computational Experiments and Discussion

A number of computational experiments were conducted to qualitatively study the behavior of the solution of (8), (9), (10), and (11) and to determine the quantitative characteristics.

The model described by (1), (2), (3), and (4) can also be used to describe thermal-induced mass loss of PC in vacuum as a result of outgassing and sublimation of material. Therefore, the effect of model parameters values on $\dot{M}(t)$ (1a), $M(t)$ (1b) and VP distribution in PC was studied in the first experiment. Results are partly presented in Fig. 1. Here it was assumed that $k = 0.01$, $S^{rad}(x,t)$.

For the calculations, the base values of the model parameters were chosen as follows: $h = 100, R = 1, k = 10^{-2}, D = 10^{-3}, \beta = 10^{-7}, \upsilon = 0$ and $S^{rad}(x,t) = 0$. Using them, $\dot{M}(t), M(t)$ (curves 1, Fig. 1a, b) were found. Then, some parameters were varied. It follows from Fig. 1 that increase of each model parameter results in significant change of behavior of $\dot{M}(t), M(t)$. Thus, increase of diffusion coefficient causes growth of mass loss, whereas increase of first-order reaction rate lowers it. Naturally, the existence of a sublimation process caused an increase of mass loss of material.

All results given below were obtained for base values of parameters h, R, k, β. Alterations of conditions of numerical experiments and material properties under irradiation were accounted by correcting VP source functions, effective diffusion coefficient and sublimation rate.

The second experiment (results are shown in Fig. 2a) was dedicated to finding the effect of initial irradiation energy on mass loss rate of PC for the same electron flux density ($\varphi_0 = 10^7$).

The third experiment was similar to the second one for the case when PC is subjected to irradiation with identical energy flux density $I = \varphi(E_0) \cdot E_0$. To satisfy this, flux densities of electrons with initial energies of 20, 30, 50, 100 and 150 keV were multiplied by corresponding coefficients: 2.5; 5/3; 1.0; 1/2; 1/3 (Fig. 2b).
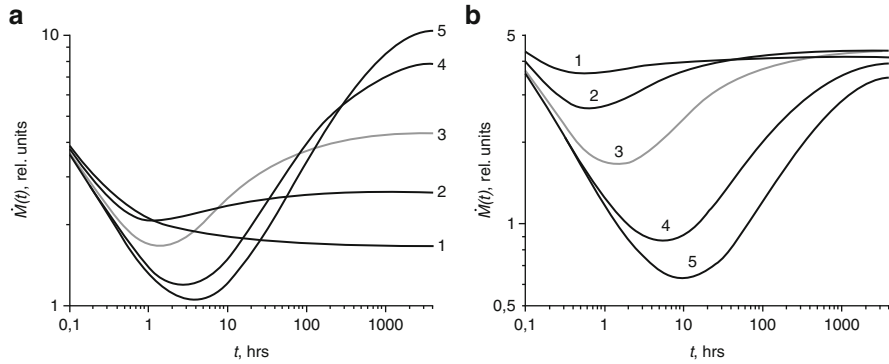
Fig. 2 Mass loss rate of material under irradiation by electrons with different energies: (**a**) – identical flux density; (**b**) – identical energy flux density

As can be seen in all plots of Fig. 2, up to the point $t = 1$ hour, the higher is E_o, the faster the PC mass loss rate decreases. Indeed, with growth of E_o for equal electron flux density (energy flux density), less energy releases in the near-surface layer and, consequently, less VP forms, but it is the VP that defines the value of $\dot{M}(t)$ at initial moments.

Towards the end of the second experiment (Fig. 2a), the pattern is reversed, i.e. the higher is the E_o, the higher is $\dot{M}(t)$. This can be explained by the fact that for equal electron flux density, the growth of E_o results in increase of absorbed dose in material and, consequently, more VP forms. The VP's distribution peak, with increase of E_o, shifts inward the material where their accumulation occurs. Therefore VP's contribute to mass loss later than VP's were formed in the near-surface layer of material.

Partial results of computational experiment simulating process of PC mass loss under irradiation by electrons with different energies but identical energy flux density are shown in Fig. 2b. Functions $\dot{M}(t)$ calculated for $E_o \leq 50 \text{keV}$ qualitatively repeat data presented in Fig. 2a. Nevertheless, increase of electron energies to 100 and 150 keV results in noticeable decrease of $\dot{M}(t)$. This is explained by the fact that when electrons with such energies interact with material, the major part of VP's is generated far from the near-surface layer and the time for their migration to the near surface layers as well as the possibility to enter into any first-order reactions significantly increases. The portion of such VP's is increasing with distance from the point of their generation to free material surface. In the case when $E_o = 150 \text{ keV}$ another factor appears: some electrons possess enough energy to pass through the 100-μm threshold with their energy not totally absorbed in the 100-μm thick material.

Below are given the results of computational experiments for electrons having different energies but identical energy flux densities.
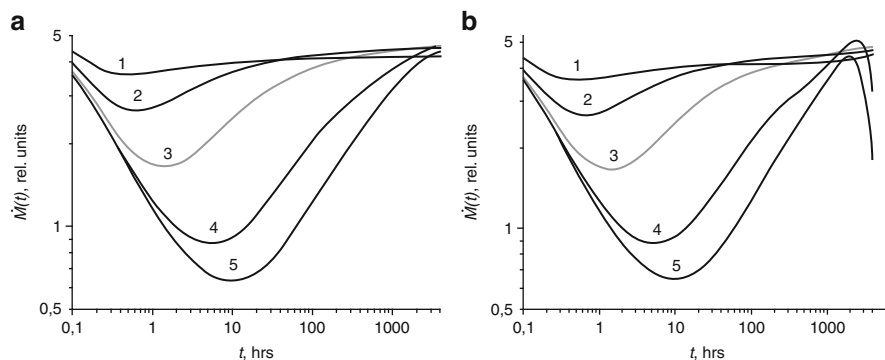
Fig. 3 PC mass loss rate with unchangeable properties under irradiation by electrons with different energies: (**a**) – for $\beta = 0$, $\upsilon = 0$; (**b**) – for $\beta = 0$, $\upsilon = 5 \times 10^{-6}$

Figure 3 shows the effect of υ on function $\dot{M}(t)$ for PC's whose properties do not change under electron irradiation. To find the influence of υ on the mass loss rate, the first-order reactions in the calculations were disregarded ($\beta = 0$). The functions $\dot{M}(t)$ of PC irradiated by electrons with $E_o = 100$ and $E_o = 150$ keV experience maximum changes. A dramatic drop of the function $\dot{M}(t)$ for these energies at the end of the experiment (Fig. 3b around 1000 h) is related to the fact that in the course of time more electrons leave PC with their energy not fully dissipated.

When planning to test materials for irradiation-induced mass loss and analyzing the test results with the purpose to forecast changes of their properties in space conditions, the following should be taken into account. Firstly, the radiation-induced VP generation potential in materials is finite. Secondly, permeability of PC increases if there is radiolysis and outgassing, that, in turn, accelerates VP migration processes in material.

The first mentioned above fact was taken into account when performing the fourth computational experiment. To do so, in (1), (2), (3), and (4) a source function was used depending not only on spatial variable but on time as well.

$$S^{rad}(x, t) = A \exp[-B(x - C)^2] \exp[-\alpha(x)t] \tag{14}$$

where $\alpha(x) \geqslant 0$ – weight function proportional to $S^{rad}(x)$ and accounting unevenness of radiolysis rate over material thickness.

Increase of PC permeability under irradiation, due to radiolysis and outgassing, was simulated by introduction in (1), (2), (3), and (4) of a temporal dependence of diffusion coefficient. It was also considered that the radiolysis intensity and the migration rate of its products in a material are determined, to a large extent, by the function $S^{rad}(x)$. Consequently, change rate of PC permeability differs in dependence on coordinate x and time t. Therefore, the fifth experiment repeats the forth one that was done using the diffusion coefficient growing with time:
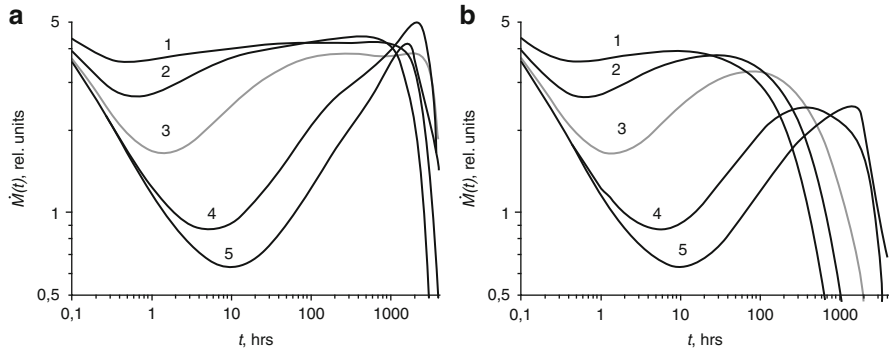
Fig. 4 PC mass loss rate: (**a**) – increase of material permeability; (**b**) – increase of material permeability and limitation of potential of VP generation in it
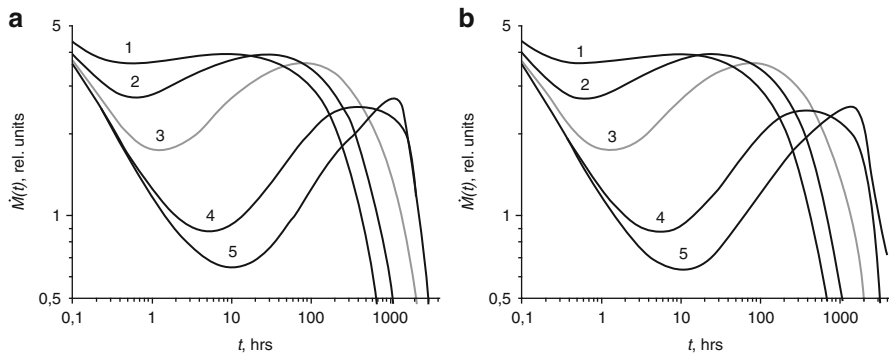

Fig. 5 Effect of sublimation rate on PC mass loss rate: (**a**) – $v = 5 \times 10^{-6}$; (**b**) – $v = v(E_o)$

$$D(x,t) = D_0 \exp[\alpha_1(x)t] \qquad (15)$$

where $\alpha_1(x) \geq 0$ – weighting function (analog of function $\alpha(x)$ in (14)) accounting for non-uniformity in property changes under irradiation over material thickness; D_o – effective VP diffusion coefficient in material before radiation.

Figure 4 shows the results of computational experiments where growth of PC permeability under irradiation (Fig. 4a) and limitation of VP generation potential in it (Fig. 4b) were taken into account. It is seen that at $t = 1$ hour, the values of $\dot{M}(t)$ calculated for $E_o \leq 50$ keV exceed the same characteristics obtained for $E_o = 100$ and 150 keV by several times, and this difference increases at the initial time span. The pattern is reversed at the end of experiments. At $t \geq 1000$ hours, $\dot{M}(t)$ of samples irradiated with high-energy electrons was many times higher than mass loss rates of samples irradiated with lower energy electrons. It is mostly due to the growth of $D(x,t)$, that is the migration rate of radiolysis products accumulated in PC to the free surface.

Figure 5 shows the results of computational experiments where limitation of VP generation potential in material and change of its permeability under irradiation are taken into account. The difference between the graphs shown in Fig. 5a, b consists

in the following. Sublimation rate in the first case was chosen equal for all energies of electrons. It was assumed in the second case that parameter $\upsilon = \upsilon(E_o)$ is directly proportional to absorbed energy in the near-surface layer of material. The most evident influence of $\upsilon = \upsilon(E_o)$ was demonstrated in behavior of the function at initial electron energies $E_o = 100$ and 150 keV. For 150 keV in the second case (Fig. 5b), values of the functions $\dot{M}(t)$ at t > 3000 h are many times greater than those shown in Fig. 5a.

4 Conclusions

Computational modeling allowed to obtain both the quantitative estimates and qualitative results, describing the process of PC mass loss under irradiation by electrons with different energies, as well as make the following observations.

1. Mass loss rates for a given PC in vacuum under irradiation by electrons with different energies can vary by orders of magnitude both for irradiation with identical particle flux density and with identical energy flux density.
2. It follows from calculations that the smaller the electron energy, the faster the component of mass loss rate, attributable to emission of radiolysis products, achieves its maximum. Major part of radiolysis products formed by action of the most energetic space ionizing particles makes contribution to the total mass loss with the maximum time delay with respect to their emergence.
3. It is necessary to take into account the irradiation-induced changes of material properties including possible limitation on potential of generation of radiolysis products in models describing PC mass loss under irradiation. Calculation results show that increase of material permeability, due to its destruction and outgassing, leads to increase of PC mass loss rate. It becomes more noticeable with growth of electron energies from 20 to 150 keV.
4. When preparing to test mass loss of polymeric composites and analyze test data, the dependence of sublimation rate on energy of radiation liberated in the near-surface layer of material should be considered.

References

1. Faye D, Marco J, (2003) Effects of ultraviolet and protons radiations on thermal control counting after contamination. In: Proceedings of the 9th European symposium on spacecraft materials in space environment, ESA SP-540, The Netherlands, pp 527–523
2. Khasanshin RH, Kostyuk VI, Kosogorov AV, Porzhezhinskaya EJu (2009) Modeling of deposition of radiation atomization products of certain materials on a quartz glass surface. Scientific and technology book. Radiation resistance of electronic systems, Resistance-2009, M.: MIFI-2009, vol 12, pp 125–126
3. Khasanshin RH (2009) On effect of electron radiation intensity on mass loss of polymeric composite. Probl Atomic Sci Technol 1:22–27
4. Khasanshin RH (2008) Effect of radiation on mass loss rate of polymeric composite for outgassing in vacuum. Problems of atomic science and technology 1:18–23

Effects of Atomic Oxygen and Grease on Outgassing and Adhesion of Silicone Elastomers for Space Applications

Henry C. de Groh, Bernadette J. Puleo, and Bruce M. Steinetz

Abstract An investigation of silicone elastomers for seals used in docking and habitat systems for future space exploration vehicles is being conducted at NASA. For certain missions, NASA is considering androgynous docking systems where two vehicles each having a seal would be required to: dock for a period of time, seal effectively, and then separate with minimum push-off forces for undocking. Silicone materials are generally chosen for their wide operating temperatures and low leakage rates. However silicone materials are often sticky and usually exhibit considerable adhesion when mated against metals and silicone surfaces. This paper investigates the adhesion unit pressure for a space rated silicone material (S0383-70) for either seal-on-seal (SoS) or seal-on-aluminum (SoAl) operation modes in the following conditions: as-received, after ground-based atomic-oxygen (AO) pre-treatment, after application of a thin coating of a space-qualified grease (Braycote 601EF), and after a combination of AO pre-treatment and grease coating. In order of descending adhesion reduction, the AO treatment reduced seal adhesion the most, followed by the AO plus grease pre-treatment, followed by the grease treatment. The effects of various treatments on silicone (S0383-70 and ELA-SA-401) outgassing properties were also investigated. The leading adhesion AO pre-treatment reduction led to a slight decrease in outgassing for the S0383-70 material and virtually no change in ELA-SA-401 outgassing.

Keywords Adhesion • CVCM • Elastomer • Outgas • Rubber • Seals • Silicone • TML

H.C. de Groh (✉) • B.J. Puleo • B.M. Steinetz
NASA Glenn Research Center, Cleveland, OH 44135, USA
e-mail: Henry.C.deGroh@nasa.gov

1 Introduction

The National Aeronautics and Space Administration (NASA) is evaluating different silicone elastomers for seals for docking and habitat systems being considered for future missions [1, 2]. In addition to exhibiting extremely low leakage, the seals must meet stringent low-outgassing requirements, operate over a broad temperature range, and exhibit low adhesion to minimize decoupling or separation forces. The primary class of elastomers that meet the wide operating temperature range for these applications are silicone-based rubbers [3]. However, these elastomers have inherent adhesive properties, which make them sticky, creating potential difficulties when trying to separate docked spacecraft or hatches [4, 5]. Three different adhesion-lowering treatments have been considered: atomic oxygen (AO), grease coating, and an AO treatment combined with a grease coating. A heat treatment plus AO treatment was examined in an effort to lower outgassing. The AO pre-treatment developed by NASA Glenn has shown excellent results in reducing seal adhesion with moderate fluence levels [4, 6]. Grease was considered in two approaches: first as a stand-alone treatment and second as an addition to the baseline AO pre-treatment method. Grease was investigated as a means to reduce adhesion for the following reasons: its effectiveness at lowering adhesion was unknown; the AO pre-treatment, though very effective, requires special equipment and a vacuum tank large enough to accommodate the seal diameter; and the special equipment costs make AO treatments expensive compared to grease. The effects of a light grease coating on adhesion and outgassing are presented here. Several different elastomer compounds have been considered and tested; this paper is limited to results from tests of the elastomer compounds S0383-70 supplied by Parker-Hannifin Corporation, and ELA-SA-401 supplied by Esterline Corporation.

Prior work has shown that atomic oxygen, characteristic of that present in Low-Earth-Orbit (LEO) combines with the silicone in silicone-based elastomers to form a very thin, glassy surface coating [4, 7]. At moderate AO levels, this SiO_x-based coating does not significantly degrade the sealing properties of the rubber [6].

Space-qualified grease has been used in the past by NASA to lubricate gears and to ease the placement of elastomer seals [8, 9]. Greases are also being considered as a way to lower unwanted seal adhesion. Braycote Micronic 601 EF, a space qualified perfluoroether grease, was examined in this study [10].

When elastomer seals are used in space, it is important for them to be stable, and have a low total mass loss (TML) and low collected volatile condensable materials (CVCM). Current requirements are for TML <1 % and CVCM <0.1 %. However, there is always motivation for outgassing to be as low as possible to minimize contamination of sensitive surfaces such as windows and tracking systems. Thus tougher requirements are frequently proposed and may be imposed in some situations in the future.

The effects of AO and grease coatings on seal outgassing were unknown, thus a campaign was begun to determine the effects of these treatments on TML and CVCM. This paper reports the results of that campaign.

2 Procedures

2.1 Specimens

This study used cylindrical button specimens cut from sheets to measureadhesion, and #2-106 o-rings to measure outgassing.

2.1.1 Buttons for Adhesion Testing

Cylindrical 9.1 mm diameter buttons of S0383-70 elastomer were cut from 5.4 mm thick sheet material using a drill press and a custom-made core drill lubricated with soap, as described previously [6]. Buttons to be tested with grease were then weighed, and an amount of Braycote Micronic 601 EF grease approximating 1.2 mg/cm^2 applied to its mating surface. Small amounts of grease were then added or subtracted to achieve the desired rate of 1.2 mg/cm^2. The adhesion buttons had an average rate of coverage of 1.17 mg/cm^2 and a standard deviation of 0.11 mg/cm^2. Only S0383-70 buttons were made; no adhesion tests on ELA-SA-401 are reported in this paper.

2.1.2 O-Rings for Outgas Testing

This study used S0383-70 and ELA-SA-401 o-rings of the size #2-106 (inner diameter = 4.42 mm and cord width = 2.62 mm) which were small enough to fit in the crucible used in outgas testing without being cut or sectioned in any way. It was believed that sectioning after AO treatment, and there-by exposing the sample's interior, could increase outgassing [6]. Sheet material was not used because the process by which the o-rings are made mimics better the docking seal manufacturing process.

2.2 Treatments

2.2.1 Atomic Oxygen

Elastomer S0383-70 button specimens to be tested with grease were AO exposed in an atomic oxygen facility, referred to as Tank 9 at the NASA Glenn Research Center (GRC) [6], to a fluence of 1.25×10^{20} atoms/cm^2. Fluence levels in the facility were determined using Kapton witness specimens. O-rings for grease and outgas testing made of S0383-70 and ELA-SA-401 were AO exposed to 1.0×10^{20} atoms/cm^2 using SPI Supplies Plasma Prep II atomic oxygen facilities at GRC [6]. O-rings were hung by a fine wire to ensure AO exposure to all surfaces.

Another set of o-rings were exposed to a fluence of 4.9×10^{20} atoms/cm^2 after a 4-day vacuum bake in a related effort to lower outgassing.

2.2.2 Heat Treatments

In an effort to lower TML and CVCM a treatment was used on S0383-70 and ELA-SA-401 o-rings which consisted of a 4-day bake under vacuum at a temperature of 205 °C, after which, the o-rings were exposed to an AO fluence of 4.9×10^{20} atoms/cm^2.

2.2.3 Grease Coating

As-received buttons and #2-106 o-rings to be greased were first wiped with 99 % isopropyl alcohol, dried, and weighed. The procedure used to grease the buttons is mentioned in Sect. 2.1.1. The o-rings were covered with Braycote Micronic 601 EF perfluoroether grease over their entire surface at an average rate of 1.19 mg/cm^2 with a standard deviation among o-rings of 0.08 mg/cm^2. The rate of coverage was measured by weighing the o-ring before and after grease application and the amount of grease adjusted until the desired coverage was achieved. To put this application rate into perspective the Sun Protection Factor (SPF) application rate for sunscreen on a person's skin is 2 mg/cm^2.

2.3 Adhesion Testing

Procedures used for adhesion testing are discussed in detail elsewhere [6]. Adhesion was measured between the flat surfaces of two buttons SoS and between a button and a flat, anodized aluminum alloy plate SoAl with the plate having an average roughness, Ra, of 13 μ in (0.33 μm). The aluminum alloy was 6061 T651 and the anodizing was MIL-A-8625 T II. Button specimens were brought together, compressed 25 %, and held for 72,000 s (20 h). The load and unload rate was 0.01 in./s (0.254 mm/s). Adhesion was measured during unloading using a force transducer. Specimens mated with other specimens with a similar grease coating were tested repeatedly. Once a grease coated button was mated with an uncoated specimen, such as an anodized aluminum plate, the greased button would not be tested again until its coating had been re-applied and measured. The anodized aluminum plate used in SoAl tests was cleaned with 99 % Isopropyl alcohol before each test.

2.4 Outgas testing

All o-ring outgas test specimens were sent to Orange County Material Test Laboratories in Anaheim, California, who used ASTM Standard Designation: E 595–93 [11] for TML and CVCM testing.
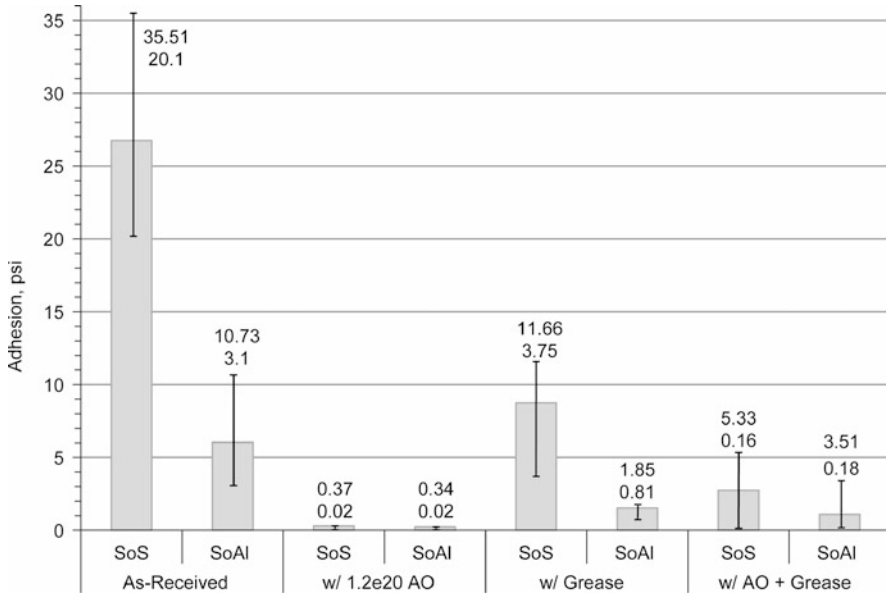
Fig. 1 Adhesion in lb/in.^{2} of S0383-70 elastomer in Seal-on-Seal (SoS) and Seal-on-aluminum (SoAl) test modes, in the following conditions: *1*. As-received; *2*. After receiving an atomic oxygen fluence of 1.25×10^{20} atoms/cm^2 AO; *3*. After application of Braycote Micronic 601 perfluoroether grease at a rate of 1.2 mg/cm^2; *4*. After 1.25×10^{20} atoms/cm^2 AO plus 1.2 mg/cm^2 Braycote Micronic 601 grease

3 Results

3.1 Adhesion

Figure 1 shows the adhesion of the compound S0383-70 in the various sealing modes of interest, seal-on-seal SoS and seal-on-aluminum SoAl and with various treatments imposed on the rubber. This group of experiments was designed to determine if Braycote Micronic 601 EF perfluoroether grease could be used to lower the adhesive characteristics of S0383-70. The bar data in Fig. 1 are the averages listed in Table 1. The lines in the bars of data represent the range of values from the tests performed and can also be found in Table 1. Figure 1 shows the as-received adhesion and how effective an AO treatment of 1.25×10^{20} atoms/ cm^2 is, effectively lowering SoS and SoAl adhesion to 0.5 psi or essentially zero. The application of 1.2 mg/cm^2 of grease to as-received S0383-70 also lowered adhesion in both SoS and SoAl arrangements. Application of the grease resulted in an approximately 70 % decrease in adhesion compared to as-received levels. This level of adhesion reduction achieved with grease only may be of value in many applications. However, the goal for future docking systems is for the seal adhesion

Table 1 Adhesion in lb/in.^{2} of S0383-70 elastomer in seal-on-seal and seal-on-aluminum test modes conditions: as received, AO fluence of 1.25×10^{20} atoms/cm^2, application of Braycote Micronic 601 EF perfluoroether grease, and a combination of AO fluence of 1.25×10^{20} atoms/cm^2 plus Braycote Micronic 601 EF perfluoroether grease

	As-received		w/AO		w/Grease		w/AO + Grease	
Test #	SoS	SoAl	SoS	SoAl	SoS	SoAl	SoS	SoAl
1	24.67	4.28	0.37	0.34	3.75	1.83	0.16	0.37
2	20.1	10.73	0.02	0.02	10.83	1.85	5.23	0.18
3	35.51	3.1	–	–	11.66	0.91	5.33	3.51
4	–	–	–	–	–	–	0.23	0.32
Average	26.76	6.04	0.20	0.18	8.75	1.53	2.74	1.10
S.D.	6.46	3.35	0.18	0.16	3.55	0.44	2.54	1.40

to be below 0.5 psi. The adhesion of AO treated S0383-70 increased with the application of the grease to about 5 psi for the SoS case, and 3 psi for SoAl. These conservative (worst case) values of 5 and 3 psi for the AO + grease tests are cited rather than the averages of 2.74 and 1.1 psi for SoS and SoAl, respectively because of the stochastic nature of adhesion and adhesion testing which is reflected by the standard deviations provided in Table 1.

4 Outgassing

Outgas testing of as-received material and after the 4-day vacuum bake + AO, AO only treatment, and grease coating, are shown below in Fig. 2. All outgassing data are from uncut, #2-106 o-rings. Per the ASTM standard each measurement was an average of 3 o-ring tests; one repeat measurement was made for the tests using grease and the two measurements then averaged.

The combined bake at 205 °C and AO treatment did not lower the outgassing of S0383-70 significantly compared to as-received S0383-70, however the combined bake at 205 °C plus AO treatments did lower TML by 78 % and CVCM by 69 % for ELA-SA-401. Thus ELA-SA-401 may be advantageous in applications where very low outgassing is needed.

Figure 2 represents the effects of the 1.25×10^{20} atoms/cm^2 AO fluence on outgassing of both the S0383-70 and ELA-SA-401 compounds. A slight decline in outgas is observed for the S0383-70 compound relative to as-received. ELA-SA-401 did not show a significant change in outgas properties after the AO treatment.

Figure 2 shows a slight increase in outgassing for S0383-70, compared to as-received, after the application of 1.2 mg/cm^2 of Braycote Micronic 601 EF perfluoroether grease. However the greased seal still achieves NASA's outgas requirements of TML <1 % and CVCM <0.1 %. Based on the standard deviation of TML and CVCM measurements and expected detection limits, the uncertainty of TML and CVCM results is judged to be +/−0.02 %: this uncertainty is shown as error bars on Fig. 2 [12].
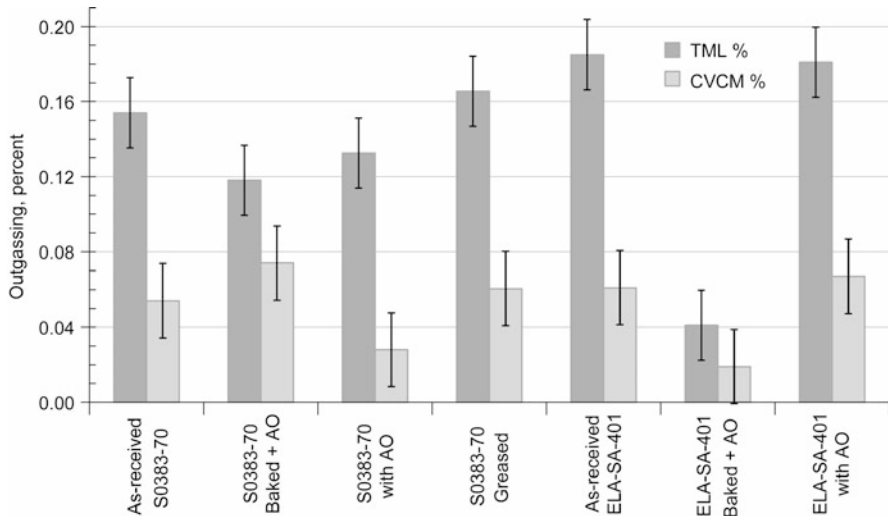
Fig. 2 Effect of heat treatment + atomic oxygen (AO), atomic oxygen, and grease coating on the outgassing of S0383-70 and ELA-SA-401

5 Conclusions

A number of adhesion tests were conducted on silicone elastomer Parker S0383-70 material. Of the various adhesion reduction techniques evaluated, the AO pre-treatment of 1.25×10^{20} atoms/cm^2 lowered adhesion the most. For seal-on-seal (SoS) operation modes the seals showed reduced unit adhesion from 26.8 to 0.2 psi and for seal-on-aluminum (SoAl) operation modes unit adhesion went from 6.04 to 0.18 psi. Application of a thin coat of Braycote 601EF perfluoroether grease also reduced adhesion, but to a lesser degree; for SoS the unit adhesion went from 26.8 to 8.75 psi and for SoAl the unit adhesion went from 6.04 to 1.53 psi. For specimens that were first pre-treated with AO and further applied with a thin coat of Braycote Micronic 601EF perfluoroether grease the reduction in unit adhesion for SoS went from 26.8 to 2.74 psi and SoAl went from 6.0 to 1.10 psi. The AO pre-treatment enables S0383-70 to achieve the low adhesion levels we expect to need for docking seal applications (<2 psi).

Outgassing in ELA-SA-401 was not changed after AO pre-treatment of 1.25×10^{20} atoms/cm^2. However, after the bake plus AO pre-treatment the TML and CVCM of ELA-SA-401 decreased by 78 % and 69 %, respectively. Outgassing in S0383-70 slightly decreased after AO pre-treatment and did not significantly change after the bake plus AO treatment. Outgassing was higher for Braycote 601EF perfluoroether grease-coated S0383-70 compared to as-received S0383-70, however the outgassing with applied grease was still below NASA's TML and CVCM percentage requirements of TML <1 % and CVCM <0.1 %.

References

 1. Dunlap P, Steinetz B, Daniels C (2008) Overview of LIDS docking seals development. NASA Seal/Secondary air system research symposium, NASA/CP—2009-215677
 2. Lewis JL, Carroll MB, Morales RH, Le TD (2002) National aeronautics and space administration (U.S. Government), Washington, DC, Androgynous, reconfigurable closed loop feedback controlled low impact docking system with load sensing electromagnetic capture ring. US Patent 6,354,540
 3. Finkbeiner JR, Dunlap Jr PH, Steinetz BM, Daniels CC (2006) Apollo seals: a basis for the crew exploration vehicle seals, AIAA-2006-5259, presented at the 42nd AIAA/ASME/SAE/ASEE Joint propulsion conference. Sacramento, 2006; also available as NASA/TM—2006-214372
 4. de Groh III HC, Miller SKR, Smith IM, Daniels CC, Steinetz BM (2008) Adhesion of silicone elastomer seals for NASA's crew exploration vehicle 44th AIAA/ASME/SAE/ASEE, joint propulsion conference, July 2008, paper no. AIAA-2008-4625, 21 July 2008. Hartford; also printed as NASA/TM—2008-215433
 5. Conrad MC, Daniels CC, Bastrzyk MB (2010) An experimental investigation of silicone-to-metal bond strength in composite space docking system seals, NASA/CR—2010-216886
 6. de Groh III C, Daniels CC, Dever JA, Miller SK, Waters DL, Finkbeiner JR, Dunlap Jr PH, Steinetz BM (2010) Space environment effects on silicone seal materials, H April 2010, NASA/TM—2010-216332
 7. Banks BA, Dever JA, Gebauer L Hill CM (1991) Atomic oxygen interactions with FEP teflon and silicones on LDEF, LDEF-69 months in space. In: Proceedings, NASA first post-retrieval symposium, p 801
 8. Morales W, Street Jr KW, Zaretsky EV (2009) Performance and analysis of perfluorinated grease used on space shuttle actuators, April 2009, NASA/TM—2009-215605
 9. Bennett JE (2007) Process specification for the application of liquid lubricants. Engineering directorate, structural engineering division, NASA JSC, Jan 2007, PRC-8002C
10. Product Data, Castrol Braycote Micronic 601 EF, Castrol Industrial North America Inc., Naperville, http://www.castrol.com/liveassets/bp_internet/castrol/castrol_advantage/STAGING/local_assets/downloads/b/am_Braycote_601_EF_Mic_USA_English_pds.pdf
11. ASTM Designation: E 595-93 (Reapproved 2003) ASTM international, 100 Barr Harbor Dr. PO Box C700, W. Conshohocken 19428–2959, USA
12. Test report for: mass loss and collected volatile condensable materials, NuSil silicone technology LLC, Carpinteria, 2006

CNES Experiments on MEDET: Lessons Learned

Ch. Durin, S. Remaury, J.C. Mandeville, V. Rejsek-Riba, S. Duzellier, L. Duffours, P. Colombel, T. Woignier, and L. Labat

Abstract The Material Exposure and Degradation ExperimenT MEDET has been successfully launched and retrieved with EuTEF from the Columbus External Payload Facility of the ISS (18 months, from February 2008 to September 2009). All experiments have been providing data as expected during the operations phase. MEDET is an active experiment that was exposed to the Low Earth orbit (LEO) environment. It combines seven sub-experiments. CNES has been proposed two experiments devoted to the measure of μ-particles:

SODAD is a MOS type impact detector, to characterise the properties of micrometeoroids and orbital debris particles.

AEROGEL is a passive detector, to capture micrometeoroid and orbital debris particles

In previous papers [1–3] we have proposed in flight results inside this paper, we describe the post-flight analysis of both CNES experiments and an analysis of all MEDET surfaces exposed to impacts effects. A correlation with simulation tools is discussed

C. Durin (✉) • S. Remaury
CNES – Centre Spatial de Toulouse, 18 avenue Edouard Belin, 31401 Toulouse Cedex 9, France
e-mail: christian.durin@cnes.fr

J.C. Mandeville
Mandespace, 8 rue des Régans, 31000 Toulouse, France

V. Rejsek-Riba • S. Duzellier
ONERA (The French Aerospace Lab), 2 Av Edouard Belin, 31055 Toulouse Cedex, France

L. Duffours • P. Colombel
Prime Verre PAT Millénaire Bât, 101350 Avenue Albert Einstein, 34000 Montpellier, France

T. Woignier
CNRS/IRD, UMR CNRS 6116 UMR IRD 193- IMEP- (PRAM-IRD), B.P. 214 Petit Morne, 97232 Le Lamentin, Martinique, France

L. Labat
Steel Electronique Zac, de Cantalauze Route de Mondavezan, 31220 Martres Tolosane, France

Keywords AEROGEL • Columbus external payload facility • MEDET • SODAD • μ-particles

1 Introduction

Precise knowledge of space environment is of prime importance for space missions. Orbital debris and meteoroids are a key parameter of this environment. The contribution of natural meteoroids is stable, however the number of orbital debris is growing steadily and recent collisions are likely to generate further more debris. During the last few years a variety of sensors were flown on satellites [1, 2, 5, 11–14, 24, 29, 30], however most of them were passive instruments. Uses of active sensors such as MOS sensors (SODAD) provide a better knowledge of evolution of debris clouds and improve existing models [28]. On their side, Aerogel sensor allows us to collect intact μ-particles and to estimate very precisely the effect of environment on fragile surfaces. All MEDET surfaces especially RAM face are very useful to study damages produce by impact on different materials.

2 SODAD Experiments

2.1 Summary Statement

The SODAD experiment was devoted to the detection of solid micro-particles [4, 6–8, 19–22, 25–27]. Moreover, after retrieval of the payload, it is possible to get additional data and to assess, if needed, the behavior of the sensors. Laboratory analysis provides data on the composition and the origin of impacting particles. Present module is $120 \times 120 \times 90$ mm^3, with 4 sensors (40.8 cm^2 = total active surface), with a mass of 1 kg and a power consumption of 1 W. In stand-by mode a bias voltage of 50 V charges the capacitor. Upon high velocity impact of an incoming particle, it is discharged and the event is monitored and stored.

Experiment was powered ON for the first time on February 22, 2008. Final shut down and retrieval was made on September 2, 2009, upon STS-128 mission. Exposure to space has been 565 days and expected measurement time 558 days. However, due to operational constraints (shuttle rendezvous, low temperature of experiment) and unexpected shut down, the effective measurement time was only 428 days (77 % of time). During the exposure, the experiment was oriented in the RAM direction for 394 days (91 % of exposure time). Precise ON/OFF operations and orientation of the payload can be retrieved from data log. Data were stored in a DTL file dedicated to SODAD experiment and retrieved periodically from the control centre [15, 17]. From the beginning of operations, one of the sectors on sensor 2, has been shorted and turned OFF, actual area of sensors was therefore reduced to 36 cm^2. During the mission, 11 impacts have been detected. As shown in
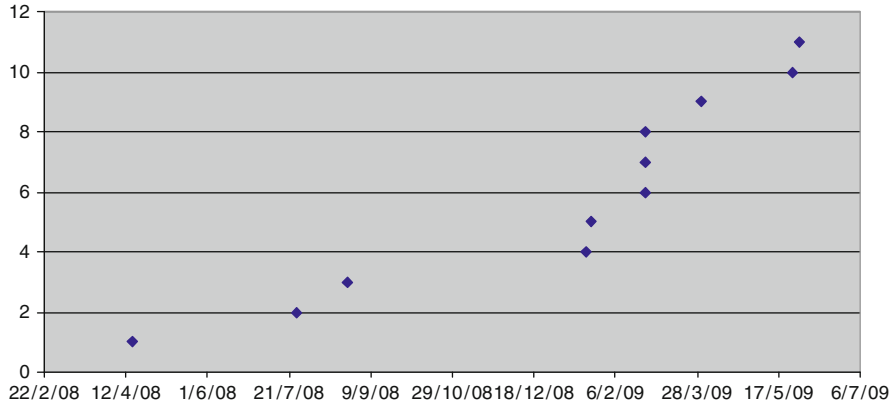
Fig. 1 SODAD results summary

Fig. 1, distribution in time is not random and appears to be linked to peculiar events. In particular, 3 impacts have been detected on February 24 2009, that could be connected to debris generated during the KOSMOS 2251/Iridium 33 collision that occurred on February 10, 2009, at an altitude of 788 km (with a relative impact velocity of 11.7 km/s). Shape and magnitude of discharge signals are similar to those obtained during laboratory tests [23].

An analysis of ISS orientation lets us to confirm that SODAD was oriented perpendicular to velocity vector [16] (i.e. MEDET/SODAD RAM facing velocity vector) during a large part of the mission. All impacts recorded were in this configuration except that of 30/03/09 on sensor 2 which does not present the same impact features.

Despite a limited number of cases, it is possible to make a correlation between the amplitude of the discharge and the diameter of the impact crater. It seems that a saturation threshold is reached for detectors used with a 200 μm diameter of impact. Taking into account actual measurement time, best estimate of the flux of meteoroids and debris as given by SODAD is 2680/impacts/m^2/year, for particles with a diameter larger than 3 μm (threshold confirmed after SEM survey and analysis of calibration data).

2.2 SODAD Experiment Results

The front face of the experiment measured 120 × 120 mm (144 cm^2). During optical survey, one large 450 μm impact was visible on the sensor n° 4. It is typical of impacts produced in brittle material: central part extensively fragmented, surrounded by a spall zone [9]. Survey at a 100 X magnification made possible the identification of 13 craters with a diameter larger than 50 μm: 2 on sensor n° 1, 2 on sensor n° 2, 4 on sensor n° 3 and 5 on sensor n° 4. In-flight impacts detected are

Table 1 SODAD results summary

Sensor	In flight	Optical	SEM
1	2	2	2
2	1	2	2
3	3	3 (4)	1
4	5	5	3
Total	11	12 (13)	8

Fig. 2 MOS sensor impact
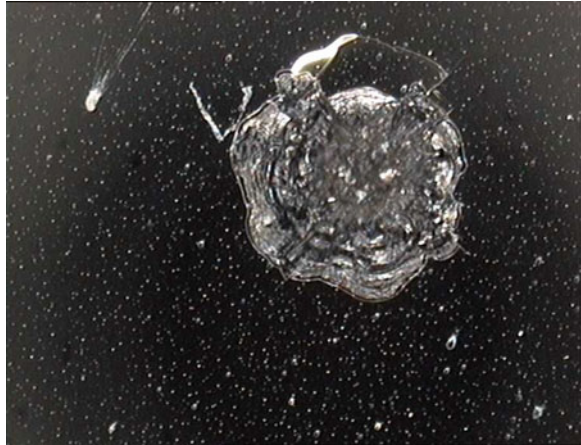
respectively: 2, 1, 3, and 5 (total 11). One 100 μm impact is visible on a bolt of sensor n° 4.

The optical analyses results [18] were confirmed with a Scanning Electron Microscope (SEM). We cannot observe smaller crater and, by the way, we can confirm minimum impact size. Table 1 summarizes the results obtained in flight and during post flight analysis.

- Regarding sensor 1, we have a good agreement between in flight data's, optical observation and SEM analysis (craters 70 and 85 μm).
- Regarding sensor 2, we have good agreement (craters 200 and 80 μm) but no record for one of them due to electrical power "off" on the sensor.
- Regarding sensor 3, three records but four optical detections (one no so clear) and only one detected by SEM
- Regarding sensor 4, we have good agreement between in flight data's and optical observation (two craters to be identified by SEM)

The impacts on MOS detectors are characteristic impacts produced on a fragile silicon material (see Fig. 2). We distinguish an irregular outline characterized by radial and concentric fractures; the diameter of this zone is called Ds. On the smallest impacts, we distinguish an almost intact semi-hemispherical zone that shows evident tracks of fusion. For the biggest impacts, (400 μm), this central part was strongly damaged and ejected. We do not find impact smaller than 40 μm; if we
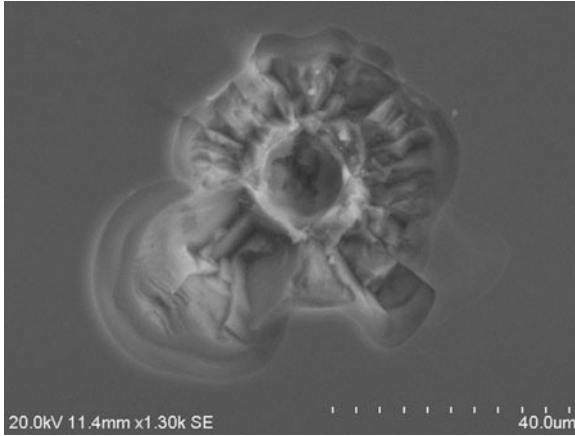
Fig. 3 SEM of the impact on MOS sensor
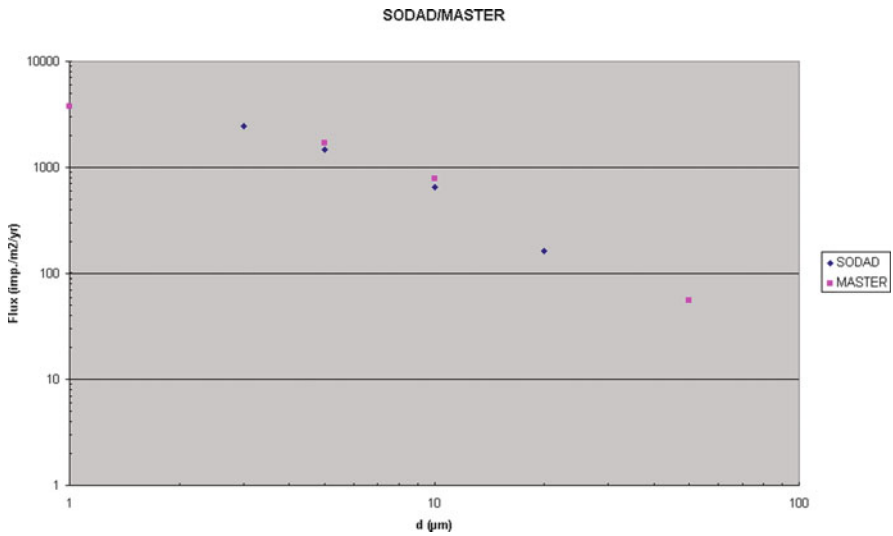
Fig. 4 MASTER/SODAD results comparison

take the ratio Ds/d = 15, this corresponds to a particle with a diameter d of about 3 μm. In these conditions the biggest impact would have been produced by a particle of the order of 30 μm. Figure 3 shows a typical SEM picture of SODAD impact. Using previous hypothesis on Ds/d ratio, a comparison of particles' flux (between 1 and 50 μm) given by the model of environment MASTERS 2005 (series 2) and by the measurements made by SODAD (series 1) is presented in Fig. 4. We see that the results are similar. We can conclude that the population of small fragments did not vary in a significant way between 2004 and 2009.

Table 2 SEM/EDS analysis results

Identification	SEM Ds, (μm)	Discharge (Volts)	Optical Ds, (μm)	Residues
MOS 1–1	85	24	135	No
MOS 1–2	**70**	**23**	**50**	**Al, Si, Mg (met)**
MOS 2–1	160 × 210	27	150	No
MOS 2–2	85	OFF	75	No
MOS 3–1	?	29	100	–
MOS 3–2	?	24	60	–
MOS 3–3	110	31	130	No
MOS 4–1	450	28	450	No
MOS 4–2	80	25	90	No
MOS 4–3	**50**	**16**	**75**	**Sn, (debris)**
MOS 4–4	?	22	40	No
MOS 4–5	?	25	40	No
Total	8	11	12	

The energy dispersive x-ray microanalysis (EDS) associated with the SEM was used to identify the residues of particles responsible for craters. This search, however, was not very productive, since the impact conditions led to evaporation and/or ejection of the residues of the particles. Only in 2 cases it was possible to identify the presence of associated residues either of a meteoroid (MOS1-2), or from debris (MOS4-3). Table 2 summarises the analysis results.

We have tested SODAD electronic box after retrieval, and we can conclude that the electronic box is operational and that the anomaly detected during flight is more linked to the sensor behaviour.

3 Aerogel Experiments

3.1 Summary Statement

Aerogel is a low density material 0.07–0.1 g/cm^3 and is a good candidate to collect small particles [33]. AEROGEL is a passive experiment exposed in the same conditions as SODAD. The size of the exposed surface was $4 \times 2 \times 2 = 16$ cm^2. A few impacts and surface degradation were observed during the Post Flight Analysis (PFA).

We have identified a few defects and some impacts on the Aerogel surface. Figure 5 shows the results from an optical and SEM analysis of the impact features. Due to their size and/or Aerogel surface aspect, some identified craters are difficult to find by optical or SEM observations. Some of the observed features must be surface defects or particle on top of the surface. During SEM observations, we were able to confirm optical results (see Tables 3 and 4). Optical and SEM observations confirmed surface degradation of Aerogel blocs induced by exposure to space. It will be induced by space environment and/or a flux of very small particles.
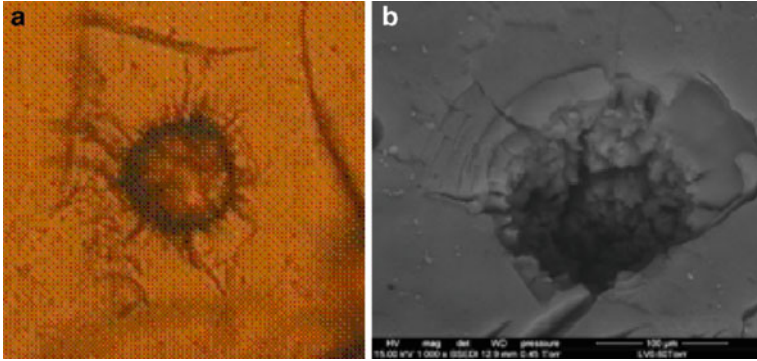
Fig. 5 Impacts in the Aerogel material. Optical (**a**) and SEM (**b**) microscopy

Table 3 Particle size results from bloc 1

Identification	Optical Ds, (μm)		SEM Ds, (μm)	
1	179	190	127	145
2			472	457
3				
4			507	392
5				
6				
Total	1		3	

Table 4 Particle size results from bloc 2

Identification	Optical Ds, (μm)		SEM Ds, (μm)	
I			138	74
II	2,800	964	2,808	825
III				
IV	338	201	323	269
V	89	137	77	106
VI	128	145	66	76
VII	75	90	54	74
Total	5		6	

Tests are in progress, in order to retrieve particles from the Aerogel. Analysis using micro confocal microscopy allows identifying the particles inside the Aerogel. It seems that many particles are detected even if no surface crater has been identified along the sample length.

A small part of the Aerogel bloc that consists of silica was dissolved and the residues were filtered. Many small particles (a few μm in size) were found in the filtered products. Presently, it is difficult to understand the finding of these particles inside the Aerogel. Spatial positions of these objects (on the surface or inside first microns of the bloc) are difficult to localize. Tests are running to add more results. We were able to identify the composition of these particles and we found different materials (stainless steel, glass, oxide..). We need to follow on our tests regarding

origins of these debris/particles. A new analysis of the Aerogel surface s had revealed many small craters (around 2 μm), not detected before. This investigation is in progress to try to understand the behaviour of the space Aerogels.

Using hypothesis [32] on Ds/d ratio = 8 a comparison of particles flux between 1 and 50 μm given by the model of environment MASTERS 2005 and by the observations on Aerogel experiment is running.

Aerogel seems to be able to collect very small particles even if they have very low velocities. Space exposure makes it difficult to analyze the surface due to the modified surface aspect. More tests are running to try to explain first results and correlation with model.

4   Other MEDET Exposed Surfaces

4.1   Summary Statement

High-resolution pictures and SEM analysis of the other faces of MEDET have been carried out and more impact craters have been found. A RSR thermal control coating covers the RAM Plate and the Starboard plate. The space environment (AO, UV, impacts) has damaged this coating. The MLI protective sheets also contain traces of space environment effects. On other MEDET experiments, we have also detected impacts features.

The RAM face has a total area of 1,368 cm^2. Taking into account the space occupied by experiments and samples, the surface for the estimation of particle flux is 600 cm^2. Three coupons with a total surface of 85 cm^2 were cut out for SEM inspection

The starboard plate with a total surface of 484 cm^2 was examined by optical microscopy (G 50–100×).

The MLI have a total surface of 4,200 cm^2. Two samples taken from the Zenith plate, with a total surface of 614 cm^2 and a coupon of 221 cm^2 taken from the Nadir face were examined with optical microscope and SEM.

4.2   RAM Plate

Made of aluminium alloy, the RAM plate is covered with a thermal control RSR (Rigid Solar Reflector thickness 50 μm made of polydimethylsiloxane). The space environment (AO, UV) has altered this protective layer, as can be seen from the collected images. Ten craters with diameters larger than 50 μm were identified on the plate and some of the experiment surfaces (8 on the plate, 2 on the wheel). The micro calorimeters were not examined. The impacts produced on the complex RSR/ Al show a particular aspect with puffiness and a delamination of the protective layer around the impact crater, the centres of the biggest craters are typical of impacts

Fig. 6 AA1 Impact on part A

15.0kV 11.9mm x210 SE   200um
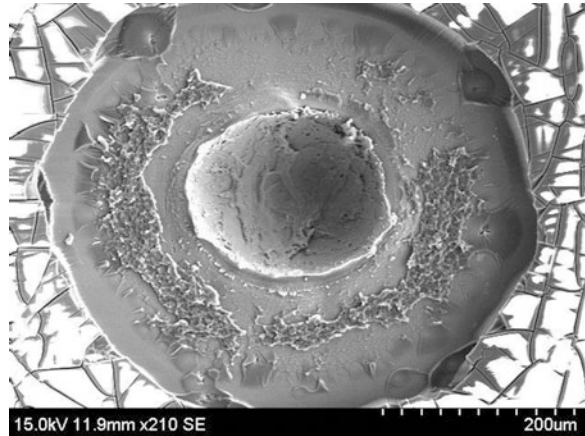
Table 5 Summary of RAM plate analysis results

Identification	Dc, optical (µm)	Dc, SEM (µm)	Residues (EDS)
AA1 (22 cm²)	180 × 260	180 × 250	No
AB1 (27 cm²)	45	45	Ag, Cu, Zn, debris?
AC1 (36 cm²)	450	480	No
AC2 (36 cm²)	280	270	Fe, Zn, Cu, debris?

produced on a ductile material: hemispherical shape, lip, projection on the surface, presence of melted zones [31].

Three samples (A, B, C) were provided by ESTEC for analysis. Four craters identified in optical microscopy were analyzed with SEM. The energy dispersive x-ray microanalysis (EDS) associated with the SEM microscope allows in certain cases to identify the presence of residues resulting from the impact (see some results in Fig. 6 and Table 5).

From these samples, we can estimate a flux for particles larger than 10 µm as ~ 300 impacts/m²/year

5 STARBOARD Plate

Made of Aluminium and covered with RSR, it measures 220 × 220 mm (surface 484 cm²). The final aspect shows no major changes, with only slight yellowing and microcracks. Nine craters of a diameter larger than 50 µm were identified in optical microscopy. The plate was not cut and craters were not examined in high magnification, or in the SEM. The flux of particles larger then 10 µm measured on the plate is 120 impact/m²/year, value lower than what is observed on the RAM face due to a different orientation and to a lower resolution in the observation. The presence of RSR infers with the impacts, the same morphology as on the craters of the RAM face.

Fig. 7 Impact on the wheel (optical)
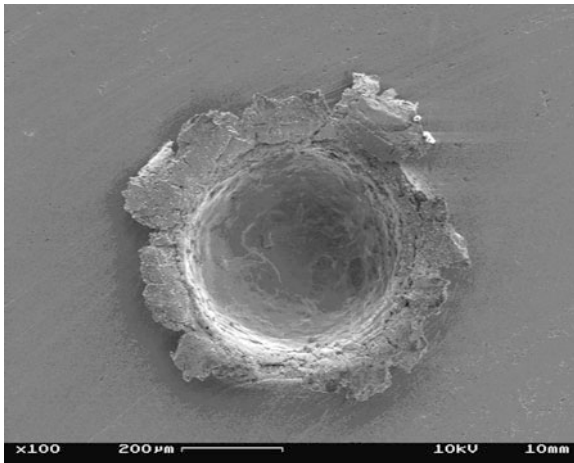
Fig. 8 Impact on the wheel (SEM)

5.1 Spectrometer Wheel

Made from Aluminium, 110 mm in diameter, it supports various material samples. Two large impacts are visible in the central part of the wheel and are typical of hypervelocity impacts produced on the aluminium, with a very visible lip (different from impact on parts with RSR). The biggest one has a diameter of 900 μm; the second one has a diameter of 450 μm. If we consider that the impact of 900 μm was produced by a particle of 150 μm, the corresponding flux (by taking into account the total surface of the plate before 1,360 cm^2) is of the order of 5 impacts/m^2/year. (see Figs. 7 and 8). EDS analysis did not allow to identify the nature of responsible

Table 6 Optical analysis results

Impact	Diameter Dc, (μm)	Depth T, (μm)	T/D
Large	900	450	0.5
Small	450	300	0.7

particles, these impacted certainly at high speed (>15 km/s). The topography of the impacts was also studied using a confocal microscope. This allows obtaining information on the profile and the depth of craters.

Table 6 presents the geometry of both impacts on the spectrometer wheel: the reported T/D value of the large impact is equal to 0.5 (hemispherical crater), indicating that the impact was produced by a particle with a density similar to the density of aluminium. The report T/D of the small impact indicates a relatively deep crater, produced by a particle of density larger than aluminium density [2, 10].

5.2 SODAD Bolt Crater

The head of one stainless steel bolt used in the assembly of the detector 4 of SODAD shows an impact crater 270 μm in diameter. This hemispherical crater is typical of a high velocity impact. The lip is pronounced with regard to the surface. It shows tracks of creep and, in one case, beginning of spalling. Walls are covered with a layer of metal melted during the impact. It was not possible to identify residues resulting from the projectile. The elemental composition obtained from the EDS analysis reflects the composition of the used steel. The particle responsible for the crater should have a diameter from 35 to 40 μm (it would have produced on the silicon a crater of 800 μm, bigger than the other craters observed on SODAD). The density of the particle seems to have been raised because the depth of the crater is important.

6 MLI

The structure of the used MLI consisted of an external sheet of Kapton: 25 μm, followed by 10 internal sheets of aluminised Mylar and 6–7 μm layers of Dacron. The external sheet is cover with Mapatox-K (5–110 μm base silica, used to protect against AO). Three coupons were extracted from the sheet of MLI (total surface 4,200 cm^2) for detailed observation: Face Zenith, MLI1: 205 × 160 mm, useful surface: 292 cm^2, Face Zenith, MLI2: 215 × 150 mm, examined surface: 322 cm^2 and Face Nadir, MLI3: 170 × 130 mm, useful surface: 221 cm^2.

The analysis was conducted under a glass plate (to avoid reflections) using an optical microscope and magnifications between 60× and 100×.

The ageing of the face Zenith (under the effect of UV and AO) is pronounced with developed cracks and embrittlement clearly visible. The phenomenon is less

Fig. 9 Impact on MLI (Optical)
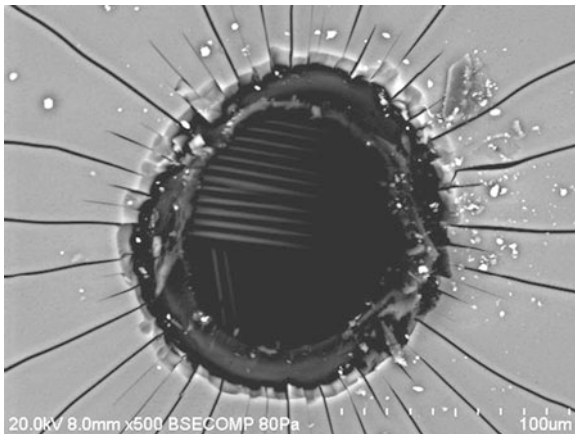
Fig. 10 Impact on MLI (SEM)

pronounced for Nadir. This is perfectly visible on Figs. 9 and 10. Several perforation due to impacts were identified (total 18: on MLI1 = 13, on MLI2 = 5) on the Zenith face. They have a characteristic aspect. The perforation of the first sheet of Kapton is surrounded with a zone where we distinguish radial concentric cracks. This is typical of impacts on a fragile material: The surface defects observed are located on the layer of Mapatox, The lips of the craters show evidences of carbonization of Kapton. We can distinguish on the biggest impacts the perforation of the layers of successive Mylar and the damage of the fibers of the nets of Dacron. The perforations found until now have diameters between 50 and 300 μm. It is difficult to identify with the video-microscope impacts smaller than 50 μm. Several

impacts have an elliptic shape. It is important to note that the primary impacts occurring on a thin sheet have the Dc/d of the order of 1–3. Until now, no impacts were found on the Nadir sample.

SEM observation in MLI confirms the general aspect of the impacts with the presence of a very visible lip, carbonized, surrounded with a ring showing the tracks of fracture and spalling of the fragile layer of Mapatox.

As it had been noticed during previous observations of materials returned after space exposure, MLI is a good material for the identification of residues inside craters. The orientation of the MLI towards the Zenith allows a majority of natural particles to be trapped. It was possible to identify effectively 5 impacts produced by meteoroids with the presence of: Na, Al, Mg, Fe, Ti, and K ... Two impacts show the presence of gold (Au), indicating an artificial fragment.

7   Post-Flight Analysis (PFA) Summary

- On the RAM plate : $S = 1,367$ cm^2, material Al + RSR, ductile, thick Material: Dc/d = 5–6 (Dc diameter of the edge-to-edge crater)

    - 8 impacts have been detected from Dc 95 to 700 μm

On the Wheel : $S = 95$ cm^2, material AL

- 2 impacts have been detected from Dc 550 to 900 μm

    On the Starboard : $S = 484$ cm^2, material AL + RSR

- 9 impacts have been detected from Dc 60 to 400 μm

    Ductile, thick Material: Dc/d = 5–6 (Dc diameter of the edge-to-edge crater, d: Diameter of the particle)
    On SODAD : $S = 41$ cm^2, material Si

- 15 impacts have been detected from Ds 40 to 450 μm
- 1 impact have been detected on a steel bolt Dc 100 μm

    Fragile, thick Material: Ds/d = 12–15 (Ds diameter of the zone of spalling, d : Diameter of the particle)
    On the MLI: $S = 835$ cm^2, material Kapton + Mylar + Mapatox

- 18 impacts have been detected from Ds 45 to 220 μm

    Thin Material: Dh/d = 1–3 (Dh diameter of the perforation, d : Diameter of the particle)
    On the Aerogel : $S = 16$ cm^2, material Si

- 9 impacts have been detected from Dc 60 to 2,000 μm

    Ds/d = 8 (Ds diameter of the perforation, d : Diameter of the particle)

Table 7 MEDET/MASTER fluxes

| d, µm | MEDET | | | | MASTER | | |
	MLI zénith	Starboard plate	RAM plate	Aerogel	SODAD MOS	Master rtp	Master RAM
1						939	3,758
2,7					2,560		
3					2,419		
3,3					1,918		
5	180				1,452	423	1,700
6,6					853		
10		120	300		645	194	780
12	160						
13					213		
20		53	86		161		
25	95						
40		27	54				
50						14	56
100	18		32				

The objective of previous studies was to allow calculating the flux of particles (meteoroides and fragments) detected on MEDET/SODAD and comparing it to that given by the available environmental models (MASTER) and to that as mesured in other experiments also exposed on the platform EuTeF and/or on other carriers. The obtained data will be of use to an improvement of the models of meteoroides and fragment environments. The presence of a variety of materials exposed on MEDET and used for the determination of the flux of solid particles makes difficult a synthetic approach. The response under impact of these materials is rather different and precise data of calibration in laboratory are missing. The results are presented in Table 7 and Fig. 11.

The cumulative fluxes deduced from the measurements are compatible with those given by the model MASTER for the RAM face (30 impact/m^2/year for d > 100 µm, 100 impact/m^2/year for d > 20 µm). Fluxes measured on faces Zenith and Starboard and RAM are consistent. It is necessary to note that the convergence between the various measurements (except for SODAD) are obtained for particles of diameters ranging from 10 to 50 µm. Concerning the RAM plate, due to a lack of resolution for craters smaller than 50 µm it is likely than the maximum flux is underestimated at least by a factor of 2. Its value is closer to the value of 300 impacts/m^2/year as obtained by the observations on the 3 coupons (85 cm^2) cut from the plate, rather than the value of 133 impacts/m^2/year as deduced from the observation of all the plate. The trend is similar for the starboard plate. Conversely, for the large craters (> 100 µm), the statistic is better for a large area, for the bigger particles, the available surface for the study limits also the precision.

With SODAD, the flux measured in flight corresponds to 2,680 impact/m^2/year. The threshold of detection corresponds certainly to particles of diameters between 2.5 and 3.5 µm. The flux obtained according to these observations after flight is

FLUX MEDET/SODAD PFA
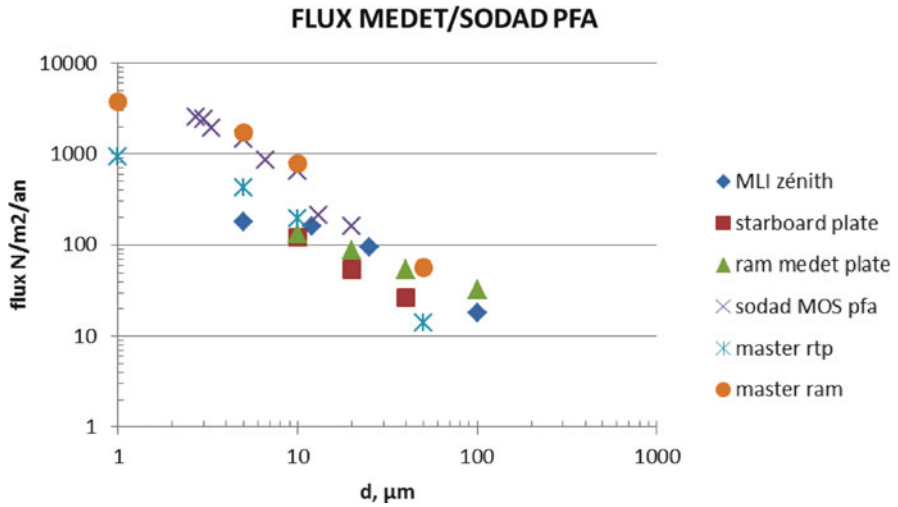
Fig. 11 MEDET/MASTER fluxes

Flux comparison for d > 10µm
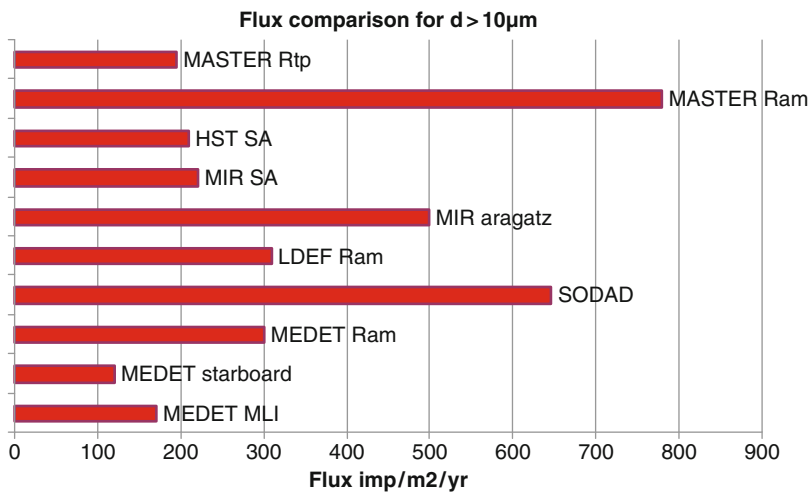
Fig. 12 Comparison with previous experiments

160 impact/m²/year for a particle of the order of 20 μm and of 2,420 impacts/m²/year for a particle of the order of 3 μm.

It is interesting to compare the flux of micro particles derived from the analysis of MEDET with similar analysis performed on experiments or materials retrieved after exposure to space on several instances. The comparison is shown in Fig. 12, particles larger than 10 μm, for LDEF (Long duration exposure facility, 1984–1990), space station MIR (Aragatz, 1988–1990, Solar arrays, 1988–1998),

Table 8 EDS analysis results and comparison with previous experiments

Experiments	μmet %	Deb.%	No %	Material sample	Axes
MEDET Aerogel	TBD	TBD	TBD	Si Aerogel	RAM
MEDET RAM	6	19	75	Al/silicon	RAM
MEDET Zenith	62	13	25	MLI	Zenith
LDEF leading	17	11	72	Al	RAM
LDEF trailing	30	15	55	Al	Wake
MIR aragatz	23	9	68	Al	Inertial
MIR PIE	27	14	59	Al	Inertial
HST (95)	26	10	64	Glass	sun
HST (02)	32	44	24	Glass	sun

HST (Hubble space telescope, solar arrays 1992 and 2002). If we take into account the underestimate of data concerning the RAM and starboard faces of MEDET (as discussed earlier), the correlation of data is good and the population of particles larger than 10 μm appears to be stable.

7.1 *Meteoroides and Fragments*

The discrimination between both populations of particles can be made by identification of residues inside craters. For the RAM face: on 16 analyzed craters, 4 show recognizable residues (25 %) among which 3 caused by fragments (75 %) and 1 caused by a natural particle. For the face Top: on 8 analyzed craters, 7 show recognizable residues (87 %) among which 5 caused by meteoroides (71 %) and 2 by fragments (29 %) see Table 8.

8 Conclusions

The analysis of the various components of the MEDET experiment after exposure in space during 18 months in 2008–2009 provide a realistic outlook of the meteoroids and debris space environment during this period.

Impact craters listed until now are with diameters ranging from 40 to 950 μm, which correspond to particles between 3 and 200 μm (it seems that one of the visible perforations on the MLI corresponds to a particle of 250 μm. On Aerogel, a crater of 2,000 μm was observed). Samples exposed to four different directions are available: RAM: plate (aluminium + RSR) and experiments SODAD (silicon), Aerogel (Si) + others, Starboard plate: aluminium + RSR, Zenith: MLI/Mapatox and Nadir: MLI/Mapatox.

The presence of samples made of a variety of different materials makes, however, it difficult to conduct an accurate comparison between the results. Until now, impacts features have been observed on the RAM, zenith and starboard faces, none

on the Earth face. High-resolution SEM scans, at least at $100\times$, of additional coupons from the RAM plate (and from the starboard plate) would increase the reliability of the data for particles smaller than 10 μm in diameter.

The active experiment SODAD dedicated to the detection of the solid particles worked satisfactory. The number of recorded impacts during the flight is comparable to that observed after the flight. We have validated the design/behaviour of the sensors and we will compare these results with a new mission on the SAC-D satellite. The temporal information shows a non-random distribution with time linked with space events. The second time, no notable change in flux is recorded and the agreement with prediction model is very good. The best reliability for small impacts is obtained from the observation of SODAD: the brittle material make identification of small impact features easy. One must note that, until now, no impacts smaller than 40 μm (made by a particle close to 3 μm) have been found on the SODAD detectors. A more detailed analysis of sensors is necessary to confirm this trend. Indeed, impacts caused by particles smaller than 3 μm have been found on surfaces and solar cells retrieved from MIR and HST. Aerogel works very well and many particles have been trapped. Work is conducted to retrieve them and analyse their shape and composition.

References

1. McDonnell JAM (ed) (1998) Meteoroid and debris flux and ejecta models, final report of ESA contract 1887/96NL/JG, ESA CR (P)- 4252
2. Berthoud L (1993) Micrometeoroids and orbital debris observed in low earth orbits. Thesis ENSAE, Toulouse
3. Durin Ch, Mandeville JC (2009) SODAD First results and post-flight analysis. In: Proceedings ISMSE 11, Aix en Provence
4. Kassel PC, Wortmann JJ (1995) MOS capacitor detectors for measuring micrometeoroid and space debris flux. J Spacecr Rocket 32:4
5. Kinard WH, Carter DJ, Jones JL (1984) NASA SP-473, (1984), p 131., LDEF mission 1 experiments
6. Durin Ch, Mandeville JC (1997) MOS sensors for detection of orbital debris, ESA SP-393
7. Sitte K (1967) Micrometeorite studies at the max planck institute Heidelberg, ESRO SN-18
8. Igenbergs E, Shriver EL (1973) Magnetogasdynamic compression of a coaxial plasma accelerator flow for micrometeoroid simulation. J Appl Phys 44:2177
9. Taylor EA, Kay L, Shrine NRG (1997) Hypervelocity impact on semi-infinite brittle materials: fracture morphology related to projectile diameter. Adv Space Res 20:1437–1440

10. Mandeville JC (1996) Impact detection in space: derivation of physical properties of meteoroids and debris. Adv Space Res 16(12):147
11. Durin Ch, Mandeville JC, Perrin JM (2005) In-situ detection of meteoroids and orbital debris. In: Proceedings 4th conference on space debris, ESA SP- 587
12. Aragatz MJC (1990) Mission dust collection experiment. Adv Space Res 10(3):397
13. Zwiener JM, Wilkes MR, Carruth RR, Kamenetzky Hörz F, Kinard WH (2000) Overview of the space environmental effects experiments flown on the MIR space station: MEEP, OPM, SPSR. In: Proceedings 8th conferences material in space environment, Arcachon
14. Graham GA, Kearsley AT, Drolshagen G et al (2001) Microparticles impacts upon HST solar cells. Adv Space Res 28:1341–1346
15. Duzelier S, et Falguère D (2008) TM-DTL dates, document exploitation MEDET, ONERA
16. Calcul de position ISS, feuille excel, ONERA/DESP
17. Berthoud L, Mandeville JC (1997) Low-Earth-Orbit micrometeoroid and debris investigations. J Spacecr Rocket 34(1):125–132
18. Mandeville JC (2009) Rapport mandespace, MDS R/02/2009
19. Canady KS, Monteith LK, Donovan RP (1968) Characterization of SiO_2 for a capacitance type meteoroid penetration detector, NASA CR-66712
20. Kassel PC (1973) Characteristics of capacitor type micrometeoroid flux detector when impacted by simulated micrometeoroids, TN-D7359, NASA
21. Mandeville JC (1998) Detection active in-situ de debris orbitaux: Réalisation et essais de capteurs MOS, Rapport final RF/456417 ONERA-DESP
22. Mandeville JC (2001) Projet DEBRIS/FBM: Essai sous impact de capteurs MOS (MPI Heidelberg) RTS 1/05030, DESP
23. Mandeville JC, Raif M (2003) Projet DEBRIS/FBM: essai sous impact de capteurs MOS (TUM Munich) RF AER CNES 06289
24. Mandeville JC, Maag CR, Durin C (2000) In situ detection of micrometeoroids and orbital debris: the PIE experiment on MIR. Adv Space Res 25:329–334
25. Oliver JP, McKisson JE, Simon GG (1993) Orbital debris environment monitor, MOS detection system, ISST paper, 1993
26. Singer SF, Stanley JE, Kassel PC (1985) The LDEF interplanetary dust experiment. In: Giese RH, Lamy P (eds) Properties and interactions of interplanetary dust. Reidel, Dordrecht, pp 117–120
27. Moussi A (2002) Impact tests on MOS sensors, CR Stage DEA, DESP
28. Labat L Dossier (2001) de définition expérience FBM/DEBRIS: FBM-DF-PL-7-DB-5516-CNS, STEEL-Electronique, Mazères, Mai 2001
29. Mandeville JC (2004) Assessment of in-situ impact detectors : MOS sensors, WP-110, Final report ESA contract 17794/03/NL/JA
30. Berthoud L, Mandeville JC (1993) Analysis of remnants found in LDEF and MIR impact craters, AIP conference proceedings 310, Houston May 1993
31. Hörz F et al (1993), Penetration experiments in aluminium and Teflon targets of widely variable thickness, AIP conference proceedings 310, Houston May 1993
32. Zolensky MEE et al (1993) Meteoroid investigations using the long duration exposure facility. In: AIP conference proceedings 310, Houston
33. Kitazawa Y (1999) Hypervelocity impact experiments on aerogel dust collector. J Geophys Res 104(E9):22,035–22,052

Molecular Contamination Analysis on *SUZAKU* X-ray Imaging Spectrometer

Fumitaka Urayama, Atsushi Fujii, Eiji Miyazaki, and Yugo Kimoto

Abstract *Suzaku* is the fifth Japanese X-ray astronomy satellite. The X-ray telescopes consist of four X-ray Imaging Spectrometer (XIS) detectors, a single X-Ray Spectrometer (XRS) detector and a single Hard X-Ray Detector (HXD). The XIS has an X-ray CCD camera, which covers an energy range of 0.2–12 keV. *Suzaku* was launched on a Japanese M-V launch vehicle on July 10, 2005. The X-ray CCD effective area below 2 keV has been decreasing with time after the launch. The degradation was characterized by X-ray absorption of carbon-rich molecular contaminants with accumulation mass of 100–140 μg cm^{-2} on the XIS Optical Blocking Filters (OBF) in 2010. The contaminant thickness was maximal at the center of an OBF, and decreased toward the edge of the OBF. The numerical analyses suggested that molecular contaminants, outgassed from the spacecraft's materials, would accumulate in sufficient quantity to explain the phenomena well.

Keywords Molecular contamination • X-ray imaging spectrometer • Suzaku astronomy satellite

1 Introduction

It has been reported that the spacecraft's materials induce molecular contaminants to accumulate onto the spacecraft's surfaces in a space environment; thus resulting in increases in the solar absorptance of the spacecraft's thermal control surfaces and

---

F. Urayama (✉) • A. Fujii
Space Engineering Development Co., Ltd., Tsukuba 305-8505, Japan
e-mail: urayama.fumitaka@sed.co.jp

E. Miyazaki • Y. Kimoto
Japan Aerospace Exploration Agency, Tsukuba 305-8505, Japan

decreases in the reflectivity or transmissivity of the spacecraft's optical components [1]. These phenomena may hinder the spacecraft in successfully completing its missions.

We developed the "Japanese SPacecraft Induced Contamination Environment" (J-SPICE) analytical software application so as to predict mass of molecular contaminants that could potentially accumulate onto the spacecraft's surfaces [2]. To enhance reliability of the software program, we improved the J-SPICE based on ground-based test data and *Hinode* (SOLAR-B) flight data [2, 3].

In this study, numerical analysis and assessment were conducted for contamination deposition on the OBFs inside *SUZAKU* (Astro-EII) satellite, by using the J-SPICE. The time dependency and spatial distribution of accumulation mass on the OBFs were discussed.

2 Contamination Inside X-ray Imaging Spectrometer

SUZAKU accommodates four XIS detectors with CCDs and OBFs. Inner surfaces of the satellite were maintained at temperature of approximately 20°C on orbit. Inner surfaces of the XIS detectors were maintained at temperature of approximately -40°C on orbit. The XIS detectors were covered with multi-layer insulations (MLI) except of apertures at topside of the XIS detectors. The bases, including CCD, were sealed structure.

The XIS effective area below 2 keV had been decreasing with time after launch. In order to examine this efficiency degradation, Astro-EII team had observed soft and stable X-ray sources, such as supernova remnant 1E0102-72, neutron star RXJ1856.5-3754 and the Cygnus loop. It was most likely some contaminants accumulating on surfaces of the OBFs, which was one of the coldest portions inside the satellite. The spectral analysis of these data was conducted to estimate thickness and element ratio of C to O for the contaminants on the OBFs. The thickness of the contaminants was different for each detector as shown in Fig. 1. The thickness became maximal at center of the XIS1's OBF and decreased toward the edge as shown in Fig. 2. The degradation was characterized by additional absorption of carbon-rich contaminants. The element ratio of O/C was less than 1/5 [4].

3 Numerical Analysis of Molecular Contamination and Discussion

Molecular contamination deposition occurs under the following mechanisms; emission, transport and deposition. We developed and have utilized Japan's first contamination analytical software, J-SPICE since 2002. The basic equations used in this software application are:
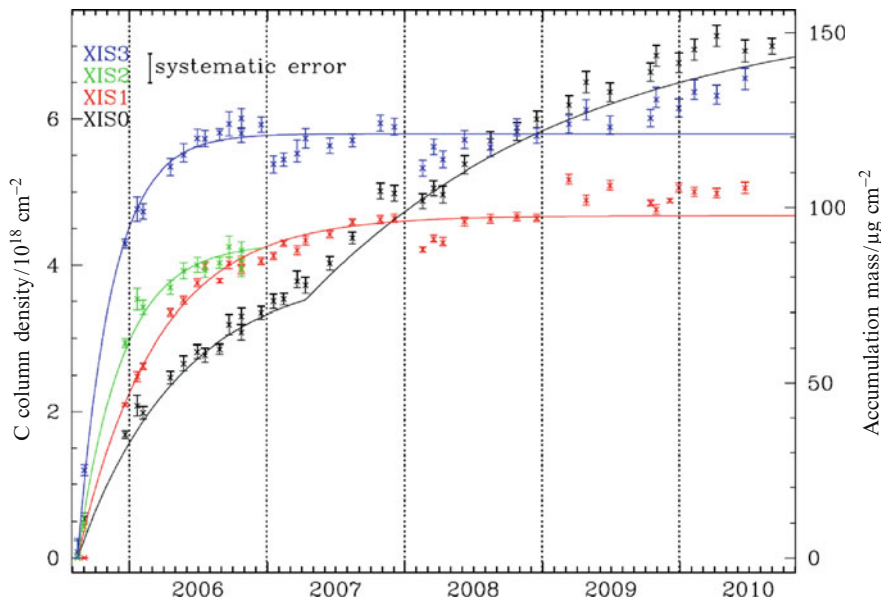
Fig. 1 Quantity of molecular contaminants on each XIS OBF, assuming diethylhexyl phthalate (DEHP, $C_{24}H_{38}O_4$) as a contaminant [4]

$$\dot{m} = \dot{M} \cdot F \cdot s \tag{1}$$

$$\dot{m} = \dot{M} \cdot F - \dot{m}_{evap} \tag{2}$$

Where $\dot{m}$ is deposition rate, $\dot{M}$ is outgassing rate, F is view factor, s is sticking coefficient and $\dot{m}_{evap}$ is re-evaporation rate. We had used (1) for design analysis of a spacecraft. Equation 2 was provided for clarifying critical determinants of the thickness and the element ratio of the contaminants on the OBFs. This is expected for applying the equation to design analysis of future spacecraft. The sources of molecular contaminants are the spacecraft's organic materials. The outgassing rate is expressed in (3) or (4).

$$\dot{M} = a \cdot t^b \cdot \exp\left[-\frac{E_S}{R \cdot T_S}\right] \tag{3}$$

$$\dot{M} = a \cdot \exp\left[-\frac{t}{b} \cdot \exp\left(-\frac{E_S}{R \cdot T_S}\right)\right] \tag{4}$$

Where a and b are constants inherent of an outgassing source, t is elapsed time, E_S is activation energy, R is gas constant and T_S is temperature of the outgassing source. The re-evaporation rate is expressed in (5).
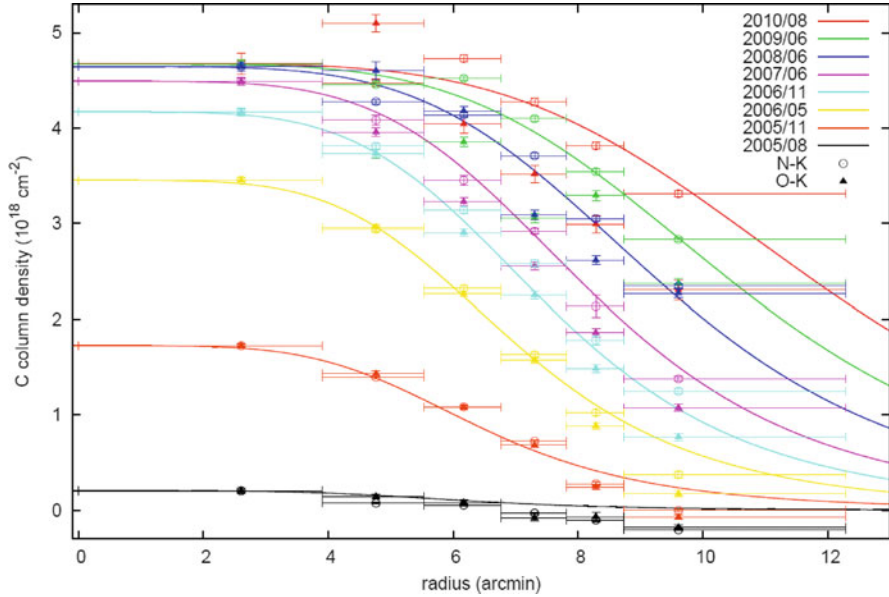
Fig. 2 Spatial distribution of C column density derived from N and O fluorescent lines from the day earth (i.e., Sun-lit Earth) atmosphere. Open circles and filled triangles represent the data points determined by the N and O fluorescence lines, respectively. The best fit curves are also shown in the figure [4]. One minute of arc is equivalent to length of 1.4 mm on the OBF

$$\dot{m}_{evap} = a_{evap} \cdot \exp\left[-\frac{E_{evap}}{R \cdot T_R}\right] \tag{5}$$

Where a_{evap} is constant inherent of a chemical compound, E_{evap} is the evaporation energy and T_R is temperature of the contaminated surface.

In order to determine the view factors, the *SUZAKU* geometric model was prepared as shown in Fig. 3. The parameters in (3) were derived by using Quartz Crystal Microbalance (QCM) measurement data, which were obtained while conducting bake-outs for the *SUZAKU* satellite in a thermal vacuum chamber [5]. It was assumed that the contaminants were diethylhexyl phthalate (DEHP, $C_{24}H_{38}O_4$, O/C = 1/6) and dibutyl phthalate (DBP, $C_{16}H_{22}O_4$, O/C = 1/4) since the element ratio of O/C was less than 1/5 based on the X-ray observation data. Plasticizers include DEHP and DBP. The parameters in (4) and (5) were derived by using the QCM data and vapor pressures of DEHP and DBP [6, 7].

Table 1 shows analysis assumptions by using (1) and (3). Figure 4 show calculation values of accumulation mass on the XIS0's OBFs by using the equations. In this analytical situation, location of the outgassing source did not contribute to the calculation values. The calculation values were approximately two or three times greater than the measurement values after a lapse of 5 years since X-ray observation started. It suggests that uncertainty on time-dependency of the
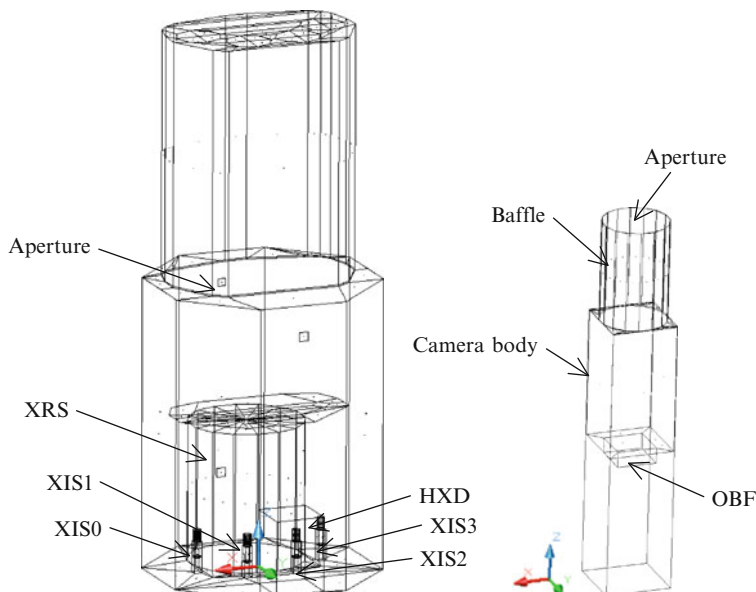
Fig. 3 Geometric model of *SUZAKU* satellite (*left*) and XIS detector (*right*)

Table 1 Analysis assumptions by using (1) and (2)

Assumptions	Descriptions
Beginning of contamination	L + 30 days (start of XIS observation)
Outgassing source	Surfaces inside *SUZAKU* satellite with temperature of $20\,^{\circ}$C, except for XIS dectcters, XRS and HXD
Contaminated surfaces	Surfaces inside XIS detectors, i.e. baffles, camera bodies and OBFs with temperature of $-40\,^{\circ}$C. Sticking coefficient is equal to one on the surfaces
Model contaminants	(Not applicable)
Transport of molecular contaminants	Diffuse reflection on surfaces inside *SUZAKU* satellite and surfaces outside XIS dectcters, XRS and HXD. Sticking coefficient is equal to zero on the surfaces

outgassing rate, which was expressed in (1), existed since the rate was extrapolated to 5 years by using the QCM data for 10 days. The calculation value of contaminant thickness at center of the OBF was nearly equal to the values at the edge. The measurement value at the center was approximately two times greater than the value at the edge on August 2010. Note that re-evaporation of the contaminants on the OBFs was not consideration in this analysis.

Re-evaporation of the accumulated contaminants was consideration for second analysis by using (2), (4) and (5) in order to explain time dependence and spatial distribution of the accumulation mass as shown in Figs. 1 and 2. Table 2 shows
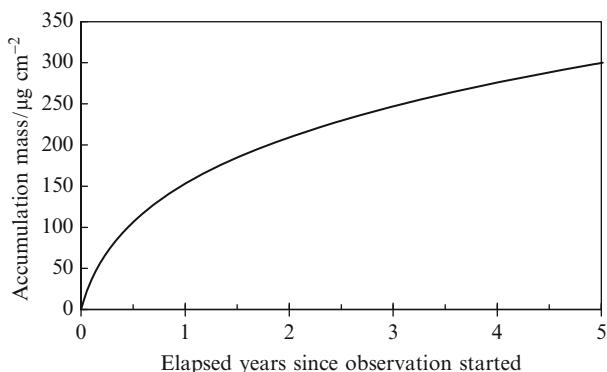
Fig. 4 Calculated values of accumulation mass on XIS0's OBF. The values for the OBF of XIS1, XIS2 or XIS3 were same as the values for XIS0

Table 2 Analysis assumptions by using (2), (4) and (5).

Assumptions	Descriptions
Beginning of contamination	L + 30 days (start of X-ray observation)
Outgassing source	Surfaces inside *SUZAKU* satellite with temperature of 20 $^\circ$C, except for XIS dectcters, XRS and HXD
Contaminated surfaces	Surfaces inside XIS detectors, i.e. baffles and camera bodies with temperature of $-50\,^\circ$C, and OBF with temperature range from $-50.8\,^\circ$C to $-50.0\,^\circ$C as below
	T0) center: $-50.0\,^\circ$C, edge: $-50.0\,^\circ$C
	T1) center: $-50.2\,^\circ$C, edge: $-50.0\,^\circ$C
	T2) center: $-50.4\,^\circ$C, edge: $-50.0\,^\circ$C
Model contaminants	Diethylhexyl phthalate (DEHP, $C_{24}H_{38}O_4$) and dibutyl phthalate (DBP, $C_{16}H_{22}O_4$)
Transport of molecular contaminants	Deposition and re-evaporation on all surfaces inside *SUZAKU* satellite

analysis assumptions by using the equations. Figure 5 shows calculation values of accumulation mass at center or edge of the OBF. The accumulation mass at the center was nearly equal to the mass at the edge while temperature of the OBF was $-50\,^\circ$C, i.e. case T0. The accumulation mass at the center was greater than the mass at the edge while temperature of the center was lower than temperature of the edge, i.e. case T1 and T2. It suggests that spatial distribution of the OBF temperature contributed spatial distribution of the accumulation mass as shown in Fig. 2.

Temperature of the OBF was approximately $-50°C$ on this analysis assumption however temperature of the OBF was approximately $-40°C$ on orbit. DBP did not accumulate permanently on the OBF with temperature of $-40°C$ on our calculation. It was assumed that interaction between DBP and DEHP was negligible weak. Polar character of DBP is similar to that of DEHP since DBP or DEHP has two carbonyl groups. It is well known that vapor pressure for mixture of chemical compounds
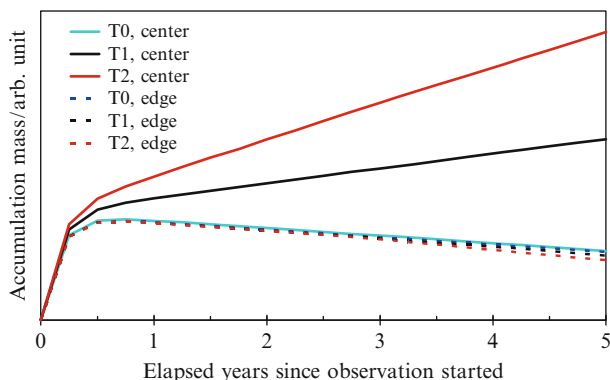
Fig. 5 Accumulation mass at center or edge of the OBF in consideration of re-evaporation phenomenon

with similar polar character is lower than sum of vapor pressure for each chemical compound. Re-evaporation rate of DBP with DEHP would be lower than the rate of DBP without DEHP. The other factors would include existence of another chemical compound such as n-butyl benzyl phthalate (BBP, $C_{19}H_{20}O_4$). Boiling points of BBP and DBP are 370 °C and 340 °C under atmospheric pressure condition, respectively.

The accumulation mass on the XIS3's OBF increased rapidly, and then became constant as shown in Fig. 1. The accumulation mass on the XIS0's OBF increased continuously. It suggests that the small difference between temperatures of the center and edge contributed time dependence of the accumulation mass on the XIS0's OBF, as shown in Fig. 5. The calculation values of accumulation mass at the center, for smaller difference of the temperatures, were smaller than that for greater difference of the temperatures. This tendency was different from the phenomena as shown in Fig. 1. Unfortunately we don't know accurate temperatures inside each XIS detector, including the baffles and the camera body. The temperatures of the OBFs would complicate our prediction of time dependence and quantity of the accumulation mass.

4 Conclusions

The accumulation mass from 100 to 140 µg cm^{-2} on the XIS's OBF of *SUZAKU* satellite were observed on November 2010. The accumulation mass at center of the XIS1's OBF was two times greater than that at the edge on August 2010. Our analysis indicated that the calculation value of accumulation mass at center of OBFs was 300 µg cm^{-2} on August 2010. A chemical compound with higher evaporation rate, including DBP and BBP, would contribute the spatial distribution of accumulation mass on the OBF.

The J-SPICE will be useful to predict accumulation mass of molecular contaminants on critical surfaces for spacecraft design. We have progressed verification and improvement for the J-SPICE prediction accuracy.

References

1. Tribble AC (2000) Fundamentals of contamination control. SPIE Press, Washington
2. Urayama F, Yano K, Yamanaka R, Miyazaki E, Kimoto Y (2008) Molecular contamination assessment on *Hinode* solar optical telescope. J Jpn Soc Aeronaut Space Sci 56:543–550
3. Hayashi T, Urayama F, Takeda N, Baba N (2004) Modeling of material outgassing and deposition phenomena. Proc SPIE 5526:137–146
4. The *Suzaku* Technical Description (2010) ISAS/JAXA and NASA/Goddard space flight center
5. Anabuki N, Astro-E2 Team (2005) Measurements of the outgassing rate during the satellite baking of Astro-E2. JAXA-RR-04-025
6. Lesvenan AL, Guyt J, Schmeitzky O, van Eesbeek M (2003) Re-evaporation of polymeric materials during outgassing experiments. In: Proceedings of the 9th international symposium on materials in a space environment, pp 211–216
7. Lide DR (ed) (2002) CRC handbook of chemistry and physics, 83rd edn. CRC Press, Colorado

First Evaluation of Contamination on the JEM/MPAC&SEED

Susumu Baba, Junko Matsuyama, Junichiro Ishizawa, and Yugo Kimoto

Abstract JEM/MPAC&SEED were exposed to the space environment for 8.5 months and retrieved via EVA in April 2010. We subsequently analyzed the surface of JEM/MPAC&SEED to determine the state of contamination.

1 Introduction

JAXA developed the Micro-Particles Capturer and Space Environment Exposure Device for material exposure experiments on the exterior of the Japanese Experiment Module (JEM/MPAC&SEED) on the ISS. The device was attached to the exterior of the JEM in July 2009 and exposed to the space environment for 259 days. After exposure, the device was retrieved via Extra-Vehicular Activity (EVA) in April 2010, whereupon its surface and the mounted SEED samples were examined to investigate the state of contamination.

A comparison was also made with the results of the Russian Service Module/ Micro-Particles Capturer and Space Environment Exposure Device (SM/ MPAC&SEED) concerning the state of contamination.

2 Overview of JEM/MPAC&SEED

JEM/MPAC&SEED consist of three parts as follows: (1) Silica-aerogel (used for capturing space debris and micro meteoroids), (2) Gold plate (used to investigate the flux of impact on the same), (3) SEED samples (experiments involving space

S. Baba (✉) • J. Matsuyama • J. Ishizawa • Y. Kimoto
Aerospace Research and Development Directorate, Japan Aerospace Exploration Agency,
2-1-1 Sengen, Tsukuba 305-8505, Japan
e-mail: baba.susumu@jaxa.jp

Silica-aelogel (MPAC experiment)

Gold plate (MPAC experiment)
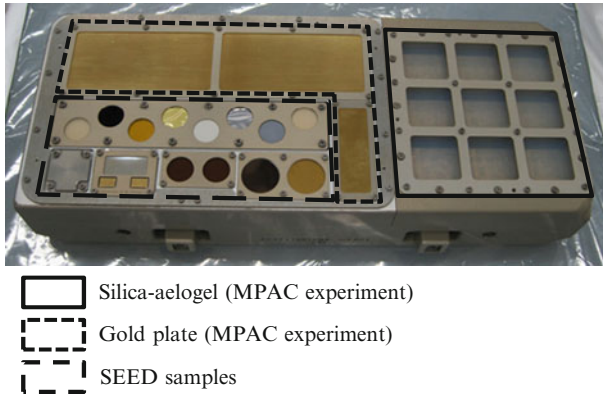
SEED samples

Fig. 1 Photographs of JEM/MPA C&SEED
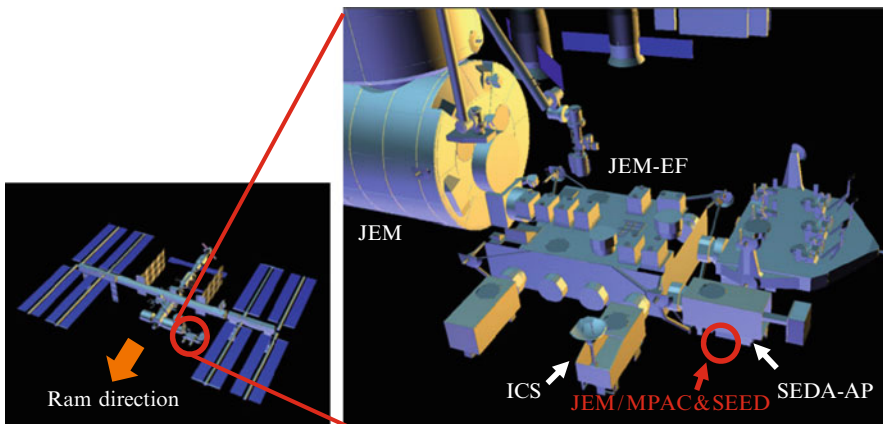
Fig. 2 Location of JEM/MPAC&SEED

material exposure to evaluate durability against the space environment) [1]. All samples were mounted on the ram face of the device using an aluminum alloy frame (Fig. 1), located at the top of the ram direction of the ISS. (Fig. 2).

3 Observation Results

After retrieval, the surface of device and the mounted samples were analyzed to investigate the state of contamination by Optical Microscopy (OM), X-ray photoelectron spectroscopy (XPS) and time-of-flight secondary ion mass spectroscopy (TOF-SIMS). XPS analyses were performed to obtain the atomic composition of the top surfaces and the depth profiles. Conversely, TOF-SIMS analyses were performed to identify the molecular composition of the top surfaces.

Table 1 Surface observation points

	Observation point	Material	Analyzed side	Method (× :Done)		
				OM	XPS	TOF-SIMS
A	Alluminium alloy frame_1	A7075-735 2alloy (with an MIL-A-8625 type 1 anodic coating)	Anodic coating	X	X	X
B	Alluminium alloy frame_2				X	
C	ITO coated UPILEX®-258	ITO/PI	ITO		X	
D	DUS-601	ITO/PU	ITO		X	
E	Ge coated Black Kapton®	Ge/PI	Ge		X	
F	Ag coated FEP	Ag/FEP	FEP		X	

Fig. 3 The aluminum holder with samples showing the surface observation points
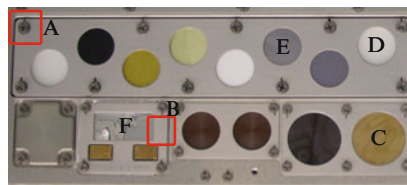
3.1 Observation Points

The observation points included the surface of the film samples and the aluminum alloy frames which had been used to hold the samples (Table 1 and Fig. 3). The selected film samples were covered with an Atomic Oxygen (AO) resistant layer to allow estimating the thickness of the contamination deposit layer. In general, materials with a low durability against AO erosion react with the AO forming rough surfaces. Therefore, contaminants deposited on such rough surfaces will adopt the morphology of the eroded surface, thus hampering efforts to estimate the layer thickness.

3.2 Optical Observation

After retrieval, the entire external surface of the aluminum alloy frame was analyzed and was found to attain a brownish discoloration except for the unexposed areas that were covered by washers (Fig. 4).
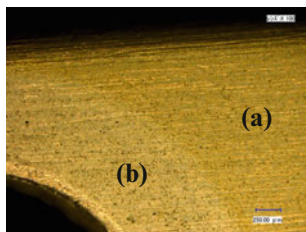
Fig. 4 Discoloration of the aluminum alloy frame 1 (**a**) exposed area (**b**) unexposed area covered by washer
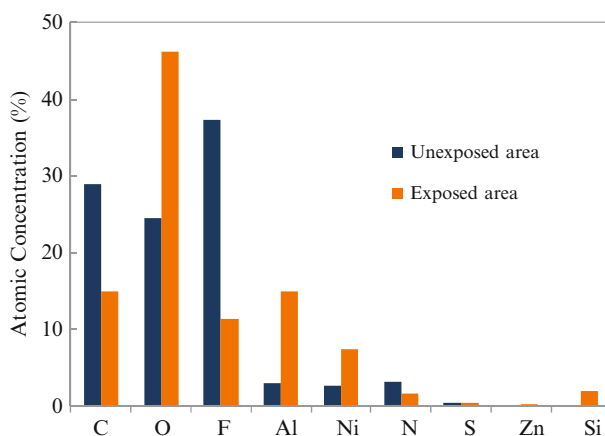
Fig. 5 Elemental composition of the top surface of the aluminum alloy frame 1

3.3 XPS and TOF-SIMS Analysis

3.3.1 Aluminum Alloy Frame 1

Figure 5 shows the elemental composition of the top surface of the aluminum alloy frames as analyzed by XPS. In all analysis points of the aluminum alloy frame, C, O, F, Al, Ni and N were detected, as well as traces of S and Zn. The aluminum alloy frames were made of A7075-7352 alloy with a MIL-A-8625 type 1 anodic coating. The coating had to be completely sealed due to its porous structure. Cobalt or nickel acetate are often used as the sealing agents. The presence of Ni, could also be explained by its out diffusion from the aluminum alloy frame itself.

Si was only detected in the exposed area, while concentrations of C, F and N showed declining tendencies due to exposure. In contrast, concentrations of O, Al and Ni increased following such exposure. In unexposed areas, carbon was mainly detected in the form of CFx, as well as C–O, C = O and COO. Conversely, in the exposed areas, it was detected mainly as CHx, C–C and C = C, as well as C–O,

Table 2 Chemical state of the elements

| | Chemical state of the elements | | |
| | C | | |
	Main	Others	F
Unexposed area	CFx	C-O,C=O,COO	CFx
Exposed area	CHx,C-C,C=C	C-O,C=O,COO	Fluoride

Table 3 Distinctive chemical groups identified in the TOF-SIMS spectra

	TOF-SIMS (Distinctive chemicals)	Element that composes	Remarks
Unexposed area	PF PE	C,F,O	Derived from fluoro chemical lubricant
	PTFE	C,F	
Exposed area	Phthalate esters	C,O,H	Derived from addition agent
	BHT	C,O,H	
	Fatty acid amines	C,N,H	
	Si inorganic compound	Si,O,H	SiO_2 etc...

$C = O$ and COO. Though the chemical state of F was CFx on unexposed areas, it was detected as fluoride on the exposed areas. (Table 2).

In addition, the top surface of the aluminum alloy frame 1 was analyzed in unexposed and exposed areas using TOF-SIMS to identify the molecular composition. Table 3 shows the chemical groups that were identified in the TOF-SIMS spectra. In the unexposed areas, chemical groups that were associated with perfluoropolyether (PFPE) and polytetrafluoroethylene (PTFE) were found that, presumably, were derived from fluorochemical lubricant. Such identification is considered reasonable, because prior to the JEM/MPAC&SEED launch, fluorochemical lubricant was used to lubricate the screws. Namely, PFPE and PTFE may be elements originating in the JEM/MPAC&SEED itself.

In contrast, the PFPE and PTFE compounds were practically not seen on the exposed areas that could be due to their removal from the surface by space environmental factors such as AO, UV.

Various forms of organic matter such as phthalate esters, butylated hydroxytoluene (BHT) and fatty acid amines were distinctively present on the exposed surfaces. Such organic matter is thought to include elements that originated from polymer additive agents. In general, additive agents are usually detected on surfaces within the storage environment at ground level, hence the organic matter concerned presumably became attached to the surface after EVA.

Si inorganic compounds, such as SiO_2, were observed on the exposed surfaces. The probability for SiO_2 to adhere in the atmosphere or for an adhering silicone to oxidize into SiO_2 in the atmosphere is considered low; another way of SiO_2 formation should be looked for. Incidentally, Miyazaki reported on the result of a ground experiment where by AO was irradiated against the surface of the polyimide film which was contaminated with silicone [2]. According to this report, the silicone that was on the surface of the polyimide film may have been changed to SiO_2 by
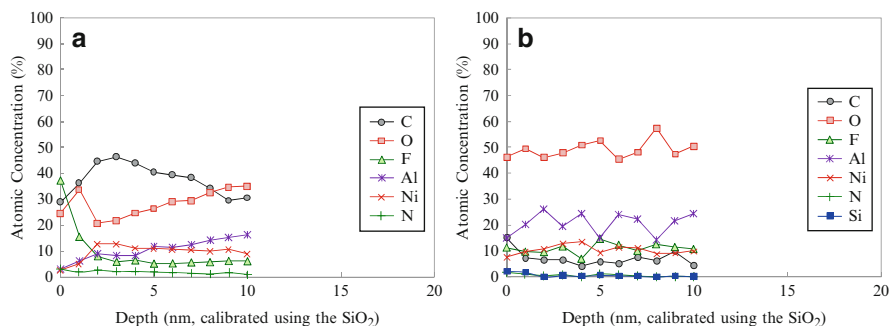
Fig. 6 XPS depth profile analysis of the aluminum alloy frame 1. (**a**) Unexposed area (**b**) Exposed area

AO. Based on the above hypothesis, it can be suggested that SiO_2 found on the exposed surfaces was formed from silicone contamination that was induced by outgassing from nearby materials and that was oxidized by AO while in-orbit.

The results of XPS depth profile analysis in unexposed and exposed areas are shown in Fig. 6. In the unexposed area, a high concentration of F was observed in the top surface to a depth of 1 nm that can be attributed to a layer of fluorochemical lubricant based on the TOF-SIMS result. Also, in the exposed area, the concentration of O was obviously higher than in the unexposed area. Si was observed in the top layers of the exposed surface to a depth of 1 nm.

3.3.2 Film Samples

The exposed surfaces of mounted film samples were also analyzed to obtain the depth profile using XPS for the purpose of estimating the thickness of the contamination layers (Fig. 7). Si has been observed besides the original elements of these samples and is thought to be a contaminant introduced during the exposure. The thickness of the contamination layer was defined as the Si thickness where the Si concentration decreased 50 % regarding the top surface concentration level.

3.3.3 ITO-Coated Upilex-S®

ITO-coated Upilex-S® is a coating of Indium Tin Oxide deposited onto a Upilex-S® (Polyimide) film. Si was observed in addition to the ITO elements in the postflight analysis. The chemical state of Si appears to be SiO_2 due to the energy of the detected Si peak. As indicated in Fig. 7 for ITO-coated Upilex-S®, the thickness of the SiO_2 layer was about 3 nm.
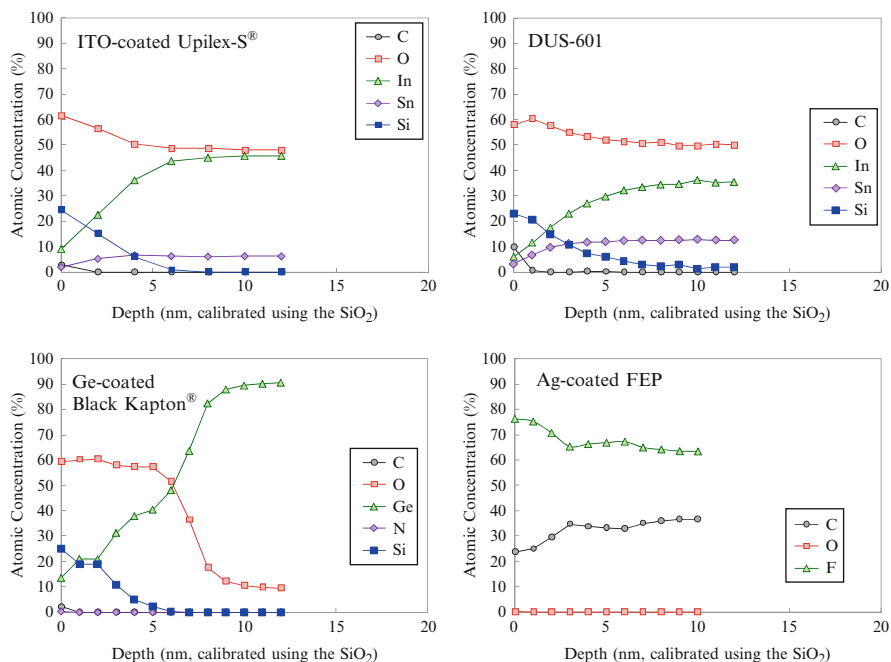
Fig. 7 XPS depth profile analyses of the exposed area of film samples

3.3.4 DUS-601

DUS-601 is a coating of ITO applied to a polyurethane film. Si was observed in addition to the ITO elements. The chemical state of Si seems to be SiO_2, as suggested by the XPS analysis. As indicated in Fig. 7 for DUS-601 sample, the thickness of the SiO_2 layer was about 3 nm.

3.3.5 Ge-Coated Black Kapton®

Ge-coated Black Kapton® is a coating of germanium, a semiconductor material that withstands the AO attack without forming an oxide, onto Black Kapton® (Polyimide) film. Si and O were observed in addition to Ge. The chemical state of Si appears to be SiO_2, as suggested by the XPS analysis. The thickness of the SiO_2 layer was about 3 nm.

3.3.6 Ag-Coated FEP

Ag-coated FEP is a coating of silver applied to fluorinated ethylene propylene (FEP) film. No Si was found on the surface of this sample in the after-flight analysis.

Fig. 8 Analyzed points of
the depth profile (**a**) exposed
area of Ag-coated FEP
(**b**) aluminum alloy frame 2
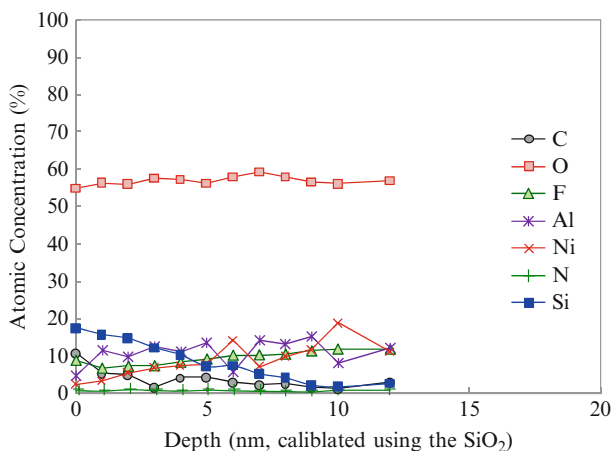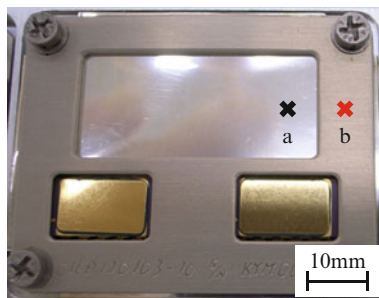
Fig. 9 XPS depth profile analysis of the aluminum alloy frame 2

The depth profiles of oxygen and carbon were found to differ from the tendencies observed with other film samples.

3.3.7 Why Si Was Not Detected on Ag Coated FEP

In an attempt to explain the absence of Si on the exposed surface of the Ag coated FEP sample, a few hypothesis were evaluated as follows.

Hypothesis #1: Silicone contamination did not affect the area around the Ag-coated FEP.
Hypothesis #2: Silicone contamination was unable to adhere to the FEP surface.

To verify hypothesis #1, an XPS depth profile analysis of the aluminum alloy frame 2 surface was performed in an area near the analyzed point on the Ag-coated FEP (Fig. 8). As can be seen from Fig. 9, that presents the result of the XPS depth
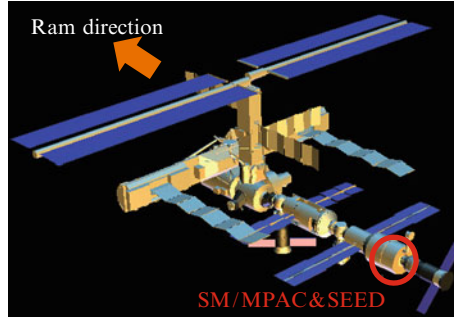
Fig. 10 The location of SM/MPAC &SEED (At the time of retrieval of #3)

profile analysis of the aluminum alloy frame 2, Si is clearly present in the spectrum, a fact that disregards hypothesis #1. Ground-based experiments are currently being prepared for verification of the hypothesis #2

4 Comparison of Present Results with SM/MPAC&SEED Experiment

4.1 Overview of SM/MPAC&SEED Experiment

SM/MPAC&SEED is a device with the same purpose developed earlier than JEM/MPAC&SEED. SM/MPAC&SEED consists of three identical units (SM/MPAC&SEED #1, #2 and #3). In October 2001 all three units were attached to the handrail outside the SM by EVA, and retrieved individually after exposure of 315 (#1), 865 (#2), and 1,403 days (#3), respectively [3]. Figure 10 shows the location of SM/MPAC &SEED on the ISS. Comparing the location of the JEM/MPAC&SEED (see Fig. 2) with the SM/MPAC&SEED (Fig. 10), it is clear that a large number of ISS structural elements were obstructing the ram face of SM/MPAC&SEED compared with JEM/MPAC&SEED.

4.2 Thickness of the Contamination Layer in SM/MPAC&SEED Experiment

A SiO_2 contamination layer was also observed in the ram direction of SM/MPAC&SEED experiment. Figure 11 presents a comparison of the SiO_2 layer thickness between the SM/MPAC&SEED and the JEM/MPAC&SEED experiments [4]. Even taking the exposure duration into consideration, the thickness of SM/MPAC&SEED exceeds that of JEM/MPAC&SEED. If to rule out any
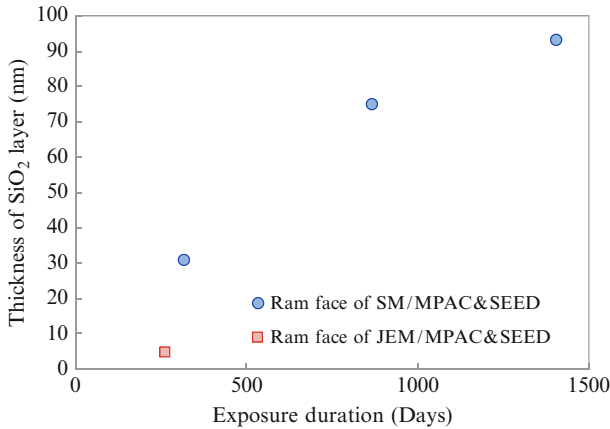
Fig. 11 Thickness of the SiO$_2$ contamination layer versus exposure duration

accidental deposition of Si, the growth rate of the contamination layer in SM/MPAC&SEED is still considered to exceed that of JEM/MPAC&SEED. The possible causes are listed as follows;

1. *Different location of the ram surfaces on the ISS*: There are many structures on the ISS located in front of the ram face location of the SM/MPAC&SEED as compared with JEM/MPAC&SEED (compare Fig. 2 to Fig. 10). If a structure containing a SiO$_2$ contamination source was located in front of the SM/MPAC&SEED experiment it could contribute to an increased level of contamination.
2. *Difference of the exposure time periods:* When SM/MPAC&SEED has been deployed, many structural elements of the ISS were still under construction. In contrast, JEM/MPAC&SEED was deployed after the ISS had almost been completed. Generally, the outgassing rates of materials exposed to vacuum are greater in the beginning of exposures. Therefore, it is possible that the contamination rates that affected the ram face of SM/MPAC&SEED were higher than for JEM/MPAC&SEED.

5 Conclusions

The contamination on the surface of JEM/MPAC&SEED experiment was investigated. A SiO$_2$ contamination layer was observed in most places, the thickness of which was under 5 nm, making it thinner than that found in the SM/MPAC&SEED experiment. The SiO$_2$ layer was not detected on the exposed surface of the Ag-coated FEP sample. Currently, we are preparing ground experiments to verify the cause.

References

1. Kimoto Y, Ishizawa J, Shimamura H (2011) Passive space environment effect measurement on JEM/MPAC&SEED. In: Proceedings of ICPMSE-10 J, June 2011, Okinawa (in press)
2. Miyazaki E, Matsumoto K, Yamanaka R, Kimoto Y (2009) Ground experiment of interaction between molecular contamination and atomic oxygen. In: Proceedings of the 53rd symposium on space science and technology, Tsukuba, July 2009, 1236–1241(in Japanese)
3. Kimoto Y, Ishizawa J, Miyazaki E, Suzuki M (2009) SM/MPAC&SEED experiment overview. In: Proceedings of international ymposium on SM/MPAC&SE ED Experiment, JAXA-SP-08-015E, 5–9
4. BABA N, Kimoto Y (2009) Contamination effect on SM/MPAC&SEED experiment. In: Proceedings of international symposium on "SM/MPAC&SEED Experiment," JAXA-SP-08-015E, 27–3

A Method of Estimating the Charge Properties of Spacecraft Materials

Yifeng Chen, Shengsheng Yang, Xiaogang Qin, and Hong Shi

Abstract The degradation law of the properties of spacecraft material is different due to the complex environment in space. It is important to estimate and improve the properties of spacecraft material for developing a long-life and high reliability spacecraft. This paper studies the degradation model of material and develops the method to investigate the charge properties (esp. surface charge and internal charge) considering the degradation of mechanical property of spacecraft material.

Keywords Dielectrics • Property • Spacecraft charge

1 Introduction

Electronic devices and insulating materials of spacecraft will be damaged in space environment. The factors inducing such damages include vacuum, thermal cycling, and high-energy radiation. High-energy radiation interacts with insulating materials causing partial decomposition and cross-linking. Atomic oxygen reacts chemically with the surfaces of organic materials causing oxidation and erosion. The low-molecular weight fractions evaporate from organic materials and the bulk of organic materials becomes micro-porous, leading to increased bulk resistivity and surface resistivity of insulating materials. Charge accumulation on the surface or in the bulk of the insulating materials and electric devices of the spacecraft may cause electrical discharge resulting in serious damage. Accidents in such an environment are thought to be strongly related to the degradation of spacecraft materials.

In the initial stage of the knowledge of material parameters determined under irradiation conditions [1], we tried to observe the mechanical properties of

---

Y. Chen (✉) • S. Yang • X. Qin • H. Shi
Science and Technology on Vacuum &Cryogenics Technology and Physics Laboratory,
Lanzhou Institute of Physics, Chinese Academy of Space Technology, Lanzhou 730000, China
e-mail: chenyifeng04@gmail.com

Table 1 The degradation law of dielectrics

	Space			Ground	
Parameters	Trend	Mechanism		Trend	Mechanism
ρ	↑	Vacuum micropores appear		↓	Low molecular weight fractions form
tanδ	↓	Micropores, polar radicals increase		↑	Micropores, polar radicals increase, polar micromolecules
ε	↓	Vacuum micropores		↑	Polar micromolecules + moisture
Surface charge trap	↑	Material surface state changes		↓	Polar radicals emerge
Electrostatic storage property	↑	Resistivity increases		↓	Polar radicals emerge

insulating material. Advanced measurement techniques for surface potential and electric-charge accumulation in dielectrics have been applied for evaluating the properties of spacecraft insulating materials [2].

2 Dielectric Properties Degradation Mechanism

The aging processes in insulator materials in ground conditions can be explained mostly by photooxidation aging and partial decomposition and microcracks formation at atmospheric conditions and applied high electric fields. When low molecular weight fractions and end groups containing polar macromolecules are formed, aging of insulator materials in atmospheric conditions on the ground is accompanied by decreasing of insulation resistance (ρ), increasing of loss tangent (tan δ), dielectric constant (ε), partial discharge (PD), etc. [3, 4]. However, because low molecular weight fractions are continuously extracted in vacuum conditions and the influence of high-energy electron irradiation, the aging of space dielectric materials is contrarily expressed by increasing of insulation resistance, decreasing of loss tangent, dielectric constant, and so forth. Moreover, the main threat of aging of space dielectric materials to spacecraft is the electrostatic discharge, therefore the change of electrical resistivity of dielectric materials especially that of electrostatic properties could be used to evaluate the reliability and the life time of space dielectric materials. The difference between the degradation law of dielectrics in space environment and in ground is shown in Table 1.

Fig. 1 Schematic
presentation of the system for
measurement of dielectric
properties
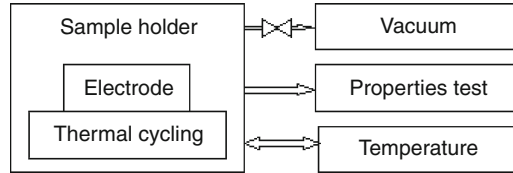
3 Method for Evaluating Dielectric Properties

There are a lot of differences in dielectrics properties of materials measured in air atmosphere and in vacuum environments because at atmospheric conditions the low-molecular weight fractions evaporate from organic materials with the bulk of such organic materials attaining a micro-porous structure. To imitate the space conditions, the dielectric materials under investigation should be irradiated with one of the space environment radiation factors in a vacuum environment. The system used in the present experiments is described below.

4 Sample Holder

Figure 1 shows the details of the sample holder.(1) The pressure of the system should be lower than 10^{-5} Pa. (2) The stainless steel metal is chosen to provide complete electrical and light shielding. (3) The thermal cycling range is 200 °C to −160 °C. (4) The electrical connection with double-shielding allows easily measuring the properties of dielectrics. (5) The electrode assembly can be used to test the absolute charge of slabs of dielectric materials.

5 Resistivity Measurement

The classical resistivity method is used to measure the bulk resistivity and surface resistivity of dielectrics. The resistivity of dielectric materials will increase after high-energy electron irradiation. The increase of surface resistivity of dielectrics is due to increased surface micro-roughness that causes an increase of the electric track (Fig 2a). And the bulk resistivity increases as a result of increased formation of micropores in the dielectric (Fig 2b). The change of the bulk resistivity and surface resistivity can be used to evaluate the degradation of dielectrics properties.
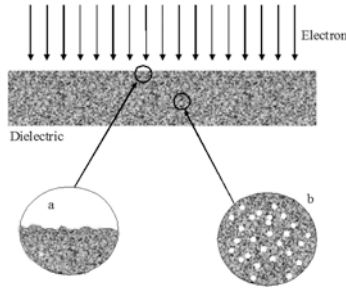
Fig. 2 The change of resistivity of dielectrics under high-energy electron irradiation
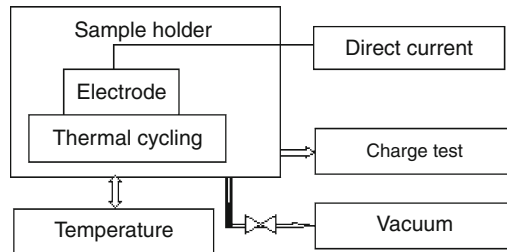
Fig. 3 Schematic diagram of the set-up for testing electrostatic properties of polymeric material

6 Estimation of Electrostatic Properties in Vacuum

High-energy electron irradiation essentially decomposes polymeric material, generates micro pores and polar micromolecules and leads to material cross-linking. Under high vacuum, the formed micromolecules may leave the bulk of the material, giving a rise in volume resistance. Also, as discussed above, the surface resistance will increase and the electrostatic storage capacity will be enhanced. The electrostatic properties of dielectric materials can be estimated by applying a DC field and then measuring material surface charges and volume charges, i.e. firstly measuring the total charges under applied DC field, then shorting out the material surface to release charges, and, finally, measuring the volume charges in the material. The surface electrostatic properties and bulk electrostatic properties could be evaluated from the electrostatic quantity, high-energy electron-beam intensity and irradiation time, as shown schematically in Fig. 3.

7 Estimation of Dielectric Properties in Vacuum

Dielectric constant ε and tan δ are the key parameters that describe the dielectric properties of materials. As material ages, these two parameters will change significantly before its mechanical properties will degrade due to the physical and
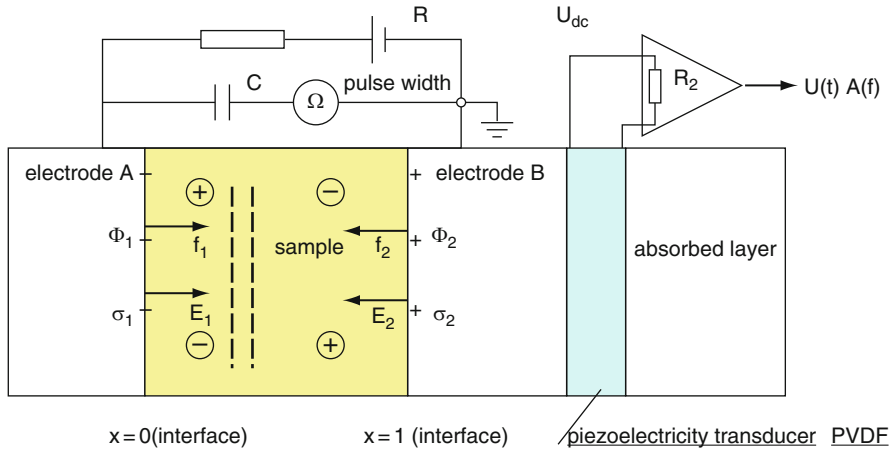
Fig. 4 The schematic diagram of space charge measurement

chemical changes in the material. Measurements of ε and tan δ values as a function of the irradiation intensity and time are sufficient for obtaining information on the reliability and lifetime of the spacecraft materials. Using the set-up shown in Fig. 1, the required information on the changes of ε and tan δ can be obtained using a dielectric spectrum analyzer system.

8 Estimation of Space Charge Properties in Vacuum

In-situ space charge measurement is a technology developed in recent 10 years to measure the internal space charge and potential distribution in dielectric materials. Presently, the research in this field has been focused on in-situ space charge distribution measurements in irradiated dielectric materials used for space applications. From these measurements the electrostatic charge distribution and the electrostatic field distribution in dielectrics could be defined. A number of instruments and set-ups have been produced [3, 5–7].

The schematic diagram of pulsed electro-acoustic (PEA) detection equipment used in this work is shown in Fig. 4. When a high voltage pulse is applied to both ends of the sample, internal space charge redistribution occurs within the sample that is transmitted in the form of mechanical or ultrasonic waves. These signals reach the grounded aluminum electrode and attached to it PVDF piezoelectric transducer and are transformed into electric signals containing the information of internal space charge distribution in the sample. We developed an in situ space charge measurement system shown in Fig. 5a, of which the key technology is the electrode system (Fig. 5b). It should be noted that in such in-situ measurements signal distortion and signal attenuation must be taken into account. Presently, experiments are in progess using the described above set-ups and the data will be published elsewhere.
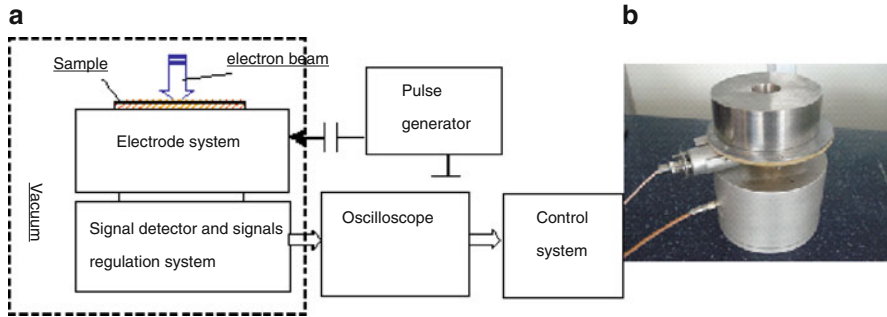
Fig. 5 In situ measurement system of internal space charge in electron irradiated sample

9 Conclusions

Estimation of spacecraft materials lifetime is very important for the safety of spacecraft. Therefore, accurate predictions of the lifetime of polymeric materials used in spacecraft design not only facilitate the evaluation of reliability and lifetime of spacecraft, but also are beneficial in selection and development of technologies used for manufacturing of these polymers.

For accurate estimates, realistic simulation of the space environment is of great importance and difficulty. Since space environmental factors that may affect a spacecraft on a space mission include a large variety of phenomena like geomagnetic substorms, sunspots, solar storms and so on, a great deal of efforts still has to be put by scientists forward to understand them. So far, we can only simulate several leading factors affecting the lifetime and reliability of spacecraft materials, such as thermal cycling, high energy particles (every cosmic radiation, plasmas), high vacuum, etc. The in-situ testing methods described in this paper are based on simple approaches and were developed to help scientists evaluating the major electric parameters of dielectric materials.

References

1. Ninghua W, Bin G et al (2004) A practical space charge testing system realized by the pulse electro-acoustic method. Electr Meas Instrum 11:12–15
2. Xiaodong L, Xiaoquan Z et al (2007) Study on space charge and dielectric character of dielectric after high energy electron radiation. Adv Technol Electr Eng Energy 26(1):55–58
3. Xiaodong L, Xiaoquan Z et al (2006) Influence of electron beam radiation on electrical parameter of polyimide. Insul Mater 39(6):38–41
4. Griseri V, Fukunaga K et al (2004) In-situ space charge distribution measurements in electron irradiated polymers for space applications. In: International conference on solid dielectrics, Toulouse, July 5–9
5. Catani JP, Payan D (2004) Electrostatic behavior of materials in a charging space environment 2004. In: International conference on solid dielectrics, Toulouse, July 5–9

6. Maeno T, Fukunaga K (2002) Portable space charge measurement system for space environ-ment monitoring. Annual report conference on electrical insulation and dielectric phenomena, pp 853–855
7. Griseri V, Lèvy L et al (2002) Space charge behavior in electron irradiated polymers. Annual report conference on electrical insulation and dielectric phenomena, pp 922–925

Registering the Elemental Composition
of Micrometeoroids and Debris

N.D. Semkin, A.M. Telegin, and K.E. Voronov

Abstract A method has been developed to obtain information about the chemical composition of micrometeoroids in laboratory conditions by analyzing the material residues of particles trapped in the craters formed on exposed to space surfaces of a matrix of thin film capacitors.

The paper presents a number of ion spectra collected by a mass – spectrometer with an electrostatic accelerator that is using a metal – dielectric – metal (MDM) film as a target. It is shown that such modification of the mass-spectrometer improved the efficiency of ion production and allowed to obtain information on elemental composition from a larger number of compounds. The theoretical basis for this phenomenon is considered.

Keywords Chemical composition • Debris • Mass spectrometer • Micrometeoroid

1   Introduction

In the exploration and development of on-board detectors of cosmic dust it is necessary to create instruments that would transform impact information and other related parameters of the particles into electrical signals. The time-of-flight (TOF) mass – spectrometers are used widely to evaluate the elemental composition of micrometeoroids [1, 2].

However, for small particle velocities, less then 6–8 km/s (including the debris), the degree of ionization of different chemical elements is small that does not allow receiving full and accurate information about their elemental composition. Basically, the resulting spectra contain information mostly from ions of alkaline elements due to their small ionization potential values.

N.D. Semkin (✉) • A.M. Telegin • K.E. Voronov
Samara State University, 443086, Russia Samara, Moscow highway, 34
e-mail: talex85@mail.ru

In order to obtain more information on the elemental composition of the particles, it is proposed to use thin metal – dielectric – metal (MDM) film structures as a target in the mass – spectrometer. When voltage is applied to the MDM structure plate, due to its potential energy, it is possible to improve the efficiency of ion formation, that are analyzed by TOF mass – spectrometer [1]. Measuring the voltage on the punched through capacitor provides additional information about the mass and energy of the micrometeoroids [3].

2   Theory

When particles collide with the target surface, both the target material and the particles undergo an ionization process [4]. The composition of the produced plasma may contain information on the elemental composition of the particles. Low temperature plasma can take into account only single ionization that allows calculating the residual charges without the use of numerical methods.

A system of equations describing the kinetics of ionization and recombination in the expanding cluster can be presented as follows:

$$
\begin{cases}
\dfrac{dx_k}{dt} = (1 - x_k) \cdot x_e \cdot \dfrac{ACt_0 n(t)}{T^3(t)} \cdot \exp\left(-\dfrac{J_k}{T_0}\right) - \dfrac{x_k x^2{}_e n^2(t) A t_0}{T^{\frac{9}{2}}(t)}; \\[3mm]
n(t) = \dfrac{n_0}{t^3}; \\[3mm]
T(t) = \dfrac{T_0}{t}; \\[3mm]
x_e = \displaystyle\sum_{k=1}^{k_{\max}} v_k x_k,
\end{cases}
\tag{1}
$$

where t – is dimensionless time normalized to t_0 that is defined as the time of establishment of the impact processes in the insulator, x_e, x_k – are the degree of ionization of electrons and ions of a k-th element, v_k – presence of heavy particles of the k-th class, J_k – ionization potential of the k-th element, T_0 - the initial temperature of the plasmoid, n(t) – is the concentration of heavy particles, $C = 6.06 \cdot 10^{21} \mathrm{cm}^{-3} \cdot (\mathrm{eV})^{-4.5} \cdot \mathrm{s}^{-1}$, $A = 8.75 \cdot 10^{27} \mathrm{cm}^{-6} \cdot (\mathrm{eV})^{-4.5} \cdot \mathrm{s}^{-1}$, T – is the temperature.

The equations for the residual charges can be expressed as follows [4]:

$$
Q_e = \frac{4}{3} \cdot \pi \cdot R_0^3 \cdot n_0 \cdot x_{e\infty},
\tag{2}
$$

$$
Q_k = \frac{4}{3} \cdot \pi \cdot R_0^3 \cdot n_0 \cdot v_k \cdot x_{k\infty}, \quad Q_e = \sum_{k=1}^{k_{\max}} Q_k.
\tag{3}
$$

When the dielectric is punched through, the space between the plates of a capacitor is filled with plasma, which can be represented as a mixture of electronic and ionic liquids. The frictional force of the electron liquid against the ionic liquid causes the heating of the plasma. The heating rate of electrons due to the friction force is determined from the following equation [5]:

$$\frac{3}{2} \cdot n_e \cdot \frac{dT_{\ddot{a}}}{dt} = \sigma_e \cdot E^2; \tag{4}$$

where n_e- is the concentration of electrons, $T_{\ddot{a}}$ – is the electron temperature, σ_e – is the electronic component of the plasma conductivity, E – the external electric field applied to the capacitor plates.

The increase in plasma temperature due to the current (Joule) heating should be taken into account in solving the problem of gas-kinetic plasma expansion, the total temperature of which can be represented as the sum of two components:

$$T_\Sigma = T + \tilde{T},$$

where T- is the temperature of the expanding cluster, $\tilde{T}$- is the temperature of the Joule heating of the plasma. This increment of temperature occurs due to the voltage applied to the plates of the MDM structure.

Thus, an increase in the field strength applied to the MDM structure, leads to an increase of the number of ions formed during the impact, which is confirmed by calculations [4]. Detectors based on such MDM – structures were used in space experiments [6, 7].

3 Experimental

Assessment of the chemical elements is carried out by an array of thin film MDM – structures deposited on a clean target (such as silver, gold). After exposure of these structures in space, they are analyzed in the laboratory by applying a voltage pulse to the shortened in space capacitors to create a breakthrough in them. The elemental composition of the residues from the impact particles remained in the formed crater are then analyzed in TOF mass spectrometers of various designs.

The advantages of such delayed measurements in their simplicity and no need in sophisticated equipment on the spacecraft. The authors developed a method to obtain information about the chemical composition of micrometeoroids in laboratory conditions by analyzing the material residues of particles trapped in the craters formed on the exposed to space surfaces that form a matrix of thin film capacitors (Fig. 1).

A thin film capacitor structure consisting of a metal (Al) – insulator (PMMA, thickness 0.3–0.6 μm)- metal (Al thickness 0.1 μm) was deposited on a glass
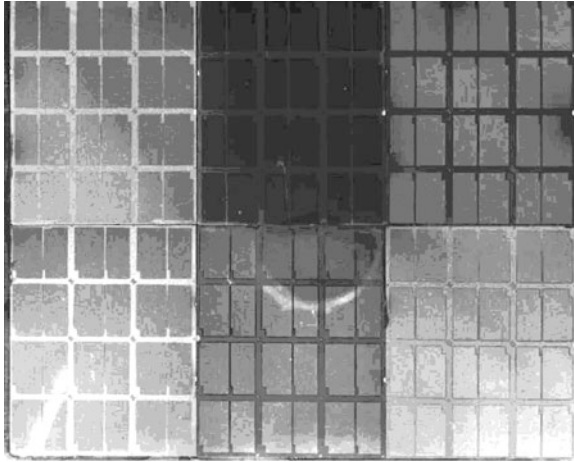
Fig. 1 A matrix of thin-film capacitors used for entrapping micrometeoroids and other particles
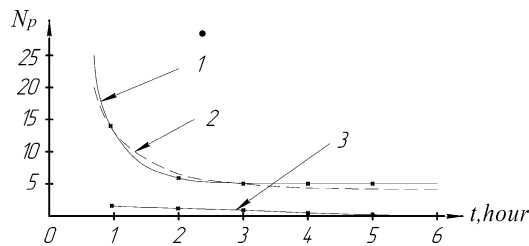
Fig. 2 Dependence of the number of breakdowns on time. (*1*) – in air under pressure p $= 10^5$ Pa; (*2*) – in vacuum at a pressure p $= 1.33 \ 10^{-3}$ Pa, T $= 100$ °C and capacitor voltage; (*3*) – at T $= 60$ °C, U$_c$ $= 30$ V, p $= 1.33 \ 10^{-3}$ Pa

ceramic substrate. The formed matrix of thin film capacitors was irradiated with Al and Fe particles in laboratory conditions using a particle accelerator. The MDM structure containing the short-circuited capacitors with the formed craters was then transferred to the vacuum chamber of the TOF mass spectrometer. A voltage pulse 100–150 V was then applied to these capacitors creating plasma in the short-circuited section of the capacitor and the spectra that contained information on the residues from the particles in the craters were recorded.

The MDM structures were created by polymerization of monomers in a high-frequency discharge. Figure 2 shows the dependence of the number of breakdowns on time in air (1) and in vacuum (2) and at different temperatures and voltages on the capacitor (2), (3). The conducted testing of the MDM structures demonstrated the high quality of the formed capacitors that confirmed their suitability for use as micrometeoroid detectors resistant to spontaneous discharges in a wide range of temperatures and stresses.
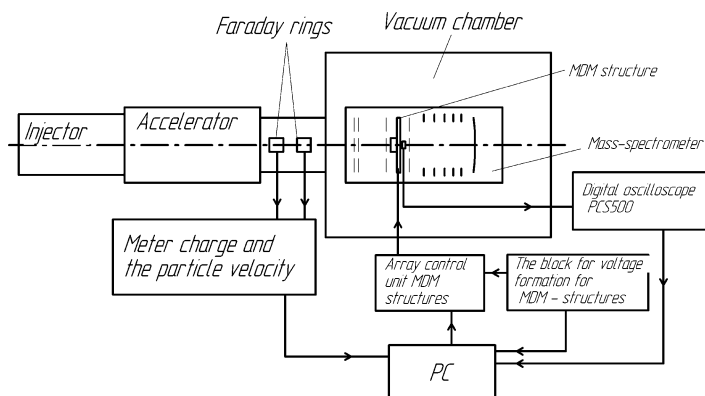
Fig. 3 Schematic presentation of the experimental set-up
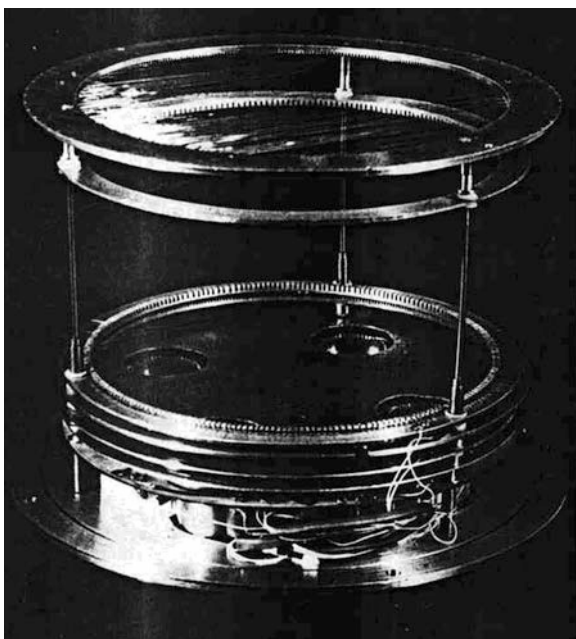
Fig. 4 Image of the mass – spectrometer used in the experiments

The experimental setup is shown in Fig. 3. The major blocks in then set-up include the electrodynamic accelerator [8] that provides acceleration of microparticles to velocities 0.3–13 $km \cdot s^{-1}$ and the vacuum chamber with the mass – spectrometer (Fig. 4) in which as a target is used a thin film MDM matrix. A schematic presentation of the mass – spectrometer is shown in Fig. 5. A detailed description of the working principle of the mass – spectrometer can be found in [2]. The mass – spectrometer design includes a focusing mirror – (1), a metal target with
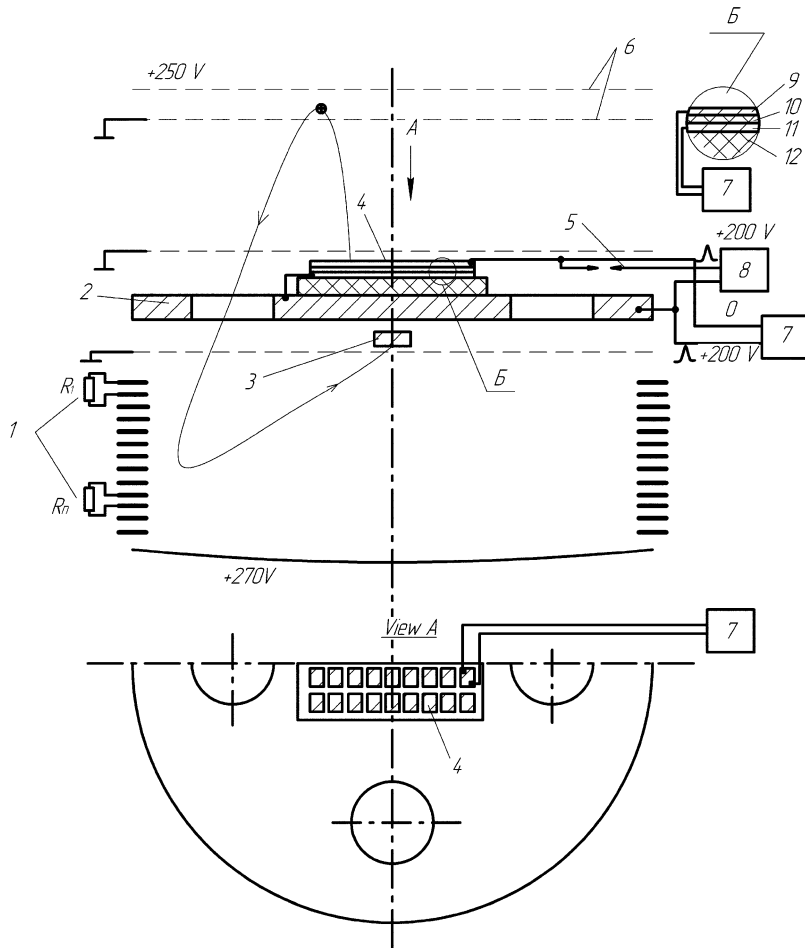
Fig. 5 Schematic presentation of the gaseous-dust mass – spectrometer with a thin film MDM matrix: *1* – focusing mirror, *2* – metal target with holes *3* – ion collector, *4* – the thin-film MDM matrix (target): *5* – needle electrodes, *6* – reflecting mirror *7* – Pulsed power supply *8* – Pulsed spark source, *9*, *10*, *11*, *12* – thin film MDM – structure (*9* – upper plate of (Al), *10* – dielectric (PMMA), *11* – lower plate, *12* – glass-ceramic substrates)

holes – (2), ion collector – (3), thin-film MDM matrix (target) – (4), needle electrodes – (5), the reflecting mirror – (6), a pulsed power supply – (7) and a pulsed spark source – (8).

The measurement of elemental composition of the high-speed particles trapped in the thin film MDM structures is done in four stages.

In the first stage, the elemental composition of the residual gas in the vacuum chamber where the mass – spectrometer is installed is measured by applying a voltage pulse to the needle electrodes that causes a discharge and ionization of residual gas in the vacuum chamber.
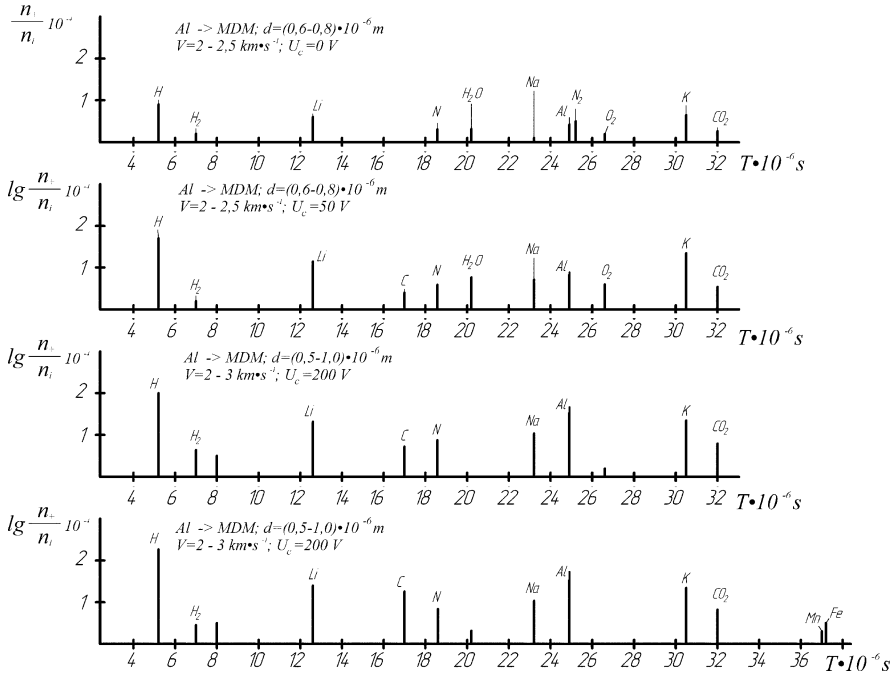
Fig. 6 Ion spectra obtained using the electrodynamic accelerator with a range of particle velocities 0.3–3 km s^{-1}

In the second stage, the effect of the elemental composition of MDM structure on the overall spectrum is measured by applying a current pulse to one of the capacitors in the MDM matrix that were not hit by particles. This causes an explosion of the capacitor and release of ions into the working area of mass – spectrometer.

In the third stage, the thin film MDM matrix structure is irradiated with particles in the absence of voltage on the MDM structure and the formed ions are analyzed.

In the fourth stage, a voltage pulse was applied to the shorted capacitors in the MDM structure and a spectrum was collected. The results of a typical set of experimental data obtained in the four stages are presented in Fig. 6. The spectra shown in Fig. 6 that were obtained using the electrodynamic accelerator with a range of particle velocities 0.3–3 km·s^{-1} were recorded in the memory of a digital oscilloscope.

As can be seen from Fig. 6, with an increase in the applied to the MDM structure voltage, an increase in the number of collected ions is seen, indicating an improvement in the efficiency of ion production by $\sim$ 1–2 orders. In the conducted experiments some spectral lines could not be identified. The experimental data agree qualitatively with the theoretical predictions. The increase in voltage across the MDM structure leads to an increase in the number of ions that is important in the analysis of low-speed particles. The comparison was based on an idealized particle

with a certain set of lines in the spectrum that can explain the mechanism for increasing the efficiency of the mass spectrometers when using thin film MDM structured targets, in the case of low particle velocity ($0.3–3$ km$\cdot$s^{-1}). It must be emphasized that the results of the analysis of mass spectra were obtained at a qualitative level only due to the fact that the spatial expansion of each chemical element occurs along different trajectories. Therefore, quantitative analysis of the spectra obtained with $U = 0$ and $U = 200$ V is very approximate. The problem of determining the movement trajectories of expanding ions of different masses in this work is not considered.

4 Conclusions

Using the thin film MDM capacitor structures as targets in mass spectrometers can improve the efficiency of ion formation during low-speed collision. Exposing the MDM matrices in open flight experiments allows using of the exposure method in the analysis of elemental composition of debris and micrometeoroids. While increasing the voltage on the MDM capacitor improves the efficiency of their use due to a larger number of ions formed during the impact, there is a limit to such increase associated limited dielectric strength. Using thin film MDM capacitor structures as a target in mass – spectrometer allows to increase its detection sensitivity of debris in the range $0.3–10$ km$\cdot$s^{-1}.

References

1. Kissel J, Sagdeev RZ, Bertaux JL et al (1986) Composition of comet halley dust particles from vega observation. Nature 321:280–282
2. Semkin ND, Voronov KE, Myasnikov SV et al (2002) Gas-dust-impact mass spectrometer. Instrum Exp Tech 1:118–124
3. Semkin ND, Voronov KE, et al (2007) The conductivity of shock-compressed channel film MDM structures in the regime of stationary radiation. JTF 77(1):85–89
4. Semkin ND, Novikov LS,Voronov KE et al (2000) Detector of micrometeoroid and artificial space debris particles. Space Debris 2(4):273–293
5. Oraevskii B (1974) Plasma on Earth and in space. Naukova Dumka, Kiev, p 170
6. Novikov JS, Voronov KE, Semkin ND et al (1997) Attempt of measurment of space debris microparticles flux in geosyncronous orbit. In: Proceedings second European conference on space debris, ESOC, Darmstadt, 17–19 Mar 1997, pp 135–138
7. Apatite I, Vasyukova ZV, Kashcheev BL et al (1981) "Intercosmos-14" and associated ground-based observations of meteors. Space Res 19(5):700–794
8. Semkin ND, Piyakov AV, Voronov KE (2007) A linear accelerator for simulating micrometeorites. Instrum Exp Tech 2:140–147

An Investigation of Stress Dependent Atomic Oxygen Erosion of Black Kapton Observed on MISSE 6

Sharon K.R. Miller, Bruce A. Banks, and Edward Sechkar

Abstract Black Kapton XC polyimide was flown as part of the Polymer Film Tensile Experiment (PFTE) on Materials International Space Station Experiment 6 (MISSE 6). The purpose of the experiment was to expose a variety of polymer films, typical of those used for thermal control blankets or supporting membranes on Earth orbiting spacecraft, to the low Earth orbital (LEO) environment under both relaxed and tension conditions. Black Kapton XC under tensile stress experienced a higher erosion rate during exposure in LEO than the same material that was flown in a relaxed condition. Testing conducted to determine the magnitude of the stress and erosion dependence using a ground-based thermal energy atomic oxygen plasma showed a slight dependence of erosion yield on stress for Kapton HN and Black Kapton XC, but not to the extent observed on MISSE 6. More testing is needed to isolate the factors present in LEO that cause stress dependent erosion.

Keywords Atomic oxygen • Black Kapton XC • Erosion yield • International space station • MISSE • Tensile stress

S.K.R. Miller (✉)
NASA Glenn Research Center, Cleveland, OH 44135, USA
e-mail: sharon.k.miller@nasa.gov

B.A. Banks
Alphaport Inc. at NASA Glenn Research Center, Cleveland, OH 44135, USA

E. Sechkar
ASRC Aerospace at NASA Glenn Research Center, Cleveland, OH 44135, USA

1   Introduction

Thin film polymers are used in many spacecraft applications for thermal control (multi-layer insulation and sunshields), as lightweight structural members (solar array blankets, inflatable/deployable structures) and have been proposed for propulsion (solar sails). Polymers in these applications are exposed to the space environment and are vulnerable to degradation by solar ultraviolet radiation, solar flare X-rays, solar wind electrons and protons trapped in Earth's magnetic field, temperature and orbital thermal cycling, and low Earth orbit atomic oxygen [1]. In applications where the polymer film is under tension while exposed to these environmental factors, it is important to understand the effect of stress in combination with the environment on the durability of thin polymer films. Polymer films were flown previously in the Polymer Film Thermal Control Experiment and the Gossamer Materials Experiment as part of Materials International Space Station Experiment (MISSE) 1 as well as on MISSE 3, MISSE 4, and MISSE 5 [2, 3]. The MISSE 6 exposure is different from prior such experiments in that a number of the samples were designed to be exposed while under tension to better simulate their use in space and determine if the stress level affects the durability. The dog-bone shaped tensile samples of polymers were flown on both the ram and wake facing sides of the MISSE 6 Passive Experiment Containers (PECs). A description of all of the samples flown as part of PFTE is contained in reference [4]. This paper focuses on the results observed for Black Kapton XC flown on MISSE 6 and the results of ground testing conducted in an attempt to gain a better understanding of the erosion observed in LEO.

2   Flight and Ground Based Experiment Description and Procedure

2.1   MISSE 6 Environment and Ground Based Atomic Oxygen Exposure

MISSE 6 was composed of two Passive Experiment Containers (PECS), 6A and 6B. Both PECS had one side of the suitcase style containers facing ram and the other side facing wake. They were both installed on the European Columbus module of the International Space Station (ISS) on March 22, 2008 during the flight of STS-123. They were retrieved on September 1, 2009 by the crew of STS-128 after slightly over 17 months in low Earth orbit (LEO). Environment exposure condition estimates that have been determined to date are the atomic oxygen exposure level on each side and the UV radiation level [5–7]. There were also two Kapton HN/VDA tensile dogbones that were flown as part of this experiment on the wake side of MISSE 6A from which scanning electron microscope images

Fig. 1 Photo of stressed (*left*) and unstressed (*right*) sample holders from above, and a side view drawing of a holder showing the unstressed sample position on the left and the stressed on the right. (Dimensions are in inches.) The stressed sample is fixed on the left side and allowed to move to the right by having the mount hole on the right slotted. Tension is supplied by compression of the spring
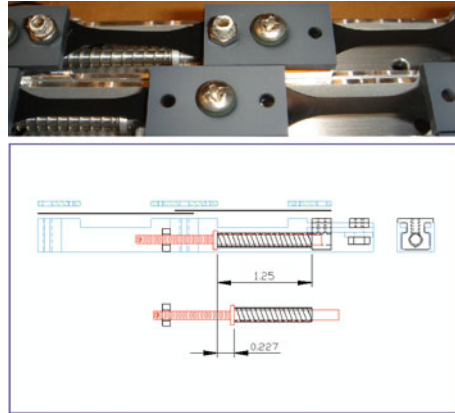
of protected locations on the surface were used to determine the erosion depth and ultimately the atomic oxygen fluence [4]. All of the data seemed in good agreement with an estimate of the atomic oxygen arrival fluence for the ram side of 6A and 6B of approximately 2×10^{21} atoms/cm^2, and for the wake side approximately 1.2–1.4×10^{20} atoms/cm^2. This indicates that the wake side of MISSE 6, which was to have received very low atomic oxygen exposure was oriented in the ram direction long enough to have received an atomic oxygen dose about 6.5% that of the ram oriented side. Estimates of the UV radiation exposure in equivalent sun hours (ESH) were 2,600 ESH for the ram sides of 6A and 6B and 1,950 ESH for the wake sides of 6A and 6B [7]. Temperature, thermal cycling, and ionizing radiation estimates were not available at this time.

Exposure to atomic oxygen for the ground based tests was conducted in an AXIC LF-5 plasma system pumped with a Varian SH110 Scroll Pump. Air was used as the feed gas and a radio frequency power of about 36 W was applied to the internal electrodes to form the thermal energy (~0.04 eV) atomic oxygen plasma that was used to expose samples placed inside the chamber. The effective atomic oxygen fluence for these tests was about a factor of 6 higher than for the flight samples.

2.2 Experiment Design for Application of Tensile Stress

The flight experiment was designed to allow some of the polymer dog-bone type samples to be exposed under a tensile load typical of expected conditions for the James Webb Space Telescope sunshield. The tensile load of approximately ~2.22 N (0.5 lb) was applied by mounting the sample in a holder similar to that shown on the left side of the photo in Fig. 1 and then compressing a spring with a spring constant of ~385 N/m (2.2 lbs/in) by approximately ~0.0058 m (0.227 in.) to put the sample under an approximately constant tensile load. The drawing in Fig. 1 shows a double sample holder where the sample on the left did not have an applied tensile stress and

the one on the right did. For the samples exposed under stress, the resulting stress was dependent on the polymer film thickness per (1) with an average gage width of approximately 0.0032 m (0.126 in.). For the Black Kapton XC samples, the applied stress was ~2.76×10^7 N/m^2 (~4,000 psi) as the films were 2.54×10^{-5} m (0.001 in.) in thickness.

$$Stress = (Force/Area) = (Force)/(Gage\ width) * (Thickness) \qquad (1)$$

For the ground based testing, the same sample holders were used but slightly modified to allow other spring compression lengths to achieve a wider variety of tensile stress on the samples. This was accomplished by modifying the rod underneath to allow greater travel of the spring and through the use of copper u-shaped shims to compress the spring and place the sample under a fixed tensile load.

2.3 Sample Description

All of the samples, both for flight and for ground testing were punched from polymer sheets using a die manufactured according to specimen "Type V" under the American Society for Testing and Materials (ASTM) Standard D-638 [8]. The dog-bone shaped die had a gage length of 7.62 mm (0.3″) and an average gage width of 3.21 ± 0.02 mm (0.126″). The Black Kapton XC (100XC10E7), a carbon pigmented polyimide, was manufactured by DuPont. It had a vapor deposited aluminum coating on the back that was originally intended to provide electrical contact for an active sample break indication but due to some wiring issues prior to fight, the flight samples were not wired for active monitoring. The unflown extra control samples were used for the ground experiment testing. There were also Kapton HN samples flown on MISSE 6 but the ones on the ram side had a SiO$_x$ protective coating on the space exposed side to prevent erosion by atomic oxygen, and the ones on the wake side were not under stress. For ground tests, Kapton HN manufactured by DuPont of 5.08×10^{-5} m (0.002 in.) in thickness was used to obtain atomic oxygen flux maps and for stress erosion comparison for the ground based experiments due to the limited supply of Black Kapton XC samples. The Kapton HN samples were punched from the same die, but a thin layer of magnetron sputter deposited gold was applied to the back of the sample to prevent atomic oxygen erosion of the back side. Thin pieces of aluminum foil were cut to fit and wrapped over the grip and transition area on the front side of the Kapton HN and Black Kapton XC samples, so that only the gauge length would be exposed to atomic oxygen for more accurate measurement of the erosion at a fixed stress level, before they were secured in the holder.

2.4   Analysis

The mass of the samples before and after exposure was measured using a Sartorius ME5 microbalance. Samples were dehydrated at a vacuum of approximately 8.67 Pa (65 mTorr) for 48 h prior to weighing to minimize errors due to absorption of moisture from the air. The change in mass of the Kapton HN was used to determine the atomic oxygen fluence at the surface according to ASTM E-2089 [9]. Change in mass was also used to determine the erosion during flight or in ground tests. Overall and close up photos were taken of the samples post flight, and before and after ground testing, using a Sony Cybershot DSC T-9 camera. Initial observations were recorded and a few selected samples were gold coated and mounted for scanning electron microscopy with a JEOL JSM-6390 LV scanning electron microscope (10 keV) with energy dispersive analysis by X-rays (EDAX).

3   Results and Discussion

3.1   Kapton XC Samples on MISSE 6

Two unstressed samples of black Kapton (XC) were exposed on the ram side of MISSE 6. Both samples appeared to show evidence of texturing of the surface with a darker appearance near each end of the dog-bone sample. One of these samples designated AO-S-1 was inadvertently put under stress when one end of the sample holder was moved, which changed the overall sample length by ~0.0017 m (~0.068 in.). This sample was installed in a sample holder initially designed for putting the sample under a tensile load so the holder on the top side of the sample had a slotted mount hole. It appears that the sample was inadvertently bumped and the one end of the holder moved putting the sample under a high tensile stress even though it was not initially intended to be stressed. There was a cable that was passed up between this sample tray (G3) and the neighboring tray very close to AO-S-1 which may have provided the opportunity for inadvertent bumping of the one end of the sample holder during experiment installation. The movement put a strain on the sample (for an undetermined length of time) of ~0.07. This represents approximately 26% of the maximum strain for Kapton XC. The resulting stress on the sample was 2.32×10^8 N/m^2 (33,600 psi) which is greater than the yield strength of Kapton XC. The sample had a silvered appearance on the end that was stretched and distorted which is evident from the photograph in Fig. 2.

The appearance of the sample raises two questions. The first is why the stretched end appears silver and the second is why the black Kapton appears to be darker in the region of higher stress? In order to try to answer these questions, SEM and EDAX analysis was performed on the sample at selected locations shown in Fig. 3.

SEM images in Fig. 3 show a significant change in surface morphology from the center to the edge. The center portion has a smooth lumpy appearance typical of

Fig. 2 Kapton XC flown on ram side of MISSE 6 (AO-S-1) showing stretching of the sample at the silver area at the top of the sample in the photograph
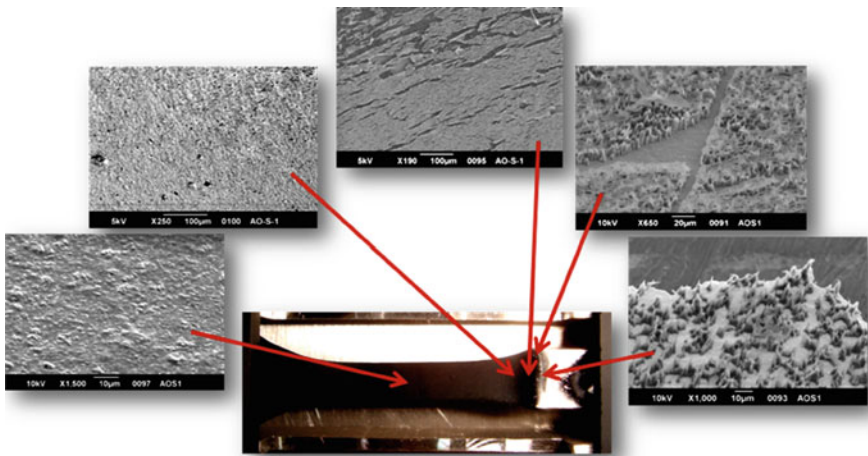
Fig. 3 SEM images of selected positions on sample AO-S-1 exposed on the ram side of MISSE 6

black Kapton which progresses to an area which looks as if it had a thin film gossamer coating on it with many cracks perpendicular to the pull direction. There are fine cone-like peaks in areas where there is cracking which progresses to almost all peaks with thin wisps of film on the surface nearer to the silver area. At the edge
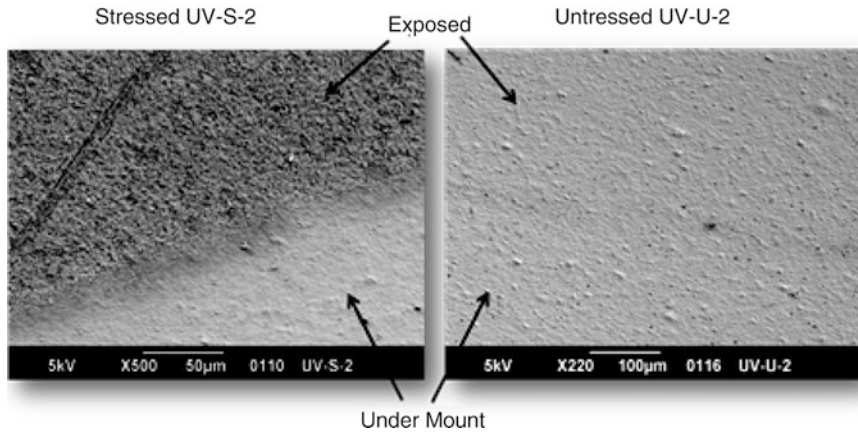
Fig. 4 Scanning electron microsope images of stressed (*left*) and unstressed (*right*) Kapton XC at 45 ° tilt. Top approximately 2/3 was exposed to the space environment on the wake side of MISSE 6 while the bottom ~1/3 was protected by the clamp holding the sample in place

where the sample separated, there are only a few short peaks remaining. EDAX scans indicate mostly carbon and oxygen signals in the central region progressing to a high concentration of aluminum near the stretched end. This sample was originally intended to be put under stress and wired so there was a vapor deposited aluminum coating on the back side. It appears that as the stress on the sample is increased, the erosion rate of the black Kapton increases which results in first development of surface texture cones and a thin film of ash from oxidation of the black Kapton. This progresses to loss of ash and erosion of the mostly carbon cones to the point at which the vapor deposited aluminum is predominantly what is left looking like a blanket of snow at the base of the remaining carbon peaks. If erosion of the Kapton XC is dependent on the level of stress, then there should be an observable difference between the stressed and unstressed samples of Kapton XC that were flown on the wake side of MISSE 6.

The stressed and unstressed samples of Kapton XC flown on the wake side did appear very different from each other. The two unstressed samples appeared slightly textured while the 2 stressed samples were very dark matte black in appearance. A photo of the two sample pairs is shown in Fig. 1. The stress level during exposure was ~2.76 × 10^7 N/m^2 (~4,000 psi) and the strain was ~0.008 which represents about 3% of the maximum strain. The stress on the sample was about 24% of the tensile strength. This does not appear to be a significant amount of strain on the material but is enough to cause a difference in the appearance of the erosion of the material due to oxidation by atomic oxygen. Figure 4 shows side-by-side SEM images at 45 ° tilt of the stressed (UV-S-2) sample of Kapton XC on the left and the unstressed (UV-U-2) sample of Kapton XC on the right. There is more surface texturing occurring on the stressed sample than the unstressed sample as can be seen in the top 2/3rds of the image. The bottom 1/3 was under the sample mount
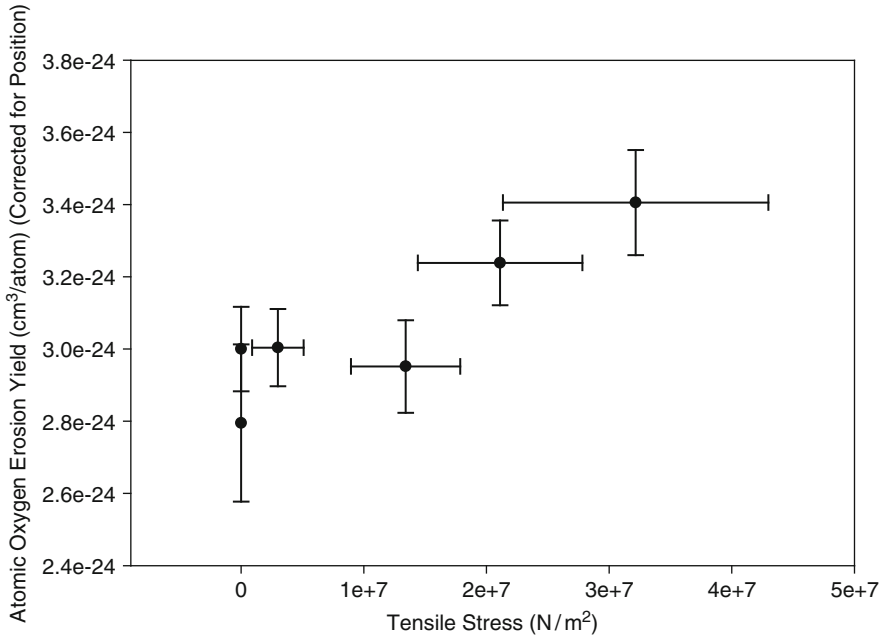
Fig. 5 Atomic oxygen erosion ratio as a function of stress for Kapton HN exposed to ground based thermal energy atomic oxygen

and protected from erosion by atomic oxygen. The unstressed sample is only slightly different in appearance to the unexposed surface, while the surface of the stressed sample has undergone very noticeable erosion.

To better quantify the erosion, both the stressed and unstressed flight samples (UV-S-1 and UV-U-1) were dehydrated and weighed. The samples had not been weighed prior to flight, so a pre-flight mass estimate was made by taking four measurements on each of 6 control specimens and using the average mass as the pre-flight mass for both samples. The resulting erosion yield for each sample (cm^3/atom) was $7.01 \times 10^{-25} \pm 9.94 \times 10^{-25}$ for the unstressed sample and $2.93 \times 10^{-24} \pm 1.84 \times 10^{-24}$ for the stressed sample. The error is large due to the very low change in mass and the error in the pre-flight mass estimate. In spite of this, the erosion yield for the stressed sample was still greater than the error. A rough estimate from this data is that the erosion yield for Black Kapton XC at a tensile stress of ~2.76×10^7 N/m^2 (~4,000 psi) is about a factor of 4 higher than for the same material not under stress.

In order to obtain a better measurement and determine if there is a stress level dependence on erosion of Kapton and Black Kapton, ground tests were conducted with the samples at different stress levels.
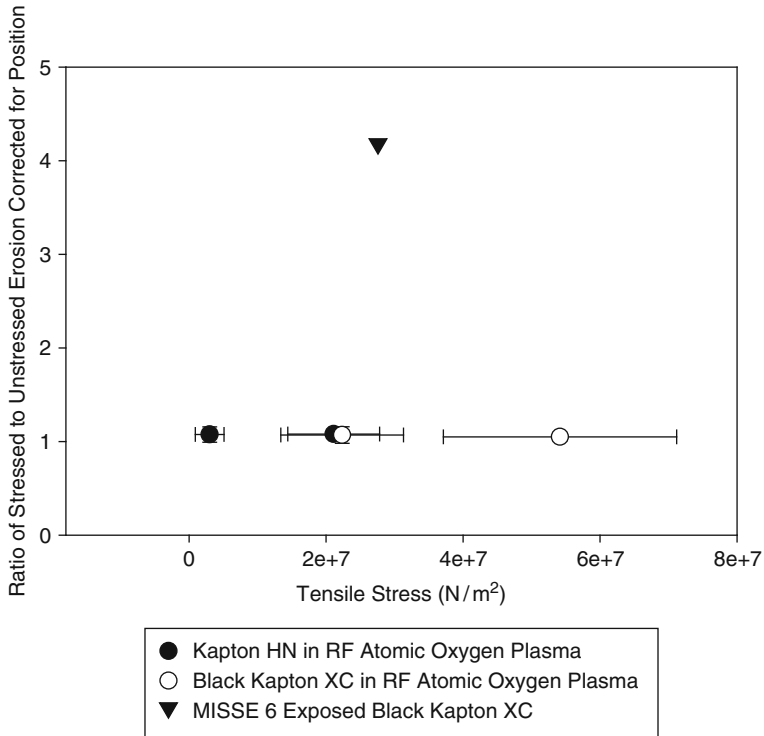
Fig. 6 Ratio of stressed to unstressed erosion yields for Kapton HN, and Black Kapton XC exposed to a ground based thermal energy atomic oxygen plasma as a function of tensile stress compared to that for Black Kapton XC exposed on MISSE 6

3.2 Ground Testing Using Thermal Energy Atomic Oxygen

Dehydrated and weighed unstressed Kapton HN tensile samples were mounted in each of eight sample positions of the four modified flight sample holders sitting on an aluminum plate. The plate was placed in the vacuum chamber and the samples exposed to the RF atomic oxygen plasma. The mass change of each sample was used to determine the atomic oxygen flux at each position and the data from the flux map was used to correct the erosion data from the exposure tests with Kapton HN and Black Kapton XC under stress to account for spatial variation in the atomic oxygen arrival.

Kapton HN samples were installed in the same sample holders and four of the samples were loaded to varying stress levels with two unstressed samples included for fluence witnesses. The atomic oxygen arrival ratio for the two unstressed samples was within error of that observed for the flux map so the fluence at the locations of the stressed samples was estimated using the flux map and fluence measured at the control locations. Figure 5 contains a graph of the resulting erosion

yield (cm^3 removed per incoming atom) as a function of tensile stress for Kapton HN. As can be seen from the graph, at stress levels above 2×10^7 Pa, the erosion yield exhibited a slight increase with increasing stress.

The erosion yield for two stress levels of Kapton HN normalized with respect to the unstressed erosion yield for that material was compared with that obtained for two Black Kapton XC samples exposed in the ground based atomic oxygen plasma chamber in the same positions and with the same spring compression level as that of the Kapton HN. The resulting stressed to unstressed erosion ratios shown in Figure 6 were within error of each other but much lower than the erosion ratio for the stressed to unstressed Black Kapton XC exposed on MISSE 6. The error in the flight data is not shown but is expected to be large in comparison to that for the ground based atomic oxygen exposure data. However, there was very little difference in the surface appearance of the ground test data compared with that observed on MISSE 6.

4   Conclusions

Black Kapton XC exposed on MISSE 6 exhibited statistically a significantly higher erosion rate when placed under tensile stress as observed for the highly stressed sample on the ram side and two stress loaded samples on the wake side. Although a slight stress dependence was also observed in the ground based thermal energy atomic oxygen chamber for Kapton HN, and Black Kapton HN, the magnitude of the difference between the stressed and unstressed samples both in appearance and in the erosion yield was not the same as that observed in LEO. There are, however, differences between the ground based and LEO exposure environments which could cause this difference. There is an energy difference for the atomic oxygen (4.5 eV in LEO compared to 0.04 eV in the ground chamber) and different levels of UV radiation, temperature, and charged particles. The ground system also lacks energetic protons, electrons, and X-rays which are present in LEO. It is possible that two or more environment factors must be present to greatly affect the erosion rate of a stressed polymer such as Kapton HN and Black Kapton XC. Further testing is needed to isolate the factors which result in increased erosion under stress.

References

1. Dever JA, Banks BA, de Groh KK, Miller SK (2005) Degradation of spacecraft materials. In: Kutz M (ed) Handbook of environmental degradation of spacecraft materials. William Andrew Publishing, Norwich
2. Dever JA, Miller SK, Sechkar EA, Wittberg TN (2008) Space environment exposure of polymer films on the materials international space station experiment, Results from MISSE 1 and MISSE 2, J High Perform Pol., Connell JW (ed), vol 20, no 4/5, Aug/Oct
3. Miller SK, Dever JA (2009) Space environment exposure results from the MISSE 5 polymer film thermal control experiment on the international space station. In: Proceedings of the 11th international symposium on materials in the space environment ISMSE-11, Aix-en-Provence, Sept
4. Miller SKR et al (2010) MISSE 6 Polymer film tensile experiment. In: Proceedings of the 2010 national space & missile materials symposium (NSMMS), Scottsdale, June 28-July 1
5. Personal electronic mail communication with Miria Finckenor, NASA Marshall space flight center, (3/30/2010)
6. de Groh KK, Banks BA, Guo A, Ashmead CC, Mitchell GG, Yi GT (2010) MISSE 6 polymers atomic oxygen erosion data. Presented at the 2010 national space & missile materials symposium (NSMMS), Scottsdale, June 28 – July 1, (2010)
7. ESH estimates provided by the Boeing ISS thermal analysis group, contact: Gary Pippin, retired, Boeing, May (2010)
8. American Society for Testing and Materials (1995) Standard test method for tensile properties of plastics, ASTM D 638-95. American Society for Testing and Materials, West Coshohocken
9. American Society for Testing and Materials (2000) Standard practices for ground laboratory atomic oxygen interaction evaluation of materials for space applications, ASTM E 2089-00. American Society for Testing and Materials, West Coshohocken

The Effect of Surface Cracks on Tensile Strength in Polyimide Films Exposed to Low Earth Orbit in MPAC&SEED Experiment

Hiroyuki Shimamura, Yugo Kimoto, and Takashi Nakamura

Abstract The surface textures of polyimide (PI) films exposed to a low Earth orbit environment in the "SM and JEM/MPAC&SEED experiments" and PI films irradiated by atomic oxygen (AO) using a ground facility were quantitatively evaluated. Additionally, the degradation in tensile strength of these PI films was assessed in terms of the surface texture changes. The exposed surfaces of the flight PI films were contaminated by silicon oxide layers and included some local valleys, or extremely deep depressions compared with the surrounding areas. The depth of the deepest local valleys on the exposed surfaces (a_{0max}), which were predicted by extreme statistics, exceeded those of the local valleys of the AO-irradiated PI films. When the tensile strength of these PI films was plotted against AO fluence, the tensile strength reduction trends clearly differed for each PI film. However, the reduction trends were shown to closely correlate when the tensile strengths were plotted against a_{0max}. These results mean that the tensile strength of the PI films attacked by AO can be evaluated based on the depth of surface cracks and that fracture mechanics is considered an effective tool to predict tensile strength reduction.

H. Shimamura (✉) • Y. Kimoto
Aerospace Research and Development Directorate, Japan Aerospace Exploration Agency, 2-1-1 Sengen, Tsukuba 305-8505, Japan
e-mail: shimamura.hiroyuki@jaxa.jp

T. Nakamura
Division of Mechanical and Space Engineering, Graduate School of Engineering, Hokkaido University, N13, W8, Kita-ku, Sapporo 060-8628, Japan

1   Introduction

Polyimide (PI) films have excellent properties such as high specific strength and
rigidity, and high dimensional accuracy, as well as high resistance to a space
environment: considerable ability to withstand UV, radiation, and high
temperatures. Based on such properties, PI films are suitable for use in space
deployable structures. They have been also applied to the base film of solar sails
and flexible solar arrays [1–4]. Their mechanical properties are the key parameter in
this application, because any decline in mechanical properties could risk deforma-
tion or rupture of the overall structure, causing a possible abortion of the spacecraft
mission. Accordingly, the mechanical properties of PI films in a space environment
should be thoroughly evaluated to predict the degree of degradation and establish a
profit margin.

In our previous experiments, the tensile properties of PI films (125-µm-thick
UPILEX-S; UBE Industries Ltd.) exposed to the low Earth orbit (LEO) environ-
ment in the "Service Module/Micro-Particles Capturer and Space Environment
Exposure Device (SM/MPAC&SEED) experiment" were evaluated, and PI films
irradiated by atomic oxygen (AO) using ground facilities were also tested [5–7]. PI
films used for the former and latter experiments are designated as "Flight-PI (SM)"
and "AO-PI" in this paper, respectively.

Figure 1 presents the relationship between tensile strength and AO fluence (F_{AO})
in Flight-PI (SM) and AO-PI [5–7]. The tensile strength of these PI films reduced
concomitantly with increasing F_{AO}. However, the Flight-PI (SM) showed a sharp
decline, compared to the AO-PI. If the tensile strength reduction of PI films exposed
to a LEO environment were determined by F_{AO}, the Flight-PI (SM) and the AO-PI
would indicate a similar decline with respect to F_{AO}. However, Fig. 1 shows that the
tensile strength behavior of the PI films cannot be interpreted only by F_{AO}.

Subsequently, the fracture surfaces of Flight-PI (SM) and AO-PI are shown in
Fig. 2 [5–7], both of which exhibited similar morphology. This result means that
the fracture process in the Flight-PI (SM) is equivalent to that in the AO-PI; AO
is regarded as the main factor behind the tensile strength reduction of PI films
exposed to the LEO environment. Additionally, based on the fracture surface
morphology, radiated patterns expanded from the eroded surfaces, the rupture of
the PI films is thought to originate from the rough surfaces formed by AO
erosion. In conclusion, the surface texture caused by AO erosion has a significant
impact on the tensile properties of PI films, meaning an accurate assessment of
surface texture is necessary to facilitate understanding of the tensile strength
reduction.

This study is intended to quantitatively evaluate the surface texture of PI films
eroded by AO and discuss the tensile strength reduction in terms of the surface
texture. In this study, exposed surfaces and cross-sections of PI films after
AO erosion were analyzed by scanning electron microscopy (SEM). Subsequently,
the depth of surface cracks that can act as fracture initiators, were defined with the
roughness profiles obtained from the cross-sections. Based on the variation of the
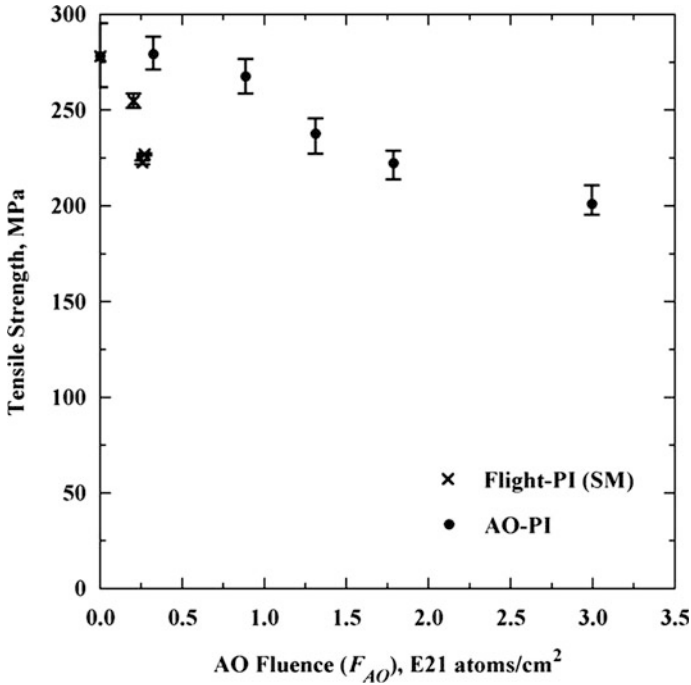
Fig. 1 Tensile strength of Flight-PI (SM) and AO-PI versus AO fluence [5–7]

crack depth with F_{AO}, the relationship between tensile strength and crack depth was investigated.

2 Experimental Procedures

2.1 Material

Flight-PI (SM) and AO-PI samples were used in this study. In addition to these samples, PI films (125-μm-thick UPILEX-S) exposed to the LEO environment in the "Japanese Experimental Module (JEM)/MPAC&SEED experiment" were evaluated; these PI films are designated as "Flight-PI (JEM)."

The exposure durations and F_{AO} of Flight-PI (SM) and (JEM) are shown in Table 1 [8, 9]. Details of the procedure and the environmental conditions of the SM and JEM/MPAC&SEED experiments are included in [10–12].

AO irradiation tests for AO-PI were conducted using the "Combined Space Effects Test Facility" [13, 14] at Tsukuba Space Center, Japan Aerospace Exploration Agency. The F_{AO} fluencies in the AO-PI experiments are indicated in Table 2. Further information concerning the AO irradiation test conditions is given in [5–7].
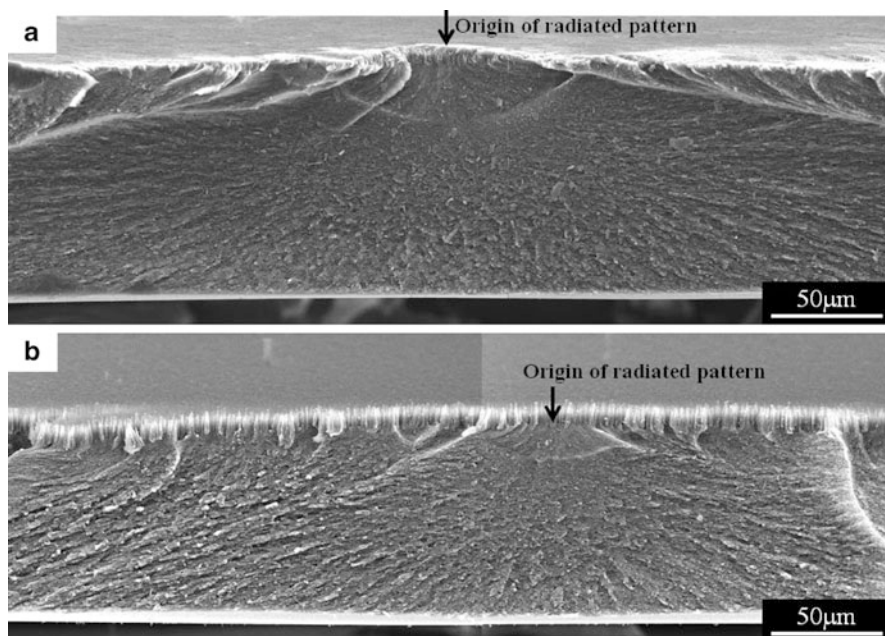
Fig. 2 Fracture surfaces of (**a**) Flight-PI (SM) (F_{AO}: 0.27E21 atoms/cm^2) and (**b**) AO-PI (F_{AO}: 0.8E21 atoms/cm^2) [5–7]

Table 1 Exposure durations and F_{AO} of the Flight-PI (SM) and (JEM) [8, 9]

Sample designation	Flight-PI (SM)			Flight-PI (JEM)
Exposure experiment	SM/MPAC&SEED			JEM/MPAC&SEED
Exposure duration, day	315	865	1,403	259
AO fluence (F_{AO}), E21 atoms/cm^2	0.20	0.26	0.27	0.59

3 Exposed Surface Observation

The exposed surfaces of Flight-PI (SM) and (JEM), and AO-PI were analyzed using SEM technique (JSM-6360NS; JEOL). As a reference, the surfaces of the pristine control PI films, designated as "Control-PI", were also analyzed. A thin Pt coating was deposited onto the samples in preparation for SEM observations and they were tilted by approximately 45 ° during observations to facilitate viewing of the surface texture.

Only the AO-PI sample was rinsed in water before the Pt deposition to remove inorganic particles accumulated on the exposed surfaces. Generally, PI films intrinsically contain inorganic particles [15, 16]. These are not subject to AO erosion, and hence accumulate in bulk on exposed surfaces after AO irradiation tests with a high F_{AO}. The particles on the AO-PI surfaces were completely rinsed off because they could otherwise interfere with the surface texture observations.

Table 2 F_{AO} of the AO-PI [5–7]

Sample designation	AO-PI				
AO fluence (F_{AO}), E21 atoms/cm^2	0.3	0.8	1.3	1.8	3.0

4 Cross-Sectional SEM Observations

All samples from Flight-PI (SM) and (JEM), AO-PI, and Control-PI were cut using a microtome (RM2265; Leica) and the formed cross-sections close to the exposed surfaces were analyzed using an SEM (JSM-6360NS; JEOL) technique.

In the process of the cross-section preparation, the samples were firstly saturated with dodecane solutions, whereupon the wetted samples were cut on a microtome at an extremely low temperature of approximately $-150\,^\circ$C. The cutting direction was perpendicular to the thickness direction of the samples. The dodecane solutions solidify at this temperature and can serve as embedding materials. Using the above method, the cross-sections of all samples could be prepared without destroying their surface texture. After the dodecane solutions had dried out, the cross-sectional observations were conducted.

5 Evaluation of the Maximum Initial Crack Depth

The surface texture of PI films eroded by AO is very rough and they are likely to have numerous initial cracks, the deepest of which are expected to trigger a rupture on the surfaces. Therefore, the depth of the deepest initial crack must be determined to assess the tensile strength degradation of the PI films.

The depth of the deepest initial crack was identified as the "maximum initial crack depth (a_{0max})" in this paper. The a_{0max} of Flight-PI (SM) and (JEM), and AO-PI samples were predicted by the following procedures.

Firstly, the roughness profiles of the exposed surfaces were obtained from their cross-sectional images and subsequently used to determine the initial crack depth (a_0). The a_0 was defined as the difference between the maximum and mean valley depths of the roughness profile within an evaluation length (ln). The length ln is in the direction of the X-axis used for assessing the roughness profile. Consequently, a_0 is calculated using the following equation:

$$a_0 = Rv - Rvm \tag{1}$$

Here, Rv is the maximum valley depth of the roughness profile within ln, and Rvm is the arithmetic mean values of the single valley depth (Rv_i). Rvm is calculated from the following equation:

$$Rvm = \frac{Rv_1 + Rv_2 + Rv_3 + Rv_4 + Rv_5}{5} \tag{2}$$

Here, Rv_i is the depth of the deepest valley of the roughness profile within sampling length (lr), which is one fifth the length of ln.

The evaluations of a_0 were conducted in approximately 10 areas per sample, avoiding overlap of the evaluated roughness profiles. Subsequently, the maximum value of a_0 in the exposed surfaces was derived from extreme statistics and designated as a_{0max}. Detailed procedures for the extreme statistical methods are included in [7].

6   Results and Discussion of Surface Texture

SEM images of the exposed surfaces and cross-sections for Control-PI, Flight-PI (SM) and (JEM), and AO-PI are shown in Figs. 3, 4, 5 and 6, respectively. In the cross-sections, the exposed surfaces are positioned almost centrally in the images; the upside of which corresponds to the space side or AO source side, while the downside corresponds to the sample cross-sections.

Control-PI exhibited considerably flat and smooth surfaces (see Fig. 3).

All Flight-PI (SM) exhibited a rough texture due to AO erosion containing a number of extremely deep depressions compared with the surrounding areas (see Fig. 4) that are defined as "Local valleys" in this paper. Additionally, contamination layers with thicknesses in the hundred-nm range were confirmed on the rough surfaces of all Flight-PI (SM) samples.

Contamination deposits and several local valleys were also confirmed on the exposed surfaces of Flight-PI (JEM) (see Fig. 5), as well as on Flight-PI (SM). The contamination layers, however, were not visible in the cross-sectional images, because they delaminated from the exposed surfaces while preparing the specimens for cross-sectional observation. The cross-section suggests that the rough surfaces caused by AO erosion existed under the contamination layers.

The main components of the contamination layers on the Flight-PI (SM) and (JEM) were considered to be silicon oxide (SiO_x), according to analyses of the exposed surfaces using an electron probe micro-analyzer (EPMA) [7, 17]. Contamination layers consisting of SiO_x had been confirmed frequently in other space environment exposure experiments [15]. The SiO_x contamination layers are expected to be formed by a reaction of contaminations, including silicone components, with AO on the exposed surfaces [15].

Numerous sharp and fine cones were also found on AO-PI exposed surfaces (see Fig. 6), which is typical in polymer materials attacked by AO [18]. The cones showed a tendency to grow in diameter and height with increasing F_{AO}. A number of local valleys were observed at intervals on the exposed surfaces for both the Flight-PI (SM) and (JEM) samples.

From the definition of a_0, the depth of each local valley can be identified as a_0 in the Flight-PI (SM) and (JEM), and the AO-PI. Subsequently, a_{0max}, which is the maximum value of a_0, might correspond to the depth of the deepest local valley on the exposed surfaces of each sample.
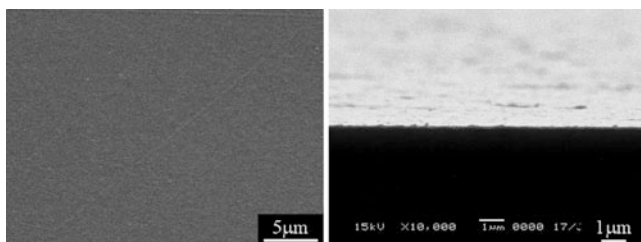
Fig. 3 Exposed surface (*left image*) and cross-section (*right image*) of Control-PI
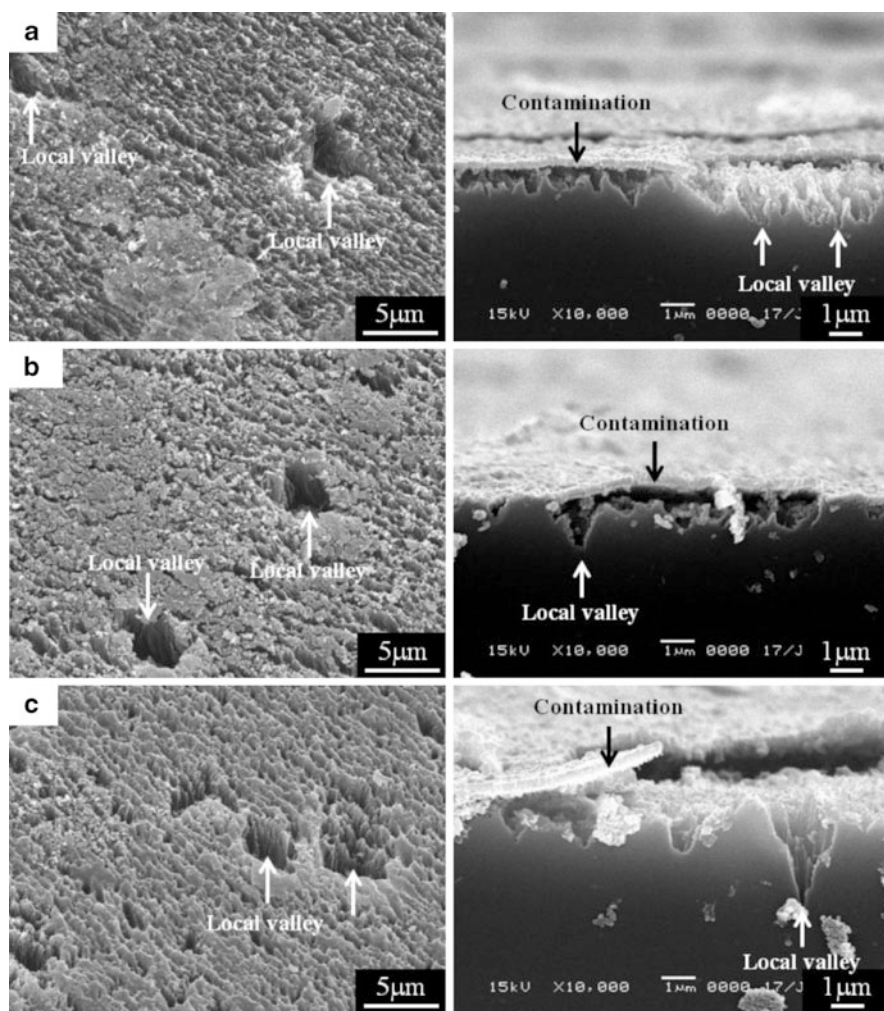
Fig. 4 Exposed surfaces (*left images*) and cross-sections (*right images*) of Flight-PI (SM). ((**a**) F_{AO}: 0.20E21 atoms/cm^2, (**b**) F_{AO}: 0.26E21 atoms/cm^2, (**c**) F_{AO}: 0.27E21 atoms/cm^2)
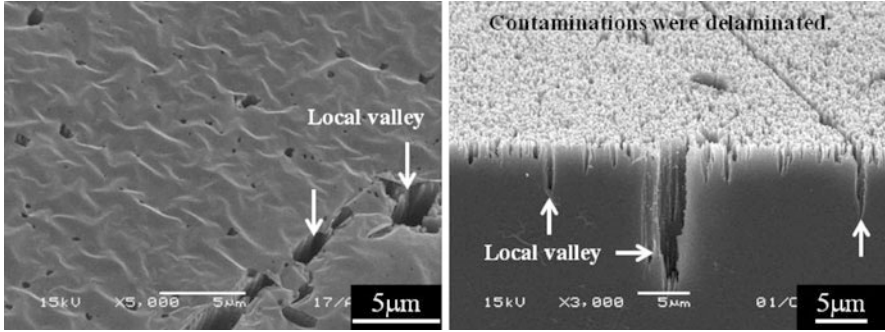
Fig. 5 Exposed surface (*left image*) and cross-section (*right image*) of Flight-PI (JEM) (F_{AO}: 0.59E21 atoms/cm^2)
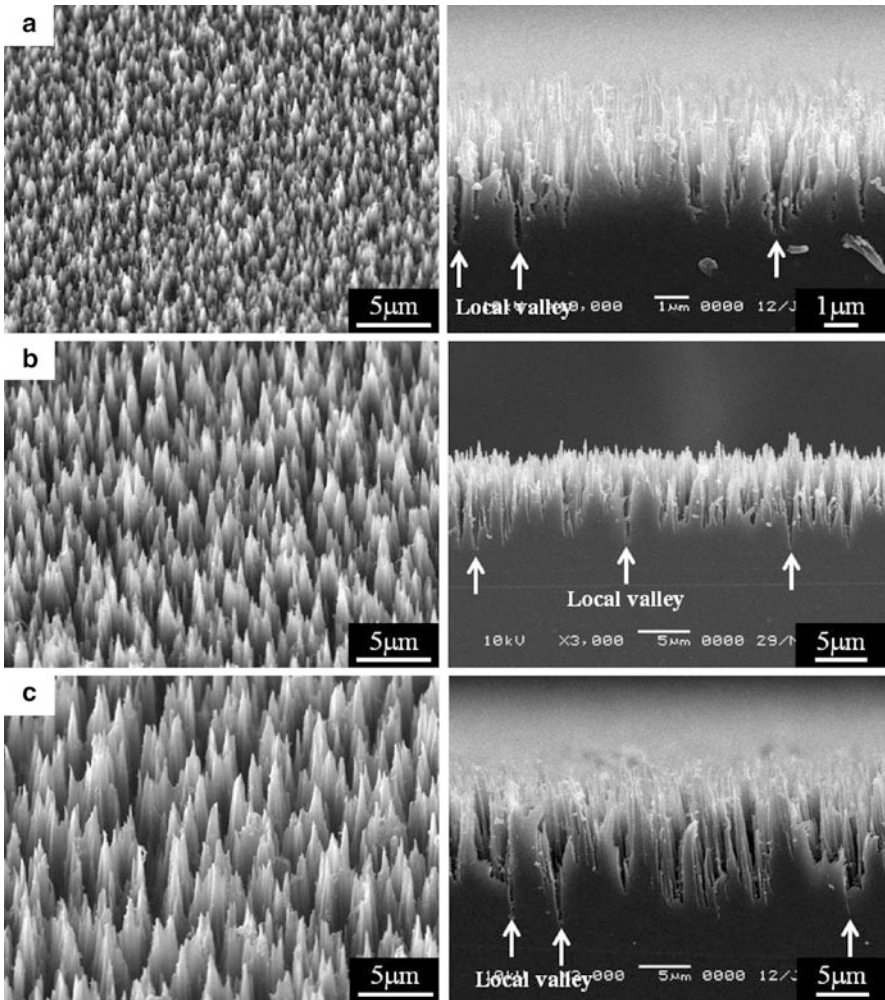
Fig. 6 (continued)
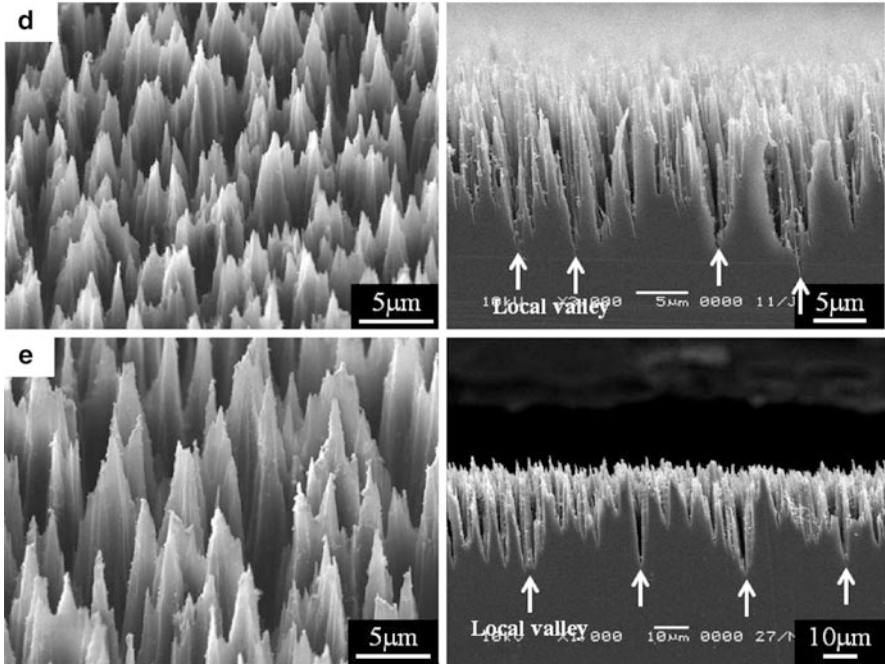
Fig. 6 Exposed surfaces (*left images*) and cross-sections (*right images*) of AO-PI. ((a) F_{AO}: 0.3E21 atoms/cm^2, (b) F_{AO}: 0.8E21 atoms/cm^2, (c) F_{AO}: 1.3E21 atoms/cm^2, (d) F_{AO}: 1.8E21 atoms/cm^2, (e) F_{AO}: 3.0E21 atoms/cm^2)

7   Relationship Between Maximum Initial Crack Depth and AO Fluence

The a_{0max} values of the Flight-PI (SM) and (JEM), and AO-PI samples versus the F_{AO} are presented in Fig. 7. The a_{0max} of AO-PI increased almost proportionally to F_{AO}. Meanwhile, the a_{0max} of the Flight-PI (SM) and (JEM) exceeded those of the AO-PI. This result means that the PI films exposed to the LEO environment had deeper local valleys than those irradiated by AO in a ground facility.

This result, namely the deeper local valleys of Flight-PI (SM) and (JEM), is attributable to the SiO_x contamination layers formed on the exposed surfaces. In the AO-PI, local valleys are assumed to gradually deepen, as all the exposed surfaces are randomly eroded by AO. Conversely, in the Flight-PI (SM) and (JEM), AO erosion might not progress on all exposed surfaces due to the SiO_x contamination layers, which can serve as an AO protective coating [19], though all exposed surfaces were slightly eroded by AO (see Figs. 4 and 5). If locally the SiO_x contamination layers were removed, only such spots would be subject to AO erosion, forming deep local valleys at a low F_{AO}. The formation processes of the
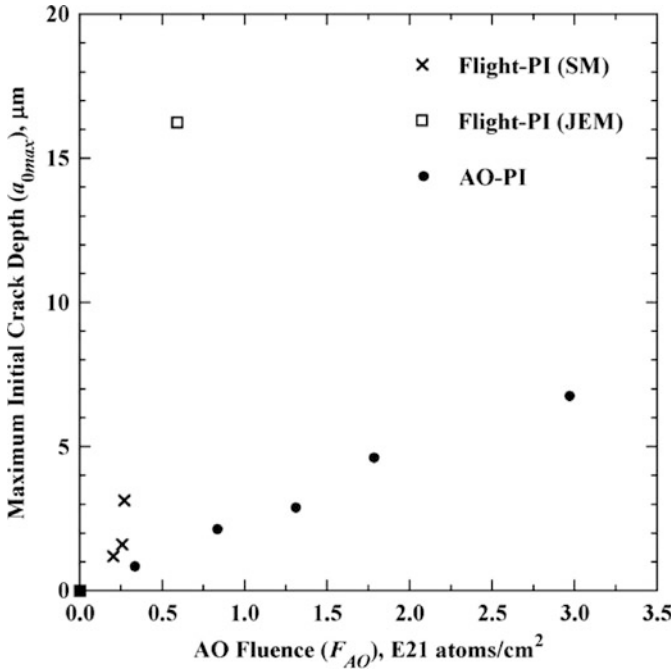
Fig. 7 Maximum initial crack depth (a_{0max}) of Flight-PI (SM) and (JEM), and AO-PI with respect to F_{AO}. [5–7]

deep local valleys are similar to those of formation of deep holes at defect sites (non-coated areas) on coated polymer films' surfaces by AO undercutting [20]. Although further detailed research is required, the SiO_x contamination layers are expected to have a significant effect on the formation of deep local valleys.

8 Relationship Between Tensile Strength and Maximum Initial Crack Depth

The tensile strength of Flight-PI (SM) and (JEM) and AO-PI samples is shown in Fig. 8 with respect to a_{0max}. The tensile strength of these samples gradually declined with increasing a_{0max}. It should be noted however that while these declining trends in these samples were closely correlated; the decrease trend of Flight-PI (SM) and AO-PI clearly differed when their tensile strength was plotted against F_{AO} (see Fig. 1). Namely, the decrease in tensile strength properties in PI films exposed to the LEO environment is explained by the depth of cracks formed on the exposed surfaces. Furthermore, this result means that fracture mechanics can be an effective tool in assessing the strength of PI films.
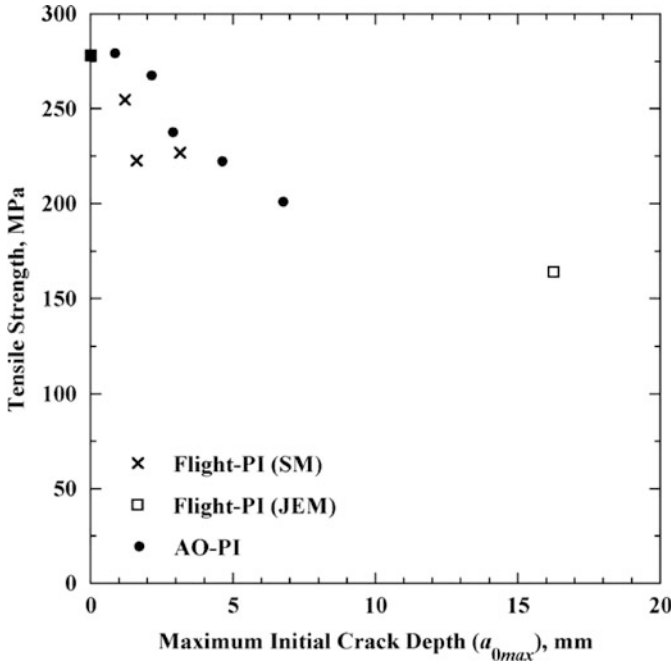
Fig. 8 Tensile strength of Flight-PI (SM) and AO-PI with respect to maximum initial crack depth (a_{0max})

9 Conclusions

Numerous sharp and fine cones were formed on the exposed surfaces of AO-PI, the diameter and height of which increased with increasing F_{AO}. Additionally, some local valleys were confirmed on the surfaces, the depth of the deepest of which (a_{0max}) increased proportionally to F_{AO}. For Flight-PI (SM) and (JEM) samples formation of contamination layers, the main component of which was SiO_x, and formation of a number of local valleys were observed on the exposed surfaces.

The a_{0max} of the Flight-PI (SM) and (JEM) samples far exceeded those of the AO-PI. The formed SiO_x contamination layers were considered to affect the formation of the deep local valleys. When the tensile strength of the Flight-PI (SM) and AO-PI samples were plotted versus the a_{0max}, the tensile strength decreasing tendency in both cases was conformed. This result means that the tensile strength of PI films exposed to the LEO environment can be evaluated based on the depth of the surface cracks.

References

1. Shibayama Y, Arai H, Matsui K, Hama K, Ushirokawa A (1989) SFU solar array. Proceedings of European space power conference, pp 557–562
2. Forkapa MJ, Stidham CR, Banks BA, Rutledge SK (2001) Atomic oxygen durability testing of an international space station solar array validation coupon. NASA TM-107212
3. Kojima Y, Tamura T, Nozaki Y, Onishi Y (2008) Dynamic simulation of stick-slip motion of a flexible solar array. Contorol Eng Pract 16:724–735
4. Tsuda Y, Mori O, Takeuchi S, Kawaguchi J (2005) Flight result and analysis of solar sail deployment experiment using S-310 sounding rocket. Proceedings of 56th ISTS, (CD-ROM)
5. Shimamura H, Nakamura T (2009) Mechanical properties degradation of polyimide films irradiated by atomic oxygen. Polym Degrad Stab 94:1389–1396
6. Shimamura H, Nakamura T (2010) Investigation of degradation mechanisms in mechanical properties of polyimide films exposed to a low earth orbit. Polym Degrad Stab 95:21–33
7. Shimamura H, Nakamura T (2011) Mechanical properties degradation and its prediction methods of polyimide films exposed to space environment. JAXA-RR-10-009, (in Japanese)
8. Kimoto Y, Yano K, Ishizawa J, Miyazaki E (2009) Post retrieval analyses of space environment monitoring samples: radiation effects, UV, and atomic oxygen fluence. JAXA-SP-08-015E pp 11–17
9. Kimoto Y, Ishizawa J, Shimamura H (2012) Proceedings of ICPMCE-10 J, (in press)
10. Kimoto Y, Ishizawa J, Miyazaki E, Suzuki M (2009) SM/MPAC&SEED Experiment Overview. JAXA-SP-08-015E. pp 5–10
11. Miyazaki E, Kimoto Y, Ichikawa S, Kubo K (2008) Two space environmental exposure experiments of materials on ISS. IAC-08-C2.I.23
12. Kimoto Y (2009) Projects for Spacecraft Materials in JAXA. IAC-09-D5.3.1
13. Shimamura H, Miyazaki E (2009) Investigations into synergistic effects of atomic oxygen and vacuum ultraviolet. J Spacecraft Rockets 46(2):241–242
14. Shimamura H, Miyazaki E (2011) Handbook of the combined space effects test facility. JAXA-RM-10-013. (in Japanese)
15. Banks BA, de Groh KK, Miller SK, Waters DL (2009) Lessons learned from atomic oxygen interaction with spacecraft materials in low earth orbit. Protection of materials and structures from space environment, Toronto, Canada, 20–23 May 2008. In: Kleiman JI (ed) Proceedings of ICPMSE-9. Published by AIP conference proceedings 1087, pp 312–325
16. Banks BA, Backus JA, Manno MV, Waters DL (2009) Atomic oxygen erosion yield prediction for spacecraft polymers in low earth orbit. NASA TM-2009-215812
17. Baba S, Matsuyama J, Ishizawa J, Kimoto Y (2012) Proceedings of ICPMCE-10 J, (in press)
18. Banks BA, de Groh KK, Miller SK (2004) Low earth orbital atomic oxygen interactions with spacecraft materials. NASA TM-2004-213400
19. Kimoto Y, Ichikawa S, Miyazaki E, Matsumoto K (2009) Space environment effects on materials at different positions and operational periods of ISS. Protection of materials and structures from space environment, Toronto, Canada, May 20–23, 2008. In: Kleiman JI (ed) Proceedings of ICPMSE-9. Published by AIP conference proceedings 1087, pp 207–211
20. de Groh KK, Banks BA (1994) Atomic-Oxygen undercutting of long duration exposure facility aluminized kapton multilayer insulation. J Spacecraft Rockets 31(4):656–664

Flight Experiment Results of the Polysiloxane-Block-Polyimide "BSF-30" on the JEM/MPAC&SEED Mission on the ISS

Eiji Miyazaki, Yugo Kimoto, and Rikio Yokota

Abstract Atomic oxygen (AO) in low Earth orbit (LEO) is one of the most dangerous environmental factors leading to erosion of the external materials of a spacecraft. As one of the methods to improve AO tolerance, the use of silicon-containing materials has been proposed. On such materials, an SiO_2 layer is formed from the reaction of the silicon contained in the material and the AO existing in orbit, which can therefore be called a "self-organized" layer. In the present study, polysiloxane-block-polyimide "BSF-30", which is a silicon-containing polyimide, was investigated by ground testing and in a flight experiment. BSF-30 was exposed to the LEO space environment on the Japanese Experimental Module/Micro Particles Capturer & Space Environment Exposure Device (JEM/MPAC&SEED) mission on the ISS for 8.5 months. As a result, a mass loss of 0.011 mg was measured, which is about 1/500 times smaller than that of a common polyimide. From a cross sectional transmission electron microscopy analysis the formation of a layer about ~50 nm thick was observed on the exposed surface, within which high fractions of Si and O were also detected. In conclusion, it is verified that BSF-30 has sufficient AO tolerance in a LEO environment by the JEM/MPAC&SEED.

Keywords Atomic Oxygen (AO) • Low Earth Orbit (LEO) • Self-organization • Space environment • Tolerance

E. Miyazaki (✉) • Y. Kimoto
Japan Aerospace Exploration Agency, Tsukuba, Ibaraki 305-8505, Japan
e-mail: miyazaki.eiji@jaxa.jp

R. Yokota
Institute of Space and Astronautical Science, Japan Aerospace Exploration Agency,
Kanagawa 252-5210, Japan

1   Introduction

In low Earth orbit (LEO), Atomic Oxygen (AO) is one of the severe environmental factors causing the materials placed on the outside of spacecraft to degrade [1, 2]. Originating from Earth's atmosphere, oxygen molecules are dissociated into neutral atoms by ultraviolet rays. The resultant AO remains at LEO altitude. Spacecraft circle the Earth in LEO orbits at a speed of around 8 km/s, colliding with AO at a high relative velocity that imparts the equivalent of around 5 eV of translational energy, thereby causing erosion called AO Attack. Polyimide is a well-known material prone to AO-attack. The AO-attack surface shows a distinctive morphology with micrometer-sized asperities: a so-called *carpet* or *needle-like shape*. The AO attack degrades the material properties. Improving space materials' tolerance against AO necessitates study of AO tolerance-improvement techniques. Coating is a standard method, for which inorganic thin coatings such as ITO and silicone resin are used [3–5]. However, such coatings must have high reliability to maintain performance during missions and very low defects during production because coating degradation engenders severe erosion of the base film. Furthermore, since hard inorganic coatings are very fragile, special care is required for handling during assembly, thereby raising production costs. With this in mind, a method to achieve AO tolerance other than coating should be considered. One such method is the use of silicon-containing materials, the AO tolerance of which has been investigated [6, 7].

A SiO_2 layer is formed from a reaction of the silicon contained in the material and AO existing in orbit; it can therefore be called a "self-organized" layer. The layer functions as an AO-protective layer and also present advantages over films with manufactured AO-tolerant layers due to its self-healing function when the layer is damaged. It is expected to facilitate handling on the ground and provide high reliability in orbit.

The polysiloxane-block-polyimide film "BSF-30" is focused on herein as one silicon-containing film, which was developed for use on the ground, rather than in space. The AO tolerance of BSF-30 has been investigated by irradiation tests on the ground, which revealed that BSF-30 is expected to show AO tolerance with SiO_2 layer formation by collision with AO [8]. Subsequently, BSF-30 was selected as one of the samples for the Japanese Experimental Module/Micro Particles Capturer & Space Environment Exposure Device (JEM/MPAC&SEED) mission on the International Space Station (ISS) [9]. BSF-30 was exposed to the LEO space environment on the ISS for 8.5 months, after which the samples were retrieved to the ground to evaluate how they had changed following exposure to the space environment.

In this study, we report on the results of the evaluations for the polysiloxane-block-polyimide "BSF-30" film on JEM/MPAC&SEED, whereupon the tolerance of BSF-30 against AO is discussed based on the results of the after-retrieval evaluation.
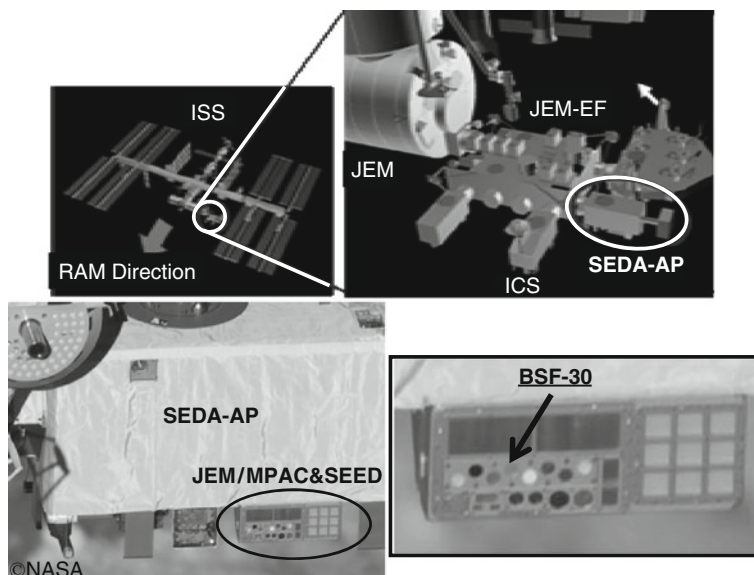
Fig. 1 Location of BSF-30 and JEM/MPAC&SEED on the ISS

2 Experimental

2.1 Sample Preparation

Polysiloxane-block-polyimide "BSF-30" manufactured by Nippon Steel Chemical Co., Ltd. mainly for terrestrial use in the electronic industry was used. For the JEM/MPAC&SEED mission, BSF-30 was supplied as a 25-µm-thick, A4-size film. 25-mm-diameter pieces were cut from the film for the JEM/MPAC&SEED specimens. The specimen was held in place using an aluminum alloy frame of the JEM/MPAC&SEED hardware with a 20-mm-diameter window, which was the area exposed to space. The initial mass of the flight specimen was 15,300 mg.

2.2 JEM/MPAC&SEED Mission

JEM/MPAC&SEED is an experimental hardware that was installed on the Space Environment Data Acquisition equipment – Attached Payload (SEDA-AP) on the JEM Exposed Facility of the ISS (Fig. 1).

The surface of the JEM/MPAC &SEED where the samples were installed faced the RAM direction of the ISS, and high AO fluence was expected.

The JEM/MPAC&SEED was launched by the Space Shuttle STS-127 in July 2009, and has begun the exposure to space on July 23, 2009 CDT. After exposure,

Table 1 AO and UV fluences calculated from monitoring samples on JEM/MPAC&SEED

Environmental factor	Value
AO	5.91×10^{20} atoms/cm^2
UV	<30 ESD

JEM/MPAC&SEED was retrieved into the ISS on April 9, 2010, and returned to the ground by Space Shuttle mission STS-131 that landed on April 20, 2010. In other words, the exposure duration of JEM/MPAC&SEED was 259 days (~8.5 months).

The environmental factors, e.g., AO and UV fluences, were measured by "monitoring samples" installed on the JEM/MPAC&SEED. AO fluence was measured by the mass loss of the polyimide sheet "VESPEL®" caused by AO erosion, which can be determined by the erosion yield measured by AO irradiation tests on the ground [10]. UV fluence was measured by the solar absorptance change of the polyurethane sheet "DUS601" [10]. Based on evaluation of the monitoring samples, the environmental factors were determined as shown in Table 1. The details of the evaluation results for the monitoring samples are described in reference [11].

2.3 Evaluation Techniques

To evaluate the space environmental influence on the BSF-30 film, macroscopic observation, mass measurement, and cross-sectional microscopic observation were carried out. For macroscopic observation, a digital still camera was used. For mass measurement, we used a microbalance (readability 1 μg, maximum load 5,100 mg, MX5; Mettler Toledo International Inc.). Water absorption into the sample was measured during weighing. Therefore, to calculate the dry mass, it must be compensated by extrapolation of the mass increase curve shown during weighing of the sample. The weighing procedure was as follows: the sample was stored in a desiccator for at least 24 h; it was brought onto the microbalance under controlled ambient conditions of $23 \pm 2\,^{\circ}$C and $50 \pm 5\,\%$ relative humidity and the mass was established after holding the sample for 180 s on the balance after removal of the sample from the desiccator. That measurement was then fitted to a quadratic curve to obtain the estimated dry mass from the intercept of the fitted curve. In particular, for initial measurements, the samples were stored in a vacuum chamber for at least 24 h in addition to the weighing procedure to eliminate errors caused by outgassing in vacuum. The cross-sectional microstructure was observed using a transmission electron microscope (TEM H-7100; Hitachi Ltd.). Samples stained using RuO_4 were sliced using an ultramicrotome to produce a cross-section, including the exposed surface. To obtain microstructural information, TEM observation was performed at an acceleration voltage of 100 kV and magnification of 200,000. Scanning TEM/energy dispersive X-ray spectroscopy (STEM/EDX, using JEM2100F/JED-2300 T; JEOL Ltd.) analysis was also performed in order to see the elemental composition at very small areas and the elemental fraction was calculated from the STEM/EDX spectrum.
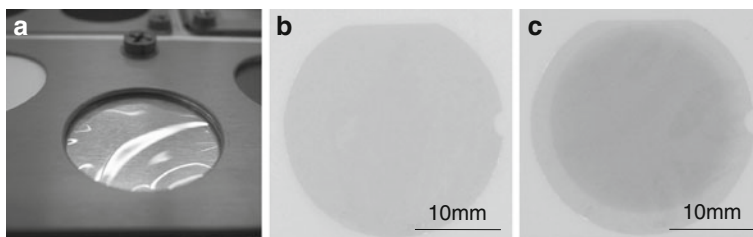
Fig. 2 Macroscopic pictures of BSF-30 flight sample for JEM/MPAC&SEED. (**a**) On JEM/MPAC&SEED hardware after flight, (**b**) pre-flight, (**c**) post-flight

Table 2 Mass measurement results of BSF-30 on JEM/MPAC&SEED

Specimen name	Pre-flight, mg	Post-flight, mg	Delta, mg
BSF-30	15.300	15.289	−0.011

3 Results and Discussion

3.1 Macroscopic Observation

Figure 2 shows a picture of the flight sample. Figure 2a was taken during disassembly of the retrieved JEM/MPAC&SEED hardware to remove the samples. As can be seen from Fig. 2a, the surface of the sample was shiny and smooth. Figure 2b, c were taken of the sample only, pre- and post-flight. We can see that the center, which was exposed to space, is darkened.

3.2 Mass Change Measurements

The measured mass is presented in Table 2. The mass loss by exposure to the LEO space environment was 0.011 mg. Compared to the mass loss of typical polyimide, assuming an AO fluence equivalent to that of JEM/MPAC&SEED, the mass loss of BSF-30 could be one five-hundredth or less of a typical polyimide.

3.3 Microscopic Observation

Figure 3 presents the cross-sectional TEM images of BSF-30. For pre-flight samples (Fig. 3a), no obvious layer is found at the exposed surface.

In the post-flight sample a layer is observed along the exposed surface (Fig. 3b) that is around 50 nm thick. From the STEM/EDX analysis the elemental composition of both surfaces was calculated (Fig. 4). For the pre-flight sample (Fig. 4a), the elemental composition of the surface layers is homogeneous and not dependent on depth. For the post-flight sample, however, (Fig. 4b), it was found that the elemental
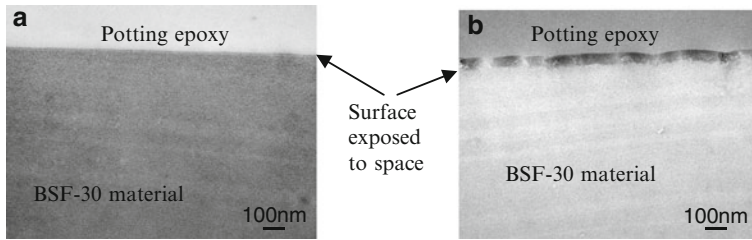
Fig. 3 Cross sectional TEM images of BSF-30 flight sample for JEM/MPAC &SEED. (**a**) Pre-flight, (**b**) post-flight
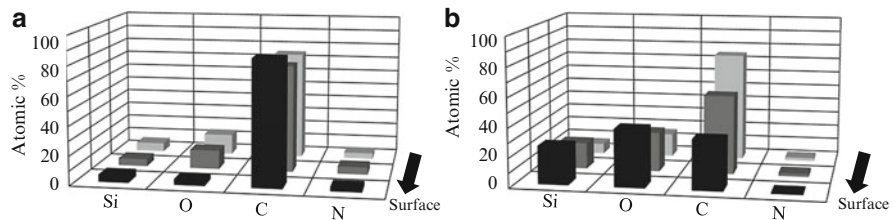
Fig. 4 STEM/EDX elemental composition of BSF-30 flight sample for JEM/MPAC&SEED. (**a**) Pre-flight, (**b**) post-flight

composition depends on depth. The concentrations of Si and O are higher at the sample surface and that of C is lower. This result indicates that the layer formed on the surface exposed to the space environment could be Si-O rich.

4 Discussion on the Tolerance of BSF-30 Against the LEO Environment

Figure 5 shows a comparison between the mass changes of the BSF-30 sample in the present flight and the mass changes obtained from the ground AO irradiation test [8]. Analyzing the data in Fig. 5, it can be suggested that the flight sample experienced a smaller mass change compared to that for AO irradiated samples on the ground. In addition, as was discussed in Sect. 3.1.2, it was 1/500th of a typical polyimide with equivalent AO fluence. Thus, the mass loss of BSF-30 caused by exposure to the LEO environment is small enough. It also should be noted that an Si-O enriched layer was formed on the surface of the flight sample as shown in Fig. 3 that was not present on the pre-flight sample surface. The thickness of the formed layer for the flight sample is ~50 nm and it exceeds the layer formed in the ground AO irradiated sample, ~10 nm [8, 12].

It could be said that the formed Si-O layer was self-organized by exposure to the AO in orbit. From the discussed above points, i.e., a small mass loss and the ability for self-organized layer formation, the BSF-30 material has a great
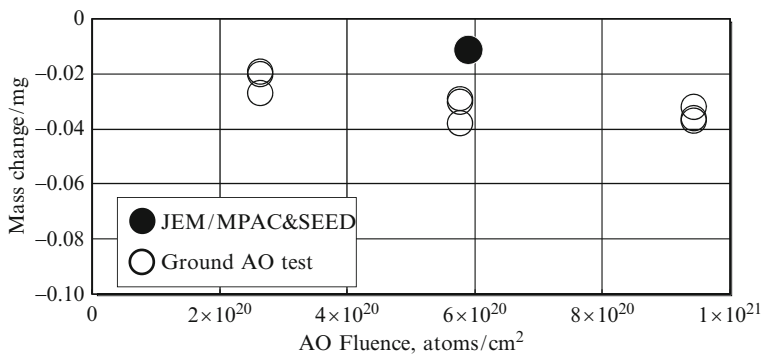
Fig. 5 A comparison between mass changes of BSF-30 flight samples on JEM/MPAC&SEED and in AO test on the ground

potential to serve as a protective layer with self-organizing capabilities upon exposure to the AO in LEO environment. It can be concluded that the tolerance of BSF-30 against AO in a real LEO environment has been verified through the JEM/MPAC&SEED mission.

As was mentioned above, the thickness of the formed layer was higher then that formed in AO ground testing (50 nm vs. 10 nm). While some of the thickness could be attributed to a Si-based contamination layer that is estimated at less than 10 nm [13, 14], the nature of the rest of the formed Si-O layer is not clear at the present. Further work is required to clarify this point.

5   Conclusions

We evaluated Polysiloxane-Block-Polyimide "BSF-30" material that was exposed to space on JEM/MPAC&SEED for 8.5 months. Based on the results, we can conclude that the BSF-30 was verified as having sufficient tolerance against AO existing in a LEO environment, based on both the mass loss, 0.011 mg, and the Si-O rich self-organized layer formation. Following a comparison of the results between Flight and AO irradiation tests on the ground, it was found that the Si-O rich layer formed on the exposed surface in flight is ~50 nm thick, and is thicker than that formed in the ground AO tests (~10 nm). With some of the thickness (less than 10 nm) attributed to a Si-based contamination layer, the nature of the rest of the formed Si-O layer is not clear at the present. Further work would be needed to clarify this point.

References

1. Crossman FW (1982) Spacecraft material applications – long-term stability questions. NASA-CP-2269
2. Tennyson RC (1993) Atomic oxygen and its effects of materials. In: DeWitt RN (ed) The behavior of systems in the space environment. Kluwer, Amsterdam
3. Smith KA (1985) Evaluation of oxygen interaction with materials (EOIM) – STS-8 atomic oxygen effects. AIAA-85-7021, AIAA shuttle environment and operations II conference, Houston, pp 190–197
4. Ishizawa J et al (2006) Results of the space-environment exposure experiment "SM/MPAC&SEED" on the international space station (2): siloxane coated polyimide films, and silicone based paints and adhesives. In: Proceedings of the 10th international symposium on "materials in a space environment" ESA-SP-616, European Space Agency, Collioure, France
5. Yan L et al (2001) Study of surface chemical changes and erosion rates for CV-1144-0 silicone under electron cyclotron resonance oxygen plasma exposure. J Vac Sci Technol A 19 (2):447–454
6. United States Patent 5073607
7. Gonzalez RI et al (2003) Synthesis and atomic oxygen erosion testing of space-survivable POSS (polyhedral oligomeric silsesquioxane) polyimides. In: Proceedings of the 9th international symposium on "materials in a space environment" ESA-SP-540, European Space Agency, Noordwijk, The Netherlands
8. Miyazaki E et al (2010) Investigation into tolerance of polysiloxane-block-polyimide film against atomic oxygen. Acta Astronaut 66:922–928
9. Ichikawa S et al (2009) Status of JEM/MPAC&SEED experiment onboard SEDA-AP on KIBO exposed facility. In: Proceedings of international symposium on "SM/MPAC&SEED experiment" JAXA-SP-08-015E, Japan Aerospace Exploration Agency, Tsukuba, Ibaraki, Japan
10. Kimoto Y et al (2009) Post retrieval analyses of space environment monitoring samples: radiation effects, UV, and atomic oxygen fluence. In: Proceedings of international symposium on "SM/MPAC&SEED experiment" JAXA-SP-08-015E, Japan Aerospace Exploration Agency, Tsukuba, Ibaraki, Japan
11. Kimoto Y et al (2011) Passive space environment effect measurement on JEM/MPAC&SEED. In: Proceedings of ICPMSE-10J, Nago, Okinawa, Japan, (in press)
12. Tagawa M et al (2000) Volume diffusion of atomic oxygen in α-SiO_2 protective coating. High Perform Polym 12:53–63
13. Baba S et al (2011) First evaluation of contamination on the JEM/MPAC&SEED. In: Proceedings of ICPMSE-10J, Nago, Okinawa, Japan, (in press)
14. Miyazaki E et al (2009) Results of space-environment exposure of the flexible optical solar reflector. J Spacecr Rocket 46(1):28–32

Development of Heat Sealable Polyimide Thin Films with High Space Environmental Stability for Solar Sail IKAROS Membrane

Rikio Yokota and Masahiko Miyauchi

Abstract A novel asymmetric thermoplastic polyimide (ISAS-TPI) with good space environmental stability was developed. The world's first solar sail mission: IKAROS consisting of four large area polyimide thin film petals (total diameter 20 m) with various attached electric devices was built and launched on May 21, 2010.

Keywords Asymmetric structure • Polyimide • Solar sail • Space environmental stability

1 Introduction

Aromatic polyimides (PIs) such as Pyromellitic dianhydride(PMDA)/4, 4′-Oxydianilie(4, 4′-ODA) and 3, 3′,4, 4′-biphenyltetracarboxylic dianhydride (s-BPDA)/4, 4′-ODA are well known for their outstanding thermal and environmental stability that is due to their planar structure in addition to their rigid wholly aromatic structures. However, these advantages cause some limitations in applications for molding or fabrication in heat sealing because of their insolubility and infusibility. Among many methods for improving the processability of aromatic polyimides, we have reported that the PI derived from an asymmetric aromatic tetra carboxylic acid dianhydride, i.e., 2, 3, 3′, 4′-BPDA:(a-BPDA) led to higher Tg's than the corresponding PIs from a symmetric one (s-BPDA) with the same diamines. In addition, the asymmetric PIs have higher thermo-plasticity than the corresponding

---

R. Yokota (✉)
IKAROS Demonstration Team, Institute of Space and Astronautical Science, Japan Aerospace Exploration Agency, Sagamihara, Kanagawa 229-8510, Japan
e-mail: yokota.rikio@jaxa.jp

M. Miyauchi
Frontier Material Development Division, Kaneka Corporation, Settsu, Osaka 566-0072, Japan
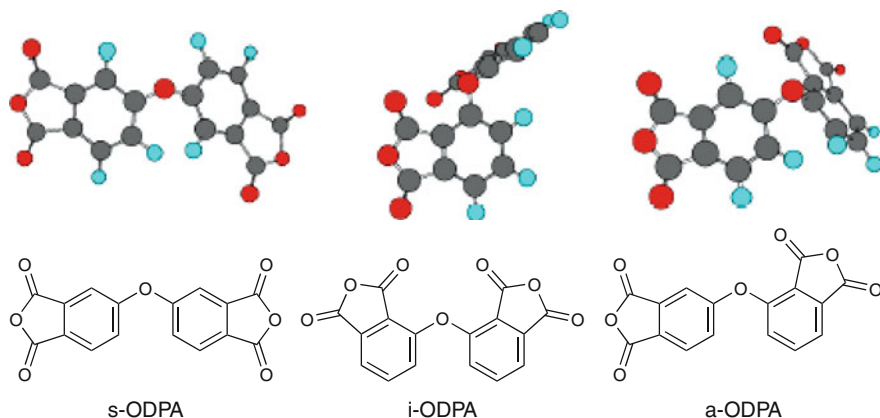
Fig. 1 Isomeric s-,a-,i- ODPA structures

symmetric PIs on the basis of their non-planar biphenyl-imide structures inhibiting intermolecular interaction (no ordered structure formation). Thus, the sterically bent/distorted but rotation-restricted structural unit induced by asymmetric aromatic monomers was greatly expected for developing new high performance polyimides [1, 2]. We successfully developed asymmetric aromatic addition-type imide oligomers (TriA-PI:a-BPDA/4.4′-ODA/PEPA) having high Tg and good processability [3]. Based on this asymmetric structure chemistry, we started the development of a heat sealable polyimide having a high space environmental stability in applications for solar sail membrane in Aug 2007. This paper presents the results on the development of a novel heat sealable asymmetric polyimide thin film and its application for solar sail IKAROS membrane [4, 5].

2 Development of a Novel Asymmetric Aromatic Polyimide; a-ODPA/4, 4′-ODA

As shown in Fig. 1, asymmetric a- or i-ODPAs (supplied by Manac Co.) are moderate stereo irregular and, more or less, flexible in comparison to isomeric BPDA.

Figure 2 shows the synthetic root of thermo-plastic and heat sealable a-ODPA/4, 4′-ODA: The ISAS-TPI. ISAS-TPI has been obtained by common two step method with rapid thermal imidization [6, 7].

Figure 3 shows dynamic tensile properties of s- and a-ODPA/4, 4′-ODA polyimides, and PMDA/4, 4′-ODA polyimide. Tg of a-ODPA/4, 4′-ODA is higher than that of symmetric s-ODPA/4, 4′-ODA and shows a large drop in storage modulus, E' without rubbery plateau above Tg as isomeric BPDAs. It means that this asymmetric polyimide can be used for heat sealable films due to very high drop of modulus E' above Tg.
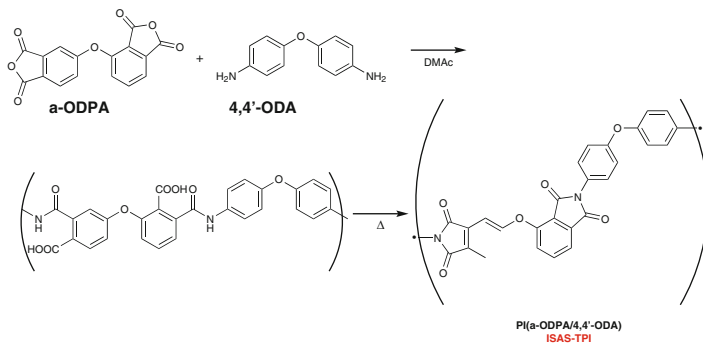
Fig. 2 Reaction scheme of thermo-plastic and heat sealable a-ODPA/4, 4′-ODA : ISAS-TPI
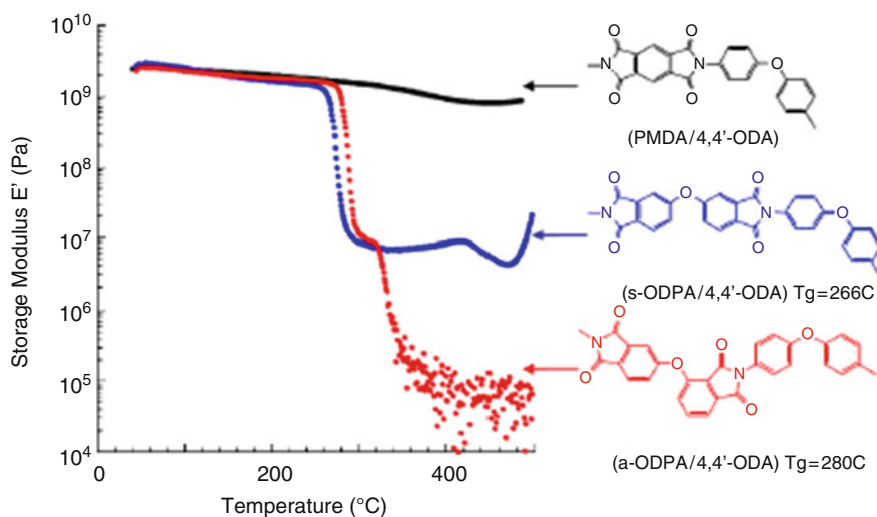
Fig. 3 Dynamic tensile properties of symmetric PMDA/4, 4′-ODA, s-ODPA/4, 4′-ODA, and a-ODPA/4, 4′-ODA polyimide films

Mechanical properties of prepared ISAS-TPI thin film, such as modulus E = 2.8 GPa and elongation at break (ε_b) = 92% are excellent. Compared with symmetric s-ODPA/4, 4′-ODA film, 7.5 μm thin film of a-ODPA/4,4′-ODA prepared from 14% polyimide solution in DMAc is easily sealed in 20 s at 350 °C and 0.1 Mpa without any problems. Proton and electron irradiation have been conducted by Japan Atomic Energy Research Institute (JAERI) and UV radiation had been performed by Tsukuba Space Center of JAXA. Physical and mechanical properties of those films were measured in our laboratory.

Figure 4 shows the elongation at break of ISAS-TPI, APICAL-AH 7.5 μm film, polyether imide (PEI, ULTEM; General Electric) and Polycarbonate (PC) irradiated by electron beam. The obtained data indicates that ISAS-TPI has enough high stability for space environment. On the other hand PEI and PC showed poor
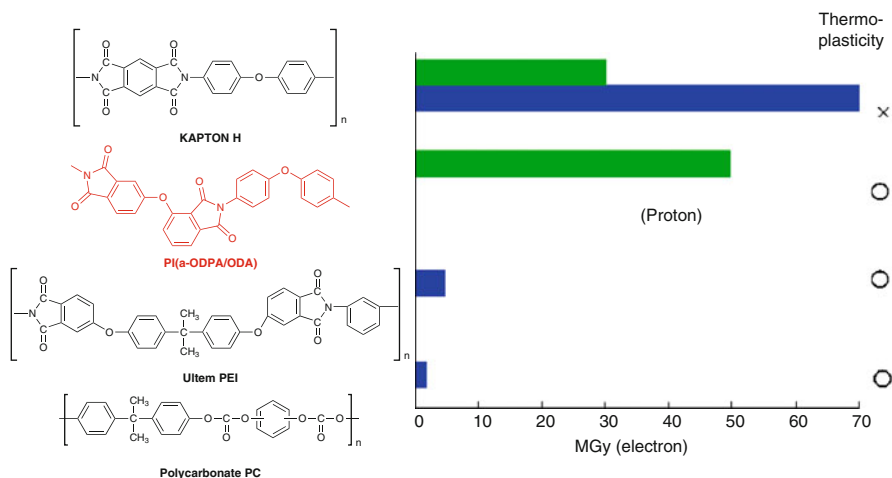
Fig. 4 Space environmental stability of ISAS-TPI and aromatic polymers irradiated by electron beam: retardation of native elongation at break (80% (1st) and 3rd bars from top) and 20% (2nd, 4th, 5th bars from top)) (JAERI)
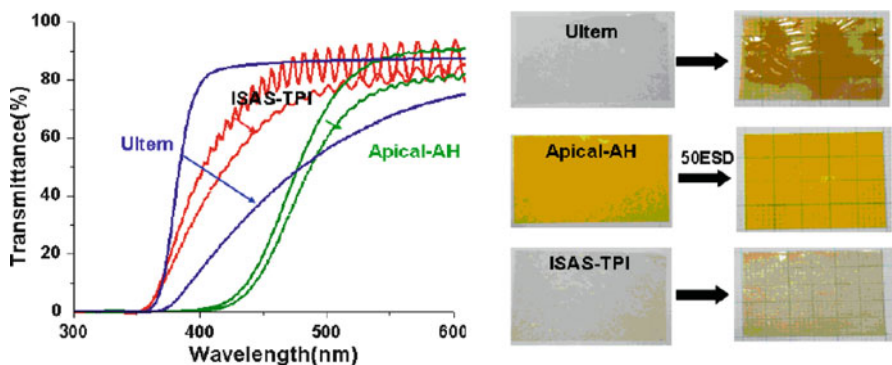
Fig. 5 Color changes of ISAS-TPI and aromatic polyimides by UV radiation (50ESD)

stabilities against irradiation by electrons because of the fast degradation at aliphatic group ($-C(CH_3)_2-$) in both main chains.

Figure 5 shows UV–vis spectra and color changes of ISAS-TPI and PEI and APICAL-AH 7.5 μm films after a 50 ESD exposure to UV irradiation. ULTEM film showed a profound color change with a greater red shift in the UV–vis spectrum. However, ISAS-TPI and APICAL-AH showed less color change, indicating that ISAS-TPI also has enough high stability for UV irradiation in space environment.

Table 1 summarizes the physical properties and space environmental stability for commercial PMDA/4, 4′-ODA film; Apical-AH (KANEKA) and ISAS-TPI prepared by Fujimori KOGYO Co., Ltd.. Novel asymmetric aromatic polyimide: a-ODPA/4, 4′-ODA indicates high solubility for NMP and DMAc and excellent heat sealing properties with having high space environmental stability as APICAL AH polyimide film.

Table 1 Summary of physical properties and space environmental stability for commercial PMDA/4, 4′-ODA film; Apical-AH (KANEKA) and a-ODPA/4, 4′-ODA film; ISAS-TPI

Polyimide	Tg (DMA) (°C)	Solubility. (NMP) (%)	Heat sealing (375°C−20 sec)	Space environmental stability elongation at break, %								
				Proton (MG y)			Electron (MG y)			U.V (ESD)		
				0	45	100	0	1	20	0	150	
Apical AH (KANEKA) PMDA/4, 4′-ODA	>360	no	no	61%	22%		62%	58%	54%	62%	62%	
ISAS-TPI a-ODPA/4,4′-ODA	265 (250°C cured)	>20	good	95%	73%	39%	81%	63%	76%	81%	71%	

Table 2 Summary of physical properties and space environmental stability for commercial PMDA/4, 4′-ODA film; Apical-AH (Kaneka) and a-ODPA/4, 4′-ODA film; ISAS-TPI

Goal			
1.	Heat sealing:	320–350 °C, <1 min	→ 340 C, 20 s
2.	Solubility in DMAc or NMP	30% <	→ 20% <
3.	Space environment;	proton 10 kGy	→ 20 MGy <
	radiation:	10~20 MGy	→ 20 MGy <
		U.V (150 ESD)	→ OK (mechanical)
			Δ (optical)
4.	Thermal stability:	Tg = 280 °C	→ Tg = 265–280 °C
5.	Film	(t) 5~7 μm, (w) 100 cm width	→ OK
6.	Mechanical properties;	σ b 100~200 MPa	→ 110 MPa
		modulus (E) 1~3 GPa	→ 2, 8–3.4 G
		elongation at break, 50–80 %	→ 80% <
7.	Cost; very expensive so far		

3 Development of Solar Sail IKAROS Membrane

What is a solar sail spacecraft ? Fridrikh Tsander proposed the concept of solar sail spacecraft with the solar-photon propulsion obtained by reflecting sunlight of a large, very thin, metalized polymer film a long time ago. However, nobody was successful to realize the theory in space because of so many challenges in technological solutions such as structure, stowage and deployment, system analysis, materials, and so on. Development of thermal and space environmentally stable polymer films is one of key requirements, in addition to the sealing, fabricating, packaging, and deployment; (1) A very thin (5–7 μm) high performance films has to be manufactured. (2) Heat sealable, thermo-plastic thin films with a high Tg and high reliability is also a key requirement (Table 2).

As was mentioned already, newly developed ISAS-TPI polyimide is a very promising material if it can be manufactured as wide, thin film. On the other hand, fortunately, there is a commercially available PMDA/4, 4′-ODA polyimide thin film; Apical AH (Kaneka). Therefore both films were selected for the IKAROS membrane. The solar sail IKAROS (Interplanetary Kite-craft Accelerated by Radiation Of the Sun) is the world's first solar powered sail craft employing photon propulsion. Thin film solar cells were also mounted on the sail surface to experimentally test the generation of solar power.

Figure 6 shows schematic representation of the principle of photon propulsion by Sun. IKAROS was launched from Tanegashima Space Center of JAXA using the H-IIA F-17 rocket on May 21, 2010.

Figure 7 illustrates mission sequence of IKAROS. ISAS-TPI covers almost 10% space of IKAROS. After separation from H-IIA rocket, IKAROS was spun up at up to 25 rpm for deploying the membrane. Figure 8 shows an illustration of IKAROS membrane. The membrane was made of two different polyimide thin films, i.e. an 80 nm aluminized APICAL AH/Al for outer area and an 80 nm aluminized ISAS-TPI/Al for near the spacecraft, respectively.
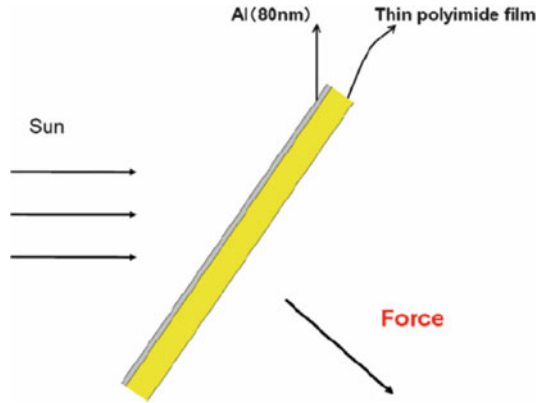
Fig. 6 Schematic representation of photon propulsion by Sun
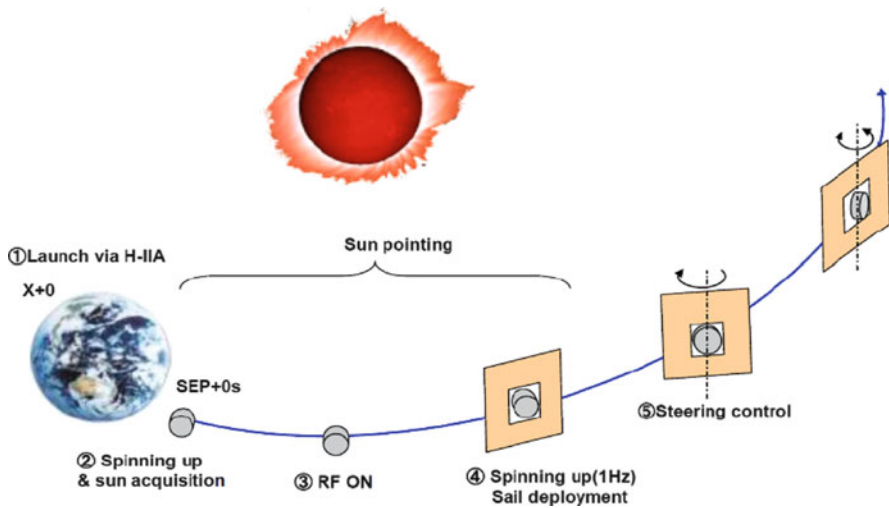
Fig. 7 Nominal mission sequence of IKAROS

Table 3 summarizes the chemical structures and physical properties of polyimide films: APICAL AH and ISAS-TPI selected for sail membranes.

Figure 9 illustrates configuration of 1/4 of IKAROS structure (one petal). As can be seen in Fig. 8, IKAROS sail was composed of four petals. The steering devices were applied by thin film liquid crystals and dust counter sensors of PVDF films, in addition to thin film polyimide solar cells, are attached on the membrane. Figure 10 shows sail design and the process of practicing the stowing of the sail.

Figure 11 illustrates the stowing of all four petals onto IKAROS spacecraft. The stowed IKAROS membrane with a diagonal of 20 m will be deployed using the spinning motion. Four weights are attached to the four tips of the membrane in order to facilitate deployment. Deployment is occurring in two stages as shown in
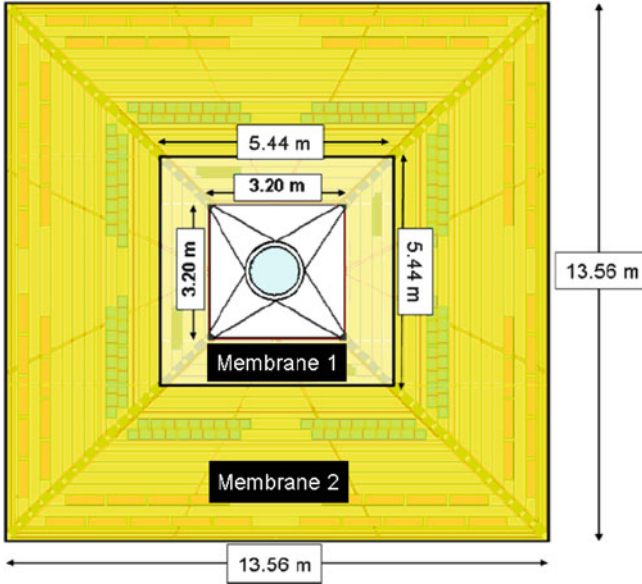
Fig. 8 IKAROS membrane:APICAL AH, 2:ISAS-TPI

Table 3 Properties of the selected for 'IKAROS' sail membrane materials
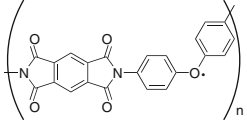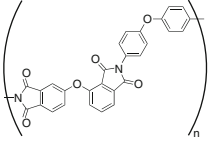
	Membrane 1 PMDA/4,4′-ODA	Membrane 2 a-ODPA/4,4′-ODA
Material	Kaneka APICAL-AH (7.5 μm) comercial polyimide film/Al	Newly developed ISAS-TPI thermoplastic polyimide film (7–8 μm)
Chemical structure		
Properties	Modulus: 3.0 GPa, elongn.:80% Tg:420°C, heat sealing: ×	Modulus: 2.8 GPa, elongn.:92% Tg:280°C, heat sealing: O
Area (173.63 m²)	154.28 (88.9%)	19.35 (11.1%)
Thickness (μm)	7.5	7.5–8.0
Sail wt. (1.849 kg)	1.643	0.206
Metal	Aluminum	Aluminum
Thickness (nm)	80	80

Fig. 12. During first stage, the membrane is static and during the second stage it is dynamic, i.e. opening up. This method can be realized with simpler and lighter mechanisms than conventional mast or boom type.
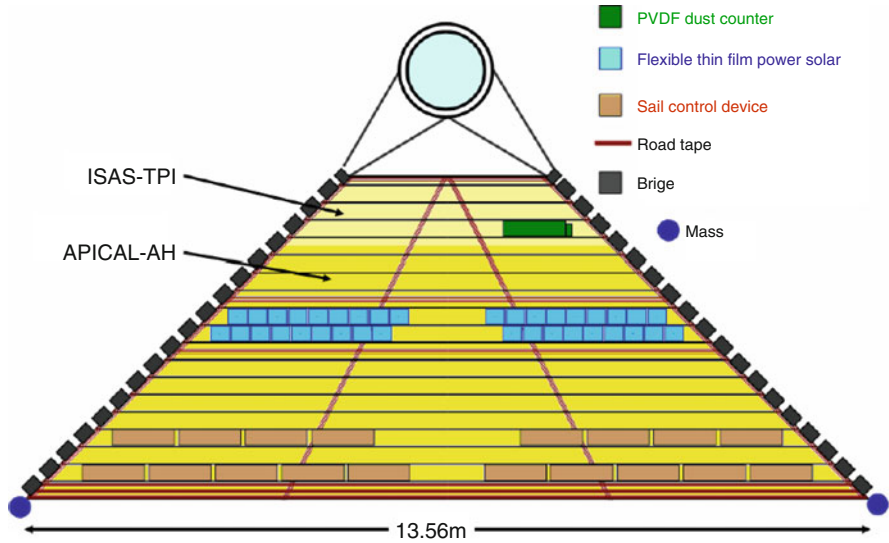
Fig. 9 Configuration of a ¼ of IKAROS Sail structure
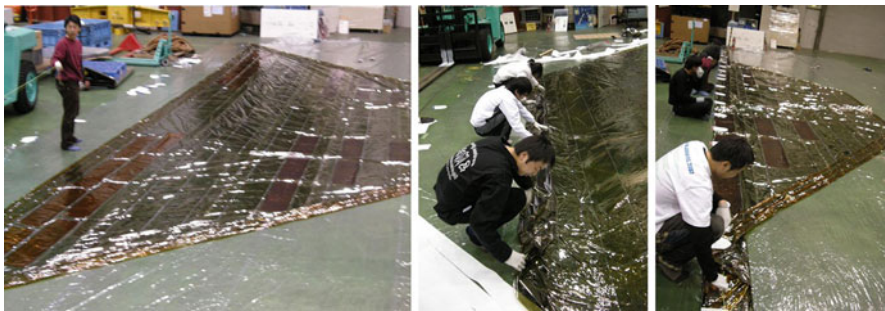
Fig. 10 Sail design and practicing the stowing

Figure 13 shows a 7.5 μm thin polyimide 1/4 IKAROS flight model (FM) membrane deployed in a clean room. Figure 14 is a picture of IKAROS spacecraft with four membranes stowed around the drum.

The world's first solar sail having 7.5 μm thin polyimide APICAL AH and novel thermoplastic asymmetric polyimide ISAS-TPI film aluminized has been launched from the Tanegashima space center in Japan on May 21 in 2010.

Figure 15 shows a picture of a released tip of mass with a piece of folded membrane (1), and a snap of second stage deployment. Both pictures were taken by a camera on the spacecraft. On June 9, 2010, the fully deployed IKAROS is photographed by its own camera attached on upper deck as shown in Fig. 16.
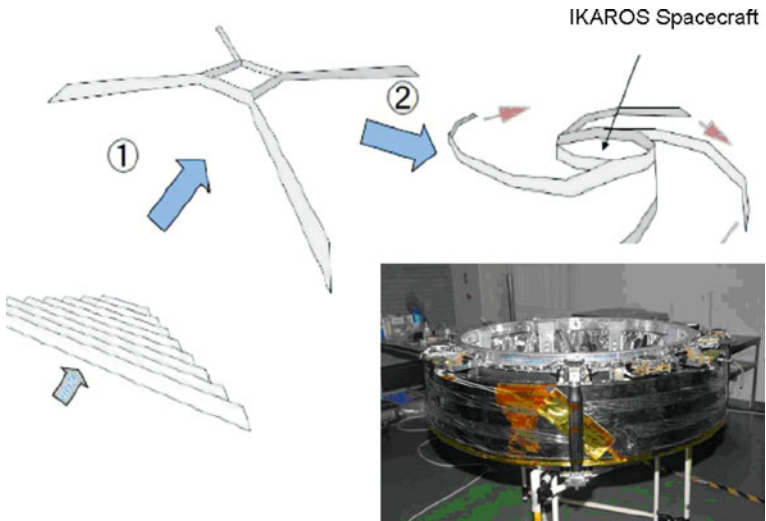
Fig. 11 Stowing a petal and mother vessel with four petals stowed
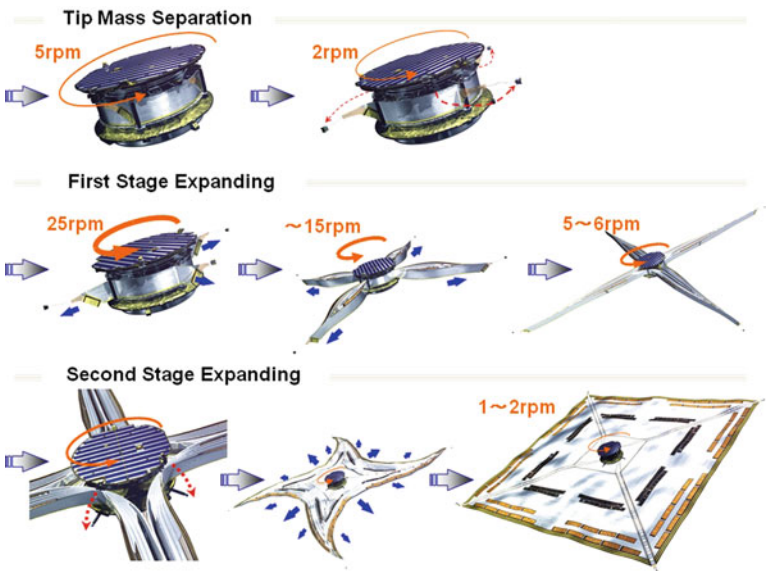
Fig. 12 Deployment sequence and mechanism
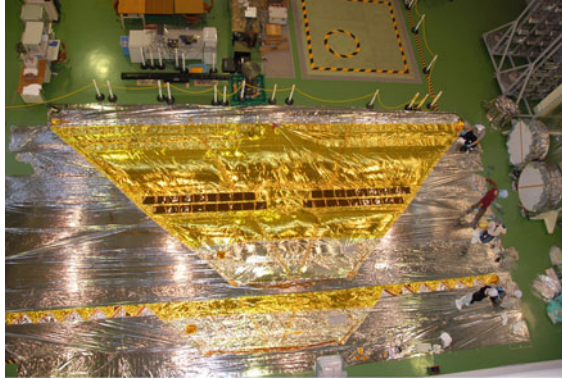
Fig. 13 Fully deployed FM membrane of ¼ IKAROS sail

Fig. 14 IKAROS FM spacecraft in clean room

4   Future Plans

We have successfully achieved the world's first solar sail mission: IKAROS. The second mission will take place in the late 2010s. It will provide a medium size solar power sail with a diameter of 50 m, and will have integrated ion-propulsion engines. The spacecraft destinations will be Jupiter and the Trojan asteroids. However, we have to overcome many technological challenges such as development of high efficiency solar cells and control devices with high space environmental stability in addition to the very light, more reliable polyimide membranes. The development of high performance polyimides is one of key factors for new space technology.
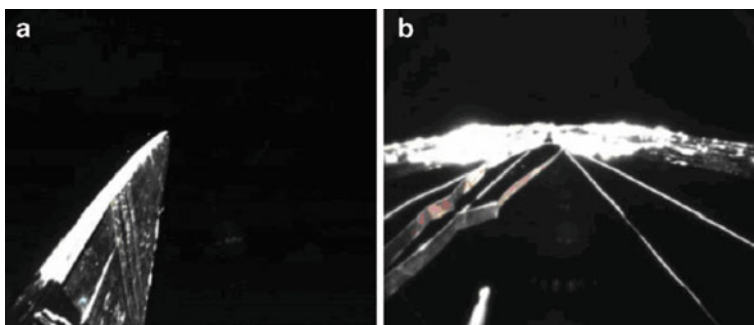
Fig. 15 (**a**) First stage deployment in space, (**b**) second stage deployment in space
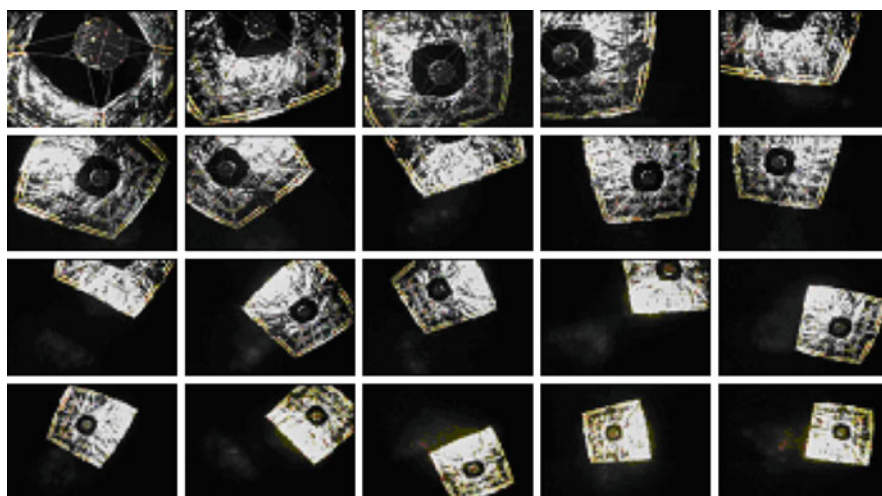
Fig. 16 Consecutive pictures of IKAROS solar sail taken by its own camera

References

1. Hasegawa M, Sensui M, Shindo N, Yokota R (1999) Structure and properties of novel asymmetric biphenyl type polyimides. Homo- and copolymers and blends. Macromolecules 32:387–396
2. Yokota R (2008) Asymmetric polyimides: creating next generation of aerospace materials. Kobunnshi 57:747–751

3. Yokota R, Yamamoto S, Yano S, Sawaguchi T, Hasegawa M, Yamaguchi H, Ozawa H, Sato R (2001) Molecular design of heat resistant polyimides having excellent processability and high glass transition temperature. High Perform Polym 13:S61–S71
4. Yokota R (2009) Novel heat sealable aromatic polyimide films with excellent space environmental stability. In: Proceedings of 4th international symposium on engineering plastics, Dalian, 23–26 Aug 2009
5. Yokota R (2001) Fundamental problems of solar sail space craft -large area polymer thin films. In: Proceedings of second space science symposium, Kanagawa, 19–20 Nov 2002, pp 89–91
6. Suzuki M, Yano S, Iwata M, Ishida Y, Yokota R (2007) Chemical structure and properties of novel asymmetric thermoplastic polyimides. Polym Prepr JPN 56:4934
7. Miyauchi M, Kazama K, Andoh A, Sawaguchi T, Iwata M, Ishida Y, Yokota R (2010) Development and fabrication of novel thermo-plastic polyimide thin films for solar sail IKAROS membrane. Polym Prepr JPN 59:1389, May/26–28/2010

Ion Beam Treatments for Enhancement of Surface Conductivity and Durability of Space Polymers: Results, Analysis, Mechanisms

J. Kleiman, Z. Iskanderova, F. Bussieres, A. Grigorevskiy, and R. Sodhi

Abstract This paper presents an overview of a few ion beam treatment technologies developed by ITL scientists and through successful national and international collaboration with other companies and research organizations.

Ion beams of medium to heavy mass elements of various natures, with energies from low keV, to moderate, few tens of keV have been used for ion beam treatment or ion implantation. A process named SurfTex^{TM} developed for treatment of the outer, mirror-like surface of Teflon used as a thermal control covering allowed to eliminate completely the specular reflections from the surface that were blinding the optical equipment, without changing the thermal optical properties of the coverings. An ion implantation process named Implantox^{TM} allowed creating on the surfaces of most treated polymers a stable protective layer that considerably decreased the erosion of the polymer materials in LEO. Another ion beam treatment technology (named CARBOSURF^{TM}) lead to surface carbonization that resulted in forming a charge dissipative top surface layer on polymer materials providing them with tunable, variable thermal optical properties in a wide range of values.

The obtained results have been used for development of a number of technological processes, followed by successful scale-up trials. A few low energy high intensity technological ion beam sources have been used in an industrial manufacturing-production environment to obtain large surface area treated polymer sheets.

J. Kleiman (✉) • Z. Iskanderova
Integrity Testing Laboratory Inc., 80 Esna Park Dr., Markham, ON L3R 2R7, Canada
e-mail: jkleiman@itlinc.com

F. Bussieres
MDA Corp., Ste-Anne-de-Bellevue, QC, Canada

A. Grigorevskiy
Kompozit, Korolev, Moscow region, Russia

R. Sodhi
Surface Interface Ontario, Deptartment of Chemical Engineering and Applied Chemistry, University of Toronto, Toronto, ON M5S 3E5, Canada

1 Introduction

The developed ion beam technological processes [1–3] were aimed at solving problems encountered by materials in space environment that can be divided into three broad classes, i.e. to prevent or eliminate completely:

(a) Effects of erosion in LEO due to atomic oxygen effects;
(b) Effects of excessive glare from mirror-like thermal optical coverings that were found to blind the optical equipment in space;
(c) Effects of surface charging and space equipment performance in GEO that include the degradation of high-voltage solar arrays due to arcing in GEO, secondary arcs on solar generators and problems in long-term modern antennae performance.

2 Classification of Ion Beam Techniques

In general, the ion beam techniques can be classified as follows:

(a) *Ion Implantation:* Accelerated ions in vacuum penetrate a solid surface. Applications depend on the ion species, energy, and fluence. Ion energies can vary from ~1 keV to ~10 MeV, with fluxes ranging form low dose (doping: semiconductors/electronics 10^{13}–10^{15} at/cm^2) to high dose (metallurgy, surface modification -10^{16} to 10^{17} at/cm^2);
(b) *Ion Beam Sputtering/Texturing*: Bombardment of a solid with a beam of energetic ions causes sputtering of the solid surface, often with significant surface morphology change/regularly repeated features development. Ion energies—of ~1–10 keV;
(c) *Ion Beam (Assisted) Deposition IB(A)D:* IB(A)D is a surface engineering technique of Ion Beam Deposition (IBD) or ion bombardment with simultaneous sputter deposition or another physical vapor deposition (PVD) technique.
(d) *Ion Beam Treatments of Organics*: classified separately because in organics volatiles may be released under ion bombardment with elemental and structural changes happening in the materials including organic–inorganic transitions.

3 Results and Discussion

3.1 Ion Beam Texturing Surface Modification Process-SurfTex[TM]

A texturing surface modification process was developed and applied to Ag/Teflon films in order to provide a matt finish [1, 4, 5]. Large areas of Teflon FEP films were successfully treated by texturing them in a continuous ion beam process using
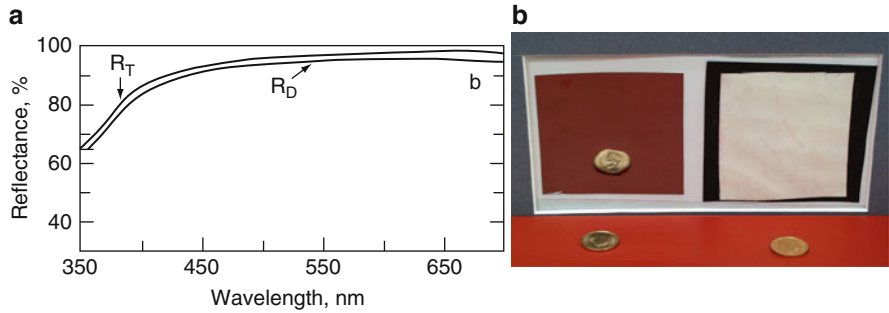
Fig.1 (a) Total (R_T) and diffuse (R_D) reflectance measurements for an Ag/Teflon sample after an exposure to a Krypton gas ion-beam; (b) Optical images of Ag/Teflon samples before (*left*) and after (*right*) treatment with the texturing process. Coins are placed in front of the samples to demonstrate the total loss of reflectance in the treated sample

Table 1 Major optical and thermal optical properties of the Ag-Teflon film before and after texturing

	Ag/Teflon original	Ag/Teflon textured
Solar absorptance α	0.08	0.07
Total emittance (ε)	0.79	0.81
α/ε	0.10	0.09
Appearance	Shiny, grey-metallic	Matte, milky-white
Total reflectance	0.95	0.93–0.95
Diffuse reflectance	0	0.92–0.93

krypton as the ion source. The developed treatment of Ag/Teflon surfaces reduced substantially the specular reflectance of the films by changing the morphological structure of their surfaces [6] through ion-beam texturing in a controlled manner from a metallic-like and shiny to complete milky-white (Fig. 1) without significantly affecting the thermal optical properties (Table 1) [1].

For enhanced protection in LEO against the effects of atomic oxygen, the treated Ag/Teflon surfaces were coated with a thin layer of SiO_2 at Sheldahl Corp.

Sheets of Ag/Teflon treated by this process were applied to cameras and lights on the International Space Station using an acrylic adhesive (3M 966). The camera/light units covered with the textured Ag/Teflon were successfully exposed to space on the ISS for a prolonged time, retaining their highly diffuse surface properties and the required thermal optical properties [7].

3.2 Ion Beam Implantation Technology: Implantox^{TM}

Mid energy ion beam sources were used to modify space-bound materials in order to provide new protective properties to their surfaces. A method of surface modification of advanced polymers, graphite and carbon-based composites named

Implantox[TM] based on high-dose ion implantation with Si, Al, Si + Al, Si + B, Si + Al + B, Y, Sm, Gd and special oxidative post-treatment was developed and patented in 1997 [2, 7–10]. The developed technology dramatically increased the erosion and oxidation resistance of polymer-based materials together with substantial improvements in mechanical, electrical, and optical properties.

In the Implantox[TM] process, a high-dose single or binary ion implantation of specially selected metals or semi-metals is performed into polymers and carbon-based composites that when combined with a special oxidation post-treatment following ion implantation produces a graded oxide(s)-based surface layer, with a variable degree of carbonization, chemically bonded to the original polymer, and highly resistant to erosion and oxidation. Based on computer simulation and experimental studies, the implantation energy range required to produce a 50–100 nm thick modified protective oxide-based layer in most of the treated materials was determined to be 20–50 keV and the required ion dose range was found to be 10^{16}–10^{17} ions/cm^2 [2]. The types of oxides, the degree of surface carbonization, i.e. the surface content of oxide(s)-based structures and the amount of carbonized (graphitized) phases in the modified surface layers can be varied and controlled in a wide range. Various surface-sensitive properties of the modified layers, such as mechanical, optical, electrical, etc. can be tailored and controlled by the conditions of ion implantation and the following oxidative post-treatment. It was confirmed in a number of studies that surface treatment by Implantox[TM]:

– Protects polymers and composites from space environment in low Earth orbits,
– Increases the oxidation resistance in highly oxidative environments, such as atomic oxygen, ozone, oxygen plasmas,
– Improves the spacedurability of polymeric materials and coatings,
– Allows tailoring of the degree of hydrophobicity and hydrophilicity
– Allows tailoring of optical and thermal-optical surface properties,
– Including refraction, reflection, color, and degree of transparency.

Since during the Implantox[TM] process the surface layers of the treated material are modified, the problems of adhesion, thermal mismatch and change in dimensions that are typical for deposition processes, disappear. Virtually all hydrocarbon polymers, carbon and carbon fiber-reinforced polymer (CFRP) composites can be modified by Implantox[TM]. The process is a non-thermal, allowing for low melting temperature materials to be treated. Since this surface treatment technology is based on ion-implantation in vacuum, it is absolutely clean and environmentally friendly. No hazardous materials are used or released in this process.

During the implantation process, the surface region is enriched with the implanted species and a release of volatiles may occur at the same time, leaving a carbonized or graphitized surface layer on the original material. The second stage in the process is carried out in appropriate oxidative environment containing atomic oxygen (AO), for instance, under exposure to FAO flux. A number of processes are happening simultaneously at this stage including the oxidation of the remaining organics and the release of the formed volatiles and the oxidation of the implanted elements with formation of oxide(s)-based precipitates. The implanted layer is then

gradually converted to a layer of oxide(s)-based compound(s) and is stabilized in this form, thus providing long-term protection of the original polymer underneath.

A few space-related thin polymer film materials, treated by Implantox™, have been included in two MISSE flights in so-called "New Atomic Oxygen Protection Concepts" experiment [11]. They have been selected based on the results of a program of space polymers' surface modification and ground-based oxygen plasma and FAO beam testing. Those studies were initiated by ITL/UTIAS team and continued at ITL for MISSE results evaluation and analysis. The samples exposed to LEO environment for 4 years in MISSE-1 and for 1 year in MISSE-3 have been analyzed by a number of surface analysis techniques. The test results of surface-modified samples confirmed full protection for those polymers in LEO environment. Figure 2 presents the data from a SIMS analysis of a Kapton HN sample implanted with ions of Si, 25 keV and B, 10 keV before (a) and after (b) open space flight outside ISS (12 months). As can be seen from the SIMS analysis results, the surface of Implantox^{TM} treated and LEO exposed sample underwent of their surfaces was also conducted to evaluate the surface chemical reconstruction. The analysis had shown that Si is present at the surface mostly in the form of oxide(s)-like chemical compounds that is indicated by the Si2p binding energy E_b^{Si} values, having $E_b = (103.3-104)$ eV that is typical for Si oxides and the shift of the oxygen binding energy for O1s up to $E_b^O = 533.2$ eV that is also indicative of silicon oxides [11]. Another implanted element, boron, has been found at the surface in small quantities, around (1–2) at.% (Table 2). The boron is present in the form of boron oxide, as shown by B binding energy value, $E_b^B = 193.2$ eV [11] that is typical for oxidized boron. It should be noted that boron appears in the subsurface layers, as indicated by SIMS results (Fig. 2)

All polymer samples, immediately after the implantation process, exhibit a carbonized surface layer and are opaque prior to exposure to FAO. The carbonization effect manifests itself by brownish surface color, and is confirmed by XPS data showing surface enrichment in carbon and reconstruction of carbon chemical states (Table 3). This surface carbonization effect is a well known adjunct of ion implantation processes in polymers. However, partial or full recovery of the original color and optical transmission was observed after FAO treatment of the implanted samples, with the degree of recovery depending on the implantation conditions and on the FAO dose

The major appeal of the ion implantation approach over conventional inorganic coatings is that the difficulties associated with brittleness, mismatch of coefficients of thermal expansion, and change in surface morphology are mitigated by creation of a graded surface modified region.

Ion-beam treatment process to form charge dissipative surfaces- Carbosurf^{TM}

A surface modification technology (tentatively named Carbosurf™) that was developed to achieve charge dissipative properties on the surface of polymers is based on the controlled carbonization of the surface layer of thin polymer films [3, 12]. Surface resistivity (SR) in the charge dissipative range, from ~2 MΩ/sq up to 150 MΩ/sq with low temperature dependence has been achieved on hydrocarbon and partially fluorinated polyimides due to surface carbonization, using specially
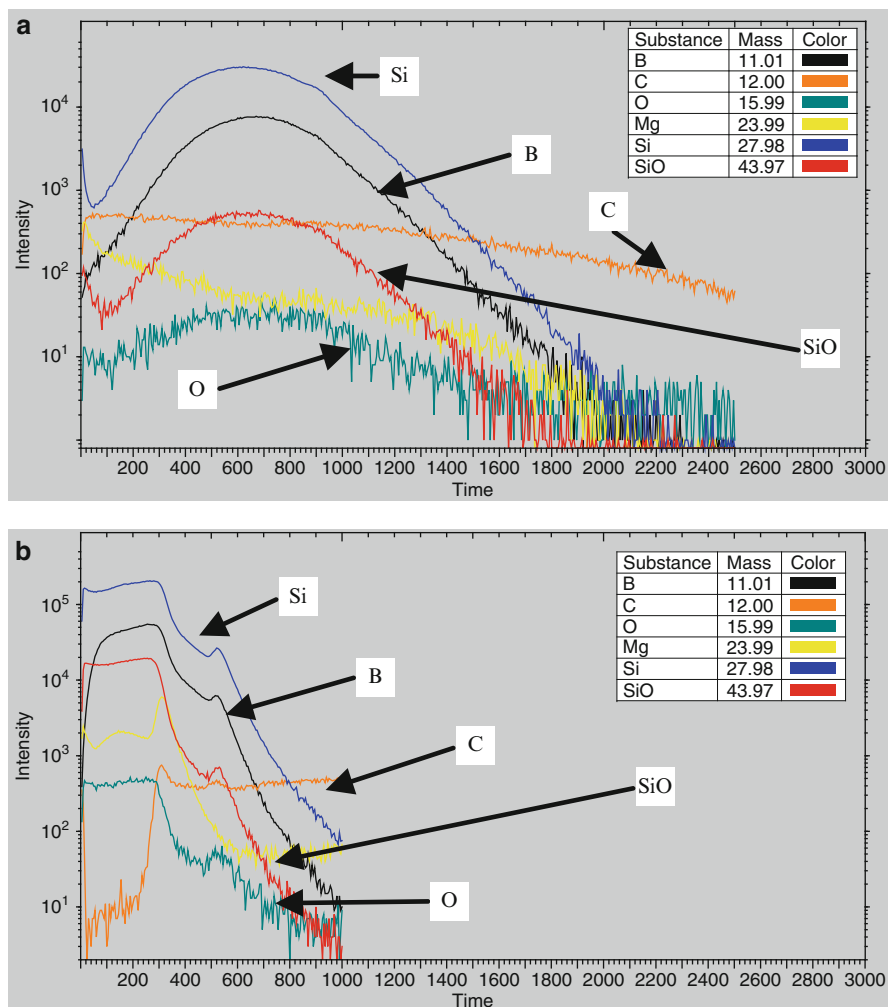
Fig. 2 SIMS depth profiling results for Kapton HN implanted with ions of Si, 25 keV and B, 10 keV before (**a**) and after (**b**) open space flight outside ISS (12 months)

Table 2 XPS data for implanted and implanted/LEO environment exposed space polymers

Film state	Mylar D		Kapton HN	
	Implanted	After space exposure	Implanted	After space exposure
Element	At. %	At. %	At. %	At. %
C1s	88.7 %	17.97	85.2 %	17.39
N1s	–	0.51	2.2 %	0.48
O1s	8.6 %	49.94	8.8 %	50.28
Si2p	2.1 %	29.68	1.6 %	30.93
B1s	0.6 %	1.90	0.4 %	0.93

Table 3 Surface resistivity and RF properties of pristine and Carbosurf™-treated Kapton HN

| Material | Treatment | SR (Ω/sq) | | Ku band insertion loss (dB) | Ku band return loss (dB) |
		As treated	After GEO Rad. testing		
Kapton 100HN	Pristine	$>10^{12}$	$\sim 10^{11}$	0.015–0.020	30–31
Kapton 100HN	Carbosurf™	$(13–25)\cdot 10^{6}$	$18\cdot 10^{6}$	0.015	31
Ge/Kapton HN	Ge (1,000 Å)	$5\cdot 10^{7}$	$1.3\cdot 10^{8}$	0.015	30

selected ion beam treatment conditions [3]. The created surface resistivity can be tailored to the desired values for particular applications on a variety of space polymer films. The Carbosurf™ treatment is performed using ion beams of rare gases, without affecting the mechanical and any other properties of the polymeric material underneath, and was scaled-up using an industrial high-intensity ion beam facility.

The main advantage of Carbosurf™ technology, for instance, for high frequency antenna applications over technologies currently available is a low temperature dependence of the achieved surface resistivity and excellent RF performance. It was shown (Fig. 3) that the temperature dependence of SR at room temperature and with temperature varying in the range from $-150\,^{\circ}$C to $+150\,^{\circ}$C for CP1 treated by Ar^{+} ion beam and Kapton HN exposed to Kr^{+} ion beam is quite slow and at low temperatures the ion beam treated samples still keep the surface resistivity in the appropriate range of values [13]. Table 3 illustrates the SR values of pristine Kapton HN and treated by Carbosurf™, measured before and after GEO imitating radiation testing as well as their RF transmittance. Similar properties for Ge/Kapton HN sample that is used routinely for such application are also shown.

Another important feature of the Carbosurf™-treated materials, i.e. their full RF permeability, is also demonstrated in Table 3. The significant distinction of the developed surface carbonization technology from deposition of semi conductive coatings is that the Carbosurf™ treatment is "graded" into the material thus eliminating any sharp interfaces that could be a weak point of the alternate coatings' technologies [12]. Figure 3 presents the semi-log graphs of the T$^{-1/4}$ temperature dependence of the surface resistivity of various polyimide samples with different Carbosurf™ treatments. Such linear dependence is a clear indication of variable range hopping conductivity mechanism in the thin Carbosurf-treated surface layer of polymers.

One of important applications of Carbosurf–treated materials is their use as feed aperture cover materials in satellite antennas performing in GEO and other orbits where thermal runaway problems may exist. With an increase in feed temperature, the RF power and the frequency comes increased risk of thermal runaway in feed aperture cover materials placed directly in front of feeds. Indeed, the conductivity of static dissipative coating increases with temperature, hence increasing RF loss. Thus the aperture cover materials can reach a thermal runaway point and burn instantly when exposed to very high RF power densities.
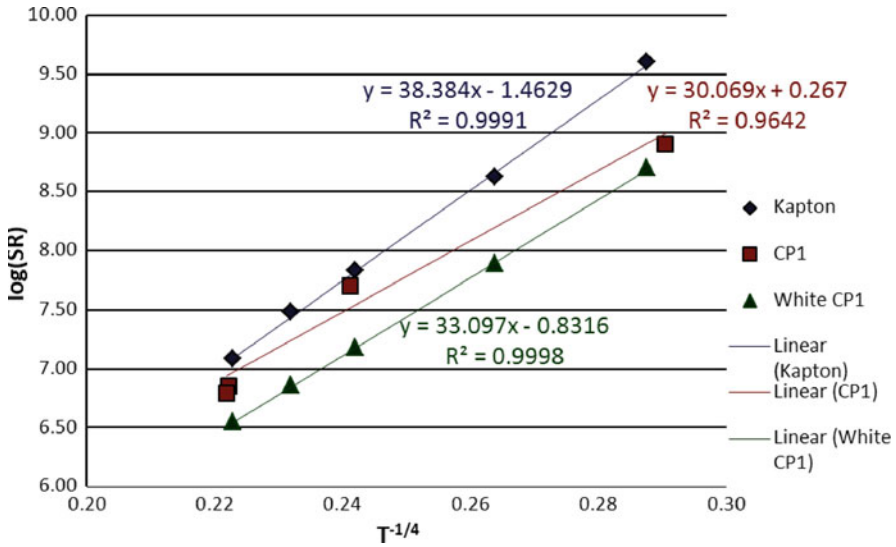
Fig. 3 Semi-log graphs of the $T^{-1/4}$ temperature dependence of the surface resistivity of various polyimide samples with different Carbosurf treatments

Table 4 Comparison of thermal runaway power density for various sunshield materials

Material (all samples 1 mil)	Approx. local power density at runaway (MW/m^2)
Kapton uncoated	More than 16.6 (no runaway reached at max. capacity of setup)
Carbo+, SR of 1.5E8 Ω/sq, (at Tamb)	14.2
Carbo+, SR of 4E7 Ω/sq, (at Tamb)	8.3
Typical Ge coated material	0.6–1.6

Waveguide tests were made in TVAC to expose a number of aperture cover material samples that included Kapton untreated, Kapton treated by a modified Carbosurf process and a typical Ge-coated material with various resistivity over temperature behaviors to very high RF power densities. The samples were placed in a special sample holder inserted between two waveguide flanges.

Table 4 below shows a comparison of the RF power density observed in tests to initiate thermal runaway for the described above materials (tests at Ka-band in WR51 waveguide).

It can be seen from Table 4 that the power handling capability of the Carbosurf[TM] treated Kapton 100HN material is at least 5 times higher (and up to ten times higher for material with higher surface resistivity) than germanium coated materials. This is due to the low temperature dependence of surface resistivity of the treated material compared to alternate static-dissipative coatings like Germanium.

4 Conclusions

It was demonstrated that ion beam surface treatment technologies present a viable option for both protection and impairment of new functional properties to space-bound materials. Surface modification processes have been developed to provide an alternative solution to the problems caused by different space environment factors to space polymers and polymer-based composites used in LEO and GEO spacecrafts.

The developed processes allowed in one case to drastically reduce the specular reflectance by surface texturing, in another case to protect from the atomic oxygen erosion in LEO by creating an oxide-based surface layer and in still another case to increase surface conductivity with low temperature dependence and full RF transmittance that extended the use of traditional space materials in space applications.

References

1. Kleiman JI, Popov O, Tong A, Molenda D (1998) Development of high diffuse reflectance surfaces on teflon. In: Kleiman JI, Tennyson RC (eds) Proceedings of the third international space conference on protection of materials and structures from the LEO space environment, ICPMSE-3. Toronto, 25–26 Apr 1996. Kluwer, 1999, pp 167–178
2. Iskanderova ZA, Kleiman JI, Gudimenko Y, Tennyson RC, Cool GR (1997) Surface modification of polymers and carbon-based materials by ion implantation and oxidative conversion. U.S. Patent #5,683,757, issued 11 Apr 1997
3. Iskanderova Z, Kleiman JI, Bussieres F (2009) Method of making charge dissipative surfaces of polymeric materials with low temperature dependence of surface resistivity and low RF kloss. US Patent Application Serial No. 12/458,486, 2009
4. Kleiman JI, Gudimenko Y (1997) Reduced glare, high diffuse reflectance teflon surfaces for improved performance of video cameras on Canadian MSS for SS alpha. In: Proceedings of the seventh international symposium on materials in space environment. Toulouse, 16–20 June 1997 (SP-399, Aug 1997), pp 419–424
5. Kleiman JI, Iskanderova Z, Antoniazzi J (2009) Long term flight performance of high diffuse reflectance AG/teflon coverings flown on Canadian mobile servicing station, MSS. In: 11th international symposium on materials in space environment, Aix en Provence, 15–18 Sep 2009
6. Kleiman JI (2010) Surface modification of space materials. Encyclopaedia of aerospace engineering, vol 4. John Wiley & Sons Canada, Limited, Toronto, Canada, doi: 10.1002/9780470686652.eae238
7. Iskanderova Z, Kleiman J, Gudimenko Y, Morison WD, Tennyson RC (1997) Improvement of oxidation and erosion resistance of polymers and composites in space environment by ion implantation. Nucl Instrum Methods Phy Res B127/128:702–709

8. Kleiman J, Iskanderova Z, Tennyson RC (1998) Ion implantation protects surfaces. Adv Mater Process 153:26–30

9. Kleiman JI, Iskanderova ZA, Gudimenko YI, Morison WD, Tennyson RC (1999) Polymers and composites in the low earth orbit space environment: interaction and protection. Can Aeronau Space J 45(2):148–160

10. Iskanderova Z, Kleiman J, Gudimenko Y, Morison WD, Tennyson RC (1999) Surface modification of polymer-based materials by ion implantation – a new approach for protection in LEO. In: Kleiman JI, Tennyson RC (eds) Protection of materials and structures in LEO space environment. Kluwer, Dordrecht, pp 225–234

11. Iskanderova Z, Kleiman JI, Tennyson RC (2009) Pristine and surface-modified polymers in LEO: MISSE results versus predictive models and ground-based testing. In: Kleiman JI (ed) Proceedings of the ICPMSE-9 conference, Toronto, 20–23 May 2008. Publisher AIP conference proceedings 1087, pp 300–311

12. Iskanderova Z, Kleiman JI, Issoupov V, Bussieres F (2009) CarboSurf™ surface modification technology for charge dissipative and radio-transparent GEO durable space polymers. In: Kleiman JI (ed) Proceedings of the ICPMSE-9 conference. Toronto, 20–23 May 2008. Publisher AIP conference proceedings 1087, pp 588–599

13. Iskanderova Z, Kleiman J, Issoupov V, Bussieres F (2009) Surface treatment technology for changing, tuning, and adjusting surface resistivity of space polymers. In: Proceedings of the 11th ISMSE international symposium on materials in a space environment, Aix-en-Provence, 15–18 Sept 2009

Comparison of Properties of Solid Lubricant Between Two Exposure Experiments Aboard the ISS

Koji Matsumoto, Mineo Suzuki, and Yugo Kimoto

Abstract To evaluate the degradation of materials in low Earth orbit space environment, the Space Environment Exposure Device (SEED) experiments were carried out on the International Space Station. As part of these experiments, changes in the tribological properties of a molybdenum disulfide bonded film that is used as a solid lubricant, were evaluated. The results of friction tests in a vacuum and surface analysis by XPS were compared between two exposure experiments aboard the Service Module (SM) and the Japan Experimental Module (JEM). The investigations revealed silicon and fluorine contaminations in the JEM/SEED flight sample, but with a lower amount of silicon contamination than the SM/SEED flight sample. The JEM/ SEED flight sample and ground-based tested samples showed lower friction coefficients than a reference sample at the beginning of the tests. The friction behavior of the JEM/SEED flight sample was similar to those of SM/SEED flight samples.

1 Introduction

The degradation of materials in extreme environments is a critical issue affecting the reliability of tribological components in space. In the low Earth orbit (LEO) space environment, materials are strongly affected by factors such as atomic oxygen (AO), ultraviolet rays (UV), and radiation.

K. Matsumoto (✉) • M. Suzuki
Spacecraft Structures and Mechanisms Group, Aerospace Research and Development Directorate, JAXA, Chofu, Tokyo 182-8522, Japan
e-mail: matsumoto.koji@jaxa.jp

Y. Kimoto
Electronic Devices and Materials Group, Aerospace Research and Development Directorate, JAXA, Tsukuba, Ibaraki 305-8505, Japan

A number of materials used in space applications (e.g., as thermal coatings, paints and lubricants) were exposed to the LEO space environment in the Service Module/Space Environment Exposure Device (SM/SEED) experiment aboard the International Space Station (ISS) to evaluate how they would be affected by a real space flight environment [1, 2]. Three sets of pallets containing the same specimens were exposed to the space environment for different durations. A molybdenum disulfide (MoS_2) film used as solid lubricant coating was selected as one of the materials in the experiment [3–7]. However, much silicon contamination was detected on the MoS_2 specimens in SM/SEED experiment, so the main factors affecting observed tribological properties, whether contamination, AO, UV or other factors, were not obvious.

The Japanese Experiment Module/Space Environment Exposure Devices (JEM/SEED) experiment is another ISS exposure experiment that uses the JEM Exposure Facility. The same MoS_2 specimen as used in the SM/SEED experiment was exposed to the LEO environment in the JEM/SEED experiment. The SM is located at the tail of the ISS, an area that appears to receive much contamination, while the JEM is located on the front of the ISS, which is thought to be a cleaner, less contamination environment. The results of friction tests and surface analyses of the MoS_2 specimen in the JEM/SEED experiment are evaluated and compared with the results of the SM/SEED experiment to understand the effects of the space environment on the tribological properties of MoS_2 film in the absence of contaminations, and differences in the space environment around a spacecraft.

2 Project Outline

Figure 1 shows two materials exposure experiments aboard the ISS. The JEM/SEED experiment was carried out as part of the Space Environment Data Acquisition equipment-Attached Payload (SEDA-AP) mission launched on Space Shuttle 2J/A (STS-127) in July 2009.

After being mounted aboard the JEM exposure facility, the JEM/SEED pallet, which held material specimens, was exposed to the space environment. The JEM/SEED pallet was retrieved to inside the ISS in April 2010 and then returned to Earth by Space Shuttle 19A (STS-131). The exposure duration was 8.5 months (259 days), and the average altitude of the ISS estimated from flight data for these days was 343.4 km. In a previous study, three pallets of specimens were exposed to the LEO environment in the SM/SEED experiment from October 2001 for durations of 315, 865 and 1403 days. The JEM/SEED experiment exposure duration was shorter, but the altitude during exposure was lower than in the SM/SEED experiment. Figure 2 shows photographs of the pallets in two SEED experiments.

The fluences of the effective factors, atomic oxygen and ultraviolet rays, calculated from the altitude and attitude of the ISS during the experiments and from monitor materials are listed in Table 1.
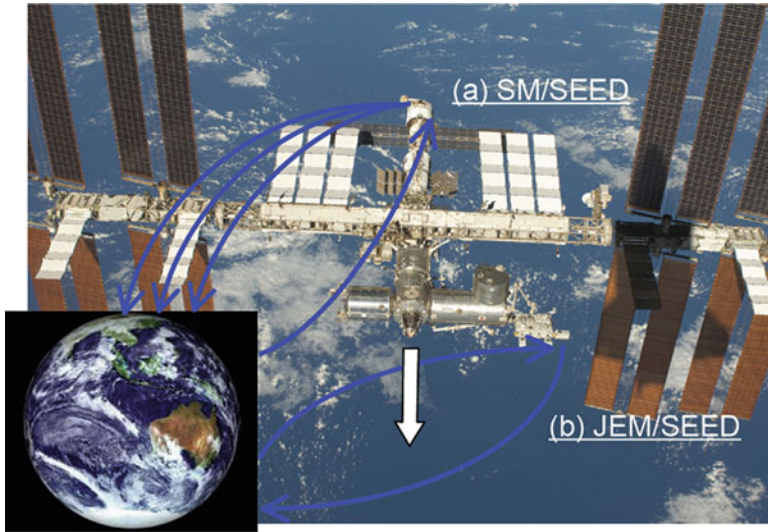
Fig. 1 Two material exposure experiments aboard the ISS in low Earth orbit
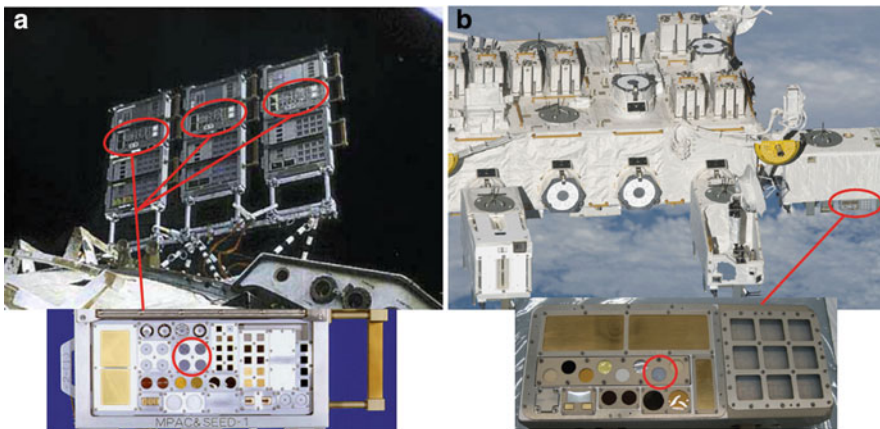
Fig. 2 SEED pallets during exposure in low Earth orbit and mounted positions of MoS_2 samples. (**a**) SM/SEED, (**b**) JEM/SEED experiments

One of the lubricant specimens tested in the SEED experiments is a bonded MoS_2 films coated onto a titanium alloy substrate. An organic binder, polyamide-imide, constitutes about 65 % of the film. The film thickness was about 10 μm. The same type of MoS_2 specimens were also used in a ground-based experiment that simulated space exposure conditions in a facility at JAXA [8]. The atomic oxygen environment was simulated by a laser-detonation source [9], while the ultraviolet ray environment was simulated by Xe shortwave arc lamp.

Table 1 Flight conditions and fluences of effective factors in flight experiments

		SM/SEED			JEM/SEED
		#1	#2	#3	
		1 year (315 days)	2 years (865 days)	3 years (1403 days)	8.5 months (259 days)
	Monitor materials	386.6 km	391.5 km	370.8 km	343.4 km
Atomic oxygen (AO) [atoms/cm^2]	(Calculation)	2.85×10^{21}	5.70×10^{21}	8.41×10^{21}	1.40×10^{21}
	Vespel	2.04×10^{20}	2.57×10^{20}	2.70×10^{20}	5.91×10^{20}
	PAMDEC	2.41×10^{21}	1.36×10^{21}	1.37×10^{21}	–
Ultraviolet rays (UV) [ESD]	(Calculation)	73.8	167	271	56.85
	PU	18.1	15.8	13.4	
	ITO/PU	–	–	–	< 30

3 Evaluation Methods

3.1 Friction Test

Friction tests were performed using a tribometer with a pin-on-flat configuration. Sliding between a flat and counterpart specimen was a reciprocating linear motion. The counterpart specimen was a 7.94 mm-diameter ball composed of 440C stainless steel. The sliding speed and applied load were, respectively, 10 mm/s and 2N. The tests were interrupted after the same number of sliding strokes, and the wear tracks were examined to understand the mechanism of any friction changes.

3.2 Surface Analysis

The surfaces of samples and the rubbing tracks after friction tests were investigated by XPS analysis. X-rays source of monochromatic Al Kα was used, focused to φ100 μm for the film surfaces and φ20 μm for the rubbing tracks.

4 Results and Discussion

4.1 Film Surface Composition by XPS Analysis

Figure 3 shows the surface composition of a JEM/SEED flight sample, a reference sample and ground test samples revealed by XPS analysis. Much carbon from the binder material was detected in the reference sample. The composition of the UV-irradiated sample was not significantly different to the reference sample, while the AO-irradiated sample had greater oxygen and lower carbon concentrations than the reference and UV-irradiated samples.
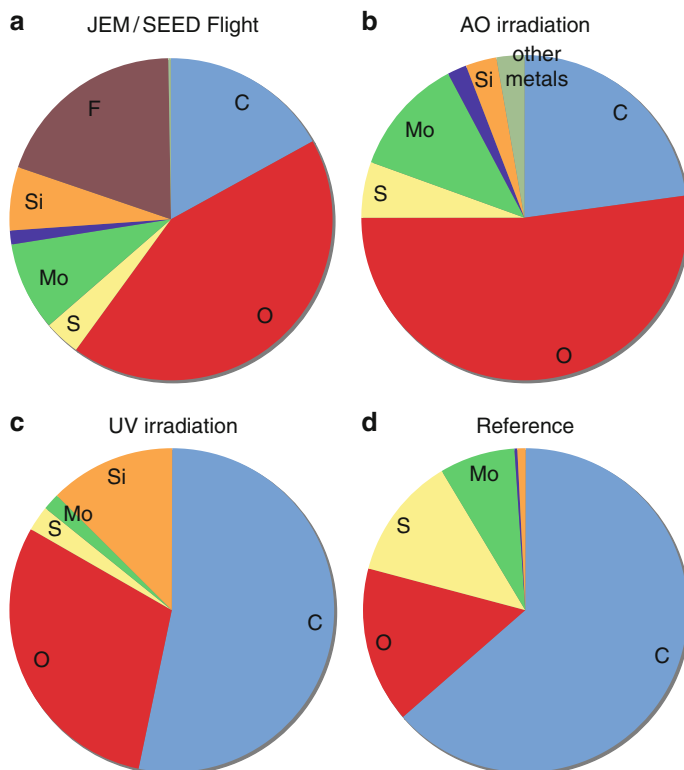
Fig. 3 Surface composition of the JEM/SEED flight sample and ground test samples by XPS analysis

Ground-based test samples might show traces of surface contaminants from the exposure facilities. Silicon and fluorine were detected on the surface of the JEM/ SEED flight sample, and these appear to be contamination. The oxygen concentration in the flight sample was higher than in the reference sample, but lower than in the AO-irradiated sample due to the detection of much contamination. Except for the presence of contamination, XPS analysis of the flight sample showed similar results to the AO-irradiated sample. Figure 4 shows narrow spectra of typical elements detected in the surfaces of the JEM/SEED flight and reference samples. For Mo 3d spectra, two peaks at 232 and 236 eV were observed in the flight sample, which indicate Mo (VI) and the presence of MoO_3. The peak at 162 eV in the S 2p spectra is a peak of sulfide, whereas a peak of SO_2, sulfone or sulfate at 168–170 eV was observed for the flight sample. For C 1s spectra, a peak of CF_x was detected at 292–293 eV on the surface of the flight sample.

To compare the surface compositions of flight samples, Fig. 5 shows XPS analysis results for film surfaces of SM/SEED flight samples with exposure durations of approximately 1 year and 3 years. The concentration of silicon in the surface of the JEM/SEED flight sample (Fig. 3) was less than in the SM/SEED
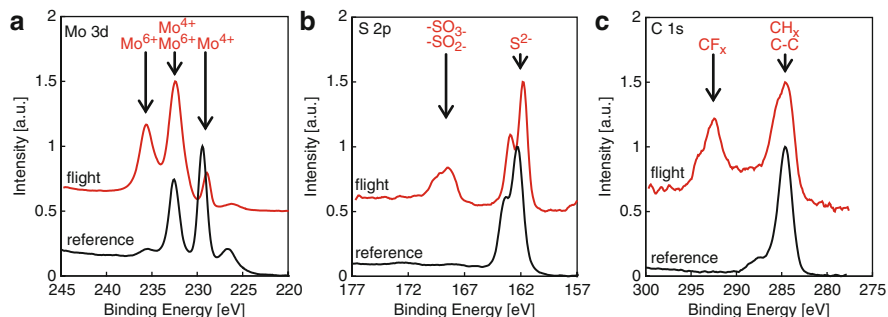
Fig. 4 Comparison of XPS spectra of film surface between JEM/SEED flight sample and reference sample. (**a**) Mo 3d, (**b**) S 2p, and (**c**) C 1s
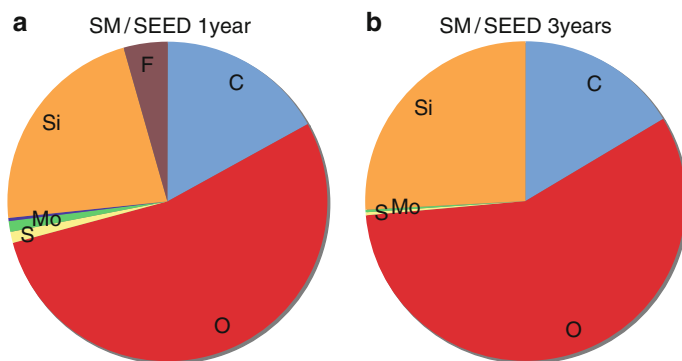
Fig. 5 Surface composition of the SM/SEED flight samples by XPS analysis

samples. The JEM/SEED experiment environment therefore seems to be cleaner, with less contamination than the previous SM/SEED experiment. On the other hand, fluorine was hardly detected in the SM/SEED samples, and seems to have come from a different source to the silicon.

4.2 Friction Behavior of JEM/SEED and Ground-Based Tested Samples

Figure 6 depicts the friction behaviors of a JEM/SEED flight sample, a reference sample, and AO and UV irradiated ground test samples. The friction coefficient of the flight sample decreased sharply from start of the test and reached a steady state earlier than the reference sample. The AO-irradiated and UV-irradiated samples also showed low friction coefficients from beginning of the tests. The AO-irradiated sample had similar behavior to the flight sample, but showed a lower friction
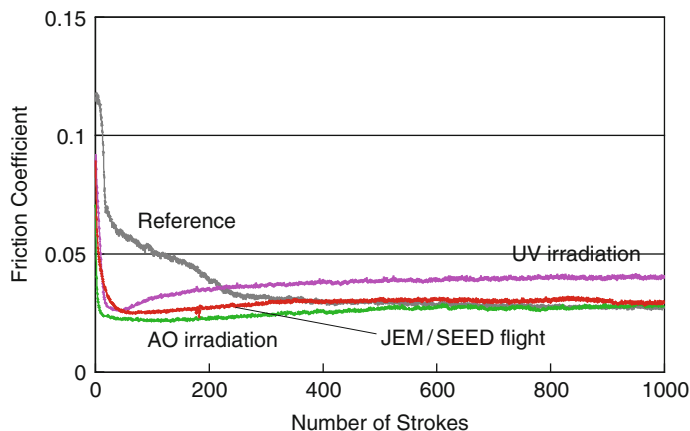
Fig. 6 Friction behavior of JEM/SEED flight sample, reference sample, and AO and UV irradiated samples

coefficient than the flight sample at the beginning of the test. The friction coefficient of the UV-irradiated sample increased slightly and became stable after decreasing at beginning of the test.

To understand wear process and mechanism of friction change, friction tests were interrupted at 100, 2,000 and 20,000 sliding strokes and spot XPS analysis of the wear tracks of the films and microscope observations of the contact area of the counterpart were carried out. The contact areas of the 440C stainless steel counterpart ball after 100 strokes and 20,000 strokes for each specimen are presented in Fig. 7. The photographs of the counterpart of the reference sample show large transfer film. Similarly for the UV-irradiated sample, hard transfer film adhered to the counterpart after 100 and 20,000 sliding strokes. In contrast, for the AO-irradiated sample, transfer film was recognized only at the entrance and exit sides of the contact area, and had not adhered to the center of the contact area of the counterpart after 100 and 20,000 sliding strokes. This indicates that the mechanism of friction change is different between the AO-irradiated and UV-irradiated samples, although both showed a sudden decrease in friction. On the counterpart of the flight sample, a little transfer was found after 100 sliding strokes, but transfer film was not recognized at the center of contact area after 20,000 strokes. The friction change mechanism of the flight sample seems to be the same as that of the AO-irradiated sample, atomic oxygen contributing to the decrease in friction.

In the spot XPS analysis of the wear tracks of the JEM/SEED flight sample, the 236 eV peak of MoO_3 in the Mo 3d spectra observed on the film surface disappeared from the wear tracks after 100 strokes. This indicates that most of oxide layer of the film surface was removed at an early stage of the friction test. This is supported by the absence of an SO_2 peak in the S 2p spectra of the wear tracks. In contrast, the CF_x peak in the C 1s spectra remained in the 100-stroke wear track. The influence of fluorine may persist for a long time [10].
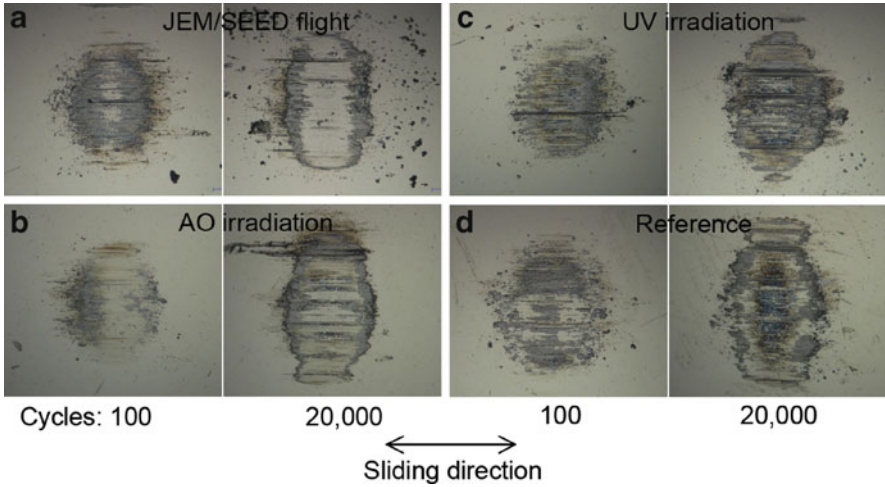
Fig. 7 Wear tracks of counterpart specimens for each sample after 100 strokes and 20,000 strokes
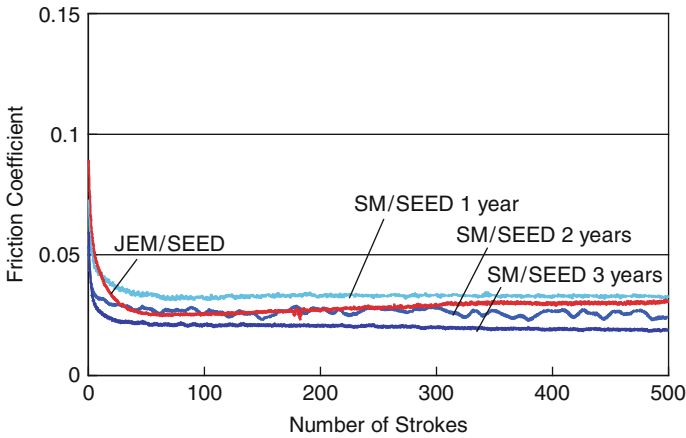
Fig. 8 Comparison of friction behavior of flight samples

4.3 Comparison of Friction Properties Between Two SEED Experiments

Figure 8 compares the friction behaviors of flight samples from the JEM/SEED and SM/SEED experiments. The friction coefficients of the SM/SEED flight samples at the beginning of the test were lower with increasing exposure duration. The friction coefficient of the JEM/SEED flight sample decreased from the start of the test in the same way as the first SM/SEED sample and reached the level of the second
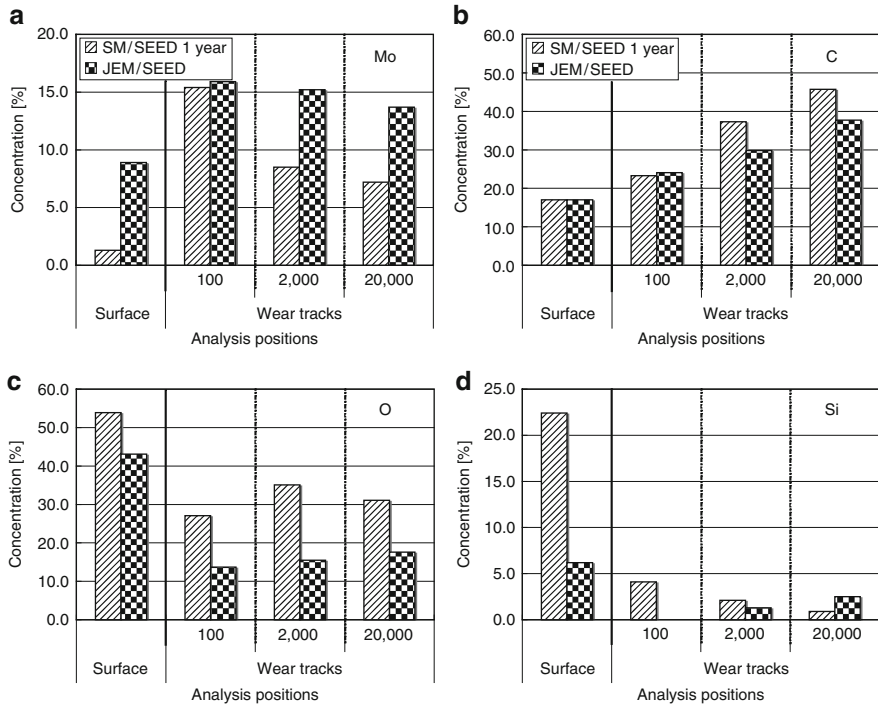
Fig. 9 Concentrations of typical elements by XPS quantitative analysis for the film surface and wear tracks of two flight samples (**a**) molybdenum, (**b**) carbon, (**c**) oxygen, and (**d**) silicon

SM/SEED sample. It then gradually increased and approached again the same level as the first SM/SEED sample. The friction behavior of the JEM/SEED flight sample was the almost same as those of SM/SEED samples. The slight differences seem to be due to differences in the fluences of AO and UV, and the amounts and types of contaminations.

Figure 9 shows the concentrations of typical elements on the film surface and the wear tracks, comparing JEM/SEED and SM/SEED flight samples. The biggest difference between the two SEED experiments is amount of silicon contaminations on the film surfaces. However, these had decreased to a few percent after only 100 sliding strokes, even for the SM/SEED flight sample that had more than 20 % of silicon detected on its surface. The molybdenum concentrations in the surfaces of flight samples differed due to contamination. However, for both JEM/SEED and SM/SEED samples, they increased to about 15 % by 100 sliding stroke and then decreased with further sliding. The carbon concentration increased as the number of sliding strokes increased. It is supposed from these results that silicon contamination was removed at early stage and molybdenum concentration increased. Due to selective etching of the binder material by atomic oxygen, the carbon concentration on the film surfaces was low. As the number of sliding strokes increased, the carbon concentration recovered and the molybdenum concentration gradually decreased.

5   Summary

Bonded MoS$_2$ film specimens were exposed to the low Earth orbit space environment in the JEM/SEED and SM/SEED experiments at different locations on the ISS. Changes in the tribological properties and surface compositions of the films after exposure were compared, with the following findings:

1. Silicon and fluorine contaminations were detected on the JEM/SEED flight sample. The amount of silicon contamination, which was detected also on the SM/SEED flight samples, was small.
2. The JEM/SEED flight sample and samples irradiated with AO and UV on the ground showed lower friction coefficients than a reference sample at the beginning of friction tests. The mechanism of the decrease in friction of the flight samples was similar to that of the AO-irradiated ground sample.
3. The friction coefficient of the JEM/SEED flight sample behaved similarly to those of SM/SEED flight samples.

References

1. Kimoto Y et al. (2009) SM/MPAC & SEED Experiment Overview. In: Proceedings of international symposium SM/MPAC&SEED experiment, JAXA special publication JAXA-SP-08-015E, 1
2. Kimoto Y et al (2009) Space environmental effect to materials on different position and operational period of ISS. In: Kleiman JI (ed) Proceedings of ICPMSE-9, Protection of materials and structures from space environment, Toronto, 20–23 May 2008. Published by AIP conference proceedings 1087, 207
3. Akiyama M et al (2005) Surface and tribological properties of the MoS$_2$-based lubricants retrieved from real LEO space environment: the first and second year results obtained by SM/SEED. In: Proceedings of 11th ESMATS, 347, Lucerne, 21–23 Sep. 2005
4. Tagawa M et al (2006) SM/SEED flight experimental results on molybdenum disulfide-based solid lubricants. In: Proceedings of 25th ISTS: 2006-c-22, Kanazawa, 4–11 June 2006
5. Matsumoto K, Akiyama M, Tagawa M (2008) Changes in triological characteristics of MoS$_2$ bonded film by exposure to low earth orbit space environment. J Vac Soc Jpn 51(8):554
6. Matsumoto K, Tagawa M, Akiyama M (2009) Effects of long-term irradiation with LEO environment effective factors on properties of solid lubricant. Trans JSASS Space Technol Jpn 7:Pc_31–Pc_36
7. Matsumoto K, Tagawa M, Akiyama M (2009) Tribological characteristics of bonded MoS$_2$ film exposed to AO, UV and real LEO environment by SM/SEED experiment. In: Kleiman JI (ed) Proceedings of ICPMSE-9, Protection of materials and structures from space environment, Toronto, 20–23 May 2008. Published by AIP conference proceedings 1087, 148
8. Tanaka Y et al (1998) New high vacuum test facilities for mechanical components (part 1) -UHV material property test facility and combined environment test facility. In: Proceedings of 21st ISTS, 98 -e-2.1
9. Caledonia GE, Krech RH, Green BD (1987) A high flux source of energetic oxygen atoms for material degradation studies. AIAA J 25:59
10. Matsumoto K, Suzuki M, Kimoto Y (2011) Evaluation of solid lubricant in JEM/SEED experiment. In: Proceedings of 28th ISTS, 2011-c-11, Okinawa, 5–12 June 2011

Instrumentation for Ground-Based Testing in Simulated Space and Planetary Conditions

Jacob Kleiman, Sergey Horodetsky, and Vitali Issoupov

Abstract This paper is an overview of instrumentation developed and created by ITL Inc. for simulated testing and performance evaluation of spacecraft materials, structures, mechanisms, assemblies and components in different space and planetary environments. The LEO Space Environment Simulator allows simulation of the synergistic effect of ultra-high vacuum conditions, 5 eV neutral atomic oxygen beams, Vacuum-Ultraviolet (VUV) and Near-Ultraviolet (NUV) radiation, and temperature conditions. The simulated space environmental conditions can be controlled in-situ using a quadruple mass-spectrometer, Time-of-Flight technique, as well as Quartz Crystal Microbalance sensors. The new NUV System is capable of delivering an NUV power intensity of up to 10 Equivalent Suns. The design of the system uses horizontal orientation of the 5 kW Mercury lamp, focusing of NUV radiation is achieved due to a parabolic reflector. To address the Lunar/Martian surface environments, the Planetary Environmental Simulator/Test Facility has been developed and built to allow for physical evaluation of the effects of the Lunar/Martian dust environments in conjunction with other factors (ultra-high vacuum or planetary atmospheric conditions, VUV/NUV radiation, thermal cycling, and darkness). The ASTM E 595/ASTM E 1559 Outgassing Test Facility provides the means for the outgassing test of materials with the objective to select materials with low outgassing properties for spacecraft use and allows to determine the following outgassing parameters: Total Mass Loss, Collected Volatile Condensable Materials, and Water Vapor Regained.

Keywords Atomic oxygen • Lunar/Martian dust • Outgassing testing • Space environment • VUV/NUV radiation

J. Kleiman (✉) • S. Horodetsky • V. Issoupov
Integrity Testing Laboratory Inc., 80 Esna Park Drive, #7-9, Markham, ON L3R 2R7, Canada
e-mail: jkleiman@itlinc.com

1   Introduction

Materials used in space are exposed to vacuum, ultraviolet radiation from the Sun, and space radiation, that results in materials and functional components damage, as well as spacecraft charging (electrostatic discharge effects), micrometeoroids and debris impacts, and thermal cycling. The significance of ground-based simulation of the near-Earth and planetary environments and their effects on spacecraft materials, systems, structures, and components consists in the major objective to create a simulation infrastructure and abilities for lifetime prediction of spacecraft materials, systems, and components through on-ground experimental simulation of the comprehensive effects of various factors of the low Earth orbit (LEO), geostationary Earth orbit (GEO) space environments, as well as surface conditions of other planets (Moon, Mars, Venus, etc.) [1–7]. The combination and comparison of both in-flight and ground-based sophisticated experiments in space simulators are needed for the development of predictive understanding of the materials degradation and protection mechanisms in various space environments. Those space science materials issues are essential for the development of advanced materials and coatings for the current and future missions.

The main innovative approach proposed by ITL Inc. for development of new space simulation technologies is the development of unique instrumentation and technology for testing and predicting the lifetime of spacecraft materials and components in simulated near-Earth environments, as well as in simulated environments of other planets (Moon, Mars, Venus, etc.). The approach to simulation of different space and planetary environments is based on the most reliable up-to-date environmental models collected from various literature sources, analyzed and implemented in the unique computer software to allow for experimental conditions to be chosen that will simulate the comprehensive effect of the environment during a space mission.

Simulation of the near-Earth and planetary space environments produces a number of strict technological and physical criteria to individual factor sources, such as, for instance, high vacuum better than 10^{-6} Torr provided by oil-free pumping. The vacuum chamber geometry should allow for simultaneous exposure to various space factors and in-situ monitoring of physical properties of the irradiated specimens, as well as physical parameters of individual simulated factors (Time-of-Flight (ToF) technique, Quartz Crystal Microbalance (QCM) sensors, atomic emission spectroscopy, etc.). The structural and chemical integrity of materials when exposed to the environmental conditions of space is evaluated using the static and dynamic outgassing tests at high temperatures.

2   The VEMES™ LEO Space Environment Simulator

Materials interaction with atomic oxygen in its main ground state $O(^3P)$ within the thermal and hyperthermal energy ranges along with other LEO environmental conditions (vacuum, UV, temperature conditions) is essential for studying materials
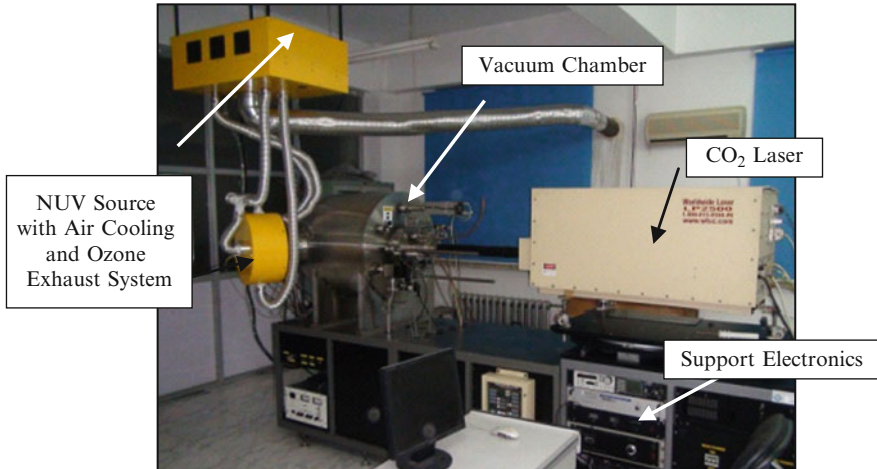
Fig. 1 General view of the VEMES™ facility with the coaxial AO source

behavior in any LEO environment. ITL Inc. in 2003–2005 has designed, developed, and created the modern fully computerized Variable Energy Multifunctional Environment Simulator (VEMES™) simulator system (Fig. 1) that has the ability to simulate the synergistic effect of a number of LEO environmental factors, including:

- Ultra-high vacuum conditions ($<10^{-7}$ Torr);
- Microwave (thermal) oxygen plasma;
- Hyperthermal Atomic Oxygen (~5 eV);
- Vacuum-Ultraviolet (VUV) radiation (115–200 nm);
- Near-Ultraviolet (NUV) radiation (1–10 Eq. Suns @ 254 nm); and
- Thermal cycling between $-160\,^{\circ}$C to $+350\,^{\circ}$C.

The VEMES™ system generally contains the following three major modules: vacuum chamber and pumping system; physical sources of space factors for accelerated testing and characterization; and an advanced computerized operational and control module. The facility is mounted on three racks, the first one serving as a vacuum chamber support, the second one containing the mechanical pumps, pneumatic and water cooling systems, with the third rack being used to support the high precision laser optical system. The main technical parameters of the VEMES™ system, its components, source, and systems are presented in Table 1. The VEMES™ facility is currently operational at Harbin Institute of Technology (China). Each individual system of the facility is described below.

Vacuum system. The vacuum VEMES™ system includes the hemispherical-cylindrical vacuum chamber that is manufactured from stainless steel with all vacuum connections designed for high vacuum conditions. The chamber has a volume of about 0.8 m^3 and allows for accommodation of relatively large samples.

Table 1 Main technical parameters of the VEMES™ facility

	Parameter	Value
Vacuum system	Volume, m^3	0.3
	Pumping speed (N_2), l/s	1,000
	Basic vacuum, Torr	10^{-7}
	Distance from nozzle to samples, cm	25–45
Pulsed laser	Laser energy, Joule	~5.5
	Laser wavelength, μm	10.6
	Maximum frequency, Hz	4
Laser AO source	Energy, eV	~5
	Beam flux, atom/cm^2/s	$(3–5) \times 10^{15}$
	Accelerating factor	10–50
	AO beam diameter/sample size	200–225 cm^2
Microwave AO source	Type of RF generator	Magnetron
	RF generator power (kW)	0.1–1.0
	RF generator frequency (MHz)	2,450
	Energy (eV)	0.5–1.5
VUV source	Type of VUV Source	Hamamatsu L2D2 lamp
	Wavelength, nm	115–200
NUV source	Type of NUV source	Mercury lamp
	Wavelength, nm	200–400
	NUV intensity	Up to 10 Eq. Suns
Thermal cycling	Temperature range, °C	−160/+350
	Temperature rate, °C/min	0–10
	Temperature control accuracy, °C	±1

The vacuum chamber is pumped by a turbo pump (Varian TV 1001 Navigator) and two auxiliary rotational mechanical pumps (DS-402 and DS-602). The pumping speed of the Varian TV 1001 Navigator turbo pump of 1,000 l/min allows for quick plasma post-discharge exhaust and for maintaining the high vacuum conditions during operation of various sources of the VEMES™ facility.

Sample Positioning System (SPS). The sample positioning system (SPS) presented in Fig. 2 is an originally designed set-up installed inside the vacuum chamber. The SPS design permits precise sample positioning within a travel distance of 250 mm and fast sample exchange, as well as computer-controlled heating, cooling, and thermal cycling. The sample holder plate representing a disc of 20 cm in diameter is attached to the front of the thermal assembly of the SPS.

Cooling of the system is provided by liquid nitrogen supplied through stainless steel tubes. Heating is done using a set of heaters located inside the cooler. To reduce cooling time when switching from high to low temperatures and heating from cryo- to room temperatures, compressed air is used. It allows significantly speeding-up the heating/cooling/heating cycle time that is very important in thermal cycling experiments simulating different environments. Compressed air is also used to maintain the achieved temperature. The temperature control system allows
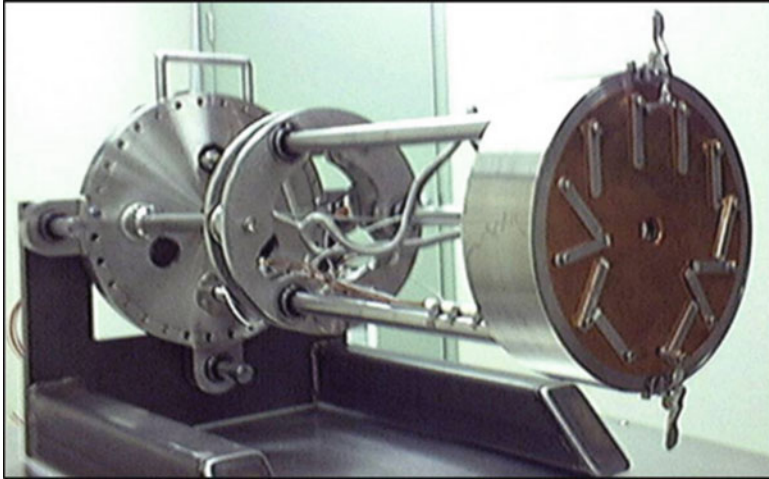
Fig. 2 Sample positioning system (SPS) of the VEMES™ facility

measuring the temperature with an accuracy of 1 °C and temperature holding (−150 °C to +150 °C) or controlled and programmable thermal cycling between −160 °C and +350 °C with an accuracy of 2 °C.

Laser AO Source. ITL Inc. has designed and manufactured several prototypes of the laser AO source with either lateral or coaxial laser beam delivery that use the common principles of formation of continuous and pulsed AO beams under high-vacuum conditions [8–10]. The main components of the AO source (see Fig. 3) are the CO_2 IR laser with an optical system, pulsed gas valve, conical nozzle and the synchronization system. Samples exposed to atomic oxygen beam are located on the sample holder (9) (see Fig. 2). In case of *lateral delivery* of the laser beam in the AO source (Fig. 3a), the laser pulse is delivered into the VEMES™ chamber by means of the optical system consisting of a light guide, ZnSe portview (6), and a set of IR mirrors, focused by a ZnSe lens with 500 mm focal distance (5) adjusted using a focusing system (4). A flat molybdenum mirror (7) fixed on a step-motor computer controlled mirror support (8) allows the incidence angle of the laser beam to be adjusted between 10 ° and 12 ° and the laser pulse to be reflected into the conical nozzle (10). In the *coaxial mode* of the AO source (Fig. 3b), the laser beam delivery system is different. In this case, the source operates without the optical system and IR mirrors, and the ZnSe focusing lens is used as a portview at the same time. Due to such a modification of the source, the laser beam energy loss could be significantly minimized [11, 12].

Microwave AO Source. In contrast to the laser AO source, the RF oxygen plasma source generates a continuous flux of atomic oxygen. When developing the microwave AO system of the VEMES™, we reviewed all known conventional designs (Surfatron [13], Resonance RF Plasma Source [14], and Plasma Torch [15, 16]) and
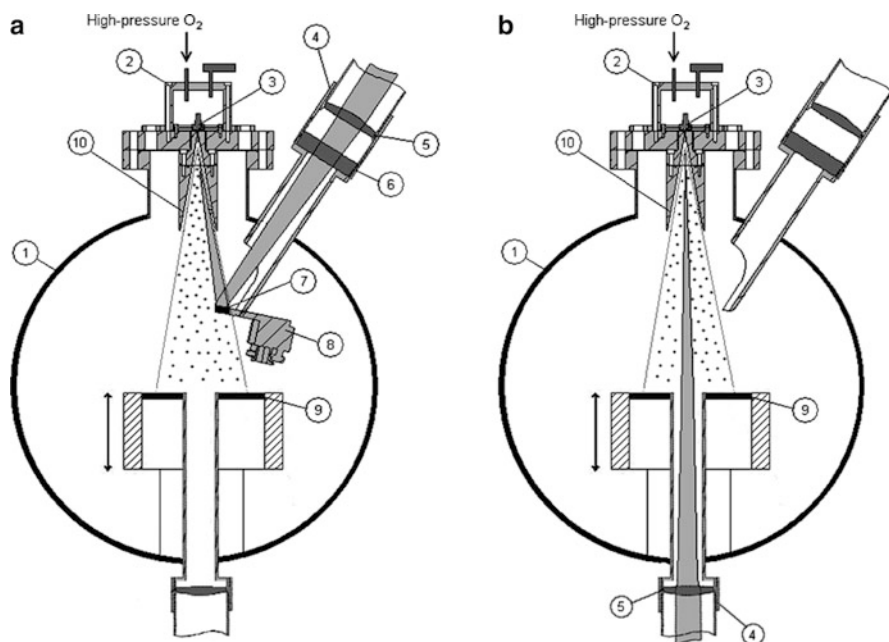
Fig. 3 Schematic presentation of the lateral (**a**) and coaxial (**b**) laser AO sources: (*1*) vacuum chamber; (*2*) high pressure gas chamber; (*3*) pulsed valve; (*4*) adjustable lens holder; (*5*) focusing ZnSe lens; (*6*) ZnSe viewport; (*7*) molybdenum mirror; (*8*) adjustable mirror support; (*9*) sample holder

employed the commercial highly reliable AX7610 microwave plasma torch. The magnetron head operates with an output frequency of 2.45 GHz and has a maximum output power of 1.2 kW. A differential pumping system provides high vacuum conditions in the VEMES™ chamber during plasma torch operation under a working pressure of 1–8 Torr. The main technical parameters of the RF oxygen plasma source are summarized in Table 1.

VUV/NUV source. The main part of the VUV source installed on the VEMES™ facility is a Hamamatsu L2D2-2000 series deuterium lamp with magnesium fluoride windows, model L7293. The body of the lamp is located outside of the vacuum chamber with its end-tube pushed through o-ring compression fittings to provide a vacuum seal. The lamp body is placed in a housing and cooled with forced air. The source provides a continuum spectral output between approximately 115 and 200 nm, with the major UV intensity peaks located at 125 and 160 nm. The newly designed and developed NUV System is presented in detail below.

Presently, ITL Inc. is developing and manufacturing two improved prototypes of the LEO simulator system that will operate at Lanzhou Institute of Physics (China) and at the Skobeltsyn Research Institute of Nuclear Physic (Moscow State University, Russia).
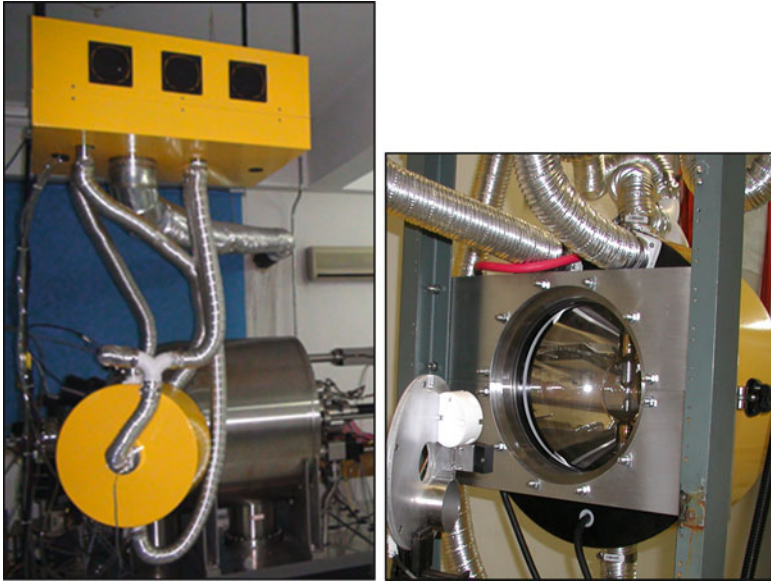
Fig. 4 NUV system installed at the VEMES™ facility (*left*) and the front view of the NUV source with IR filter (*right*)

3 Near-Ultraviolet (NUV) System

ITL Inc. has recently designed and built a Near-Ultraviolet (NUV) System capable of delivering a peak NUV intensity of up to 10 Equivalent Suns (ES) in the vicinity of the 254 nm wavelength. The NUV Source is adapted for installation on the vacuum chamber of the VEMES™ simulator facility as shown in Fig. 4. The NUV System is also serving a 12″ flap door to the interior of the vacuum chamber (see Fig. 1) for sample introduction and exchange.

A 5 kW Mercury lamp (Bachur and Associates Co.) having radiation output in the range of 180–400 nm and providing greater intensity in a smaller area (greater brightness) than the Xenon lamp, because of the smaller arc size, has been chosen for the present design. The created NUV System can be used to conduct accelerated testing of candidate spacecraft materials and thermal control coatings in the VEMES™ simulator chamber.

The NUV System includes the following main parts:

• Mercury NUV lamp;	• IR filter;
• NUV lamp housing;	• NUV intensity control sensors;
• Parabolic reflector;	• Intensity-controlling 5,000 W power supply; and
• Cooling system;	• Mechanical attachment to the VEMES™ facility.

Three types of reflectors (semi-spherical, elliptical, and parabolic) can be used for focusing NUV radiation of the NUV source. In the design stage, computer

modeling of systems with three different types of reflectors (semi-spherical, elliptical, and parabolic) for focusing the NUV radiation has been performed in order to calculate the NUV power intensity in the focal points of each type of the reflector. An elliptical reflector would require an Optical System containing one condenser lens and 1–2 focusing lenses to deliver the NUV radiation from the NUV source to the vacuum chamber. Therefore, the developed NUV System includes the parabolic type of reflector, as it allows operating the NUV source without any additional Optical System.

Cooling System. Due to high operation temperatures, an efficient cooling system was designed to overcome the overheating problem of the NUV lamp and heat sinks for reliable performance of the NUV source. Taking into account high voltage isolation problems, the air cooling system was chosen. The cooling system uses a cooler blowing air into the NUV system and expelling hot air through an outlet vent. Calculations for efficient air flow have been performed to help with the design of the geometry for air flow inside the NUV system housing, as well as the cooling pump. The required output of the cooler pump was estimated to be, at least, 4.4 m³/min. Temperature feedback is provided by a special temperature sensor that allowed monitoring the temperature of inlet and exhaust air. Incoming air will be filtered to keep out dust and contaminants. The built-in forced-air cooling functions ensure long-term life of the NUV lamp.

Temperature control of the inlet and exhaust air is used to adjust the air flow rate and to ensure the optimal operation temperature of the NUV Mercury lamp (around 200 °C), providing the optimal performance of the lamp. Operation of the NUV system requires extra security to prevent overheating of the NUV lamp that could lead to lamp explosion. By measurement and monitoring the inlet and exhaust air temperature, the NUV source control system is able to provide security features for reliable performance of the NUV source. Note that the air cooling system exhaust contains ozone that represents a danger for the operational personnel, with a maximum safe allowable level in the air of 0.10 ppm.

IR Filter. It was estimated that the 5 kW Mercury lamp generates more than 1 kW of IR radiation. Therefore, an IR filter was suggested to avoid excessive overheating of the NUV system and thermal damage to the samples. The IR water filter (see Fig. 4, *right picture*) was designed in the form of a leakproof cavity placed between two discs transparent for NUV radiation and filled with distilled water, to absorb most part of IR radiation generated by the powerful NUV lamp. Based on ITL's experience, a layer of water 1″ in thickness absorbs almost 100% of IR radiation. The IR filter is integrated into the NUV system support, with the back plate of the IR filter serving as a portview for the vacuum chamber of the VEMES™ facility.

As far as the implemented IR filter absorbs most part of IR radiation generated by the NUV lamp, the filter would become overheat within a few minutes. A closed-loop running water system was designed, built, and used to avoid the water overheating problem. Water running through the IR filter cavity is cooled down in a specially designed heat exchanger by using an external closed-loop running water of a laboratory chiller. Monitoring the IR filter temperature during operation of the NUV source indicated that the water cooling system was able to prevent

water inside the IR filter from boiling. The IR filter allowed achieving good results in terms of reducing the IR part of NUV lamp radiation.

NUV Intensity Control Sensors. An NUV intensity control sensor was developed using special NUV photodiodes from Bachur and Associates Co. intended to monitor the NUV power intensity at two specific wavelengths: 254 and 260 nm. Since the objective was to create a powerful NUV source with peak intensity in the region of wavelengths most harmful to the polymers, it was required to develop a control sensor for NUV power intensity measurement as a function of the wavelength, distance from the NUV source, as well as input power and operational conditions of the NUV source. This intensity control sensor would also be used to compensate for NUV power intensity drift during source operation.

The UV measurement systems have the capability to function over a wide range of selected spectrums, intensities (mW/cm^2) and/or energy (mJ/cm^2). It is known that each type of NUV lamps has a specific dependence of NUV power intensity on the input power, i.e. the $I = I(P)$ curve. For the 5 kW Mercury lamp, a range of input power from 0.35 to 5 kW was investigated. It was found that the NUV intensity was varying between 0.5 and 10 ES. The input power should be from 2.5 to 4.5 kW to achieve an intensity of the NUV radiation from the NUV source between 3.5 and 10 ES. The selected operational conditions of the NUV source guarantee its normal operation. The characteristic irradiation spectrum delivered by the NUV source compared to the Solar spectrum [17] is shown in Fig. 5.

Power Supply. The designed NUV system uses an intensity-controlling 5,000 W power supply from Bachur and Associates Co. The Control Sensors provide the capability of monitoring and controlling the intensity within a specific spectrum. Dual channel optical feedback loop allows better than ±2% intensity precision and long term repeatability. The power supply also incorporates a "Change Lamp" and "Maximum Power Operation" alarm. The power supply has a detachable, three-wire power cord for connection to the power source and to a protective ground.

4   The Planetary Environmental Simulator/Test Facility

To respond to the space technology development strategies of the Canadian Space Agency, ITL Inc. has designed, developed, and manufactured a Planetary Environmental Simulator/Test Facility (see the general design of the facility in Fig. 6) that will be used for testing and lifetime evaluation of candidate spacecraft materials and mechanical systems, space suits, and planetary mission crew habitats [18, 19]. The facility includes a vacuum chamber and a number of environmental sources to provide the following environmental factors of the planetary surface conditions of the Moon and Mars:

Ultra-high vacuum or atmospheric conditions;
Lunar/Martian dust conditions;
VUV/NUV radiation;
Thermal conditions/thermal cycling; and
Darkness/illumination conditions.
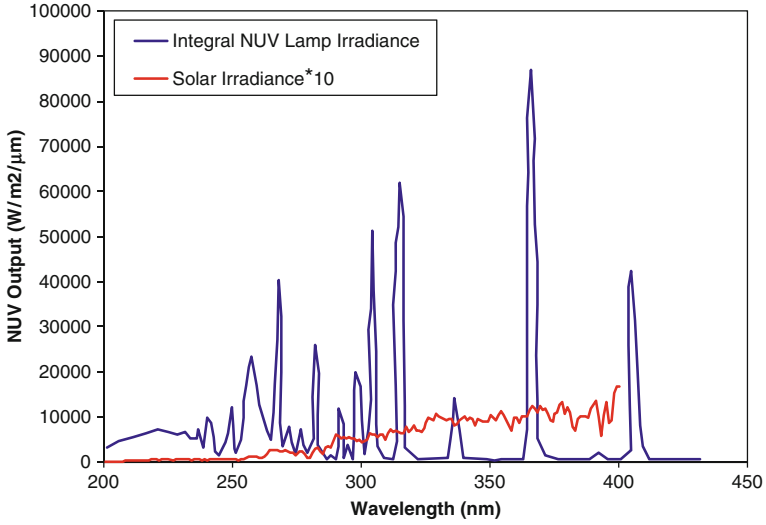
Fig. 5 NUV output of the 10 ES mercury lamp compared to the solar spectrum [17]

Fig. 6 General view of the planetary environmental simulator/test facility

The facility can be equipped with drive systems for translational and rotational movements and with thermal-vacuum test rigs to allow for mechanical testing and life time evaluation of various spacecraft and planetary rovers mechanisms (robotics arms, bearing units, vision sensors, solar arrays, thermal protection structures and thermal condenser materials, power systems, etc.) in simulated Lunar/Martian

planetary environments. The design of the simulator facility allows testing where dust would be the most important environmental factor to verify the operational hardware, including drive, deployment, docking, and vision systems, mechanical mechanisms and tribological components. The main objective of testing would be verification of dust tolerant designs, as well as studying and improvement of the dust and other environmental factors mitigation strategies. The technical parameters of the facility are summarized in Table 2.

The high-vacuum chamber is cylindrical in shape made of stainless steel with one of its ends designed to have a semi-spherical shape. The cylindrical part of the simulation chamber is 30″ in diameter and ~51″ long. The design of the vacuum chamber includes a detachable semi-spherical front for installation of a larger sample, a cylindrical base, and a flat back plate. All flanges are of ConFlat (CF) type with copper gaskets sealing. The facility is equipped with all necessary electrical, control, and motion feedthroughs. A pumping system to evacuate the chamber includes oil-free mechanical scroll and rotary pumps with up to 4,500 l/s pumping speed to achieve high vacuum (better than 10^{-7} Torr). The vacuum pumping system of the simulator facility has an essential requirement of being robust to any dust that would find its way into it, therefore, a Dust Filter has been developed and used to prevent dust particles from getting into the vacuum pumps. The Dust Filter includes five baffle plates with alternating windows at the "top-bottom-top-bottom-top" positions covered with a fine metallic.

The sample holder/sample transfer system is an ultra-high vacuum set-up installed inside the vacuum chamber and designed to hold and position samples of different shapes and nature, allowing for heating, cooling, and thermal cycling of the samples (see a system prototype in Fig. 2). The sample holder system can be installed either from the back side or on the top at a 12″ flange of the vacuum chamber to allow for appropriate mounting and testing of the samples. Heating and cooling of the thermal control platform can be provided at a maximum temperature rate of ~8 °C/min, temperature holding (−150 °C to +150 °C) or controlled and programmable thermal cycling between −160 °C and +350 °C are allowed through a computer-controlled program. To allow for durability testing of mechanical systems in simulated Lunar/Martian environment, a rotation feed-through and drive system can be mounted at the sample holder system (see the internal configuration of the simulator chamber in Fig. 7).

The dust particles source developed to produce a dust cloud in the facility includes a paddle actuator located inside the source driven by a computer-controlled step-motor. JSC-1A lunar soil simulant or similar can be used for operation of the dust source. The source allows obtaining different configurations and intensity of generated dust cloud. It is used for studying the tribological aspects of lunar dust and dust-related phenomena within mechanical components, such as adhesion, abrasion, and wear mechanisms, as well as the effects of vacuum, lunar thermal cycles, radiation, and electrostatics. A Vacuum-UV (VUV) source providing a continuum spectral output between approximately 115 and 400 nm is

Table 2 Main technical parameters of the planetary environmental simulator/test facility

	Parameter	Value
Vacuum system	Volume, m^3	~0.7
	Pumping speed (N_2), l/s	2,050
	Basic vacuum, Torr	$<2 \times 10^{-7}$
Dust source	Lunar soil simulant	JSC-1AF
	Dust thermal conditioning	RT/+200
	Dust activation	VUV
Sample holder/sample transfer system	Holder size, cm^2	314
	Temperature range, °C	$-180/+200$
	Mechanical testing	Rotary or translational
VUV source	Type of VUV source	Hamamatsu L2D2 lamp
	Wavelength, nm	115–200
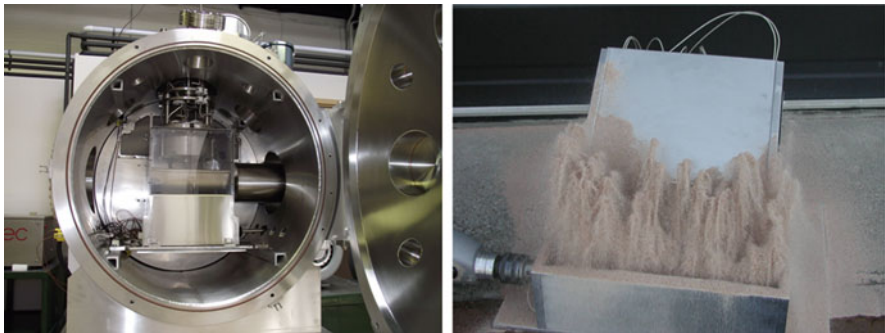
Fig. 7 Internal configuration of the simulator chamber with dust source (*left*) and an example of generated dust cloud (*right*)

used to achieve electrostatic charging of dust particles. Vacuum pressure sensors, electrical probe to monitor the dust particles charge (Langmuir probe) and thermocouples are the basic instrumentation to monitor the exposure conditions and to follow degradation of the performance and physical properties of exposed specimens.

The modular design of the facility allows to include a number of modular space environment sources such as Near-UV (NUV), variable-energy proton and electron radiation, rocket's exhaust contaminations, microgravity, etc., as well as a variety of fixtures and rigs for testing of spacecraft systems and mechanisms, tribological testers, etc. The Lunar Environmental Simulator/Test Facility and its advanced versions can be considered as the most comprehensive and sophisticated space and planetary environmental simulators created to support the design, testing, and validation of newly developed space and planetary robotic hardware for long-term safe space exploration missions.

5 The ASTM E595/E1559 Outgassing System

Outgassing of organic materials can be approached as a surface evaporation combined with diffusion for bulk contaminant species. These species can be either initially present components, or decomposition products. Contamination exists in many forms, e.g. particulates, chemical species, vapor condensation, corrosion, etc. Materials should have low outgassing rates at normal operating temperatures and the outgassing should consist of a minimum of condensables at the temperatures of nearby surfaces.

The ASTM E595 [20] characterizes the outgassing property of candidate materials and components in a controlled and repeatable way by measuring the amounts outgassed from the bulk of a material normalized with respect to sample size. This test method serves as a screening technique for critical items when exposed to specific environmental conditions. NASA historically has used the following screening levels for rejection of spacecraft materials: no more than 1.00% Total Mass Loss TML, and no more than 0.10% Collected Volatile Condensable Materials (CVCM). Individual users may have particular requirements for outgassing that are not directly considered by this method.

Responding to the growing demand from international community, ITL Inc. has developed a general design of an outgassing facility that accommodates the set-up for both ASTM E595 and ASTM E1559 test methods. The developed Outgassing System features oil-free pumping with a scroll pump and two turbo pumps (77 l/s and 250 l/s) to obtain vacuum conditions better than 10^{-6} Torr and the test operation is made fully computer-controlled. The general view and the specification of different components of the ASTM E595/E1559 Outgassing System are presented in Fig. 8.

In the ASTM E595 test material testing is carried out by placing known amounts of material in $10 \times 12 \times 6$ mm^3 container boats that are placed inside a receptacle within a temperature controlling heated copper bar. The receptacle has a venting port facing a collector plate to measure the materials with lower volatilities. The design of the copper heating bar of the ASTM E595 sample set-up is shown in Fig. 9. For the test, the copper bar and the materials under test are held at 125 °C and the collectors at 25 °C and the outgassing test is continued for 24 h. A forming press to produce Al container boats for sample enclosure is offered as an option.

The ASTM E1559 Standard test method [21] was established in 1993 as an improved version of the ASTM E595 Standard in order to provide a method for the characterization of materials outgassing kinetics. Test ASTM E1559 uses a method that allows the total mass loss to be determined through the use of three Quartz Crystal Microbalances (QCMs) to be maintained at 90 K (−183 °C), 160 K (−113 °C), and 298 K (25 °C).

The ASTM E1559 requires that the QCMs consist of two crystals (one for mass collection and one for reference) and that they have a sensitivity of at least 1×10^{-8} g/cm^2/Hz at 298 K (25 °C). This is typically accomplished with crystals that have natural frequencies of 10 MHz to 15 MHz. The E1559 test facility
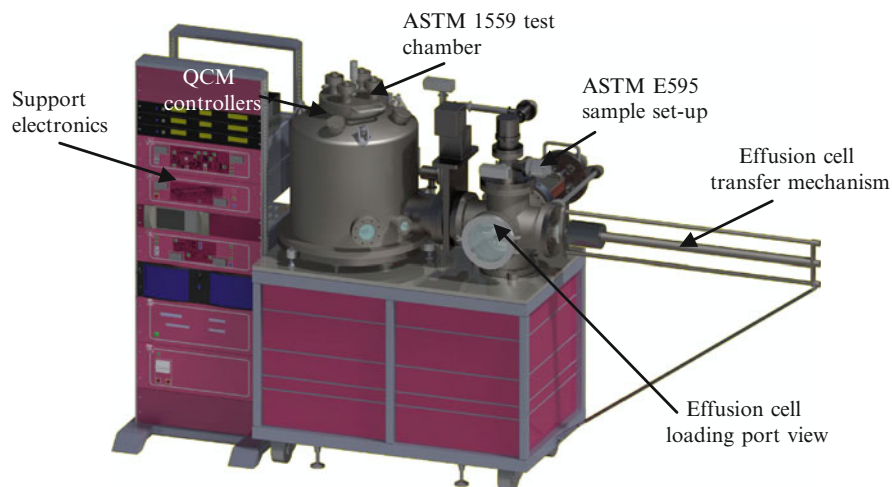
Fig. 8 General view of the ASTM E595/E1559 outgassing system
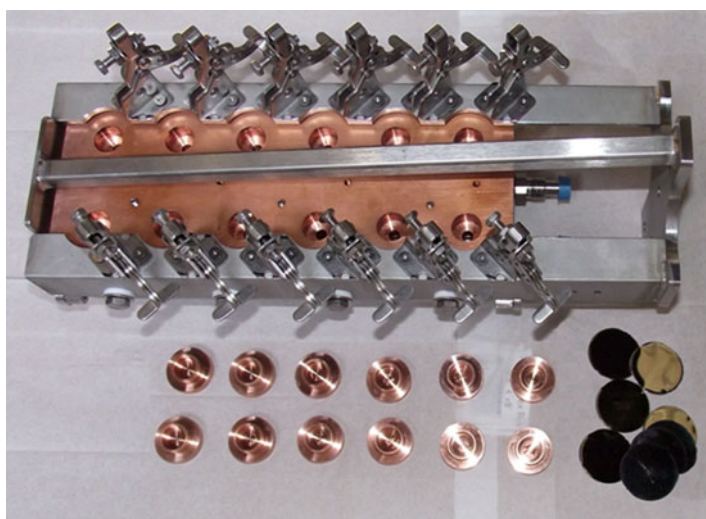
Fig. 9 Heating bar with 12 specimen compartments and 12 collector plates

offered by ITL uses QCMs with 15 MHz crystals that have a sensitivity of 1.73×10^{-9} g/cm^2/Hz. The crystals are 1.27 cm in diameter and optically polished and plated with gold [22]. The pair of crystals is designated as a sensor crystal and a reference crystal.

The effusion cell is a cylindrical container approximately 65 mm inside diameter by 50 mm deep, and is machined from stainless steel 304. The integrated heater ensures uniform temperature distribution throughout the inner cavity. The effusion cell has a detachable cover plate which allows for insertion of material samples.

This lid has a cylindrical orifice of 3.0 mm in diameter by 3.0 mm long providing the appropriate flux distribution. The cell has an integral temperature sensor and heater, and control system which permits operating the cell from ambient to 398–573 K (125–300 °C) with a precision of 0.5 K or better. The effusion cell is positioned inside the test chamber at 150 mm from the surface of the sensing crystal in each QCM so that the center of the cell orifice exit plane coincides with the intersection point of the QCM axes. The cell orifice thus has the same view factor of 415.08 cm^2 to the all QCMs.

The test chamber is evacuated to a vacuum level on the order of ~10^{-7} Torr before QCM cooling is commenced. The QCMs are maintained at approximately 298 K until the chamber liner and baffles have reached temperatures of less than ~75 K. At this point, the QCMs heaters are set to temperatures varying from 90 K for the coldest to as high as 298 K for the warmest. To provide low temperature, the QCM sensors are attached to liquid nitrogen reservoirs. The QCMs are thermally shielded from each other to allow the temperatures to be independently controlled. Once these temperatures have become constant, outgassing data can be collected.

The sample, on the order of 10–20 g, is placed inside the effusion cell that is mounted in the interlock chamber (see Fig. 10). After the interlock chamber has been evacuated to a level of approximately 10^{-9} Torr, the gate valve is opened and the effusion cell is moved manually using the transfer mechanism shown in Fig. 9 to its location inside the main chamber as shown in Fig. 10. Once the effusion cell is in place, the effusion cell temperature controller is set to the desired temperature, usually to 398 K (125 °C), and the frequencies of all QCM's are recorded as a function of time with a 1 min time interval. The time required for completion of an outgassing test varies depending on the needs of the user. In many instances outgassing times of up to 5 days are used in order to determine the long-term outgassing rates.

After the condensed mass of the outgassing products has reached a plateau, the effusion cell is withdrawn from the chamber and back into the interlock chamber. At this point the QCM temperatures are commanded to a much warmer temperature, usually to 398 K (125 °C) at 1 K/min, to boil off the condensed contaminants. An RGA 300 quadruple mass spectrometer is used to analyze the partial pressure of the residual gas atmosphere during the QCM sensor warm-up and to quantitatively determine the species observed. Identification of outgassed species is usually not within the normal scope of work for this testing because of the requirement for more sophisticated analytical capabilities.

Upon completion of the testing, the material test sample is removed from the effusion cell and weighed. The value obtained is compared to the value prior to the start of the outgassing measurements. The total mass loss is determined from these data and then compared with that obtained from the calculated values determined using the QCM deposition data.

The ASTM E595/E1559 Outgassing System is well suited to measure outgassing/deposition kinetics of volatiles released from materials. It can be used also to produce the data necessary to support mathematical models used for the prediction
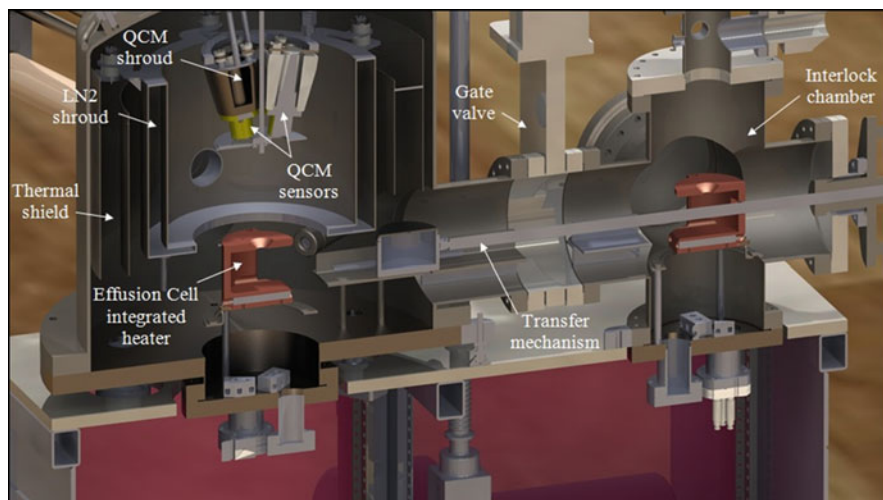
Fig. 10 Transferring the effusion cell from Interlock chamber into ASTM E1559 test chamber

Table 3 Main technical parameters of the ASTM E595/E1559 outgassing system

	Parameter	Value
Vacuum system	Volume, m^3	~0.2
	Pumping speed (N_2), l/s	81/300
	Basic vacuum, Torr	$<10^{-9}$
E595 test	Test temperature, °C	125
	- Measuring the TML, CVCM, and WVR	
E1559 test	QCM frequency, MHz	15
	Sensor sensitivity, g/cm^2 Hz	1.73×10^{-9}
	Sensors temperature, °C	$-183/-113/+25$
	Mass range, AMU	1–300
	- Outgassing and deposition kinetics testing	
	- Measuring the TML, CVCM, and OGR	
	- QCM thermogravimetric analysis (QTGA)	

of molecular contaminant generation, migration, and deposition. Table 3 provides the technical characteristics of the ASTM E595/E1559 Outgassing System.

References

1. Tribble AC (2003) The space environment: implications for spacecraft design. Princeton University Press, Princeton
2. Huheey JE, Keiter EA, Keiter RL (1993) Inorganic chemistry: principles of structure and reactivity, 4th edn. Harper Collins College Publishers, New York

3. Scurat VE, Nikiforov AP, Ternovoy AI (1994) Investigations of reactions of thermal and fast atomic oxygen (up to 5 eV) with polymer films. In: Proceedings of the 6th international symposium on materials in a space environment, Noordwijk
4. Koontz SL, Albyn K, Leger LJ (1991) Atomic oxygen testing with thermal atom systems: a critical evaluation. J Spacecr Rocket 28(3):315–332
5. Heiken GH et al (1991) Lunar sourcebook: a user's guide to the Moon. Cambridge University Press, New York
6. Gaier JR et al (2009) Lunar simulation in the lunar dust adhesion bell jar. Report NASA/TM-2007-214704
7. Craven P, Vaughn J, Schneider T, Norwood J, Abbas M, Alexander R (2009) MSFC lunar environments test system (LETS) system development. Third lunar regolith simulant workshop, Huntsville, 17–20 Mar 2009
8. Caledonia GE, Krech RH, Green BD (1987) A high flux source of energetic oxygen atoms for material degradation studies. AIAA J 25:59–63
9. Caledonia GE, Krech RH, Green BD, Pirri AN (1990) US Patent No 4,894,511
10. Krech RH, Caledonia GE (1993) AO Experiments at PSI. Report PSI
11. Kleiman J, Horodetsky S, Sergeyev V, Issoupov V (2006) Critical review of the design of space environment simulators: lessons learnt. In: Proceedings of the 10th international symposium on materials in a space environment/8th international conference on protection of materials and structure from the LEO space environment, Collioure, 19–23 June 2006
12. Kleiman J, Horodetsky S, Sergeyev V, Issoupov V (2006) CO_2-laser assisted atomic oxygen beam sources: research, development, and optimization of operational parameters. Ibid
13. Tennyson RC (1991) Atomic oxygen effects on polymer-based materials. Can J Phys 69:1190–1208
14. Kudryavtsev NN, Mazyar OA, Sukhov AM (1993) Apparatus and techniques for the investigation of methods of generating molecular beams. Physics-Uspekhi 36(6):513–528
15. Kleiman JI, Iskanderova Z, Gudimenko Y, Horodetsky S (2003) Atomic oxygen beam sources: a critical review. In: Proceedings of the 9th international symposium on materials in a space environment, Noordwijk, 16–20 June 2003
16. Morison D, Tennyson RC, French YB (1988) Microwave oxygen atom beams source. In: 4th European symposium on spacecraft materials in space environment, CERT, Toulouse
17. Standard Solar Constant and Zero Air Mass Solar Spectral Irradiance Tables (2006) ASTM E490-00a
18. Horodetsky S, Issoupov V, Kleiman J (2010) A planetary environmental simulator/test facility. In: Proceedings of the 26th space simulation conference, Annapolis, 18–21 Oct 2010
19. Kleiman J, Horodetsky S, Issoupov V (2011) A planetary environmental simulator/test facility. In: Proceedings of the 10th international conference on protection of materials and structure from the LEO space environment, Okinawa, 12–17 June 2011
20. Standard Test Method for Total Mass Loss and Collected Volatile Condensable Materials from Outgassing in a Vacuum Environment (2007) ASTM E595
21. Standard Test Method for Contamination Outgassing Characteristics of Spacecraft Materials (2009) ASTM E1559
22. CrystalTek TQCM Operation Manual (2011) CrystalTek

A Planetary Environmental Simulator/ Test Facility

Jacob Kleiman, Sergey Horodetsky, and Vitali Issoupov

Abstract   Under a 2-year program funded by the Canadian Space Agency, ITL Inc. is developing and manufacturing a Planetary Environmental Simulator/Test Facility to be used for testing and life-time evaluation of candidate spacecraft materials and mechanical systems, space suits, and planetary mission crew habitats. The *basic* facility will include a vacuum chamber and a number of environmental sources to simulate the planetary surface environments, including dust particles, UV radiation, temperature conditions and darkness, as well as simple fixtures and test rigs enabling to conduct mechanical testing of planetary rovers' components.

The stainless steel high-vacuum chamber is cylindrical in shape with one of its ends designed to have a semi-spherical shape. The cylindrical part of the simulation chamber is $30''$ in diameter and $\sim51''$ long. The sample holder/sample transfer system allows a total displacement of $\sim12''$ inside the chamber and allows for heating, cooling, and thermal cycling of the samples. The *basic* dust particles' source includes a lunar/Martian soil simulant container, a dust refill compartment, and a funnel-like enclosure in which the dust cloud is generated and designed to confine the dust and prevent it from spreading all over the chamber. The dust is activated by a paddle actuator located inside the source, allowing generating dust clouds of different intensity and configuration. The source is designed also to mix the particles during the dust simulant conditioning stage.

A multi-stage evolutionary path of the facility is outlined with the aim to create an *advanced* test facility that will be used to support the design, testing, and validation of Canadian space robotic hardware.

Keywords   Lunar dust • Lunar environment • Planetary environment simulator

J. Kleiman (✉) • S. Horodetsky • V. Issoupov
Integrity Testing Laboratory Inc., 80 Esna Park Drive, #7-9, Markham, ON L3R 2R7, Canada
e-mail: jkleiman@itlinc.com

1 Introduction

The Moon remains a favored target for the human exploration missions outlined in the "Global Exploration Strategy" by 14 space agencies around the world [1, 2]. The strategy supports international space exploration and calls for further studies of the Moon and Mars – places where humans will 1 day live and work.

Facilities for simulation of lunar conditions had evolved along with increased knowledge of the planetary conditions on the Moon, starting with very simple simulation chambers to highly sophisticated systems [3–16]. Initially, the functionalities of such facilities were based on a number of capabilities that matched the requirements. Particular emphasis was placed on the ability to handle various amounts of simulated lunar regolith while still being able to maintain vacuum and temperature requirements. Some of the facilities seem to address the majority of the requirements, however, the severity of the lunar dust problems encountered during the Apollo missions were consistently underestimated by ground tests, illustrating the need to develop significantly better lunar dust simulants and simulation facilities.

All experience with extravehicular activity (EVA) systems on the lunar surface comes from the six Apollo missions that landed two-man crews (Apollo 11, 12, 14, 15, 16 and 17) and took place between 1969 and 1972 [17, 18] and information from lunar landings of Russian automated stations. One of the unexpected findings of the Apollo experience was how troublesome the lunar dust turned out to be. The dust-related hazards could be sorted into nine categories described in [17] as follows:

- Vision obstruction;	- False instrument readings;
- Dust coating and contamination;	- Loss of traction;
- Clogging of mechanisms;	- Abrasion; and
- Thermal control problems;	- Seal failures.
- Inhalation and irritation.	

While simple dust mitigation measures were sufficient to address some of the problems, like loss of traction, for many other problems, like thermal control, adhesion and abrasion, new technologies must be developed. Some mitigation strategies, such as vibration have been tried with little success [19–21]. Others, such as brushing appeared to work much better in ground tests than they did in the lunar environment.

ITL Inc., based on its previous accumulated experience with design and building of space environment simulators [22, 23], proposed to create an advanced planetary simulation facility and associated with it methodology that will involve the development of simulation environments to address the harsh conditions of the Moon in a more efficient way. This will include the use of better simulants, creation of more efficient ways of interaction of the dust simulant with samples, higher vacuum, better correlated simulation scenarios, and more realistic thermal and illumination environments.

2   General Design Criteria

In the early stages of system design, the environmental factors to be simulated in the facility were discussed with potential customers developing the planetary robotics hardware in order to take into account their needs for testing. Based on these discussions, ITL has developed a facility to conduct simulated testing where dust would be one of the most important environmental factors to verify the operational capability of the newly developed hardware, including drive systems, deployment systems, vision systems, mechanical mechanisms, seals, docking systems, etc.

To allow for durability testing of mechanical systems in simulated lunar environment, a rotation feed-through and drive system will be mounted as part of the sample holder system. Vacuum pressure sensors, electrical probe to monitor the dust particles charge (Langmuir probe) and thermocouples will be the basic instrumentation to monitor the exposure conditions in simulated lunar vacuum, dust and temperature environment. The facility is controlled by powerful user-friendly software that allows the operator to control different sources and components.

The main objective of testing would be verification of dust tolerant designs, as well as studying and improving of dust and other environmental factors mitigation strategies. Figure 1 provides the schematic view of the Lunar Environmental Simulator/Test Facility and shows the major components and systems of the designed system that are expected to be created by the end of the present project.

3   Vacuum Chamber and System

Based on the requirements to space and planetary environmental simulators and on previous ITL experience, the design of the vacuum chamber includes a detachable semi-spherical front, a cylindrical base, and a flat back plate. The vacuum chamber is manufactured from Stainless Steel 304 with vacuum connections (flanges). All flanges are of ConFlat (CF) type with copper gaskets sealing. Five $12''$ CF flanges, one $8''$ CF flange, three $6''$ CF flanges, two $4.5''$ CF flanges, and thirteen $2.75''$ CF flanges are mounted on the vacuum chamber.

The developed design of the vacuum chamber has the highest axial symmetry of all flanges, thus facilitating the alignment of various environmental sources, measurement sensors and instrumentation. To allow for easy sample exchange and for accommodation of more sophisticated objects, the vacuum chamber combines two independent ways of samples change: a detachable semi-spherical front for installation of a larger sample and an access door for routine sample change (optional).

The oil-free vacuum pumping system includes a roughing mechanical pump Varian TriScroll 600 (500 l/min pumping speed), a special dust-proof Varian Turbo-V 3 K-T turbomolecular pump (2,050 l/s pumping speed), an XGS-600 vacuum gauge controller, as well as the required vacuum gauges, feedthroughs, gaskets, and connectors. Testing and adjustment of the vacuum pumping system has
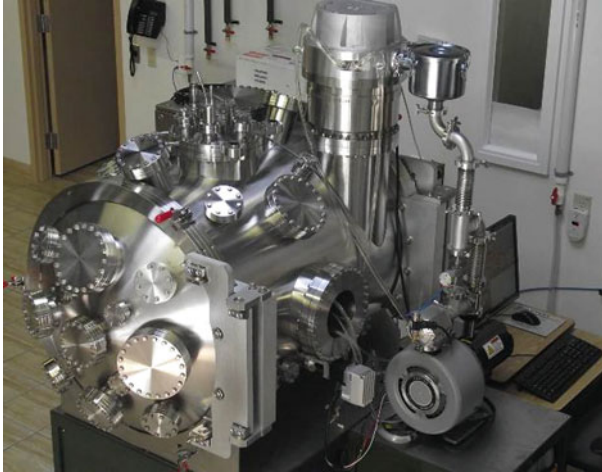
Fig. 1 The lunar environment simulator/test facility (general view)

been conducted with the objective to determine the optimal pumping rates during different pumping regimes. Typical curves for vacuum pressure during pumpdown of the simulator's chamber using different regimes of fore-pumping (low- and high-pumping speed) are presented in Fig. 2 that shows the vacuum pressure vs. time of pumping during the fore-pumping stage of the simulator chamber. As can be seen from Fig. 2, the minimum pressure achieved in the facility chamber within ~6,500 s (~1.8 h) of pumping with one Varian Turbo-V 3 K-T turbomolecular pump (2,050 l/s pumping speed) is lower than 1×10^{-7} Torr.

The vacuum pumping system of the facility includes a low/high pumping switch designed to allow for fore-pumping the simulator's chamber with low or high pumping speed. Low fore-pumping speed is used when pumping the chamber with lunar soil simulant loaded into the dust source. A number of engineering solutions have been used to protect the vacuum pumping system of the facility from possible damage by dust particles. The vacuum chamber is pumped by the turbomolecular pump from the top. The vacuum vent is located at the back part of the facility's chamber which is partitioned from the front part where the dust source is operating. Since the bottom of the vent opening is off the dust source, no dust should be able to flow to the pump.

4 Design and Operation of Dust Filter

The vacuum pumping system of the Planetary Environmental Simulator/Test Facility has an essential requirement of being robust to any dust that would find its way into it. Therefore, to provide an extra security and to preserve the vacuum pumps, a dust filter has been developed, designed, and manufactured.
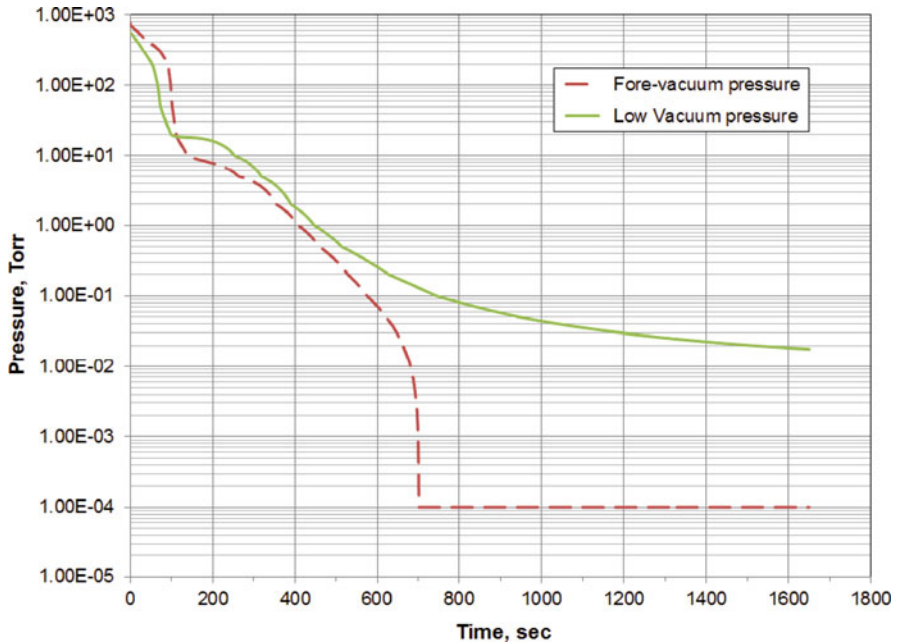
Fig. 2 Fore-pumping stage of the simulator vacuum chamber

Figure 3 shows the dust filter assembled according to the developed design. The filter includes five baffles with alternating windows at the "top-bottom-top-bottom-top" positions. The widows are covered with a fine metallic mesh to prevent dust particles from getting into the vacuum pump. The baffle system is fitted in the vacuum chamber and fixed at the rails on the walls of the chamber. Each of the baffle plates has a widow covered with a fine metallic mesh. In this way, the set of baffles with alternating windows position is used to stop dust particles from getting into the vacuum pump. The baffle system will be fitted in the vacuum chamber due to air-tight rubber gaskets (see Fig. 3) and fixed at the rails on the walls of the chamber by the angle pieces at four corners of the structure.

4.1 Sample Holder System

It was shown that using a liquid nitrogen shroud to cool a sample in a vacuum chamber is an extremely inefficient approach. Thus, taking into account only the radiative heat transfer mechanism between the sample and the shroud, the time needed to cool the sample down to −150 °C from room temperature was estimated at several days. In the present design, a Sample Holder System (SHS) is proposed and designed to allow for efficient high/low temperature conditioning and temperature cycling of the samples.

Fig. 3 Dust filter installed in the simulator chamber

Figure 4 shows the design of the sample holder assembly. The sample holder system is an ultra-high vacuum set-up installed inside the vacuum chamber and designed to hold and position samples of different shapes and nature, allowing for heating, cooling, and thermal cycling of the samples. The Sample Positioning System (SPS) consists of the following main parts: Sample holder plate; Thermal control platform, and Holder/thermal control platform moving system. The assembly is mounted on a 12″ flange equipped with all necessary electrical, control, and motion feedthroughs.

The technical specifications of the sample holder system are as follows:

- Fully compatible ultra-high vacuum design;
- Temperature range (-150 °C to $+250$ °C);
- Controlled and programmable thermal cycling (-150 °C to $+250$ °C) modes;
- Built-in accelerated heating/cooling options by forced air;
- Integrated thermocouples for temperature measurements;
- Full computer control over all system functions.

The thermal control platform consists of a pair of disks 200 mm in diameter and 4.76 mm thick made from stainless steel and copper (not shown in Fig. 4). The disks could be made either solid or with a concentric hole, ~33 mm in diameter, depending on the experimental set-up (use of dust, UV sensors, etc.). The hollowed disks allow also introducing rotary or translational motion using a mechanical feedthrough. The sample transfer system is designed to allow for a total displacement of 300 mm. The sample holder can accommodate samples up to 200 mm in diameter. The fastening of samples onto the platform is achieved through the use of special clamps.

The thermal control platform is used for cooling, heating, constant temperature maintenance, and thermal cycling of the samples. Effective temperature range is

from -150 °C to $+250$ °C. The temperature is measured using K-type thermo-couples and sustained with ± 1 ° accuracy. The sample holder system uses six 400 W cartridge heaters (Omega Engineering Inc.), connected in series, liquid nitrogen and compressed air supply, and two control thermocouples mounted on the sample holder disk.

A testing program of the sample holder system was conducted by placing it in a vacuum chamber with a base vacuum of ~10^{-6} Torr with the main objective to adjust the control software for thermal cycling operation, to determine the temperature rate during the heating and cooling stages of a thermal cycle, as well as to develop recommendations for future adjustments and improvement of the system.

A typical thermal cycle consists of a heating ramp, a cooling ramp and dwell times at each target temperature during the user-defined soak time. Thermal cycling of the samples attached to the sample holder is achieved by alternating the cooling and the heating modes through a computer-controlled program. During the heating stage, when the heaters are on, when the temperature registered by the control thermocouple approaches a certain set temperature (8 °C, 4 °C, and 1 °C below the setpoint), the thermal controller starts turning the pairs of heaters off one by one. When the target temperature setpoint is reached, all heaters are turned off. The sample holder temperature, however, will continue to increase, due to thermal inertia. The constant dwell temperature conditions are maintained by turning on the heaters for a time t_1 followed by turning on the liquid nitrogen for a time t_2 and repeating this action during the user-defined soak time.

The time required to achieve the upper and the lower set temperature points varies and needs to be adjusted independently for each set temperature. To increase the heating/cooling rates and to allow for quick heating from the cryo temperatures to zero compressed air is used. When switching from high to low temperatures, compressed air is used to reduce the cooling time since it would quickly cool down the sample holder to approximately 110 °C and it can also be used for high accuracy temperature maintenance. When switching from low to high temperatures,
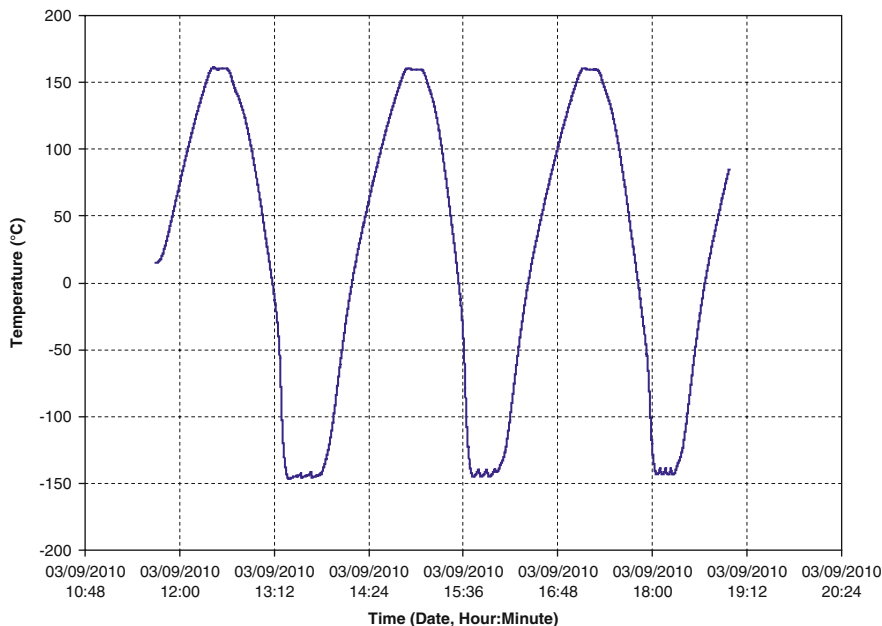
Fig. 5 Best profile of thermal cycles achieved in the *advanced* configuration of the sample holder system

compressed air is used to quickly clear the system of liquid nitrogen. Two additional drain valves are required for system's drainage.

The performance of the sample holder system was tested and the results of a thermal cycling experiment conducted in accordance with the described above methodology area shown in Fig. 5. The temperature rate achieved during thermal cycling operation testing could be considered to consist of two parts in each heating or cooling stage. The minimum and maximum temperature rates for the heating and cooling stages observed during thermal cycling experiments as shown in Fig. 5 were found to be equal to ~7.6 °/min.

4.2 Dust Particles Source

A dust particles source has been developed to produce a dust cloud in the Lunar Environmental Simulator/Test Facility. The dust particles source includes three main parts: Dust container (Dust activation compartment); Dust storage compartment; and Foldable plates to form a funnel-like closed structure in which dust cloud is generated. Dust is stored, pre-treated and agitated in the dust activation compartment. The dust cloud in the chamber will be created by a paddle actuator located inside the source that will be driven by a computer-controlled step-motor (a 400 W servo motor Cool Muscle CM2-C-60A40A-K providing a more important torsional

moment). This method of creation of the dust cloud allows controlling the flux and the velocity of dust particles, as well as forming different configuration of generated dust cloud. The system can also be used to mix the particles during the stages of lunar dust simulant preparation. Foldable plates are used to form a funnel-like closed structure to ensure that the dust is confined only to the test area and is not spreading uncontrollably throughout the chamber. The present source can hold about 3 kg of lunar soil simulant. The JSC-1A simulant has been purchased and is planned for future testing.

The manufactured dust particles source prototype has been tested using regular sand to evaluate the generated dust cloud. During the operation of the source, different configurations of generated dust clouds were observed. The optimal configuration of dust cloud is achieved by varying the rotation speed of the step motor. Testing of the dust source prototype has allowed choosing a rotation speed of ~180 pps (pulse per second) to obtain a desired form, height and concentration of the cloud. A similar optimization procedure will be used for optimization of the lunar simulant cloud parameters when the dust source will be installed in the vacuum chamber.

A special housing for dust source operation inside the simulator facility was designed and manufactured. The chamber for dust source operation has a maintenance door made of Plexiglas that will be used when service of the dust source, placing the samples or dust source refill are required. The upper part of the chamber has a sliding gate for installation of the sample holder/sample transfer system inside the simulator facility for testing of the samples in the generated dust cloud together with temperature conditions. Figure 6 shows the housing incorporating the dust source and sample holder installed in the simulator chamber.

4.3   Vacuum UV Source

The VUV radiation of wavelengths between 115 and 200 nm produced by the Sun can cause degradation to materials, producing changes in optical, mechanical, and chemical properties. The VUV radiation arriving to the Moon surface with the solar wind is also known to be responsible for electrostatic charging of lunar dust. The VUV source developed for the Lunar Environmental Simulator/Test Facility includes a Hamamatsu VUV deuterium lamp (Model L1835) with magnesium fluoride windows which provides a continuum spectral output between approximately 115 and 400 nm and a Hamamatsu power supply for deuterium lamps (Model C9935).

The VUV lamp is installed on a 4.5″ stainless steel standard ConFlat flange using an ITL-designed vacuum flange adaptor. The body of the lamp is located outside of the vacuum chamber with its end-tube pushed through o-ring compression fittings to provide a vacuum seal. The lamp end-tube window is thus located inside the vacuum chamber. The lamp body is placed into a water-cooled housing.

The lamp housing fully accommodates the lamp with the flange so that no optical alignment is required, allows for easy lamp installation, operation and replacement.

Fig. 6 Housing incorporating the dust source and sample holder installed in the simulator chamber
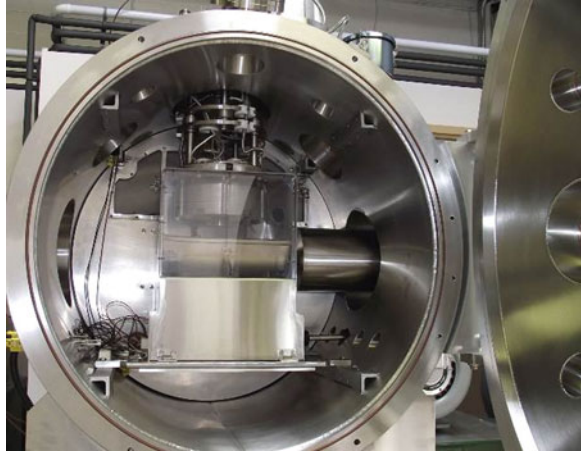
5 Support Electronics and Control Blocks

Four support electronic and control blocks have been designed and manufactured for operation of the facility that includes the following modules:

- Main power supply;	- Vacuum system controller; and
- Dust source drivers;	- Sample holder controller.

All of the components, systems and sources of the facility will be connected through and controlled by the developed modules. The Programmable Logic Controller (PLC SIEMENS SIMATIC S7-200) performs the operation and controls every electrical socket via a set of Solid State Relay (SSR) to ensure the proper operation of connected devices.

The Planetary Environmental Simulator/Test Facility will be operated using ITL's original proprietary control software. The software is being developed using the Visual Studio 2010 platform. The control software will allow to operate the facility in either Manual or Automatic modes. The Manual mode allows the operator to set the parameters and to manually control all the components, systems and sources of the facility. The manual mode of operation is now fully tested and ready for use while the development of the automatic mode has been started and is in progress.

6 Lunar Soil Simulant Pre-Treatment and Activation

Testing in simulated environmental conditions of lunar dust requires an appropriate preparation of the lunar regolith simulant (JSC-1A or similar). The most advanced lunar simulator facilities [3–6] have the ability to bake out lunar dust simulants, or

actual lunar regolith, under vacuum, then subjecting them to a hydrogen/helium plasma and UV environment. Once activated, the dust can be applied to a sample and the coverage, adhesion of dust particles to the surfaces can be determined in such systems.

A number of physical properties of the lunar dust simulant (particles' microstructure, area of contact between particles, thermal conductivity, electrical charge, etc.) can be proposed to control the activation of the lunar regolith simulant and consequently, its behavior. Based on the described approach, further investigation and development of a methodology for lunar soil simulant pre-treatment and activation will be conducted in the next stage of the project.

To establish the optimum conditions for activation of JSC-1AF lunar dust simulant in the lunar simulator environment, i.e. vacuum, temperature and VUV or plasma conditions that should be used for actual testing in the Planetary Environmental Simulator/Test Facility, a plasma asher chamber will be used. It will allow simulating low-vacuum conditions ($\sim 10^{-3}$ torr), temperature (up to +200 °C), as well as oxygen, helium or argon plasma produced using a radio-frequency (RF) generator and study which of them will have the most effect on the mechanical, chemical, microstructural and electrical properties of the lunar soil simulant. Once a methodology for pre-treatment and activation of the lunar soil simulant is developed, preliminary testing will be conducted in the plasma asher chamber to investigate the adhesion of dust to the surfaces of interest, such as stainless steel or thermal control coating surfaces.

In accordance with the philosophy described above, ITL has conducted preliminary investigation of the morphology, chemical composition and thermal physical properties of JSC-1AF lunar dust simulant. Figures 7 and 8 show the surface morphology and elemental composition of the JSC-1AF simulant as obtained from a SEM/EDS analysis.

7   Simulating the Effect of Lunar Dust on the Thermal Control Surfaces

The thermal optical performance of spacecraft materials and external thermal control coatings, such as black and white paints, second-surface mirrors and thermal radiators, can significantly degrade under simulated lunar conditions, as was shown in tests carried out at NASA GRC lunar dust adhesion bell jar (LDAB) facility [3], [24–26]. The lunar simulation facility at NASA enables the simulated lunar dust to be heated, dried, plasma cleaned, chemically reduced, and delivered to the samples surface in-situ through either a 25 or a 32 μm sieve so that only the dust fraction would be applied. Sub-monolayer coatings of dust were formed on the surface of the samples in all cases in these tests [25, 26].
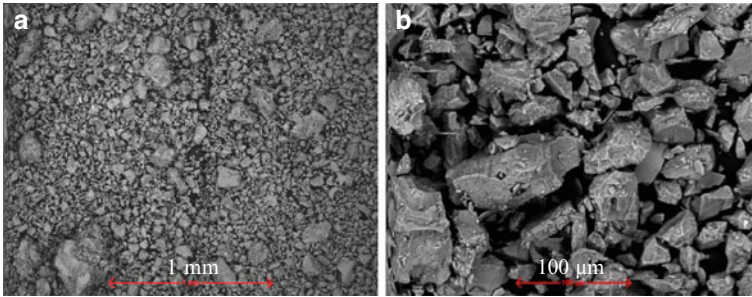
Fig. 7 Secondary electron SEM image showing the surface morphology of JSC-1AF lunar dust simulant (**a**) Magnification 50×; (**b**) Magnification 350×
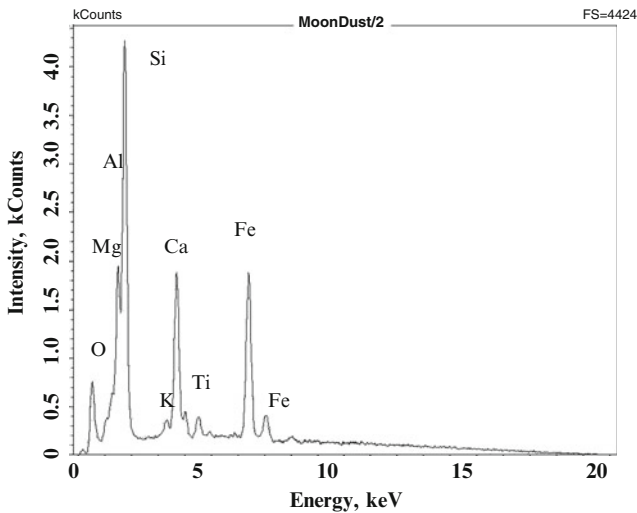
Fig. 8 Energy dispersive x-ray microanalysis of JSC-1AF lunar dust stimulant.

Thermal modeling is used to determine the absorptivity (α) and emissivity (ε) of the thermal control surfaces in both the clean and the dusted states. It was found that even a sub-monolayer of simulated lunar dust can significantly degrade the performance of both white paint and second-surface mirror type thermal control surfaces under these conditions. Contrary to earlier studies [26], dust was found to affect ε as well as α. ITL is going to implement the testing methodology used at NASA GRC to conduct thermal control coatings testing in simulated lunar surface environment and appropriate dust adhesion studies.

8   Thermal-Vacuum Test Rigs and Fretting Fatigue Set-Up

As part of future development of the Lunar Environmental Simulator/Test Facility and test methodologies, the facility chamber will be equipped with a number of driving mechanisms and motion feed-throughs for translational and rotational movements, fretting and fretting fatigue rigs for mechanical testing and life time evaluation of spacecraft materials, assembly units, mechanical systems and mechanisms, tribological testers, etc.

The fretting fatigue rig is a unique instrument to evaluate the performance of materials and coatings in harsh conditions that could imitate terrestrial and space environments. ITL has developed a fretting fatigue set-up that has been used in a testing program of fretting fatigue of titanium and aluminum samples in a vacuum environment with different coatings [27]. The fretting rig loading to produce normal loads on the specimen is controlled by a load cell. The drive system is based on a set of piezoelectric actuators. The loading system would provide tensile pre-loads and provide peak loads of up to 12 kN and cycle at ~2–100 Hz. A modified fretting fatigue apparatus can be mounted inside the Lunar Environmental Simulator/Test Facility chamber to work in vacuum and/or gas environments (like the Martian carbon-dioxide atmosphere).

The sample during the fretting fatigue testing could be subjected to simulated lunar dust and temperature conditions (cooling, heating, or thermal cycling). The system can be remotely powered via accessible port connections to monitor the transversal and longitudinal loads on the tested specimen that can be provided in real time by precision strain gauges mounted on the specimen, as well as other sensors. The control software being developed to operate the facility can be used to set up the parameters of the fretting fatigue testing (frequency, amplitude, duty cycle, and temperature) and to change them dynamically during the test.

9   Tribology Concerns About Lunar Dust and Dust Mitigation Strategies

In preparing for long term operations within a dusty lunar environment, the three fundamental approaches to keeping mechanical equipment functioning are dust avoidance, dust removal, and dust tolerance, with some combination of the three likely to be found in most engineering designs. Methods to exclude dust from contact with mechanical components would constitute mitigation by dust avoidance, so testing seals for dust exclusion efficacy as a function of particle size provides useful information for mechanism design.

A number of dust mitigation methods that can be explored include application of self-cleaning transparent coatings with low surface energy, non-uniform electrostatic fields of fibrous electrets protective systems and electric fields generated with

help of external AC power sources, detachable and recyclable electret dust absorbers and surface cleaning with the help of mechanical vibrations going along the surface.

Three promising strategies to mitigate the effects of dust combined with other Lunar/Martian environmental factors on surface system components can be tested and evaluated in the Planetary Environmental Simulator/Test Facility. First, components designed so that they can better tolerate the effects of dust will be tested in the simulated lunar dust environment. An example might be a space suit fabric that has better resistance to abrasion by lunar dust [21]. Second, testing will be done on components designed so that less dust attaches to it. For example, a space suit fabric can have a smooth outer layer so that dust cannot so easily work its way between the fibers, so there is less dust on the fabric to abrade it [21], [22]. Third, techniques can be developed to clean dust from surfaces. Another dust mitigation method may consist in using a large-size platform to prevent dust particles from flying and deposition on the surface of space suits and system components.

10 Conclusions

This paper provided a brief but comprehensive review of the progress made by ITL Inc. in designing and building a Planetary Environmental Simulator/Test Facility for future space exploration missions. It summarized the most relevant information about the Lunar and Martian planetary simulator systems, lunar soil simulants, as well as outlined the testing methodologies and approaches for in-situ mechanical testing of the durability and performance of planetary exploration surface systems. A multi-stage evolutionary development path of the simulator/test facility is outlined, with its first stage, i.e. design, development and manufacturing of the lunar environmental simulator/test facility simulating the vacuum, temperature, UV, dust and darkness factors is being accomplished as part of a 2-year project supported by CSA.

The proposed modular design will allow to upgrade the planetary environmental simulator/test facility to include a number of modular space environment sources such as VUV/NUV, variable-energy proton and electron radiation, rocket's exhaust contaminations, microgravity, etc., as well as a variety of fixtures and rigs for fretting and fretting fatigue mechanical testing of spacecraft materials, mechanical systems and mechanisms, tribological testers, etc. It is safe to say that no universal planetary environmental simulator/test facility does exist in the world presently, that would allow simulating the synergistic influence of the most important factors of the lunar planetary environment, including appropriate lunar soil simulant preparation, mechanical/tribological testing, and characterization and monitoring of simulated conditions, and post-test measurements of the samples. The present model of the Lunar Environmental Simulator/Test Facility and its advanced

versions that can be created in the future will undoubtedly be among the most comprehensive and sophisticated space and planetary environmental simulators created.

References

1. The global exploration strategy: The framework for coordination. April 2007
2. European Space Agency (2010) The global space exploration strategy. http://www.esa.int/SPECIALS/Space_Exploration_Strategy/SEMDAM0YUFF_0.html. Accessed 19 Aug 2011
3. Gaier JR, Sechkar EA (2009) Lunar simulation in the lunar dust adhesion bell jar. Report NASA/TM-2007-214704
4. Craven P, Vaughn J, Schneider T, Norwood J, Abbas M, Alexander R (2009) MSFC lunar environments test system (LETS) system development. Third lunar regolith simulant workshop, Huntsville, 17–20 Mar 2009
5. Vaughn JA, Schneider T, Craven P, Norwood J (2008) LETS: lunar environments test system. Lunar regolith behavior workshop, Houston, 12–14 Aug 2008
6. NASA scientific and technical aerospace reports (2009) 47(15): 134
7. NASA GSFC lunar systems capabilities. http://explorationatgoddard.gsfc.nasa.gov/pubs/gsfc-lss.pdf. Accessed 19 Aug 2011
8. NASA GSFC dust environmental effects particle chamber (DEEP). http://explorationatgoddard.gsfc.nasa.gov/techpdf/DeepChamber_Goddard.pdf. Accessed 19 Aug 2011
9. Davies GR, Mason NJ, Gómez F, Prieto O, Helbert J, Colangeli L, Srama R, Barnes D, Merrison J (2009) Europlanet research infrastructure: planetary simulation facilities. European planetary science congress, EPSC abstracts vol 4, p 63
10. Kochan H et al (1991) Laboratory comet simulation experiments. Geophys Res 18(2):243–291
11. Kochan H, Feibig W, Möhlmann D, Willnecker R et al (1997) The new planetary simulation facility of DLR – and its first full operational performance during a breadboard – test of a small sample acquisition and aistribution tool (SSA/DT) for space mission applications to Mars, Moon, and Comets. In: Proceedings of the 3rd international symposium on environmental testing for space programs, ESTEC, Noordwijk, 24–27 June 1997
12. Tankosic D, Abbas MM (2008) Measurements on charging of Apollo 11 and 17 lunar dust grains by low energy electrons. In: Proceedings of the 39th lunar and planetary science conference (Lunar and planetary science XXXIX), League city, 10–14 Mar 2008
13. Abbud-Madrid A, Dreyer CB, Nakagawa M, Olhoeft GR, King R, Eustes AW, Moore JJ (2008) Lunar science capabilities at the Colorado School of Mines. In: Proceedings of the NLSI lunar science conference, Moffett Field, 20–23 July 2008
14. Smithers GA, Nehls MK, Hovater MA, Evans SW, Miller JS, Broughton RM, Beale D, Kilinc-Balci F (2007) A one-piece lunar regolith bag garage prototype. Report NASA/TM-2007-215073
15. Fan SC, Feng YQ, Zheng QJ (2005) A study of experimental facility for lunar rover development. In: Proceedings of the international lunar conference, Toronto, 13–19 Sept 2005
16. The large space simulator. http://ams.cern.ch/AMS/CGSE/Documents/SJTU/CD%20From%20SJTU%20(March%2014,%202008)/lss.pdf. Accessed 19 Aug 2011

17. Gaier JR (2008) The effects of lunar dust on EVA systems during the Apollo missions. Report NASA/TM-2005-213610
18. International Association for the Advancement of Space Safety. Newsletter. July 2008
19. Calle CI, McFall JL, Buhler CR, Snyder SJ, Arens EE, Chen A, Ritz ML, Clements JS, Fortier CR, Trigwell S (2008) Dust particle removal by electrostatic and dielectrophoretic forces with applications to NASA exploration missions. In: Proceedings of the electrostatics society of America Annual meeting, Minneapolis, 17–19 June
20. Marcy JL, Shalanski AC, Yarmuch MAR, Patchett BM (2004) Materials choices for Mars. J Mat Eng Perform 13(2):208–217
21. ASTM D3884 – 09 Standard Guide for Abrasion Resistance of Textile Fabrics (Rotary Platform, Double-Head Method)
22. Kleiman J, Horodetsky S, Sergeyev V, Issoupov V (2006) Critical review of the design of space environment simulators: lessons Learnt. In: Proceedings of the 10th international symposium on materials in a space environment/8th international conference on protection of materials and structure from the LEO space environment, Collioure, 19–23 June
23. Kleiman J, Horodetsky S, Sergeyev V, Issoupov V (2006) CO_2-laser assisted atomic oxygen beam sources: research, development, and optimization of operational parameters. In: Proceedings of the 10th international symposium on materials in a space environment/8th international conference on protection of materials and structure from the LEO space environment, Collioure, 19–23 June
24. Gaier JR, Jaworske DA (2007) Lunar dust on heat rejection system surfaces: problems and prospects. Report NASA/TM-2007-214814
25. Gaier JR, Siamidis J, Larkin EMG (2008) Extraction of thermal performance values from samples in the lunar dust adhesion bell jar. In: Proceedings of the 25th space simulation conference, Annapolis, 20–23 Oct
26. Gaier JR, Siamidis J, Panko SR, Rogers KJ, Larkin EMG (2008) The effect of simulated lunar dust on the absorptivity, emissivity, and operating temperature on AZ-93 and Ag/FEP thermal control surfaces. Report NASA/TM-2008-215492
27. Kleiman J (2002) Fretting and fatigue damage in the space environment: design and test evaluation of fretting fatigue rig in vacuum environment. Final Report ITL-061202-0620, Orenda Aerospace Corp Contract Project ID RD6941

Influence of Atomic Oxygen Exposure on Friction Behavior of 321 Stainless Steel

Y. Liu, J. Yang, Z. Ye, S. Dong, L. Zhang, and Z. Zhang

Abstract Atomic oxygen (AO) exposure testing has been conducted on a 321 stainless steel rolled 1 mm thick sheet to simulate the effect of AO environment on steel in low Earth orbit (LEO). An atomic oxygen exposure facility was employed to carry out AO experiments with the fluence up to $\sim 10^{21}$ atom/cm^2. The AO exposed specimens were evaluated in air at room temperature using a nanoindenter and a tribological system. The exposed surfaces were analyzed usign XPS technique.

The experimental and correlated analytical results indicated that long term exposure to atomic oxygen results in formation of a metallic oxide in the surface layer of the stainless steel that leads to surface hardening. With increasing AO fluence, the surface microhardness is increased. The friction behavior during starting period is influenced by AO exposure. The maximum friction coefficient of run-in stage is decreased after AO exposure.

Keywords Atomic oxygen • LEO • Stainless steel • Friction • Hardening

1 Introduction

The results of in-space tests had shown that atomic oxygen (AO) is considered as a major critical factor of LEO environment. Materials used in spacecraft operating in LEO orbit must be designed and selected to withstand the attack by atomic oxygen [1]. In order to explore and evaluate the effect of atomic oxygen on materials in laboratory conditions, many AO simulation facilities were established using

Y. Liu (✉) • J. Yang • Z. Ye • S. Dong • L. Zhang
School of Materials Science and Engineering, Harbin Institute of Technology,
Harbin 150001, China
e-mail: liuy@hit.edu.cn

Z. Zhang
Department of Materials Science and Engineering, Tsinghua University, Beijing 100084, China

various technologies. Extensive investigations were carried out on erosion effect, undercutting mechanism and modeling of interaction between atomic oxygen and polymers as well as protective coatings [2].

Many metals and alloys have wide applications in spacecraft. A previous study showed that most pure metals are stable to atomic oxygen while some active metals such as Ag, In, and Cu etc. are easily oxidized [3–9]. When the aluminum surface is irradiated by AO beam, the formed dens aluminum oxide will prevent the further oxidation. Thus, the oxidation rate decreases with the oxidizing volume [10]. The oxidation of pure silver by AO involves two steps, i.e. firstly an Ag_2O layer is produced and then an AgO on the top of Ag_2O layer forms. The Ag_2O is a loose oxide layer with a number of defects, such as pores and grain boundaries that allow AO diffusion into the interface of Ag_2O and Ag, leading to continuous oxidation of Ag substrate. With the growth of Ag_2O, the inner stress within the Ag_2O film increases, resulting in corrugation, cracking and spallation of the formed Ag_2O. The pure copper can be oxidized into CuO and Cu_2O by AO [4, 7, 8]. The oxidation reaction of pure copper and AO is sensitive to the temperature. At lower temperatures, the oxidation production of copper mainly consists of Cu_2O. With increasing temperature, a CuO layer forms on the surface of Cu_2O. The copper oxides will flake away under the impact of energetic AO, generating contaminations to the other materials or components of spacecraft. Although it is easy to oxidize Ag and Cu, the Ag-Cu alloy shows higher AO resistance than the pure Ag film [3, 11]. The oxidation of nickel, which produces NiO, has higher oxidizing rate in atomic oxygen than in molecular oxygen [12]. The reason for that is the chemical absorption of AO on the NiO surface is easier than that of molecular oxygen.

The 321 stainless steel is a candidate alloy for space mechanisms especially in tribological systems. During operation in LEO orbit, the steel will be attacked by atomic oxygen which unavoidably diffuse and accommodate onto the surface of the steel. When a certain stainless steel is designed and selected to be used in LEO environment, the level of its susceptibility to tribological behavior needs to be investigated. However, very little data are available on AO exposure test of stainless steel both in space as well as ground simulations. The present study describes tests conducted on 321 stainless steel subjected to AO exposure, with the aim to explore the effects of AO exposure on its friction behavior.

2 Experimental Procedure

The exposure tests were conducted in a microwave induced atomic oxygen beam facility using a space environment complex simulation facility. The facility consists of a microwave source, vacuum chamber, magnet roll, cooling system and neutralization target. The oxygen gas flowing into the vacuum chamber is ionized into plasma by synchronization of RF and magnetic field. The oxygen ion beam will be reflected by the positive metal target, forming neutralized AO beam, as shown in
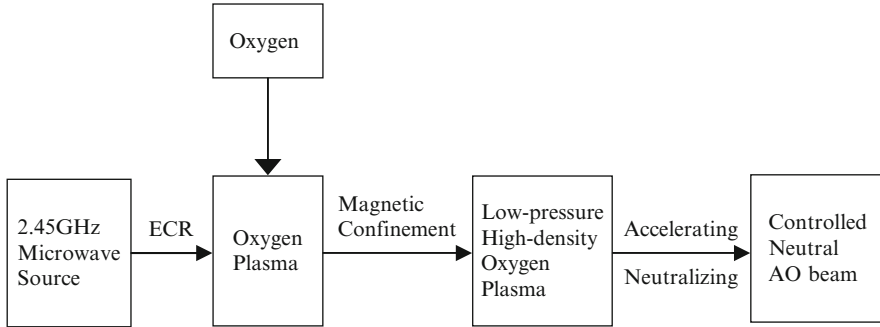
Fig. 1 Schematic graph showing generation of AO beam

Table 1 Composition of 321 stainless steel (wt %)

Element	Cr	Ni	Ti	C	Si	Mn	S	P	Fe
Content	17.5	9.1	0.25	0.025	0.61	1.05	0.027	0.010	Balance

Fig. 1. Changing the distance from target to specimen holder can provide different AO flux. The energy of AO beam can be adjusted by tuning the positive voltage of neutralization target. In the present test, the AO exposure was conducted under energy of 5 eV and flux of 5×10^{16} atoms$\cdot$cm$^{-2}\cdot$s^{-1}. The RF power is controlled by a 500 W power supply. The vacuum system is capable of maintaining a pressure of 0.4 Pa with an input gas flow of 9 standard cubic centimeters/min of oxygen. The positive voltage of neutralization target is 15 V. Under these conditions, the 321 stainless steel specimen was irradiated with a directed AO beam to various fluencies of 1×10^{20} atom/cm^2, 2×10^{20} atom/cm^2, 5×10^{20} atom/cm^2 and 1×10^{21} atom/cm^2.

The 321 stainless steel in the form of rolled sheet was chosen for the tests. Table 1 lists the chemical composition of the 321 stainless steel. The shape of the specimen is 10 mm $\times$ 10 mm square sheet of 1 mm thick. The surface of the specimen was mechanically polished to Ra 3.2 μm before the exposure.

The friction tests were performed in a pin-on-disk type tribometer under a dry sliding condition in air. A 321 steel specimen was installed into the fixed pin holder sliding against the rotated disk of 52,100 steel to form a friction couple. The normal load of 20 N and the sliding velocities of 0.4 m/s were chosen as parameters for the tribological test. The friction coefficient of the specimen subjected to AO exposure with different AO fluence was measured. The sliding distance of all tribological tests was 1,000 m in order to obtain a stable friction. The disk and pin specimens were cleaned with acetone in an ultrasonic cleaner before test. Each test point value is calculated from the average of three specimens under the same friction condition.

An XP type Nano Indenter was utilized to measure surface hardness with test depth of 2,000 nm. An X-ray photoelectron spectroscopy system made in USA (PHI 5700 ESCA) was employed to determine the chemical status of the original and the AO exposed surfaces, using an Al Kα source with energy of 1,486.6 eV.
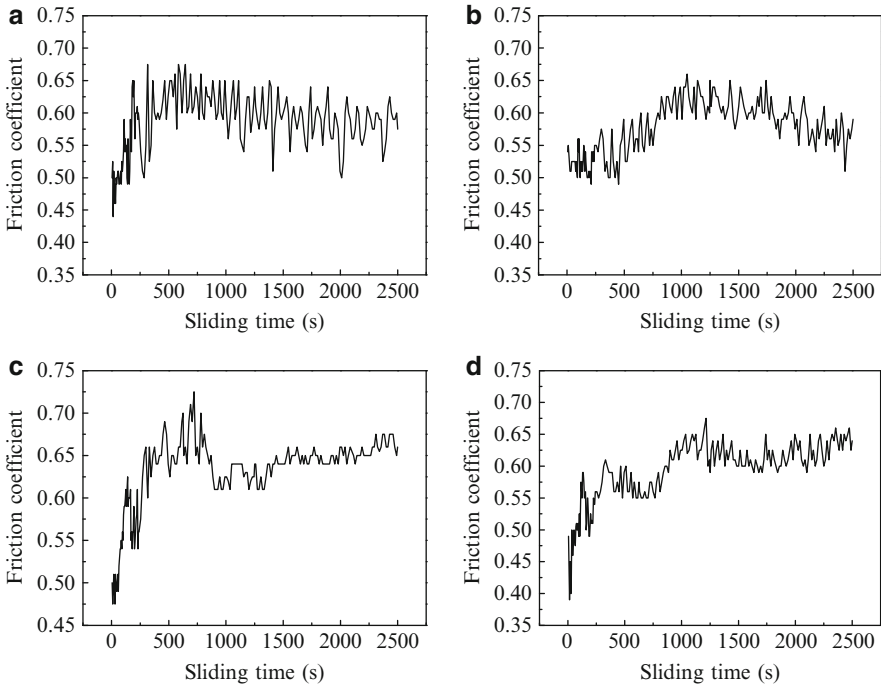
Fig. 2 Friction coefficient as a function of time for (**a**) unexposed and AO exposed specimen with fluence of (**b**) 1×10^{20} atom/cm^2, (**c**) 5×10^{20} atom/cm^2 and (**d**) 1×10^{21} atom/cm^2

3 Results and Discussions

3.1 Friction Coefficient

Figure 2 shows the friction coefficients of steel specimens exposed to different AO fluence. In contrast with the curve of friction coefficient versus time of the unexposed specimen as shown in Fig. 2a, the run-in period of the AO exposed specimen is extended, as shown in Fig. 2b–d. The two counter surfaces are polished by each other through friction and contact under nominal load during run-in period. The run-in process is resulting in attaining a stable real contact area and friction coefficient as well. The development of friction coefficient during run-in period reflects the status of interaction between surfaces. Thus, the above phenomenon indicates that the influence of AO exposure on steel specimen only located within a very thin surface layer, leading to an extended run-in period in the friction process.

In addition, the friction coefficient is increased quickly to reach a maximum value within run-in period. The calculation on this value demonstrates that the maximum friction coefficients of AO exposed specimen are lower than that of the original specimen, as shown in Fig. 3. It is also can be seen from Fig .3 that the maximum
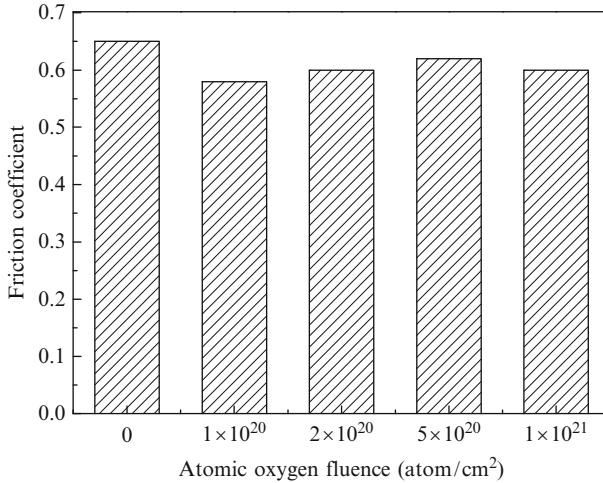
Fig. 3 The calculated maximum friction coefficient under different AO fluence

friction coefficient is increased with increasing AO fluence. These results indicate that the AO exposure affects the surface status of steel, such as changing run-in stage and the maximum friction coefficient during friction.

4 Microhardness of the Exposed Surface

Figure 4 shows the microhardness distribution in the surface layer of the unexposed and the exposed specimens. All the tested specimens exhibit similar trend of microhardness variation with depth. The hardness, of which has maximum value on the surface, decreases slowly to a stable value with increasing the depth from surface. Comparing the curves in Fig. 4, it is demonstrated that the AO exposure results in surface hardening. The hardening effect is increased with increasing AO fluence. The measurement of surface hardness is in accordance with above results, as shown in Table 2.

When friction occurs between two counter surfaces, one surface suffers adhesion and mechanical action from the other surface, leading to surface deformation and wear. The AO exposure induced hardening will protect the surface of 321 stainless steel from the deformation in contacting spot and damage by mechanical collision of the counter surface. As a result, the real contact area is decreased during the starting period of sliding friction, leading to a decrease in maximum friction coefficient of run-in stage of friction, as shown in Fig. 3. However, the AO induced hardening takes place in a very thin layer below the surface. Thus, the AO exposure only delays the stable stage of friction and expands run-in stage, as shown in Fig. 2.
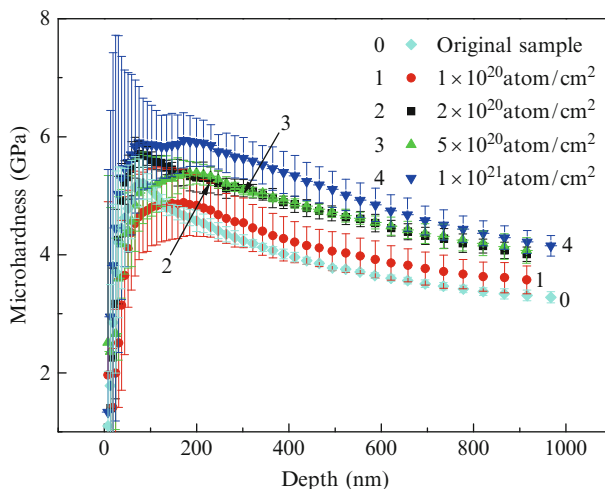
Fig. 4 Nano-hardness distribution along the depth before and after AO exposure

Table 2 Surface nano-hardness before and after AO exposure

AO fluence	Nano-harness/GPa				
atoms/cm^2	Pot 1	Pot 2	Pot 3	Pot 4	Average
0	3.211	3.123	3.016	3.057	3.102
1×10^{20}	3.943	3.716	3.676	–	3.778
2×10^{20}	3.095	3.594	3.379	3.487	3.389
5×10^{20}	3.646	3.56	3.845	4.089	3.808
1×10^{21}	3.806	3.775	3.89	4.102	3.893

5 Chemical Composition of the Exposed Surface

In order to explore the reason of surface hardening induced by AO exposure, the chemical status of the exposed surface was analyzed by means of XPS. The surface layer was also examined after sputtering for 2 min, of which will erode material on the utmost surface to avoid the influence of absorbed oxygen during analysis in air. Figure 5 gives the analysis result of the unexposed surface. Figures 6 and 7 show the Ols absorptive spectra from the AO exposed surface and the sputtered surface of AO exposed specimens, respectively. The Ols absorptive band composes two peaks locating around 532 eV corresponding to absorbed oxygen and 530.5 eV attributing to metallic oxide.

Comparing Figs. 5a and 6, it is found that the amount of absorbed oxygen is distinctly decreased after AO exposure. The comparison between Figs. 5b and 7 shows the same result for the sputtered specimens exposed to AO. On the other hand, the amount of metallic oxide is increased after AO exposure, as shown in Figs. 6 and 7.
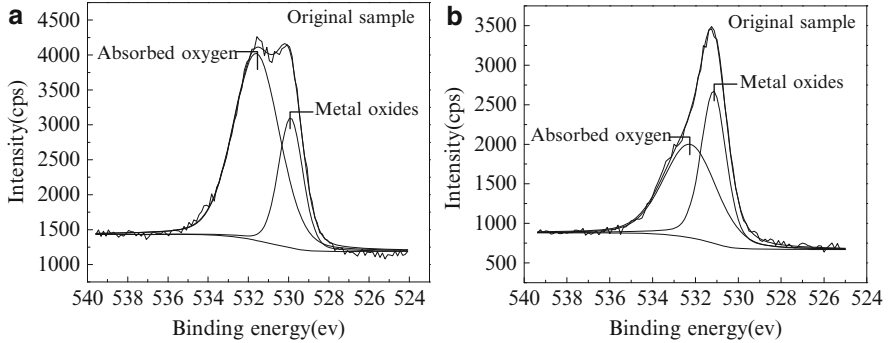
Fig. 5 OlS XPS peak for (**a**) unexposed and (**b**) sputtered unexposed surface
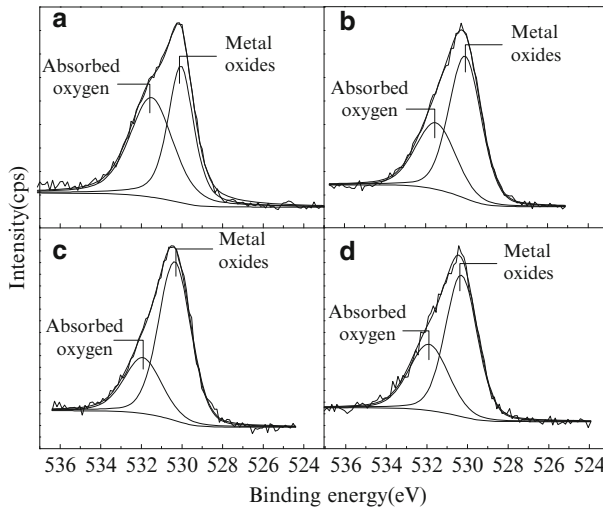
Fig. 6 The OlS spectra of the exposed surfaces with fluence of (**a**)1×10^{20} atoms/cm^2, (**b**) 2×10^{20} atoms/cm^2, (**c**) 5×10^{20} atoms/cm^2, and (**d**) 1×10^{21} atoms/cm^2

Based on the above analyses, it can be suggested that the exposure of 321 stainless steel surface to AO flux results in an increase in oxygen content of the surface layer, forming a metallic oxide. Although the mechanism of interaction between atomic oxygen and steel needs further investigation, the increase of metallic oxide should be one of major reasons for the surface hardening induced by AO exposure.

6   Conclusions

The change in friction coefficient, microharness and chemical status of AO exposed surface were investigated. The obtained results are as follows.
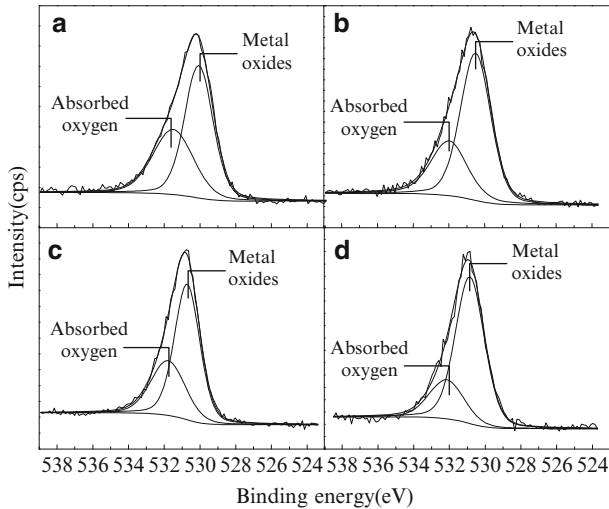
Fig. 7 The Ols spectra after sputtering for the exposed surfaces with AO fluence of (**a**)1×10^{20} atoms/cm^2, (**b**) 2×10^{20} atoms/cm^2, (**c**) 5×10^{20} atoms/cm^2, and (**d**) 1×10^{21} atoms/cm^2

1. The AO exposure results in formation of metallic oxide in the surface layer of the 321 stainless steel, leading to surface hardening. The surface microhardness is increased with increasing AO fluence.
2. The AO exposure influences the starting period of friction. The run-in stage is expanded after AO exposure. The maximum friction coefficient of run-in stage is decreased after AO exposure.

References

1. Banks BA, Miller SKR (2006) Overview of space environment effects on materials and GRC'S test capabilities. NASA CP 214383, vol 1, pp 485–505
2. Tagawa M (2008) Atomic oxygen-induced polymer degradation phenomena in simulated LEO space environments: how do polymers react in a complicated space environment? Acta Astronaut 62:203–211
3. Peters PN, Gregory JC, Christl LC, Raikar GN (1991) Effects on LDEF exposed copper film and bulk. LDEF first post-retrieval symposium, NASA CP-3134, pp 755–762
4. Raikar GN, Gregory JC, Christl LC, Peters PN (1993) The interaction of atomic oxygen with copper: an XPS, AES, XRD, optical transmission and stylus profilometry study. LDEF second post-retrieval symposium, NASA CP 3194, pp 1169–1186
5. Christl LC, Gregory JC (1991) Measurements of Erosion characteristics for metal and polymer surfaces using profilometry. LDEF first post-retrieval symposium, NASA CP-3134, pp 723–735
6. Whitaker AF et al (1993) Atomic oxygen effects on LDEF experiment A0171. LDEF second post-retrieval symposium, NASA CP 3194, pp 1125–1134
7. Mirtich MJ, Rutledge SK (1991) Ion beam textured and coated surfaces experiment (IBEX). LDEF first post-retrieval symposium, NASA CP-3134, pp 989–1004

8. Franzen W, Brodkin JS, Sengupta LC,Sagalyn PL (1991) Ellipsometric study of oxide films formed on LDEF metal samples. LDEF first post-retrieval symposium, NASA CP-3134, pp 1005–1021
9. Whitaker AF, Little SA, Harwell RJ et al (1985) Orbital atomic oxygen effects on thermal control and optical materials. STS-8 Results, AIAA paper 85–01415 presented at the 23rd Aerospace Science Meeting, 14–17 Jan 1985
10. Whitaker AF (1993) Atomic oxygen effects on LDEF experiment AO171. LDEF second post-retrieval symposium, NASA CP-3194, pp 1125–1135
11. Gregory JC (1986) Interaction of hyperthermal atoms on surfaces in orbit: the university of alabama experiment. In: Proceedings of the NASA workshop on atomic oxygen effect, 31–35 Nov 1986
12. Raspopov SA, Gusakova AG, Voropayev AG et al (1995) Enhanced oxidation of nickel in atomic oxygen. J Alloy Comp 227:5–9

Study of Tensile Properties of Mg-Rare Earth Alloys at Cryogenic Temperatures

Hao Wang, Shangli Dong, and Gang Lu

Abstract To evaluate the effects of cryogenic temperatures on mechanical properties of a thermo-mechanically treated Mg-rare earth (RE) alloy, tensile tests were carried out from room temperature to liquid nitrogen temperature (LNT) to study the deformation and fracture behavior of the selected magnesium alloy. The results showed that the ultimate strength and yield strength increased while elongation decreased as the testing temperature decreased. The as-forged specimen exhibited higher strength and ductility than the aged specimen.

Further scanning electron microscopy (SEM) investigation and optical observation illustrated that the deformation mechanism of the Mg-RE alloy changed from slip to twinning with a decrease in testing temperature. Furthermore, the fracture of tensile specimen transformed from boundary to twin plane as observed by SEM. The brittleness of the second phase at cryogenic temperature is taken into account in discussing the transition of the fracture mode of the Mg-RE alloy from intergranular to transgranular with the decrease of temperature.

Keywords Cryogenic temperature • Deformation • Fracture behavior • Mg-RE alloy • Tensile property

1 Introduction

Magnesium alloys are widely used in aerospace engineering, auto industry, electronic information industry and defense & military because of the advantages they offer, i.e. low density, high specific strength, good castability and good machining properties [1, 2]. The limitations for magnesium alloy applications stem from

H. Wang (✉) • S. Dong • G. Lu
School of Material Science and Engineering, Harbin Institute of Technology,
No.92, West Da-Zhi Street, Harbin 150001, China
e-mail: wewhl7r@gmail.com

Table 1 Composition of the Mg-RE alloy (wt.%)

Element	Zn	Zr	Y	C	N	H	O	other
Content	5.6–6.0	0.4–0.7	1.0–1.2	0.008	0.03	0.003	0.13	> 0.4

essential lack of a possible slip system at room temperature that is due to their hexagonal closed-pack (HCP) lattice structure [3]. The basal slip plane can be activated and it is the only slip deformation system at room temperature. Prismatic slip and pyramidal slip would be activated just after the temperature raising to 177°C [4] and 300 °C [5] respectively.

A common way to improve magnesium alloy's mechanical properties is, according to Hall-Petch law [6], through the control of the grain size by using appropriate solutions and/or through plastic deformation. Rolling, extrusion, hot forging and severe plastic deformation (SPD) could all have a significant effect on reducing the size of grains [7, 8]. Also solutions with Zr and rare earth (RE) elements would produce the same effect [9]. RE solution can even enhance the deformation ability by changing the c/a ratio to coordinate the slip system. Except the slip mechanism, twinning also plays an important role in Mg alloy deformation. Although twinning could not cause a large deformation, twinning can adjust the grain orientation for following slip [10] that makes it irreplaceable at room temperature or/and at high strain rate.

Due to the extensive applications of Mg alloys in space engineering, it is necessary to understand the behavior and properties of Mg alloys at extreme conditions. In this study, the tensile property of a Mg-RE alloy at cryogenic temperature is evaluated and the related deformation and fracture behavior are also examined.

2 Experimental Details

A forged Mg-RE alloy billet, having a composition as shown in Table 1, was employed as the experimental material for tensile testing. The specimens were machined from the blanks along the length direction (LD) as seen in Fig. 1.

After machining of the specimens, heat treatment was carried out at a number of different conditions, i.e. at 490°C for 4 h and aging at 180°C for 0–24 h, and solution at 420°C for 4 h and aging at 180°C for 0–24 h, and only aging at 170°C for 10 h, respectively. The hardness test was used to verify the peak heat-treatment. The maximum hardness was found for the solutions prepared at 490°C * 4h + 180°C * 20 h, and at 420°C * 4h + 180°C * 8 h that were used in the tensile testing and were named as Case1 and Case 2, respectively.

Tensile test was carried out at a constant crosshead speed of 1mm/min in MTS 810 machine equipped with a cryogenic system. After tensile test at various temperatures the fracture surfaces or adjacent regions of the fractured specimens were metallographically examined by SEM and optical microscopy.
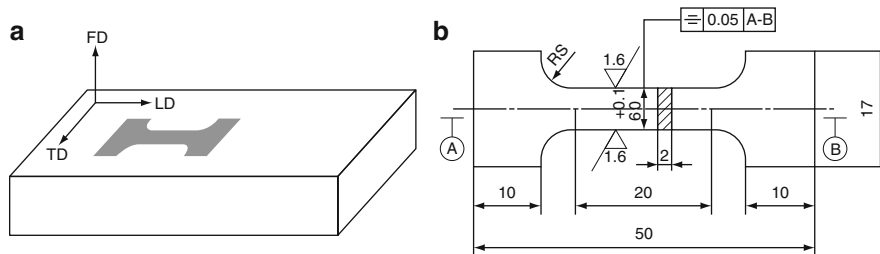
Fig. 1 Schematic presentation of the tensile samples used in the testing. (**a**) Tensile samples cut out geometry from the as-forged stock (**b**) Specimen shape and dimension for tensile test

3 Results and Discussion

3.1 Tension Test Results

The dependence of the ultimate tensile strength (UTS), yield strength (YS) and elongation of the as-forged, case 1 and case 2 treated specimens versus the testing temperature is shown in Fig. 2. It can be seen that the strength increased but elongation decreased with decreasing temperature. The as-forged specimen exhibits superior tensile properties, and its UTS changes to 395.9 MPa at LNT from 274.5 MPa at RT, YS increases to 317.1 MPa from 274.5 MPa, and the elongation drops to 3.8 % from 18.1 %. It is interesting to note that as epy temperature decreases, the strength does not increase monotonously, and there is a range of temperatures at which the UTS and YS are near constant, implying the deformation mechanism variation with decrease in testing temperature.

As it is well known, slip plays against twinning in deformation of metallic materials [11]. Slip and twinning are competitive factors when the stress reaches its critical resolved shear stress (CRSS). Generally, slip mechanism takes a dominating role at RT and high temperatures. Once slip releases strain concentration, it is impossible for twinning processes to form as a strain activator. In tensile tests, twinning mechanism contributes more in deformation with decrease of temperature, also in improving slip condition by orientation modification [12]. The slip deformation decrement caused by temperature decrease would be compensated by twinning. As temperature drops, the domination of slip will be limited by the lacking of thermal activity, and twinning deformation will stand out and support continuous deformation and cause possible slip plane rotated for subsequent deformation. The flat in Fig. 3 reveals that during these periods, the activated slip systems reduce and twinning occurs simultaneously, and deformation continues.

The discussed results indicate that the as-forged specimens exhibit better performance in both strength and ductility. As a conjecture, the effect of heat treatment which maybe promotes recrystallization in the Mg-RE alloy will be discussed in the following section.
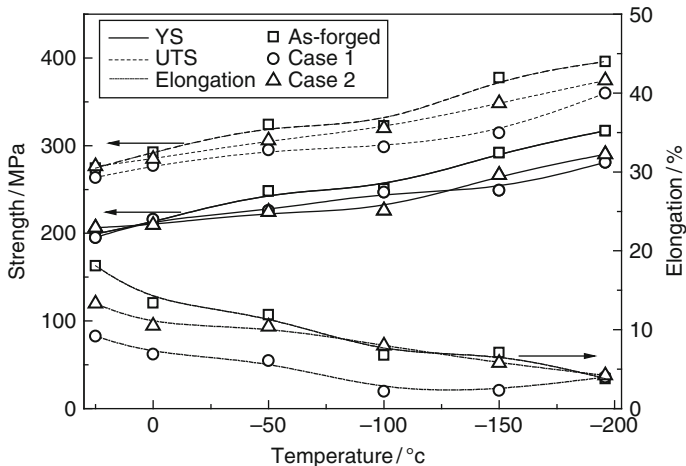
Fig. 2 Relationship of UTS, YS and elongation of Mg-Re alloy specimens with three processing histories versus the tensile test temperature
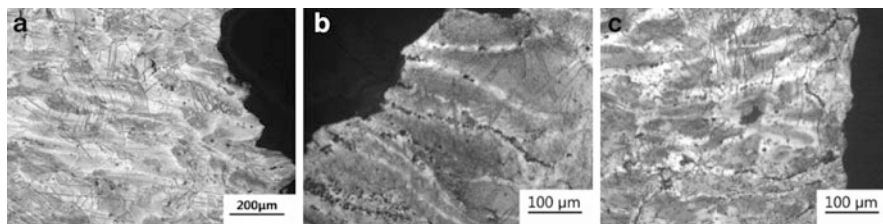
Fig. 3 Metallographic analysis near fracture surface of Mg-RE alloy tensile tested at RT. (**a**) as-forged specimen, (**b**) case 1 treated specimen, (**c**) case 2 treated specimen

3.2   Metallographic Examination

After tensile tests, sections of specimens near the fracture surface were selected for metallographic observation. Figures 3 and 4 show the microstructure features near fracture surface of the as-forged, case 1 and case 2 treated specimens at RT and LNT, respectively. Due to forging, the forged billet shows abundant recrystallization grains along the boundary of matrix grains, and these recrystallization grains would grow during heat treatment process. As seen in Fig. 3, the as-forged specimen exhibits more uniform deformation than others, and that the deformation is promoted by recrystallization structure in the heat-treated specimens. Therefore, the cracks in the heat-treated specimens are most likely formed at grain boundaries rather than inside grains. At the same time, all specimens experienced the transformation from slip dominated to twinning during the deformation with decreasing test temperature from RT to LNT.
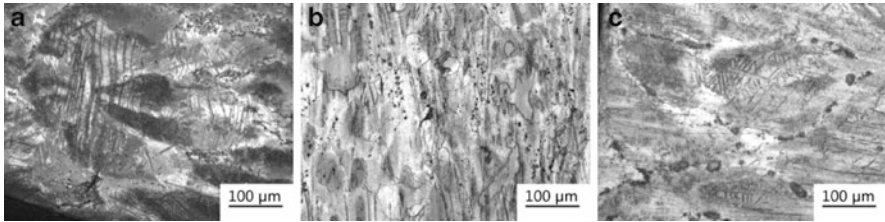
Fig. 4 Metallographic analysis near fracture surface of Mg-Re alloy tensile tested at LNT . (**a**) as-forged specimen, (**b**) case 1 treated specimen, (**c**) case 2 treated specimen
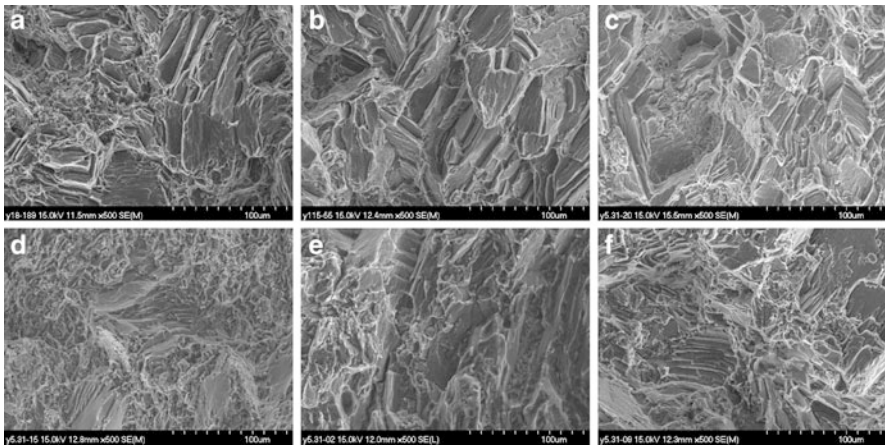
Fig. 5 Fractography of the specimens fractured at RT and LNT (**a**)as-forged specimen, RT; (**b**) case 1 treated specimen, RT; (**c**) case 2 treated specimen, RT; (**d**) as-forged specimen, LNT; (**e**) case 1 treated specimen, LNT; (**f**) case 2 treated specimen, LNT

3.3 SEM Observations

The fracture surfaces of the as-forged and heat-treated specimens tested at RT and LNT were carefully analyzed with SEM, and the typical fracture features are shown in Fig. 5. The predominant feature of the fracture surface is the occurrence of tear edges and steps, with some shallow dimples dispersed among them. Variation in both the height and the direction of the tear edges were found in the specimens fractured at LNT. With decreasing temperature, the edges and steps become lower and more uniform in orientation, implying the variation from intergranular fracture to transgranular fracture.

A noticeable plastic deformation in the heat-treated specimen before fracture with a large number of dimples is shown in Fig. 6. It should be noted that the size and the shape of the dimples are influenced by the stress state of the matrix and the size, shape and dispersion of the precipitates, as well as temperature. As seen in
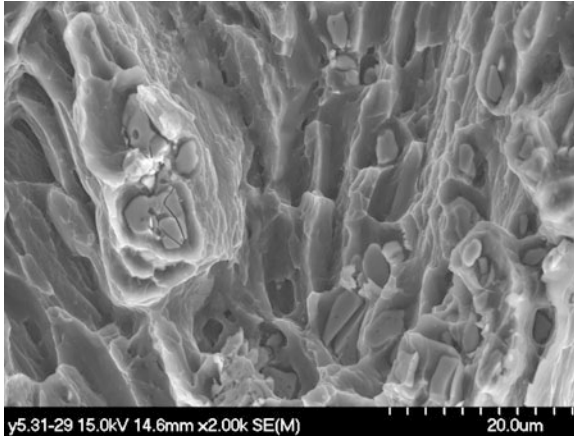
Fig. 6 Fracture observation of a case 2 treated specimen tensioned at 0 °C
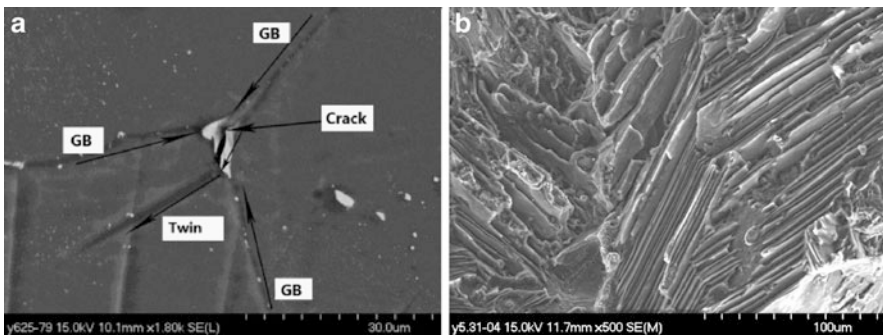
Fig. 7 SEM observation of (**a**) the surface of case 2 treated specimen at −100 °C perpendicular to fracture surface and (**b**) the fracture surface of case 1 treated specimen tensioned at LNT

Fig. 6, if the fracture occurred by void coalescence, the dimples would be shallow, especially as the precipitates cracked into pieces.

While a growing crack interacting with grain boundary and twinning is formed, it would propagate along the twinned plane since the twinning oriented the atoms plane to adjust the deformation and lower the Schimd Factor of twinned plane. The presence of transgranular cracks is more important at cryogenic temperatures. With decreasing temperature, the stress concentration especially shown in the Fig. 7a case, would allow the cracks to propagate along the twinning and induce fracture features as shown in Fig. 7b, resulting in cryogenic brittleness.

It was also found that, in addition to the predominant mechanism of quasi-cleavage fracture of the matrix, the brittleness of second phase among the grain boundary at cryogenic temperature would contribute to crack nucleation mechanism. As shown in Fig. 8, grain boundary crack is found to nucleate at the interface of

Fig 8 Fracture features of case 2 treated specimen tensioned at $-100\ ^{\circ}$C
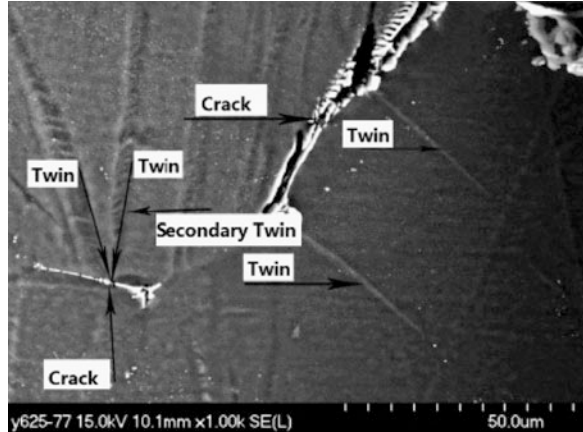
grain boundary, precipitates and the matrix under the stress concentration caused by interaction of twinning and grain boundary. Secondary twinning was also observed which indicates twinning is the predominant deformation at low temperature.

4 Conclusions

With decreasing tensile temperature, the ultimate strength and yield strength of the either as-forged or heat-treated Mg-RE alloy specimen increase, while the elongation decreases. The as-forged specimens exhibit superior properties than the samples prepared at 490 $^{\circ}$C * 4 h +180 $^{\circ}$C * 20 h and at 420 $^{\circ}$C * 4 h +180 $^{\circ}$C * 8 h at both room temperature and cryogenic temperature. The tensile fracture surface of the heat-treated specimen exhibited more obvious features of quasi-cleavage fracture than as-forged specimen at cryogenic temperature. As the second phases become brittle at cryogenic temperature, fracture mode of the Mg-RE alloy changed from intergranular fracture to transgranular fracture with decreasing tensile temperature. And it was found that twinning seemed to be the dominating deformation mechanism at cryogenic temperature, by various ways, in the Mg-RE alloy.

References

1. Zeumer N (1988) Magnesium alloys in new aeronautical equipment. Magnesium Alloys Appl. Wolfsburg, 28–30 Apr 1988, pp 125–132
2. Kainer KU, Bala Srinivasan P, Blawert C, Dietzel W (2010) Corrosion of magnesium and its alloys. In: Tony JAR (ed) Shreir's corrosion. Elsevier, Oxford, pp 2011–2041

3. Lou XY, Li M, Boger RK, Agnew SR, Wagoner RH (2007) Hardening evolution of AZ31B Mg sheet. Int J Plast 23(1):44–86. doi:10.1016/j.ijplas.2006.03.005

4. Flynn W (1961) On the thermally activated mechanism of prismatic slip in magnesium single crystals. Trans TMS-AIME 221:33

5. Obara T, Yoshinga H, Morozumi S (1973) {112-2} <11-23 > Slip system in magnesium. Acta Metall 21(7):845–853. doi:10.1016/0001-6160(73)90141-7

6. Barnett MR, Beer AG, Atwell D, Oudin A (2004) Influence of grain size on hot working stresses and microstructures in Mg-3Al-1Zn. Scr Mater 51(1):19–24. doi:10.1016/j.scriptamat.2004.03.023

7. Kim HK, Kim WJ (2004) Microstructural instability and strength of an AZ31 Mg alloy after severe plastic deformation. Mater Sci Eng A 385(1–2):300–308. doi:10.1016/j.msea.2004.06.055

8. Barnett MR, Nave MD, Bettles CJ (2004) Deformation microstructures and textures of some cold rolled Mg alloys. Mater Sci Eng A 386(1–2):205–211. doi:10.1016/j.msea.2004.07.030

9. Yang Z, Li JP, Zhang JX, Lorimer GW, Robson J (2008) Review on research and development of magnesium alloys. Acta Metall Sin 21(5):313–328. doi:10.1016/s1006-7191(08)60054-x (English Letters)

10. Yoo M (1981) Slip, twinning, and fracture in hexagonal close-packed metals. Metall Mater Trans A 12(3):409–418. doi:0.1007/bf02648537

11. Christian JW, Mahajan S (1995) Deformation Twinning. Prog Mater Sci 39:1–157

12. Jiang L, Jonas JJ, Mishra RK, Luo AA, Sachdev AK, Godet S (2007) Twinning and texture development in two Mg alloys subjected to loading along three different strain paths. Acta Mater 55(11):3899–3910. doi:10.1016/j.actamat.2007.03.006

Embrittlement of MISSE 5 Polymers
After 13 Months of Space Exposure

**Aobo Guo, Grace T. Yi, Claire C. Ashmead, Gianna G. Mitchell,
Kim K. de Groh, and Bruce A. Banks**

Abstract Understanding space environment induced degradation of spacecraft materials is essential when designing durable and stable spacecraft components. As a result of space radiation, debris impacts, atomic oxygen interaction, and thermal cycling, the outer surfaces of space materials degrade when exposed to low Earth orbit (LEO). The objective of this study was to measure the embrittlement of 37 thin film polymers after LEO space exposure. The polymers were flown aboard the International Space Station and exposed to the LEO space environment as part of the Materials International Space Station Experiment 5 (MISSE 5). The samples were flown in a nadir-facing position for 13 months and were exposed to thermal cycling along with low doses of atomic oxygen, direct solar radiation and omni-directional charged particle radiation. The samples were analyzed for space-induced embrittlement using a bend-test procedure in which the strain necessary to induce surface cracking was determined. Bend-testing was conducted using successively smaller mandrels to apply a surface strain to samples placed on a semi-suspended pliable platform. A pristine sample was also tested for each flight sample. Eighteen of the 37 flight samples experienced some degree of surface cracking during bend-testing, while none of the pristine samples experienced any degree of cracking. The results indicate that 49% of the MISSE 5 thin film

A. Guo · G.T. Yi · C.C. Ashmead · G.G. Mitchell
Hathaway Brown School, 19600 North Park Boulevard, Shaker Heights, OH 44122, USA

K.K. de Groh (✉)
Space Environment and Experiments Branch, NASA Glenn Research Center, 21000 Brookpark Rd., M.S. 309-2, Cleveland, OH 44135, USA
e-mail: kim.k.degroh@nasa.gov

B.A. Banks
Alphaport at, NASA Glenn Research Center, 21000 Brookpark Rd., M.S. 309-2, Cleveland, OH 44135, USA

polymers became embrittled in the space environment even though they were exposed to low doses (~2.75 krad (Si) dose through 127 μm Kapton) of ionizing radiation.

Keywords Low Earth orbit • Radiation • Spaceflight experiment • Polymers • Bend-test • Embrittlement

1 Introduction

As a result of space radiation, debris impacts, atomic oxygen interaction, and thermal cycling, the outer surfaces of space materials degrade when exposed to low Earth orbit (LEO) [1]. Ionizing radiation is known to embrittle polymers, and has severely embrittled the Teflon fluorinated ethylene propylene (FEP) outer layer of the multilayer insulation covering the Hubble Space Telescope [2]. A study was conducted to measure the embrittlement of 37 thin film polymers after LEO space exposure. The polymers were flown aboard the International Space Station and exposed to the LEO space environment for 13 months as part of the Materials International Space Station Experiment 5 (MISSE 5).

MISSE is a series of spaceflight experiments designed to test the performance and durability of materials and devices exposed to the low Earth orbit (LEO) space environment. MISSE consists of 11 flight experiment trays (10 Passive Experiment Carriers (PECs) and one smaller tray being flown with MISSE 8) that are mounted to the exterior of the International Space Station (ISS). Each two-sided tray contains numerous individual flight experiments and are positioned in either a ram/wake orientation or a zenith/nadir orientation [3]. The MISSE 5 polymer samples were from the Polymer Erosion and Contamination Experiment (PEACE) and were flown in a nadir-facing position for 13 months, which resulted in exposure to omni-directional charged particle radiation, thermal cycling, and low doses of atomic oxygen and direct solar radiation [3]. The samples were analyzed for space-induced embrittlement using a bend-test procedure in which the strain necessary to induce surface cracking was determined. Details on the MISSE 5 experiment, polymer flight samples, test procedures and bend-test results are provided.

2 MISSE 5 Experiments and Exposure

MISSE 5 contained two active and one passive experiments: The Forward Technology Solar Cell Experiment (FTSCE), an active experiment that tested the performance of 36 current and advanced generation solar cells for use on future spacecraft; the active Second Prototype Communication Satellite System (PCSat-2) that provided a communications system and tested the Amateur Satellite Service off-the-shelf solution for telemetry command and control; and the passive
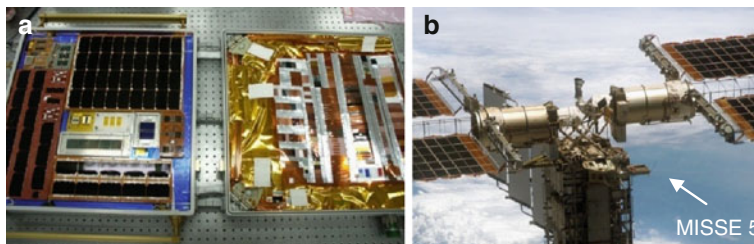
Fig. 1 MISSE 5: (**a**) Pre-flight, and (**b**) On-orbit photo taken during STS-114 of the zenith facing experiments

MISSE 5 Thermal Blanket Materials Experiment, which consisted of several individual experiments to measure the degradation of more than 200 materials in the space environment [3]. The 37 PEACE samples were flown as part of the MISSE 5 Thermal Blanket Materials Experiment.

MISSE 5 was placed in a zenith/nadir position on the P6 Trunion Pin Handrail of the International Space Station (ISS) during the STS-114 mission on August 3, 2005. Figure 1 shows a pre-flight photograph of MISSE 5 and an on-orbit photo taken during the STS-114 mission. MISSE 5 was exposed to the LEO space environment for 13 months, and was retrieved on September 15, 2006 during the STS-115 mission.

It is estimated that the polymers received an ionizing radiation (also called charged particle radiation) dose of ~2.75 krads(Si) through 127 μm Kapton, 165 ± 25 direct Sun hours (~360 Earth reflected), an atomic oxygen fluence of ~$1.8 \times o.10^{20}$ atoms/cm^2, and 6,400 thermal cycles [4]. Temperature range was estimated from the experiment deck temperature for the Forward Technology Solar Cell Experiment on the solar facing side of MISSE 5 [5].

3 MISSE 5 PEACE Polymers Experiment

The MISSE 5 PEACE Polymers experiment consisted of 49–0.5″ (1.27 cm) × 1.5″ (3.81 cm) rectangular polymer material samples with 53 polymer materials. The majority of samples were thin film flexible polymers. A few rigid samples were also flown sandwiched between two pieces of either Kapton H or Kapton HN with Y966 acrylic adhesive. The primary experiment objective was to determine the atomic oxygen erosion yield (Ey, cm^3/atom) of polymers after space exposure in a nadir orientation. As the Thermal Blanket Materials Experiment needed to be thin and flexible, samples were taped and then sewn onto a Kapton blanket substrate therefore making determination of the Ey based on mass loss impossible. Therefore, all samples were dusted with fine salt-spray particles to provide isolated locations of protection from atomic oxygen erosion so that recession depth measurements could be made post-flight for Ey determination [3]. Figure 2 is a
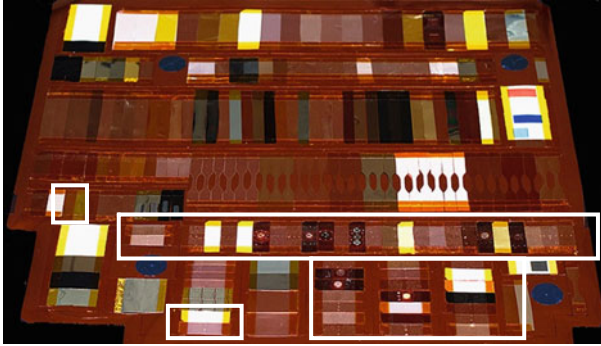
Fig. 2 Pre-flight photograph of the MISSE 5 Thermal Blanket Experiment (before the stitching and additional tape was applied). The PEACE Polymer samples are outlined in white

pre-flight photograph of the MISSE 5 Thermal Blanket Experiment with the PEACE Polymer experiment samples highlighted.

Thirty-seven of the 49 PEACE polymer samples were in a configuration that could be evaluated for surface embrittlement through bend-testing. The other 12 samples were not in thin film form and hence were not tested. A list of the flight samples that were tested along with the MISSE 5 flight sample number, the polymer name, the polymer abbreviation, trade names an d the film thickness, are provided in Table 1 in the Results and Discussion section.

4   Experiment Procedures

4.1   Sectioning Bend-Test Samples

Because the MISSE 5 PEACE polymers were multi-purpose samples, only a portion of each sample was bend-tested for strain-induced surface cracking. A piece measuring $0.5''$ (1.27 cm) $\times$ $0.2''$ (0.508 cm) of each sample was sectioned for bend testing. The small salt particles were removed from the samples prior to bend-testing by carefully brushing off the dust with a small horse-hair water color brush. The salt was washed off a few samples (M-2, M-18, M-24, T-1, T-6) by rinsing with water and then gently drying the sample with pressurized nitrogen.

4.2   Bend-Test Procedures

The samples were analyzed for space-induced embrittlement using a bend-test procedure in which a surface strain was applied to the sample without adding overall tensile load. The strain necessary to induce surface cracking was determined

Table 1 MISSE 5 bend-test results

MISSE ID	Material	Thickness (µm)	% strain
M-02	Cellulose acetate (CA), Clarifoil	50.8	DNC
M-03	Polybutylene terephthalate (PBT), GE Valox 357	76.2	DNC
M-04	Chlorotrifluoroethylene (CTFE), Neoflon M-300	127	DNC
M-05	Crystalline polyvinylfluoride w/white pigment (PVF), White Tedlar TWH10BS3	50.8	DNC
M-07	Perfluoroalkoxy (PFA), Teflon PFA 500 LP	127	DNC
M-08	Tetrafluoroethylene-ethylene (ETFE), Tefzel ZM	76.2	4.26
M-11[a]	Fluorinated ethylene propylene (FEP), Teflon FEP	50.8	2.09
M-13	Ethylene-chlorotrifluoroethylene (ECTFE), Halar 300	76.2	DNC
M-14	Polyimide BPDA (Upilex-S) (PI), Upilex-S 25 S	25.4	DNC
M-16	Polyamide 6 (PA 6), Nylon 6	50.8	DNC
M-17	Polyamide 66 (PA 66), Nylon 66	50.8	5.61
M-18	Polyacrylonitrile (PAN), Barex 210	50.8	8.60
M-19	Polybenzimidazole (PBI), Celazole PBI 22	50.8	DNC
M-21	Poly(p-phenylene-2 6-benzobisoxazole) (PBO), balanced biaxial film	25.4	DNC
M-23	Polyetheretherketone (PEEK), Victrex PEEK 450	76.2	9.92
M-24	Polyethylene terephthalate (PET), Mylar A-200	50.8	0.76
M-25	Polyimide (CP1) (PI), CP1	76.2	1.51
Q-2	Tetrafluoroethylene-ethylene (ETFE), Tefzel 500 LZ	127	6.91
T-1	Polymethyl methacrylate (PMMA), Plexiglas	50.8	0.40
T-4	Polysulphone (PSU), Thermolux P1700	50.8	DNC
T-5	Polyurethane (PU), Duraflex PS S010	50.8	DNC
T-6	Polyvinylidene fluoride (PVDF), Kynar 740	76.2	2.16
T-7	Polyvinyl fluoride (PVF), Tedlar TTR10SG3 (clear)	25.4	0.38
U-1	Polyetherimide (PEI), Utem 1000	254	DNC
U-2	Amorphous fluoropolymer (AF), Teflon AF 1601	50.8	1.45
U-3	Polyimide PMDA (PI), Kapton E	50.8	1.28
U-5	Ultra high molecular weight polyethylene (UHMWPE)	254	DNC
U-7	Polyvinyl chloride (PVC), clear-lay rigid PVC	127	DNC
V-1	Tetrafluoroethylene hexafluoro-propylene vinylidene fluoride (THV), Clariflex	254	25.72
V-2[b]	Expanded polytetrafluoroethylene (ePTFE) (ISS cable material)	228.6	DNC
V-3	Polytetrafluoroethylene (PTFE), PTFE T-100 virgin skived sintered film	76.2	5.03
V-4	Polyimide (PI), Kapton 100 CB	127	DNC
V-5	Poly arylene benzimidazole (TOR)	38.1	0.46
V-6	Poly arylene benzimidazole (COR)	38.1	0.70
V-7	Polysulfone (PSO)	50.8	DNC
X-1	Polyethersulfone (PES)	76.2	DNC
X-2	Polymethylpentent (PMP)	50.8	0.40

[a]FEP had cracks in the surface before bend-testing
[b]ePTFE is bright white and cracks may be hard to see

by bending the samples over mandrels. Bend-testing was conducted using an apparatus with a semi-suspended pliable platform, and a set of mandrels varying in diameter. A total of 23 mandrels were used, ranging in diameter from 1.253 to 0.052 cm. The diameter of each mandrel was calculated by using the mean diameter obtained by averaging four measurements made using Fowler & NSK Max-Cal electronic digital calipers. Each sample was bend-tested using successively smaller mandrels, with the sample being inspected after being bent around each mandrel. This procedure was continued until cracks were visible or until the sample did not experience any cracking with the smallest mandrel, in which case the sample was recorded as having not cracked.

During bend-testing, the sample was placed with its space-exposed face down onto the semi-guided apparatus. The mandrel was pushed down onto the sample, forcing the material to bend against a pliable surface that spanned two supports on the apparatus. The sample was bent in a U-shape, where the space-exposed surface was in tension and the backside surface was under compression. As the diameter of the mandrels decreased, the tension on the space-exposed surface of the sample increased because the sample was forced to bend more tightly around the mandrel.

Optical microscopy was used to document any surface features in the bend-test area prior to testing, and the same area was examined after bending around each mandrel to identify and document any induced surface cracks. The samples were examined at magnifications of approximately 10X to 13.8X with an Olympus SMZ stereo-zoom optical microscope outfitted with a Canon digital camera. An electronic coordinate system, the Boeckeler Microcode II Digital Readout, was used to find the same test location for microscopy examination before and after bend-testing at each mandrel, always centered at a dot that had been marked on the sample so that it would always be bent in the same location. Depending on the size of the sample, nine to fifteen optical microscopy pictures of each sample were taken before bending so that the entire bend-test sample was documented. When the sample was first observed to crack during the bend test process, the mandrel, and hence the strain, were recorded and the sample was not tested further. If no cracks could be detected under the optical microscope, the sample was bend-tested again with the next smaller mandrel, and the procedure was repeated. To verify the test results, several samples were bend-tested more than once.

4.3   Strain Calculations

Equation 1 allows the percent strain (E) to be calculated based on the thickness of the sample (t) and the diameter of the mandrel (d). This equation was derived from the bend-test configuration shown in Fig. 3.

$$E = \left(\frac{t}{d+t}\right) \times 100 \tag{1}$$
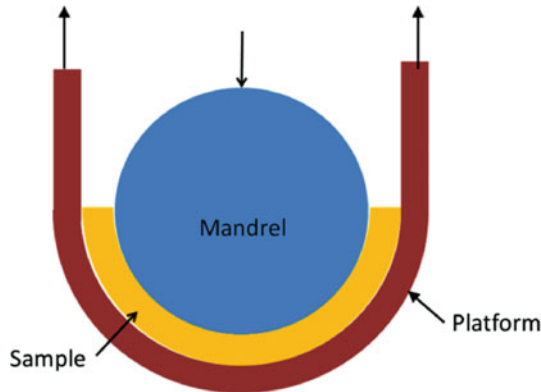
Fig. 3 Illustration of the bend-test configuration showing a cradle platform used to bend the sample around the mandrel

The percent strain for each individual material, as stated before, was determined based on the mandrel at which it initially cracked and the thickness of the sample.

5   Results and Discussion

Two of the PEACE Polymers samples were found to have cracked in half while on-orbit: Sample T-1 polymethyl methacrylate (PMMA, 50.8 μm thick) and Sample X-2 polymethylpentent (PMP, 50.8 μm thick). Close-up post-flight photos of Samples T-1 and X-2 are shown in Fig. 4a, b, respectively.

The set of photos in Fig. 5 is an example of the microscope images obtained before and after bend-testing with each mandrel. The sample in Fig. 5 is polyvinyl fluoride (PVF), also known as clear Tedlar (MISSE T-7). The box in each figure shows where cracks developed during bend-testing. This 25.4 μm thick sample cracked under a surface strain of only 0.38%.

While the PVF polymer shown in Fig. 5 is representative of typical MISSE 5 PEACE polymer behavior, with the formulation of very small but visible vertical cracks, Fig. 6 shows Sample X-2 (PMP), which exhibited more extreme behavior. This is one of two samples that cracked on-orbit. It was found to be extremely embrittled and fractured into pieces during bend-testing.

In Fig. 6 similar features are circled to facilitate the comparison process. Space exposure embrittled this polymer to a degree where the sample fell apart upon bend-testing with the largest mandrel (1.25 cm dia.), which provided a surface strain of only 0.4%. Sample T-1, PMMA, also cracked with the largest mandrel and fractured into pieces.

An example of a sample that did not crack during bend-testing, and hence remained ductile, is shown in Fig. 7. This is Polyurethane (PU), MISSE 5 sample T-5.
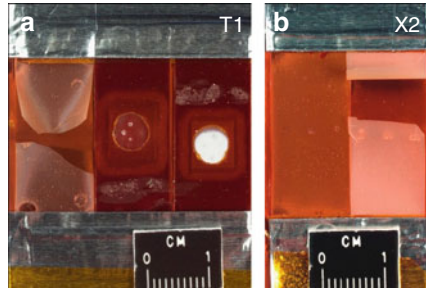
Fig. 4 Post-flight photographs of cracked PEACE samples: (**a**) sample T-1, PMMA (*left* sample), and (**b**) sample X-2, PMP (*right* sample)
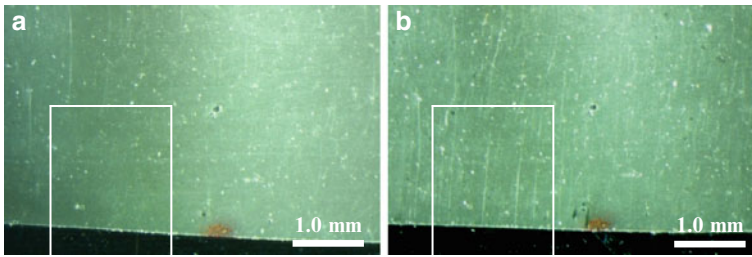
Fig. 5 Sample T-7, PVF: (**a**) before bend-testing and (**b**) after bend-testing
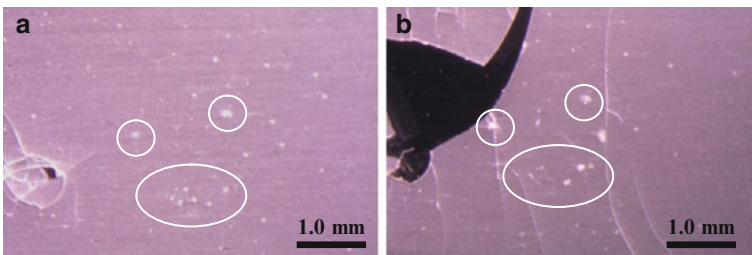
Fig. 6 Sample X-2, PMP: (**a**) before bend-testing, and (**b**) after bend-testing
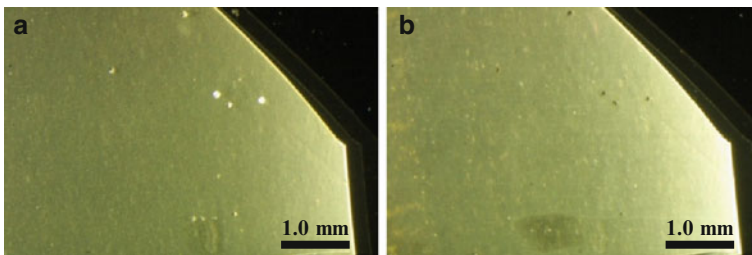
Fig. 7 Sample T-5, PU: (**a**) before bend-testing, and (**b**) after bend-testing

In summary, 17 of the 37 flight samples experienced some degree of surface cracking during bend-testing, while none of the pristine samples experienced any degree of surface cracking.

A list of the tested MISSE 5 PEACE samples, and their bend-test results, are provided in Table 1. In Table 1, DNC means Did Not Crack. It should also be noted that bright white materials such as Sample V-2, expanded polytetrafluoroethylene (ePTFE), would be particularly hard to see very fine surface cracks. Also, sample M-11, fluorinated ethylene propylene, appeared to contain surface scratches or cracks prior to bend testing, which may have impacted the bend-test results. Because the bend-test procedure relies on optical microscopy for identification of very small surface cracks, it is desirable to verify these bend-test results by examining the bend-tested samples with scanning electron microscopy or another technique that can verify the development of surface cracks.

The fact that surface strain induced cracking occurred in FEP (M-11), Kapton E (U-3), PTFE (V-3), and TOR (V-5), and that Upilex-S (M-14) did not crack, is consistent with results by Miller and Dever who characterized the tensile properties of these same polymers flown on the MISSE 5 Thermal Blanket Experiment as part of the Polymer Film Thermal Control Experiment (PFTC) [4].

6 Summary and Conclusions

A study was conducted to characterize the embrittlement of thin film polymers after exposure to the space environment. In these investigations a bend test procedure was used to characterize the embrittlement of 37 different polymers that were exposed to LEO aboard the ISS for 13 months in a nadir-facing orientation as part of the MISSE 5 PEACE polymers experiment. Using mandrels of different diameters combined with optical microscopy, the strain necessary to induce surface cracking was determined for flight samples and compared with that of pristine samples. While none of the pristine materials cracked at the highest strain available, 18 of the 37 flight samples (49%) experienced embrittlement, shown by surface-tensile-induced cracking, after just 13 months of exposure in LEO. Two of the polymers, PMMA and PMP, had cracked while on-orbit and were so brittle that they fractured when bend-tested with the largest mandrel. These results indicate that many thin film polymers are susceptible to embrittlement in the LEO space environment, even after low solar and particle radiation exposures. Therefore, even "minimal" amounts of radiation exposure must not be overlooked when designing spacecraft components based on expected mechanical properties.

References

1. Dever JA, Banks BA, de Groh KK, Miller SK (2005) Degradation of spacecraft materials (Chapter 23). In: Kutz M (ed) Handbook of environmental degradation of materials. William Andrew Publishing, Norwich
2. Townsend JA, Hansen PA, Dever JA, de Groh KK, Banks BA, Wang L, He C (1999) Hubble space telescope metallized teflon FEP thermal control materials: on-orbit degradation and post-retrieval analysis. High Perform Polym 11:81–99
3. de Groh KK, Banks BA, Dever JA, Jaworske KJ, Miller SK, Sechkar EA, Panko SR (2008) NASA Glenn Research Center's Materials International Space Station Experiments (MISSE 1–7). In: Proceedings of the international symposium on SM/MPAC&SEED experiment, Tsukuba, 10–11 March 2008. JAXA-SP-08-015E, March 2009, pp 91–119; also NASA TM-2008-215482, Dec 2008
4. Miller SKR, Dever JA (2011) Materials international space station experiment 5 polymer film thermal control experiment. J Spacecr Rocket 48(2):240–245, March–April 2011
5. Walters RJ et al (2005) Forward technology solar cell experiment first on-orbit data. In: 19th space photovoltaic research and technology conference, Brookpark, Ohio, 20–22 Sept 2005, NASA/CP-2007- 214494

Temperature Effects of Ultraviolet Irradiation on Material Degradation

Kazuyuki Mori and Junichiro Ishizawa

Abstract Ultraviolet rays (UV) cause organic materials to deteriorate. UV irradiation ground testing is therefore important to understand the "adequate lifetime assessment" and the "end-of-life (EOL) characteristic" of materials used in space. In previous experiments, high temperatures were found to accelerate the UV degradation of cross-linked ethylene tetrafluoroethylene (X-ETFE). This causes concern of potentially similar effects in other materials. In this study, we evaluated UV degradation at high temperatures and subsequently determined materials usable in space that had shown accelerated degradation due to UV irradiation at high temperatures.

Keywords Ultraviolet • Degradation • Temperature • Thermo-optical property

1 Introduction

In 2003, Midori-II (Advanced Earth Observing Satellite-II: ADEOS-II) stopped supplying observation data. When troubleshooting Midori-II, high temperatures were found to have accelerated the UV degradation of X-ETFE [1]. There was a concern that similar effects could appear in other materials. And, indeed, similar temperature dependence was observed for X-ETFE, F-OSR, PEN, polyurethane. To shed more light on this problem, the behavior of X-ETFE/F-OSR/PEN was analyzed in detail. It was observed that reflectance and transmittance spectra changed greatly. The deterioration of the thermal-optical properties were observed over a range of UV wavelengths and could not be connected to a specific

K. Mori (✉) • J. Ishizawa
Aerospace Research and Development Directorate, Japan Aerospace Exploration Agency,
Tsukuba 305-8505, Japan
e-mail: mori.kazuyuki@jaxa.jp

Table 1 UV irradiation conditions

Irradiation fluence (ESD[a])	30		
Irradiation flux (solar)	10		
Target temperature	below 313 K	353 K	423 K

[a]Equivalent solar day, 1 ESD $= 1.02 \times 10^3$ J·cm^{-2}
(Quantity survey of solar spectrum 200–400 nm)

Table 2 Equipment for thermo-optical property measurement

	Name	Manufacturer
Solar absorptance	U-4100	Hitachi High-technologies
Normal infrared emittance	TESA2000	AZ technology

Table 3 Equipment for spectrum measurement

	Name	Baseline	Manufacturer
Reflectance spectrum	U-4100	SRS-99	Hitachi High-technologies
Transmission spectrum	U-4100	–	Hitachi High-technologies

wavelength. In the observed degradation, the temperature was found to play an important role during UV irradiation testing. We recommend that the ground test temperature be kept at the same level as in-orbit temperature.

2 Experimental Procedures

UV irradiation was performed using JAXA's ground test facilities. The UV irradiation conditions are shown in Table 1. In the experiments the specimen surfaces were subjected to three target temperatures, i.e. below 313, 353 and 423 K. In general, the thermo-optical properties of thermal control materials are influenced by UV. Before and after the UV irradiation tests, the solar absorptance (α_S), normal infrared emittance (ε_N) and reflectance spectra (%R) of the specimens were measured. Tables 2 and 3 show the equipment used in the measurements.

3 Results and Discussion

A number of different polymers were selected for testing. The specimens used in this work and the results of the thermo-optical properties measurements are shown in Tables 4 and 5. As can be seen from Table 4, the UV degradation of solar

Table 4 Solar absorptance of specimens UV-irradiated at different temperatures

Specimen		Solar absorptance/U-4100			
		Initial	30 ESD @ below 313 K	30 ESD @ 353 K	30 ESD@423 K
X-ETFE	Cross-linked ethylene tetrafluoroethylene	0.19	0.40	0.57	0.75
NOVA astro white	White paint/organic (silicone)	0.29	0.31	0.34	0.34
S13GP L0-1	White paint/organic (silicone)	0.20	0.20	–	0.21
Flexible-OSR	IT O/CeO/polyetherimide/Ag/Ni	0.12	0.15	0.19	0.26
Ag/FEP	Ag coated perfluoro ethylene-propylene	0.02	0.02	0.02	–
Upilex-R t = 25 μm	Polyim ide film/Ube Industries, Ltd.	0.18	0.18	0.18	0.18
Upilex-R t = 50 μm	Polyim ide film/Ube Industries, Ltd.	0.20	0.21	0.20	–
Upilex-S t = 50 μm	Polyim ide film/Ube Industries, Ltd.	0.40	0.40	0.40	0.40
Upilex-S t = 125 μm	Polyim ide film/Ube Industries, Ltd.	0.44	0.44	0.44	–
Apical AH t = 25 μm	Polyim ide film/Kaneka Corporation	0.22	0.23	0.23	0.24
Kapton 100 H	Polyim ide film/Du Pont-Toray Co., Ltd.	0.23	0.26	0.25	0.27
Modified PI	Poly silox ane coated polyim ide film	0.23	0.33	0.31	–
SiOx Kapton H	SiOx coated Kapton H	0.22	0.23	0.22	–
PEN t = 50 μm	Poly ethylene naphthalate	0.03	0.11	0.17	Tg/428K
DUS202 t = 0.1 mm	Polyurethane/Sheedom Co., Ltd.	0.02	0.16	0.32	–
DUS451 t = 0.2 mm	Polyurethane/Sheedom Co., Ltd.	0.08	0.17	0.35	–
DUS601 t = 0.8 mm	Polyurethane/Sheedom Co., Ltd.	0.21	0.30	0.33	[a]0.34
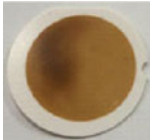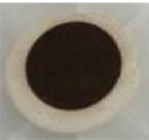
[a]383K

Table 5 Infrared emittance of specimens UV-irradiated at different temperatures

Specimen		Normal infrared emittance/TESA 2000			
		Initial	30 ESD @ below 313 K	30 ESD @ 353 K	30 ESD @ 423 K
X-ETFE	Cross-linked ethylene tetrafluoroethylene	0.89	0.91	0.91	0.90
NOVA astro white	White paint/organic (silicone)	0.94	0.93	0.94	0.94
S13GP L0-1	White paint/organic (silicone)	0.95	0.95	–	0.95
Flexible-OSR	IT O/CeO/polyetherimide/Ag/Ni	0.87	0.87	0.88	0.87
Ag/FEP	Ag coated perfluoro ethylene-propylene	0.59	0.59	0.61	–
Upilex-R t = 25 μm	Polyim ide film/Ube Industries, Ltd.	0.51	0.51	0.51	0.51
Upilex-R t = 50 μm	Polyim ide film/Ube Industries, Ltd.	0.65	0.65	0.64	–
Upilex-S t = 50 μm	Polyim ide film/Ube Industries, Ltd.	0.65	0.65	0.64	0.65
Upilex-S t = 125 μm	Polyim ide film/Ube Industries, Ltd.	0.80	0.79	0.79	–
Apical AH t = 25 μm	Polyim ide film/Kaneka Corporation	0.51	0.52	0.51	0.51
Kapton 100 H	Polyim ide film/Du Pont-Toray Co., Ltd.	0.52	0.52	0.51	0.51
Modified PI	Poly silox ane coated polyim ide film	0.70	0.69	0.70	–
SiOx Kapton H	SiOx coated Kapton H	0.54	0.53	0.54	–
PEN t = 50 μm	Poly ethylene naphthalate	0.58	0.60	0.59	Tg/428K
DUS202 t = 0.1 mm	Polyurethane/Sheedom Co., Ltd.	0.80	0.79	0.82	–
DUS451 t = 0.2 mm	Polyurethane/Sheedom Co., Ltd.	0.92	0.91	0.92	–
DUS601 t = 0.8 mm	Polyurethane/Sheedom Co., Ltd.	0.97	0.94	0.96	[a]0.92

[a]383K

Table 6 Photographs of UV-irradiated X-ETFE (Raychem Spec 55/) at temperatures below 313, 353 and 423 K

X-ETFE	Testing temperature		
UV fluence (ESD)	Below 313 K	353 K	423 K
0			
30			

absorptance of X-ETFE and F-OSR was found to accelerate at higher temperatures. Polyethylene naphthalate (PEN) also demonstrated accelerated degradation at high temperatures. No degradation, however, was observed in the infrared emittance values for all of the tested samples regardless of temperature (Table 5). Table 6 shows the photographs of the UV-irradiated samples. A strong effect of the temperature on UV degradation of the surface is clear. The surface color changed significantly, from white to dark brown, at 353 and 423 K (higher temperature) respectively, compared with the specimen below 313 K.

The quantitative thermo-optical properties of UV-irradiated X-ETFE, F-OSR and PEN specimens are shown in Fig. 1. As can be seen from Fig. 1, the degradation of solar absorptance for all three materials is accelerated with increasing temperature for all UV irradiation fluencies, while the normal infrared emittance does not depend on UV irradiation at temperatures below 313, 353, and 423 K. In addition, the data at 423 K for the PEN (TeonexFilm CLA-50 μm) was indicative of the glass-transition temperature (Tg) for this material at 428 K [2].

The short wavelength UV is very energetic. The reflectance spectra of X-ETFE and F-OSR are shown in Figs. 2 and 3, respectively. As can be seen from Figs. 2 and 3, the degradation effect is seen over a wide-range of wavelengths and not at any specific wavelength. For X-ETFE (Fig. 2), deterioration in the reflectance properties is clearly visible with the increased temperature. In addition, although no deterioration of the reflectance is observed in the wavelength area exceeding 1200 nm at a temperature below 313 K, deterioration of the reflectance is observed up to 2,200 nm at 353 and 423 K. This supports the theory that the temperature change alters the thermophysical properties of X-ETFE constitution materials, at 313 and 353 K.
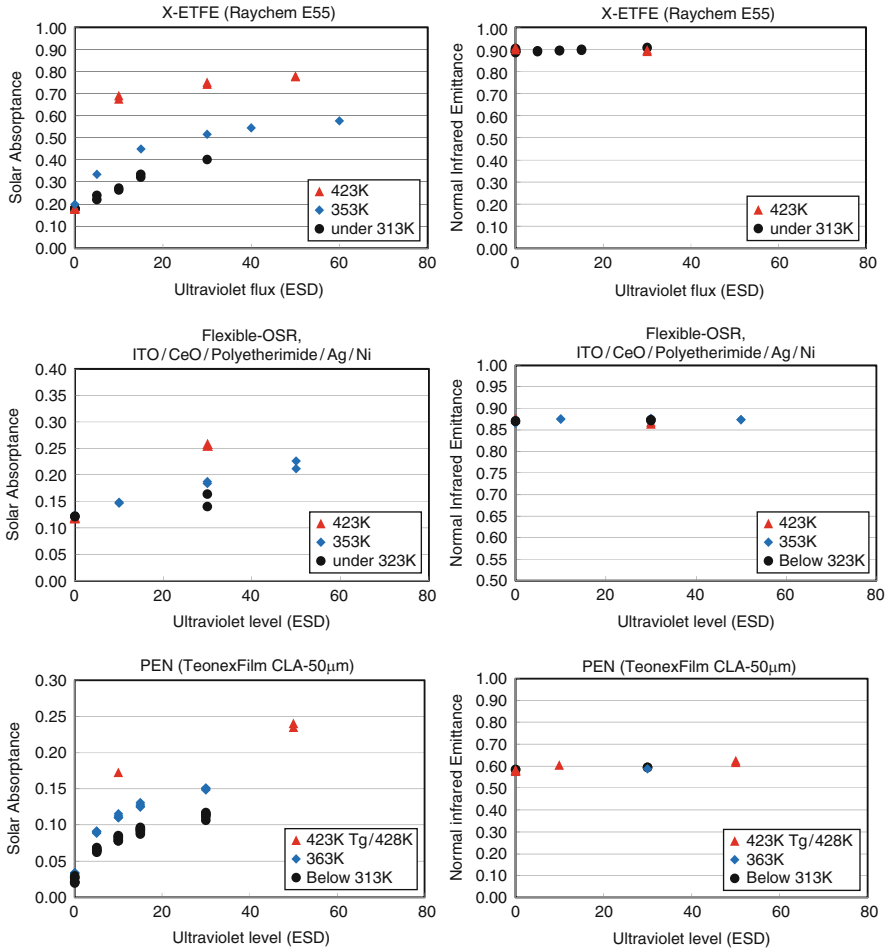
Fig. 1 Solar absorptance and normal infrared emittance changes versus the UV irradiation intensity

In F-OSR the reflectance deteriorates with the increase in temperature through UV irradiation. However, no deterioration in reflectance is observed in the wavelength areas of 250–350 nm and 850–1,150 nm respectively, regardless of temperature. In the wavelength area exceeding 1,150 nm, no deterioration of the reflectance spectrum was observed by UV irradiation at 313 K. but such deterioration was observed by UV irradiation at 353 and at 423 K. This supports the theory that the change in temperature also alters the thermophysical properties of F-OSR constitution materials, at 423 and 353 K, similar to X-ETFE.
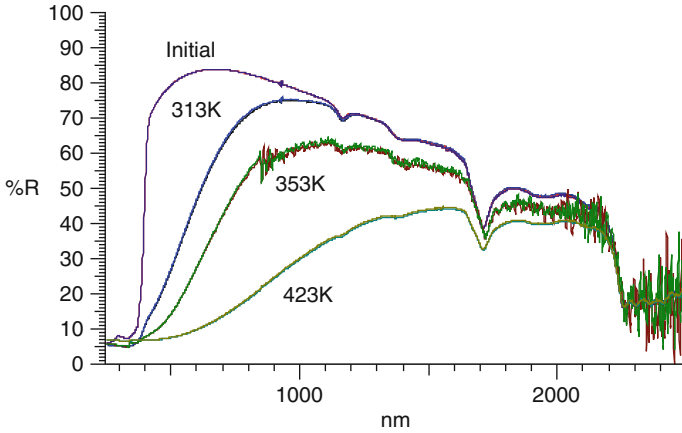
Fig. 2 Reflectance spectrum of X-ETFE. Initial, 30ESD@313 K, 30ESD@353 K, 30ESD@423 K
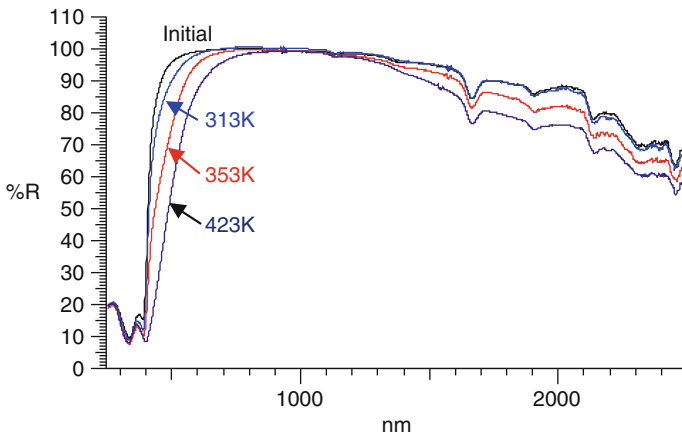
Fig. 3 Reflectance spectrum of F-OSR. Initial, 30ESD@313 K, 30ESD@353 K, 30ESD@423 K

In PEN (Fig. 4) deterioration of reflectance is observed by UV irradiation at both temperatures and in a wavelength region of less than 450 nm. The reflectance increases by more than 1%, within the range 450–800 nm. The deterioration in reflectance is small with UV irradiation below 313 and at 353 K above 800 nm.

X-ETFE and F-OSR are materials with very low transmission, but PEN is a material with high transmission. The transmissivity deteriorates significantly in the wavelength area less than 550 nm, with deterioration exceeding 1 % observed until 800 nm (Fig. 5). The deterioration of solar absorptance is significant (Table 4), because there is significant deterioration of transmissivity and 450~500 nm is where the solar spectral irradiance (Fig. 6) peaked [3].
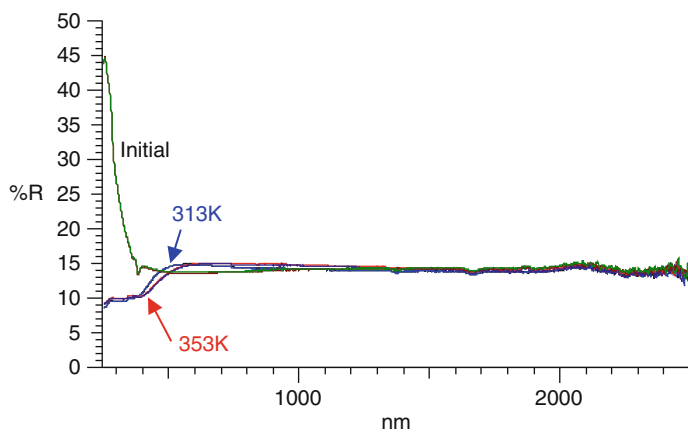
Fig. 4 Reflectance spectrum of PEN. Initial, 30ESD@313 K, 30ESD@353 K
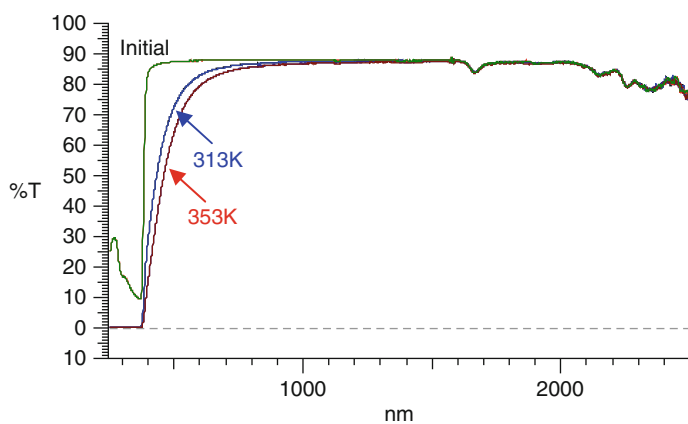
Fig. 5 Transmission spectrum of PEN. Initial, 30ESD@313 K, 30ESD@353 K
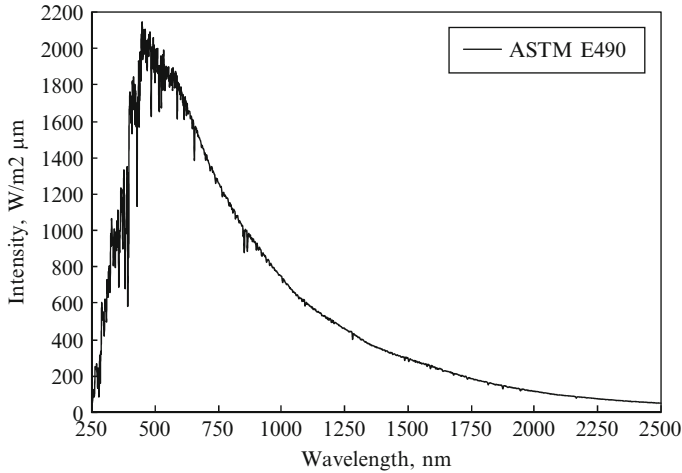
Fig. 6 Solar spectral irradiance according to ASTM E490-73a [3]

4 Summary

We evaluated the UV degradation at high temperatures, using ground irradiation facilities. Some materials for use in space showed accelerated degradation due to UV irradiation at high temperatures. Temperature was an important factor during the UV irradiation testing. We recommend that the ground test temperature be kept at the same level as in-orbit temperature. It is insufficient to keep the UV irradiation temperature at a level lower than orbit. In particular, for X-ETFE, F-OSR and PEN, the test temperature under UV irradiation must be monitored. In future, there should be a guideline to set the temperature for the ground UV irradiation examination, by thermal analysis.

References

1. Ishizawa J et al (2009) Space environment effects on cross-linked ETFE polymer. In: Proceedings of the 11th ISMSE: on CD-ROM
2. http://www.teijindupontfilms.jp/english/product/pen_teo.html
3. ASTM E490 - 00a (2006) Standard solar constant and zero air mass solar spectral irradiance tables. ASTM International, Philadelphia

GEANT4 Simulation of Interplanetary Proton Induced Deep Dielectric Charging

Qin Xiaogang, Wang Ji, Yang Shengsheng, Chen Yifeng, and Shi Hong

Abstract Energetic protons with high fluence are a major reason for internal charging of dielectrics in interplanetary spacecraft. In this paper, the proton induced internal charging of dielectrics is predicted based on radiation induced conductivity (RIC) model and particle transfer software package GEANT4. With GEANT4-RIC simulation, the fluence and dose depth profiles in Kapton and Teflon under 10 MeV proton radiation are obtained. These results are introduced into the RIC model containing the current continuity equation, the Poisson equation and the trapped charge equation to solve the internal charge and electric field distributions. The latter is compared with insulation disruption field as a guideline for discharging behavior.

The performed simulations validated a common experimental result that discharge occurs in Kapton after it was irradiated with protons at a fluence of $3 \times 10^{12}/cm^2$ and Teflon does not exhibit such phenomena. The obtained results confirm that the GEANT4-RIC method can be used to evaluate the proton induced dielectric charging and that it provides a basis to understand better the interplanetary proton induced internal charging problem.

Keywords Dielectrics • GEANT4s • Internal charging • Interplanetary • Proton

1 Introduction

Deep dielectric charging is one of the important environment effects to consider for satellites orbiting Earth. Electrons injected into dielectric material would result in deep dielectric charging and discharging that may cause data flipping, command

Q. Xiaogang • W. Ji • Y. Shengsheng • C. Yifeng (✉) • S. Hong
Science and Technology on Vacuum &Cryogenics Technology and Physics Laboratory,
Lanzhou Institute of Physics, Chinese Academy of Space Technology, Lanzhou 730000, China
e-mail: chenyifeng04@gmail.com

errors and changes in dielectric material properties, all of which may lead to final serious consequences that are difficult to predict. At Earth orbits, being shielded and protected by the Earth's magnetic field, the primary charging factor is electrons in the Van Allen radiation belt and just the outer radiation belt. For the inner radiation belt the proton fluence has no influence on the spacecrafts behavior [1, 2].

In deep space exploration, however, the spacecrafts will encounter the interplanetary space environments that are composed mostly of low energy plasma from the solar wind and high-energy protons from solar energetic particle events. Generally speaking, such radiation environments take Galactic Cosmic Rays (GCR) and Solar Particle Events (SPE) into account, for example, solar protons with high energy from solar events will be the leading cause of interplanetary spacecraft deep charging [3].

In 1991, a model was proposed by Akishin based on studies of dielectric charging under proton irradiation that allowed calculating the inner field according to the ionization processes. The relationships between the discharge and the proton energy as well as beam density were established [4, 5]. In 1992, Gromov performed ground-based experiments to simulate charging and charge distribution under solar proton irradiation, in which Mylar and Teflon samples were exposed to proton beams. The proton fluence was $5 \times 10^{10}/cm^2$ with energy range from 0.23 to 0.8 MeV with the irradiation times around 3–9 s. The obtained results demonstrated that time evolution of surface charge was nonlinear that indicated that charge storage was dependent on irradiation and leakage currents [6]. In a different work by Khorasanov, studying the influence of proton irradiation on polymethyl methacrylate and epoxy resin boards, the critical proton fluence causing breakdown was 10^{12}–$10^{13}/cm^2$ for proton energies between 10 and 70 MeV [7]. In 2005, at Crocker Nuclear Laboratory Cyclotron at the University of California, Nelson conducted proton beam exposure tests to simulate dielectric internal charging processes that materials would experience when traveling between planets, or on the Moon, or Martian surface at CME [3]. Materials he selected included Teflon, cream and circuit board material. It was shown that at the dose of $3 \times 10^{12}/cm^2$, in both the circuit board material and the cream pulsed discharges occurred, while no discharge phenomenon was observed for Teflon. Based on a large difference observed between the computation results based on a simplified parallel plate capacitor model and the experimental result of proton beam irradiation, Nelson concluded that the model wasn't sufficient enough to explain internal discharge induced by proton irritation [3]. As a result, more accurate models and further experiments were expected for proton irritation issue. Boev et al. have experimentally and theoretically confirmed that under irradiation the electric field in dielectrics was related to the incident energy and radiation induced conductivity of the material [8]. Based on that conclusion, in this paper it is pointed out that radiation induced conductivity (RIC) model and particle transfer software package GEANT4 can be used to simulate proton radiation induced charging, and to predict electric field distribution in dielectrics. The feasibility and accuracy of using GEANT4-RIC to calculate the internal discharge have been determined preliminarily.

Fig. 1 Proton induced internal charging
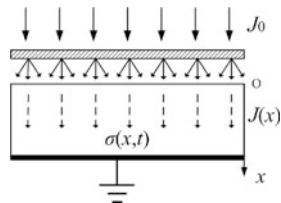
2   GEANT4-RIC Models

2.1   RIC Model

Figure 1 present schematically the RIC model. As can be seen from Fig. 1, protons, incident on dielectric with a certain energy spectrum and a certain flux, lead to the formation of deep dielectric charging. Back surface of the dielectric is grounded for charge leakage, so this kind of connection is called back surface grounding structure.

Similar to the electrons radiation induced conductivity (RIC) model, the RIC model for protons is also described by three equations, i.e., the Poisson equation, the continuity equation and the rate equation for deep trapping of positive charges [9]. Therefore the basic governing equations are described as:

$$\varepsilon \frac{\mathrm{d}E(x,t)}{\mathrm{d}t} + [\sigma(x) + \mu_+\rho_f(x,t)]E(x,t) + J(x) = J_0(t) \tag{1}$$

$$\varepsilon \frac{\mathrm{d}E(x,t)}{\mathrm{d}x} = -\left(\rho_f(x,t) + \rho_t(x,t)\right) \tag{2}$$

$$\frac{\mathrm{d}\rho_t(x,t)}{\mathrm{d}t} = \frac{\rho_f(x,t)}{\tau_+}\left(1 - \frac{\rho_t(x,t)}{\rho_m}\right) \tag{3}$$

In the equations, ε is the dielectric permittivity of the material, μ_+ and τ_+ are the mobility and trapping time, respectively, of the free positive charges, ρ_m is the density of the proton traps, $E(\chi,t)$, $\rho_f(\chi,t)$ and $\rho_t(\chi,t)$ are the electric field, the free charge density and the trapped charges density at position x and at moment t, respectively. The $J_o(t)$ is the flux of the incident particles that is computed by GEANT model. The $J(x)$ is the density of the proton beam current, σ is the electric conductivity of the material that depends on the dose rate under irradiation and it can be expressed by the relation:

$$\sigma = \sigma_d + \sigma_r = \sigma_d + k\dot{D}^\Delta \tag{4}$$

where σ_d is the dark conductivity or intrinsic conductivity, while σ_r is radiation induced conductivity, k and Δ are the coefficient and exponent of σ_r, is the radiation dose rate that are also derived from GEANT4.

3   MULASSIS Model

Geant4 is a toolkit for simulating the transfer of particles through matter that is a result of worldwide collaboration that grew to include the efforts of hundreds of scientists and engineers from Europe, Japan and the United States. The origin of Geant4 development can be traced back to 1993. It has been designed and constructed to simulate a great variety of particles, cover a wide energy range, provide choices of physics models to handle interaction between particles and matter, enable its easy adaptation for optimal use. As a result, the model has been used in applications in High-Energy Physics (HEP), medical physics and space engineering [10]. Based on Geant4, the MULASSIS model is a Multi-Layered Shielding Simulation Software that can provide quantitative measurements of particle fluence, energy deposition, Non-Ionizing Energy Loss (NIEL) and Pulse height energy-deposition spectra (PHS) for 1-D flat-panel or Spherical shields [11]. Here, the progress for protons and dielectrics interaction is directly simulated using MULASSIS, and the flux and dose distributions varying with depth are obtained

Using GEANT4 as a simulation toolkit, a right physical propagation model, according to incident-particle energy, should be selected. For interaction between protons and material, GEANT4 makes the choices of the Bertini intra-nuclear cascade model and the Precompound Model. The former deals with energy range from 100 to 5 GeV, while the latter expands hadrodynamics model and turns into an inelastic collision model about the low-energy nucleons [12]. The MULASSIS covers the physics models mentioned above that constitute Hardon physics script. In addition, we take it into consideration that making a comparison with the electron effects requires standard electromagnetism propagation rules. Here we adopt "Hardron + em-ln", and the particles incident energy range is 1 keV ~ 100TeV [11]. Figure 2 shows the trajectory of protons with 10 MeV in Teflon Multilayer of 5 mm thickness which is made up of 100 layers and each layer's width is 50 μm.

It solves for the protons rang in Teflon from the model shown in Fig. 2. Figure 3 plots the dose and fluent profiles along with depth. It is clear that the 10 MeV proton fluence reaches its maximum at 0.7 mm and at 0.75–0.80 mm is near zero. This numerical date proves that the model we introduced and the result we calculated are correct and believable, for in Ref.13 it had been shown that 10 MeV protons rang in Telfon was 0.70832 mm. The patterns in Fig. 3 also demonstrate that most protons are highly concentrated around the range, which is a very difference phenomenon from electrons incidence.

Compared with particle incidence time, the duration of interaction between protons and dielectric is actually very short and negligible. Therefore, the previous fluence result being normalized can be used to calculate different radiation dose and fluence.
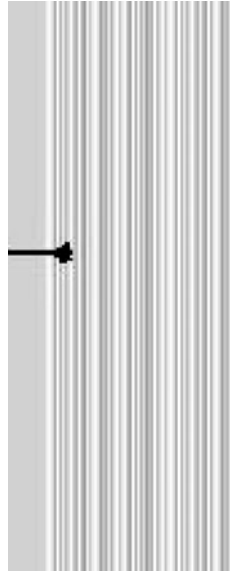
Fig. 2 10MeV protons incidence trajectory in Teflon of 5 mm thickness
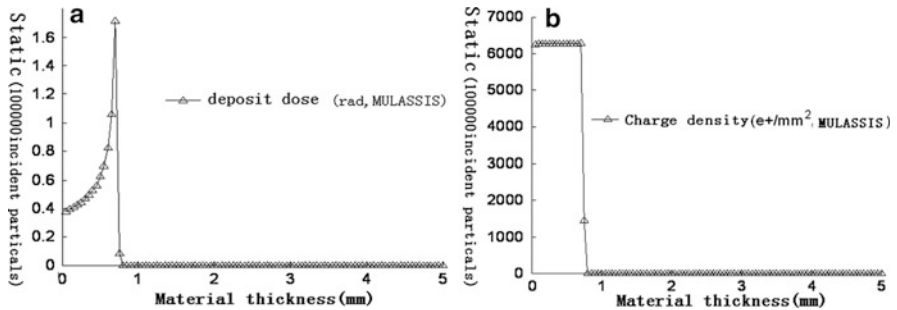
Fig. 3 MULASSIS numerical result of proton radiation. (**a**)- 10 MeV protons dose distribution along with depth in Teflon; (**b**) 10 MeV protons fluence distribution along with depth in Teflon

4 Simulation Validations

Nelson experimental result showed that Kapton occurred discharge after radiation with the fluence of $3 \times 10^{12}/\text{cm}^2$ lasting 20 min ~ 2 h and Teflon did't give such a phenomenon [4]. In order to make a comparison with the experimental results, here both Kapton and Teflon are assumed 1.5 mm in the same as experiment parameters besides the protons energy is fixed at 10 MeV and the duration 20 min. Then beam density is $4 \times 10\text{-}10\text{A/cm2}$ at $3 \times 10^{12}/\text{cm}^2$. Apparently the parameters in proton RIC model such as free-charge mobility, trapping time, the maximum trapped

Table 1 Simulation parameters in dielectric material internal charging

Parameters	Material	
	Kapton	Teflon
ε_r	3.4	2.1
$\sigma_d(\Omega^{-1}\,\mathrm{m}^{-1})$	10^{-16}	10^{-16}
$k(\Omega^{-1}\,\mathrm{m}^{-1}\,\mathrm{rad}^{-1}\,\mathrm{s})$	2.0×10^{-15}	1.6×10^{-14}
Δ	0.8	0.6
Dielectric strength (V/m)	1.96×10^8	7.8×10^7
Density (kg/m^3)	1.42×10^3	2.1×10^3
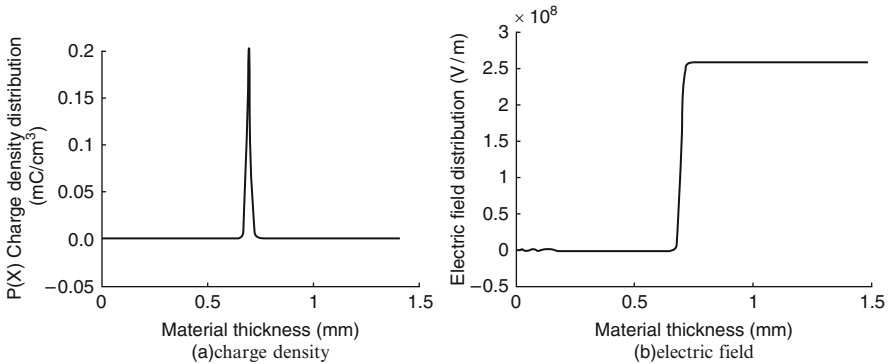
Fig. 4 Calculation of internal charging in Kapton upon proton irradiation

charge density, radiation induced conductivity exponent and coefficient are different from electrons radiation. the radiation induced conductivity exponent relies on electrons, and the radiation induced conductivity coefficient is attained from Ref.3 by normalizing experimental surface potential to RIC model.

$$\mu_+ = 2.0e^{-17}\,m^2V^{-1}S^{-1} \quad \tau_+ = 1.0s$$

That is to say, in the experiment under 10 MeV protons radiation with the density of $2 \sim 4\,\mathrm{nA/cm}^2$ for the duration of 10 min, the potential on Kapton surface is 101 V and the Teflon surface voltage is 45 V. We select a set of parameters mostly corresponding to the experiment result and process GEANT4-RIC simulation. Parameters for GEANT4-RIC are shown in Table 1.

Figures 4 and 5 show the simulation results for Kapton and Teflon with 10 MeV radiation. MULASSIS incident particles are normalized to $10^5/\mathrm{cm}^2$. It is obvious that with fluence of $3 \times 10^{12}/\mathrm{cm}^2$, Kapton voltage surpasses the discharge threshold 1.96×10^8 V/m, while Teflon is far less than 7.8×10^7 V/m, corresponding with experimental results.
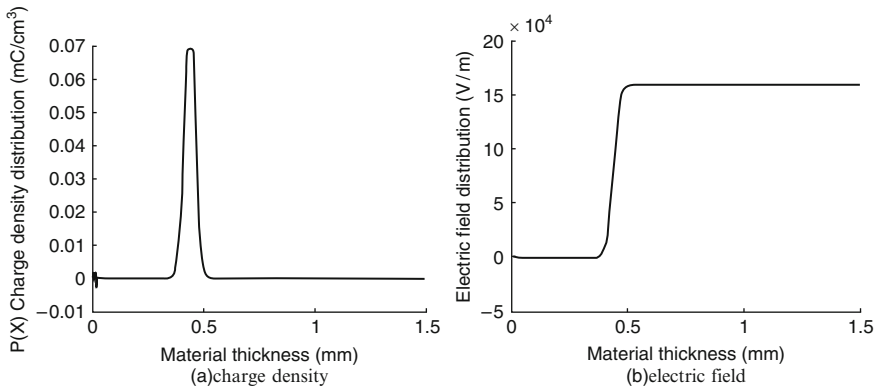
Fig. 5 Calculation of internal charging in Teflon upon proton irradiation

5   Conclusions

Based on Monte Carlo Toolkit Geant4 particles transfer software, we have respectively figured out the dose and fluence along with depth in Kapton and Teflon, and subsequently input it into radiation induced conductivity charging dynamic model. The results show the distribution of charge density and electric field within dielectric of 1.5 mm thickness and proton energy of 10 MeV. Calculations display that Kapton occurs discharge after radiated with the fluence of $3 \times 10^{12}/cm^2$ and Teflon does not give such a phenomenon, which agrees with the published experimental result. Electric field built by proton radiation induced internal charging in dielectrics is also obtained from preliminary numerical simulation. The correctness of usage GEANT4-RIC in simulation of proton charging and discharging is verified, and a solid foundation has been established for solving interplanetary spacecraft dielectric internal charging and discharging problems.

References

1. Jian-Guo HUANG, Dong CHEN (2004) A study of characteristics for deep dielectric charging on satellites. ACTA Physica Sinica 53(3):961–966, in Chinese
2. Jian-Guo HUANG, Dong CHEN (2004) A study of deep dielectric charging on satellites for different grounding patterns. ACTA Physica Sinica 53(3):1611–1616, in Chinese
3. Nelson WG (2007) Proton induced internal electrostatic discharges and charge storage in spacecraft dielectrics. In: 45th AIAA aerospace science meeting and exhibit, Reno
4. Akishin I, Dunaev NM et al (1999) Model of radiation electri-fication of dielectrics in simulating the effects of protons in space. Phys Chem Mater Treat 25(4):380–382
5. Akishin I, Bithoshkin EA et al (1996) Electric Discharge Mechanism of Failure of Solid Dielectrics under Proton Radiation. Phys Chem Mater Treat 30(5):197–199
6. Gromov VV, Sessler G et al (1992) A study of spacecraft charging due to exposure to interplanetary protons. Phys Chem Mater Treat 26(3):255–257

7. Khorasanov GL, Rodionov BN (1994) Electric discharges in dielectrics irradiated by fast protons. In: Proceedings of the sixth international symposium of materials in a space environment, ESTEC, Noordwijk
8. Boev SG et al (1991) Bulk charging of dielectrics by irradiation with charged particles. J Electrost 8:133–142
9. Sessler GM (2004) Quasistatic and dynamic piezoelectric coefficients of polymer foams and polymer film systems. IEEE Trans Dielectr Electr Insulation 11(2):192–202
10. Agostinelli S, Allison J et al (2003) Geant4–a simulation toolkit. Nucl Instrum Methods Phys Res A 506:250–303
11. Lei F, Truscott PR (2002) Multi-layered shielding simulation software user's manual. http://reat.space.qinetiq.com/mulassis/mulassis_files/mulassis%20sum.pdf
12. Hong-Gang XIE, Sheng-Li NIU, Liu-Xing HUANG (2007) Simulation of Single Event Effects in Semiconductor Devices with Geant4. ACTA J Tsinghua University(Sci Technol) 47 (S1):1036–1039, in Chinese
13. Janni JF (1982) Energy loss, range, path length, time-of-flight, straggling, multiple scattering, and nuclear interaction probability: In two parts. Part 1. For 63 compounds Part 2. For elements $1 \leq Z \leq 92$. Atomic Data Nucl Data Tables 27(2/3):147–339

Microstructure and Properties of Pure Zirconium After Irradiation by Charged Particles

Hai Liu, Hongpeng Zhang, Shangli Dong, Jingdong Xiao, Yong Liu, and Zhengjun Zhang

Abstract In order to estimate the possible application of zirconium-based alloy in space craft, the space irradiation effects have been studied using ground simulation testing of a model material, pure zirconium, in this paper. The irradiation tests of charged particles such as protons, argon ion and nitrogen ion on a pure zirconium, UNS R60702 (denoted as Zr 702 herewith), was carried out in a ground space simulation irradiation facility.

X-ray diffractometry (XRD), transmission electron microscopy (TEM), scanning electron microscopy (SEM), Nanoindentation, dynamic mechanical analyzis (DMA) and tensile testing were employed to examine the microstructure and properties of the proton, nitrogen ion or argon ion irradiated Zr 702.

It is shown that after irradiation with 120 keV protons and argon or nitrogen ions, the specimen surface morphology practically did not change and no new phases could be detected within the surface layer of Zr 702. Dislocation configurations in the irradiated region of Zr 702 were however affected by proton and nitrogen and argon ion irradiation. The bulk mechanical properties such as tensile strength and fracture strain of Zr 702 were mostly not influenced by 120 keV protons and argon or nitrogen ion irradiation. The local properties such as nano-hardness of the irradiated surface were found to vary with the fluence or type of the charged particles.

Keywords Zirconium and zirconium alloy • Irradiation • Charge particles • Protons • Argon ions • Nitrogen ions

H. Liu • H. Zhang • S. Dong (✉) • J. Xiao • Y. Liu
School of Materials Science and Engineering, Harbin Institute of Technology,
Harbin 150001, China
e-mail: sldong@hit.edu.cn

Z. Zhang
Department of Materials Science and Engineering, Tsinghua University, Beijing 100084, China

1 Introduction

Zirconium and zirconium alloys have been widely used in nuclear industry because of the appreciative combination of mechanical properties, much lower thermal neutron absorption cross-section and good corrosion resistance, as well as desirable processing characteristics [1–3]. Recently, zirconium-based materials are attracting much attention of chemical engineers, biomedical researchers and aerospace designers and engineers due to their excellent properties and potential in the desired service [4, 5]. Using alloying approaches, zirconium-based alloy is being developed for structural or component application in flight vehicles. To be used in spacecraft, the microstructure development and properties degradation of the zirconium-based alloy relevant to space environment have to be carefully estimated. And the issue due to space radiation is an essential subject [6].

On the other hand, numerous investigations were conducted in the past decades on irradiation effects of zirconium and zirconium alloys applied in nuclear reactors. In these studies, the irradiation tests were mainly performed by high energy protons, electrons, neutrons and ions by bombardment and field-driven techniques or even in real reactors. In such investigatons, the irradiation effects on solute redistribution [7], grain growth [8, 9], microstructural defects evolvement [10, 11], deformation [12], electrochemical behaviors [13] and stress corrosion [14] in zirconium and zirconium alloys have been well examined. Undoubtedly, the obtained irradiation relevant results from nuclear grade zirconium and zirconium alloys will be beneficial to the potential application of zirconium-based materials in space vehicle, but are not adequate.

As a first step of a research, the current work aims at investigation of the response of pure zirconium to low energy charged particles. A UNS R60702 zirconium was selected as the experimental material and a ground space irradiation simulation facility was employed to provide the irradiation environment. The results, mainly related to microstructure and mechanical properties of the investigated pure zirconium irradiated with 120 KeV protons and nitrogen or argon ion beams are summarized herewith.

2 Experimental

The studied plate specimens (as shown in Fig. 1) were cut from a 2 mm rolled Zr 702 sheet with the actual composition of zirconium bigger than 99.95 % (w.t.). After careful polishing of one surface, the above specimens along with the TEM foil specimens were irradiated in vacuum (less than 10^{-3} Pa) at room temperature with 120 keV protons, nitrogen and argon ions, respectively, with the charged particles fluence up to 5×10^{16}/cm^2. The irradiation conditions are listed in Table 1.

After the irradiation exposures, several measurement and analytical techniques such as computerized tensile testing, nanoindentation, dynamic mechanical

Fig. 1 Typical Nano-Indentation test and XRD specimen (**a**), tensile test specimen (**b**) and DMA specimen (**c**) used in this study

Table 1 Irradiation test conditions

Charge particles	Energy (keV)	Fluence (ions/cm^2)
Proton	120	$1 \times 10^{15}, 5 \times 10^{15}, 1 \times 10^{16}, 5 \times 10^{16}$
Nitrogen ion	120	$1 \times 10^{15}, 5 \times 10^{15}, 1 \times 10^{16}, 2 \times 10^{16}$
Argon ion	120	$1 \times 10^{15}, 5 \times 10^{15}, 1 \times 10^{16}, 2 \times 10^{16}$

analysis (DMA), X-ray Diffraction, transmission electron microscopy and scanning electron microscopy were applied to examine microstructure and properties of the proton, argon ion or nitrogen ion irradiated Zr 702, especially within irradiated surface region. All the microstructural analyses and mechanical tests were performed in accordance with the appropriate standards.

3 Results and Discussion

3.1 Microstructure

After irradiation by the selective charged particles, the phase structure features of the specimens, especially within the irradiated surface of Zr 702, were investigated by XRD technique at an incident angle of 3°. Typical XRD patterns of the specimens irradiated by protons, nitrogen ions and argon ions with the energy of 120 keV and various fluences are given in Fig. 2. It is shown that only hexagonal α-zirconium can be remarkably detected in all the irradiated specimens, similar as in the original un-irradiated specimen.

While it could not be directly confirmed that new phase(s) were not formed upon irradiation with 120 keV proton, nitrogen ion or argon ion just based on the results described in Fig. 2, taking into account the previous investigations [6, 11, 14] and referencing the XPS examination carried on irradiated specimens in current research, it is reasonable to speculate that the low energy charged particles employed herein did not lead to generation of new phase in pure zirconium.

Direct examination of the irradiated foil specimens by TEM observation revealed minimal microstructure differences in zirconium after experiencing 120 keV proton, nitrogen ion or argon ion irradiation. Figure 3 shows several typical TEM
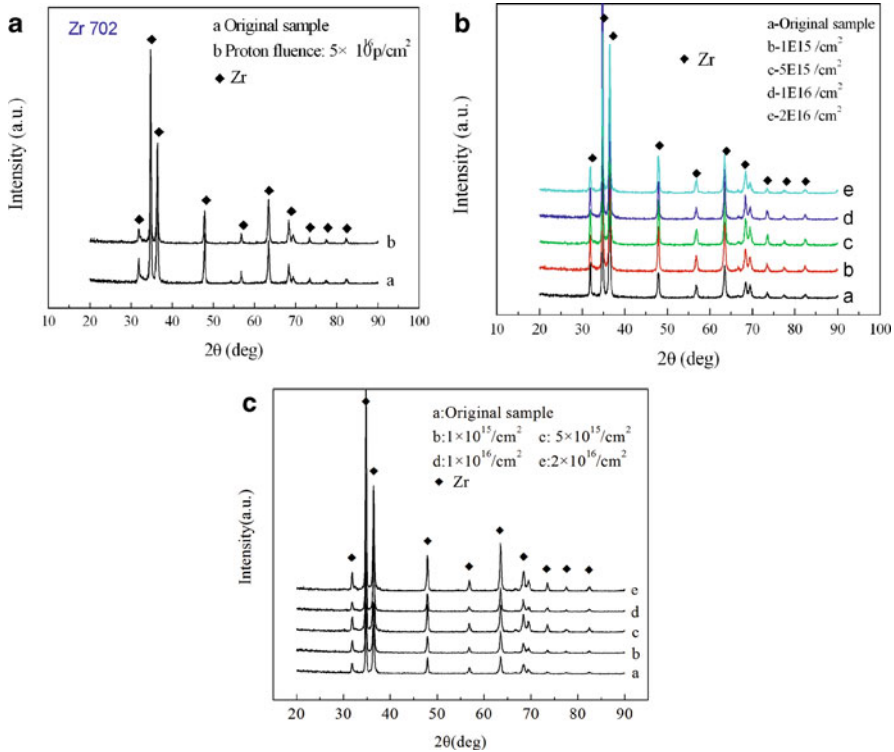
Fig. 2 XRD patterns of the Zr 702 specimens before and after irradiated by 120 keV proton (**a**), nitrogen ion (**b**) and argon ion (**c**)

micrographs taken in the specimens irradiated by the charged particles applied in this work. The TEM morphology in the proton-irradiated pure zirconium specimen is similar to that in the as-received un-irradiated specimen, while that in the nitrogen ion-irradiated pure zirconium specimen matches the argon ion -irradiated specimen. As shown in Fig. 3, after irradiation with 120 keV nitrogen ions or argon ions, a high density of very small defect clusters with the size of several nm are produced in pure zirconium. And the argon ion irradiation seems to induce more defects than nitrogen ion (compare Fig. 3b with Fig. 3d, and Fig. 3c with Fig. 3e).

But such phenomenon was not found in the 120 keV proton-irradiated specimens even with the fluence up to 5×10^{16} p/cm^2.

A previous study [15] has indicated that high density of small defect clusters, consisting predominantly of dislocation loops, would be produced in pure zirconium after irradiated by higher dose neutron. In addition to irradiation hardening, these defects were also thought to be responsible for the occurrence of dislocation channeling in local regions and thus leading to the loss of strain hardening capacity of the neutron-irradiated zirconium [15]. It is interesting to reveal the presence of high density of small defect clusters in pure zirconium irradiated by low energy
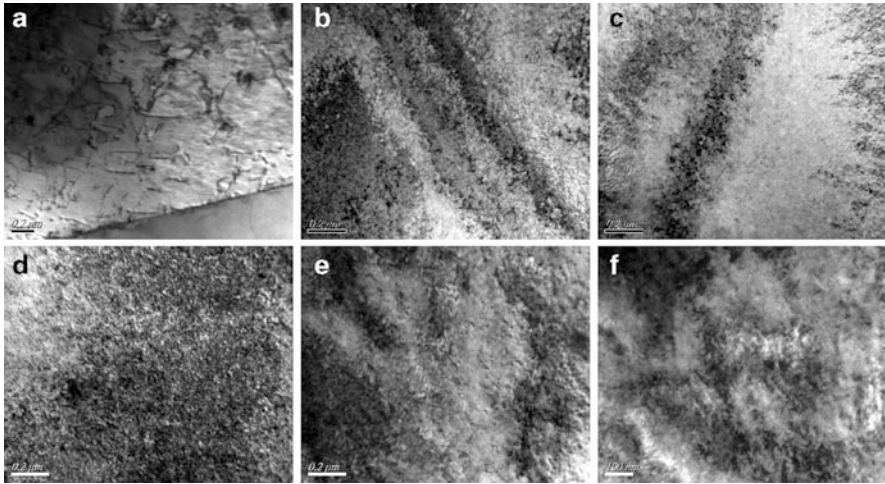
Fig. 3 TEM micrograph showing typical dislocation features in the Zr 702 specimens before and after irradiation: (**a**) as –received; (**b**) nitrogen ion irradiated, 1×10^{16} ions/cm^2; (**c**) nitrogen ion irradiated, 2×10^{16} ions/cm^2; (**d**) argon ion irradiated, 1×10^{16} ions/cm^2; (**e**) argon ion irradiated, 2×10^{16} ions/cm^2; (**f**) argon ion irradiated, 2×10^{16} ions/cm^2

nitrogen ion or argon ion, and the relevant effects on mechanical behaviors of pure zirconium, such as deformation, is worthy of further investigation.

4   Mechanical Properties

The mechanical properties of the irradiated Zr 702 were firstly evaluated by a uniaxial tensile test at room temperature. The results show that the tensile property of Zr 702 are not remarkably affected by 120 keV proton, nitrogen ion or argon ion irradiation. As seen in Figs. 4 and 5, the engineering stress–strain behaviors of the as- received Zr 702, proton, nitrogen-ion or argon ion irradiated Zr 702 are almost similar (Fig. 4). The ultimate strength and fracture strain of Zr 702 are also not varied with the increase of irradiation fluence (Fig. 5). And almost no difference could be observed on the fractography after irradiation (Fig. 6). According to the previous studies [6, 14], such results are reasonable due to the limited irradiation effects of low energy charged particles on macro-mechanical property of zirconium and zirconium alloys. Meanwhile, the DMA investigation into the proton, nitrogen-ion or argon-ion irradiated specimens showed that the dynamic modulus of Zr 702 within the temperature range RT→ –120°C→150°C was also not affected by the charged particles employed for this study.

    Estimation of surface hardness of the proton, nitrogen ion and argon ion irradiated specimens by nanoindentation technique reveals another profile of the microscopic mechanical property of pure zirconium, as shown in Figs. 7 and 8. The
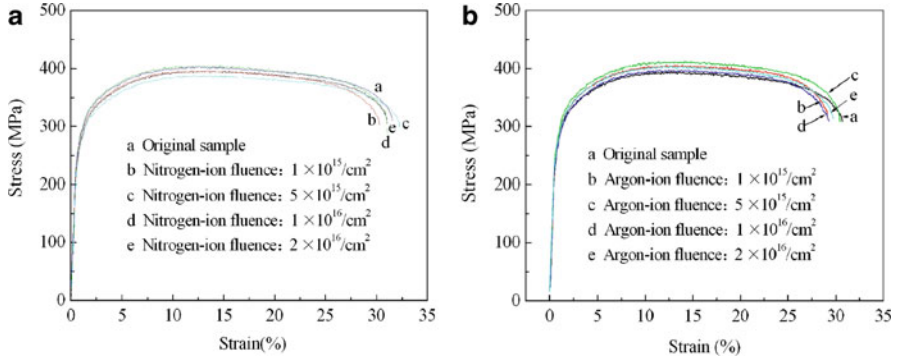
Fig. 4 Typical engineering stress–strain curves of the Zr 702 specimens after irradiation by nitrogen ion: (**a**) and argon ion (**b**)
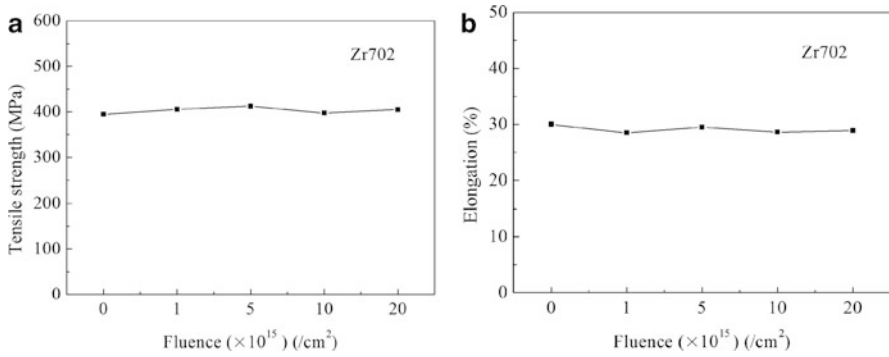
Fig. 5 UTS vs fluence (**a**) and fracture strain vs fluence (**b**) of Zr 702 irradiated with 120 keV argon ions
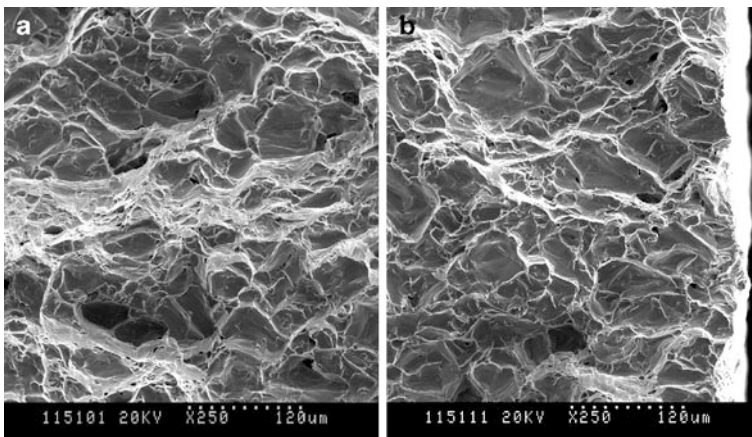
Fig. 6 Fractography of the un-irradiated (**a**) and argon-irradiated (**b**) specimens
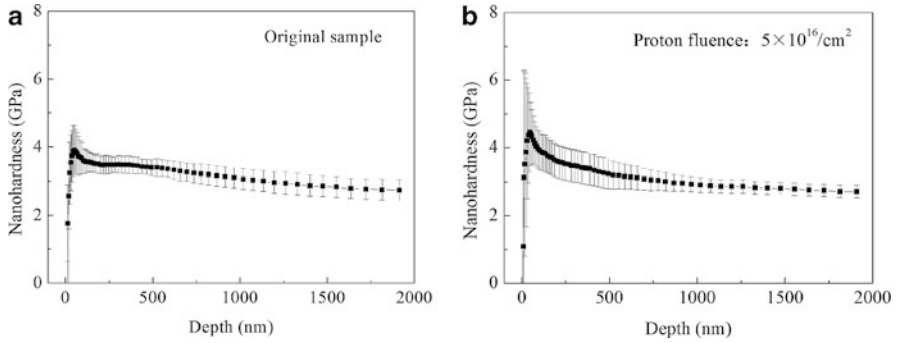
Fig. 7 Typical surface hardness profile estimated by nanoindentation method for the un-irradiated (**a**) and proton -irradiated (**b**) specimens
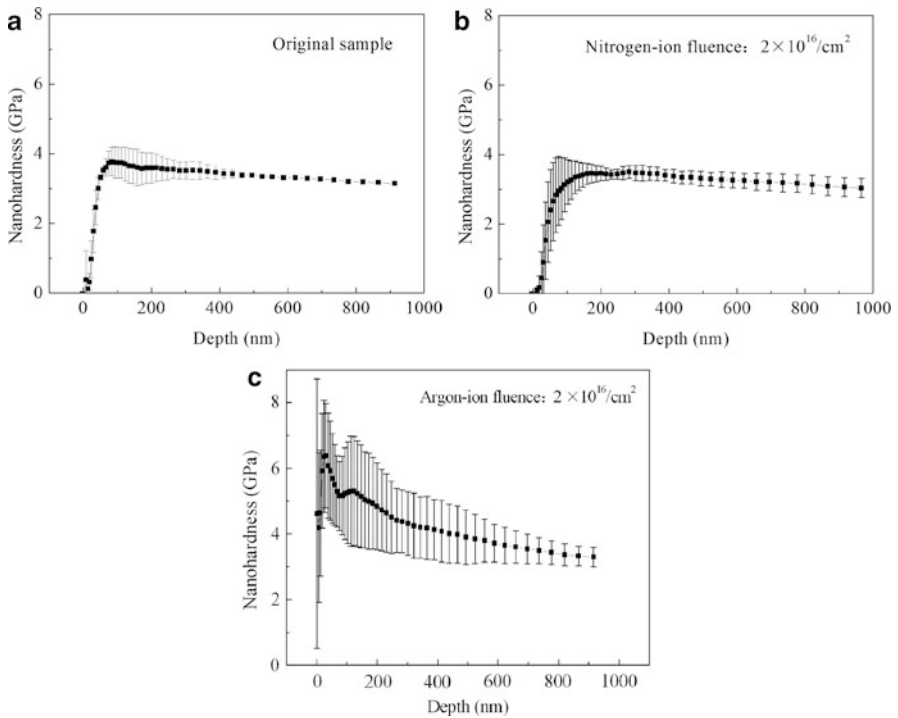
Fig. 8 Typical surface hardness profile estimated by nanoindentation method for the (**a**) un-irradiated, (**b**) nitrogen ion and (**c**) argon ion-irradiated specimens

hardness of pure zirconium within the surface layer of 2,000 nm is little affected by 120 keV proton irradiation (Fig. 7). But ion irradiation, especially argon ion irradiation induces obviously surface hardening effect within the depth of 300 nm
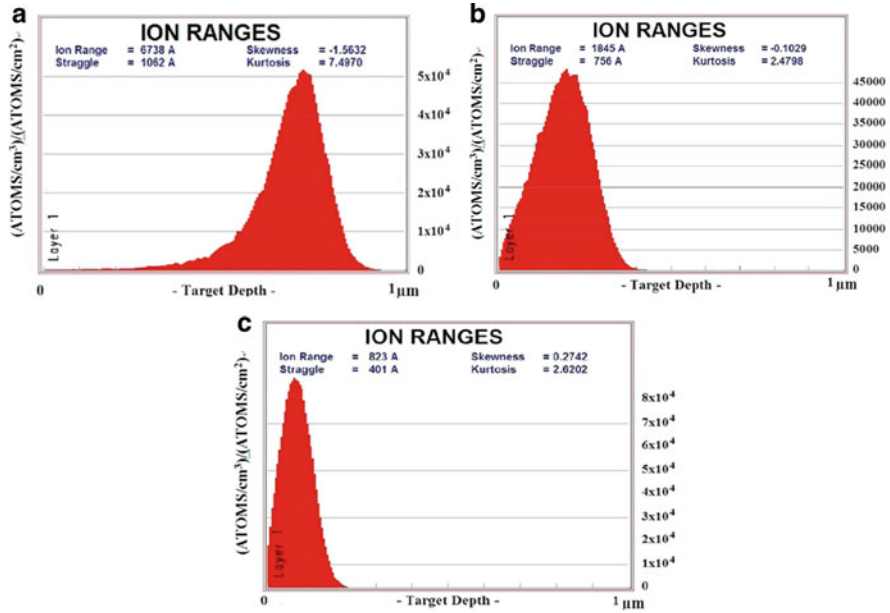
Fig. 9 Estimated profile of (**a**) proton, (**b**) nitrogen ion and (**c**) argon ion with energy of 120 keV basing on the simulated calculations of SRIM program

in pure zirconium (Fig. 8). These results correspond with the high density of small defect clusters observed by TEM, implying the importance of local mechanical property examination by appropriate technique for the irradiated samples by charged particles with low energy or low fluence.

5 Irradiation Effects

Based on the above microstructure and mechanical property experimental results, along with applying Monte Carlo method, the related irradiation effects of low energy protons, nitrogen ions and argon ions on pure zirconium have been discussed. The distribution of 120 keV proton, nitrogen ion and argon ion and the irradiation damage efficiency along the incidence direction were calculated using the SRIM 2008 program. The obtained profiles of proton, nitrogen ion and argon ion distribution in pure zirconium are shown in Fig. 9. It can be seen that penetrating range of argon ions is smaller than for nitrogen ions and protons, resulting in a faster energy loss along the incidence direction and thus formation of high density defects within the limited depth.

On the other hand, the atom of argon is larger than nitrogen or proton, and higher solute hardening is expected in zirconium if no second phase is formed. With the increase of argon ion irradiation fluence, the crystal aberration extends and large size defects form with the movement of point defects, resulting in the increased hardening effect.

6   Conclusions

The influence of 120 keV protons, nitrogen ions and argon ions on microstructure and mechanical properties of a pure zirconium have been investigated in this paper, simulating the low energy charged particles radiation effects in space. It is found that the tensile strength and fracture strain of Zr pure zirconium are almost not affected by proton, argon ion or nitrogen ion irradiation, but the surface hardness estimated by nanoindentation varies with the fluence and type of the charged particles.

Argon ion irradiation could produce remarkable hardening within the surface layer, enhanced with an increase of argon ion fluence and reaching a peak along the incidence direction. While no new phased were detected in all irradiated specimens, high density of small defect clusters were observed in the ion-irradiated specimens. Solute strengthening and defects' strengthening are thought to be responsible for the ion irradiation hardening in pure zirconium. Attention should be paid to the microscale property of metallic materials as irradiated by low energy charged particles.

References

1. Northwood DO (1985) The development and applications of zirconium alloys. Mater Des 6 (2):58–70
2. Motta AT, Yilmazbayhan A, Gomes da Silva MJ et al (2007) Zirconium alloys for supercritical water reactor applications: challenges and possibilities. J Nucl Mater 371:61–75
3. Banerjee S (2001) Nuclear applications: zirconium alloys, in encyclopedia of materials: science and technology. Elsevier, Oxford, pp 6287–6299
4. Stojilovic N, Bender ET, Ramsier RD (2005) Surface chemistry of zirconium. Prog Surf Sci 78:101–184
5. Ehrman JD, Bender ET, Stojilovic N et al (2006) Microbial adhesion to zirconium alloys. Colloids Surf B Biointerfaces 50(2):152–159
6. NASA (1970) Nuclear and space radiation effects on materials. NASA SP-8053
7. Zou H, Hood GM, Roy JA, Packwood RH (1997) Irradiation-driven solute redistribution in Zr alloys. J Nucl Mater 245:248–252
8. Fortis AM, Gonzalez HC (2000) The initial transient of the irradiation growth in a zirconium alloy. J Nucl Mater 279:301–307
9. Kaoumi D, Motta AT, Birtcher RC (2006) Grain growth in Zr-Fe films during in-situ in irradiation in a TEM. Nucl Instr Meth Phys Res B 242:490–493
10. Mukherjee P, Nambissan PMG, Barat P et al (2001) The study of microstructural defects and mechanical properties in proton-irradiated Zr-1.0%Nb- 1.0%Sn-0.1%Fe. J Nucl Mater 297:341–344
11. Sarkar A, Mukherjee P, Barat P (2008) Effect of heavy ion irradiation on microstructure of zirconium alloy characterized by X-ray diffraction. J Nucl Mater 372:285–292

12. Chow CK, Holt RA, Woo CH, So CB (2004) Deformation of zirconium irradiated by 4.4 MeV protons at 347 K. J Nucl Mater 328:1–10
13. Xu J, Bai XD, An J, Fan YD (2000) Effect of Ar ion irradiation on electrochemical behaviors of zircaloy-4. Appl Radiat Isot 53:1005–1010
14. Fournier L, Serres A, Auzoux Q, Leboulch D, Was GS (2009) Proton irradiation effect on microstructure, strain localization and iodine-induced stress corrosion cracking in Zircaloy-4. J Nucl Mater 384:38–47
15. Hashimoto N, Byun TS, Farrell K, Zinkle SJ (2004) Deformation microstructure of neutron-irradiated pure polycrystalline metals. J Nucl Mater 329–333:947–952

Application of Dust Detection Techniques in Space Science and Spacecraft Projects

Danming Li, ChengXuan Zhao, Ziyu Ye, Chunyong Wang, Lianjun Jia, and Xing Guo

Abstract Detection of the interplanetary dust or on the surfaces of planets occupies an important place in space exploration science. Dust detection techniques have a special practical project value in deep-space spacecraft missions. In addition, dust monitoring inside the manned spacecraft cabins is necessary. This paper illustrates several techniques of dust detection and their applications in space and presents an advanced technique for detection of space dust.

Keywords Detection technique • Dust • Space application

1   Introduction

"Space dust" is a concept that belongs to space environment categories; it covers many research aspects, including dust in open space environment and in man-made space platforms, as well as planetary conditions like on Moon, Mars, Earth stratosphere, etc.

Space dust detection plays an important role in science and aerospace project applications. Dust detection techniques differ in different environments. Several developed aerospace countries have conducted extensive research, designed experiments and application techniques with resulting accumulation of data in this field. With the development of aerospace science and technology, the space dust detection techniques will be more and more miniaturized, consuming less energy and increasing at the same time their capabilities.

In this paper, the dust detection methods for application on planet surfaces, in interplanetary space, or in manned spaceflights are described. Some related detection techniques are introduced. New application of an advanced detection technique is also described.

D. Li (✉) • C. Zhao • Z. Ye • C. Wang • L. Jia • X. Guo
Lanzhou institute of Physics, Lanzhou 730000, China
e-mail: lidanming@sina.com

2 Development of the Dust Detection Techniques

Many countries have developed, tested or employed many types of detectors for dust detection on the surface of the moon, Mars, in the interplanetary space or inside manned spacecraft. All these techniques, without doubt, will develop widely in the future [1].

3 The Cosmic Dust Analyzer (CDA)

The collection and analysis of extraterrestrial dust particles is important to exobiology because it provides information about the sources of biogenically significant elements and compounds that accumulated in distant regions of the solar nebula and that were later accreted onto the planets. Both interstellar and interplanetary dust seeded the Earh with elements and compounds that may have played important roles in the origin and development of life.

The exploration of the physical, chemical and dynamical properties of cosmic dust particles in interplanetary space will help us understand the mass distribution in the solar system, asteroids and Saturnian environment.

The parameters to be studied by the Cosmic Dust Analyzer (CDA) include mass, composition, electric charge, flux, speed, and flight direction of individual particles [2].

The CDA instrument consists of two subsystems, the dust analyzer (DA) and the high rate detector (HRD), as shown in Fig. 1.

The high rate detector subsystem, using two separate polyvinylidene fluoride (PVDF) sensors, for the determination of high impact rates, masses, flux of the cosmic dust particles, as shown in Fig. 2.

The Dust Analyzer (DA) is using impact ionization. The DA measures the electric charge carried by dust particles, the impact direction, the impact speed, mass and chemical composition, whereas the high rate detector is capable of determining particle mass for particles with a known speed.

The DA itself consists of three subsystems, the charge detector (entrance grids, EG), the impact ionization detector (IID) and the chemical analyzer (CA), as shown in Fig. 3.

The Dust Analyzer was used in the Cassini-Huygens mission which was the first spacecraft to orbit Saturn.

4 The Lunar Dust Detector (LDD)

A relative simple lunar dust detector (LDD) was first used in the Apollo 11 Mission. The detector evaluated the deposited thickness of the lunar soil by measuring the differences in solar reflectivity on the surface. In Apollo 12–13 Missions, a modified LDD was continuously loaded, as shown in Fig. 4, where cell-3 was used to monitor
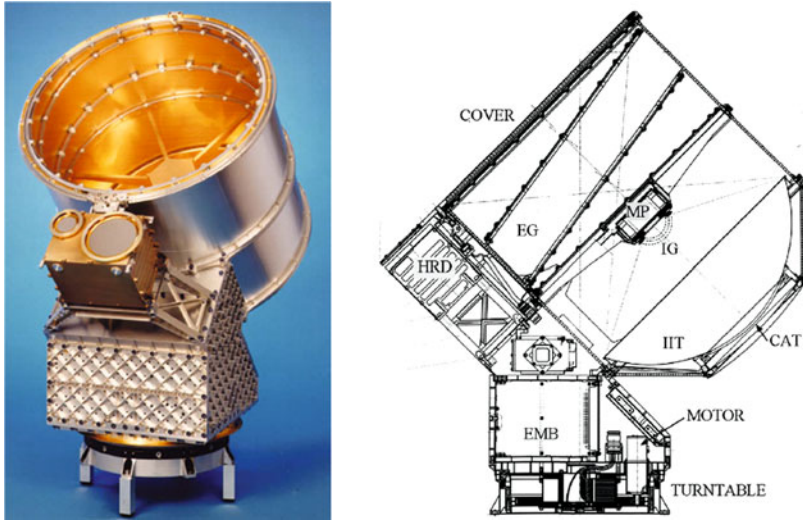
Fig. 1 The cosmic dust analyzer
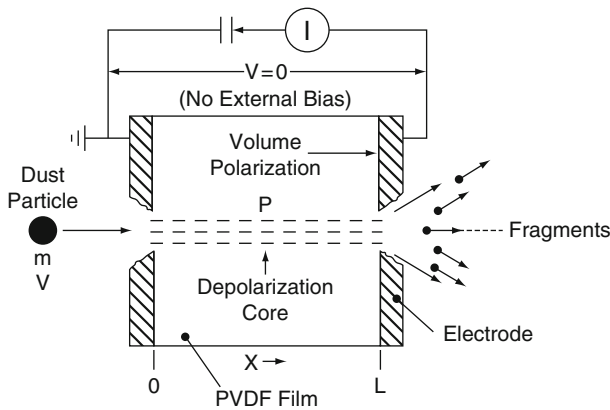
Fig. 2 Schematic drawing of a polarized PVDF sample with conducting contact electrodes

the number of accumulating dust particles on the sensitive surface of the lunar rover. In the following Apollo Missions, the lunar dust detector had become a lunar exploration payload from a simple scientific experimental instrument.

In recent years, measuring the particles and dust by Quartz Crystal Microbalance (QCM) is the main method. A thin layer of low outgassing adhesive (e.g. Apiezon grease) is spread on the quartz crystal to capture and measure the particles impacted on the surface. This kind of QCM called "adhesive" QCM. This method had been validated in missile wind tunnel experiments and spacecraft engine plume pollution monitor experiments. The Lanzhou Space Technology Institute of Physics had successfully developed a lunar dust detector based on "adhesive" QCM, and the
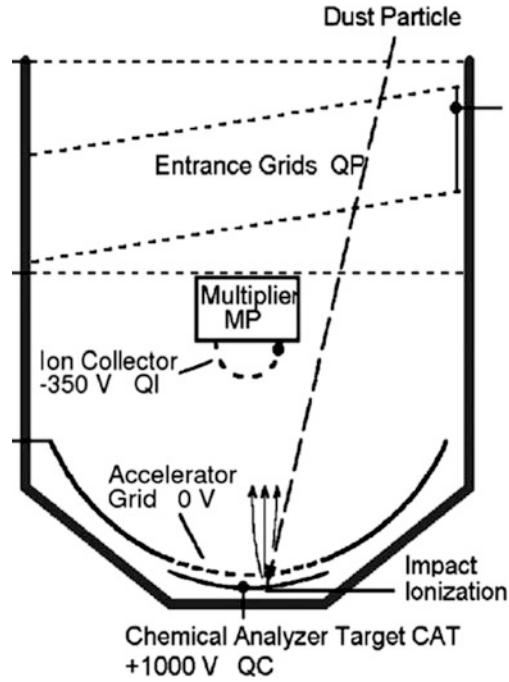
Fig. 3 Schematic drawing of dust analyzer
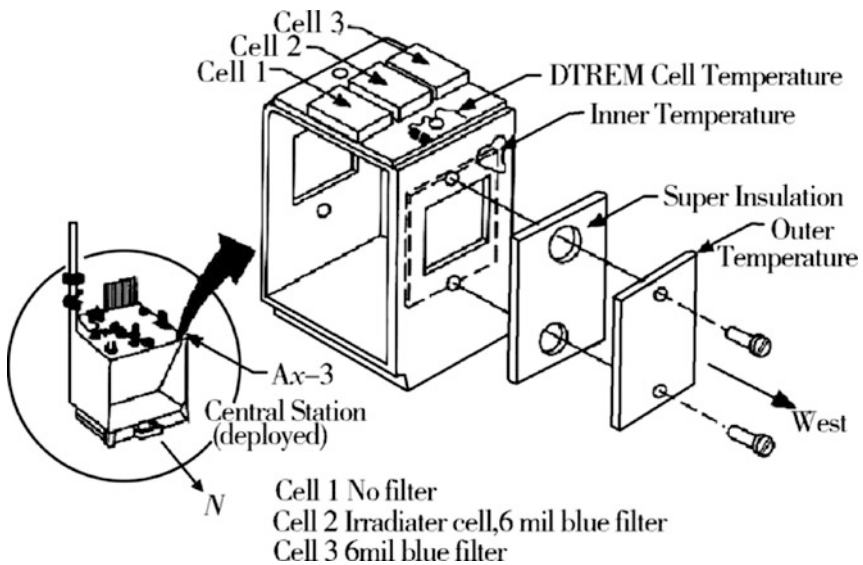
Fig. 4 Schematic diagram of lunar dust detector (LDD M-515)

Fig. 5 "Adhesive" QCM Probe

Fig. 6 Main electronics box of the LDD

detector will be used in China's Lunar Exploration Program, as shown in Figs. 5, 6, 7, and 8.

5 The Mars Dust Detector

There had been many exploration activities of Mars, Saturn and Jupiter so far, in which there were several dust detection objectives. Large amounts of suspended dust exist in Martian atmosphere. According to estimation, the basic dust density is

Fig. 7 Dust simulator
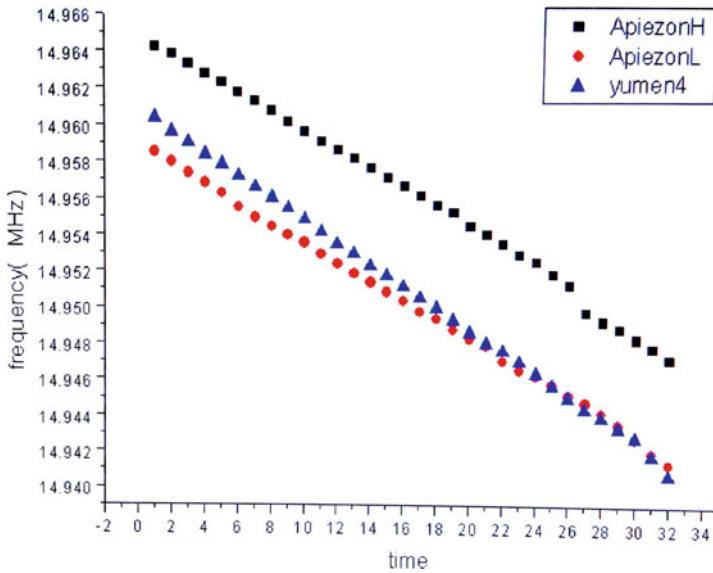
Fig. 8 Response of the SQCM to dust accummulation

1.8×10^{-7} kg/m^3. For Mars Exploration Programs, dust in the atmosphere can affect remarkably Martian rovers and modules landed on Mars surface. Once the dust particles will deposit on surfaces of solar batteries and optical sensors, the efficiency and life of the power system, optical characteristic of the optic sensors and image quality would be affected dramatically. Mars observation studies indicate that dust storms exist in the Martian atmosphere, similar to dust clouds on Earth that diffuse, expand and envelop the entire surface of Mars.

Research on dust characteristics and monitoring of the dust deposit velocities will help us not only understand the environment, atmosphere and climate of Mars, but also will allow improving the design, functions and exploration objectives of the spacecraft landed on the surface.

Table 1 Examples of Mars dust exploration missions

Launch time	Name	Spacecraft	Objectives	Nation
1998	Mars dust counter	PLANET-B	Measure surrounding particles of the Mars, uncover the expected dust zone	Japan
2011	Dust detector	Phobos-Grunt	Measure the characteristics of the particles on Phobos and Deimos	Russia
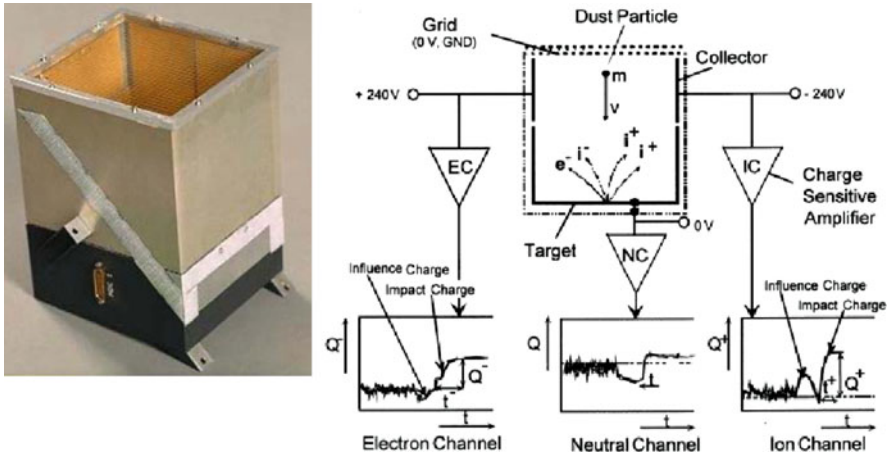
Fig. 9 The Mars dust detector and its measurement principle

The Mars Dust Detector determines mass, velocity, electric charge, and flux of a particle [3]. This technique also can be used to measure other particles, such as interplanetary dust, interstellar dust and debris around the Earth.

The dust detectors were used in Mars missions (Table 1) and lots of data were obtained.

So far, there are three types of Mars dust detection techniques, that is optical detection, impact detection and deposit detection. Impact-ionization type dust detector is light, low-power and simple-structure, which can be used to measure physical characteristics of the dusts directly (Fig. 9).

6   Dust Detectors in Manned Spaceflights

Dust in manned spaceflights is a cause for serious danger to the health of astronauts. Possible material burning and processes creating smoke in the cabin may present additional dangers to the health of astronauts. So it is imperative to create efficient techniques for detection of dust and smoke.
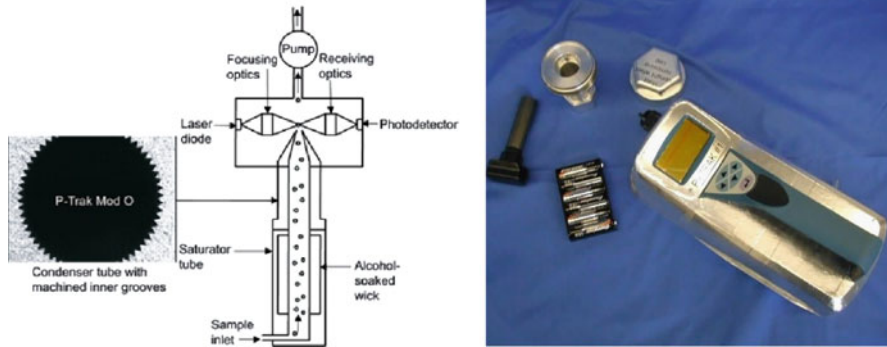
Fig. 10 Schematic diagram of P-Trak and its components

Dust measurement experiments had been done in the space shuttle (STS32) and the International Space Station. The Smoke and Aerosol Measurement Experiment (SAME) was planned to gather information on particulate size and distribution of particles on ISS. And the SAME is also used to evaluate the performance of future smoke detectors.

The DAFT (dust and aerosol measurement feasibility test) experiments, which measured dusts in the air inside ISS, were performed by NASA on station in 2005 and 2006. The main measurement instruments include P-Trak Ultrafine Particle Counter and Dust Trak [4, 5].

The P-Trak, a hand-held instrument, can count individual particles as small as 20 nm in diameter in an aerosol stream, whose number concentration can be 0–10^5/cm^3. Particles are drawn into the device by a built-in suction pump. Upon entering the instrument, these particles pass through a saturator tube where they mix with an alcohol vapor (see Fig. 10). This mixture then flows through a cooled condenser tube where some of the alcohol condenses onto the sample particles, and the droplets grow in a controlled fashion until they are large enough to be counted. These larger droplets pass through an internal nozzle and past a focused laser beam, producing flashes of light that are sensed by a photo detector and then counted to determine particle number concentration. DAFT experiments demonstrated that P-Trak performed successfully.

The DustTrak's operating range is from 0.001 mg/m^3 to 100 mg/m^3. To minimize the assumptions required about the particle size distribution, a model of the operation of the DustTrak instrument was developed using Mie scattering theory. The device uses a 90° light scattering signal to quantify the aerosol mass density. The device is equipped with an aerodynamic impactor at the inlet which captures particles larger than the selected size. The SAME experiment included two DustTraks one with a 1 μm impactor and one with a 10 μm impactor, as shown in Fig. 11.

The experiments results indicated that the average size of the particles were larger on orbit than on Earth. From the Comparative Soot Diagnostics Experiment, we know: the size of hydro-soot particles are more than 1 μm, while solid particles are still at sub-micron level.
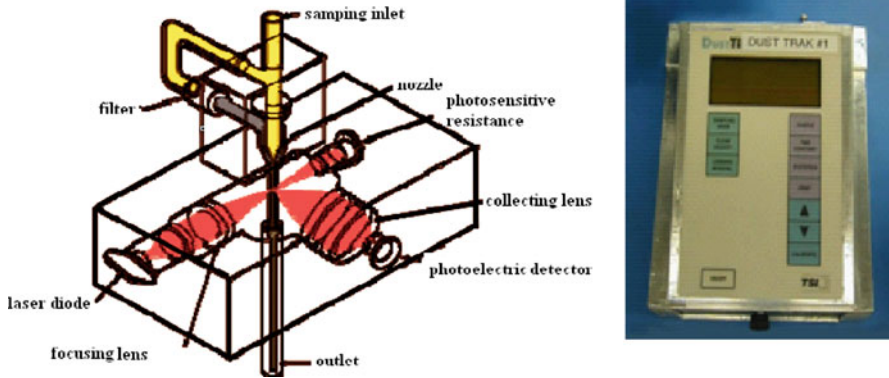
Fig. 11 Schematic diagram of DustTrak and its image
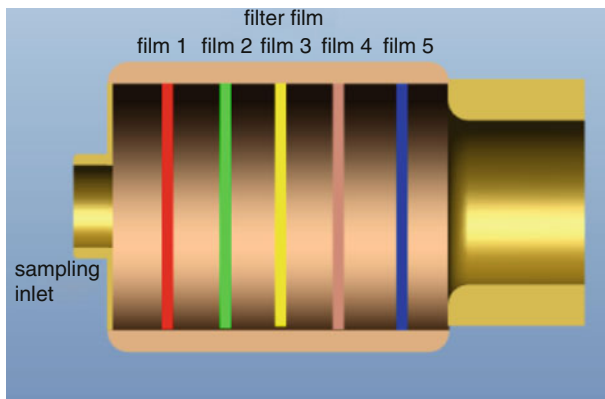
Fig. 12 Schematic diagram of multistage-separation filter film collector

7 A Novel Dust Detection Technique for Space Application

In this paper, a new type of dust detection technique suitable for space application is proposed. By using multistage filter membrane respirable collector, the dust particles with different sizes can be collected efficiently and separated accurately. For instance, the five-stage collector can collect the dust particles in five size ranges. The proposed collector head is shown in Fig. 12. It is suitable for capturing the space dust particles outside a spacecraft. A sampling pump can be used to collect the dust in the manned environment inside the cabin of a spacecraft. After the filter/collector is removed, mass analysis, chemical analysis and microscopic analysis can be peorformed on the samples accumulated on the different grade filter membranes. Figure 13 shows, as an example the difference between the
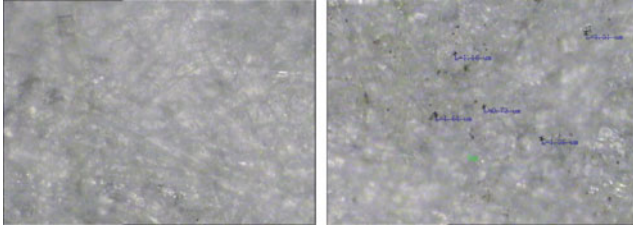
Fig. 13 The microscopic images of a clean filter membrane (*left*) and filter membrane with collected dust particles (*right*)

microscopic images obtained from a clean filter membrane and that of a filter membrane with collected dust particles. Polytetrafluoroethylene (PTFE) can be adopted as the filter membrane to reduce the rebound of the particles and to preserve the unstable compounds. Depending on the application, quartz filter membranes and coating collecting filter membranes can also be used.

8 Concluding Remarks

As the development of space technology and space exploration of interplanetary space and planetary bodies like Moon, Mars, asteroids, etc. continues, the construction of Moon and Mars bases and space stations, will necessitate the development of various dust detection techniques aimed at different requirements based on charge sensing, impact ionization, solar batteries, "adhesive" QCM, condensation nuclei counter, light scatter and Multistage-Separation Filter Film, etc..

With the development of airship technology aimed at the Earth stratosphere, it is practical to equip them with dust detectors to measure mass, velocity, altitude, etc.. Installing dust detectors on the stratosphere airship is a new concept. For this purpose, in-situ dust detectors that transport data to ground are required. The ideas proposed in this paper have not been implemented yet, and their feasibility needs to be explored further.

References

1. Grün E, Srama R, Krüger H et al (2004) 2002 Kuiper prize lecture: dust astronomy. Icarus 174:1–14
2. Srama R, Ahrens TJ, Altobelli N et al (2004) The Cassini cosmic dust analyzer. Space Sci Rev 114:465–518
3. Igenbergs E, Sasaki S, Münzenmayer R et al (1998) Mars dust counter. Earth Planets Space 50:241–245
4. Allen JS (2003) An analytical solution for determination of small contact angles from sessile drops of arbitrary size. J Colloid Interface Sci 261:481–489
5. David LU, Gary AR, William S (2009) 47th AIAA aerospace science meeting including the new horizons forum and aerospace exposition 5–8 Jan 2009, Orlando

Electron Beam Induced Charging and Secondary Electron Emission of Surface Materials

Haruhisa Fujii and Yuhki Ishihara

Abstract Many kinds of insulating materials are used outside a spacecraft. Those are FEP films, polyimide films and so on as thermal control materials. These materials are exposed to charged particles environment around a spacecraft. So these materials charge up due to the charged particles, especially electrons. It is pointed out that charge-up on these materials is likely to cause discharges on the surfaces. Therefore we have investigated the charging potential characteristics by irradiating electrons with various energies below 20 keV. In the dependence of the charging potential on the electron energy, we found that the electron energy at which no charge-up occurs exists below 5 keV. It is thought to be the energy at which secondary electron emission yield becomes one. Each material has the different value of the energy. For example, in the case of Teflon FEP, the energy is about 2.7 keV. This indicates that electron irradiation to the FEP film with the energy lower than 2.7 keV induces positive charging.

Keywords Electron irradiation • Charge-up • Thermal control materials • Teflon FEP • Secondary electron emission • Volume resistivity

1 Introduction

Many satellites for communication, broadcasting, Earth observation and so on have been launched into Earth orbits with the progress of space development and have given much benefit to our social lives. These satellites must continue to function for long life time under severe environment conditions such as vacuum, thermal cycles, high-energy charged particles, plasma and solar UV light. The large area of the

H. Fujii (✉) • Y. Ishihara
Nara National College of Technology, Department of Electrical Engineering,
Yamato-koriyama, Nara 639-1080, Japan
e-mail: fujii@elec.nara-k.ac.jp

satellite surfaces is covered with various thermal control materials in order to protect on-board electronic equipments from the thermal vacuum environment. Those thermal control materials are silvered Teflon FEP (Fluorinated Ethylene Propylene copolymer), aluminized Kapton (poly-imide), aluminized Mylar (poly-ethylene terephthalate), OSR (Optical Solar Reflector) and so on. In these thermal control materials, the insulating film materials like FEP in silvered Teflon are exposed to space. So these materials are charged up by space plasma. Especially electrons in space plasma are likely to induce charge-up phenomena to the space-craft surfaces [1]. These phenomena possibly cause ESD (Electrostatic Discharge) on the surfaces of the spacecraft. As these charge-up and discharge phenomena are great threat to the operation and the reliability of the spacecraft systems, many studies have been carried out [2–4]. In these studies, relatively high energy electron beams of the energy of a few tens of keV simulating hot plasma in space were irradiated to the insulating materials in order to investigate the charge-up characteristics as ground tests. The energy spectrum of electrons in space plasma, however, spreads widely and so electrons with lower energy exist in great numbers [5]. Therefore charge-up characteristics of these thermal control materials were investigated by irradiating electrons with various energies below 20 keV. From the experimental results secondary electron emission properties and volume resistivity of these materials were also discussed.

2 Experimental Procedure

Figure 1 shows the outline of our experimental setup. One test sample was set on the sample holder in the vacuum chamber and the lead wires of the sample were connected to the high-voltage lead terminals of the chamber. After setting it, the chamber was evacuated to the pressure lower than 1×10^{-6} Torr by a rotary pump and a turbo-molecular pump. Keeping the pressure stable, electron beam with the energy of E and the current density J_b was irradiated to the sample for 60 min.

Surface potential during and after electron beam irradiation was measured with a non-contacting electrostatic voltmeter (TREK 341B) by moving the probe (TREK 3450E) over the sample keeping the distance of 3–5 mm from the sample surface. The surface potential over the center of the test sample was recorded by a pen recorder.

By the way, in the case of electron beam irradiation with the energy in the range of 3–10 keV the sample was directly connected to the electrometer measuring the current through the sample. On the other hand, in the cases of the electron energy lower than 3 keV and higher than 10 keV, the test sample was electrically biased by a DC high-voltage power supply. In the electron energy lower than 3 keV, the sample was negatively biased to decelerate electrons impinging on the sample and in the energy higher than 10 keV it was positively biased to accelerate electrons.

All experiments were carried out at room temperature, about 20 °C. In this study, 127 μm thick silvered Teflon FEP film was used for test. The size of the sample was
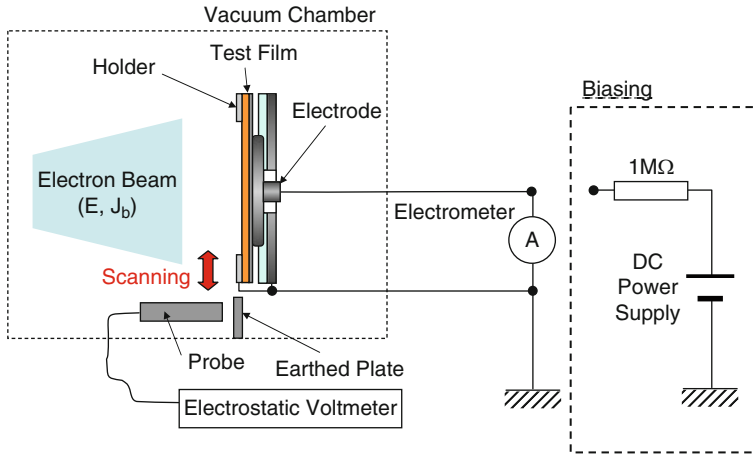
Fig. 1 Experimental set-up

about 90 mm square. Each one of the samples was set in the sample holder. The sample was covered with an aluminum frame of the thickness of 1 mm and 100 mm square with a hole of the radius of 80 mm. So the electron irradiated area was $4^2\pi$ (=50.3) cm^2. A lead wire was connected to the backside of each sample in order to measure the current during electron irradiation and to apply the biasing voltage to the sample.

3 Experimental Results

3.1 Charge-Up Characteristics During Electron Beam Irradiation

Firstly we show the time dependences of the surface potential and the current during electron irradiation with the electron energy $E = 5$ keV in Fig. 2. Three levels of the beam current density J_b were used. In each case the surface potential negatively increased with time and had a tendency to saturate to the constant potential of about -2200 V. In the case of large J_b the surface potential reached to the saturation potential in a short time. In Fig. 2b, we can see that the currents rapidly decreased with time and had a tendency to become constant values after the surface potential reached to the saturation potential.

Figure 3 shows the time dependences of the surface potential and the current during electron irradiation with constant $J_b = 0.1$ nA/cm^2 at $E = 5, 7$ and 10 keV. The rise speeds of the negative surface potentials are nearly constant after the beginning of the beam irradiation irrespective of the energy E as the values of J_b were nearly equal. And in the case of high energy E, the surface potential reached to
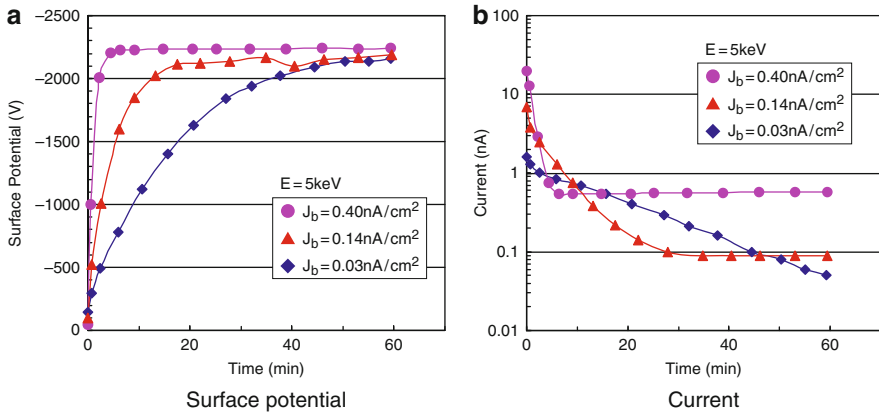
Fig. 2 Charge-up characteristics of Teflon FEP during electron irradiation with $E = 5$ keV (**a**) surface potential (**b**) current
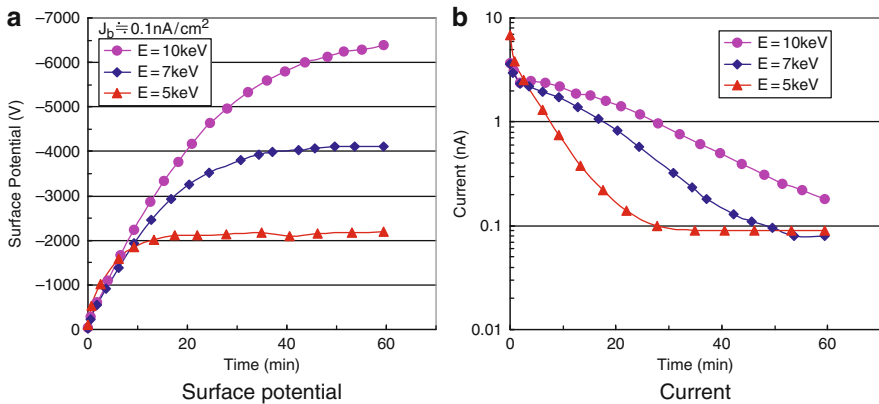
Fig. 3 Charge-up characteristics of Teflon FEP during electron irradiation with $J_b = 0.1$ nA/cm^2 (**a**) surface potential (**b**) current

the high level. So, from this Fig. 3a, we can see that the saturation surface potential depends on the electron energy.

Next we show the time dependences of the surface potentials with various electron energies E lower than 5 keV at constant $J_b = 0.1$ nA/cm^2 in Fig. 4. Similar to Figs. 3 and 4 shows that the saturation surface potential depends on the electron energy E. From this figure we can see that the FEP film charged up negatively for the electron energy E higher than 3 keV but positively for E lower than 2 keV.

We carried out the electron irradiation experiments with various electron energies lower than 20 keV at $J_b = 0.1$ nA/cm^2 including the experiments shown in Fig. 4. Figure 5 shows the electron energy dependence of the surface potential of the FEP film irradiated for 60 min with $J_b = 0.1$ nA/cm^2. The surface potential linearly depends on the electron energy E. And the negative charging occurred in
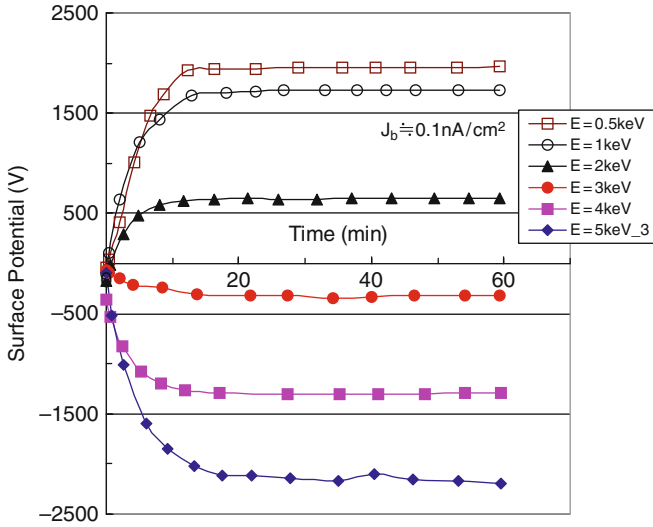
Fig. 4 Time dependences of surface potential of Teflon FEP irradiated with various electron energies lower than 5 keV
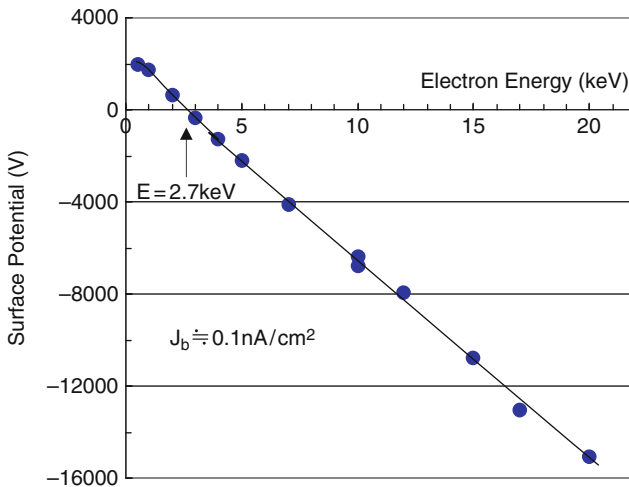
Fig. 5 Electron energy dependence of surface potential of Teflon FEP irradiated with $J_b = 0.1$ nA/cm^2 for 60 min

the case of electron irradiation with E higher than 2.7 keV and the positive charging in the case of electron irradiation with E lower than 2.7 keV. It seems that this energy $E = 2.7$ keV is the energy that secondary electron emission yield becomes one. However, in any case of electron irradiation with the energy lower than 20 keV, no discharge occurred.
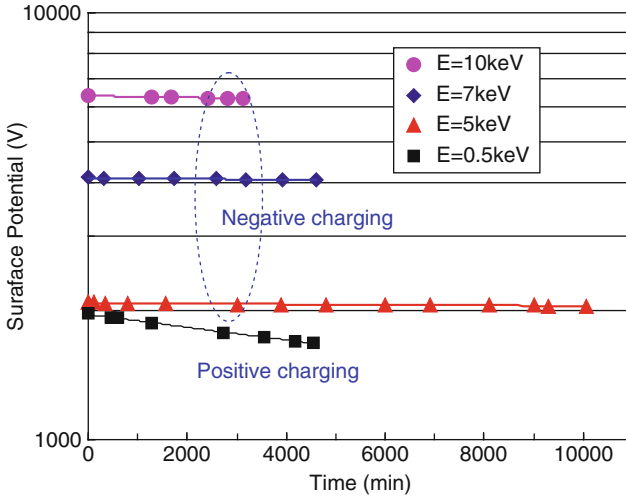
Fig. 6 Examples of decay of surface potential of Teflon FEP after electron irradiation

3.2 Charge Decay Characteristics

After each of the electron irradiation experiments under the various conditions described above, the charge decay was measured as the surface potential. Examples of the decay of the surface potential are shown in Fig. 6. The measurement of the surface potential after stopping electron irradiation was done by the probe moved over the center of the FEP sample for long time. It seems that each decay was much small from this figure and could be approximated by one linear line.

In general, the decay of the surface potential V_s of the charged insulator is expressed by the next (1).

$$V_s = V_{s0} \cdot \exp\left(-\frac{t}{\tau}\right), \tag{1}$$

where, V_{s0}, t and τ are initial surface potential, time and time constant of decay, respectively. And τ is expressed as follows.

$$\tau = \varepsilon \cdot \rho = \varepsilon_0 \varepsilon_r \cdot \rho, \tag{2}$$

where, ε is permittivity, ρ is volume resistivity, ε_0 is permittivity in vacuum ($= 8.9 \times 10^{-12}$ F/m) and ε_r is dielectric constant of the insulating material.

The volume resistivity ρ of the Teflon FEP was obtained using the (1) and (2). We used the dielectric constant $\varepsilon_r = 2.1$. Figure 7 shows the volume resistivity ρ of the FEP. The volume resistivity in Fig. 7a is as a function of irradiated electron energy E and in Fig. 7b is as a function of the surface potential at 60 min irradiation. Analizing the data in Fig. 7, we can obtain the following.
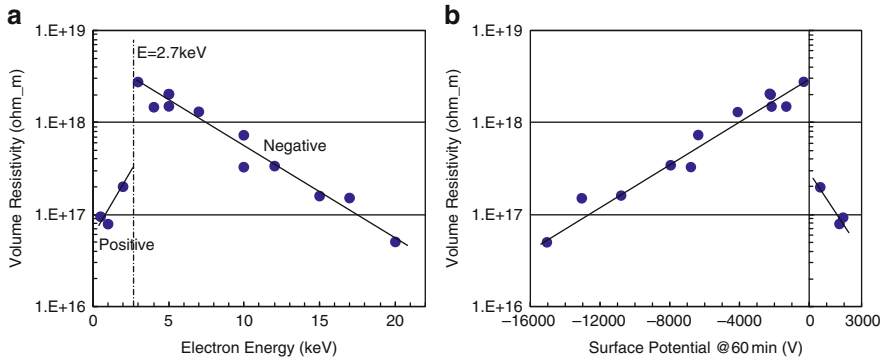
Fig. 7 Volume resistivity of Teflon FEP obtained from the decay of surface potential (**a**) electron energy dependence (**b**) surface potential dependence

1. In the case of $E > 2.7$ keV, the volume resistivity of the FEP film decreased with increase of the electron energy E which increases the surface potential.
2. In the case of $E < 2.7$ keV, the volume resistivity of the FEP film decreases with decrease of the electron energy E which increases positive surface potential.
3. Compared with the volume resistivity in negative charging, that in positive charging is nearly one digit smaller at the similar absolute surface potential.

4 Discussion

4.1 Charge-Up Characteristics and Secondary Electron Emission

The charge-up characteristics of Teflon FEP were obtained by means of electron irradiation with energy E lower than 20 keV simulating electrons in space plasma. It seems that incident electron energy exists at which no charge-up occurs. Electron irradiation with higher energy than the incident energy induces negative charging. On the other hand, electron irradiation with lower energy than the incident energy induces positive charging. It seems that the incident energy is the energy at which secondary electron emission yield becomes one. Figure 8 shows a general secondary electron emission yield of insulating material as a function of the incident electron energy [6]. In this figure, an energy range exists at which secondary electron emission yield is larger than one. At the highest energy E_{II} in the range no charge-up occurs, because the number of the incident electrons becomes equal to that of the emitted secondary electrons. In the case of Teflon FEP, E_{II} is 2.7 keV.

As the secondary electron emission yield is lower than one in the case of electron irradiation with higher energy than E_{II}, FEP film negatively charges up and then the incident electrons are decelerated by negative charging. Irradiation of the decelerated electrons causes the increase of the number of secondary electrons. When the real incident energy of electrons impinging to the negatively charged

surface becomes E_{II}, the increase of negative surface potential stops, that is, the surface potential saturates at the potential $(E-E_{II})$.

On the other hand, as the secondary electron emission yield becomes larger than one in the case of electron irradiation with lower energy than E_{II}, the film positively charges up and then the incident electrons are accelerated by positive charging. Irradiation of the accelerated electrons causes the decrease of secondary electrons. So the positive surface potential saturates at the potential $(E-E_{II})$.

4.2 Volume Resistivity

The volume resistivity of Teflon FEP film obtained from the decay characteristics after the electron irradiation decreased with increase of the surface potential as shown in Fig. 7b. That is to say, the volume resistivity depends on the electric field in the bulk of the material. Therefore the potential distribution analysis of a satellite is thought to be necessary to take this electric field dependence of the volume resistivity into consideration. On the other hand, the resistivity of Teflon FEP became low in the case of positive charging than in the case of negative charging. This indicates that the possibility of hole conduction mechanism in the bulk of Teflon FEP [7] exists in positive charge decay.

5 Conclusions

The charge-up characteristics of Teflon FEP films are evaluated by means of electron beam irradiation with the energy lower than 20 keV simulating hot electrons in space environment. The obtained results are as follows.

1. Negative charging occurred in case of electron irradiation with higher energy than some threshold energy. On the other hand, positive charging occurred in case of electron irradiation with lower energy than the threshold energy.

2. The threshold energy is thought to be the energy that secondary electron emission yield becomes one. The value is 2.7 keV for Teflon FEP.
3. From the decay of the surface potential after electron irradiation the volume resistivity was estimated. Teflon FEP has high volume resistivity, of the order of 10^{18}–10^{17} Ωm which decreases with increase of the surface potential, that is, depends on the electric field in the bulk of Teflon FEP film.

References

1. Garrett HB (1981) The charging of spacecraft surfaces. Rev Geophys Space Phys 19:577–616
2. Purvis CK, Stevens NJ, Oglebay JC (1977) Charging characteristics of materials: comparison of experimental results with simple analytical models. In: Proceedings of the spacecraft charging technology conference, NASA TMX-73537, Colorado, U.S.A, pp 459–486
3. Fujii H, Shibuya Y, Abe T, Kasai R (1988) Electrostatic charging and arc discharges on satellite dielectrics simulated by electron beam. J Spacecr Rocket 25:156–161
4. Hiro S, Fujii H (1997) Electron-beam-induced charging of polymer films for space use. Trans IEE of Jpn 117-A:805–812, in Japanese
5. Hastings D, Garrett H (1996) Spacecraft – environment interactions. Cambridge University Press, Cambridge, pp 53–70
6. Willis RF, Skinner DK (1973) Secondary electron emission yield behaviour of polymers. Solid State Commun 13:68
7. Gross B, Sessler M, von Seggarn H, West J (1979) Hole transit in Teflon films. Appl Phys Letter 34:555

Observation of Surface Discharge Phenomena on Dielectric Films Under Low Pressure Using Pockels Effect

Yohei Komiyama, Shota Suzuki, Hiroaki Miyake, Yasuhiro Tanaka, and Tatsuo Takada

Abstract Dynamic two-dimensional discharge patterns on various polymeric materials under atmospheric and low pressures are carried out using a newly developed measurement system based on Pockels effect. Spacecraft in space environment are exposed to high energy particles and radio-active rays. When the high energy particles impinge onto the surfaces of spacecraft polymeric materials they are charged, bringing sometimes to surface discharges that often can cause serious accidents. Since many accidents due to such irradiation effects are reportedther is a need to investigate deeper the discharging effects on the surface of polymeric materials under low pressure.

We developed a measurement system to observe the surface discharge pattern under low pressure conditions. In this experiment, the discharge is generated by applying high voltage to a needle on the material. Using the system, we observe various streamer patterns of the surfaces of investigated materials. Judging from the results, we found that there are two kinds of positive streamer patterns. By using numerically calculated ionization energies of various materials, we found that the formed patterns can be classified by the ionization energies.

Keywords Surface discharge • Pockels effect

Y. Komiyama (✉) • S. Suzuki • H. Miyake • Y. Tanaka • T. Takada
Department of Mechanical System Engineering, Tokyo City University, Tamazutsumi 1-28-1, Setagaya, Tokyo 158-8557, Japan
e-mail: g1081207@tcu.ac.jp

1 Introduction

A surface discharge on dielectric materials of space satellites affects the aging of the material or operation of the satellites. Many researchers have measured the surface discharge propagation characteristics like developing length, velocity, inception voltage, or flashover voltage of the surface discharge using a dust figure method or a potential probe method. While a still discharge pattern with high resolution is observed using the dust figure method, it just shows the pattern after discharging. On the other hand, a time dependent potential value at one point is measurable using the potential probe method. However, it is difficult to get a two-dimensional distribution image using this method. Therefore, we have been developing a measurement system using Pockels effect, which enables the observation of two-dimensional dynamic discharge patterns. It is well known that the pattern of the surface discharge is strongly affected by the surrounding atmosphere. Furthermore, in our previous work [1, 2], it was found that the surface discharge patterns are strongly affected by the type of materials. Therefore, the observations of the patterns on various materials in various atmospheres are necessary to investigate the surface discharge characteristics on dielectric materials for space satellites. To observe the surface discharge under low pressure atmosphere, we need to put the measurement system in a small vacuum chamber. However, an ordinary surface discharge system set-up is too large to fit into the small chamber. Therefore, we have developed a small system [1] using LED (light emitting diode). In this paper, some typical observed patterns of surface discharge on various polymeric materials under air atmospheric or low pressures are introduced.

2 Configuration of the Measurement System

Figures 1a, b show the configurations of the newly developed and the conventional surface charge measurement systems, respectively. The measurement of the surface charge is based on the electro-optic Pockels effect. When there is an electric field in so-called Pockels cell, the incident polarized light to the cell comes out from the cell with a retardation $\Delta\theta$. When the charge is distributed on a surface of a thin dielectric film that is placed on the Pockels cell, the electric field distribution corresponding to the charge distribution is generated in the cell. Therefore, the electric field distribution generates the distribution of the retardation in the cell when the polarized light is illuminating the cell. Since the retardation is corresponding to the intensity of outgoing light through the optically orthogonal analyzer, the retardation distribution can be measured using video camera [3–6]. Details of the measurement principle are described elsewhere [3, 4]. As shown in Fig. 1b, a He-Ne laser with beam expander is
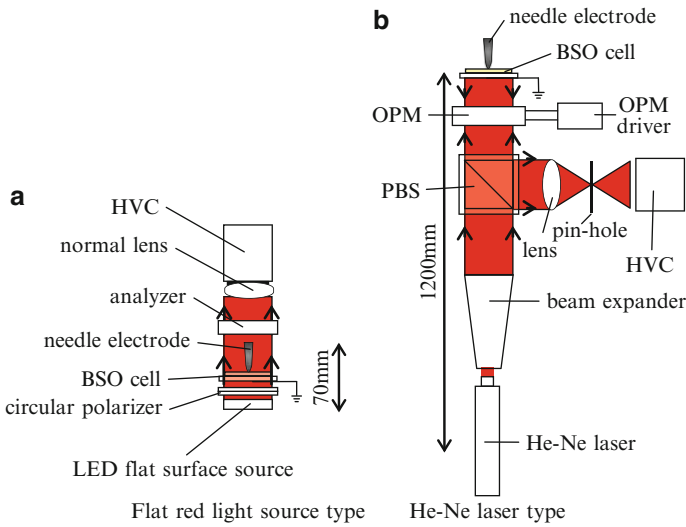
Fig. 1 Surface electric potential distribution of electro-optical measurement system

used in conventional system as a flat light source for measurement. In this system, optical phase modulation technique is used to increase the sensitivity of the measurement [3, 4]. However, the laser and the beam expander are too large to put them in the small vacuum chamber. On the other hand, a flat type LED light source is used in the newly developed system, as shown in Fig. 1a that allows to reduce the size of the system. Furthermore, the intensity of the LED light source is powerful to measure the retardation distribution without modulation technique [3, 4]. It means that there is no need anymore to use the OPM (optical phase modulator) in the developed system that allows making the size smaller than that of the conventional one.

However, the new system is build as a "transmission type" to reduce the light pass, while the conventional one is a "reflecting type". In case of the transmission type, a sample film placed on Pockels cell must be transparent, while the conventional reflecting type system allows to measure opaque samples. This is one of disadvantages of the new system and it should be improved in future.

Figure 2 shows the configuration of the developed system placed in a small vacuum chamber. Since the chamber is made of transparent PMMA (Poly-methyl-methacrylate) walls, the observation can be carried out using HVC (high speed video camera) put on outside of the chamber. The HVC allows recording the events at a speed of 1,000 frames per second. The air pressure in vacuum chamber is reduced down to about 60 and 21 kPa using a rotary pump.
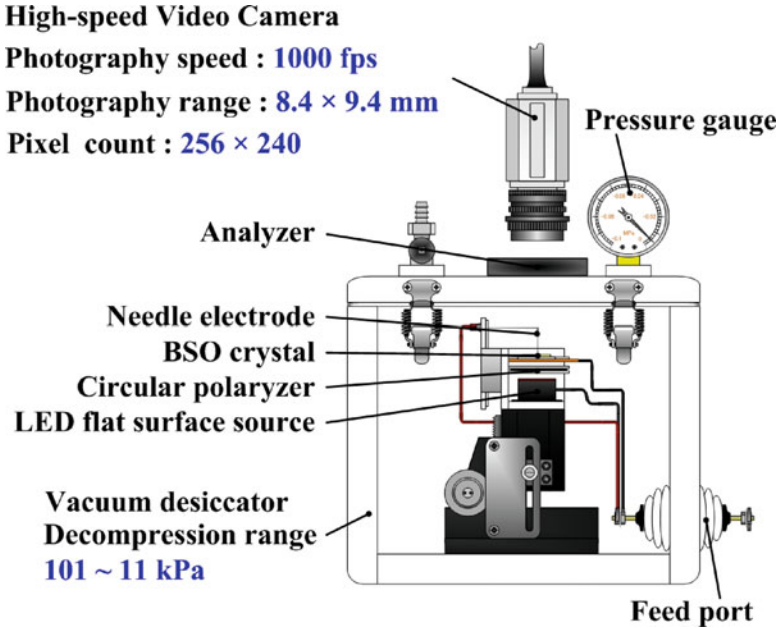
Fig. 2 Compact surface discharge measurement system under low pressure conditions

3 Samples and Experimental Procedure

3.1 Samples

Samples used for the measurements are Kapton-H, Upilex-S, PVDF (Polyvinylidene difluoride) and ETFE (Ethylene tetrafluoroethylene) thin films. In the measurement technique, the surface charge patterns are observed by charging the samples. Since the charges are located on the dielectric films that are placed on the Pockels cell, the electric field in the cell is shared by the film and the cell. If the capacitance of the film is large, the electric field in the cell becomes relatively small. That the reason why the thin films are used as the measurement samples. The sample that are all available commercially and their thicknesses are listed in Table 1.

3.2 Experimental Procedure

The surface discharges on the sample materials are generated by applying one cycle of positively or negatively started sinusoidal voltage to a needle electrode mounted on the samples. The discharge patterns are observed using HVC placed on top of the

Table 1 Description of the samples

Polymer	Thickness [μm]
Kapton-H	7.5
Upilex-S	7.5
PVDF	4.5
ETFE	12.5
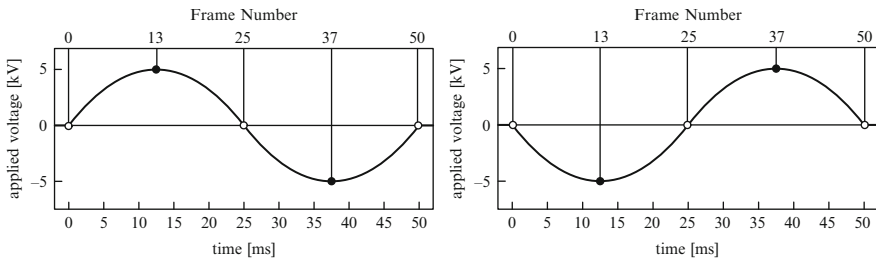
Fig. 3 Applied voltage wave pattern. The frame numbers at which the discharge images are shown are marked

transparent vacuum chamber as shown in Fig. 2. The amplitude of the applied sinusoidal voltage (peak) is 5 kV and the frequency is 20 Hz (period: 50 ms). Figure 3 shows the relationship between the applied sinusoidal voltage and the measurement timings. Since we can take the images of surface discharge pattern with 1 ms intervals using the HVC, 50 images are observed in each measurement. However, since it is impossible to show all data in the limited scope of this paper, the images obtained at the timings shown in Fig. 3 are introduced as the typical results. The discharge pattern in atmospheric (101 kPa) and low (61 kPa, 21 kPa) pressures are carried out in this work.

3.3 Results

Figures 4 and 5 show typical observation results of discharge patterns on thin films of (a) Kapton-H, (b) Upilex-S, (c) PVDF, (d) ETFE under (I) atmospheric (101 kPa) and (II) low (61 kPa) pressures respectively, with positively (Fig. 4) and negatively (Fig. 5) started sinusoidal voltage waves. In these figures, the numbers beside the patterns stand for the frame numbers of observation timing shown in Fig. 3. In these measurements, the observed data should be described using the unit of charge density $[C/m^2]$. However, it is difficult to calibrate the measured retardation accurately into the charge density. Therefore, the results shown in Figs. 4 and 5 are described using the color chart with measured retardation. As shown in figures, the positive and the negative retardations are described using "warm colors" (white > red > yellow) and "cool colors" (light blue > blue > dark blue), respectively. The zero level is described using green color. Each "color bar" on the top of the result stands for the relationship between color and retardation.

Fig. 4 Patterns of surface
charge distribution. (applied
positive started sine wave)
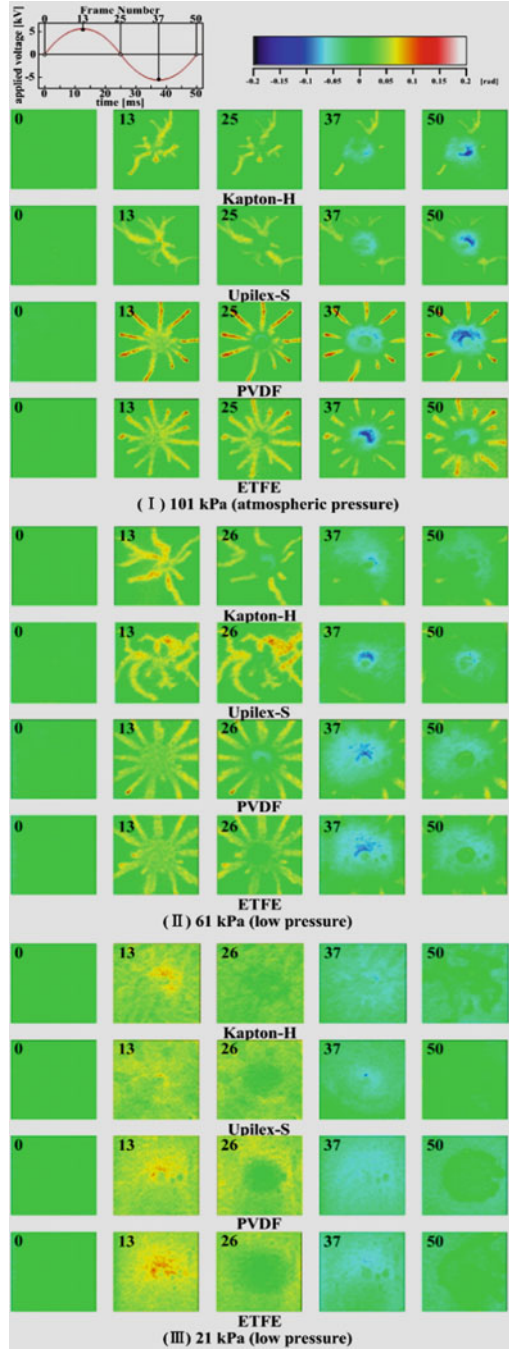
Fig. 5 Patterns of surface charge distribution. (applied negative started sine wave)
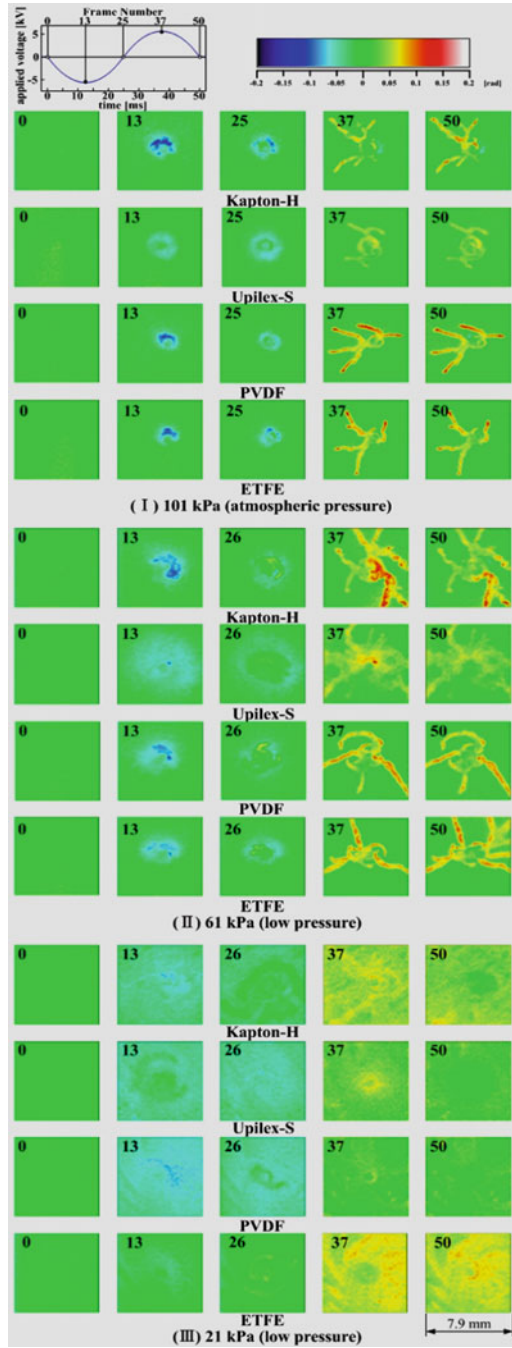
Positive and negative retardations stand for the existence of positive and negative charges on the sample, respectively.

3.4   Discussion

AC electrical surface discharge phenomena of positive streamers and negative streamers have been observed by using the electro-optic Pockels effect and a high-speed CCD camera recording system. Measured positive discharge patterns; such as radial branches, or negative discharge patterns, such as the small circles in Fig. 5, are almost the same as previously measurement results. We also observed the propagation phenomena of positive discharge streamers and the neutralization behavior of negative discharge on the solid dielectric material. At the same time we found that the difference in the surface discharge pattern was depend on the properties of the dielectric materials of the polymer films and atmospheric pressure.

3.5   Influence of the Atmospheric Pressure

Upon decompression of the chamber, the width and length of positive and negative streamers increases. The width of positive streamers under the atmospheric pressure is around 0.38 mm, but becomes wide at about 0.67 mm under the low pressure (61 kPa). With the rising pressure, the positive discharge shape shifts to glow discharge. The shape of the negative discharge streamers always progresses regardless of atmospheric pressure concentrically. In addition, the diameter of the negative charge distribution increases with decompression. The reason for these phenomena is thought to be due to the electron's mean free path.

3.6   Influence of the Polymer Film Type

The development of the positive streamer shape depends on the type of the polymer material. The positive streamer with no residual electric charge develops as a straight line on PVDF and ETFE films, as was shown in Fig. 4. In addition, streamers on Kapton® and Upilex® films developed as curves showing characteristics of meandering and branching. It can be seen from Figure 5 that the positive streamer in the negative charge area is the development of BSO bent on making progress and the entire crystalline polymer insulator, insulator type dependence is not observed. In addition, we focus on the development of positive streamer shape other than the negative charge region in Fig. 5, PVDF, ETFE on the crystallization is linear, and features shown on the Kapton® and Upilex® films curved branches. This figure matches Fig. 4 dependence shown in the sample. Thus, if the supply of electrons to

Fig. 6 Energy bands of polymer materials
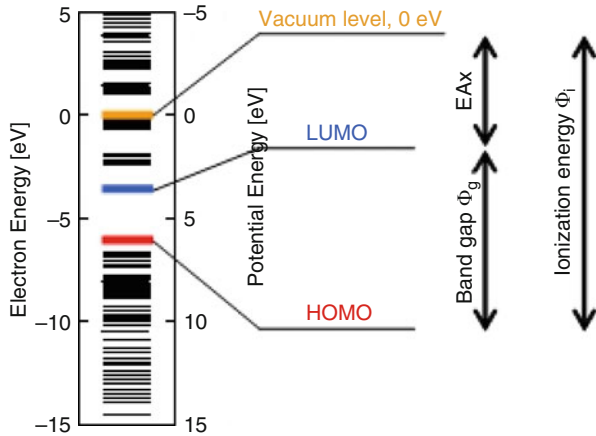
Fig.7 Energy structure of samples
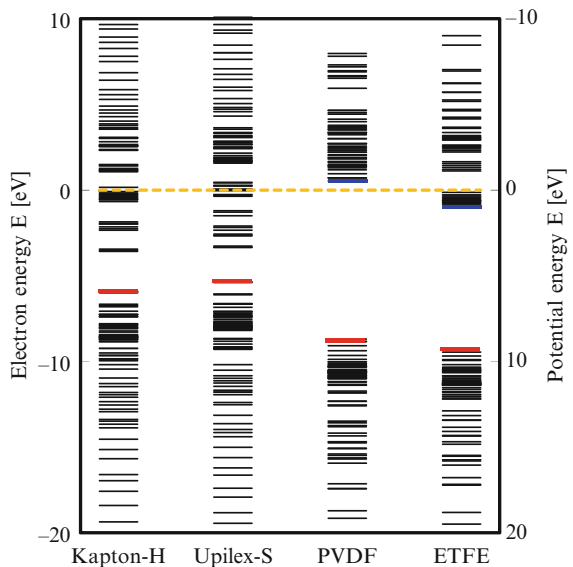
electron ionization of air is positive, the streamer would curve. When electrons are supplied to non-ionized air molecules, positive streamer is curved. In this experiment conditions, the photoelectric emission from an insulator by emission of light by the recombination is thought about as an electronic source of supply.

So far, it has been reported to have been confirmed by photoelectric emission from a sample of the discharge emission. In addition, that an emission of light wavelength with the electric discharge was observed with spectrum measurement technology in a range of 200 ~ 800 nm is reported.

Focusing on photoemission from a sample where the insulation, density-functional calculation to calculate the energy band structure for each polymeric materials. Figure 6 shows an example of the energy structure calculations. In Fig. 7, the red line indicates the highest occupied molecular orbital (HOMO), the blue line

Table 2 Electron affinity, ionization and band gap energies of various samples

Polymer	Electron affinity [eV]	Ionization energy [eV]	Band gap energy [eV]
Kapton-H	3.58	5.9	2.32
Upilex-S	3.34	5.36	2.02
PVDF	−0.53	8.69	9.22
ETFE	0.86	9.46	8.59

indicates the lowest unoccupied molecular orbital (LUMO), the yellow line presents the vacuum level (0 eV). In addition, band gap energy Φg, electron affinity x, ionization energy Φi are also marked in Fig. 6. The band gap energy, electron affinity and ionization energy of each sample are summarized in Table 2 and Fig. 7.

From Table 2 and Fig. 7 it can be seen that the ionization energy of PVDF and ETFE films is higher than for Kapton® and Upilex® films. This shows that Kapton® and Upilex® films emit electrons to the sample surface easier than PVDF. In addition, LUMO of the Kapton® and Upilex® are lower than the vacuum level. On the other hand, LUMO of the PVDF is higher than the vacuum level. Therefore, photoelectric emission from the polymeric materials due to the emission from the discharge is possible in Kapton® and Upilex®, but impossible in PVDF. In other words it could be said that the shape development of positive streamer shows dependence such as curve, meandering and branching by the photoelectric emission from polymeric materials.

Therefore, it can be suggested the energy band structure of the insulator samples is an important factor affecting the curving mechanism of positive streamers.

4 Conclusions

Surface discharge patterns on dielectric materials are observed using a newly developed system based on Pockels effect. The developed compact system enables to observe the surface charge patterns on various polymeric materials in a small chamber under low pressure condition. We have found that the width of positive streamers under low pressure is larger than those formed under atmospheric pressure. Furthermore, branched and curved streamers are observed on PI films while only straight streamers are observed on PVDF and ETFE films. It is found that the calculated ionization energy of materials is useful to classify the discharge patterns.

References

1. Tanaka Y, Komiyama Y, Suzuki S, Miyake H, Takada T (2010) Observation of surface charge distribution on dielectric films using Pockels effect. In: 15th Asian conference on electrical discharge, Xi'an Jiaotong University, Xi'an, China, pp 258–261
2. Mu HB, Zhang GJ, Komiyama Y, Suzuki S, Miyake H, Tanaka Y, Takada T (2011) Investigation of surface discharges on different polymeric materials under HVAC in atmospheric air. IEEE Trans Dielectr Electr Insul 18:485–494

3. Zhu Y, Takada T, Tu D (1995) An optical measurement technique for studying residual surface charge distribution. J Phys D; App Phys 28:1468–1477
4. Zhu Y, Takada T, Inoue Y, Tu D (1996) Dynamic observation of needle-plane surface discharge using the electro-optical Pockels effect. IEEE Trans DEI 3:460–468
5. Kawasaki T, Terashima T, Suzuki S, Takada T (1994) AC surface discharge on dielectric materials observed by advanced Pockels effect technique. J Appl Phys 76:6
6. Murookam Y, Takada T, Hidaka K (2001) Nanosecond surface discharge and charge density evaluation part I: review and experiments. IEEE Electr Insul m 17:6–16

Charging and Discharging Characteristic on PI Films Irradiated by Protons

Ryo Uchiyama, Hiroaki Miyake, Yasuhiro Tanaka, and Tatuo Takada

Abstract We evaluate the dielectric characteristic of polymeric materials for MLI (Multi Layer Insulator, a kind of thermal insulation material) for spacecraft under high energy proton irradiation using results of space charge distribution. Space-crafts have a serious damage due to the electro-static discharge accident. The electric charges are accumulated in the polymeric materials due to radioactive rays, especially electrons and protons. The charge accumulation is the origin of aging and discharging phenomena, furthermore those become trigger for spacecraft operation anomaly. Therefore, we need to obtain the space charge distribution in the bulks. In this study, we especially focused polyimide films for MLI irradiated by high energy proton. We measured the space charge distribution in the bulks during and after proton beam irradiation. From the results, it is found that positive charges accumulate in the bulk at the position of proton penetration depth. We also obtained same tendency from the results of conductivity measurement treated by ASTM method. From the above reason, we have studied the dielectric characteristics of MLI materials irradiated by radioactive rays, especially we focused the condition of proton irradiation. In this paper, we discuss the dielectric phenomena and the relationship between conductivity and charge accumulation in bulks.

Keywords Charge distribution • Conductivity • Dielectric material • PEA method • Polyimide. • Proton-beam • Spacecraft

R. Uchiyama (✉) • H. Miyake • Y. Tanaka • T. Takada
Graduate School of Engineering, Tokyo City University, Tokyo 158-8557, Japan
e-mail: g1181204@tcu.ac.jp

1 Introduction

Spacecrafts use multilayer insulators (MLI) to keep the temperature constant of those inside. It is made up dielectric materials, especially polyimide (PI) films. As MLI are always exposed to high energy radioactive rays such as electrons and protons, those charged particles are injected and accumulated in those bulks. The electric filed differential or enhancement is produced due to those charged particle accumulations. It is the origin of an electro-static discharge (ESD) on MLI. The discharge sometimes gives the serious damage for spacecrafts operation [1, 2]. Therefore, it is necessary to discuss the dielectric characteristic, such as internal charge accumulation, in the polymer irradiated by radioactive rays.

We and Griseri et al. have many experiences to measure the charge distribution in dielectric materials under electron beam irradiation using Pulsed Electro-Acoustic (PEA) and Pressure wave propagation (PWP) method [3, 4]. However, many researchers never focused to measure the charge distribution under proton irradiation condition. Therefore, we have tried to evaluate the dielectric characteristic of PI irradiated by proton beam using PEA method and ASTM method.

In this paper, we discuss the dielectric phenomena and the relationship between the charge accumulation in bulks and the conductivity.

2 Experimental Apparatus

2.1 PEA Apparatus

Figure 1 shows a schematic diagram of a developed PEA measurement system for radioactive rays irradiation condition [5]. The apparatus has the window for the irradiation of the charged particles to the sample [3, 6]. Therefore, we can measure the charge distribution under beam irradiation. This apparatus is developed with concept of downsizing to be applicable for the measurement in a small chamber. The size of the apparatus is $68 \times 48 \times 25$ mm. By using a piezo-electric transducer of PVDF (Poly Vinylidene Fluoride) with thickness of 9 кm, a spatial resolution of the PEA apparatus is about 10 кm. Therefore, we are able to measure a sample with thickness of 100 кm with resolution of 10%. This system is controlled to obtain the charge accumulation data by PC.

3 ASTM Method

Figure 2 shows a principle of ASTM method [7]. The sample is sandwiched three electrodes, which is upper and detection and electrical grounded electrodes. By applying the high electric field E to the sample from the upper electrode, the
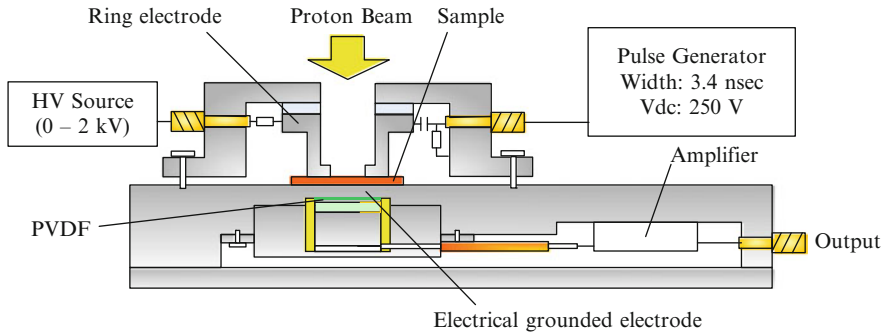
Fig. 1 Schematic diagram of the measurement apparatus
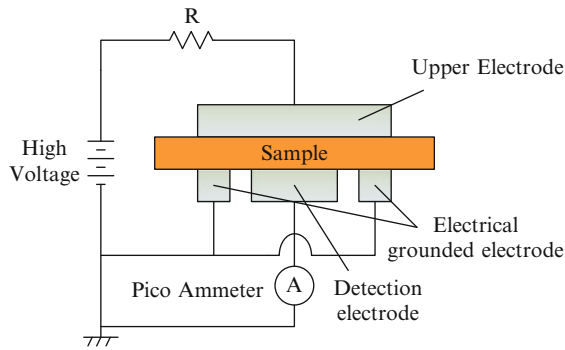
Fig. 2 Principle of the ASTM method

conduction current flow from in the sample to the detection electrode. And it measures the pico ammeter. The conduction current is described the detection electrode area S. Therefore, current density J is described using I, S with

$$J = \frac{I}{S} \tag{1}$$

Therefore, electrical conductivity κ is described using J, E with

$$\kappa = \frac{J}{E} \tag{2}$$

From (2), electrical conductivity in the sample is calculated by J and E.

4   Experimental Procedure

The sample were used the Polyimide(PI) film (Upilex®-S) of 50 and 125 μm thickness. In the experiments, the same grade samples of MLI for the actual spacecraft are used. And the samples of 125 μm thickness have an Al evaporation layer on the irradiation surface due to applied pulse voltage to obtain charge distribution. We irradiated mono energetic proton with the energy of 1.5, 2.0 MeV and current density of 30 nA/cm^2. The proton irradiation was carried out under vacuum atmosphere (1×10^{-5} Pa) for 30 min. The irradiation was carried out using 3 MeV tandem type ion accelerator facility of Takasaki Advanced Radiation Research Institute of Japan Atomic Energy Agency (JAEA), 3.75 MV Van de Graff of High Fluence Irradiation Facility at the University of Tokyo. We measured the charge distribution in the bulk of PI during and after proton beam irradiation using PEA system. After irradiation, we obtained conduction current on the irradiated energy of 1.5, 2.0 MeV and current density of 30 nA/cm^2 samples under 100 kV/mm applied by ASTM method after 1 h from irradiation [7]. The electrical conductivity was calculated from the measurement current. Furthermore, in case of 2.0 MeV, those measurements were carried out after 1 h, 1 day and 3 days protons irradiation.

5   Results and Discussion

5.1   Measurement of Charge Distribution Under Proton Beam Irradiation

Figure 3 shows the charge distributions on the maximum charge accumulation of the bulk of PI under proton beam irradiation. These figures are described as the irradiations side of right hand side. From these figures, it is found that positive charge accumulation was observed in the bulk, respectively. And the charge distribution shape has two peaks. We also calculated the penetration depth using the numerical calculation software "SRIM" [8]. From the simulations, those depths with acceleration energy of 1.5, 2.0 MeV are 37, 59 μm from the irradiation surfaces. These results are also shown in Fig. 3 using broken line. Judging from the charge distribution of Fig. 3, the peak of accumulated positive charges are about 37, 57 μm in the result of 1.5, 2.0 MeV. As we can obtain the position of positive charge accumulation is very close to calculated penetration depth, the positive charge in the bulk was generated by proton beam irradiation.

    In other words, the maximum penetration depth of the injected proton in PI is dependent on acceleration energy.
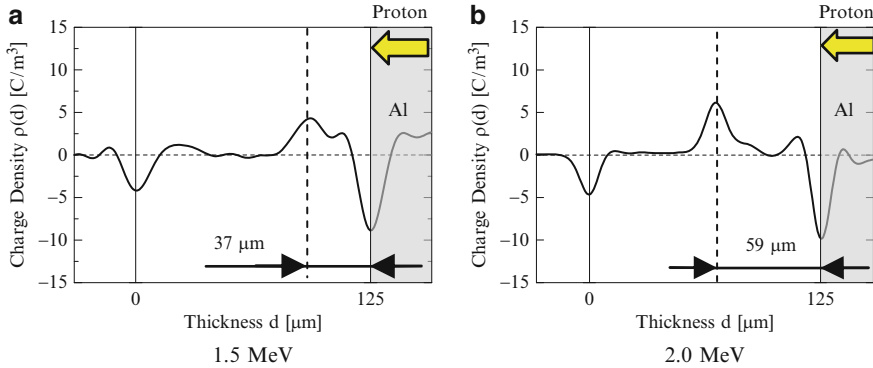
Fig. 3 Charge distribution under proton beam irradiation
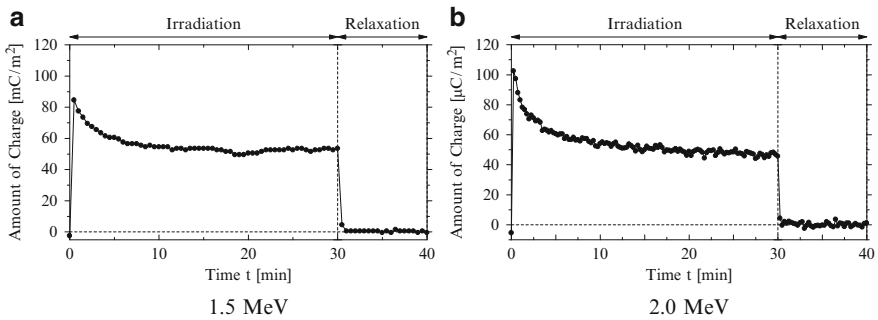
Fig. 4 Time dependence on accumulated total amount of charge

Figure 4 shows the time dependence of integral accumulated charges in the bulk which is calculated using Fig. 3.

From these figures, the Positive charges were observed just after irradiation. The amount of the positive charge saturate with irradiation time progress. The charge accumulation becomes maximum accumulation immediate after irradiation within 30 sec, respectively. After saturation, charge accumulation decrease regardless of during irradiation.

We discuss about the accumulation behavior in during irradiation. From these results, the amount of charge accumulation became a maximum immediate after irradiation and gradually decreased and saturated during irradiation. After irradiation, the accumulated charge disappeared, rapidly within 30 sec. It is the reason that the decay speed of accumulated charges became first due to rise of the electrical conductivity on irradiated area. We thought that the origin of those phenomena was produced due to the radiation induced conductivity (RIC).

6 Electrical Conductivity in Proton Beam Irradiated Polyimide Under High Electric Field

Figure 5 shows the time dependence of current density on irradiated PI with 50 μm thickness under 100 kV/mm applied non-irradiation and after 1 h from irradiation. As can be seen fom Fig. 5, the current density became maximum immediate after applied high electric field. In case of irradiated samples, the current density is higher than non-irradiation sample. After saturation, current density decrease and stabilized by 50 min, respectively.

Figure 6 shows the electrical conductivity σ that was calculated using Fig. 5. In this figure, the broken line shows the current density in non-irradiation level. From the figure, the conductivity of irradiated sample becomes 10^2, 10^3 times higher than non-irradiation after 1 h from irradiation in the result of 1.5, 2.0 MeV, respectively. As we can obtain the conductivity was generated by proton beam irradiation.

In other words, the conductivity on PI is dependent on acceleration energy.

Furthermore, in case of 2.0 MeV, we measure the current density after 1 h, 1 day, 3 days from irradiation. Fig. 7 shows the time dependence of current density on irradiated PI with 50 μm thickness under 100 kV/mm applied. From the figure, current density becomes maximum immediate after applied high electric field, respectively. And the current density of irradiated samples is higher than non-irradiation sample. After saturation, the current density decrease and stabilized by 50 min, respectively. However, in case of after 1 day from irradiation, the current density rose after about 60 min. We thought that the accumulated positive charge in the bulks of sample was generated by applying high electric field.

Figure 8 shows the time dependence of the electrical conductivity σ, which is calculated using Fig. 7. In the figure, the broken lines show the current density in non-irradiation level. From the figure, the conductivity of irradiated sample
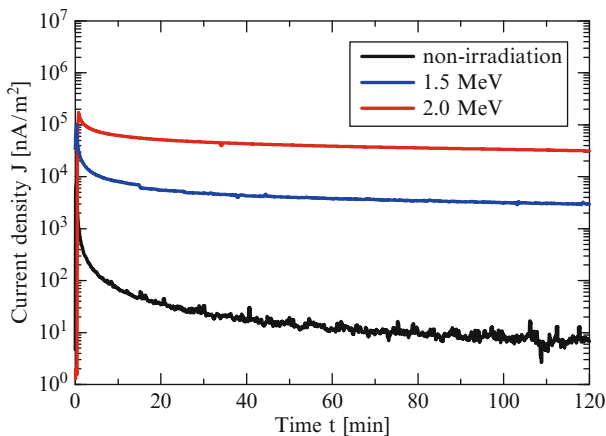
Fig. 5 Time dependence of current density
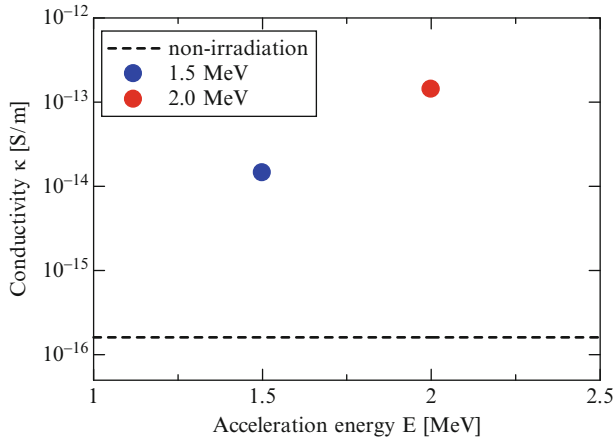
Fig. 6 Conductivity versus acceleration energy
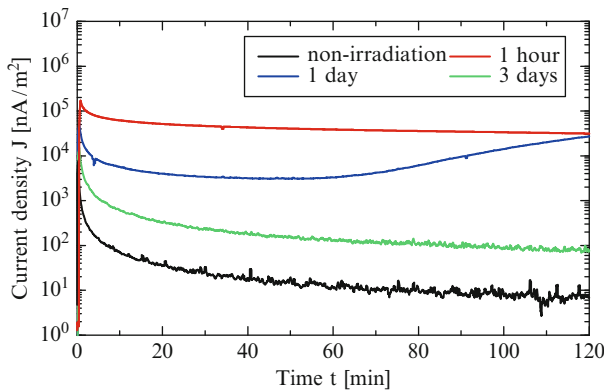
Fig. 7 Time dependence on current density

becomes 10^3 times higher than non-irradiation sample after 1 h from irradiation. Although, σ decreased with time, we can confirm σ is kept high level compared with non-irradiation level in our experiments.

We discuss about the conductivity behavior on irradiated sample. From these figures, the conductivity of irradiated sample became higher than non-irradiation sample and it was decreased in time progress. We thought that the origin of those phenomena was produced due to the radiation induced conductivity (RIC). Therefore, the conductivity induced by proton in the bulks. However, the RIC was decreased in time progress. As we can obtain the RIC were relaxed by time progress.

In other words, the conductivity of irradiated sample is dependent on time dependence.
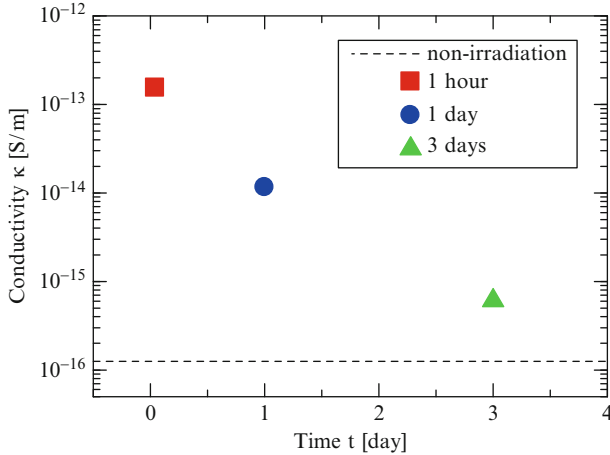
Fig. 8 Time dependence on electrical conductivity

7   Conclusions

Using the PEA method, we have observed the space charge distribution in PI which is used for spacecrafts under proton beam irradiation. After irradiation, using the ASTM method, we observed the current density and the conductivity. The following results were obtained.

(a) Positive charge accumulated just after irradiating proton beam in the bulk of PI. However, the amount of the positive charge seems to saturate with increase of the irradiation time, while after that decrease regardless of irradiation duration.

(b) By applying dc electric field to the proton beam irradiated samples, the electrical conductivity became higher than non-irradiated sample. However, the conductivity decreased with time.

References

1. Koons C, Mazur JE, Selesnick RS, Blake JB, Fennell JF, Roeder JL, Anderson PC (1998) The impact of the space environment on space systems. In: Proceedings of the 6th Spacecraft Charging Technology Conference, (Air Force Research Laboratory Science Center, Hanscom Air Force Base, MA, 2000), pp 7–11
2. Payan D, Reulet R, Dirassen B (2005) Elecrtostatic behavior of dielectrics under GEO-like charging space environment simulated in laboratory. In: Proceedings of 9th spacecraft charging technology conference, Tsukuba (Japan), 4–9 April

3. Griseri V, Perrin C, Fukunaga K, Maeno T, Payan D, Levy L, Laurent C (2005) Analysis of electron behavior in polymeric films during electronic irradiation. 2005 annual report CEIDP, pp 645–648
4. Dang W, Tahara M, Taima J, Tanaka Y, Watanabe R, Takada T (2006) Observation of charge distribution in electron beam irradiated polymers using pulsed electro-acoustic method. 2006 annual report CEIDP, pp 138–141
5. Takada T, Miyake H, Tanaka Y (2006) Pulse acoustic technology for measurement of charge distribution in dielectric materials for spacecraft. IEEE NPSC Trans Plasma Sci 34 (5):2176–2184
6. Takada T (1999) Acoustic and optical methods for measuring electric charge distributions in dielectrics. IEEE Trans DEI 6(5):519–547
7. Metrology of volume resistivity and solid electric insulating material-surface resistivity: JIS C 2139 and 2008
8. Ziegler JF, Biersack JP, Littmark U (1985) The stopping and range of ions in solids. Pergamon Press, New York

Degradation of Mechanical Properties of Spacecraft Polyimide Film Exposed to Radiation Environments

Shen Zicai, Liu Yuming, Feng Weiquan, Zhao Chunqing, and Ding Yigang

Abstract Polyimide films are widely used in spacecraft, but their mechanical properties would degrade in radiation environments that include electrons, protons, atomic oxygen, near ultraviolet or far ultraviolet, etc. Implications of using polyimide films in spacecraft are reviewed in this paper. The degradation of mechanical properties of Kapton film exposed to electrons and far ultraviolet radiation environments were studied. It is known that the tensile strength and the rupture elongation of Kapton film decrease with the increase of the tensile deformation rate and the electron and far ultraviolet radiation. The far ultraviolet radiation will cause the rupture and cross linkage of molecular bonds in the film, deoxidation of C-CO, denitrification of C-N. The increase of C-H percentage is attributed mainly to the mechanical property degradation of Kapton film under far ultraviolet irradiation.

Keywords Mechanical property • Irradiation environment • Tensile strength • Rupture elongation

1 Introduction

With the progress in space science and technology, the spacecraft structures and their weight become larger and larger. The preparation and launch of traditional space structures is usually restricted by the effective available space and maximum loads of the carriers. So improvement of spacecraft function and reduction in total mass is an important way for spacecraft design. Deployable structures are an excellent way to reduce launch costs. They require little storage room, are light weight, possess high reliability and can provide some special capabilities that traditional structures cannot.

S. Zicai (✉) • L. Yuming • F. Weiquan • Z. Chunqing • D. Yigang
Beijing Institute of Spacecraft Environment Engineering, Science and technology on reliability and environmental engineering laboratory, 100094 Beijing, China
e-mail: zicaishen@163.com
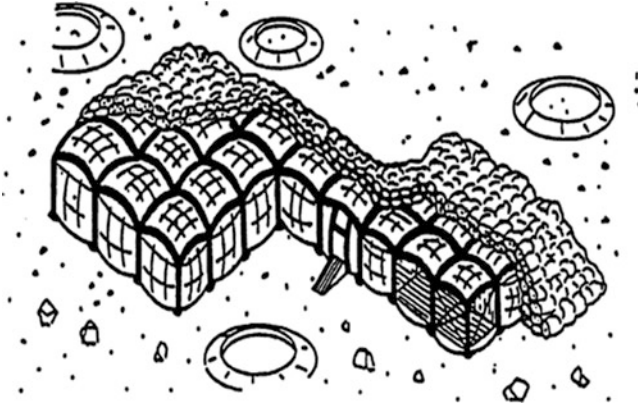
Fig. 1 Assembled modules of lunar base
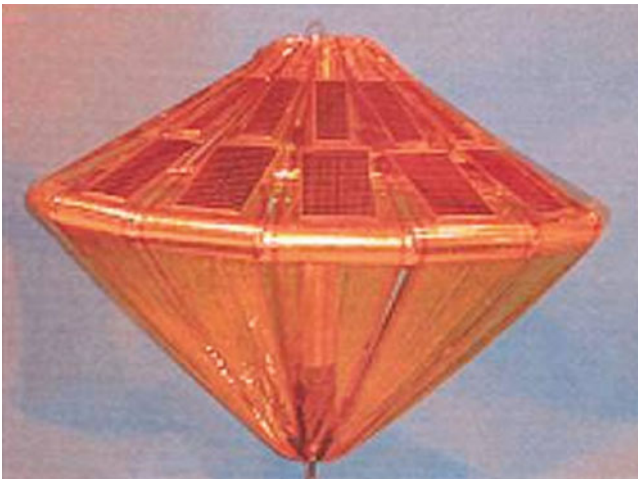
Fig. 2 Deployment of solar battery

Space deployable structures can be used in construction of future lunar bases, deployment of solar batteries, solar sails, sunshields of next generation space telescope, etc. [1–8], as shown in Figs.1 and 2. Thin polymer films are an important part of such structures.

The polymer films that are used on the outside of the spacecraft are usually exposed to the space environment and their mechanical properties will degrade severely with time [9–11]. The major space environment factors that induce such deterioration in properties are atomic oxygen (AO) in low Earth orbit (LEO), orbital thermal cycling, micrometeoroids, orbital debris and space radiation environments such as electrons, protons, near ultraviolet (NUV), far ultraviolet (FUV), etc.

So it is essential to study the mechanical degradation of spacecraft film exposed to the space environments with the results of such studies providing help to the design of spacecraft and ensuring the reliability of spacecraft in orbit.

Fig. 3 Brugger film parting tool

2 Sample Description

Kapton polymer film, 50 μm thick was selected for this study. It was cut into special samples 150 mm long and 15 mm wide using the Brugger parting tool as shown in Fig. 3, taking special care of the sample edges to remain smooth. Five samples were prepared as a group in each experiment.

3 Test

3.1 Test Facility

The test was performed in a low-energy combined environment test facility built by Beijing Institute of Spacecraft Environment Engineering (BISSE), as shown in Fig. 4. This facility can provide environments of low-energy electrons, low-energy protons, NUV (near ultraviolet), FUV (far ultraviolet), neutral plasma, thermal cycling, and vacuum [12]. The in situ measurement of αs, spectral reflectance, spectral transmittance, surface resistance and mechanical properties of the test specimens can be performed inside the facility.

The mechanical properties in this work were tested using a vertical tensile testing system as shown in Fig. 5. The tensile test is controlled by a computer and provides many parameters such as tensile strength, rupture elongation, etc.. The test samples were removed from the environmental chamber at specially selected doses to test their mechanical properties.

Fig. 4 Combined environment test facility

Fig. 5 Vertical tensile testing machine

3.2 Electron Irradiation

Electrons, especially the low-energy electrons, are most detrimental to the space-craft surface films because they constitute the majority of electrons in space and deposit their energy at the surface.

We used the AE8 radiation model. To get the low-energy data below 40 keV for electrons, we extrapolated AE8 model to the kilo electron volt range of energies. The codes ITS 3.0 was used for calculation of the dose profile. Using the conducted

simulations, the following parameters were selected for the simulation testing: electron energy -40 keV, the doses at which tests were stopped and samples were removed for testing their mechanical properties -0, 2×10^{15} e/cm^2, 6×10^{15} e/cm^2, 1.0×10^{16} e/cm^2, 1.4×10^{16} e/cm^2, 1.7×10^{16} e/cm^2.

3.3 Far Ultraviolet (FUV) Exposure

The FUV irradiation with higher energy photons can break the bonds in the surface layers of the spacecraft polymer films. A number of FUV exposures, i.e. 0ESH, 300ESH, 600ESH, 1000ESH were used separately in tests. The acceleration factor was about 10.

3.4 Temperature and Vacuum

The temperature of the samples was controlled by afixing them to a big metal plate whose temperature was maintained at about 20 °C to ensure the sample temperature was less than 50°C since too low temperatures are harmful and may affect the mechanical properties. The facility shroud temperature was controlled at -35°C. The sample temperature needs to be much higher than the shroud temperature. The vacuum system consisted of a turbo-molecular pump and mechanical pump. The vacuum was better than 3.0×10^{-3} Pa during the whole test period.

4 Results and Discussions

4.1 Tensile Deformation Rate Effect

The rupture elongation results of Kapton films without any irradiation obtained in tensile tests performed at tensile deformation rate of 50, 100, and 150 mm/min are shown in Fig. 6.

As can be seen from Fig. 6, the rupture elongation of Kapton film is decreasing with the increase of the tensile deformation rate.
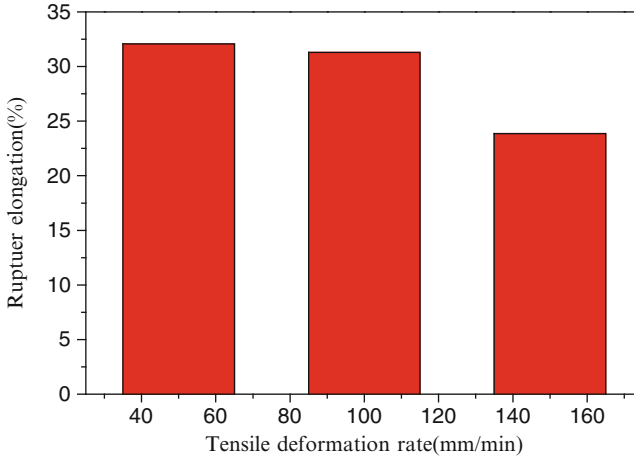
Fig. 6 Rupture elongation of Kapton film at different deformation rates

Table 1 Rupture elongation of Kapton film at different electron dosage

Dosage (e/cm^2)	Rupture elongation (%)
0	31.29
2.0×10^{15}	25.67
6.0×10^{15}	24.84
1.0×10^{16}	20.7
1.4×10^{16}	19.31
1.7×10^{16}	23.4

Table 2 Tensile strength of Kapton film at different electron dosage

Dosage (e/cm^2)	Tensile strength (MPa)
0	105.813
2.0×10^{15}	103.439
6.0×10^{15}	101.35
1.0×10^{16}	97.14
1.4×10^{16}	95.39

5 Electron Irradiation Effect

After the electron irradiation test at different doses of 0, 2×10^{15} e/cm^2, 6×10^{15} e/cm^2, 1.0×10^{16} e/cm^2, 1.4×10^{16} e/cm^2, 1.7×10^{16} e/cm^2, the tensile elongation test were conducted. The rupture elongation and tensile strength are listed at Tables 1 and 2.

Ignoring of singular result, the rupture elongation data of Kapton film can fit an exponential decrease with the increase of irradiation dose, as shown in Fig. 7. The fitted expression between rupture elongation and irradiation dose can be written as follows

$$y = 17.41 + 13.05 \exp(-x/7.69) \tag{1}$$
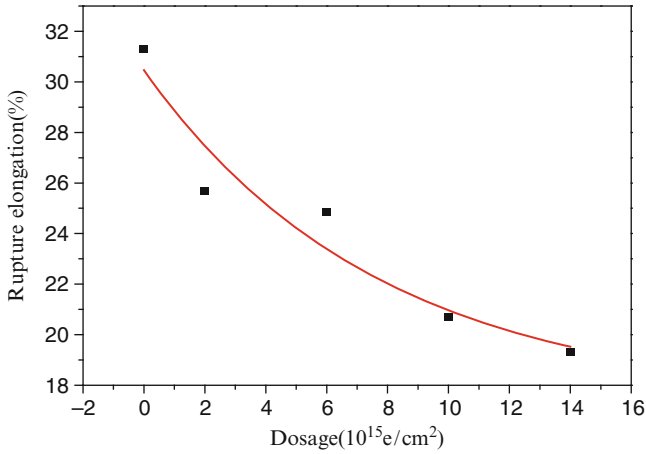
Fig. 7 Fitting curve of Kapton film rupture elongation at different doses
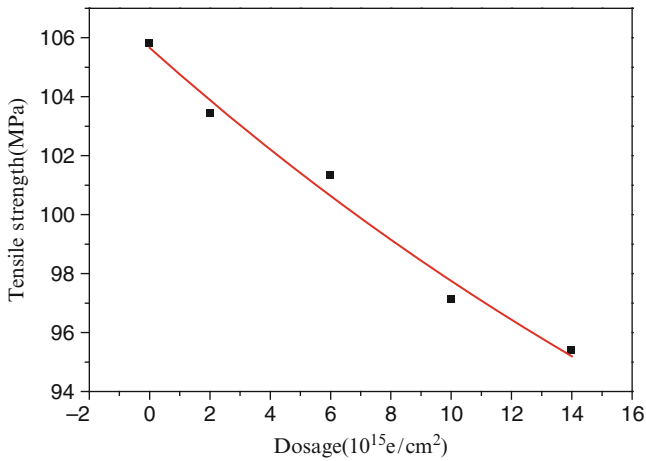
Fig. 8 Fitting curve of Kapton film tensile strength at different doses

Here, y is rupture elongation (in %); x is dose measured in unit of $10^{15}e/cm^2$.

The exponential decrease of Kapton film's tensile strength with the irradiation dosage is shown in Fig. 8 and can be expressed by the following approximation:

$$y = 75.05 + 30.61 \exp(-x/33.44) \tag{2}$$

Here, y is tensile strength, MPa; x is dose ($10^{15}e/cm^2$).

Table 3 Rupture elongation of Kapton in different FUV exposure

Dosage (e/cm^2)	Rupture elongation (%)
0	31.29
300ESH	29.91
600ESH	25.76
1000ESH	25.12

Table 4 Tensile strength of Kapton in different FUV exposure

Dosage (e/cm^2)	Tensile strength (MPa)
0	105.813
300ESH	104.98
600ESH	101.83
1000ESH	99.77
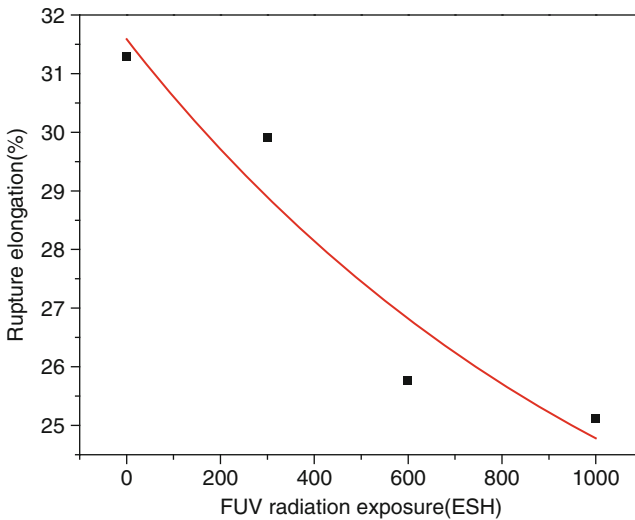
Fig. 9 Fitting curve of Kapton film rupture elongation at different radiation exposure

6 FUV Irradiation Effect

After the FUV irradiation test at different exposures of 0, 300ESH, 600ESH, 1000ESH, the tensile elongation test were performed. The rupture elongation and tensile strength are listed in Tables 3 and 4.

The rupture elongation of Kapton film irradiated by FUV can be fitted by an exponent decrease with the increase of irradiation exposure, as shown in Fig. 9. The fitted expression between rupture elongation and irradiation dosage can be written as follows

$$y = 19.89 + 11.69 \exp(-\frac{x}{1145.82}) \tag{3}$$
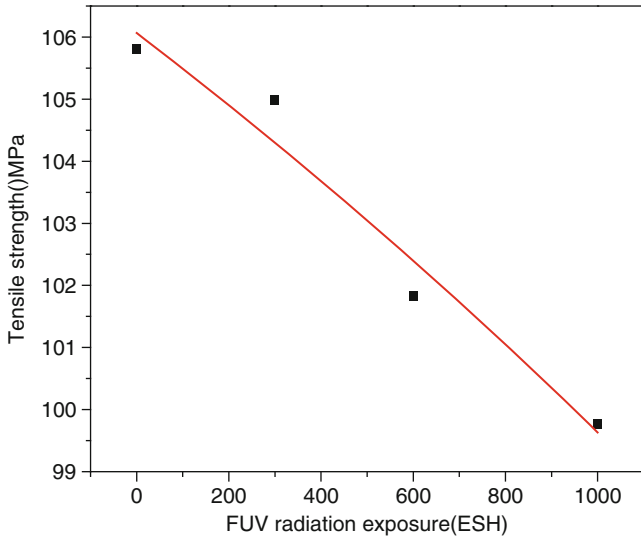
Fig. 10 Fitting curve of Kapton film tensile strength at different radiation exposure

Here, y is rupture elongation, %; x is exposure, ESH.

The tensile strength of Kapton film exponentially decreases with the radiation exposure, as shown in Fig. 10.

The fitted expression can be presented as follows

$$y = 128.98 - 22.92 \exp(\frac{x}{4044.47}) \tag{4}$$

Here, y is tensile strength, MPa; x is exposure, ESH.

7   Discussion

Kapton is an organic high molecular weight polymer, its molecular composition is $[(C_{22}H_{10}O_5N_2)_n]$. The elemental composition of Kapton can be described as C 75.9%, O 17.2%, N 6.9%

Using XPS analysis, the surface composition of Kapton irradiated with electrons with doses of 0.2×10^{15} e/cm^2, 6×10^{15} e/cm^2, 1.0×10^{16} e/cm^2 was established as shown in Table 5.

As can be seen from Table 5, the surface composition of Kapton, without irradiation, consists of C and O. The O and N concentrations increase sharply at the initial stages of irradiation that may be due to the electron irradiation, when O and N acquire electrons and exist in active state. But with an increase in electron irradiation, the component percentage of C increases while O and N decrease, suggesting that the

Table 5 Component percentage of Kapton irradiated with different electron doses

Dosage (e/cm^2)	C1s (at.%)	O1s (at.%)	N1s (at.%)
0	88.3	11.7	0
2×10^{15}	77.01	16.55	6.44
6×10^{15}	79.45	14.92	5.62
1×10^{16}	83.04	13.3	3.66

Table 6 Elemental composition of Kapton before and after FUV irradiation

Dosage (ESH)	C1s (at.%)	O1s (at.%)	N1s (at.%)
0	69.33	24.87	5.8
1,000	79.57	17.05	3.38

Name	Pos.	FWHM	Area	% Area
C1s_a	284.41	1.49	22555.37	50.70
C1s_b	285.18	1.58	15738.38	35.38
C1s_c	288.19	1.33	6194.907	13.92
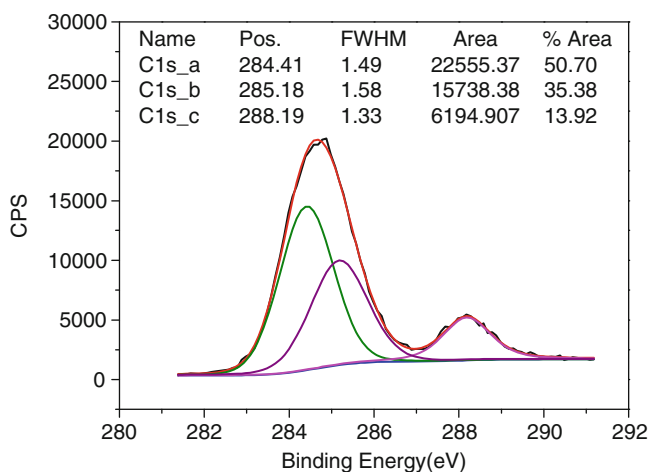
Fig. 11 XPS of C1s in Kapton before FUV irradiation

sample structure has changed with the electron irradiation, i.e. the surface becomes enrich in C, while the O and N are released gradually, resulting in the increase of sample rigidity and decrease of rupture elongation and tensile strength.

The component percentage of Kapton irradiated by FUV with dosage of 1000ESH and without irradiation is listed in Table 6.

It is clear from Table 6 that the surface composition of Kapton irradiated by FUV has significantly changed, with the C concetrnation increasing while O and N decreasing. These changes confirmed that the sample structure has changed with FUVirradiation, resulting in the increase of sample rigidity and decrease of rupture elongation and tensile strength.

Further analysis of Kapton film was performed using high-resolution XPS, with the binding energies and the high-resulution deconvoluted spectra peaks of C1s and O1s shown in Figs. 11, 12, 13, and 14, Tables 7 and 8.

From Figs. 11, 12, 13, and 14, Tables 7 and 8, we can learn that C = O turns to C-O after FUV irradiation, and there are rupture and cross linking of molecular bond of Kapton, deoxidation and denitrification happens with the rupture of C-CO and C-N by FUV irradiation, while content ratio of C-H increases.

Name	Pos.	FWHM	Area	% Area
C1s_a	284.67	1.38	24061.35	52.19
C1s_b	285.18	1.38	19166.07	41.58
C1s_c	288.47	1.61	2873.334	6.23
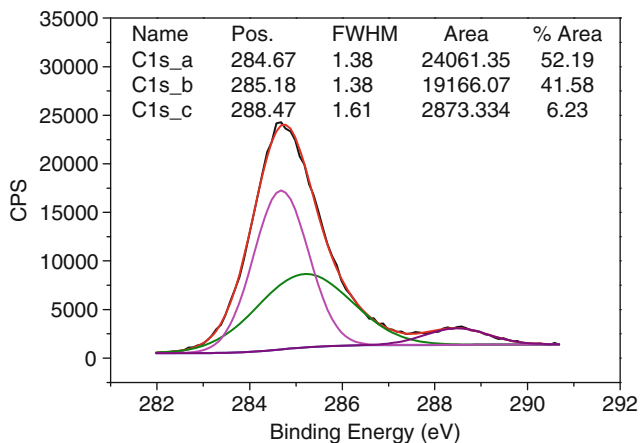
Fig. 12 XPS of C1s in Kapton after 1000ESH FUV irradiation

Name	Pos.	FWHM	Area	% Area
O1s_a	532.09	2.256	23535.46	57.24
O1s_b	531.65	1.746	17580.34	42.76
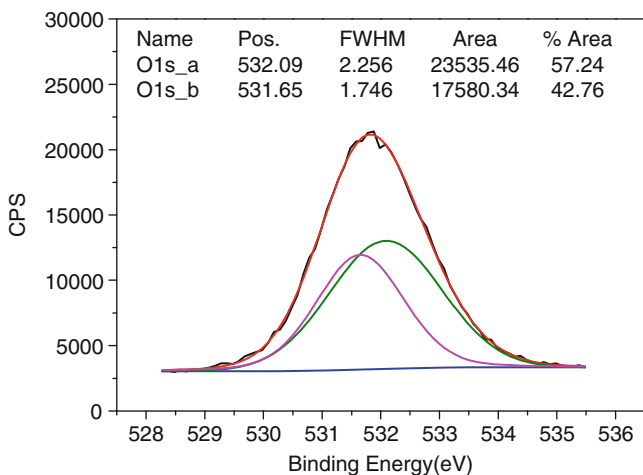
Fig. 13 XPS of O1s in Kapton before FUV irradiation
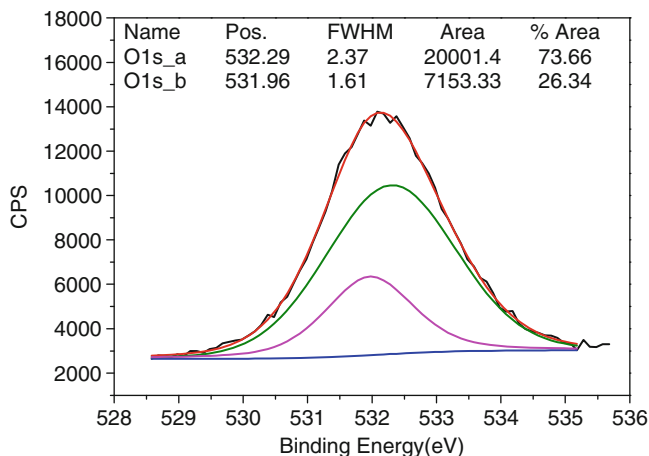
Fig. 14 XPS of O1s in Kapton after 1000ESH FUV irradiation

Table 7 Binding energy and area percentage of C1s in Kapton before and after FUV irradiation

	Binding energy/eV; area percentage/%			
Dose (ESH)	C-H	C-N, C-H, C-CO	C-O, C = O	
0	284.41;50.7	285.5;35.38	288.19;6.86	288.47;C-O
1,000	284.67;52.19	285.5;41.58	288.47;45.30	288.2;C = O

Table 8 Binding energy and area percentage of O1s in Kapton before and after FUV radiation

	Binding energy/eV; area percentage/%	
Dose (ESH)	C = O	C-O
0	531.65;42.76	532.09;57.24
1,000	531.96;26.34	532.29;73.66

8 Conclusions

The tensile strength and the rupture elongation of Kapton film decrease with the increase of the tensile deformation rate and the electron or far ultraviolet irradiation. The far ultraviolet irradiation will cause the rupture and cross linking of molecular bonds in the film, deoxidation of C-CO, denitrification of C-N. The increase of C-H percentage attributes mainly to the mechanical property degradation of Kapton film under far ultraviolet irradiation.

References

1. Joyce AD, Kim KG, Jacqueline AT et al (1998) Mechanical properties degradation of Teflon FEP returned from the Hubble Space Telescope. AIAA 0895:1–12
2. Michael LA, Harry LC, David MK et al (2000) Design and flight testing of an inflatable sunshield for the NGST. AIAA 1797:1–8

3. Grahne MS, Cadogan DP, Sandy CR (2000) Development of the inflatable shield in space (ISIS) structure for the NGST program, IAF-00-I.1.04, 1-12
4. Charles G, Humphrey P (2010) Developments and activities in solar sail propulsion. AIAA 3234:1–18
5. Nathan WG, James IC (2006) Deployment modeling of an inflatable solar sail spacecraft. AIAA 6336:1–15
6. Lichodziejewski D, Cassapakis C (1999) Inflatalble power antenna technology, AIAA, 1074, 1-11
7. Larry L, Hamid H, Michael LT (2001) Dynamic characterization of an inflatable concentrator for solar thermal propulsion. AIAA 1406:1–7
8. Dennis AR, John WC, Lawrence BF et al (2002) Electron, proton, and ultraviolet radiation effects on thermophysical properties of polymeric films. J Spacecr Rocket 39(6):833–838
9. David E, Mary H, Whitney H et al (2004) Characterization of candidate solar sail material exposed to space environmental effects. AIAA 1085:1–10
10. David E, Whitney H, Tesia S et al (2003) Characterization of space environmental effects on candidate solar sail material. SPIE 4823:67–74
11. Shimamura H, Yamagata I (2009) Degradation of mechanical properties of polyimide film exposed to space environment. J Spacecr Rocket 46(1):15–21
12. Feng W, Ding Y, Yan D et al (2009) Combined low-energy environment simulation test of geosynchronous satellite thermal control coatings. J Spacecr Rocket 46(1):11–14

Deposition of Outgassed Products and Products of Radiation-Induced Atomization of Polymeric Composite on Quartz Glass Surfaces

R.H. Khasanshin, V.I. Kostyuk, A.N. Galygin, and N.G. Alexandrov

Abstract Results of experimental simulation of deposition of spacecraft outer atmosphere products on high-orbit spacecraft optical surfaces are given. Basic data have been obtained when studying changes of quartz glass transmittance due to the influence of outgassed products of polymeric composite and electron irradiation.

1 Introduction

Major reason, why optical properties of high-orbit spacecraft skin material changes, is, as a rule, action of space electromagnetic and ionizing radiations [1–4], and their contamination by spacecraft outer atmosphere (SOA) products.

SOA is generated from a great number of various sources of volatile products (VP). Flux density of VP in a certain point in the vicinity of spacecraft is determined by source activities and their arrangement about the chosen point. Thus, spacecraft surfaces are not only in different conditions (temperature, illumination, electrostatic charging, etc.) but are subjected to different VP fluxes. Contamination of optical surfaces by SOA products is the issue of the day for modern spacecraft equipped with a great number of highly sensitive devices.

In general, the efficiency of energy and mass exchanges between SOA products and contaminable surface is defined by accommodation and condensing coefficients

R.H. Khasanshin (✉) • V.I. Kostyuk • A.N. Galygin
OAO "Kompozit", Korolev, Moscow region, Russia
e-mail: rhkhas@mail.ru

N.G. Alexandrov
Krunichev State Research and Production Space Center, Moscow, Russia
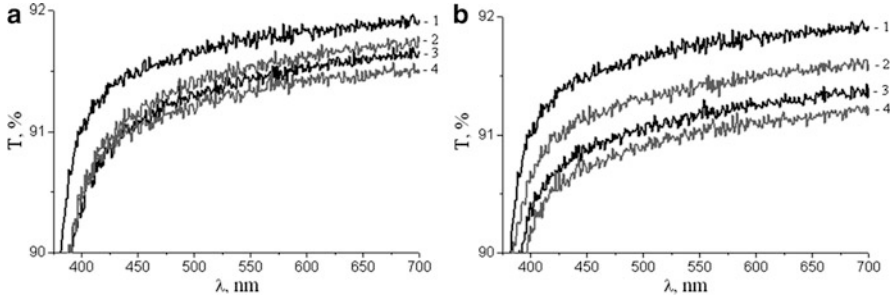
Fig. 1 Spectral transmittances of quartz glass samples irradiated: (a) – by different electron fluxes; (**b**) – by molecular flux and different electron fluxes ($1 - \Phi = 0$; $2 - \Phi = 1.5 \times 10^{14}$; $3 - \Phi = 3 \times 10^{14}$; $4 - \Phi = 6 \times 10^{14}\ cm^{-2}$)

as well as by adsorption probability. Hitting the solid surface, the adsorbing molecules turned out to be in loosely-coupled states in which they may diffuse over the surface until desorption occurs or when strong bonds are formed.

This work is dedicated to studying processes exerting influence on contamination level of quartz glass surfaces by thermal-induced and radiation-induced outgassed products of polymeric composites.

2   Experimental Results

Changes of optical properties of spacecraft skin materials in service conditions are mainly tied with generation of radiation-induced color centers and with their contamination by SOA products. To find contribution of the first process to the change in transmittance, quartz glass samples were subjected to ionizing radiation. Figure 1a shows spectral transmittances (parameter $T(\lambda)$) of samples irradiated by 40-keV electrons with flux density $\varphi \cong 10^{10}\ cm^{-2}\ s^{-1}$. It is seen that increase of electron flux results in growth of quartz glass optical density (reduction of the parameter T). Figure 1b presents the spectral transmittances of samples subjected to combined action of molecular flux (MF) of similar VP sources and different electron fluxes.

To evaluate the changes in transmittance that are directly linked with contamination of sample surfaces by outgassed products, not only initial energy of particles but also the electron fluxes were selected the same in experiments on combined and separate action of electron radiation and MF. Changes of spectral transmittances of glasses were obtained after irradiation of samples with electron fluxes: $(1) - \Phi = 0$; $(2) - \Phi = 1.5 \times 10^{14}$; $(3) - \Phi = 3 \times 10^{14}$; $(4) - \Phi = 6 \times 10^{14}\ cm^{-2}$. Analysis of data had shown that simultaneous bombardment of samples by outgassed VP and electrons gave more significant reductions of transmittances as compared with separate action.
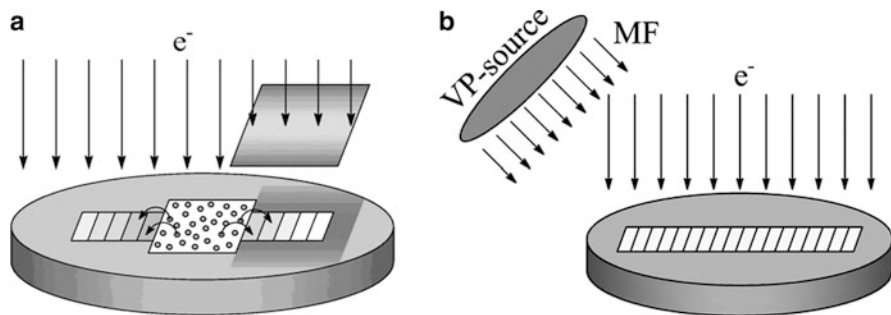
Fig. 2 Schematic presentaiton of the second (**a**) and the third (**b**) series of experiments
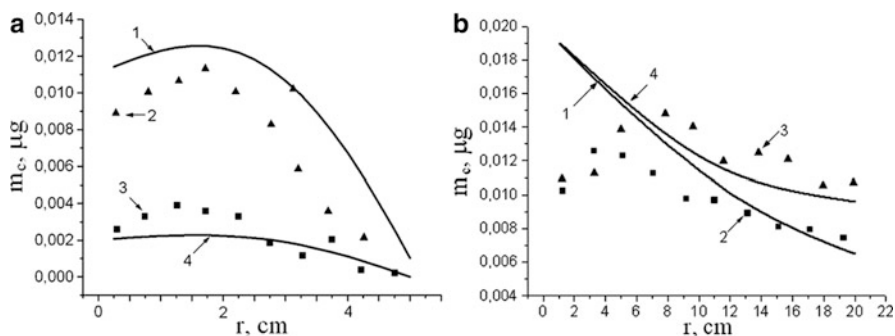
Fig. 3 Mass distribution in case of atomization (**a**) and outgassing (**b**) of products in dependence on distance from the source edge to glass surfaces and from the source center to glass surfaces respectively

The second series of experiments was carried out to study deposition of products of the radiation-induced outgassing process within the vicinity of VP source. The VP source was a sample of a polymeric composite. Symmetrically to this source there were two "rulers" with quartz glass samples. Kinetics of radiation-induced outgassing process and composition of VPs were known in advance. This assembly was fixed to a cooling plate for subsequent electron irradiation. In our case only the source and one "ruler" were irradiated whereas the second "ruler" was radiation-protected but open to VP coming from the source. The schematic presentation of this series of experiments is shown in Fig. 2a.

Results of the second series of experiments are given in Fig. 3a. Here 1 and 4 – calculation data of VP mass deposited on surfaces of radiation-open and radiation-protected "rulers" respectively, in dependence on distance from VP source edge to geometrical centers of glasses. Dependencies 2 and 3 – experimentally obtained VP mass distributions of products of outgassing and radiolysis of polymeric composite accumulated on surfaces of radiation-open and radiation-protected "rulers" respectively. Analysis of the data has shown that radiation resulted in increase of VP mass deposited on quartz glass samples.

Fig. 4 Geometric presentation of the relationship of angular distribution of VP leaving the VP source
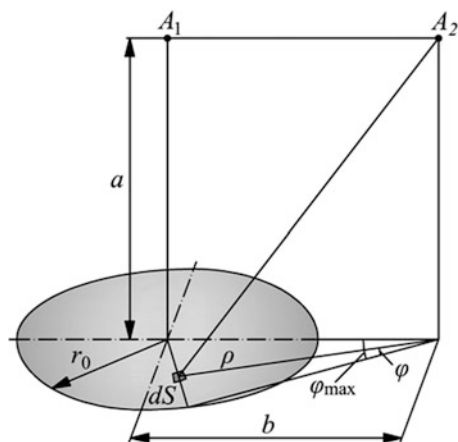
Mass dependence of outgassed products deposited on quartz glass surfaces irradiating by equal electron flux densities of $5 \times 10^{10} \ cm^{-2} \ s^{-1}$ on flux density of incident VP was studied in the third series of experiments. For this purpose, a "ruler" with glass samples was attached to surface of the cooling table in such a way that each glass was at a preset distance from the center of the VP source – sample of a polymeric composite 100 mm in diameter. The VP source temperature was maintained at 100 ± 0.2°C. Scheme of this experiment is given in Fig. 2b.

Results of the third series of experiments are shown in Fig. 3b (2 and 3). The greatest difference of experimental data from calculations was obtained for glasses at minimal distance from VP source. Actually, maximum mass m of outgassed products was deposited on glasses which were positioned nearer to the centre of the "ruler" that is out of keeping with calculations. This difference can be explained by the fact that these glasses are subjected to maximum heat flow from the source. Analogous discrepancies were also obtained when the "ruler" with glasses was subjected to simultaneous action of MF and 40-keV electrons. Curves of Fig. 3b demonstrate mass distributions of outgassed products deposited on glass surfaces. 1 and 4 – calculated estimates of contaminations, 2 and 3 – experimental data without and with radiation of glasses respectively.

When analyzing data of the first and third series of experiments, some assumptions on angular distribution of VPs leaving the VP source surface have been made.

In the case of "easy" and "moderate" molecules the disk-shape VP source was considered as isotropic in numerical calculations approximately simulating laboratory experiments. MF density at a distance a from such source on the axis of symmetry (point A_1, Fig. 4) is bound with the outgassing rate from the surface unit of the VP source df_i/dt as follows

$$\Phi_{1i}(t) = \frac{1}{2\pi} \frac{df_i}{dt} \int_0^{r_o} \frac{2\pi r dr}{a^2 + r^2} = \frac{1}{2} \frac{df_i}{dt} \ln \frac{a^2 + r_o^2}{a^2},$$

where r_o – radius of the disk, whereas the outgassing rate is found by solving equations describing the process and using the models presented in [5, 6]

$$\frac{df_i(t)}{dt} = k_i C_i(h, t) = 2k_i R_i \sum_{n=1}^{\infty} \frac{\exp[-(\lambda_{ni}^2 D_i + \sum_{j=0}^{J} \sigma_{i \to j} + \chi_i)t]}{1 + h(k_i/D_i + \lambda_{ni}^2 D_i/k_i)};$$

where D_i – effective diffusion coefficient of i–type VP in source material, $\mu m^2 \times s^{-1}$; k_i – effective desorption coefficient of i–type VP from surface of source material, $\mu m \times s^{-1}$; R_i – concentration of i–type VP in material at initial moment; h – thickness of sample, μm; $C_i(h, t)$ – concentration of i-type VP in the near-surface layer of source material; $\sigma_{i \to j}$, χ_i – weighting coefficients of thermal destruction of i-type component through j-channel, and chemical reaction rate with involvement of i-type VP respectively; λ_{ni} – eigenvalues of differential operator of the equation describing the outgassing process and being solution of the transcendental equation:

$$tg\lambda_{ni}h = k_i/(\lambda_{ni}D_i).$$

MF density at a distance a from the source plane and at a distance b from the axis of symmetry (point A_2, Fig. 4)

$$\Phi_{2i}(t) = \frac{1}{2\pi} \frac{df_i}{dt} \int_{\varphi} d\varphi \int_{\rho} \frac{\rho d\rho}{a^2 + \rho^2}$$

$$0 \le \varphi \le arctg(r_o/b); \; b\cos\varphi - (r_o^2 - b^2\sin^2\varphi)^{1/2} \le \rho$$
$$\le b\cos\varphi + (r_o^2 - b^2\sin^2\varphi)^{1/2}.$$

$$\Phi_{2i}(t) = \frac{1}{2} \frac{df_i}{dt} \ln \frac{r_o^2 + a^2 - b^2 + [r_o^4 + 2r_o^2(a^2 - b^2) + (a^2 + b^2)^2]^{1/2}}{2a^2}.$$

If $b = r_o$, $\Phi_{2i}(t) = \frac{1}{2} \frac{df_i}{dt} \ln \frac{a+(a^2+4r_o^2)^{1/2}}{2a} .,$

In the case of "heavy" molecules, direction of their escape from the disk-shape VP source is described by cosine distribution

$$df_i/dt(\theta) = (2\pi)^{-1} \cos\theta \cdot df_i/dt.$$

Mass of i-type VP in sample at time t:

$$M_{si}(t) = m_i S_0 \int_0^h C_i(x, t)dx,$$

where $C_i(x, t)$ – distribution of i-type VP concentration in source sample by time t; m_i – mass of i-type VP molecule; S_0 – surface of VP source sample.

In material sample, rate of i–type VP mass change $dM_{si}(t)/dt$ is related with its rate of concentration change $\partial C_i(x,t)/\partial t$ as follows:

$$\frac{dM_{si}(t)}{dt} = m_i S_0 \int_0^h \frac{\partial C_i(x,t)}{\partial t} dx = m_i S_0 \int_0^h \left(D_i \frac{\partial^2 C_i(x,t)}{\partial x^2} - \beta_i C_i(x,t) \right) dx,$$

or, taking into account the boundary conditions of differential equations describing the outgassing process of polymeric composites [5, 6]

$$\frac{dM_{si}(t)}{dt} = -m_i S_0 \left[k_i C_i(h,t) + \beta_i \int_0^h C_i(x,t) dx \right].$$

In turn, rate of i–type VP mass change $dM_{ci}(t)/dt$ on unit surface of the pattern material is described by the differential equation [6, 7]

$$\frac{dM_{ci}(t)}{dt} = \alpha_{cs} m_i S_0 k_i C_i(h,t) - k_{ci}^{rad} M_{ci}(t) - \chi_{ci}^{rad} M_{ci}(t),$$

where k_{ci}^{rad} – effective coefficient of re-emission of i-type VP from the condensation surface under radiation, s^{-1}; χ_{ci}^{rad} – chemical reaction rates with involvement of i-type component on the condensation surface under radiation, s^{-1}; α_{cs} – geometric factor depending on arrangement of VP source and with respect to unit of the condensation surface.

Total contribution of i-type VP to mass of outgassed products deposited on the condensation surface can be found from equation

$$M_{ci}^{sum}(t) = M_{ci}(t) + \Delta_{ci}(t),$$

where $\Delta_{ci}(t, \chi_i)$ – mass of i-type VP that has chemically reacted or chemisorbed on the condensation surface by time t

$$\Delta_{ci}(t, \chi_i) = \alpha_{cs} S_0 \int_0^1 \frac{df_i(\tau)}{d\tau} - M_{ci}(t) - k_{ci} \int_0^1 M_{ci}(\tau) d\tau.$$

Mass of outgassed products that have chemically reacted on surface and total mass of organic film that has formed on it by time t are determined respectively from equations

$$\Delta_{total}(t) = \sum_{i=1}^I \Delta_i(t, \chi_i); \quad M_{c\,total}(t) = \sum_{i=1}^I [M_{ci} + \Delta_i(t, \chi_i)].$$

3   Discussion

It should be noted that if radiation flux density exceeds $5 \times 10^{10}\,\mathrm{cm}^{-2}\,\mathrm{s}^{-1}$ action of electrons on glasses causes an inverse effect that is quantity of deposited mass reduces. Action of high-intensive low-energy radiations on quartz glass can cause local temperature jump of material that, in turn, will intensify the processes like VP surface diffusion and desorption. Electron flux density in space environment is more than twice below of this marginal value. But in radiation spectrum there are both particles having lesser energy and high-energy ones which action leads to formation of stable radiation defects.

Thus, experimental and numerical simulation data shown that action of low-intensity electrons (below $5 \times 10^{10}\,\mathrm{cm}^{-2}\,\mathrm{s}^{-1}$) causes increase of growth rate of organic film on quartz glass sample surfaces if subjected to outgassed products of polymeric composite.

Growth of outgassed products deposition rate can be partly tied with the following reasons. First, when irradiating quartz glass by 40-keV electrons, in the near-surface layer (thickness of about 10–12 µm) there occur accumulation of volume charge. Its electric field pulls the radiation-ionized molecules to sample surface.

Second, irradiation of quartz glass results in increase of number of defects on its surface where nuclei of contamination film form. This takes place because the threshold energy of chemical adsorption on defects is less than elsewhere. Then islands of chemical adsorption expand around the nuclei. This is attributed to the fact that adhesion of molecules to periphery of these islands occurs easier as a result of lowered threshold energy that facilitates chemical adsorption. Threshold of free energy needed to make transference from physically sorbed into chemisorbed state is significantly less near previously chemisorbed particles due to lateral attraction to them. This attraction can be tied with oscillatory indirect interaction between adsorbed substance particles through substrate electron subsystem.

4   Conclusions

Analysis of experimental data concerning study of irradiation effects on deposition of outgassed products of polymeric composite on quartz glass surface has shown that:

- Action of electron irradiation with intensity below $5 \times 10^{10}\,\mathrm{cm}^{-2} \times \mathrm{s}^{-1}$ on quartz glass samples results in growth of the deposition rate of outgassed products on their surfaces, i.e. in increase of the growth rate of the contamination film;
- To analyze numerically and interpret experimental data one should use mathematical models describing contamination of optical surfaces by outgassed products with allowance for time dependencies of electrical field of volume charge and chemical reaction rates that take place on quartz glass surfaces.

When preparing and conducting tests of optical materials of high-orbit spacecraft skin, authors recommend to take into account results of the work to predict changes of their spectral characteristics due to contamination caused by spacecraft outer atmosphere products.

References

1. Sergeev PM et al (2004) Electron-induced absorption in quartz glasses. Opt J 71(6):93–97
2. Gusev AP, Zabelin IA (2001) Isothermal relaxation of induced absorption of glasses after action of ionizing radiation. Opt j 68(6):79–84
3. Arbuzov VI, Suchkov FV (2001) Stability of radiation color of glasses. Opt j 68(6):85–96
4. Fong MC, Lee AL, Ma PT (1987) External contamination environment of space station customer servicing facility, Lockheed Missiles Space Company, Inc. Sunnyvale. In: CAAAIA 22nd thermophysics conference, 8–10 June 1987, Honolulu, AAIA-87-1623
5. Khassanchine RH, Kostiuk VI (2002) On simulation of outgassing process by spacecraft coatings in the course of thermal vacuum influence. Cosmonaut Rocket Prod 28:155–163
6. Khassanchine RH, Grigorevskiy AV, Galygin AN (2004) Simulation of outgassing processes in spacecraft coatings induced by thermal vacuum influence. AIAA J Spacecr Rocket 41(3): 384–388

Contamination of Outer Surfaces of International Space Station Studied by Non-Destructive Techniques

V.A. Borisov, S.F. Naumov, S.P. Sokolova, A.O. Kurilenok, V.E. Skurat, A.N. Zhigach, N.G. Beriozkina, I.O. Leipunsky, P.A. Pshechenkov, E.S. Zotova, I.O. Volkov, A.V. Naumkin, and V.V. Artemov

Abstract The aim of this work is to study non –volatile components of contamination deposits on outer surfaces of International Space Station (Russian segment) by a complex of non-destructive techniques – X-ray photoelectron spectroscopy (XPS), diffuse reflection infrared spectroscopy, scanning electron microscopy and local X-ray microanalysis (LXMA). These methods were used for investigation of 40 samples of materials and coatings after their exposure to residual atmosphere of Earth and external conditions of spacecraft. Elemental and chemical composition of surface and sub-surface layers is varied in very broad limits due to concurrence of many processes changing the sample composition. Contamination deposits contain nitrogenous components besides ubiquitous carbonaceous and siliceous components that are typical for spacecraft surface contamination.

Keywords ISS • Contamination deposits • SEM • LXMA • XPS • DRIFTS

1 Introduction

Contaminations of outer surfaces of spacecraft can greatly influence their thermo optical properties inducing the undesired changes of thermal regimes of spacecraft. These contaminations are caused by various sources. Among them, the important

V.A. Borisov (✉) • S.F. Naumov • S.P. Sokolova • A.O. Kurilenok
S.P. Korolev Rocket and Space Corporation Energia, Korolev, Moscow region, Russia
e-mail: vladimir.borisov@rsce.ru

V.E. Skurat • A.N. Zhigach • N.G. Beriozkina • I.O. Leipunsky • P.A. Pshechenkov • E.S. Zotova • I.O. Volkov • A.V. Naumkin
Institute for Energy Problems of Chemical Physics, Russian Academy of Sciences, 38, bldg.2, Leninsky prospect, Moscow 119334, Russia

V.V. Artemov
A.V. Shubnikov Institute of Crystallography, Russian Academy of Sciences, 59, Leninsky prospect, Moscow 119333, Russia
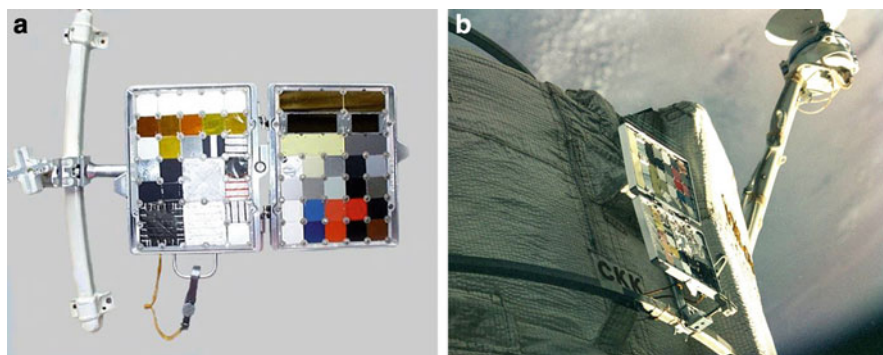
Fig. 1 Removable cassette – container (RCC) –(**a**) and an example of RCC placement on outer surface of ISS (**b**)

role is played by volatile effluents from drainage holes and by products of incomplete combustion of fuel for control and orientation engines (thrusters) (1,1-dimethylhydrazine and dinitrogen tetraoxide). The composition of products of incomplete combustion is complex and diverse. More than 20 species were discovered among these products. In most studies, the identification of products was performed by methods of gas, liquid and ion chromatography and, in many cases, in combination with mass spectrometry. These methods give the possibility to determine the volatile components of contamination deposits or the components of extracts from deposits by organic and inorganic solvents. The procedure of solvent extraction as such can be accompanied by changes of chemical composition because of poorly controlled processes of solvolysis (hydrolysis). Besides that, non-volatile and (or) insoluble species are not detected using these approaches.

2   Results and Discussion

The aim of this work is the study of non–volatile components of contamination deposits on outer surfaces of International Space Station (Russian segment – ISS-RS) by a complex of non-destructive techniques – X-ray photoelectron spectroscopy (XPS), reflection infrared spectroscopy, scanning electron microscopy, and local X-ray microanalysis (LXMA).

Removable cassette – container (RCC) is shown in Fig. 1a. An example of RCC placement on outer surface of ISS is shown in Fig. 1b.

A combination of various methods – scanning microscopy (SEM), local X-ray element microanalysis (LXMA), optical microscopy (OM), diffuse reflection IR spectroscopy (DRIFTS), X-ray photoelectron spectroscopy (XPS) – was used for investigation of 40 samples of materials and coatings after their exposition on the outer surface of International Space Station (Russian segment). The elemental and chemical composition of surface and sub-surface layers is varied in very broad

f EDS Quantitative Results

Element	Wt%	At%
CK	28.97	38.97
NK	9.74	11.23
OK	33.48	33.80
SiK	27.82	16.00

g EDS Quantitative Results

Element	Wt%	At%
CK	40.15	49.12
NK	19.26	20.20
OK	23.90	21.95
SiK	16.69	8.73

h EDS Quantitative Results

Element	Wt%	At%
CK	1.60	2.70
OK	48.09	60.96
SiK	50.31	36.34
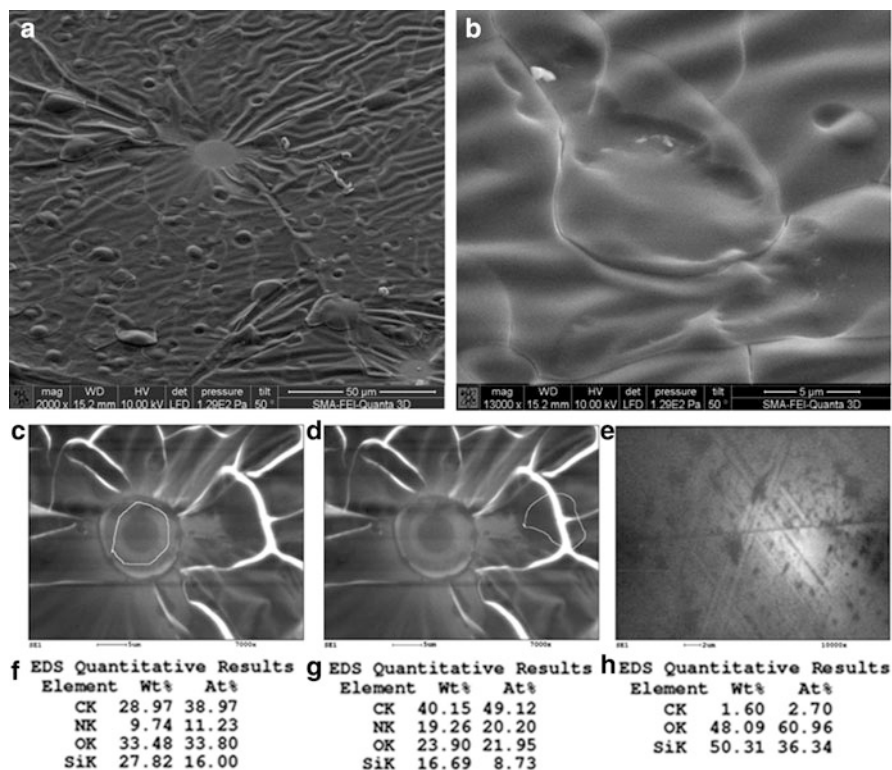
Fig. 2 SEM images of deposits (**a**, **b**, **c**, **d**) and their elemental composition (**f**, **g**) found on a sample of vitreous quartz K5 after flight. The SEM image of a control sample (**e**) and its elemental composition (**h**)

limits due to concurrence of many processes affecting the sample composition: surface destruction by vacuum UV (VUV) component of solar radiation and atomic oxygen from residual Earth atmosphere; deposition of contamination layers from intrinsic outer atmosphere of space station; deposition of contamination layers from products of incomplete combustion from orientation engines; chemical reactions of surfaces with these products.

Investigations of some samples exposed on ISS in 2006 and 2007 had shown the presence of relatively thick deposits, yellow in color and with a high content of nitrogen (Fig. 2). Such nitrogen-rich deposits were never observed in our earlier investigations of contamination on ISS and space station MIR [1, 2]. In order to determine the origin of these novel deposits, RCC with samples of various materials (enamels, Al, polymer foils) were placed in 2008 on ISS-RS in a peripheral zone of contact with jets of orientation engines, i.e. in places where the greatest changes of surface color were observed. Study of surface changes of samples from this RCC is the aim of this paper.

SE1   ├────┤100um   400x   SE1   ├────┤50um   600x

EDS Quantitative Results

Element	Wt%	At%
CK	11.80	18.00
NK	1.38	1.81
OK	46.50	53.23
MgK	0.93	0.70
AlK	34.39	23.34
SiK	0.86	0.56
SK	4.14	2.36

Before flight

EDS Quantitative Results

Element	Wt%	At%
CK	54.73	60.59
NK	21.16	20.09
OK	22.12	18.38
SiK	1.99	0.94

After flight

XPS Results

Element	at%
C 1S	70
O 1s	18,4
N 1s	8,3
F 1s	1,9
Al 2p	0,4
Si 2P	0,9
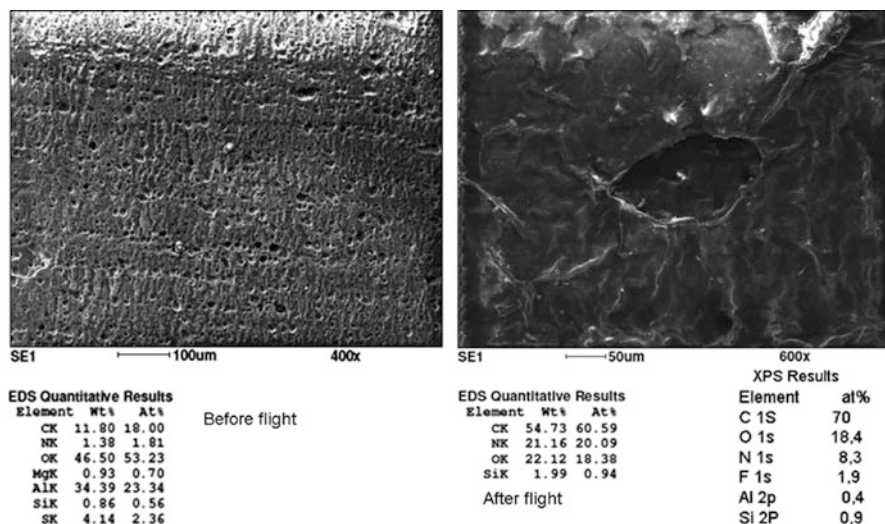
Fig. 3 SEM/EDS analysis of coating AOP-6 before and after flight

SE1   ├────┤50um   800x   SE1   ├────┤50um   600x

EDS Quantitative Results

Element	Wt%	At%
CK	17.05	25.74
NK	1.69	2.19
OK	38.82	44.00
MgK	1.50	1.12
AlK	34.52	23.20
SiK	1.35	0.87
SK	5.08	2.87

Before flight

EDS Quantitative Results

Element	Wt%	At%
CK	54.28	60.15
NK	20.97	19.93
OK	22.88	19.00
SiK	1.86	0.88

After flight

EDS Quantitative Results

Element	Wt%	At%
CK	17.05	25.74
NK	1.69	2.19
OK	38.82	44.00
MgK	1.50	1.12
AlK	34.52	23.20
SiK	1.35	0.87
SK	5.08	2.87

Fig. 4 SEM/EDS analysis of coating AOP-3 before and after flight

Thick films of deposits were observed on the surfaces of 63% of samples removed from the above mentioned RCC, with thicknesses up to several micrometers. The deposits contained carbon (59–79%), nitrogen (9–24%), and oxygen (11–23%) (and also hydrogen as determined by DRIFTS) and fully changed the structure of the surface layer. The deposit films were non-homogeneous in
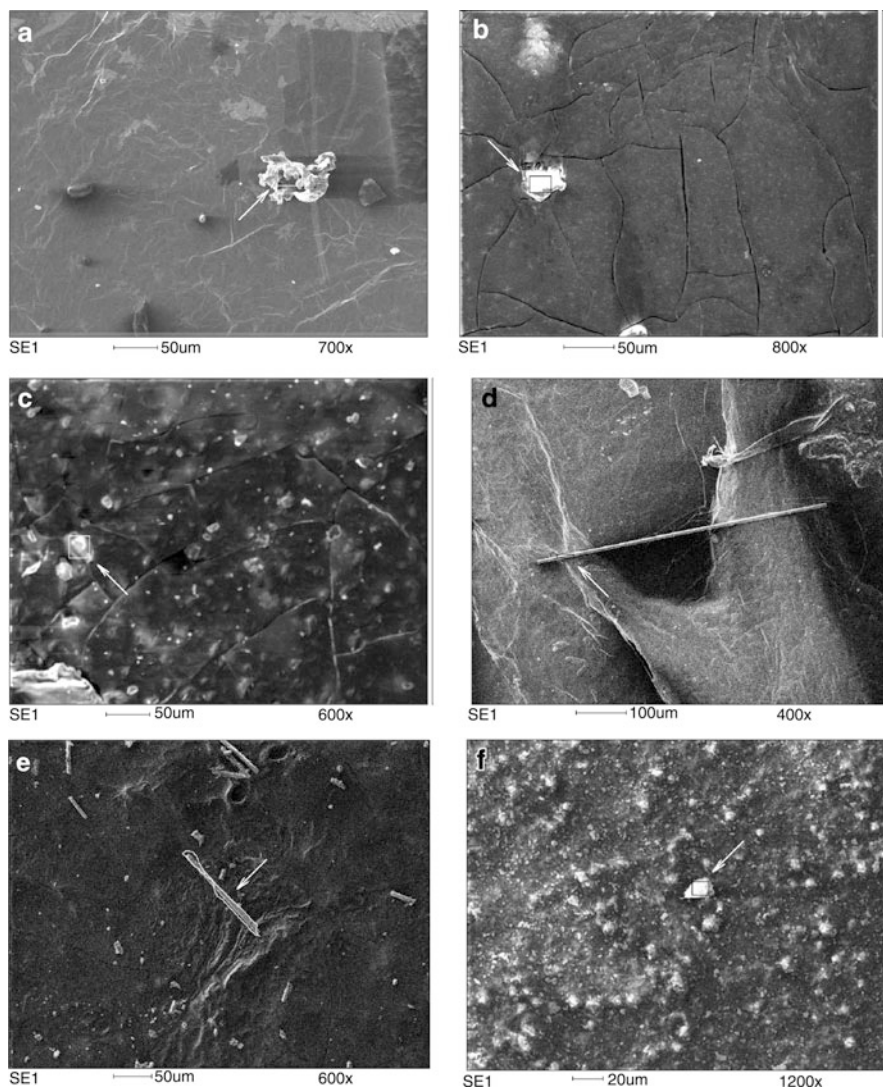
Fig. 5 SEM images of typical contamination deposits found on the samples after flight. (**a**, **b**, **c**) - Particles with high content of Al; (**d**) – Silica fiber and a fragment of the film; (**e**) -Fibers with high % of Si, Al, O; (**f**) – A particle with a high content of Mg, Fe, Zn, K, S, O

thickness. On many samples the formed films were covered with cracks and often the flaking of the upper layers was observed. These films usually contained in homogeneously distributed silicon. The average composition of these deposits as determined by LXMA contained $62.8 \pm 0.7\%$ of carbon, $18 \pm 0.7\%$ of nitrogen and $17.8 \pm 0.7\%$ of oxygen (See Figs. 3 and 4).
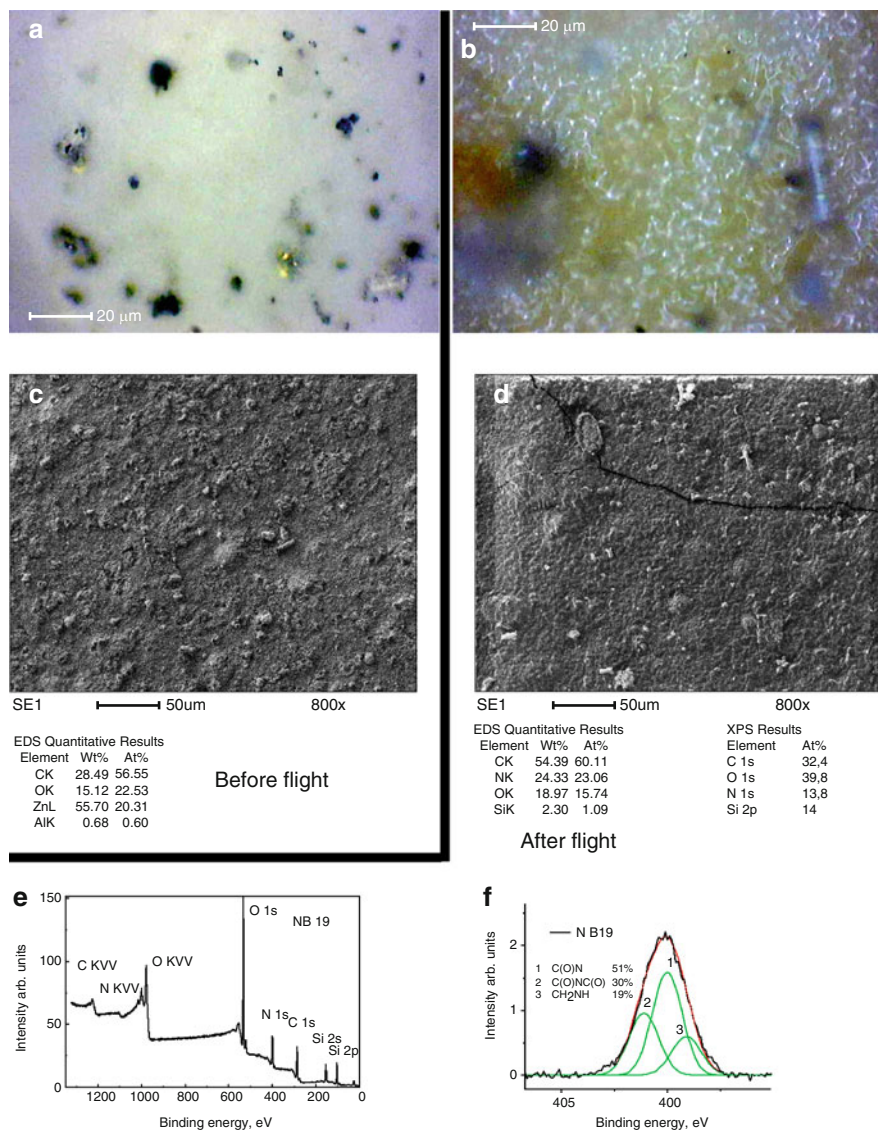
Fig. 6 Optical (**a**, **b**) and SEM (**c**, **d**) images and elemental composition of ECOM-1 coating surfaces before and after flight and XPS general survey spectrum (**e**) and a high resolution XPS analysis of the 1s nitrogen peak after flight

Single spots of deposits consisting of carbon, oxygen, and nitrogen were observed on 15 % of samples. The analysis conducted with LXMA technique didn't find nitrogen on the surfaces of 22% of samples.

Surfaces of many samples after flight contained various particles and inclusions that were absent on pristine samples and were distinctly different in their

composition from surrounding surface. Inclusions with high sodium content were found on surfaces of two samples.

Local spots and inclusions containing sodium, sulphur, potassium, and chlorine or most of these elements were found on three samples (Fig. 5). The deconvolution of the N1s signal in high resolution XPS for sample # B19E suggested presence of three bands at 399.1 eV (19%); 400.3 eV (51%) and 401.6 eV (30%) that are associated with CH_2NH, C(O)N C(O)NC(O), respectively. Some samples also contained a band at 406.8 eV (NO_3^-). Bands at 399.1 and 401.6 eV can be ascribed also to NH_x and $N(CH_3)_2$ respectively (Fig. 6).

The DRIFTS analysis allows detecting the presence of hydrogen-containing group OH, CH_x (x = 1, 2, 3) in contamination films. In particular, the increase of CH_x – groups content takes place in many cases, as also nitrogen-containing groups (NH_x, HN^+ and, possibly, NO_x) and oxygen-containing groups (in carboxy- and aldehydo – ketonic form). The chemical composition of deposits in a number of samples contained a very small content of CH_x - groups with x >1. A marked increase of OH – groups in most samples should be noted. They can be included both in organic substances (for example alcohols) and in inorganic matters (hydroxides). For a number of samples, like the surfaces of the enamel samples, the observed spectral changes were indicative of the destruction of polymeric binder component, showing a marked decrease of CH_x - groups.

3   Conclusions

The diversity of the ways and mechanisms the degradation of material surfaces of ISS is taking under the destructive action of space environment factors requires a complete set of investigation techniques based on various physical principles.

The structure and chemical composition of contaminating nitrogenous deposits found on many samples flown on ISS show that the deposits are the products of incomplete combustion of fuel in orientation engines of spacecraft in transition mode (regime). Among them, the main component – 1,1 dimethylhydrazinium salt of nitric acid – was identified.

Investigation of contamination deposits gives the possibility to establish the processes that take place in station sections that are in contact with hazardous environment and must become one of methods for inspection and prediction of residual resource of manned and unmanned space stations.

References

1. Skurat VE, Tantsyrev GD, Beriozkina NG, Volkov IO, Jigatch AN, Leipunsky IO, Pshechenkov PA, Samsonov PV, Toropov VP, Demidov SA, Naumov SF, Sokolova SP (2001) Surface contamination of some materials of the space station "MIR". High Perform Polym 13 (4):337–353
2. Naumov SF, Domoratsky AN, Sokolova SP, Kuriljonok AO, Kosnina EV, Alexashin VA, Skurat VE, Volkov IO, Berioskina NG, Leipunsky IO, Pshechenkov PA, (2003) Investigation of materials of insurance and fixation arrangements (tapes, ropes, cords, halyards and others) that are used by cosmonauts during their work in open space. In: Proceedings of the ninth international symposium on materials in a space environment, Noordwijk, 16–20 June 2003, pp 595–602. (ESA SP-540, Sept 2003)

Passive Measurement of Dust Particles on JEM/MPAC&SEED – Experiment Summary, Particle Fluxes

Miyuki Waki and Yugo Kimoto

Abstract JEM/MPAC experiments are installed in the outboard platform of "KIBO". JEM/MPAC is an experiment to capture space debris or micro-meteoroids, and clarify the origin and amount of distribution. Silica-aerogels and Au-plates of MPAC samples were exposed to space for about 8.5 months. This paper presents the distribution, impact velocity, kinetic energy, and flux in impact holes confirmed with these samples.

Keywords Debris • Impact hole • JEM/MPAC&SEED • Silica aerogel

1 Introduction

JEM/MPAC&SEED experiments are composed of a Micro-Particles Capturer (MPAC) and Space Environment Exposure Device (SEED), which are installed in the outboard platform of "KIBO" in the ISS. MPAC is an experiment to capture space debris or micro-meteoroids, and to clarify their origin and distribution. Silica-aerogels (hereafter, aerogels) and Au-plates of MPAC samples had been exposed to space for about 8.5 months (259 days). Aerogel was prepared to capture the particles and estimate the impact parameters, while Au-plate was used to measure the number of impact holes and observe the shape. This paper reports on the impact holes and the number of observed impacts in these samples.

Moreover, we compared the results of the JEM/MPAC and SM/MPAC experiments [1–8]. SM/MPAC was the first debris capture experiment installed on the Russia Service Module (SM). JEM/MPAC was installed at the front of the

M. Waki (✉)
Advanced Engineering Services Co., Ltd., Tsukuba 305-0032, Japan
e-mail: m_waki@aes.co.jp

Y. Kimoto
Japan Aerospace Exploration Agency, Tsukuba 305-8505, Japan
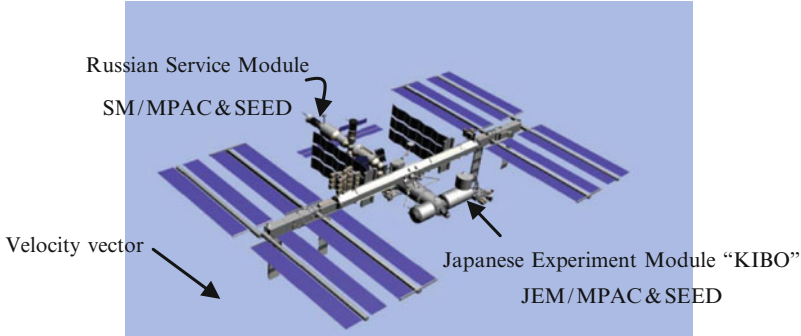
Fig. 1 Position of each MPAC experiment installed in the ISS [10]
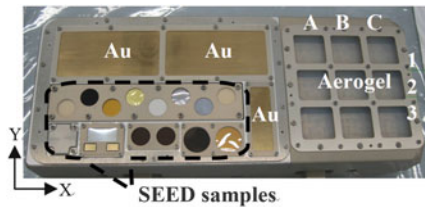
Fig. 2 JEM/MPAC&SEED structure. Nine Aerogels (exposure area:37 × 37 mm) and three Au-plates (exposure area for two 115 × 56 mm, and one 72 × 22 mm) were installed on the structure. The *upper part* of the figure is the SEDA-AP side, and the *lower part* is the space side

ISS, and the exposure side was only RAM (front face). SM/MPAC was installed behind the ISS, and the exposure side was both sides of the RAM and WAKE (rear face). In addition, the service module (SM) is composed of three units with different exposure periods.

The assumptions of the impact velocity of a micro particle onto the aerogel and the kinetic energy of the particle to the Au-plate were made based on the hypervelocity impact experiment on the ground [9] (Figs. 1 and 2).

2 Observation Method

All the samples were observed by the CCD scope while searching for impact features with an overlapped view. The impact features were left in the photograph, and classified according to the following criteria:

1. The feature had a crater-like rim and/or central peak.
2. The feature had radial cracks and/or ejecta.
3. The feature had a shape similar to those induced by hypervelocity impact experiments.
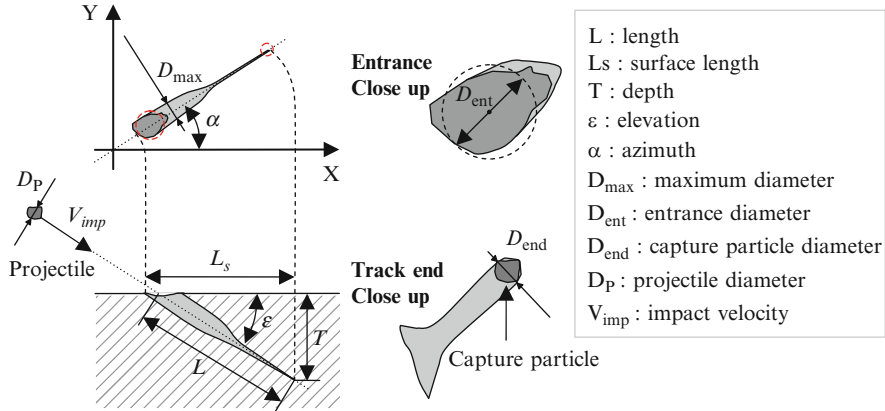
Fig. 3 Impact hole parameters

Class I satisfied all (1)–(3) criteria, and Class II satisfied one or two criteria. Classes I and II are defined as "Impact holes" made by a hypervelocity impact of micro particles such as the space debris and micro-meteoroids. Class III was assumed to be "Track". Though track is not a hypervelocity impact-induced feature, signs of some impact are visible.

The impact holes discovered on the aerogel were recorded with details of coordinates, depth, length, azimuth, elevation, entrance diameter, maximum diameter, and particle diameter. In the impact holes on the Au-plate, coordinates, depth, and diameter were respectively recorded (Fig. 3).

3 Observation with a CCD Scope

3.1 Observation Results

Hardly any degradation was observed on the surface of aerogels, and there was no discoloration extending to the entire exposure side with the SM/MPAC sample [1–3]. However, considerable solid contamination was confirmed on the surface of the aerogels, which came in various shapes, e.g. film, fibers, etc.

Forty-one impact holes and eighty-three tracks were found on the aerogels. The density of the impact holes was about $3.3E + 03$ [Number/m^2]. This means that about $4.7E + 03$ [Number/m^2/year] particles collided with the ISS in 1 year. The position distribution of impact holes and tracks in each aerogel were uniform.

In Au-plates, 15 impact holes were found. The impact holes distribution density in the Au-plate was about $1.0E + 03$ [Number/m^2]. When the number of collisions to the ISS in 1 year was calculated, it amounted to about $1.5E + 03$ [Number/m^2/year] (Fig. 4).
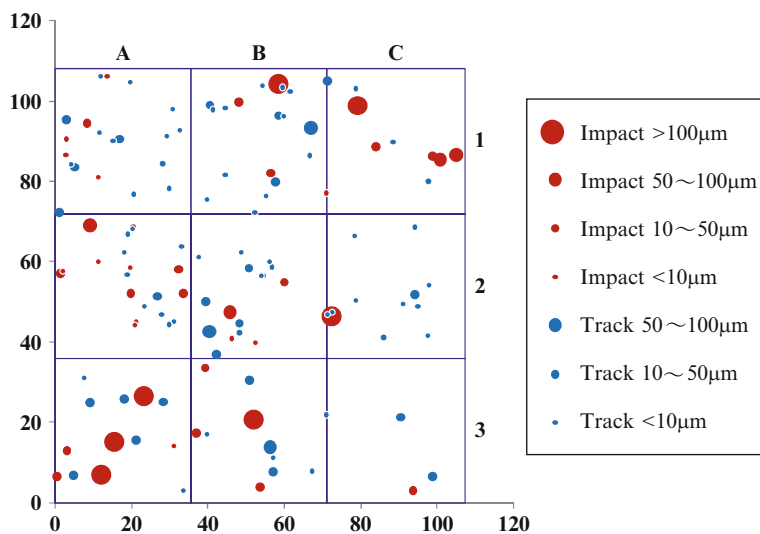
Fig. 4 Distribution of impact holes and tracks on aerogels. The size of each circle corresponds to the entrance diameter. *A, B, C* and *1, 2, 3* in the figure show the ID of aerogels in Fig. 2

(i) Super-depth synthesis chart   (ii) Impact hole entrance   (iii) Capture particle
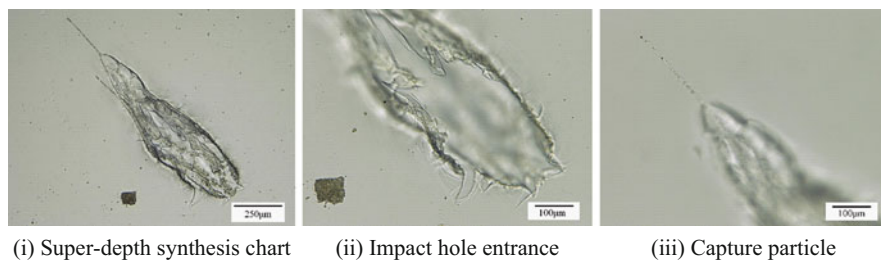
Fig. 5 Example of an impact hole on aerogel. This is the largest impact hole in the JEM sample. Entrance diameter: 293.94 μm, length: 1320.26 μm, depth: 416 μm, azimuth: −43.97°, elevation: 18.37°

3.2   CCD Images

The shapes of the impact holes on aerogels are elongated and slender and the point is extremely thin. There were impact holes including one or multiple small termination particles (several microns in size) at the aerogel, while 15 impact holes were confirmed on Au-plates. The latter featured a rim around all holes, and resembled craters having a distinctive rim on the outside of the crater. No captured particles could be confirmed (Figs. 5 and 6).

Super-depth synthesis chart   Cross-sectional shape measurement result
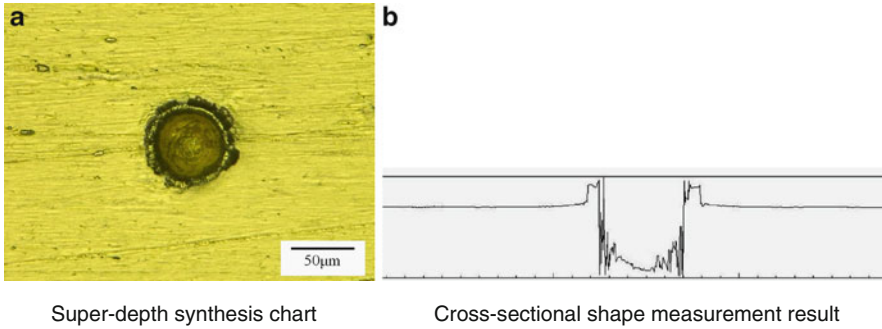
Fig. 6 Example of impact hole on Au-plate. Diameter: 48.63 μm, depth: 22.63 μm
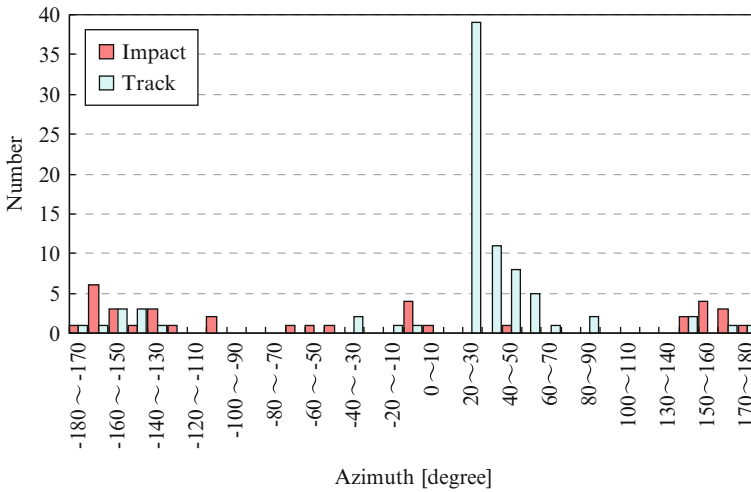
Fig. 7 Azimuth distribution

4 Distribution of Azimuth and Elevation in Aerogel

Figure 7 shows the azimuth distribution of impact holes and tracks. The azimuth of impact holes was evenly distributed, and the bias was small. Conversely, the azimuth of tracks was centered on the range 20–60°. The distribution of the elevation of impact holes and tracks is shown in Fig. 8, with both distributions concentrated within the range 20–40°. Moreover, there were some impact holes with an elevation near 90°.

The circle in Fig. 9 is a concentrated area in the track (α: 20–40, ε: 20–40). Many tracks were within the range of this circle, and with similar shapes, which suggests they may have been formed at the same time. Their origin might be the JEM Inter-Satellite Communication System or the Orbiter. Orbiter thrusters may fire during
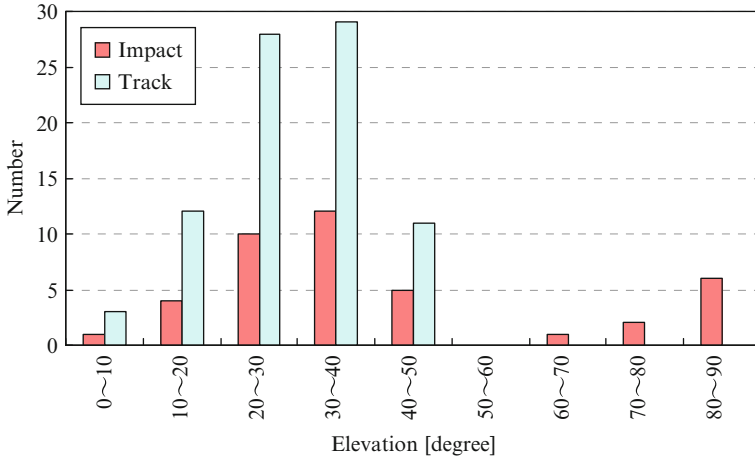
Fig. 8 Elevation distribution
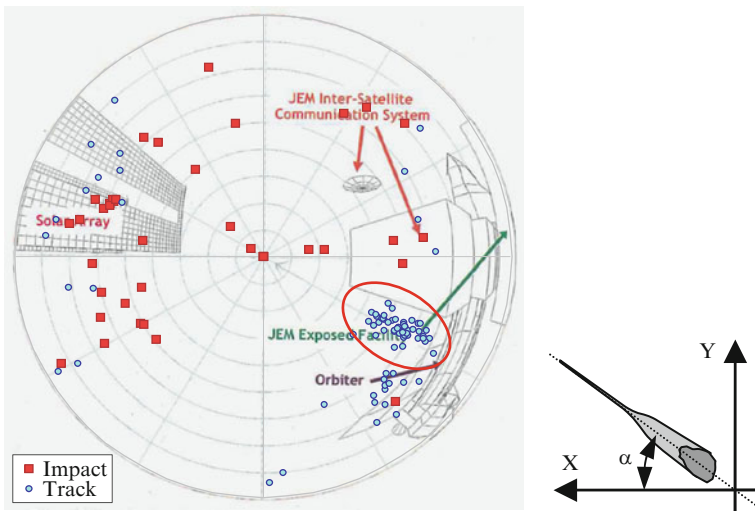
Fig. 9 Hemispherical view from JEM/MPAC&SEED (RAM direction). The Solar Array, the JEM Inter-Satellite Communication System (ICS), Orbiter, and part of the JEM Exposed Facility (EF) are seen. (Steagall et al. [7])
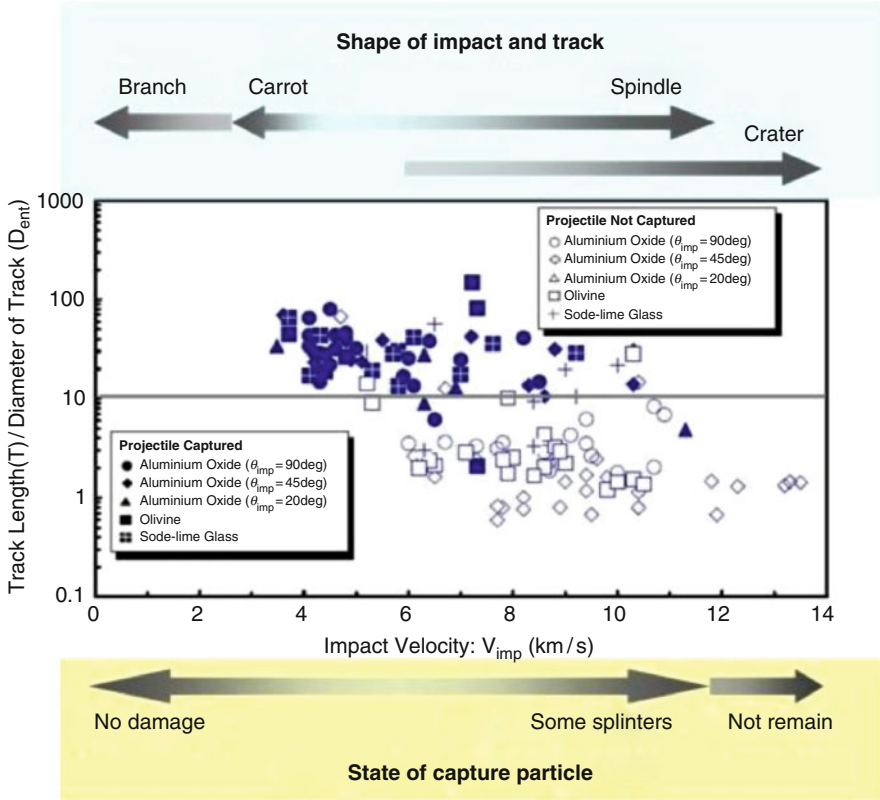
Fig. 10 Relation of the aspect ratio of the impact hole (L/D$_{ent}$) with impact velocity (V$_{imp}$) (Kitazawa et al. [1, 4])

docking/undocking operations, which may be one of the causes of these tracks, according to the result of a detailed future analysis of particles.

5 Establishment of the Impact Velocity of Projectiles on the Aerogel

5.1 The Ground Hypervelocity Impact Experiment

The impact velocity of the projectile (V$_{imp}$) was established based on the results of the ground hypervelocity impact experiment by Kitazawa et al. [1].

According to the correlation diagram of L/D$_{ent}$ (Length/Entrance Diameter) and V$_{imp}$, the impact hole becomes either of the carrot type, the spindle type, or a branch type at L/D$_{ent}$ >10 (Fig. 10). The branch type has a crack like a branch in the
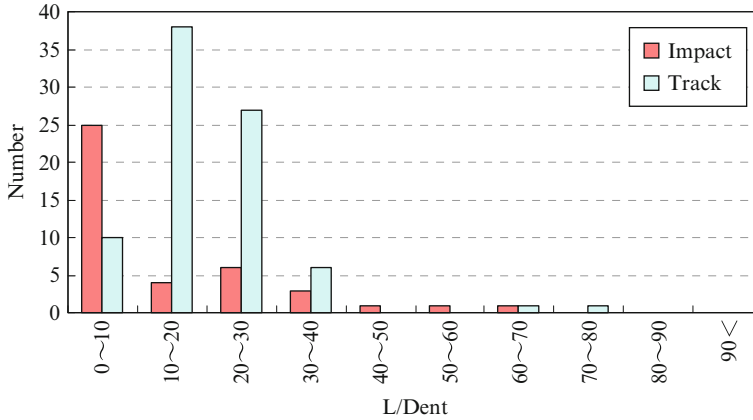
Fig. 11 Distribution of L/D$_{ent}$ for impact holes on JEM aerogels
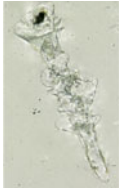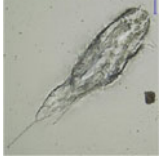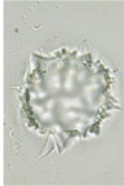
sidewall and the bottom of the impact hole, with an impact velocity of less than 3–4 km/s. The shape of the branch type resembles the hole made when the aerogel is pierced with the needle. There are many presumption impact velocities of the carrot type within the range 3, 4–5 km/s. In the spindle type, the impact velocity is presumed to be 5–12 km/s. L/D$_{ent}$ < 10 is the crater type, with impact velocity of 6 km/s or more.

The state of the captured particle differs depending on the impact velocity (V$_{imp}$). When V$_{imp}$ is less than 6 km/s, the damage to the particle is slight, and the particle remains unchanged compared with the shape of the projectile. When V$_{imp}$ exceeds 6 km/s, the captured particle breaks up into several smaller pieces but remains visible. When V$_{imp}$ exceeds 12 km/s, the captured particle is destroyed and doesn't remain in the impact hole.

5.2   JEM Sample

According to Fig. 11, many of the impact holes on JEM aerogels had L/D$_{ent}$ < 10, and of the crater type, with a presumed impact velocity (V$_{imp}$) of 6 km/s or more. The impact holes for which no capture particles were confirmed were potentially due to impact velocities exceeding 12 km/s. Many tracks had L/D$_{ent}$ = 10–30 and of the carrot or branch type. Based on the shape, the velocity of such tracks can be estimated at 3–5 km/s. Table 1 presents a summary of observed shapes and SEM examples of JEM aerogel impact features and their relationship to the V$_{imp}$.

Table 1 Presumed impact velocity and observation example on JEM aerogels

Shape	Branch	Carrot	Spindle	Crater
V imp	<3.4 km/s	3.4 –5 km/s	5 –12 km/s	6 km/s<
JEM observation example				
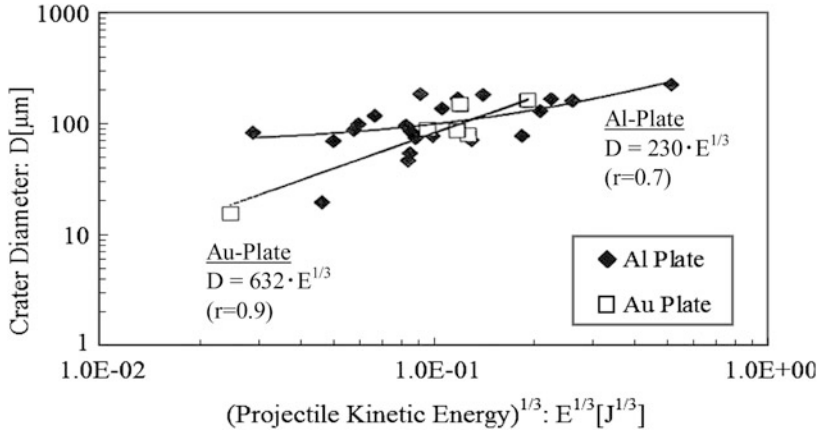
Fig. 12 Relationship between diameter (*D*) and projectile kinetic energy$^{1/3}$ (*E$^{1/3}$*) (Kitazawa et al. [1, 9])
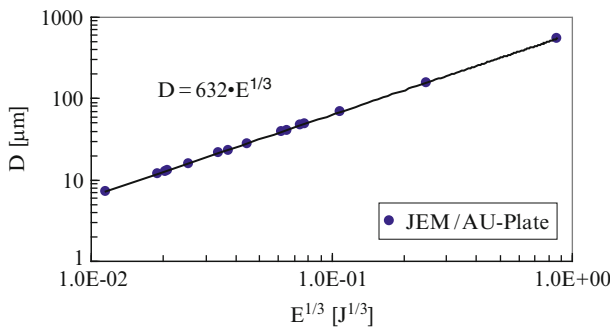
Fig. 13 Relationship between the kinetic energy$^{1/3}$ (*E$^{1/3}$*) and diameter (*D*) in JEM Au-plate

6 Establishment of Kinetic Energy in Au-Plate

The relationship between diameter (D) and projectile kinetic energy$^{1/3}$ (E$^{1/3}$) in a metallic plate according to the results of the ground hypervelocity impact experiment by Kitazawa et al. [1, 2] is shown in Fig. 12. The kinetic energy$^{1/3}$ (E$^{1/3}$) of the projectile transferred to the Au-plate in the JEM sample can be estimated using the expression D = 632·E$^{1/3}$.

The relationship between the kinetic energy$^{1/3}$ (E$^{1/3}$) and diameter (D) in JEM Au-plate is shown in Fig. 13. If the size of the projectile is understood, the impact velocity might be calculable, though no particle was confirmed in impact holes.
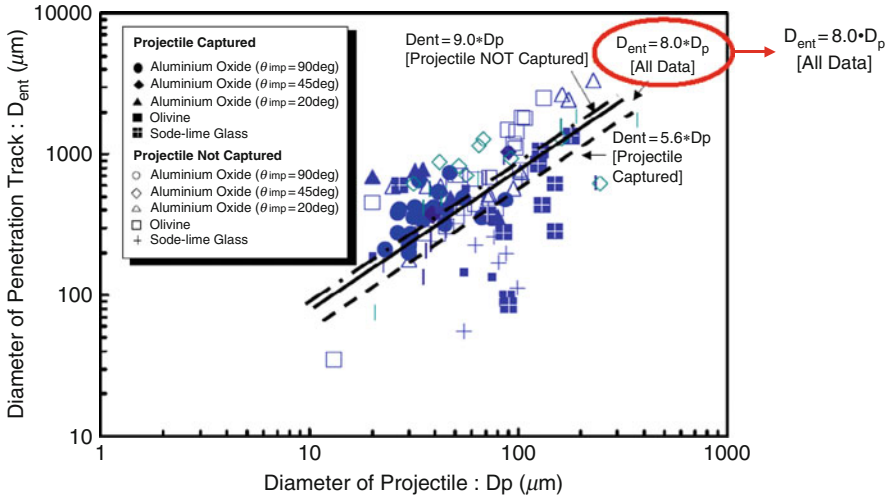
Fig. 14 Relationship between the diameter of the projectile (D_P) and the entrance diameter of the impact hole (D_{ent}) (Kitazawa et al. [1, 4])

Table 2 Impact hole flux

	JEM	SM1 (RAM)	SM2 (RAM)	SM3 (RAM)
Exposure period (days)	259	315	865	1,403
D_P (um)	Flax [Number/m^2/year]			
<5	3.50E + 03	–	–	–
5	4.90E + 02	5.10E + 03	–	–
10	3.60E + 02	1.60E + 03	–	–
20	6.00E + 02	6.30E + 02	3.90E + 02	2.10E + 02

7 Flux

7.1 Impact Hole Flux of Aerogel

Figure 14 shows the relationship between the diameter of the projectile (D_P) and the entrance diameter of the impact hole (D_{ent}) in the hypervelocity impact experiment [1]. D_P was calculated from the expression $D_{ent} = 8.0 \cdot D_P$ in Fig. 14, and individual impact hole fluxes for $D_P < 5$, and for 5, 10, and 20 μm were obtained.

Table 2 and Fig. 15 show the numerical result of flux determination [1]. The observation of impact holes of $D_P < 5$ μm is off the subject in the SM sample. Moreover, due to severe surface deterioration of SM2 and SM3, the observation of small impact holes is difficult, meaning only impact holes with an entrance diameter (D_{ent}) of 100 μm or more were recorded in SM2 and SM3. The impact hole flux
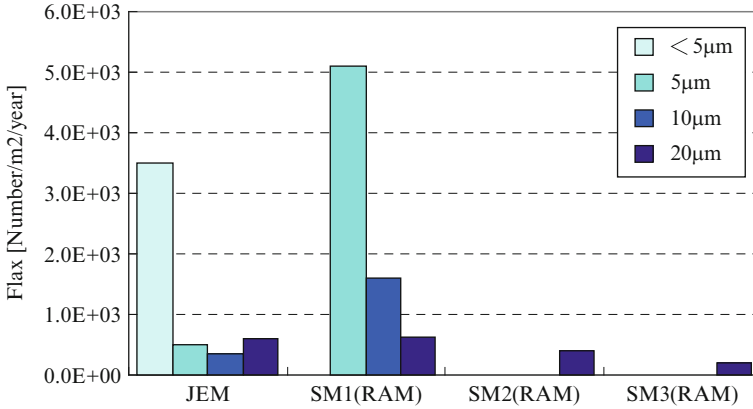
Fig. 15 Comparison of impact hole flux
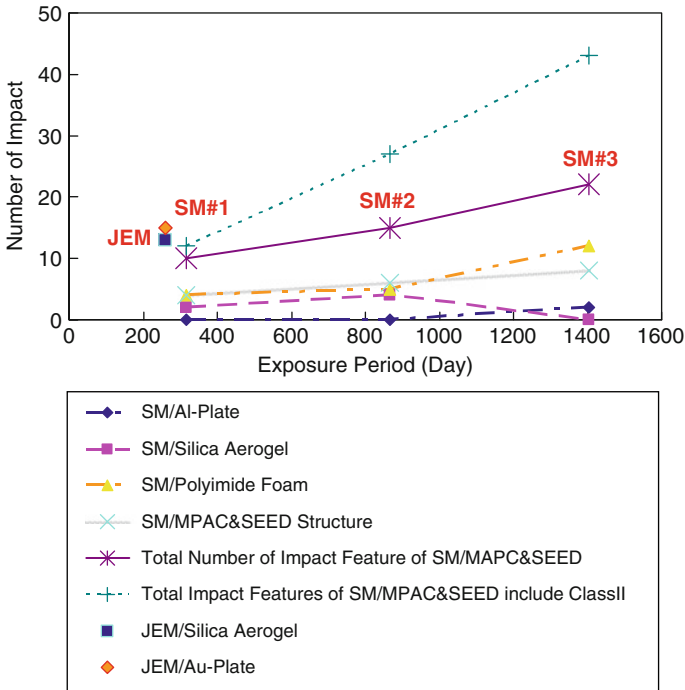
Fig. 16 Number of impact holes (Class I) (Kitazawa et al. [1])

data of SM2 and SM3 was only for $D_P = 20$ µm, because it will not record projectile diameters (D_P) of less than about 11 µm when the entrance diameter is converted into a projectile diameter.

When the impact hole flux of JEM is compared with SM1 (near the same exposure period), the impact hole fluxes of $D_P = 20$ µm are close. However, the JEM flux is smaller than that of SM1 for 5 and 10 µm, with the flux of $D_P = 5$ µm in particular very small. The major flux for the JEM sample is $D_P < 5$ µm.

7.2   Comparison of the Overall Numbers of Impact Holes

The total for class I impact holes in the JEM aerogel was 13, while all 15 impact holes in the JEM Au-plate were class I. Figure 16 shows the locations of the total Class I impact holes for SM and JEM samples. Although JEM/MPAC was smaller than SM/MPAC and also had a shorter exposure period, the number of impacts on JEM/MPAC exceeded that on SM/MPAC#1.

8   Result and Future Prospects

A number of micro-particles were captured in open space experiments and an initial analysis started of the impact morphology and particle traces. Hereafter, a detailed analysis of the particles captured in the JEM aerogel will be performed. Micro particles originating from a micro-meteoroid were found in the SM aerogel [3, 11]. There is also the potential for micro-meteoroids to be captured in the JEM aerogel. The understanding of the main elemental composition of the particles may, likely, lead to discovery of micro-meteoroids. In addition, we believe the origin of micro-meteoroids can be researched, if a detailed and advanced analysis is performed. We want to examine this in future.

References

1. Kitazawa Y, Fujiwara A, Kadono T, Imagawa K, Okada Y, Uematsu K (1999) J GEOPHYS RES 104(E9):22035–22052
2. Kitazawa Y, Fujiwara A, Kadono T, Noguchi T, Yamanaka R, Kimoto Y, Suzuki M (2009) Overview of the MPAC experiment -development of dust collectors, hypervelocity impact experiment, and post flight analysis. In: Proceedings of the international symposium on SM/MPAC&SEED experiment, Tsukuba, 10–11 Mar 2008, JAXA-SP-08-015E, pp 49–58
3. Noguchi T, Nakamura T, Kitazawa Y, Yamanaka R, Kimoto Y, Suzuki M (2009) Initial investigation of silica aerogel equipped on SM/MPAC&SEED recovered from the ISS in 2002, 2004, and 2005. In: Proceedings of the international symposium on SM/MPAC&SEED experiment, Tsukuba, 10–11 Mar 2008, JAXA-SP-08-015E, pp 59–65

4. Kitazawa Y, Noguchi T, Neish MJ, Inoue T, Ishizawa J, Fujiwara A, Imagawa K, Yamaura Y, Nakazato S, Murakami A (2004) First year mission results of passive measurement experiment of dust particles on ISS (MPAC), PDF, 24th ISTS (2004) in Miyazaki, 30 May–6 June 2004

5. Ichikawa S, Kimoto Y, Miyazaki E, Kubo K, Yano K, Matsumoto K, Ishizawa J, Shimamura H, Yamanaka R, Suzuki M (2008) Status of JEM/MPAC&SEED experiment onboard SEDA-AP on Kibo exposed facility. In: Proceedings of the international symposium on "SM/MPAC&SEED Experiment", Tsukuba, 10–11 Mar 2008

6. Kimoto Y, Ichikawa S, Miyazaki E, Matsumoto K, Ishizawa J, Shimamura H, Yamanaka R, Suzuki M (2009) Space environmental effect to materials on different position and operational period of ISS. In: Kleiman J (ed) Proceedings of the 9th international conference "Protection of Materials and Structures from Space Environment", Toronto, 20–23 May 2008. AIP conference proceedings 1087. Melville, pp 207–211

7. Steagall C, Smith K, Huang A, Soares C, Mikatarian R (2009) Induced contamination predictions for JAXA's micro-particles capturer and space environment exposure devices. In: Proceedings of the international symposium on SM/MPAC&SEED experiment, Tsukuba, 10–11 Mar 2008, JAXA-SP-08-015E, pp 19–25

8. Yamanaka R, Noguchi T, Kimoto Y (2011) Analysis results of SM/MPAC experiment samples. J Spacecraft Rockets 48(5):867–873

9. Kitazawa Y, Kawachi K, Fukasawa K, Yamaura Y, Miyadera T, Nakamura R, Imagawa K, Kamakura C, Nakayama Y, Tachi Y (2000) MPAC: passive measurement experiment of dust particles on ISS. In: Proceedings of the ISTS 2000, Morioka, pp 2077–2082

10. Japan Aerospace Exploration Agency Home Page. http://iss.jaxa.jp/

11. Noguchi T, Nakamura T, Ushikubo T, Kita NT, Valley JW, Yamanaka R, Kimoto Y, Kitazawa Y (2011) A chondrule captured by space exposed aerogel on the international space station. Earth Planet Sci Lett 309(3–4):198–206

Degradation of Optical Elements of Spacecraft Under the Impact of High-Velocity Particles

N. Semkin, L. Novikov, and M. Kalaev

Abstract The results of a study of crater's size distribution that are formed in optical glass as a result of bombardment by high-velocity particles of submicron and micron dimensions are described. An electrodynamic accelerator with a built-in system for recording particles' parameters was used as the particle's source. A function that establishes the relationship between particles' dimensions and the crater size for a particular material is determined.

1 Introduction

In long duration flights the open elements of a spacecraft gradually change their characteristics. Knowing the average particle flux impinging on the surface of the spacecraft, it is possible to simulate the processes of degradation of elements of the spacecraft in the laboratory. The shape and size of the defects depend on the size, velocity and physical properties of particles and the target. Produced defect sizes also have some distribution. Information about the form of these distributions and correlation between them can be used to predict damage of spacecraft elements.

According to available data, the most common surface damage to external parts comes in form of craters. The crater depth and diameter can be calculated using well-known empirical relations. Nevertheless, when a micrometeoroid flow affects optical elements, the actual area of the surface damage may be substantially larger than the estimated value, since an impact initiates cracking of the near-crater zone.

N. Semkin (✉) • M. Kalaev
Samara State Aerospace University, Samara, Russia
e-mail: sgau5@yandex.ru

L. Novikov
SINP, Moscow State University, Moscow, Russia

The resultant damage area, S_d, therefore, can be defined as

$$S_d = \pi(kd_c)^2/4; \tag{1}$$

where d_c is the crater diameter; and k is the coefficient describing the damage to the near-crater zone that is assumed to be 2–3.

The k value depends on a variety of factors; therefore, it is necessary to experimentally determine k for a particular glass type. Diameter d_c of the crater produced by a particle with the known mass and velocity can be estimated using the following equation [1]

$$d_c = 5 \cdot 10^{-4} d_p^{1,076} \, \rho_m^{-0.5} \, \rho_p^{0.743} V^{0.727} \cos^{0.601} \Theta \tag{2}$$

where ρ_m is the density of the barrier material, d_p is the particle diameter, ρ_p is the density of the particle material, V is the impact velocity, and θ is the angle of impact.

2 Experimental

The theoretical results are compared to the experimental data obtained using the linear accelerator simulation of micrometeoroid impacts [2]. The system consists of an injector, a linear electrostatic accelerator, a linear electrodynamic accelerator, three measuring lines and the vacuum chamber (Fig. 1).

Velocity separators are installed in the output path of the accelerator that can cut the flow of particles with unwanted parameters. A schematic diagram of the experiment is shown in Fig. 2.

In the accelerator, particles are accelerated one by one and their parameters can be recorded using the Faraday rings 1,2 (marked as FR1,2 in Fig. 2). If the particle velocity does not meet the specified parameters, it is rejected while passing through the separator, and is trapped. The remaining particles hit the surface of the glass samples. This fact is recorded by means of Faraday rings 3 and 4, which are located close to the glass samples.

3 Results and Discussion

The aluminum particle velocity distribution is shown in Fig. 3.

After accumulation on the glass sample surface of the required number of craters, the sample stage is rotated so that a new glass sample is introduced into the interaction region, and the previous sample is moved to a region where optical characteristics are measured. There is a red, 20 mW power semiconductor laser in

Fig. 1 The linear accelerator for simulation of micrometeoroid impacts
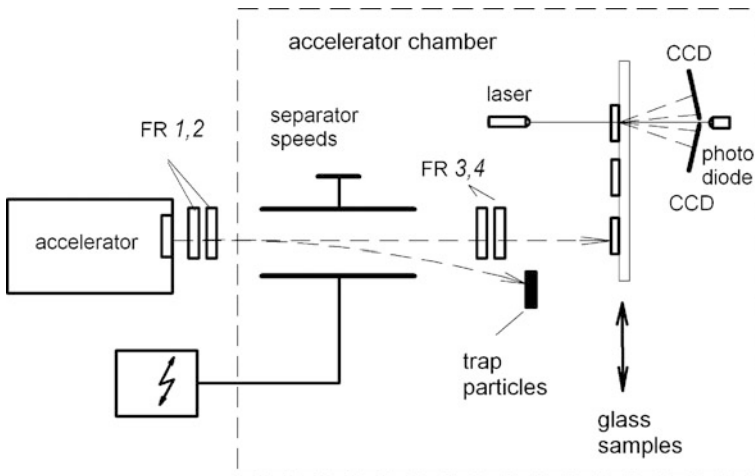
Fig. 2 Schematic diagram of the experiment
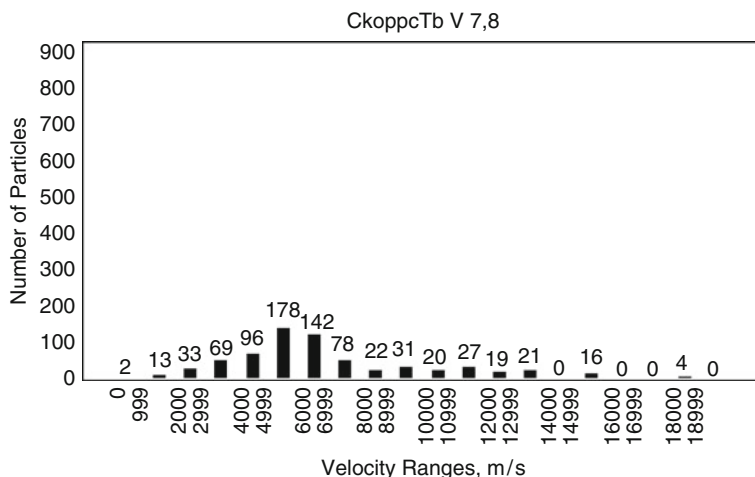
Fig. 3 Particle distribution over the velocity ranges
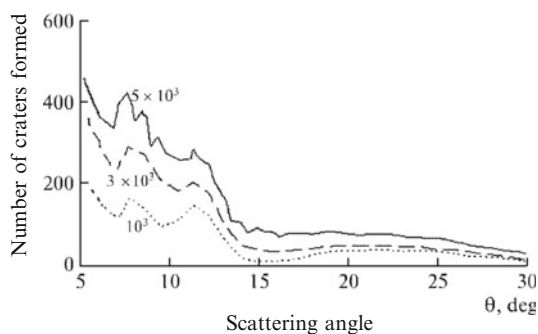
Fig. 4 Scattering indicatrices for different numbers of craters/particles

front of the glass in the measurement zone and the focused beam is scattered by the microdefects formed upon the impact of the particles and recorded with the help of the CCD detectors.

After processing the information, the dispersion indicatrix is restored for determination of the distribution of formed crater sizes on the surface of the glass. To exclude the influence of the initial light beam on the CCD, which impedes the signal discrimination at small scattering angles; measurements are performed beyond the limits of the focal spot. Measurements of $I(\Theta)$ are performed for angles $\Theta > \Theta_{min}$ and cover a $\gamma \approx 4°$ region.

The test samples were made of K-8 optical glass coated with a 0.2 μm thick platinum film. The samples were exposed to a flow of 5,000 aluminum particles. Figure 4 shows the scattering indicatrices for different numbers of particles. The

Transmittance variation T, %
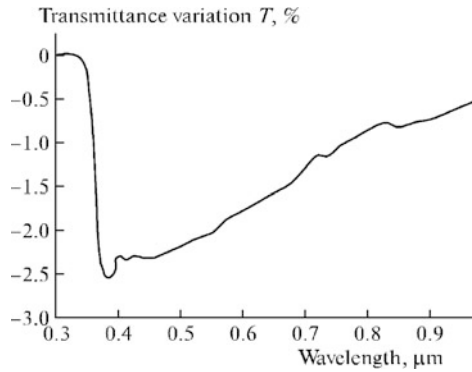
Fig. 5 Spectral transmittance of the K-8 optical glass sample

plots show that as the number of craters on the glass surface increases, a virtually linear increase in the amplitudes of the peaks of these functions is observed, thus indicating that the average crater size during the experiment remained constant.

To study the parameters of craters, it is desirable to use the nephelometric method (measurement of the scattered light intensity during passage through a dispersed system) for determining the concentration and size distribution of deposited particles/craters. The particle size distribution for the accumulated experimental data is determined from the solution of an integral equation of the first kind. If the elementary volume of a dispersed medium is illuminated with a parallel light beam, in this case, the problem of determining the particle size distribution function f(r) and the numerical particle concentration N is reduced to the inversion of the integral equation of the first kind:

$$I(\theta, \lambda) = N \int_{a_{min}}^{a_{max}} S(\theta, \lambda, a) f(a) da \qquad (3)$$

where I(Θ,λ) is the scattering coefficient at a fixed angle Θ at wavelength λ of incident radiation; N is the total concentration; f(a) is the particle size distribution function; a_{min} and a_{max} are the limiting radii of the particles in the suspension; and S (Θ,λ,a) is the scattering function of a particle with a radius "a" at wavelength λ.

The variation in the spectral transmittance of the glass, measured using the UV-1800 spectrophotometer, is shown in Fig. 5.

From Fig. 5, it is apparent that the maximum change in transmittance that is equal to 2.4% happens in the UV spectral region at a wavelength of 0.38 µm. The attenuation efficiency decreases substantially with an increase in the wavelength. At wavelengths of <0.35 µm, the intrinsic glass transmittance approaches zero; therefore, it is impossible to estimate the influence of surface defects in this region. A typical image of a crater in the glass sample with the accompanying debris
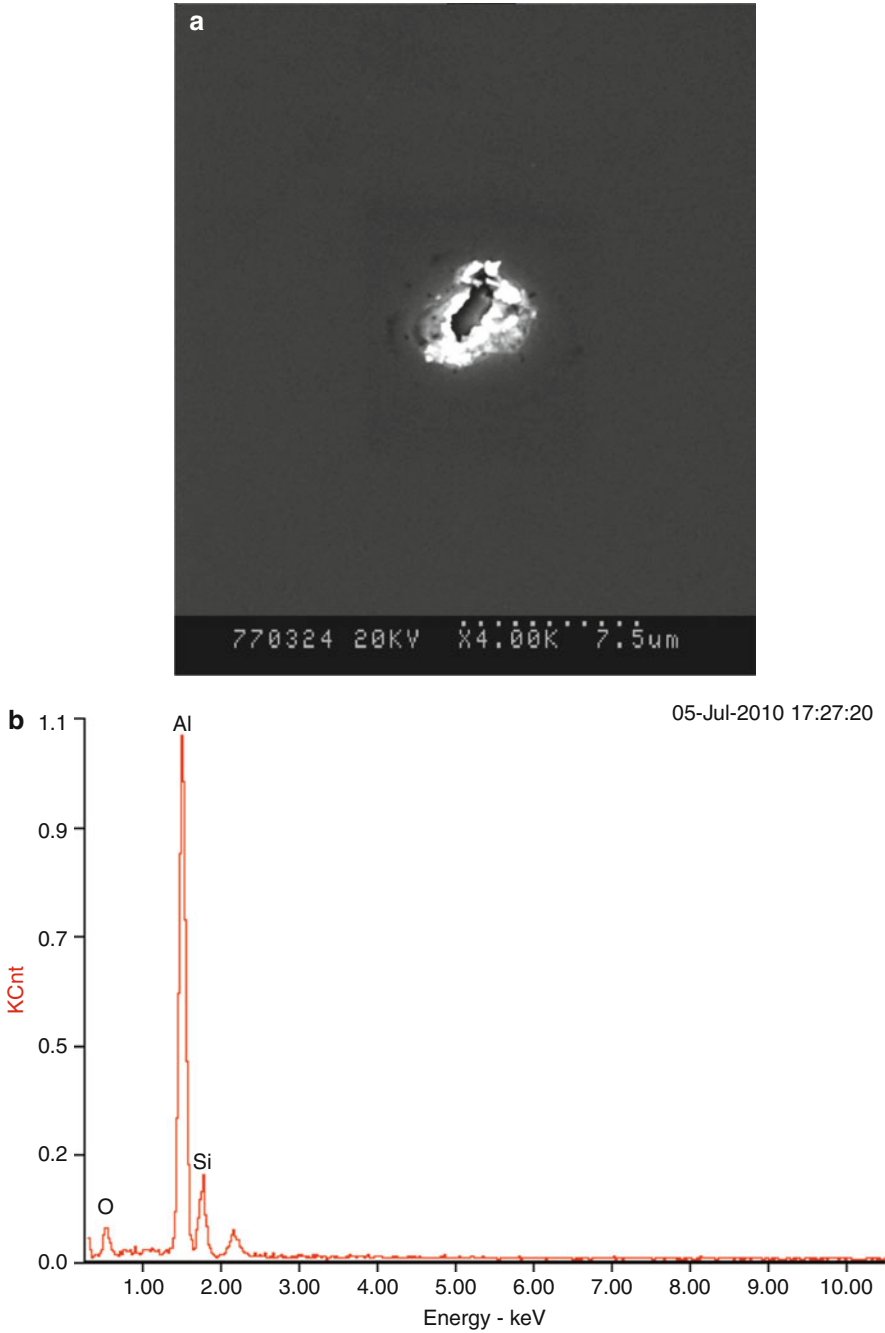
Fig. 6 Scanning electron microscopy (**a**) combined with energy dispersive x-ray microanalysis (**b**) of a crater formed upon impact of one of the particles

around it is shown in Fig. 6a. Figure 6b presents a typical energy dispersive x-ray microanalysis result of the debris.

4 Conclusions

Glass plates made from K-8 glass were exposed to a flux of 5,000 aluminum particles. The accumulated data had shown that the real area of surface damage is much higher than estimated, due to the appearance of microcracks on the sample surface. Based on the conducted studies, it can be suggested that the relative area of surface damage from micrometeoroid fluxes that have a similar distribution of particle mass and velocity, may reach 1.5 % per year. Since modern spacecrafts are designed to withstand more than 10–15 years in service life, the accumulated damage from the micrometeoroids may lead to substantial degradation of surfaces.

References

1. Semkin ND, Kalaev MP (2011) Prib Tekh Eksp (1):136 [Instrum Exp Tech (Engl Transl) 54 (1):126]
2. Semkin ND, Piyakov AV, Voronov KE et al (2007) Prib Tekh Eksp (2):140 [Instrum Exp Tech (Engl Transl) 50(2):275]

Initial Sticking Rate of O_2 Molecular Beams on Ni (111) Surface Depending on Kinetic Energy

Keisuke Inoue and Yuden Teraoka

Abstract Space structures in a low Earth orbit collide with gaseous atoms and molecules with a relative kinetic energy of several electron volts. The action of high speed reactive atoms and molecules accelerates the degradation of material surfaces. In this study, the oxidation states of Ni (111) surfaces that were prepared by irradiation with supersonic O_2 molecular beams were analyzed by soft x-ray photoemission spectroscopy with synchrotron radiation. An oxygen uptake curve and an initial sticking rate were remarkably changed depending on the O_2 incident energy. An intermediate plateau shown in an oxygen uptake curve disappeared with increasing incident energy due to the change of dissociative adsorption mechanism from a two-dimensional island growth model to a direct activated adsorption model.

Keywords Ni(111) • Oxygen • Photoemission spectroscopy • Supersonic molecular beam • Synchrotron radiation

1 Introduction

The Ni (111) surface reacts with O_2 molecules to form a thin oxide layer on the surface even at 147 K [1] showing a Langmuir-type oxygen uptake curve. When the clean Ni (111) surface is exposed to O_2 gas at higher temperatures, a plateau appears in an intermediate region of an oxygen uptake curve [1]. These characteristics are also observed in the oxidation of Ni (001) surface [2]. Such a behavior of oxygen uptake curves can be explained by a two-dimensional (2D) oxide island growth model [2, 3]. Generally speaking, a chemical reaction rate of atoms and molecules

K. Inoue • Y. Teraoka (✉)
Graduate School of Material Science, University of Hyogo, 3-2-1 Kouto, Kamigori-cho, Ako-gun, Hyogo 679-1297, Japan

Japan Atomic Energy Agency (JAEA), 1-1-1 Kouto, Sayo-cho, Sayo-gun, Hyogo 679-5148, Japan
e-mail: yteraoka@spring8.or.jp

possessing a hyperthermal translational kinetic energy (incident energy) with some solid surfaces differs from that of reactants possessing a thermal energy. Indeed, an oxygen uptake curve for the Ni (111) oxidation by O_2 molecular beams with a hyperthermal energy at a surface temperature of 300 K changed from the 2D island growth model at 0.06 eV to the Langmuir type in the case of O_2 molecular beam incidence with 0.6 eV [4]. The fact implies that the kinetics of oxygen adsorption changed depending on a translational kinetic energy of O_2 molecules to a direct activated adsorption mechanism [4]. The oxygen uptake is finally saturated at 3.0 ML followed by the intermediate plateau of 0.2 ML [4] at 300 K. The oxygen coverage was maintained to be 0.2 ML at 120 K [4]. Translational kinetic energy effects had been also shown for initial sticking coefficients of O_2 molecules at the Ni (111) surface [5]. Although a trapping-mediated adsorption mechanism was apparent at 123 K in an incident energy region lower than 0.05 eV, an activated adsorption took place in the higher incident energy region up to 0.4 eV [5].

The translational kinetic energy of O_2 molecules can be accelerated up to 2.3 eV by using our supersonic molecular beam techniques [6]. By applying such techniques, the effects of translational kinetic energy of O_2 molecules on the O_2 adsorption at the Ni (111) surface have been studied using a soft x-ray photoemission spectroscopic surface analysis with high brilliance and high energy-resolution synchrotron radiation (SR-XPS). A surface chemistry experimental station (SUREAC2000) of BL23SU, one of Japan Atomic Energy Agency (JAEA) contract beamlines in the SPring-8 facilities has been used in these experiments [7]. It is possible to irradiate the sample surface with both beams, i.e. the supersonic O_2 molecular beam (SSOMB) and the soft x-ray monochromatic synchrotron radiation beam, simultaneously at the SUREAC2000. Real-time in-situ photoemission spectroscopic observations of chemical bonding states at the oxidized Ni (111) surface can be performed during oxidation reactions. Practically, oxidation states formed by irradiation of O_2 molecular beam onto the Ni (111) surface to some extent have been observed by the SR-XPS method for constituents of the surface (Ni2p, Ni3p and O1s). Oxygen uptake curves have been obtained by a cyclic performance of the SSOMB irradiation and the SR-XPS measurement. The translational kinetic energy dependence on an oxygen uptake curve has been evaluated by changing incident energy of O_2 molecular beam. Furthermore, the translational kinetic energy dependence on an oxygen initial sticking rate has been also estimated from an initial slope of an oxygen uptake curve.

Consequently, a plateau region shown in an intermediate region of an O_2 uptake curve was found to decrease with increasing incident energy of O_2 molecules, and an initial sticking rate showed the maximum at 1 eV followed by remarkable re-increase at 2.3 eV. The first increase of initial sticking rate shown in the incident energy region below 1 eV implies that a direct activated adsorption takes place. A potential energy barrier height should be 1 eV. The remarkable re-increase of initial sticking rate at 2.3 eV indicates that the existence of second potential energy barrier in an inner region than the first potential energy barrier. The decrease of the intermediate plateau region, shown clearly in an oxygen uptake curve for low incident energies, is corresponding to the change of adsorption mechanism from a
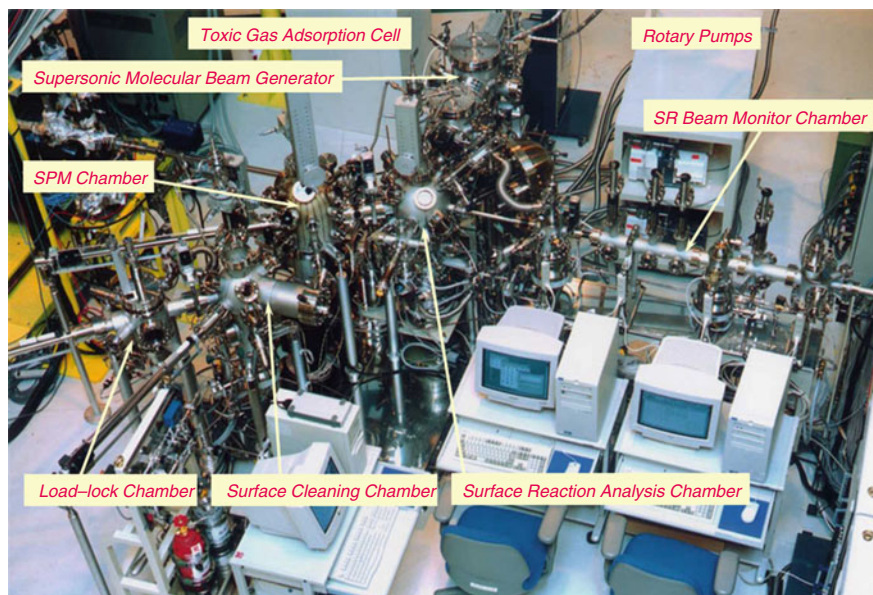
Fig. 1 General view of the SUREAC2000 system

2D island growth model to a direct activated adsorption model even in the initial reaction stages.

2 Experimental Apparatus and Samples

2.1 Surface Chemistry Experimental Apparatus

All experiments were conducted at the SUREAC2000 complex. Figure 1 shows a general view of the SUREAC2000 system with its major blocks marked. A typical experimental setup and a close-up of the sample position in the SR-XPS measurements are shown in Figs. 2 and 3, respectively. The surface reaction analysis chamber is evacuated by two turbo-molecular pumps connected in tandem so that a base pressure less than 5×10^{-9} Pa is achieved. The chamber is also equipped with a hemispherical electron energy analyzer (Omicron EA125-5MCD) and a conventional twin anode (Al/Mg-K$_\alpha$) x-ray source to facilitate the photoemission experiments.
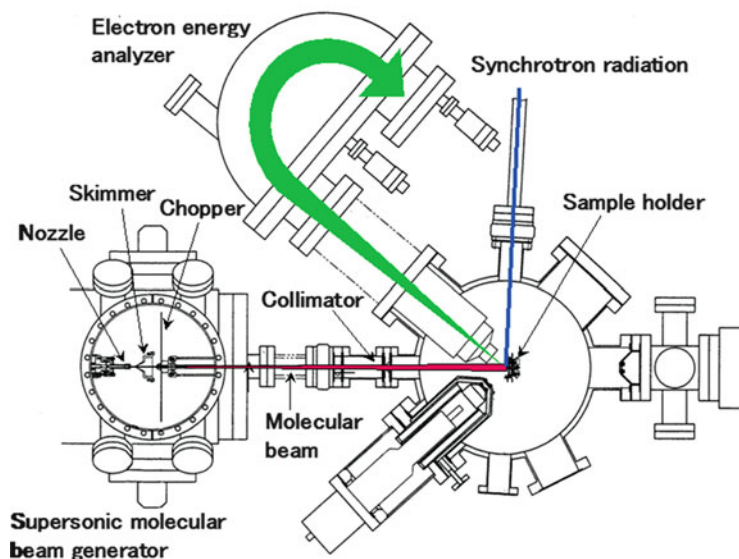
Fig. 2 Cross-sectional top view of the main parts of SUREAC2000
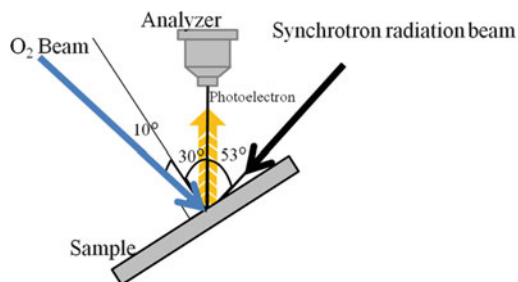
Fig. 3 Sample position and the O_2 and SR beam directions in the SR-XPS measurements

2.2 Oxygen Molecular Beam Source

The O_2 beam in the SSOMB system is continuously generated by an adiabatic expansion of O_2, He and/or Ar mixture. The free expansion nozzle can be heated up to about 1,400 K so that the upper limit of translational kinetic energy of O_2 molecules is estimated from calculations to be 2.3 eV. The incident energy value is controllable by varying the gas mixing ratio and the nozzle temperature. Usually, the incident energy is changed by varying the gas mixing ratio, keeping the nozzle temperature at 1,400 K. The sample surface was irradiated with the SSOMB at an incident angle of 10° with respect to the surface normal as shown in Fig. 3.

The incident energy of SSOMB was ranging from 0.06 to 2.3 eV. The incident energies less than 0.2 eV were achieved at the nozzle temperature of 300 K and larger energies were obtained at the nozzle temperature of 1,400 K. A backfilling experiment (exposure to O$_2$ gas) was also conducted to obtain 0.02 eV data.

2.3 Surface Preparation Procedures

A clean Ni (111) surface was made by a cyclic Ar$^+$ ion beam sputtering treatment (Ar pressure; 2×10^{-4} Pa, applied voltage; 1 kV, ion current; 1 μA) and thermal annealing (1,273 K flashing followed by 923 K for 20 min). The cleanliness of Ni (111) surface was checked by measuring an SR-XPS wide spectrum and observing low energy electron diffraction (LEED) patterns.

2.4 Photoemission Spectroscopy with Synchrotron Radiation

After initial irradiation of the clean Ni(111) surface with the SSOMB, the core level photoemission spectra of Ni2p, Ni3p and O1s were measured. Cycles of SSOMB irradiation and SR-XPS measurement were repeated up to oxygen saturation at the sample surface. The surface temperature was kept at 300 K during SSOMB irradiation and SR-XPS measurements. The SR energy was set at 680 and 1,150 eV.

3 Results and Discussion

3.1 Oxygen Uptake Curves

The time evolution of O1s photoemission spectra is shown in Fig. 4 at O$_2$ incident energy of 2.3 eV. All O1s photoemission spectra show a broad and asymmetric profile. This fact indicates that the O1s peak consists of several components. A typical peak deconvolution result is shown in Fig. 5. The main component is corresponding to (d) NiO. We assume (f) Ni$_x$O$_y$ (x > y) and (c) Ni$_x$O$_y$ (x < y) components, in addition to (e), as oxygen chemisorption components. A peak around 531 eV may be responsible for (b) OH radicals generated from dissociative adsorption of residual H$_2$O molecules during measurements [8]. Residual (a) H$_2$O molecules adsorb gradually at the oxidized Ni (111) surface during experiments.

Area intensity of an O1s peak corresponds to the oxygen content at the Ni (111) surface. We can obtain an oxygen uptake curve by plotting the area intensities of O1s peak as a function of O$_2$ dose. Figure 6 shows the dependence of oxygen uptake on the incident O$_2$ energy. In the backfilling condition, the uptake curve shows an
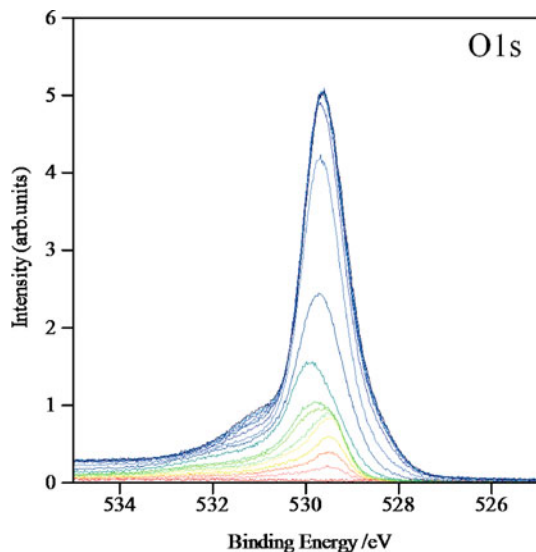
Fig. 4 Time evolution of O1s SR-XPS spectra observed in an O_2 incident energy of 2.3 eV
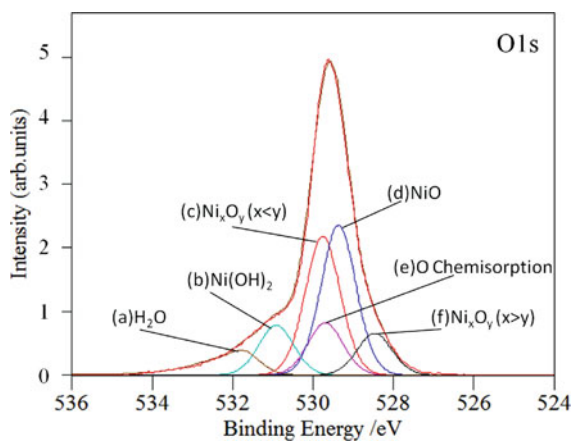
Fig. 5 Deconvolution of O1s SR-XPS peak collected from the oxygen-saturated Ni (111) surface; (**a**) H_2O, (**b**) OH, (**c**) Ni_xO_y (x < y), (**d**) NiO, (**e**) O chemisorption, and (**f**) Ni_xO_y (x > y)

intermediate plateau followed by further increase of oxygen coverage. This curve behavior is the same as previously reported [1, 4]. The oxygen content at saturation is reported to be 3 ML [4]. In the case of incident energy 0.7 eV, the intermediate plateau region was shortened and the oxygen coverage increased in the whole O_2 dose region. At the incident energies larger than 1.0 eV, the plateau almost disappeared and the oxygen saturation content increased by a factor of 5 comparing to that at the backfill condition (at incident energy of about 0.02 eV). This fact
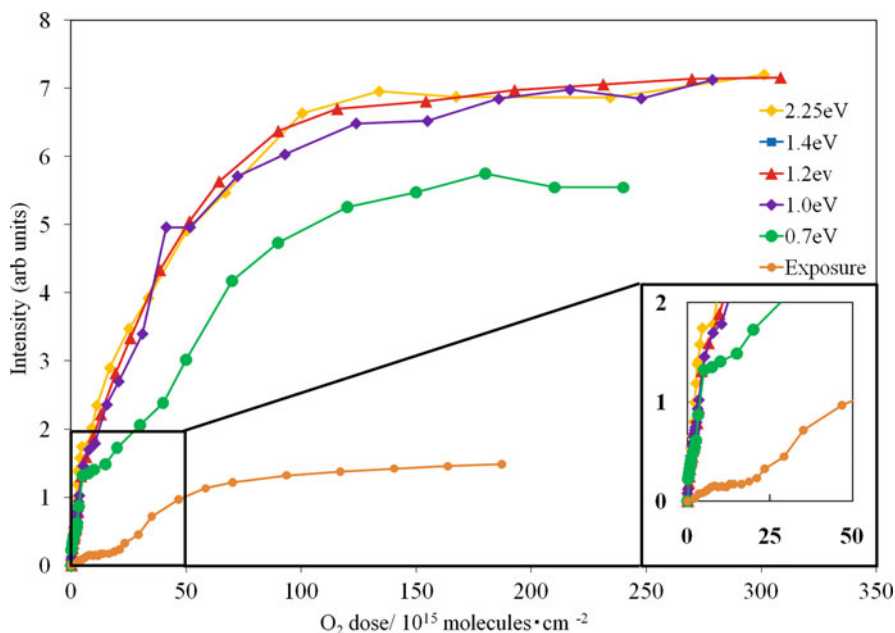
Fig. 6 Oxygen uptake dependence on the O$_2$ incident energy at the Ni (111) surface. The oxygen dependence is plotted in arbitrary units on the vertical scale

implies that the mechanism of O$_2$ dissociative adsorption changes from a 2D island growth model to the Langmuir-type direct activated adsorption model from the initial stages of O$_2$ irradiation. The increase of oxygen saturation content is attributed to the increase of main components shown in Fig. 5. These components are assigned to be a peroxide component; (c) Ni$_x$O$_y$ (x < y) and a nickel oxide component; (d) NiO.

3.2 Initial Sticking Rates of O$_2$ Molecules

A relative initial sticking rate of an O$_2$ molecule at the clean Ni (111) surface was evaluated from the initial slope of the oxygen uptake curve. Figure 7 shows relative initial sticking rates as a function of O$_2$ incident energy. The initial sticking rate increased gradually as incident energy increased, after the maximum value at 1.0 eV, the sticking rate decreased slightly and a remarkable sharp increase was observed in the region around 2.3 eV. The first increase implies that the dissociative adsorption of O$_2$ molecules takes place by an activated adsorption mechanism. The maximum initial sticking rate at 1.0 eV implies that the potential energy barrier height is 1.0 eV. The slight increase of initial sticking rate shown in the region below 1.0 eV is attributed to a quantum mechanical tunneling effect. The second
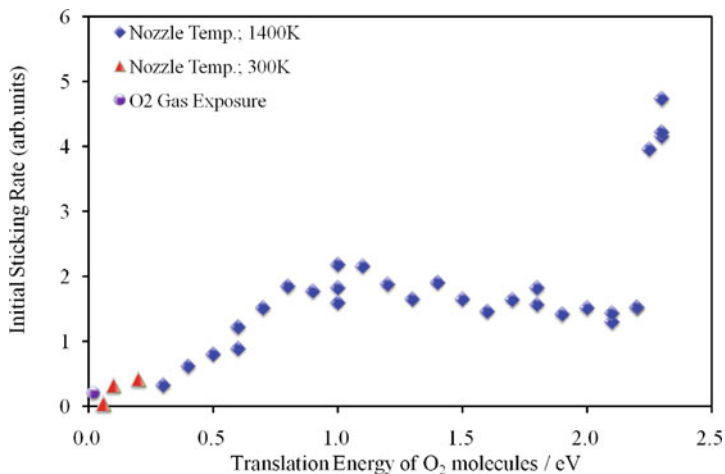
Fig. 7 Relative initial sticking rate of O_2 molecules at a clean Ni (111) surface as a function of O_2 incident energy

increase around 2.3 eV implies that high speed O_2 molecules are adsorbed by a new adsorption mechanism. That is, another potential energy barrier larger than 2.3 eV exists in a position closer to the surface than the first potential energy barrier.

4   Conclusions

Oxidation processes of a clean Ni (111) surface with hyperthermal O_2 molecular beams have been studied using soft x-ray photoemission spectroscopy with synchrotron radiation. Oxygen uptake has been observed at various translational kinetic energies (incident energies) of O_2 molecules. Although the first plateau, shown in an intermediate region of an oxygen uptake curve, is observed, as in previous reports, at O_2 incident energy of thermal energy region. The plateau disappeared with increasing O_2 incident energy. Furthermore, the oxygen content at the Ni (111) surface, formed by irradiation with 2.3 eV O_2 molecules, also increased up to about five times, compared to that observed at thermal energy. These facts correspond to some kind of activated adsorption that takes place at the Ni (111) surface.

Initial sticking rates of O_2 molecules were also evaluated from initial slopes of oxygen uptake curves. The initial sticking rate increased as incident energy increased from 0.3 to 1.0 eV, after that slightly decreased toward 2.2 eV, and finally a remarkable sharp increase was observed in the region around 2.3 eV. The first increase of sticking rate implies that the activated dissociative adsorption of O_2 molecules takes place through a potential energy barrier of 1.0 eV, and the second increase around 2.3 eV implies that high speed O_2 molecules adsorb by a new

adsorption mechanism. Another potential energy barrier exists with the height larger than 2.3 eV in the closer region to the surface.

References

1. Holloway PH, Hudson JB (1974) Kinetics and the reaction of oxygen with clean nickel single crystal surfaces II. Ni(111) surface. Surf Sci 43:141–149
2. Holloway PH, Hudson JB (1974) Kinetics and the reaction of oxygen with clean nickel single crystal surfaces I. Ni(100) surface. Surf Sci 43:123–140
3. Holloway PH (1981) Chemisorption and oxide formation on metals: Oxygen-nickel reaction. J Vac Sci Technol 18(2):653–659
4. Zion BD, Hanbicki AT, Sibener S (1999) Kinetic energy effects on the oxidation of Ni(111) using O$_2$ molecular beams. Surf Sci 417:L1154–L1159
5. Beutl M, Rendulic KD, Castro GR (1997) Does the rotational state of a molecule influence trapping in a precursor? An investigation of N$_2$/W(100), CO/FeSi(100) and O$_2$/Ni(111). Surf Sci 385:97–106
6. Teraoka Y, Yoshigoe A, Moritani K (2008) Mechanisms of concurrent SiO desorption with oxide layer formation at Si(001) surface. Elect Eng Jpn 164(3):60–68
7. Teraoka Y, Yoshigoe A (1999) Design of surface chemistry end-station of BL23SU in SPring-8. Jpn J Appl Phys 38(38–1):642–645
8. Biesinger FU, Fuggle JC, Bennett PA, Zolnierek Z, Freiburg Ch (1983) X-ray photoelectron spectroscopic chemical state quantification of mixed nickel metal, oxide and hydroxide systems. Phys Rev B 27(4):2179–2193

Hydrogen Removal from Hydrogenated Diamond-Like Carbon Films by Exposure to Photon and Energetic Atomic Oxygen Beams

Kumiko Yokota, Masahito Tagawa, Koji Matsumoto, Yuichi Furuyama, Akira Kitamura, Kazuhiro Kanda, Mayumi Tode, Akitaka Yoshigoe, and Yuden Teraoka

Abstract Stability of hydrogen in diamond-like carbon (DLC) film under simulated space environment, i.e., hyperthermal atomic oxygen, vacuum ultraviolet (VUV) and soft X-ray exposures has been studied. Hydrogen in DLC was released by exposure to low-energy atomic oxygen beam, whereas the gasification reaction of carbon atom needed collision energy above 3 eV. The desorption process in the deep region required a higher collision energy. The density of hydrogen decreased 11% by atomic oxygen exposure, and was independent of the collision energy. Photon exposure also releases hydrogen from DLC. High-energy photons in soft x-ray promote the hydrogen desorption even from deeper region with high efficiency. It was considered that soft x-ray could release bonded hydrogen which is not released by VUV or atomic oxygen exposures.

Keywords Atomic oxygen • Diamond-like carbon • Hydrogen • Soft x-ray • Ultraviolet

K. Yokota • M. Tagawa (✉)
Graduate School of Engineering, Kobe University, Kobe 657-8501, Japan
e-mail: tagawa@mech.kobe-u.ac.jp

K. Matsumoto
Japan Aerospace Exploration Agency, Chofu, Tokyo 182-8522, Japan

Y. Furuyama • A. Kitamura
Graduate School of Maritime Sciences, Kobe University, Kobe 658-0022, Japan

K. Kanda
University of Hyogo, Kamigori, Hyogo 678-12058, Japan

M. Tode • A. Yoshigoe • Y. Teraoka
Japan Atomic Energy Agency, Sayo, Hyogo 679-5148, Japan

1 Introduction

Diamond-like carbon (DLC) is an advanced carbon material, which shows many attractive properties, including low friction, high hardness, high infrared transmission, and inertness. The hydrogen content of a DLC film depends on the fabrication method and can range from 0 to more than 40 at%, (5.3 wt%). It has been well known that the hydrogen content in DLC film drastically affects the properties of DLC, for example, friction or hardness. For example, Donnet et al. showed that the ultralow friction properties of DLC in vacuum could be achieved only in the case of highly hydrogenated DLC [1, 2]. It is natural to consider that such attractive DLC performance may be affected if hydrogen in DLC is not stable in space environment. Stability of hydrogen in DLC film under space environment is a key for space applications.

In this study, hydrogen removal process from DLC film under simulated low Earth orbit space environment (atomic oxygen, ultraviolet and x-ray exposures) has been investigated. Surface properties of DLC after atomic oxygen exposure were analyzed by synchrotron radiation photoelectron spectroscopy (SR-PES) and Rutherford backscattering spectroscopy (RBS). Depth profiling of hydrogen was achieved by elastic recoil detection analysis (ERDA). Desorption properties of hydrogen from DLC film (dehydrization process) as well as of carbon (etching process) by atomic oxygen and photon exposures were studied.

2 Experimental Apparatus and Samples

The DLC films used in this study were prepared by conventional plasma enhanced chemical vapor deposition (PECVD) using CH_4 gas, and were commercially available. A DLC film was formed on a Si(001) wafer with a film thickness of approximately 0.6–1 μm. The hydrogen contents of DLC used in this study were 40 at% and 54 at%.

A hyperthermal atomic oxygen beam, which was formed by a laser detonation beam source [3–5], was used to study the effect of atomic collisions on hydrogen removal. This type of atomic beam source provided a high-intensity pulsed hyperthermal atomic beam (typical average translational energy of 5 eV). Adjusting the laser flash timing tuned the incident energy of the atomic oxygen beam. However, the energy distribution of the atomic oxygen beam was not small enough to study the energy dependence of the reaction (full with at half maximum of approximately 5 eV). Thus, to increase the energy resolution of the measurement, a high-speed mechanical chopper wheel (9,000 rpm) was installed at a distance of 82 cm from the nozzle throat. The atomic oxygen beam sliced by the chopper wheel was characterized by a time-of-flight (TOF) distribution measured by the quadrupole mass spectrometer (QMS) installed in the beamline. Because of the combination of mechanical chopper wheel and broad atomic beam, the energy of atomic

oxygen at the DLC surface was dependent on the location on the sample surface. This experimental configuration enabled to investigate the incident energy dependence of the hydrogen desorption by analyzing different sample locations. Depending on the sample location, the average energy of the atomic oxygen beam was distributed from 2.0 eV to 5.7 eV.

Ultraviolet exposure was made by a commercially available 30 W deuterium lamp source (L2D2 L7292, HAMAMATSU) with a wavelength of 115–400 nm. The deuterium lamp was attached to the atomic oxygen source chamber. The sample was exposed to the vacuum ultraviolet radiation through a MgF_2 window and evacuated light guide in order to avoid absorption of vacuum ultraviolet by air (wavelength of <200 nm). Soft x-ray exposure was done by the synchrotron facility at University of Hyogo, NewSUBARU (BL-6). The SR at the BL-6 sample stage film had a continuous spectrum from IR to soft X-ray, which was lower than 1 keV. All exposure experiments were carried out at room temperature.

ERDA and RBS measurements were performed using the 5SDH-2 tandem electrostatic accelerator located at Kobe University [6]. We used a focused He^{++} 100 μm diameter beam for RBS and ERDA measurements. To study the effect of incident energy of atomic oxygen, the RBS and ERDA measurements were performed every 3 mm along the direction of the movement of the chopper slit. The hydrogen content in an atomic oxygen exposed film was quantitatively analyzed using ERDA with He^{++} ions (incident energy: 4.2 MeV). RBS was used for depth profiling of the carbon density. The incident angle of He^{++}, the scattering angle of He^{++} for RBS measurements, and the recoil angle of H$^+$ for ERDA measurement were $75°$, $160°$, and $30°$, respectively.

SR-PES spectra were measured at the SUREAC2000 surface chemistry endstation installed in BL23SU beamline at SPring-8 synchrotron radiation facility, Japan [7]. Unlike conventional x-ray photoemission spectroscopy, SR-PES provides high-spatial resolution (less than 0.5 mm) spectra with extremely high-signal-to-noise ratios, which were suitable for spatially resolved PES.

3 Results and Discussion

3.1 Atomic Collision-Induced Hydrogen Removal

Figure 1a displays the RBS spectra of DLC film with hydrogen content of 40% exposed to atomic oxygen beams at various energies ranging from 2.0 to 5.7 eV. Figure 1b shows that depth profile of the carbon density in the DLC film analyzed by RBS. It is expressed as a function of the position from the DLC/Si interface. The thickness of DLC decreased upon atomic oxygen exposure, and was dependent on the average energy of the impinging oxygen atoms.

Figure 2 depicts the relationship between the collision energy and DLC film thickness of atomic oxygen was less than 3 eV, but the thickness decreased
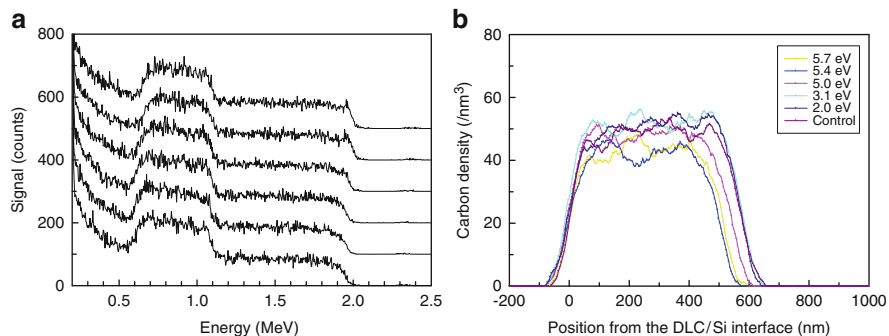
Fig. 1 RBS spectra of atomic oxygen-exposed DLC. *Left panel*: raw data, and *right panel*: depth profile of carbon density in the DLC film analyzed by RBS
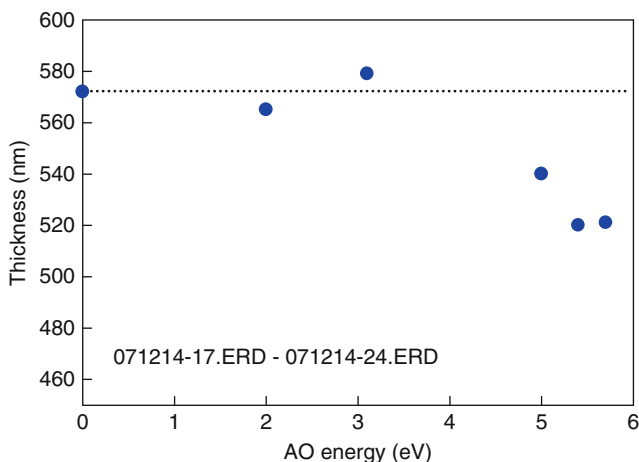
Fig. 2 Relationship between the collision energy of atomic oxygen and DLC film thickness measured from FWHM of RBS data

significantly with collision energies above 3 eV. Because an accurate fluence of atomic oxygen at the analyzed position of the DLC was unknown, a quantitative analysis of the reaction efficiency of atomic oxygen could not be obtained from the data.

However, the fluencies of 5.4 and 5.7 eV atomic oxygen beams were smaller than that of 5.0 eV beam. (It is assumed that the atomic oxygen beam intensity is proportional to the area of the spectrum). Therefore, it could be stated, at least, that the collisional energy of atomic oxygen strongly affected the yield of the gasification reaction in DLC.

Figure 3 (lower panel) displays the depth profile of the hydrogen density analyzed by ERDA where the profiles are represented as functions of the position measured from the DLC/Si interface (surface recession is obvious). Due to the
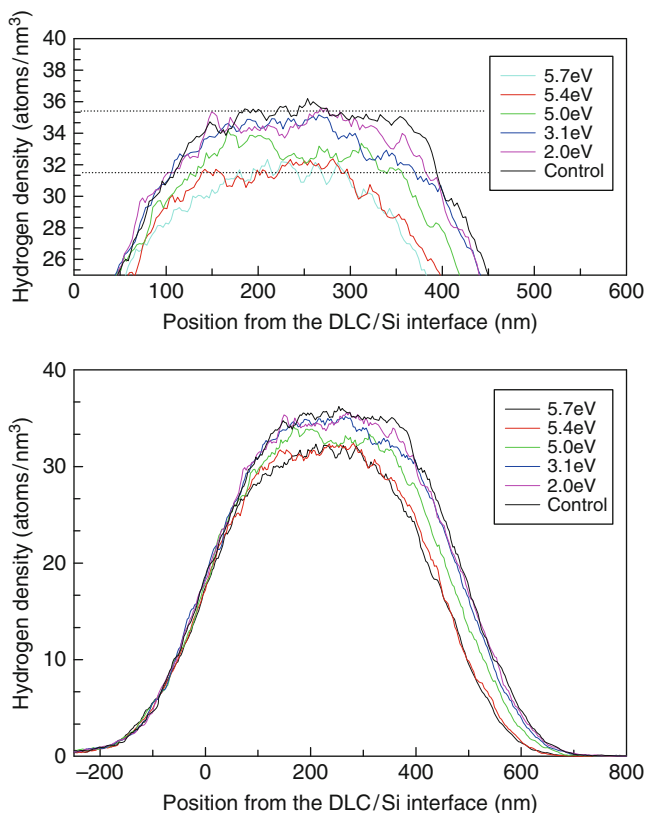
Fig. 3 Depth profile of the hydrogen density analyzed by ERDA. *Lower panel*: entire data, and *upper panel*: close-up view of the summit of the peak

thickness loss of DLC (Fig. 2), the width of the peak distribution became smaller at the analyzed position where atomic oxygen arrived with collisional energies above 3 eV. Not only the distribution width, but also the hydrogen density decreased. The peak intensity indicated that approximately 6% of the hydrogen at the DLC surface was lost even with an atomic oxygen collisional energy of 3.1 eV. In contrast, a change in DLC thickness was not detected by RBS with this collision energy. Thus, hydrogen was desorbed, but carbon remained at atomic oxygen exposure under 3.1 eV. A hydrogen abstraction reaction, which is the most probable surface reaction when hyperthermal atomic oxygen reacts with polymeric materials [8], is a possible mechanism. Figure 3 (upper panel) is a magnification of the summit of the peaks in Fig. 3 (lower panel). In addition, Fig. 3 (upper panel) shows that a decrease in hydrogen density (from 35.5 to 31.5 atom/nm^3) was initially observed in the shallow region, but gradually progressed into deeper regions as the collisional energy increased. The collisional energy of atomic oxygen was transferred to DLC at the first collision with surface atoms, and it was used for release of hydrogen.
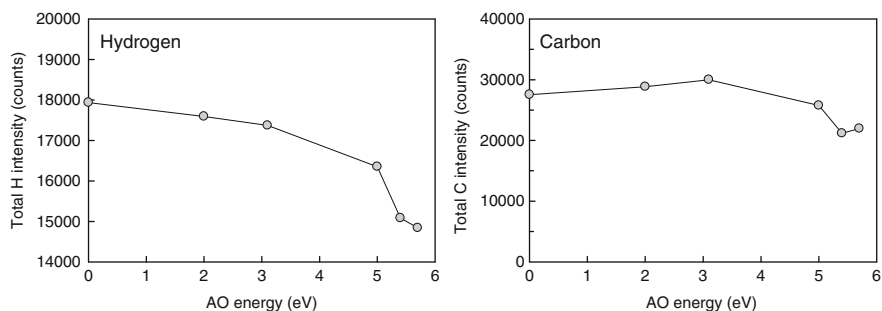
Fig. 4 Total hydrogen (*left panel*) and carbon (*right panel*) signal intensities as a function of collisional energy of atomic oxygen measured by ERDA and RBS, respectively

Table 1 Relative hydrogen fraction ratio (H/(H + C)) before and after atomic oxygen beam exposure

O-atom energy (eV)	H/(C + H) (at%)	Relative H intensity
Control	39.4	100
2.0	37.9	98
3.1	36.7	97
5.0	38.8	91
5.4	41.6	84
5.7	40.3	83

The collisional energy released at the surface promoted the hydrogen release in a deeper region, suggesting a high diffusivity of hydrogen stored in the DLC film.

Figure 4 shows the total hydrogen and carbon signal intensities as a function of collision energy of atomic oxygen measured by ERDA and RBS, respectively. The signal intensity of hydrogen decreased as the collision energy increased. In contrast, the signal intensity of carbon began decreasing at a collisional energy above 3 eV. Consequently, the relative hydrogen fraction (H/(H + C)) ratio, which is commonly used to characterize DLC property, was minimized at an atomic oxygen exposure of 3.1 eV (Table 1).

Figure 5 (left panel) and (right panel) show the C1s SR-PES spectra of DLC before and after atomic oxygen exposure (collision energy of 5.7 eV), respectively. The measurements were conducted at excitation energy of 850.37 eV with a take-off angle of 90°.

A high-energy tail near 286–287 eV and the small hump at 289.2 eV were obvious in these spectra. The region of small humps was fitted with three peaks; i.e., -OH (256.5 eV), $>C = O$ (257.9 eV), and –COOH (259.3 eV) [9]. The deconvolution result revealed that the DLC surface after exposure to atomic oxygen beam contained carbon atoms, which formed hydroxyl groups (14%), carbonyl groups (4%), and carboxyl groups (7%). Thus, the majority of the surface carbon atoms (77%) remained unoxidized.

The estimated escape depth of the C1s photoelectron (kinetic energy of 590–595 eV) was approximately 1.0 nm [10]; only 23% of the carbon atoms formed oxidized states within 1 nm from the surface. The SR-PES measurements clearly
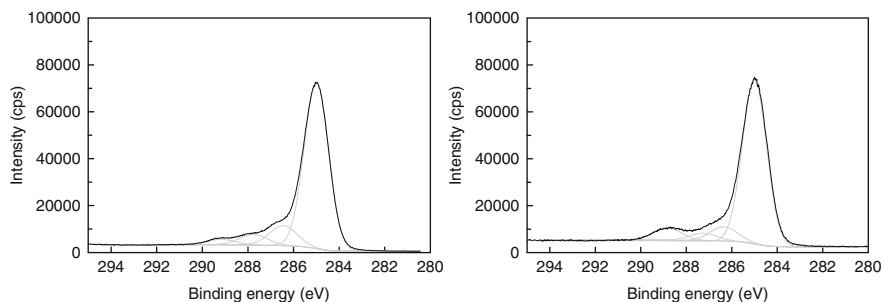
Fig. 5 C1s SR-PES spectra of DLC before (*left panel*) and after atomic oxygen exposure with collision energy of 5.7 eV (*right panel*)
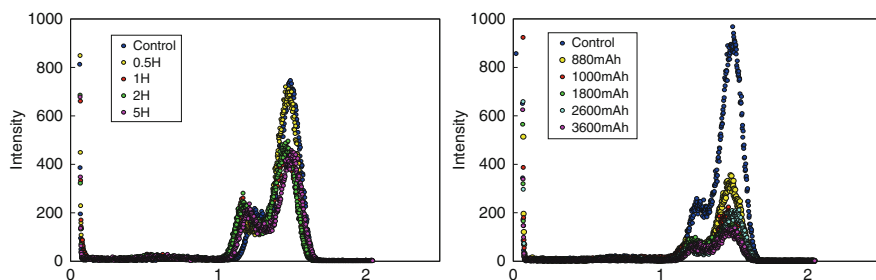
Fig. 6 ERDA spectra of VUV- and x-ray-exposed DLC with hydrogen content of 54 %. *Left panel*: VUV exposure, and *right panel*: soft x-ray exposure

indicated that DLC suffered from a severe surface etching reaction by hyperthermal atomic oxygen exposure with a collisional energy above 5 eV, but the reaction products covered only part of the outermost DLC surface.

3.2 Photon-Induced Hydrogen Removal

Figure 6 (left panel) and (right panel) show the ERDA spectra of VUV- and x-ray-exposed DLC with hydrogen content of 54%. VUV exposures were carried out using a deuterium lamp with exposure time from 0.5 to 5 h. It was obvious that the amount of hydrogen with higher energy decreased with VUV exposure. This result clearly indicated that the hydrogen atoms in a shallow region (less than 0.5 μm from the surface) were desorbed by VUV exposure, but hydrogen in deeper region was not affected by VUV exposure. Moreover, decrease in amount of hydrogen was saturated with exposure time. Figure 6 (left panel) clearly suggested that the VUV exposure promotes the removal of hydrogen in DLC, however, only a limited amount of hydrogen atoms were removed by VUV exposure. In contrast, it was observed that soft x-ray exposure to DLC promotes hydrogen departure more

efficiently (Fig. 6 (right panel)). The decrease in hydrogen is detected even in the deeper region of DLC. It was also confirmed that the amount of hydrogen left in the DLC film is decreased with increasing soft x-ray exposures. Based on the experimental results shown above, the following conclusions were obtained: the high-energy photon exposure leads to hydrogen desorption from deeper region of DLC with higher efficiently without saturation. Nyaiesh et al. and some other groups have also reported the presence of two types of hydrogen in DLC film: bonded and non-bonded hydrogen [11, 12]. The hydrogen not bonded to carbon easily diffused in DLC and terminated the dangling bonds or was released from DLC with small activation energies. Therefore, such non-bonded hydrogen could be released by VUV exposure. However, not only non-bonded hydrogen, but also bonded-hydrogen released by soft x-ray exposure which has high-photon energy could be used to scissor the C-H bonding. From the experimental results obtained in this study, it was suggested that the function of DLC film might be strongly affected by soft x-ray exposures in space environment even though soft x-ray does not show the remarkable etching of DLC.

4   Conclusions

The hydrogen content and surface properties of a diamond-like carbon (DLC) film exposed to a hyperthermal atomic oxygen beam were investigated by Rutherford backscattering spectroscopy, elastic recoil detection analysis, and synchrotron radiation photoelectron spectroscopy. Hydrogen in DLC was released by exposure to low-energy atomic oxygen beam, whereas the gasification reaction of carbon atom needed collision energy above 3 eV. The desorption process in the deep region required a higher collision energy. The density of hydrogen decreased 11% by exposure to atomic oxygen and was independent of the collisional energy. Exposure to photons also releases hydrogen from DLC. High-energy photons in soft x-ray promote the hydrogen desorption even from deeper region with high efficiency. It was considered that soft x-ray could release bonded hydrogen which is not released by VUV or atomic oxygen exposures.

References

1. Erdemir A, Erylimaz OL, Fenske G (2000) Synthesis of diamondlike carbon films with superlow friction and wear properties. J Vac Sci Technol A18(4):1897
2. Fontaine J, Le Mogne T, Loubet JL, Belin M (2005) Achieving superlow friction with hydrogenated amorphous carbon: some key requirements. Thin Solid Films 482:99

3. Tagawa M, Yokota K, Ohnae N, Henoshita H, Umeno M (2001) Oxidation properties of hydrogen-terminated Si(001) surfaces following use of a hyperthermal broad atomic oxygen beam at low temperatures. Jpn J Appl Phys 40:6152
4. Tagawa M, Yokota K, Ohki Y, Ohnae N (2004) Spatially resolved wettability control of polymer surfaces using laser-detonated hyperthermal atomic beams. J Adhes Sci Technol 18:243
5. Yokota K, Tagawa M (2007) Comparison of polyethylene and polyimide as a fluence monitor of atomic oxygen. J Spacecraft Rockets 44(2):434–438
6. Taniike A, Kubota N, Takeuchi M, Furuyama Y, Kitamura A (2002) Ion-irradiation induced hydrogen loss from polyethylene film. J Appl Phys 92(11):6489–6494
7. Saitoh Y, Nakatani T, Matsushita T, Agui A, Yoshigoe A, Teraoka Y, Yokoya A (2001) First results from the actinide science beamline BL23SU at SPring-8. Nucl Instrum Method Phys Res A 474:253
8. Minton TK, Garton DJ (2000) Dynamics of atomic-oxygen-induced polymer degradation in low earth orbit. In: Dressler R (ed) Chemical dynamics in extreme environments, vol 11. World Scientific, Singapore, p 420
9. Beamson G, Briggs D (1992) High resolution XPS of organic polymers: the Scienta300 database. Wiley, Chichester
10. Tanuma S, Powell CJ, Penn DR (1994) Calculations of electron inelastic mean free paths. V. Data for 14 organic compounds over the 50–2000 eV range. Surf Interface Anal 21:165
11. Nyaiesh AR, Nowak WB (1983) Chemisorbed hydrogen on α-carbon films. J Vac Sci Technol A1(2):308
12. Tait NRS, Tolfree DWL, John P, Odeh IM, Thomas M, Tricker M, Wilson J, England J, Newton D (1980) The hydrogen and oxygen content of self-supporting carbon foils prepared bydc glow discharge in ethylene. Nucl Instrum Method 176:433

Resistance of Silicon-Containing Carbonized Lignin to Atomic Oxygen Erosion

Takeshi Kajimoto, Toshimitsu Hata, Masahito Tagawa, Hirotsugu Kojima, and Hajime Hayakawa

Abstract Spacecraft in low Earth orbit (LEO) are exposed to atomic oxygen (AO). It is thus important to develop an environmentally friendly material that can be applied to the outer surfaces of spacecraft in LEO to protect them against AO. Carbonized material containing electroconductive graphitic microlayers is promising for this purpose. We produced carbonized lignin (CW) by separating wood in L-lactic acid and we investigated the AO erosion resistances of CW and CW containing Si. X-ray photoelectron spectroscopy (XPS) revealed that the O/C ratio increased on AO exposure. The CW sample without Si and CW samples containing 20% and 40% Si exhibited less erosion than CW samples containing 5% and 10% Si. XPS revealed that the presence of Si resulted in the formation of SiO_2 on the sample surface. For CW with Si contents of 20% and 40%, the SiO_2 coverage may be sufficiently large to prevent attack by AO.

Keywords LEO • Carbonized lignin • AO

1 Introduction

Highly reactive atomic oxygen (AO) is produced in the atmosphere by ultraviolet radiation reacting with molecular oxygen. The surfaces of spacecraft in low Earth orbit (LEO; 200–700 km above the Earth) are susceptible to oxidation through

T. Kajimoto (✉) • H. Hayakawa
Industrial Technology Center of Wakayama Pref., Ogura 60, Wakayama 649-6261, Japan

Japan Aerospace Exploration Agency, JAXA Sagamihara, Japan
e-mail: kaji@wakayama-kg.go.jp

T. Hata • H. Kojima
Research Institute for Sustainable Humanosphere, Kyoto University, Uji, Japan

M. Tagawa
Graduate School of Engineering, Kobe University, Kobe, Japan

ionization by ultraviolet radiation and by reacting with AO, which is a dominant chemical constituent at such altitudes [1–3]. Various macromolecular and carbon-containing coatings have been developed to prevent spacecraft surfaces from being eroded by AO. However, they do not have very high AO erosion resistances. There is no single element that offers protection from AO exposure and composites suffer from poor adhesion at the interface [4]. Therefore, a new material needs to be developed that can protect the outer surfaces of spacecraft in LEO against AO.

Carbon materials have recently been recognized as promising candidates for this purpose. Carbon materials are inflammable, light, and robust. Furthermore, since they consist of carbon, oxygen, and hydrogen, it is difficult for them to become space debris because of constituted organic materials. Si-doped diamond-like carbon (DLC) prevents AO erosion through the formation of a protective layer of Si [5]. Crystallization of carbon fibers is also used to protect from AO erosion [6]. Wood carbons become electrically and thermally conducting when they are heated [7], which makes them suitable surface coatings for spacecraft in LEO.

Although the components of wood (i.e., cellulose, hemicellulose, and lignin) have been isolated from wood and carbonized, carbonized lignin has found few applications except as a fuel that is similar to coal. If carbonized lignin, which is a renewable resource, can be used in applications, it could be used to produce aromatic compounds that are thermally stable on carbonization for industrial applications. Using biomass materials will reduce the energy required for carbonization.

We have carbonized organosolv lignin produced by cooking wood in L-lactic acid. In the present study, we investigate its resistance to AO erosion in the presence of carbonized wood (CW) and CW containing Si [8].

2 Experiments

2.1 Separation of Lignin from Wood for Carbonization

Sugi (*Cryptomeria japonica*) wood was milled to a powder, sieved (<2 mm), and dried at 383 K for 24 h. The sugi powder was mixed with lactic acid and heated in a pressure vessel at 473 K for 1 h. The resulting mixture was filtered and washed with organic solvents. Finally, lignin powder was obtained by liquefaction.

2.2 Carbonization and Sintering of Lignin

Lignin was carbonized by heating it to 973 K at a rate of 4 K/min in a N_2 atmosphere, maintaining it at 973 K for 1 h and then cooling it to room temperature. This process produced carbonized lignin (CW). CW samples with and without Si

Table 1 Concentration of Cw and Si for samples

Sample	Cw (wt%)	Si (wt%)
OA	100	0
OB	95	5
OC	90	10
OD	80	20
OE	60	40

Note: Cw means lignin carbonized at 973 K
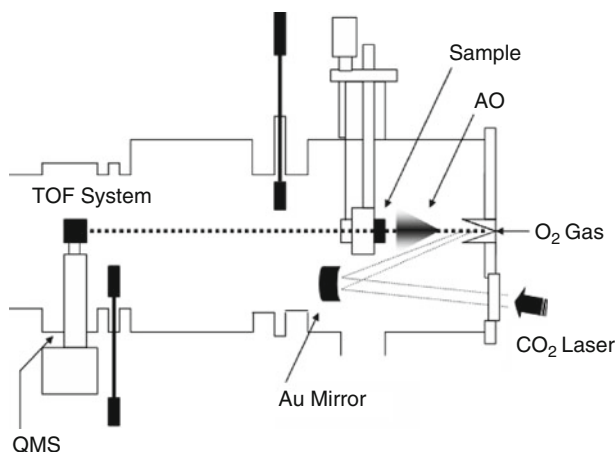
Fig. 1 Schematic drawing of laser detonation atomic oxygen (*AO*) beams source facility. *QMS* quartz crystal microbalance, *TOF* time of flight (of AO)

were mixed in a glove box in the ratios shown in Table 1 and then sintered at 1,323 K and 50 MPa. The samples were 10 mm in diameter and 1 mm thick.

2.3 Simulation Experiment Using AO

All samples were exposed to an AO beam that was produced by exciting molecular oxygen using a CO_2 laser beam (Fig. 1; wavelength: 10.6 μm; pulse energy: 5–7 J). The energy distribution of the AO beam was calculated (Fig. 2).

In this study, the average energy was about 5 eV and the flux was 2×10^{15} atoms/cm^2; this energy is equivalent to that of AO in LEO. Samples were placed in the system with their surface perpendicular to the AO beam. Two AO irradiation schemes were applied in this experiment: the whole sample surface was irradiated and half the sample surface was irradiated.

Fig. 2 Typical translational energy distribution of AO beam
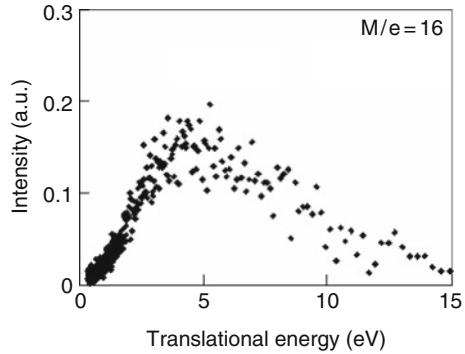
2.4   Analysis of Surface Chemistry

We used a laser microscope (VK-9710; wavelength: 408 nm) to measure the thicknesses of the exposed and unexposed surfaces of the samples whose surfaces had been half irradiated. The erosion depth was defined as the difference between the thicknesses of the exposed and unexposed surfaces. The samples were analyzed by scanning electron microscopy (SEM) and X-ray photoelectron spectroscopy (XPS).

3   Results and Discussion

3.1   Laser Microscopy

Figure 3 shows the results of erosion depth measurements using a laser microscope. Samples with Si concentrations of 0, 5, 10, 20, and 40 wt% had erosion depths of 2.5, 8.0, 3.5, 0, and 0.4%, respectively (the Si concentrations in order of increasing erosion depth are 5% > 10% > 0% > 40% > 20%). Samples with Si concentrations of 20% or more were resistant to erosion. Although a different measurement method was used, these erosion depth results are similar to those obtained in a previous study for DLC with a Si concentration of 20% [9].

3.2   SEM Analysis

Figure 4a and b show sample OB, Fig. 4c and d show sample OE. Figure 4a and c were SEM images of samples without AO irradiation and Fig. 4b and d were SEM images with AO irradiation. For the samples with AO irradiation; each sample was eroded and formed an oxide which was either SiO_2 or SiOC. Figure 3 indicates the

Fig. 3 Relationship between
erosion depth and Si
concentration for samples that
had been exposed to AO
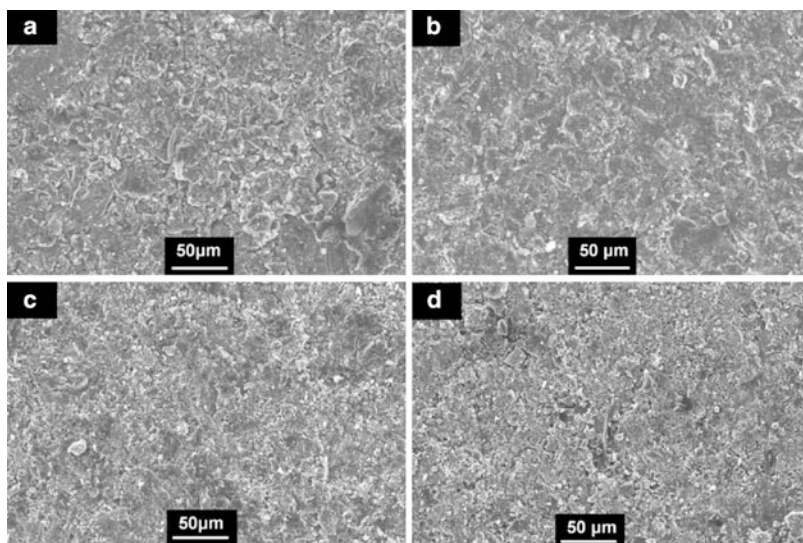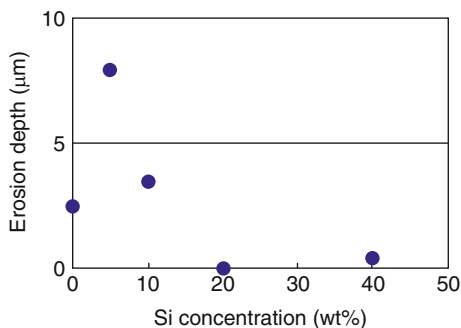
Fig. 4 SEM images of samples consisting of (**a**) 5 % Si and 95 % CW (before AO exposure), (**b**) 5 % Si and 95 % CW (after AO exposure), (**c**) 40 % Si and 60 % CW (before AO exposure), and (**d**) 40 % Si and 60 % CW (after AO exposure)

erosion depth for the five samples, of which OB was the most eroded. Sample OB was both uniformly and equally eroded from the surface. Sample OE was partially eroded because 40% of the sample was silicon.

3.3 XPS Analysis

The atomic concentration of carbon bonded to oxygen doubled during AO exposure, whereas the concentrations of C–C and C–H bonds decreased during AO exposure. Carbons on the CW surface appear to be oxidized by radical reactions and

removed as vapor during exposure. C–C and C–H bonds had higher atomic concentrations than COO– and C=O bonds; thus, oxidization can be controlled by controlling the chemical structure of CW separated with L-lactic acid.

4   Conclusions

In this study, Si was reacted with carbonized lignin by sintering, which prevented AO erosion when there was sufficient Si to react with carbon. On the other hand, when there was insufficient Si, AO reacted with carbon on the sample surfaces and erosion occurred by evaporation of CO and CO_2 gases. For CW without any Si, it is possible to control the reaction with AO by varying the Si concentration. The aromatic structures in CW played an important role in preventing reactions with AO and adsorption of AO.

References

1. Miyazaki E, Tagawa M, Yokota K, Yokota R, Kimoto Y, Ishizawa J (2010) Investigation into tolerance of polysiloxane-block-polyimide film against atomic oxygen. Acta Astronaut 66:922–928
2. Crossman FW (1982) Spacecraft material applications – long-term stability questions. NASA-CP-2269, NASA
3. Tennyson RC (1993) Atomic oxygen and its effects on materials. In: DeWitt RN (ed) The behavior of systems in the space environment. Kluwer, Amsterdam, pp 233–357
4. Longfei H, Meishuan L, Caihong X, Youngming L, Yanchun Z (2009) A polysilazane coating protecting polyimide from atomic oxygen and vacuum ultraviolet radiation erosion. Surf Coat Technol 203:3338–3343
5. Tagawa M, Yokota K, Ohara H, Miyake K, Nakahigashi T (2008) Patent no 2008-266704 Japan
6. Fujimoto K, Satoh K, Shioya T, Seki N, Fujita K (2003) Degradation of materials by high-energy atomic oxygen. JSME Int J Ser A 6:283–289
7. Hata T, Joko S (2007) Carbon materials based on tropical fast growing trees. Research Institute Humanosphere 3:59–63
8. Kajimoto T, Hata T, Tagawa M, Kojima H, Imamura Y (2010) Resistance for erosion on carbonized lignin and Si in combined materials. J High Temp Xoc 36:185–191
9. Zhang J, Lindholm NF, Brunsvold AL, Upadhyaya HP, Minton TK, Tagawa M (2009) Erosion of FEP Teflon and PMMA by VUV radiation and hyperthermal O or Ar atoms. Appl Mater Interfaces 1(3):653–660

Survivability of Silicon-Doped Diamond-Like Carbon Films in Energetic Atomic/Molecular Oxygen Beam Environments

Masahito Tagawa, Kazuhiro Kishida, Kumiko Yokota, Koji Matsumoto, Akitaka Yoshigoe, Yuden Teraoka, Jianming Zhang, and Timothy K. Minton

Abstract Volatile products were measured from two types of diamond-like carbon films under the hyperthermal atomic oxygen (AO) beam bombardment. It was clearly observed that CO and CO_2 were formed at the conventional hydrogenated DLC surface when exposed to hyperthermal AO beam. Desorption rates of CO and CO_2 are constant with AO fluence which reflects the constant erosion rate of the hydrogenated DLC. In contrast, Si-doped DLC shows decrease in amount of CO and CO_2 with increasing AO fluence. Oxidation of Si atoms at the DLC surface was detected by X-ray photoelectron spectroscopy, confirming the formation of SiO_2 film formed at the DLC surface that could prevent AO reaction with C atoms in DLC which leads to loss of DLC. Since a self-healing capability can be expected on Si-doped DLC, metal doping is a promising technology for space application of DLC.

Keywords Atomic oxygen • DLC • Volatile products • Space environment • SR-PES

M. Tagawa (✉) • K. Kishida • K. Yokota
Graduate School of Engineering, Kobe University, Kobe 657-8501, Japan
e-mail: tagawa@mech.kobe-u.ac.jp

K. Matsumoto
Japan Aerospace Exploration Agency, Chofu, Tokyo 182-8522, Japan

A. Yoshigoe • Y. Teraoka
Japan Atomic Energy Agency, Sayo, Hyogo 679-5148, Japan

J. Zhang • T.K. Minton
Montana State University, Bozeman, MT 59717, USA

1 Introduction

Diamond-like carbon (DLC) is an advanced carbon material that includes amorphous sp^2 and sp^3 carbon phases. DLC has many unique properties for mechanical, optical and microelectronics applications. DLC films had already been applied as lubricants in air/water, protective layers on hard disk drive, on automobile engine parts, cutting tools, optical coatings, gas barrier layer and hydrogen absorbing material [1]. Since in space engineering, application of DLC as a new generation solid lubricant is of great interest [2] that authors initiated such a study.

The study described in the present report had shown at the ultralow friction capability (friction coefficient smaller than 0.01) of the hydrogenated DLC in vacuum [3]. Space tribologists are expecting the excellent friction capabilities of DLC as a solid lubricant usable in space (a low friction coefficient both in air and vacuum is required). However, ultralow friction property of the hydrogenated DLC is unstable and further research is performed to achieve stable low friction of DLC in vacuum. On the other hand, when DLC is applied to the exposed section of spacecraft, it may be affected by the space environments. Since DLC is a carbon material, reaction with hyperthermal atomic oxygen (AO) is one of the keys for evaluating the survivability of DLC in space environment. In our previous study, we have reported that hydrogenated DLC is eroded away by the hyperthermal AO reaction [4]. It has also been clarified that the tribological property of hydrogenated DLC was affected by AO exposure [5]. These experimental results suggested that the proper protection method is required for the use of DLC in space environment.

In this paper, we will represent the results of measurements of volatile products during the energetic AO bombardment of Si-doped DLC surface. The effect of Si doping to form a non-volatile protective layer is also reported.

2 Experimental Apparatus and Samples

2.1 Specimen

Two types of DLC films were used in this study; conventional hydrogenated DLC and Si-doped DLC films. They were prepared by plasma chemical vapor deposition (CVD) method. The Si-doping was achieved by adding Si-containing gas into the CVD process. Si-doped DLC contains approximately 10 at.% of Si atoms. Hydrogen concentration in the specimen was about 30 at.%. Thickness of DLC film was approximately 500 nm, and Si (001) was used as a substrate.

2.2 Atomic Oxygen Beam Source

Two atomic oxygen beam facilities at Kobe University (Fig. 1-left panel) and Montana State University (Fig. 1-right panel) were used in this study [6].

Fig. 1 Laser detonation beam facilities used in this study. *Left panel*: Kobe University, and *right panel*: Montana State University

Both facilities have the same configuration. The AO beam was formed using a combination of pulsed supersonic valve and TEA CO_2 laser (wavelength: 10.6 μm, output power: 5 ~ 7 J/pulse). The average translational energy of the AO beam was measured by the time of flight of oxygen atoms. The atomic oxygen facility at Kobe University equipped with a fixed quadruple mass spectrometer for the beam characterization, in contrast, the facility at Montana State University has a rotatable quadrupole mass spectrometer to measure the volatile reaction products from the sample surface. Volatile products with mass/charge ratio of 17 (OH), 18 (H_2O), 28 (CO), 44 (CO_2) were measured during the atomic oxygen beam exposure with the sample temperature held at approximately 200 °C. Flux of the AO beam was calculated from the mass gain of the silver film measured by a quartz crystal microbalance or etching depth of Kapton-H.

2.3 Surface Analytical Methods

The DLC surfaces before and after AO exposure were analyzed by synchrotron radiation photoelectron spectroscopy (SR-PES) at BL23SU in the SPring-8 facility (SUREAC 2000 end-station) in Hyogo, Japan. The high-intensity monochromatic synchrotron radiation provides high energy resolution, high signal to noise ratio, and extreme surface sensitivity of photoemission spectra. The measurement was carried out with excitation energy of 1,252.3 eV, which was calibrated by the Au $4f_{7/2}$ peak position. Take–off angle of photoelectron was settled at 0°, 30°, 45° and 60° with respect to the surface normal.

3 Results and Discussion

3.1 Volatile Products

Figure 2 shows typical TOF spectra of volatile products with m/e = 17 (OH) and 18 (H_2O) from the non-dope DLC. Incident and final angles of atomic oxygen are
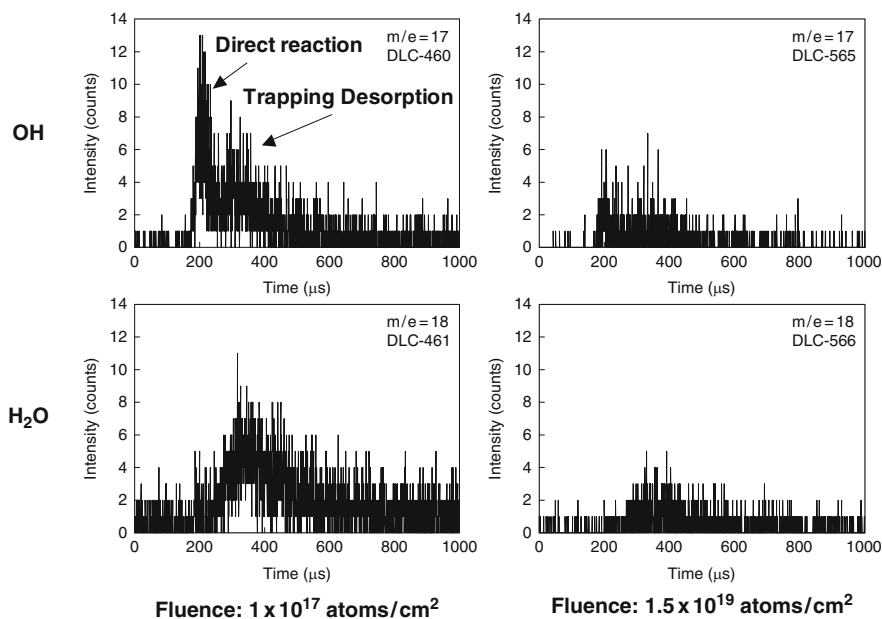
Fig. 2 TOF spectra of volatile products with m/e = 17 (OH, *upper panels*)

$\theta_i = 45°$ and $\theta_f = 45°$, respectively. The left panels are TOF spectra collected at the atomic oxygen fluence of 1.0×10^{17} atoms/cm^2, and the right panels show similar spectra collected at 1.5×10^{19} atoms/cm^2. Bimodal structure of TOF spectrum is clearly observed in OH spectra. The sharp peak at 200 μs is due to the direct reaction and that at 350 μs is due to the trapping desorption. Both peaks are decreased in higher atomic oxygen fluences at 1.5×10^{19} atoms/cm^2. On the other hand, the signal from direct reaction is small and that from trapping desorption is dominant in H_2O (lower panels). Similar results are observed for the Si-doped DLC as shown in Fig. 3. However, decreases in OH and H_2O signals are more significant in the Si-doped DLC.

Figure 4 shows typical TOF spectra of volatile products with m/e = 28 (CO) and 44 (CO_2) from the non-doped DLC. Incident and final angles are $\theta_i = 45°$ and $\theta_f = 45°$. The left panels are TOF spectra collected at the atomic oxygen fluence of 1.0×10^{17} atoms/cm^2, and the right panels shows spectra collected at 1.5×10^{19} atoms/cm^2. High background in m/e = 28 spectra is due to the presence of N_2. Bimodal structure of TOF spectrum is also observed both in CO and CO_2 spectra. The peak at 300 μs is due to the direct reaction and that at 420 μs is due to the trapping desorption. Signal intensity of direct reaction for CO_2 at 300 μs becomes weaker at high atomic oxygen fluence. However, signal intensity of trapping desorption (420 μs) does not change even in higher atomic oxygen fluencies at 1.5×10^{19} atoms/cm^2. No clear atomic oxygen fluence dependence on the TOF spectrum of CO is obvious. Figure 5 shows typical TOF spectra of
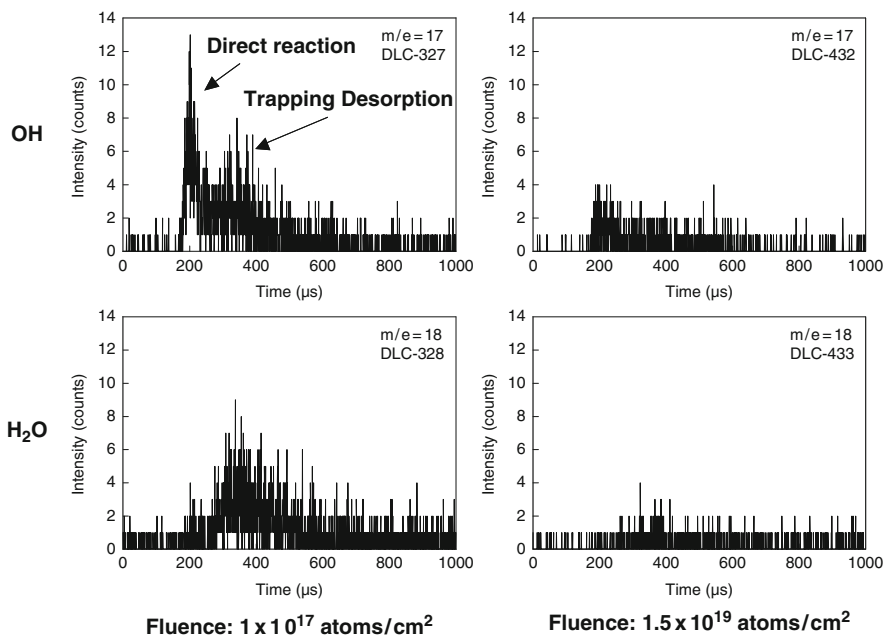
Fig. 3 TOF spectra of volatile products with m/e = 17 (OH, *upper panels*) and 18 (H_2O, *lower panels*) from the Si-doped DLC
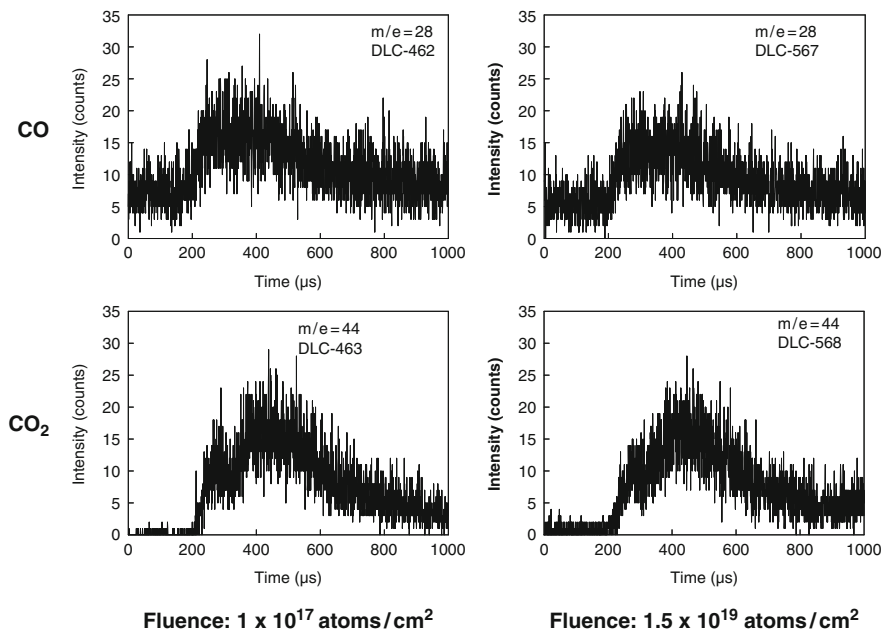
Fig. 4 TOF spectra of volatile products with m/e = 28 (CO, *upper panels*) and 44 (CO_2, *lower panels*) from the non-dope DLC
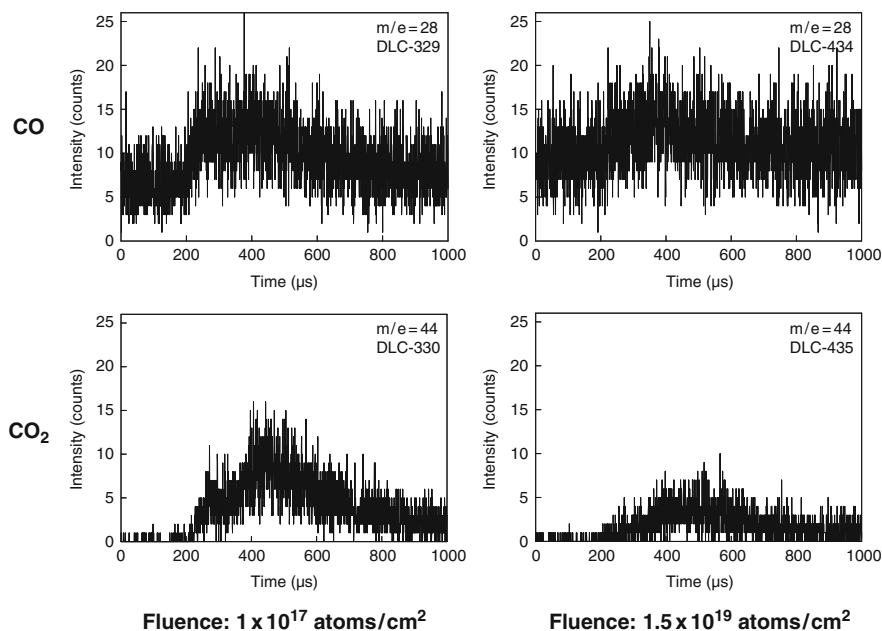
Fig. 5 TOF spectra of volatile products with m/e = 28 (CO, *upper panels*) and 44 (CO_2, *lower panels*) from the Si-doped DLC

volatile products of CO and CO_2 from the Si-doped DLC. Peak position and spectral features are similar to those in non-dope DLC (Fig. 4), however, signal intensities of CO and CO_2 deceases at high atomic oxygen fluence.

Figure 6 shows the intensity variation of CO_2 signal from DLC under hyperthermal AO beam exposure ($\theta i = 45^\circ$ and $\theta_f = 45^\circ$). It was clearly indicated that the CO_2 signal from non-dope DLC maintained constant during the AO beam exposure. This result is consistent with the fact that linear erosion was confirmed by the frequency shift of DLC-coated QCM (not shown). In contrast, CO_2 intensity from Si-doped DLC decreased with AO fluences and it reached noise-level at the AO fluence of 1×10^{19} atoms/cm^2. Same trend was observed for the CO signal, but the CO intensity decreased more rapidly. These characteristic features were observed at all final angles observed.

3.2 SR-PES Analysis

Figure 7 (left panel) shows Si 2p core level spectrum of Si-doped DLC containing 10% of Si before AO exposure. A photoelectron peak is obvious at the binding energy of 101 eV. A strong shoulder is observed at 102.9 eV, which is 1.8 eV higher than the main peak. Figure 7 (right panel) shows the SR-PES spectra of Si-doped
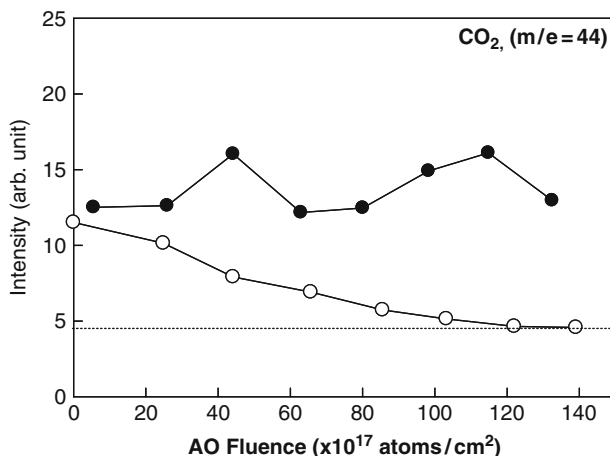
Fig. 6 Intensity variation of CO_2 signal from DLC under hyperthermal AO beam exposure. *Open circle*: Si-doped DLC, *filled circle*: non-dope DLC
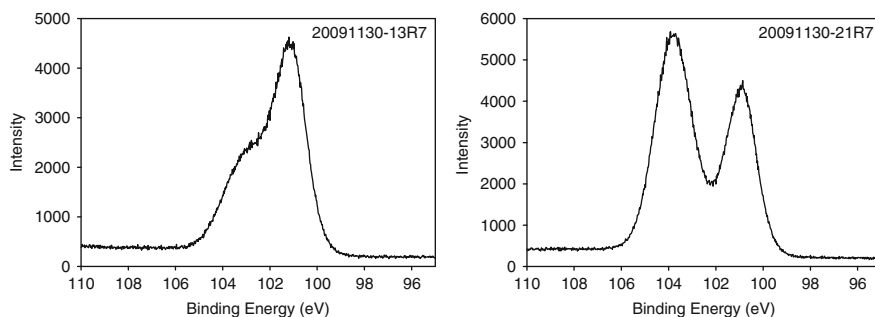
Fig. 7 SR-PES Si2p spectra of Si-doped DLC. *Left panel*: control, *right panel*: after exposure

DLC containing 10 % of Si after AO exposure. Total AO Fluence was estimated to be 1.5×10^{19} atoms/cm^2 before SR-PES measurement. Two peaks are clearly separated in the binding energies at 101 eV and 103.8 eV. Chemical shift of Si2p core level spectrum has been intensively studied. The peak deconvolution of Si 2p photoelectron spectra was performed with relative binding energies of 0.9–1.3 eV for Si^{1+}, 1.7–2.1 eV for Si^{2+}, 2.5–3.0 eV for Si^{3+} and 4.0–4.6 eV for Si^{4+} depending on the oxide thickness [7]. Details of the peak synthesis in this study were based on the previous studies [8].

The peak deconvolution results are summarized in Table 1. It was shown that 72% of Si atom remain in the SiC state (Si^{1+}) and 22 % of Si atom form SiCO (Si^{3+}). In contrast, after AO exposure, the major Si state is SiO_2 (Si^{4+}, 60 %). Depth profile of Si oxide states is analyzed by changing the take-off angle of photoelectrons. Figure 8 compares the Si 2p spectra of AO-exposed specimen collected with take-off angles of 0°, 30° and 60°. Photoelectron spectra in Fig. 8

Table 1 Atomic concentration of the Si states at the DLC surface before and after AO exposure

	Before exposure	After exposure
Si^{0+}	0	0
Si^{1+}	72	40
Si^{2+}	0	0
Si^{3+}	22	0
Si^{4+}	6	60
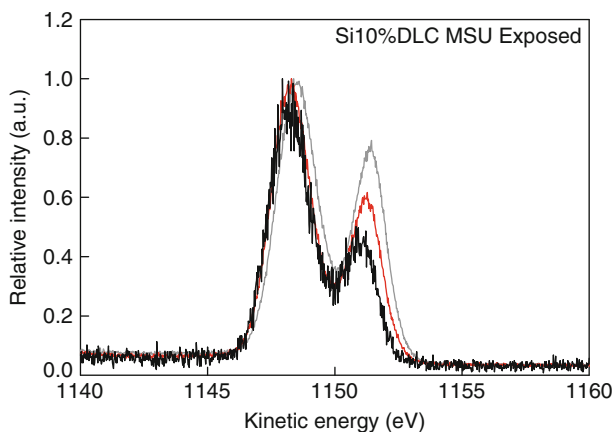
Fig. 8 Si 2p spectra of AO-exposed DLC measured with take-off angles of 0° (*gray*), 30° (*red*) and 60° (*black*)

are normalized to the peak height at 103.8 eV. It was clearly shown that the peak height of 101 eV decreases with increasing the take-off angle of photoelectrons. This spectroscopic feature indicates that the Si atoms forming SiC (Si^{1+}) distribute deeper than the Si oxides (Si^{4+}), i.e., the topmost layer consists of mainly Si oxide.

Oxide thickness at the surface could be evaluated by the SR-PES spectra. With considering the simple model which assumes a homogeneous oxide layer at the top surface, relative intensity of photoelectron Si oxide is given by the following equation [9];

$$I_{oxide}/(I_{oxide} + I_{Si}) = 1 - \exp[-d/(\lambda \cos \phi)] \tag{1}$$

where, I_{oxide} and I_{si} are the intensities of photoelectron signal of oxide and metallic Si. d is the thickness of the oxide, λ is the mean free path of the photoelectron in Si oxide, and ϕ is the take-off angle of the photoelectron. Assuming the $\lambda = 3.2$ nm for SiO_2, the thickness of surface oxide layer is calculated to be 2.8 nm. This value agrees with the previous results for the minimum thickness of protective SiO_2 layer [9]. SR-PES analysis clearly indicated that the surface of Si-doped DLC was covered by SiO_2 layer which was formed when exposed to the AO beam. The SiO_2 layer formed at the top surface prevents direct reaction of AO and carbon atoms in DLC and plays a role of a protective layer of DLC film underneath.

4 Conclusions

It was clearly observed that CO and CO_2 were formed at the DLC surface when exposed to hyperthermal atomic oxygen. Desorption rates of CO and CO_2 are constant with AO fluence which reflects the constant erosion rate of DLC. In contrast, Si-doped DLC shows decrease in amount of CO and CO_2 from the surface with increasing AO fluence. This is the evidence that SiO_2 film formed at the DLC surface can prevent AO reaction with C atoms in DLC which leads to loss of DLC and contained hydrogen. Since a self-healing capability could be expected on Si-doped DLC, metal doping is a promising technology for space application of DLC.

References

1. Donnet C, Erdemir A (eds) (2008) Tribology of diamond-like carbon films: fundamentals and applications. Springer, New York
2. Vercammen K, Meneve J, Dekempeneer E, Smeets J, Roberts EW, Eden MJ (1999) Study of RF PACVD diamond-like carbon coatings for space mechanism applications. Surf Coat Technol 120–121:612–617
3. Anderson J, Erck RA, Erdemir A (2003) Frictional behavior of diamondlike carbon films in vacuum and under varying water vapor pressure. Surf Coat Technol 163–164:535–540
4. Tagawa M, Yokota K, Matsumoto K, Suzuki M, Teraoka Y, Kitamura A, Belin M, Fontaine J, Martin J-M (2007) Space environmental effects on MoS_2 and diamond-like carbon lubricating films -atomic oxygen-induced erosion-. Surf Coat Technol 202:1003–1010
5. Muromoto M, Yokota K, Tagawa M. Unpublished
6. Tagawa M, Muromoto M, Hachiue S, Yokota K, Matsumoto K, Suzuki M (2005) Hyperthermal atomic oxygen interaction with MoS_2 lubricants relevance to space environmental effects in low earth orbit -effects on friction coefficient and wear life-. Tribol Lett 18(4):437–443
7. Moulder J, Stickle WF, Sobol PE, Bomben KD (1995) In: Chastain J, King RC Jr (eds) Handbook of x-ray photoelectron spectroscopy. Physical Electronics, Inc, Eden Prairie
8. Tagawa M, Yokota K, Yoshigoe A, Teraoka Y, Shimura T (2006) A comparison of ultra-thin SiO_2 films formed by hyperthermal O-atom beam and rapid thermal oxidation; synchrotron radiation photoemission and crystal truncation rod scattering study. Appl Phys Lett 88:133512
9. Tagawa M, Yokota K (2000) Volume diffusion of atomic oxygen in α-SiO_2 protective coating. High Perform Polym 12(1):53–63

Measurement of Surface and Volume Resistivity for Silver Coated FEP Used for Spacecraft

Hirofumi Suda, Yasushi Yamano, Shinichi Kobayashi, and Kumi Nitta

Abstract This paper reports on surface and volume resistivity of thermal control materials used for spacecraft measured in atmospheric and vacuum conditions. The investigated materials included silver coated FEP samples with or without holes and with or without an adhesive layer. The volume and surface resistivity in vacuum were about 10^{16} Ωm and 10^{17}–10^{18} Ω, respectively, for the FEP samples with holes and an adhesive layer. The values of volume and surface resistivity were almost the same for the FEP sheet without the holes and the adhesive layer. From the electrical point of view, the resistivity of the FEP sheet with holes and an adhesive layer, under vacuum conditions, is equivalent to that without holes and the adhesive.

Keywords FEP • Surface resistivity • Thermal control materials • Vacuum • Volume resistivity

1 Introduction

A large variety of materials are used in spacecraft design, among them thermal control materials. These materials greatly contribute to the reliability of the spacecraft in severe space environments. Silver coated FEP (Fluorinated Ethylene-Propylene) is actually used as one of thermal control materials. It has superior heat control properties in addition to a range of other good properties such as wide temperature range, low sunlight absorption rate, high emissivity rate, being at the same time flexible, thin and strong. However, in regular conditions, FEP is an

---

H. Suda • Y. Yamano (✉) • S. Kobayashi

Saitama University, 255 Shimo-Okubo, Sakura-ku Saitama-Shi, Saitama 338-8570, Japan

e-mail: yamano@epower.ees.saitama-u.ac.jp

K. Nitta

Japan Aerospace Exploration Agency, Chofu, Tokyo 182-8522, Japan

insulator with high electrical resistivity. This feature causes the charge accumulation under the electron irradiation when it is used as a thermal control material in space environment. In some cases, it may cause electrical breakdown.

When the silver coated FEP is used as a thermal control material, the back is coated by an adhesive and holes are formed in the material. Therefore, it is necessary to examine the influence of the holes and the adhesive on the resistivity and to understand the basic characteristic of the resistivity of the silver coated FEP. In this paper we measured the surface and the volume resistivity in atmosphere and in vacuum for four kinds of silver coated FEP (with or w/o holes and with or w/o adhesive).

2 Measurement Method

Figure 1 shows experimental setup for the measurement of surface and volume resistivity in vacuum. The chamber is evacuated to 10^{-5} Pa by a turbomolecular pump. The stage is insulated from the chamber and connected to an external terminal by an electric cable. The movable probe, which is connected to another external electrical terminal, is positioned inside the chamber to measure the surface current or to connect the grounding of the electrode to the sample. DC voltage is applied to the upper central electrode of the sample. The current through the sample bulk or along the sample surface is measured by a picoammeter (ADVANTEST R8252) that provides current sensitivity up to 10^{-15}A. The samples were measured at applied DC voltages of 100, 150, and 200 V. The duration of the measurement was 50 min. The measurement in the vacuum was conducted under vacuum conditions of 10^{-5} Pa. The resistivity was calculated from the data at 50 min after the voltage application [1].

Figure 2 shows the electrode configuration for the measurement of surface and volume resistivity according to [1]. The electrodes consist of an inner (central) electrode; a guard electrode and a backside electrode that are deposited onto the sample by Au sputter coating. The sample structure (with or without the holes and the adhesive layer) is also shown schematically in Fig. 2.

Figure 3 shows the surface resistivity measurement circuit set-up. The guard electrode is connected to the picoammeter using the movable probe and the backside electrode is connected to the ground. A DC voltage is applied to the inner electrode. We measure the surface current Is and calculate surface resistivity from (1).

$$\sigma = \frac{P}{g} \frac{V}{I_s} [\Omega] \tag{1}$$

where V- is the applied voltage, Is - surface current, g - inter electrode distance, P - effective circumferential length.
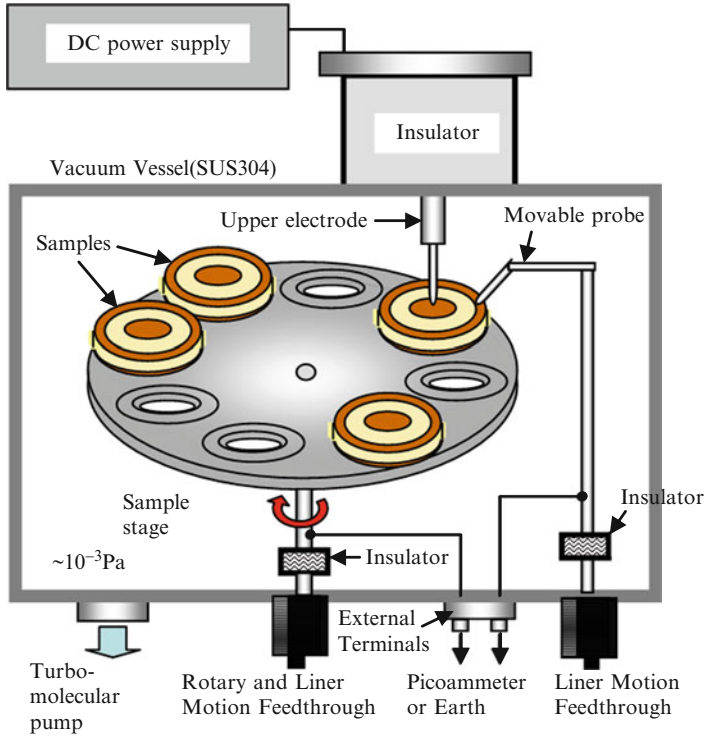
Fig. 1 Schematic of experimental setup for the measurement of surface and volume resistivity
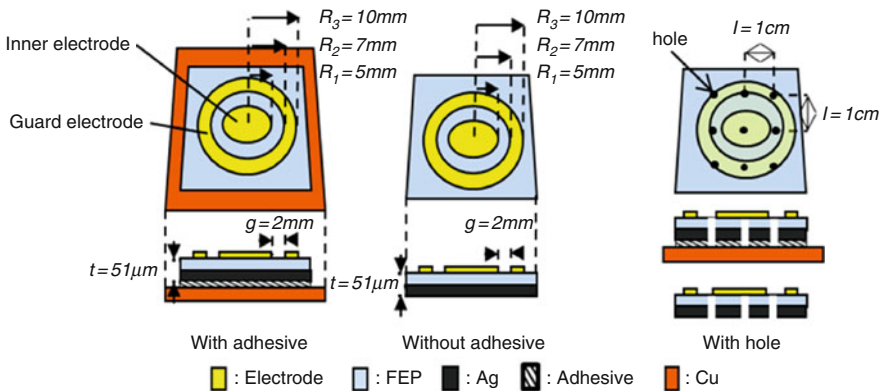
Fig. 2 Sample configuration

Figure 4 shows the volume resistivity measurement circuit set-up. In this case we can measure the current through the sample bulk by exchanging the cable of the picoammeter and the cable of the ground as shown in Fig. 3. The volume resistivity is calculated from (2), [2].
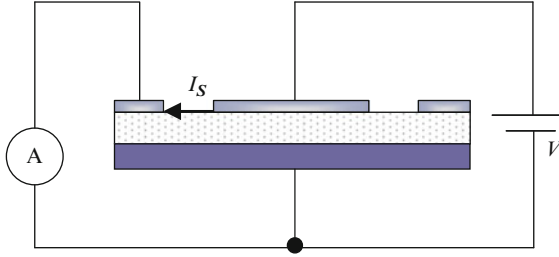
Fig. 3 Schematic presentation of the surface resistivity measurement circuit set-up
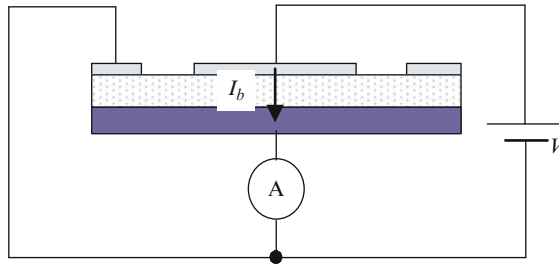
Fig. 4 Schematic presentation of the volume resistivity measurement circuit set-up

$$\rho = \frac{A}{t}\frac{V}{I_b}\,[\Omega m] \tag{2}$$

where I_b is the bulk current, t - sample thickness and A is the effective area.

3 Samples

Fluorinated Ethylene-Propylene (FEP) in sheet form was used as the sample material in the measurements. The thickness of the sample is 51 μm. To attach the FEP sheet to the spacecraft structure, the adhesive material is applied to the back side of the FEP sheet. The thickness of the adhesive layer is 58 μm. Samples B and D contained an array of holes punched in the sheets at 1 cm interval. Table 1 summarizes the information on the features of samples. Gold electrodes were deposited onto the sample surfaces by a sputtering process.

4 Results

Figures 5 and 6 show typical time charts of the bulk current for sample A and the surface current for sample C, respectively. As can be seen from Figs. 5 and 6, the absorption current, due to the polarization, flows in the beginning of the DC voltage

Table 1 Summary of sample features

Sample	Hole	Adhesive
A	×	○
B	○	○
C	×	×
D	○	×
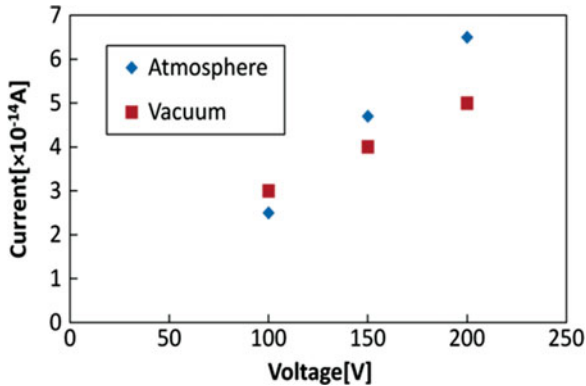
Fig. 5 Time dependence of bulk current as measured for atmospheric and vacuum conditions for sample A (applied voltage 100 V)
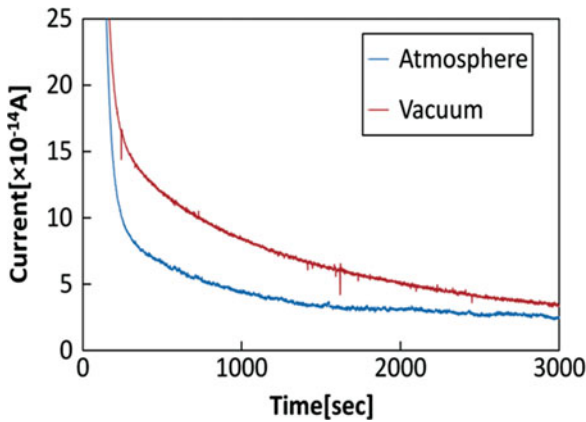
Fig. 6 Time dependence of surface current as measured for atmospheric and vacuum conditions for sample C (applied voltage 100 V)

application and decays with a certain elapsed time. The true conductive current flows stably and continuously after the sufficient decrease of the absorption current.

Figure 7 shows the relationship between applied voltage and bulk current for sample A under vacuum and atmospheric conditions. Since these bulk current characteristics are proportional to the applied voltage, it is found that they show ohmic conductivity under the applied electric field. The bulk current under vacuum condition almost coincide with that under atmospheric condition.
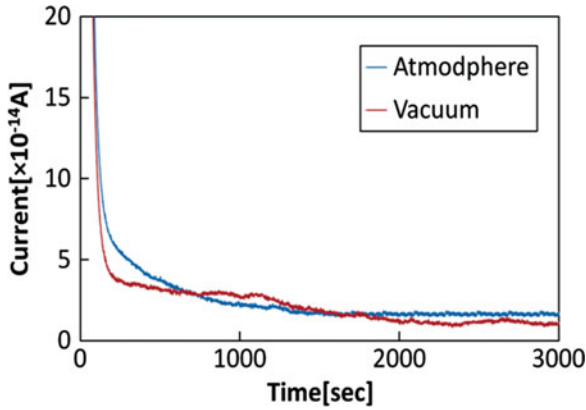
Fig. 7 Relation between applied voltage and bulk currents for sample A
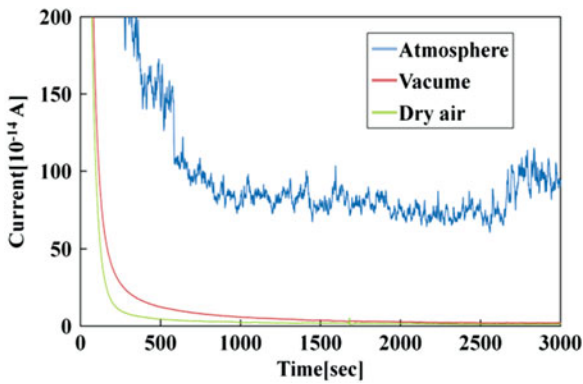
Fig. 8 Volume resistivity of each sample

Figure 8 shows volume resistivity for each sample. For samples A and C with no holes in the sample, the volume resistivities under atmospheric condition are not so different from those under vacuum condition. However, for sample D, with the holes, it is confirmed that the volume resistivity under atmospheric condition is lower than in vacuum conditions.

Figure 9 shows the comparison of bulk currents measured under atmospheric, vacuum and dry air condition for samples with holes. The current measured in dry air is almost the same as that in vacuum. However, the current measured at atmospheric conditions is higher than that under vacuum and dry air. The main reason for such results may be attributed to impurities such as water adhered or included in the holes.

Figure 10 shows the relationship between applied voltage and surface current for sample C under vacuum and atmospheric condition. Since these surface current characteristics are proportional to the applied voltage, it is found that they show
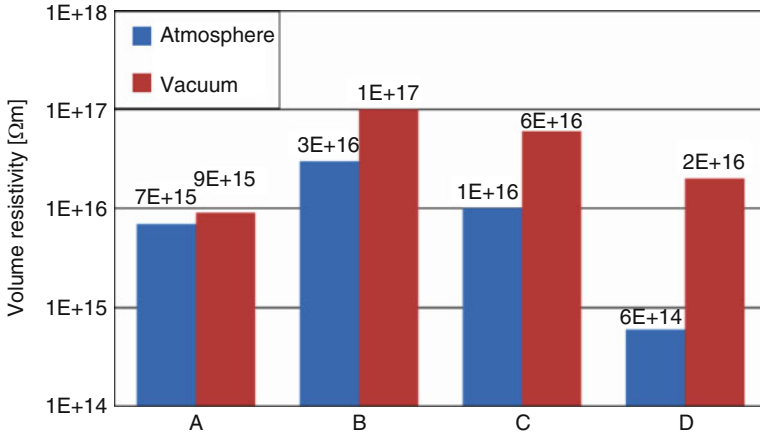
Fig. 9 Time dependence of bulk current at 200 V application for sample D
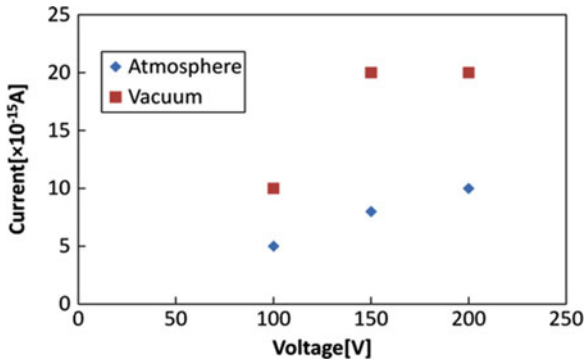
Fig. 10 Dependence of surface current (in vacuum and in atmosphere) on applied voltage for sample C

ohmic conductivity under applied electric field. Surface current under vacuum condition is higher than that under atmospheric condition.

Figure 11 shows surface resistivity for each sample. For samples A and B, which have adhesive in the back side, it was not possible to measure surface current accurately. For samples C and D, which have no adhesive on the back side, the surface resistivities under atmospheric condition are not different from those under vacuum condition.

Figure 12 shows an example of time dependence of surface current when a voltage is applied to a sample with a back adhesive layer. After the absorption current had decreased, surface current reached negative value. Though the cause of this property is uncertain, there is a possibility that the adhesive layer influences surface current characteristic.
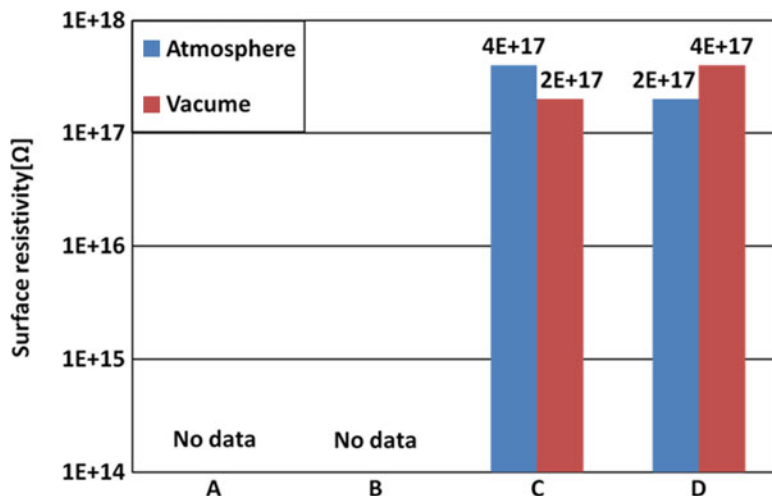
Fig. 11 Surface resistivity of each sample
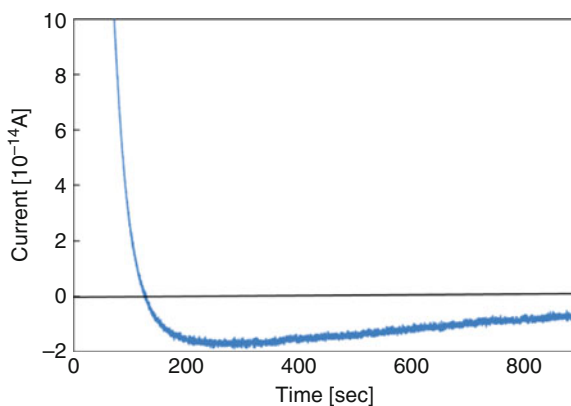
Fig. 12 Time dependence of surface current at 100 V application for sample A

5   Discussion

We have measured the volume and surface resistivity for FEP sample with or without holes and with or without adhesive under vacuum and in atmospheric conditions. The volume and surface resistivity of FEP sample are very high reaching $\sim 10^{16}$ Ωm and 10^{17}–10^{18} Ω, respectively. According to the obtained data for the sample with holes and adhesive, in vacuum conditions, these resistivities, practically, are not influenced by the presence of holes and the back adhesive. Generally, surface resistivity under atmospheric condition is quite lower than that under vacuum condition due to water vapor absorbed on the sample. However there

is almost no difference in surface resistivity for FEP sample without holes and adhesive between vacuum and atmosphere condition. Of course there is no difference in volume resistivity for it between vacuum and atmosphere condition. Note that the FEP sample with holes and adhesive has much different volume resistivity depending on the ambient condition, i.e. under atmosphere or vacuum condition, because of impurities such as water adhered or included in the hole.

6   Conclusions

This paper reported surface and volume resistivity under atmospheric and vacuum conditions for silver coated FEP used for spacecraft. The results are summarized as follows.

The volume resistivity is about 10^{16} Ωm under atmospheric and vacuum conditions.

Under vacuum conditions, it is not necessary to consider the influence of impurities such as water adhered in the hole. Therefore, there is practically no influence on the volume resistivity by the hole and the adhesive when using it under the space environment.

For samples without the adhesive, the surface resistivity is about 10^{17} Ω regardless of the presence of holes.

For samples with adhesive, because the adhesive might have some influence on the surface current, surface current can not be measured accurately.

When silver coated FEP is used as a thermal control material for spacecraft, it is not necessary to consider the influence of the holes and the adhesive on the resistivity used for the potential analysis.

References

1. Japanese Standards Association (2002) JIS handbook ceramics, vol 35, pp 140–207
2. Yamano Y et al (2008) Measurement of surface and volume resistivity for alumina ceramics under vacuum condition. In: Proceedings of the ISDEIV, Bucharest, Romania

Measurement of Quantum Efficiency for Spacecraft Materials and Noise Reduction of Photoelectron Current Waveform

Yuta Nanjou, Yasushi Yamano, Shinichi Kobayashi, Kumi Nitta, Hiroaki Miyake, and Kenji Ito

Abstract Photoelectron emission is one of important factors in analyzing the spacecraft potential. In order to calculate the spacecraft potential in a space environment, it is necessary to know the characteristics of the quantum efficiency of the materials use in spacecraft design. Quantum efficiency measurements of spacecraft materials have been carried out by irradiating them with a pulsed monochromatic vacuum ultraviolet light using the beam line 20A of the High Energy Accelerator Research Organization (KEK-PF). The photoelectron current from cover glass materials was measured in the range 30–200 nm. A system for reducing the nois was designed that enabled accurate measurements in longer wavelength range (near 200 nm). The quantum efficiency characteristics of the cover glass materials had shown that for longer wavelength their value decreased from the maximum value 0.13 electrons/photons at 30 nm.

Keywords Photoelectron emission • Quantum efficiency • Vacuum

Y. Nanjou • Y. Yamano (✉) • S. Kobayashi
Saitama University, 255 Shimo-Okubo, Sakura-ku, Saitama City, Saitama 338-8570, Japan
e-mail: yamano@epower.ees.saitama-u.ac.jp

K. Nitta
Japan Aerospace Exploration Agency, Chofu, Tokyo 182-8522, Japan

H. Miyake
Tokyo City University, 1-28-1 Tamazutsumi, Setagaya-ku, Tokyo 158-8557, Japan

K. Ito
High-Energy Accelerator Research Organization, 1-1 Oho, Tsukuba, Ibaraki 305-0801, Japan

1   Introduction

Recently, some accidents in spacecraft due to charging and discharging have been reported. To avoid such accidents, the intensive analysis and estimation of charging of satellites is required. The electrical potential of a spacecraft is determined by the incidence and emission of charged particles, such as ions, photoelectrons, and secondary electrons. Under the sunlight irradiation period, the photoelectron emission is the dominant process rather than the electrons irradiation from ambient plasma and the secondary electron emission. It is necessary to estimate the photoelectron current to analyze the potential of a spacecraft. To estimate the photoelectron current, characteristics of the quantum efficiency of spacecraft materials is necessary.

However, little data on the quantum efficiency of the spacecraft materials, especially insulating materials is available. In addition, it is difficult to measure accurately quantum efficiency of the insulating materials used in spacecraft because of the charge accumulation caused by photoelectron emission. We have carried out the quantum efficiency measurements of spacecraft materials aiming at obtaining accurate values. Nitta et.al reported the waveforms of the photoelectron emission current from cover glass of solar panel [1]. In that paper, the photoelectron currents were measured by irradiating the insulating material samples with a pulsed beam of vacuum ultra-violet light to reduce the effect of charging. However the measurements in the wavelength range from 150 to 200 nm were not good enough because of the relation of the waveforms of the photoelectron current to the noise signal coming from vibration of the experimental systems. Figure 1 shows the solar spectrum at a distance of 1 AU from the sun. Because the solar spectrum at 200 nm is 10^3 times stronger than it is at 30 nm, the data on quantum efficiency at around 200 nm is also important to take into consideration in analyzing the charge accumulation.

This paper reports on work conducted to reduce the noise on the waveforms of photoelectron current and on results on quantum efficiency of cover glass and gold.

2   Experimental System and Method

2.1   *Experimental System*

The synchrotron radiation source at beam line 20A of KEK-PF was used as a source of vacuum ultraviolet light (wavelength range of 30–250 nm). The schematic illustration of the experimental system is shown in Fig. 2. The light was transiently irradiated on the sample by a mechanical shutter to reduce charging on the surface of the insulating material. The duration for the open period of the mechanical shutter is 30 ms. The sample was fixed to a sample folder which is connected to
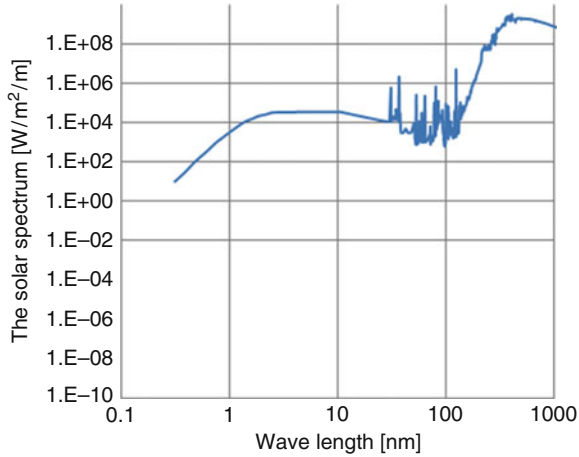
Fig. 1 The solar spectrum at a distance of 1 AU from the sun [2–6]
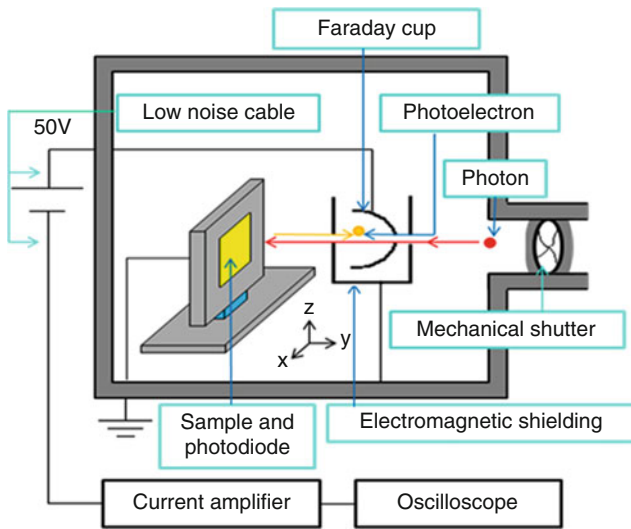
Fig. 2 The experimental system

the x-y-z stage. The Faraday cup to collect the photoelectrons emitted from the sample is connected to a feedthrough and biased to 50 V to collect the electrons. The photoelectron current signal is amplified and converted to a voltage waveform by the current amplifier (KEITHLEY 428 CURRENT AMPLIFIER). The amplification rate is 10^8 V/A. Although the sample holder and the Faraday cup are fixed in the vacuum chamber, due to various vibrational sources of the experimental system like the ground, the pumping system, etc. they experience some vibration. Such

vibrational gives rise to the distance change between the sample and the Faraday cup. This, in turn, gives rise to displacement current and thus appears as the noise on the waveform.

To eliminate or reduce substantially this factor, electromagnetic shielding was set around the Faraday cup to avoid changing the number of the electric field lines into it. In addition, the vibration of the experimental system is transferred to the coaxial cables that are used to transmit the photoelectron current between the BNC connector of the vacuum chamber to the amplifier. As a result, the dielectric material (Polyethylene) in the coaxial cable is charged generating the noise component. Therefore, a low noise cable was used for reducing noise caused by cable vibration.

2.2 Experimental Method

The synchrotron radiation is irradiated to the photodiode and the current I_P[A] is measured. The photon flux n_P [photons/s] is calculated from (1).

$$n_P = \frac{I_P}{ek} \tag{1}$$

Where, k [electrons/photons] is number of electrons generated when one photon enters photodiode. The value of k is given by National Institute of Standards and Technology (NIST). e[C] is elementary charge. A photoelectron current of the sample I_e [A] is measured and the number of photoelectron emitted at the unit time n_e [electrons/s] is calculated from (2).

$$n_e = \frac{I_e}{e} \tag{2}$$

The quantum efficiency QE [electrons/photons] of the sample is calculated from (3)

$$QE = \frac{n_e}{n_P} \tag{3}$$

The effect of the electromagnetic shielding and the low noise cable on the photoelectron current was examined by using a cover glass sample. In addition, the quantum efficiency of the cover glass and the gold which is used as the reference data was measured for the wavelength range of 30–200 nm.
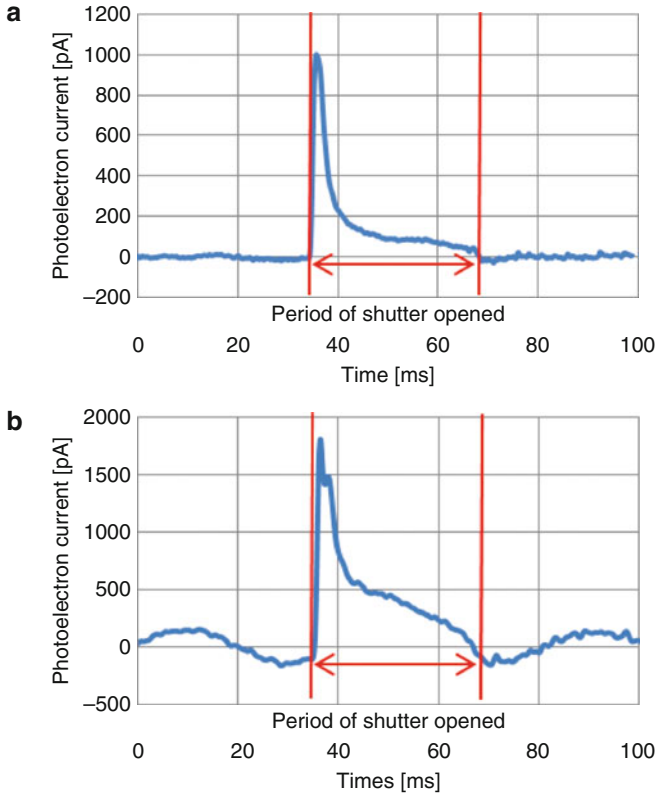
Fig. 3 Waveforms of photoelectron current for the cover glass at 50 nm irradiation. (**a**) Before noise reduction. (**b**) After noise reduction

3   Results and Discussion

3.1   *Effect of Noise Reduction*

The waveforms of photoelectron current for the cover glass with 50 nm irradiation are shown in Fig. 3. When the mechanical shutter is opened, transient photoelectron current is observed. After that, the current decays due to the charge accumulation on the cover glass. Noise current was in about 150pA without the electromagnetic shielding and the low noise cable. After setting up the electromagnetic shield and using the low noise cable, the noise was significantly reduced (Fig. 3b). With the noise reduction, the measurements of photoelectron current in the wavelength range of 180–200 nm became possible. The photoelectron current signal for the cover glass with the 200 nm irradiation is shown in Fig. 4. According to the obtained signal, the photoelectron current is quite low. It is difficult to measure the photo-electron current from the cover glass under the irradiation condition with
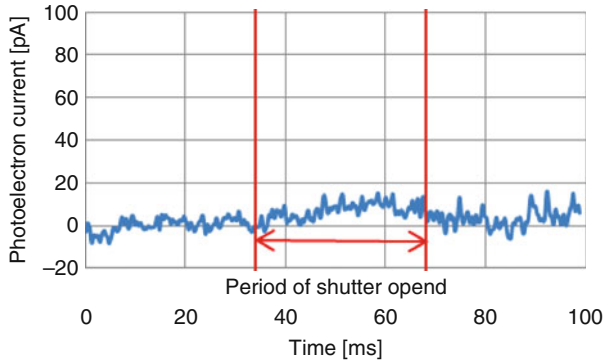
Fig. 4 Waveforms of photoelectron current for the cover glass at the 200 nm irradiation
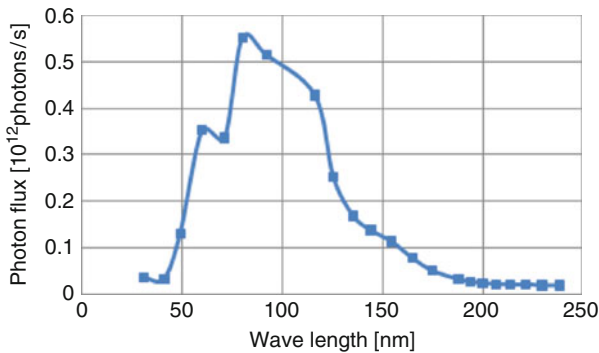
Fig. 5 Photon flux measured with the photodiode

wavelength longer than 200 nm, mainly because of a weak photon flux and the noise. Photon flux measured with the photodiode is shown in Fig. 5. The photon flux of the synchrotron radiation in 200 nm range was quite lower than in the 50–150 nm range in this beam line. If the data at wavelength longer than 200 nm are needed, a higher photon flux or lower noise level of the current measurement are necessary.

3.2   Quantum Efficiency of the Cover Glass and Gold

The quantum efficiency of the cover glass before and after the noise reduction is shown in Fig. 6. Quantum efficiency after the noise reduction exhibits the value of 0.13 electrons/photons at 30 nm, and decreases monotonically to ~0.02 at about 170–200 nm with longer wavelength. This result could be obtained by the noise reduction procedure. Quantum efficiency of the gold is shown in Fig. 7. Quantum efficiency exhibits the peak value of 0.7 electrons/photons, and approaches zero longer wavelengths.

In case of gold the measurements were possible up to 250 nm.
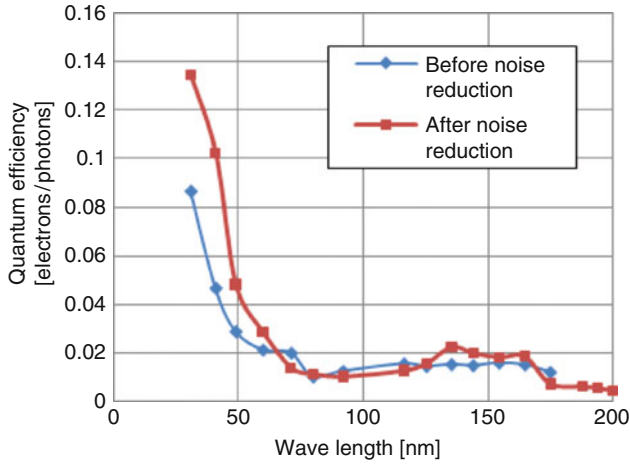
Fig. 6 Quantum efficiency of the cover glass
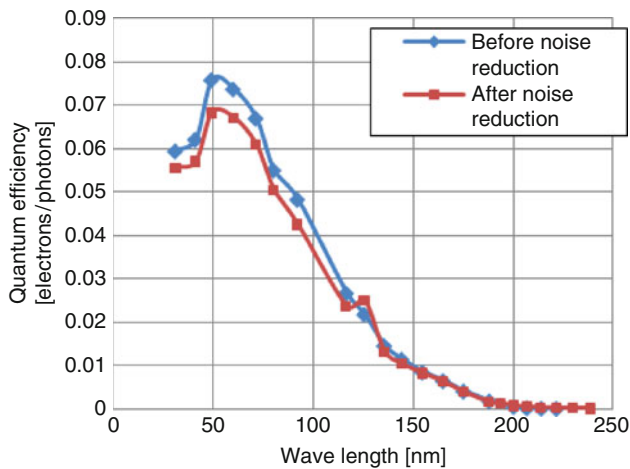
Fig. 7 Quantum efficiency of gold

3.3 Validity of Measurement Results

To compare obtained results with values published in literature, the horizontal axis of the wavelength in Fig. 7 is converted into the photon energy [eV]. The recalculated experimental values of quantum efficiency of gold are shown in Fig. 8 and the reference value [7] of quantum efficiency of gold is shown in Fig. 9. In the range of 10–25 eV (30–120 nm range), the obtained quantum efficiency of gold is 0.24 electrons/photons, while the reference value is
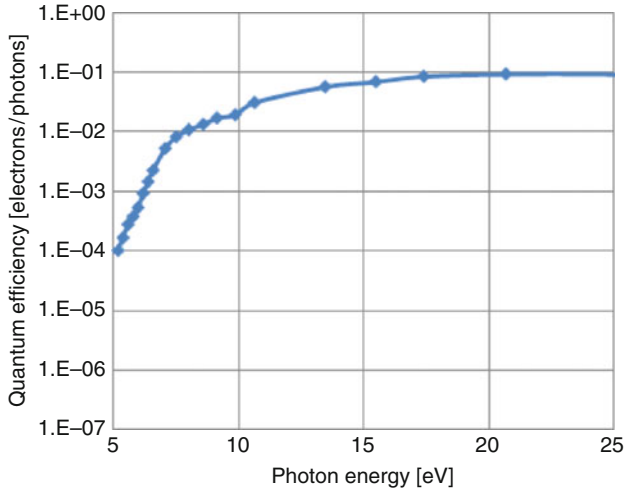
Fig. 8 Experiment value of the quantum efficiency of the gold
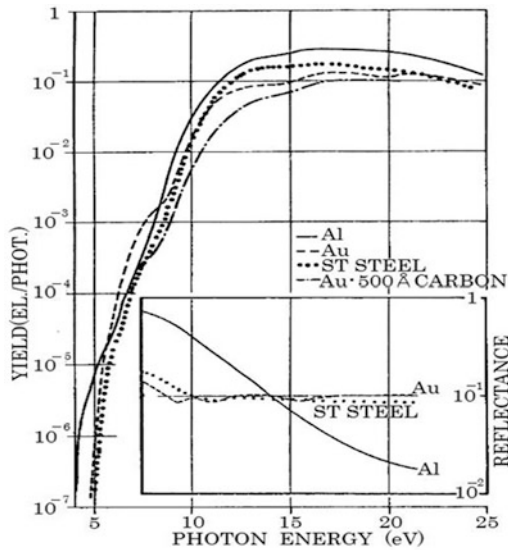
Fig. 9 Reference value of quantum efficiency of gold [7]

0.20 electrons/photons. Both values correspond to the range of 10–25 eV. However, in 5–10 eV (120–250 nm) range the obtained values are 100 times or more larger than the reference values. The difference of the data might be caused by the low level of the photon flux.

4 Conclusions

This paper described our efforts to reduce noise in the photoelectron current signal and on quantum efficiency measurements of the cover glass and gold conducted after noise reduction. The results can be summarized as follows.

1. Noise reduction in a photoelectron current signal was carried out by electromagnetic shielding and using a low noise cable.
2. It was not possible to measure the photoelectron current in the wavelength range longer than 200 nm because the photon flux in the used beam line was very low in that range.
3. Characteristic of quantum efficiency of the cover glass showed that the value decreased with the longer wavelength from the maximum value 0.13 electrons/ photons at 30 nm.
4. Quantum efficiency of gold exhibited the peak value of 0.7 electrons/photons and approached 0 at longer wavelengths.

References

1. Nitta K, Takahashi M, Miyake H, Yamano Y, Ito K (2010) A measurement of light intensity and quantum yield in photoelectron emission from satellite surface materials in the 30–250-nm range. In: Proceedings of the XXIVth ISDEIV, Braunschweig, Germany, vol 2, pp 540–542
2. Heath DF, Thekaekara MP (1997) The solar spectrum between 1200 and 3000 A. In: White OR (ed) Colorado Assoc Univ Press, Boulder, Table 1
3. Timsthy JG (1977) The solar spectrum between 300 and 1200 A. In: White OR (ed) Colorad Assoc Univ Press, Boulder, Table 1
4. Heath DF, Thekaekara MP (1977) The solar spectrum between 1200 and 3000 A. In: White OR (ed) Colorado Assoc Univ Press, Boulder, Table 2
5. Neckel H, Labs D (1981) Improved data of solar spectral irradiance from 0.33 to 1.25 μ. Sol Phys 74:P246, Table 2, x
6. Labs D, Neckel H (1968) The radiation of the solar photosphere from 2000A to 100 μ. Z f Astrophysik, vol 69, Table 7
7. Feuerbacher B, Fitton B (1972) Experimental investigation of photoemission from satellite surface materials. J Appl Phys 43(4):1563–1572

Microtribological Properties of Molybdenum Disulfide Bonded Film Exposed to Space Environment by SM/SEED Mission

Masahito Tagawa, Kumiko Yokota, Kunitaka Ochi, Masao Akiyama, Koji Matsumoto, and Mineo Suzuki

Abstract Macroscopic and microtribological properties of MoS_2 films exposed to atomic oxygen, ultraviolet rays and radiation both in low earth orbit (LEO) and in ground-based facility were evaluated. The MoS_2 samples are exposed to LEO space environment in the Space Environment Exposure Device (SEED) experiment on International Space Station (ISS). Laser-detonation atomic oxygen beam source was used for atomic oxygen simulation on the ground. It was found that the macroscopic friction coefficient of the flight sample was similar to that of the control sample. In contrast, remarkable increase in friction coefficient in microscopic properties was observed.

1 Introduction

The degradation of materials in extreme environment is a critical issue for the reliability of mechanical systems in space. Especially, in low Earth orbit (LEO) environment, various factors (e.g.; atomic oxygen, ultraviolet rays and radiation) affect materials greatly. In order to evaluate the effect of real space flight environment on the materials, several materials for space applications were exposed

M. Tagawa (✉) • K. Yokota • K. Ochi
Graduate School of Engineering, Kobe University, Kobe 657-8501, Japan
e-mail: tagawa@mech.kobe-u.ac.jp

M. Akiyama
IHI Aerospace Co., Ltd., Tomioka Gumma 370-2398, Japan

K. Matsumoto • M. Suzuki
Japan Aerospace Exploration Agency, Chofu, Tokyo 182-8522, Japan

to LEO space environment on Service Module/Space Environment Exposure Device (SM/SEED) experiment aboard the international space station (ISS) [1].

One of the target materials to be evaluated in SM/SEED was a molybdenum di-sulfide (MoS_2) film that is widely used as a solid lubricant based on its excellent properties in vacuum. Various evaluations of surface and tribological properties of MoS_2 have been performed in LEO environment [2, 3] and in ground-based atomic oxygen exposure facilities [4, 5]. In these reports, surface oxidation by atomic oxygen was commonly reported, however, different results related to friction coefficient and wear life have been reported [6, 7]. These reports are focused mainly on practical space applications so that macroscopic tribological properties have been evaluated. However, future small-size spacecraft needs different tribological properties, i.e., microtribological properties. It has been well known that macroscopic and microscopic tribological properties may differ in properties.

In this study, microtribological properties of the MoS_2 film, relevant to micro/nano satellites, exposed to atomic oxygen, UV and radiation both in LEO and in ground-based facility were evaluated.

2 Samples and Experiments

The MoS_2 samples used in this study are commercially available organic binder-type MoS_2 films (HMB34, Kawamura Research Laboratory Inc.) deposited on a titanium substrate. Polyamide-imide is used for the organic binder. The MoS_2 constitutes about 65 % of the film. The film thickness was about 10 μm.

Each SM-SEED pallet includes four MoS_2 specimens. Three pallets were launched in August 21, 2001 and have been attached to the outside of the Russian service module of ISS on October 10, 2001. Figure 1 shows the image of the three pallets attached to the SM of ISS. The first SM-SEED pallet was retrieved to inside the ISS on August 26, 2002 (Exposure: 315 days). Exposures of the second and third pallet were terminated on February 27, 2004 (865 days) and August 18, 2005 (1,404 days).

In this study, MoS_2 specimens exposed to LEO for 1-year and 2-years were used. The space environment that the specimens are facing is strongly dependent on the ISS attitude and orbit. During the first year, average altitude of ISS was 386.6 km with inclination of 51.6°. ISS attitude was 59 % in XVV (x-axis in velocity vector) and 41 % in XPOP (x-axis perpendicular to orbital plane). Table 1 presents the environment factors, atomic oxygen, ultraviolet rays and radiation, as calculated from the altitude and attitude of the ISS. Atomic oxygen fluence was evaluated both by polyimide and carbon films. Polyurethane film was used for ultraviolet measurement. Radiation was analyzed by three different methods; thermo luminescent dosimetry, alanine dosimetry and radiation sensitive field effect transistor.

On the other hand, the same type of specimens was also used for ground-based experiment, which simulates the space environment for 1- and 2-years in orbit.
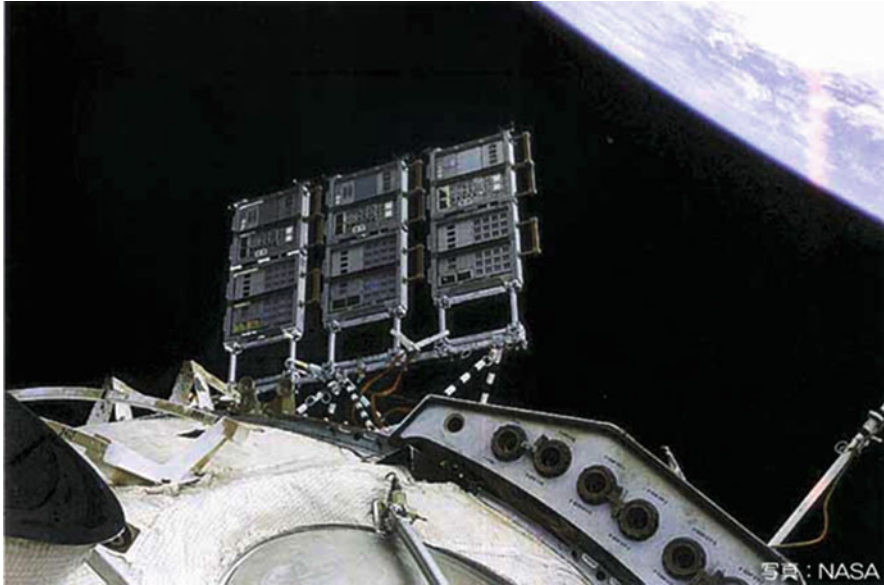
Fig. 1 SM-SEED pallets located at the exterior of ISS in low Earth orbit

Table 1 Fluencies of ultraviolet, electrons and atomic oxygen on the SM-SEED flight sample evaluated by monitoring materials (1 year in orbit)

Atomic oxygen (atoms/cm^2)	2.3×10^{20} to 6.6×10^{21}
Ultraviolet (ESD)	1–3
Radiation (Gy)	0.4–65

The samples were individually exposed in ground-based facilities to atomic oxygen, ultraviolet and electron fluxes. Laser detonation atomic oxygen beam source was used for atomic oxygen simulation (1.3E21 and 3.7E21 atoms/cm^2). VUV from deuterium lamp (35 and 69 ESD) and high-energy electron beams (1.6E16 and 3.3E16 electrons/cm^2) were used for simulating UV and radiation conditions in LEO [8]. Surface analysis of the exposed samples was performed by Auger electron spectroscopy (AES) and X-ray photoelectron spectroscopy (XPS). Scanning electron microscopy and electron dispersive X-ray spectroscopy were also utilized. Macroscopic tribological properties were evaluated by a ball-on-disc type friction tester in vacuum. SUS440C ball (R = 4.8 mm) is used. Load and speed of the sliding were 2.0 N and 2.2 mm/s, respectively [8].

Microtribological properties were analyzed by friction force microscopy (FFM) with a Si cantilever in ambient air condition. Friction force was calculated from the difference in torsion signal (d_{trace}) of the Si cantilever using (1) below:

$$F_t = \frac{S_{input}k_\varphi k_z(h + t/2)}{C_n \eta S_{A+B}} d_{trace} \qquad (1)$$
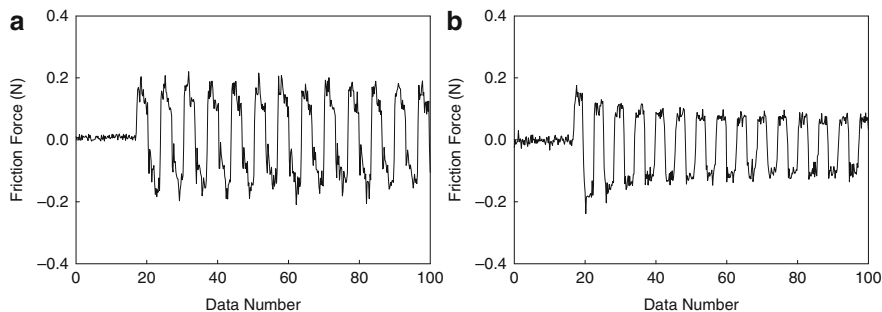
Fig. 2 Typical friction force traces of the MoS$_2$ samples. (**a**) Control and (**b**) flight sample (2 years in orbit)

where, S_{input} is the sensitivity factor of torsion of the cantilever, kj, kz are the spring constants of the cantilever for the direction of torsion and bending, respectively. h and t are the height and thickness of the cantilever. C_n, h, and S_{A+B} are the constants for converting the output of position sensitive detector to the friction force. The friction coefficient was evaluated by friction forces with different applied loads. Load and speed of the sliding were 0–700 nN and 500 nm/s, respectively.

3 Results and Discussion

3.1 Macroscopic Friction Coefficient

Friction coefficient of the selected sample is evaluated by the vacuum friction tester. Typical friction force of the control and flight samples are shown in Fig. 2. The friction coefficient of the flight sample (Fig. 2b) is divided into two parts; an initial friction and steady-state friction. Table 2 lists initial and steady-state frictions of each exposure condition. It is obvious that the friction coefficient of all samples is distributed between 0.03 and 0.06 except for UV-exposed sample; the UV-exposed sample showed lower friction coefficient compared to the other samples. This is considered to be due to the UV-induced hardening effect of polyamide-imide. It was, thus, concluded from the first and second year results that the space environment including silicon contamination does not affect tribological properties of the organic binder-type MoS$_2$ lubricant greatly. In more detail, the friction coefficient of the flight samples was even lower than the control sample.

3.2 Microscopic Tribological Properties

Figure 3 shows the topographic and friction force images of the control sample. Scanning area is 500 × 500 nm. MoS$_2$ pigment is shown as a hillock with 10 nm in

Table 2 Macroscopic friction coefficients of the MoS_2 samples exposed to simulated/real space environments

Sample	Initial friction coefficient	Steady-state friction coefficient
Control	0.059	0.033
UV-exposed	0.039	0.018
AO-exposed	0.063	0.031
Flight sample, (1 year in orbit)	0.047	0.024
Flight sample (2 years in orbit)	0.062	0.027
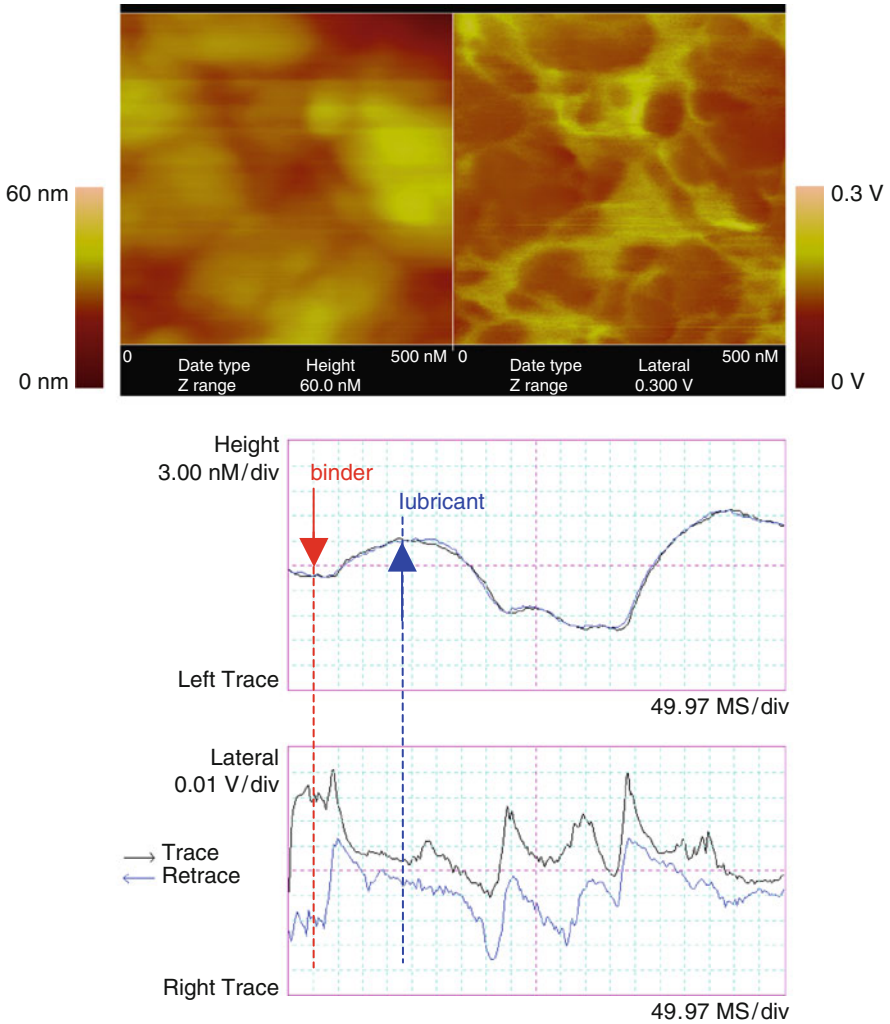
Fig. 3 Topographic (*upper left panel*) and friction force (*upper right panel*) images of the control sample. Scanning area is 500 × 500 nm. *Lower panel* shows the cross sectional data of the height and lateral force
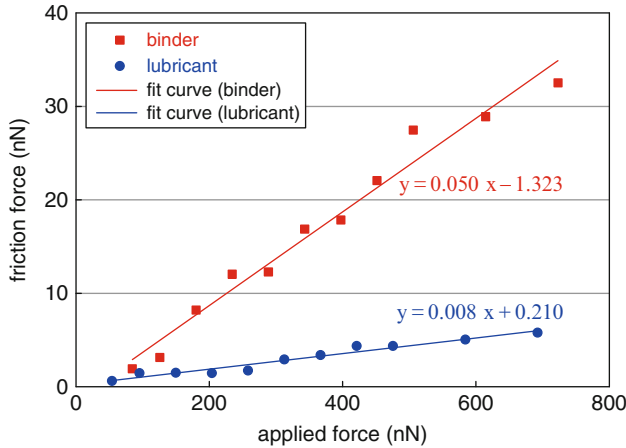
Fig. 4 The relationship between applied load and friction force for control sample calculated from (1). The *squares* are the data at the binder area and the *circles* are those at MoS$_2$ pigment. The *lines* are linear regression results

height in the topographic image. In the corresponding friction force trace image, low-friction is obvious at the MoS$_2$ pigment. Figure 4 shows the relationship between applied load and friction force calculated from (1). Squares are the data at the binder area and circles are those at MoS$_2$ pigment. Solid lines are linear regression results. A good linear relationship between applied load and friction force is observed both on MoS$_2$ pigment and binder. The calculated friction coefficients are 0.008 on the MoS$_2$ pigment and 0.05 on the binder.

The same analysis was applied for the retrieved samples and samples exposed in the ground-based facilities. Figure 5 shows the topographic and friction force images of the MoS$_2$ sample exposed to LEO for 1-year. Figure 6 indicates the relationship between applied load and friction force calculated from (1). A good linear relationship between applied load and friction force is also observed both on MoS$_2$ pigment and binder. The calculated friction coefficients are 0.03 for MoS$_2$ pigment and 0.08 for binder. The friction coefficients measured at the MoS$_2$ pigment and binder, for all samples, are summarized in Table 3. It is found that the friction coefficient of the flight and atomic oxygen-exposed samples are one order of magnitude greater than that of the control sample. On the other hand, the macroscopic friction coefficient of the same sample does not show remarkable change as shown in Table 2. Thus, it is experimentally demonstrated that the microscopic tribological properties with a small load of MoS$_2$ lubricants are easily affected by the space environment compared with the macroscopic properties. This is due to the fact that the microtribological properties are more sensitive to the surface oxidation, because of no delamination of oxide layer was expected.

Thus, the tribological systems on future small satellites would be more sensitive to space environments compared with conventional satellites.
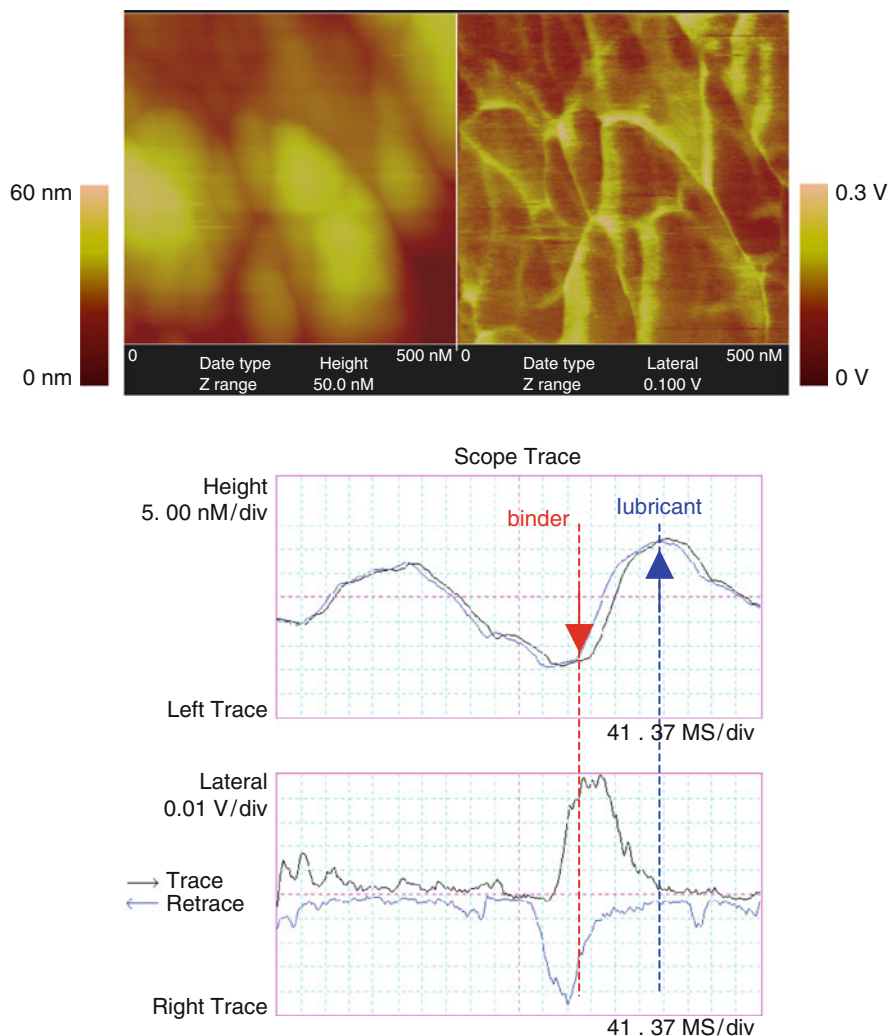
Fig. 5 Topographic (*upper left panel*) and friction force (*upper right panel*) images of the 1-year flight sample. Scanning area is 500 × 500 nm. *Lower panel* shows the cross sectional data of the height and lateral force

4 Conclusions

Surface and tribological properties (macroscopic and microscopic) of MoS_2-based lubricants that were exposed to real low Earth orbit space environment are analyzed. It is found that the friction coefficient of the flight sample is similar to that of control sample for macroscopic test ($\mu = 0.03$). This is due to the delamination of oxidized layer. However, increase in friction coefficient is detected in
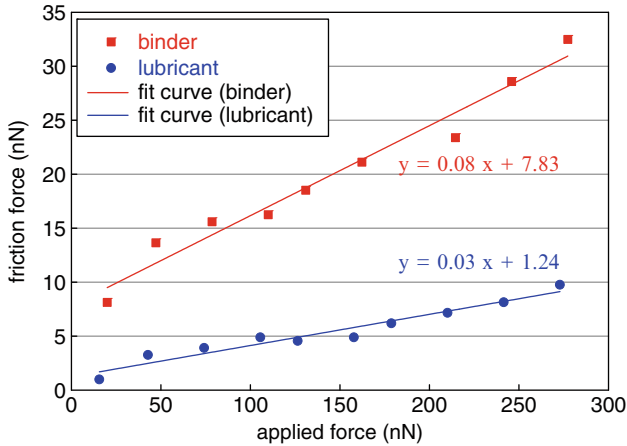
Fig. 6 The relationship between applied load and friction force calculated by the (1) for 1-year flight sample. The *squares* are the data at the binder area and the *circles* are those at MoS_2 pigment. The *lines* are linear regression results

Table 3 Microscopic friction coefficients of the 1-year flight MoS_2 samples at MoS_2 pigment and binder

Sample	MoS_2 pigment	Binder
Control	0.008–0.013	0.05
UV-exposed	0.06	0.1–0.13
AO-exposed	0.2–0.3	0.2–0.4
Flight sample, (1 year in orbit)	0.03–0.05	0.08–0.1
Flight sample (2 years in orbit)	0.05–0.08	0.15–0.19

microtribological tests ($\mu = 0.008$ to 0.03). It was demonstrated that tribological systems on future micro/nanosatellites are sensitive to space environments.

References

1. Papers in the proceedings of international symposium on SM/MPAC-SEED experiment, JAXA-SP-08-015E, (2008) Tsukuba, Japan
2. Dursch H, Keough B, Pippin G (1992) In: Proceedings of the LDEF-69 month in space second post-retrieval symposium, 1041, San Diego, CA, USA
3. Dugger MT (1993) Tribology and surface chemistry of sputtered MoS_2 solid lubricants exposed to atomic oxygen. In: Chung SY et al (eds) Flight-and ground-test correlation study of BMDO SDS materials, phase 1 report. JPL Publication, Pasadena CA, USA, 93-31, A1

4. Yamaguchi M, Hosoya T, Nishimura M (1989) Effect of atomic oxygen irradiation on tribological properties of sputtered MoS_2 film. In: Proceedings of the 34th JAST tribology conference, Toyama, Japan, p 661
5. Tagawa M, Ikeda J, Ninomiya Y, Umeno M (1998) Protection of space materials from the space environment. In: Kleiman JI, Tennyson RC (eds) Proceedings of the ICPMSE-4, fourth international conference, Toronto, 23–24 Apr 1998. Space technology proceedings, vol 4, Kluwer
6. Cross JB, Martin JA, Pope LE, Koontz SL (1990) Atomic oxygen-MoS_2 chemical interactions. Surf Coat Technol 42:41
7. Wei R, Wilbur PJ, Bughholz BW, Kustas FM (1995) In situ tribological evaluation of greases and solid lubricants in a simulated atomic oxygen environment. Tribology Transac 38:950
8. Matsumoto K, Tagawa M, Akiyama M (2008) Protection of materials and structures from the LEO space environment. In: Kleiman JI (ed) Proceedings of the 9th international space conference, Toronto, 20–23 May 2008. Published by AIP conference proceedings 1087, 148

Extreme Ultraviolet Emission from a Carbon Dioxide Laser-Sustained Oxygen Plasma

Akira Mizutani, Kazuhiro Kishida, Kumiko Yokota, Masahito Tagawa, Hiroyuki Shimamura, Yugo Kimoto, Mayuko Koga, and Hiroaki Nishimura

Abstract Extreme ultraviolet (EUV) spectrum emitted from laser-sustained oxygen plasma in a laser detonation atomic oxygen beam source was investigated. In order to measure EUV spectra, specially designed flat-field grazing-incidence EUV spectrometer was designed. The EUV spectra were recorded on an imaging plate which provides quantitative analysis capability. It was confirmed that EUV emission in the range of 20 –50 nm was included in the emission from laser-sustained oxygen plasma in a laser detonation source. The experimental results clearly indicated that the EUV intensity depends strongly on the translational energy of atomic oxygen. Even though the effect of EUV on the material erosion has not been confirmed, presence of high-energy photon need to be considered for better understanding of the reaction of hyperthermal atomic oxygen in the ground-based facility.

Keywords Atomic oxygen • EUV • Ground simulation • Space environment

1 Introduction

Space shuttle and international space station (ISS) are orbiting in low Earth orbit (LEO) which is 200–500 km above the sea level. Many environmental factors exist in LEO such as thermal cycling between $-150\,^{\circ}\mathrm{C}$ and $200\,^{\circ}\mathrm{C}$, ultraviolet, high vacuum, space debris, microgravity, radiation and neutral species. It has

A. Mizutani (✉) • K. Kishida • K. Yokota • M. Tagawa
Graduate School of Engineering, Kobe University, Kobe 657-8501, Japan
e-mail: tagawa@mech.kobe-u.ac.jp

H. Shimamura • Y. Kimoto
Aerospace Research and Development Directorate, Japan Aerospace Exploration Agency,
Tsukuba 305-8505, Japan

M. Koga • H. Nishimura
Institute of Laser Engineering, Osaka University, Suita, Osaka 565-0871, Japan

been well known that the major composition of upper atmosphere of the Earth is atomic oxygen which is formed by the photo-induced decomposition of oxygen molecules. Spacecraft traveling in LEO collides with atomic oxygen at a relative velocity of 8 km/s which corresponds to an orbital velocity of spacecraft. Because of such high collision velocity, the collision energy of atomic oxygen reaches values as high as 5 eV that is higher than the interatomic bonding energy of many materials. In the mid 1980s, it was discovered that many polymeric materials used in the spacecraft were eroded by the collision with atomic oxygen. Many flight experiments have been conducted to study the reaction efficiency of spacecraft materials with atomic oxygen, for example Evaluation of Oxygen Interactions with Materials 3 (EOIM-3). It was reported that reactive efficiency of fluorinated polymer was 1/60 and 1/88 of that of polyimide and polyethylene, respectively [1]. Similar results are reported by many flight experiments and it was believed that the survivability of fluorinated polymers, such as fluorinated ethylene propylene (FEP) Teflon, in the atomic oxygen environment in LEO was much higher than that of hydrocarbons such as polyimide. In contrast, it was reported that the erosion rate of fluorinated polymer measured in the ground-based experiments using laser detonation atomic oxygen beam source as well as other type of sources was much higher than that measured in LEO [2]. This is one of the major problem to study the ground-based atomic oxygen tests, i.e., quantitative discussion on the survivability of materials cannot be made through ground-based researches. The origin of the remarkable inconsistency in erosion rates of fluorinated polymer is considered due to the effect of ultraviolet emission from the oxygen plasma. Therefore, synergistic effect of atomic oxygen and ultraviolet, especially in vacuum ultraviolet region has been studied by several groups [3]. However, the UV emission characteristics from the oxygen plasma have not been fully performed, i.e., only limited wavelength regions were measured in the previous study [4].

On the other hand, photon emission from a laser-sustained plasma has been intensively studied relating to the development of new generation light source for semiconductor lithography. Extreme ultraviolet lithography (EUVL) is the most promising technology for next generation lithography [5]. To generate EUV emission, gas-jet-target laser plasma source have been intensively studied. This type of EUV source has a very similar configuration with laser-detonation atomic oxygen beam source used for space environmental simulation studied. A similarity of configuration of the facility arises the question that EUV emission (high energy UV, photon energies approximately 20–40 eV) might be involved in the photons from a laser-sustained oxygen plasma in the laser-detonation beam source used for atomic oxygen simulation.

In this paper, we measured EUV spectra (5–50 nm) from laser-sustained oxygen plasma in the laser detonation atomic oxygen beam source. The relationship between atomic oxygen beam energy and the EUV intensity is also studied.
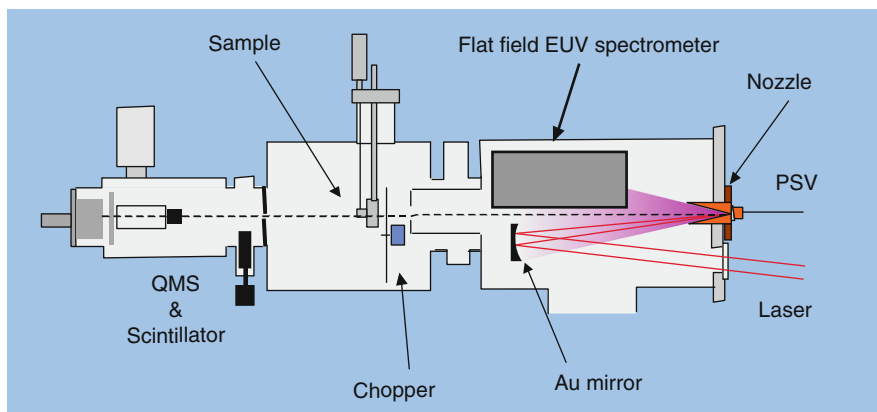
Fig. 1 Schematic drawing of the laser detonation hyperthermal atomic oxygen beam source used in this study

2 Experiments

2.1 *Atomic Oxygen Beam Facility*

Figure 1 shows the laser detonation hyperthermal atomic oxygen beam source used in this study. The atomic oxygen source is based on the laser breakdown phenomenon and was originally invented by Physical Science Inc. This method could simulate the collision energy of atomic oxygen with materials in LEO (approximately 5 eV). The atomic oxygen beam was generated by shooting a focused CO_2 laser light (typically 5–6 J/pulse) into an oxygen gas-jet introduced by a pulsed supersonic valve. The high-temperature laser-sustained oxygen plasma expands in the conical nozzle and forms a supersonic broad atom beam. The velocity and the composition of the beam thus formed were analyzed by a quadrupole mass spectrometer (QMS) with a scintillation detector. Figure 2 represents typical time-of-flight (TOF) spectrum of the m/e = 16 species in the atomic oxygen beam. Time zero corresponds to the moment when CO_2 laser emits the pulse. Thus the signal at t = 0 μs corresponds to the photon signal from the oxygen plasma in the nozzle. A large peak is obvious at t = 300 μs which comes from atomic oxygen pulse (m/e = 16) formed by the laser-induced decomposition and acceleration of the oxygen gas.

2.2 *EUV Spectrometer*

Figure 3 shows the photograph of grazing-angle flat-field spectrometer developed in this study. This spectrometer includes a grating with 1,400 line/mm. This spectrometer design was based on that reported by Kita [6], however, it was designed specifically
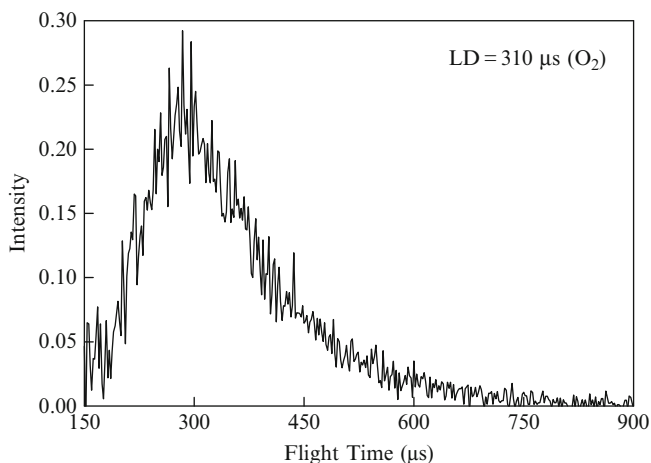
Fig. 2 Typical time-of-flight (TOF) spectrum of the m/e $= 16$ species in the atomic oxygen beam
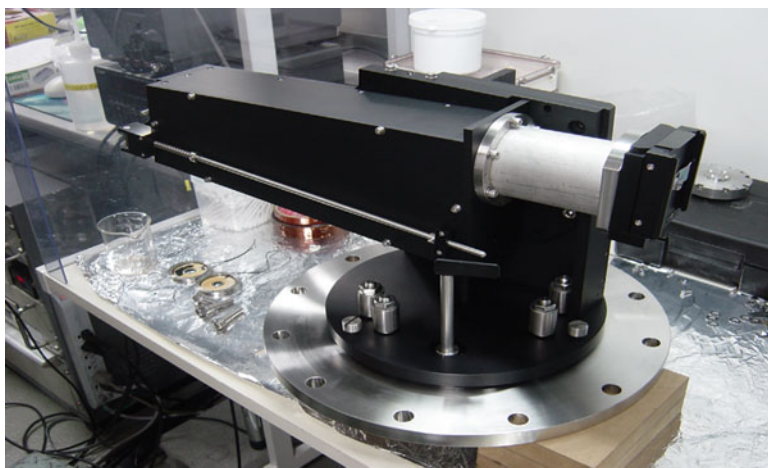
Fig. 3 Photograph of the grazing-angle flat-field spectrometer developed in this study

for the beam facility at Kobe University in order to measure the TOF and EUV spectra, simultaneously. The basic configuration of the spectrometer is shown in Fig. 4. The incident angle was settled to be 87°, and entrance slit and shutter were located at 237 mm from the grating. An imaging plate, located at the spectral plane, located 235 mm from the grating, was used for the detection of the EUV spectrum.
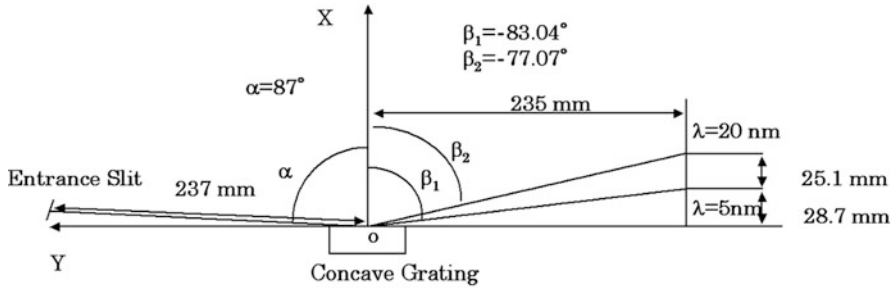
Fig. 4 Basic configuration of the spectrometer
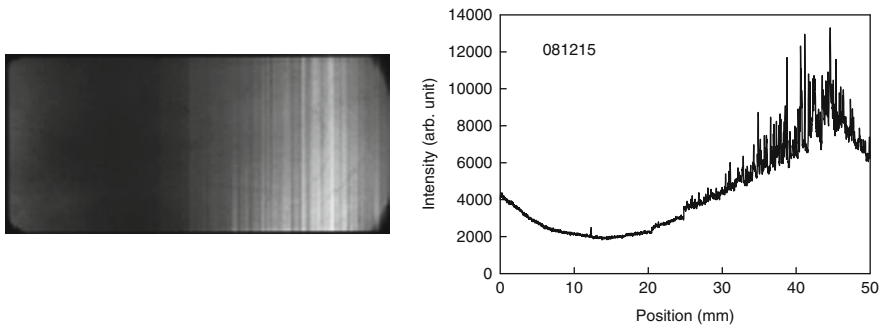
Fig. 5 Recorded EUV emission on an imaging plate from Ar plasma (*left*) and line profile (*right*)

2.3   Calibration of the Spectrometer

The grazing-angle flat-field spectrometer was calibrated by the Ar plasma. This is due to the fact that the number of spectral lines from Ar plasma (42 lines between 20 and 50 nm) is less than that from oxygen plasma (729 lines between 20 and 50 nm). Figure 5 represents the image recorded on an imaging plate exposed to Ar plasma and its line profile. According to the NIST database [7] and the basic design by Kita, spectral lines in Fig. 5 are characterized to the electron transition of *3s3p – 3s4p* (25 nm) *3s²3p – 3s²4s* (29 nm) and *2p⁶3d – 2p⁶4p* (33 nm), respectively. From the calibration by Ar, the position on the imaging plate and the wavelength were correlated by the formula shown below:

$$\lambda = 88 \times \exp(-24.1/X) - 0.726 \tag{1}$$

where, λ is the wavelength in nm and X is the position from the edge of the exposed area on the imaging plate (mm). Wavelengths of the spectral lines in all follow up experiments were defined using (1).
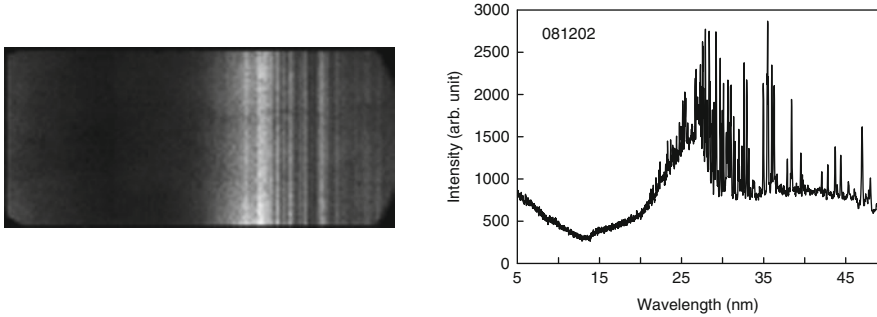
Fig. 6 Recorded EUV emission on an imaging plate from oxygen plasma (*left panel*) and corresponding EUV spectrum that was analyzed with the help of (1) (*right panel*)

3 Results and Discussion

3.1 EUV Spectrum from Oxygen Plasma

Figure 6 represents the image of exposed imaging plates and corresponding spectrum analyzed using (1). This spectrum was taken at the following conditions: PSV voltage: 1 kV, PSV opening time 400 μs, oxygen backpressure: 0.2 MPa, laser power: 6.3 J/ pulse. AS can be seen from Fig. 6 (right panel), many spectral lines are present in the range of 25–45 nm, i.e., 25, 26, 28, 29, 30, 31, 32, 34, 35, 43 and 45 nm. These spectral lines are due to the electron transition of *2p – 3d* orbits. In contrast, no strong emission is measured in the wavelength range 10–15 nm.

The TOF distribution measured simultaneously with the EUV emission is presented in Fig. 7. The velocity of atomic oxygen is approximately 8 km/s that corresponds to the relative collision velocity in LEO. A peak near 100 μs is coming from the charged particles in the beam, since it is obvious even after the electron impact ionizer of the QMS off. Analyzing the data in Figs. 6 and 7 obtained in 8 km/s atomic oxygen ground tests, it can be concluded that EUV radiation with wavelength range 20–30 nm (photon energy > 30 eV) is present in the photon emission from the oxygen plasma.

3.2 Correlation Between EUV Spectrum and TOF Distribution

A series of EUV and TOF spectra were measured with various laser delay timings that influence the velocity of atomic oxygen beam. Figure 8 shows TOF distributions of atomic oxygen beam with translational energies of (a): 2.6 eV, (b): 3.9 eV, (c): 4.2 eV, (d): 4.9 eV, (e): 6.2 eV and (f): 7.5 eV, respectively. Figure 9 indicates the corresponding EUV spectra measured simultaneously with TOF spectra shown in Fig. 8. It was clearly confirmed that the peak wavelength is

Fig. 8 TOF distributions of atomic oxygen beams. Translational energies of the beam are calculated to be (**a**) 2.6 eV, (**b**) 3.9 eV, (**c**) 4.2 eV, (**d**) 4.9 eV, (**e**) 6.2 eV and (**f**) 7.5 eV, respectively
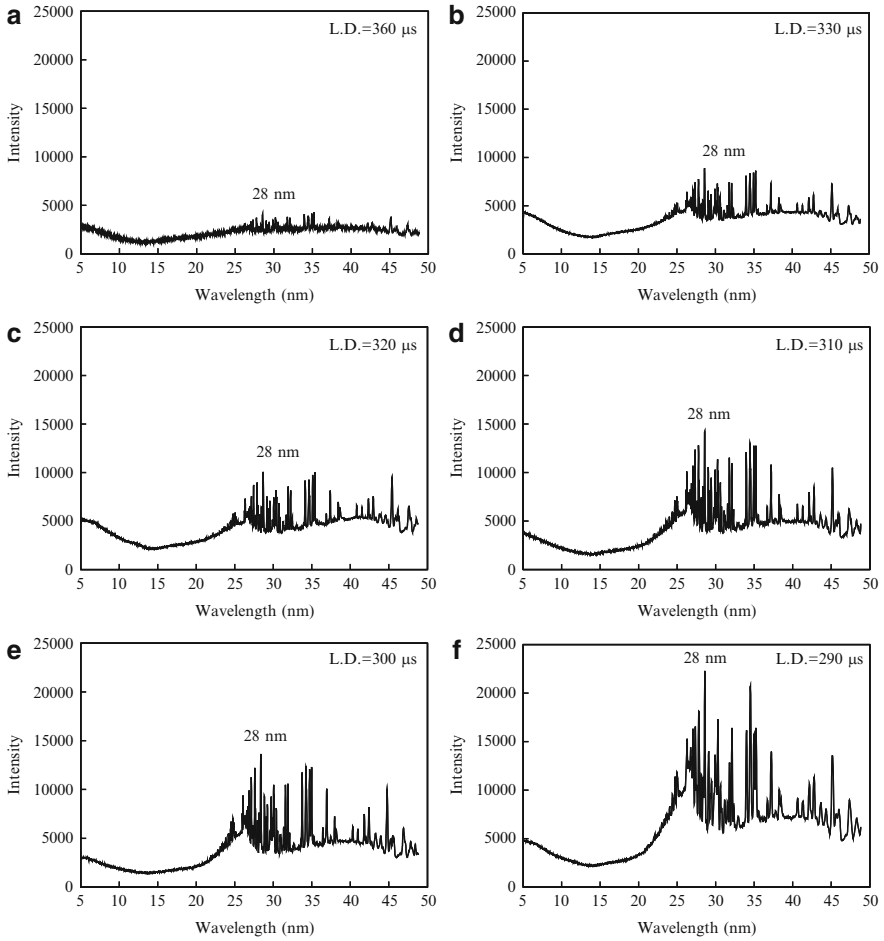
Fig. 9 EUV spectra from oxygen plasma forming atomic oxygen beams with translational energies of (**a**) 2.6 eV, (**b**) 3.9 eV, (**c**) 4.2 eV, (**d**) 4.9 eV, (**e**) 6.2 eV and (**f**) 7.5 eV, respectively

independent of the AO beam energy because the EUV peak was originated in the electron transition phenomena. However, a dramatic increase in peak intensity was observed with increasing the AO beam energy. The experimental results clearly indicated that high-intensity EUV has generated with AO with collision energy of 5 eV in the ground test and it decreases when the translational energy of atomic oxygen is reduced.

4 Conclusions

EUV spectrum emitted from laser-sustained oxygen plasma in a laser-detonation atomic oxygen beam source was measured. The grazing-angle flat-field spectrometer was designed specially for the atom beam source for Kobe University to measure the EUV spectrum and TOF distribution simultaneously. The experimental results clearly indicated that many spectral lines between 25 and 45 nm are included in the photon emission from the laser-sustained oxygen plasma. Origin of these spectral lines is considered to be the electron transition in oxygen gas, thus line position is unchanged even when plasma condition is changed. However, spectral intensity depends strongly on the plasma condition and collated to the translational energy of the atomic oxygen formed in this system. It was confirmed in this study that the materials tested in the laser detonation atomic oxygen beam source experiencing also high-energy photon exposures (>30 eV) during the tests.

References

1. Koontz SL, Leger LJ, Viserntine JT, Hunton DE, Cross JB, Hakes CL (1995) EOIM-III mass spectrometry and polymer chemistry – STS-46. J Spacecraft Rockets 32(3):483–495
2. Shepp A, Haghighat R, Lennhoff J, Schuler P, Connell J, St. Clair T, Vaughn J, Swiener J (1999) TOR and COR AO-VUV resistant polymers for space. In: Kleiman JI, Tennyson RC (eds) Protection of materials and structures from the low Earth orbit space environment. Kluwer, Dordrecht, pp 235–254
3. Grossman E, Gouzman I, Lempert G, Noter Y, Lifshitz Y (2004) Assessment of atomic-oxygen flux in low-Earth-orbit ground simulation facilities. J Spacecraft Rockets 41:356–359
4. Weihs B, van Eesbeek M (1994) Secondary VUV erosion effects on polymers in the ATOX atomic oxygen exposure facility. In: Proceedings of the 6th international symposium on materials in a space environment, ESA SP-368, Noordwijk, pp 277–283
5. Kondo H, Kandaka N, Sugisaki K, Oshino T, Shiraishi M, Ishiyama W, Murakami K (2000) Development of an EUV reflectometer using a laser plasma x-ray source. SPIE Proc 4144:76–81
6. Kita T, Harada T, Nakano N, Kuroda H (1983) Mechanically ruled aberration-corrected concave gratings for a flat-field grazing-incidence spectrograph. Appl Opt 22(4):512–513
7. Ralchenko Y, Kramida AE, Reader J, NIST ASD Team (2008) NIST atomic spectra database (version3.1.5)

Measurement of Atomic-Oxygen Flux Distribution

Takuya Hisashiba, Kazutaka Kuroda, Hirokazu Masui, Minoru Iwata, Kazuhiro Toyoda, and Mengu Cho

Abstract Since material surfaces on the outside of spacecraft are exposed directly to the space environment, material having high tolerance to atomic oxygen, ultraviolet rays and radiation are preferred for long time spacecraft operation. In order to examine the influence of atomic oxygen (AO) on space grade materials, an atomic oxygen simulation chamber was developed. A system was developed that generates AO using a laser detonation method. A CO_2 gas laser (5 J) irradiates the oxygen gas in a vacuum chamber (2 MPa) to dissociate the molecular oxygen into atomic. The velocity of AO can be controlled based on the timing between the laser and the gas pulse valve that injects oxygen gas into the chamber. The AO velocity generated by this system is measured using a QMASS (Quadruple Mass Spectrometer) and found to be 8 km/s. It was necessary to measure the AO flux distribution in the chamber at the location where the material samples are exposed to AO. The AO flux distribution was evaluated by measuring the mass gain on a QCM (QuartzCrystal Microbalance) coated with a silver film upon exposure to the AO.

Keywords Atomic oxygen flux • LEO simulator • QCM

1 Introduction

The spacecraft surfaces are exposed to a severe environment in space with the main environmental factors being atomic oxygen, ultraviolet rays, high energy electrons and protons, etc. They cause deterioration in the properties of material surfaces that affect the performance of satellites designed to operate for long periods of time. The molecular oxygen contained in Earth atmosphere is dissociated by absorbing energy of ultraviolet rays from the sun forming atomic oxygen. The atomic oxygen

T. Hisashiba (✉) • K. Kuroda • H. Masui • M. Iwata • K. Toyoda • M. Cho
Kyushu Institute of Technology, Kitakyushu 804-8550, Japan
e-mail: k349527t@tobata.isc.kyutech.ac.jp

is very active and collides with the spacecraft with a speed of 8 km/s that corresponds to collision energies of 5 eV. The deterioration of the spacecraft material surfaces by atomic oxygen in the low Earth orbit space environment is a serious problem. In addition, material deterioration causes the change of secondary electron emission coefficient and the photoemission coefficient, etc., that ultimately affects the charging effects for satellite and other spacecraft. Therefore, we need to make a standard data base of various coefficients after the space environment effects are taken into account. Hence, our research aim is to develop an atomic oxygen generator and form a standard data base for various materials after being exposed to AO.

2 Atomic Oxygen Source

2.1 The Generation Method of Atomic Oxygen

The developed atomic oxygen generator is based on a laser detonation method [1]. Figure 1 is a schematic view, and Fig. 2 is a photograph of the atomic oxygen generator designed and constructed based on the laser detonation method. The vacuum chamber where the atomic oxygen is generated is called AO chamber. The pressure in the AO chamber is kept around 5.0×10^{-5} Pa by a rotary pump and a turbo molecular pomp.

Oxygen molecules are introduced into the AO chamber by the pulse valve. The introduction pressure into the pulse valve is set to 2 MPa and is controlled by a regulator installed on the oxygen cylinder. The amount of the oxygen gas is controlled by the pulse valve. The oxygen gas infusion time can be controlled by using this pulse valve. The oxygen gas is introduced into the AO chamber by this pulse valve. After gas injection, the laser (5 J, 3 Hz) is fired into the AO chamber. The laser has been synchronized with the gas pulse valve. The laser beam collides with the oxygen gas in the nozzle and the atomic oxygen is formed. Moreover, the atomic oxygen is accelerated due to the excess energy from the laser. This time, the velocity of the atomic oxygen can be changed by adjusting the interval time of gas injection and the laser firing.

2.2 The Velocity of Atomic Oxygen

The velocity of the atomic oxygen is a very important parameter in exposures of spacecraft materials being exposed to AO. To evaluate the material in conditions imitating the LEO environment, it is necessary to control the velocity and ensure it is close to 8 km/s that simulates the atomic oxygen in LEO environment.

In our research, QMASS (Quadruple Mass Spectrometer) is used to detect the atomic oxygen and velocity. The QMASS is composed of an ionization source,
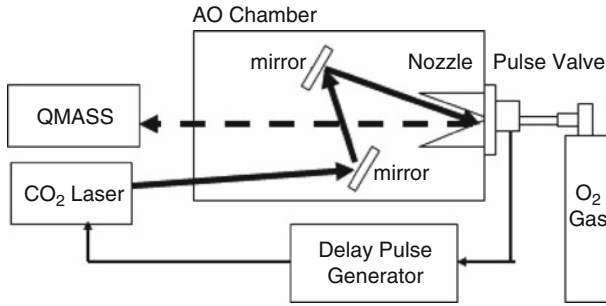
Fig. 1 AO generation systems by laser detonation
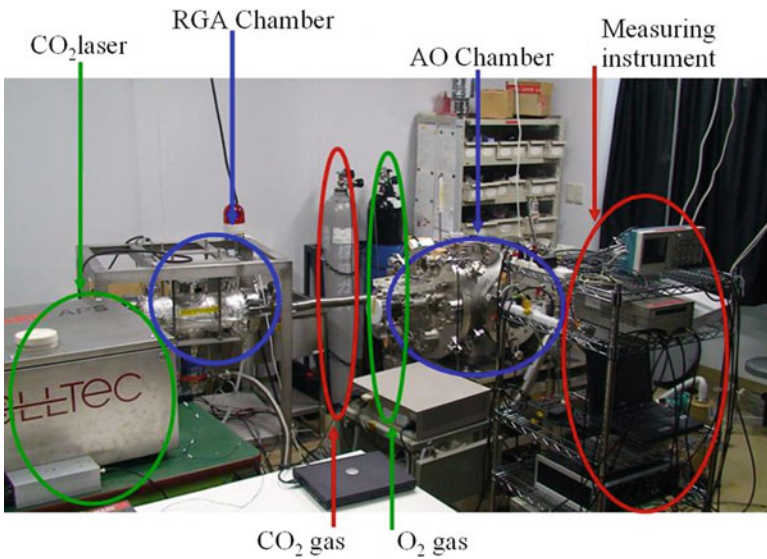
Fig. 2 Photograph of AO generation system with laser detonation

quadruple electrodes, and the detecting element (the secondary electron multiplier). The sample (atoms and molecules) is ionized in the ionization source. The quadruple electrode is comprised of electrodes positioned in four columns. Only ions with a specific mass to charge ratio can pass these electrodes and produce current in the electron multiplier that is measured by the oscilloscope. The velocity of the atomic oxygen is calculated by the time of flight and flight length. When oxygen molecules dissociate, they emit light with a wavelength of 777 nm that is detected by a photodiode. The time between atomic oxygen generation and detecting by QMASS is defined as time of flight (T). The distance from a nozzle to QMASS (flight length) is 1.9 m. Therefore, atomic oxygen velocity is calculated from (1).
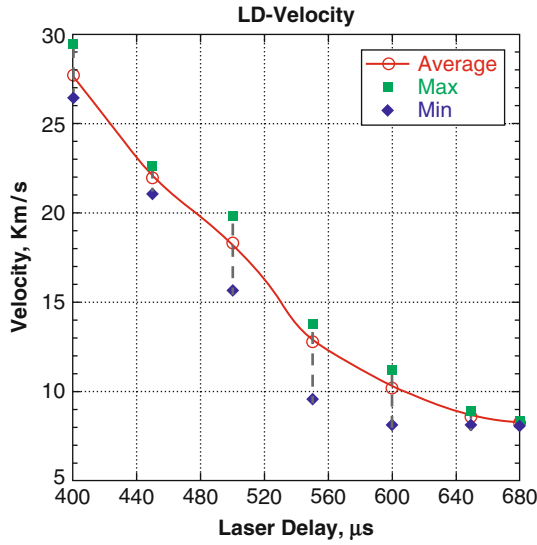
Fig. 3 The relation between the laser delay and the AO velocity
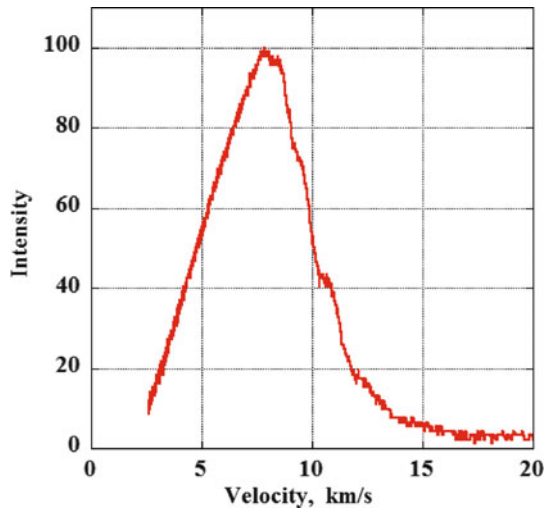
Fig. 4 The relation between the AO velocity and the intensity of the signal from QMASS

$$V = \frac{1.9 \times 10^{-3}}{T} \, [\text{km/s}] \tag{1}$$

The velocity of the atomic oxygen changes depending on the delay time between the laser pulse and the gas pulse opening. Figure 3 shows the relation between the delay time of the laser and the velocity of the atomic oxygen. Figure 4 shows the

velocity spectrum when the peak velocity of the atomic oxygen is 8 km/s. The x-axis is velocity, and the y-axis is signal strength from QMASS.

3 Measurement of Atomic Oxygen Flux

3.1 The Atomic Oxygen Flux

It is necessary to measure the flux of atomic oxygen that arrives at the material under test. In space, the atomic oxygen flux depends on the solar activity and the orbit. Thus, it is intended to calculate the number of the pulse and the irradiation multiple according to orbit and the condition of the solar activity.

3.2 How to Measure

QCM (Quartz Crystal Microbalance) is used for flux measurement of the atomic oxygen [2]. The atomic oxygen collides with the silver (Ag) coated quartz causing oxidation of the silver. The AO flux is calculated by measuring mass increase on this crystal.

$$2Ag + O \rightarrow Ag_2O \tag{2}$$

The AO flux is calculated from (3). Here, Δm is mass change, R is the Avogadro constant, M is the mass of atomic oxygen (16 g), s is the exposure time. The mass change is calculated by measuring the resonance frequency of the quartz crystal. Moreover, because the atomic oxygen is generated as pulses, the flux per pulse (shot) is obtained from (4).

$$O\_flux = \frac{\Delta m \times R}{M \times sec} [atom/cm^2/s] \tag{3}$$

$$O\_flux = \frac{\Delta m \times R}{M \times shot} [atom/cm^2/shot] \tag{4}$$

Ten QCM crystals are set up on a net, as shown in Fig. 5 and the net is affixed at a distance of 63.8 cm from the nozzle where the atomic oxygen generates. Figure 6 is a photograph of the net with the nozzle.

During measurement, the temperature of the sample holder head is kept constant using a water cooling system. The reason to keep the temperature constant is that an error can be caused in the mass calculation because the variations in temperature are influencing the resonance frequency of the quartz crystal.
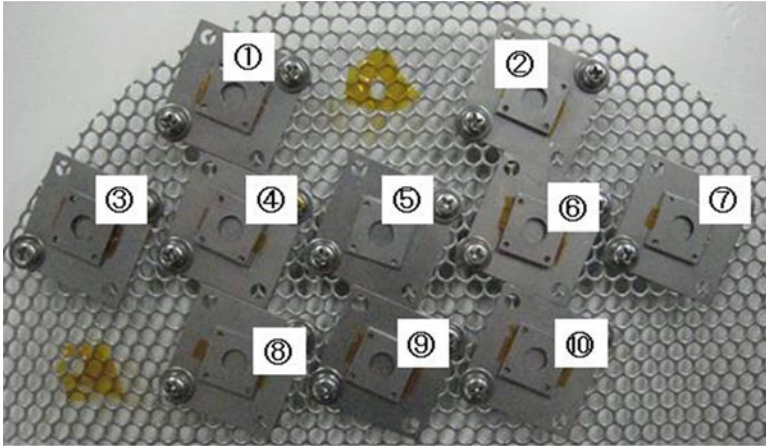
Fig. 5 The net with ten crystals affixed to it
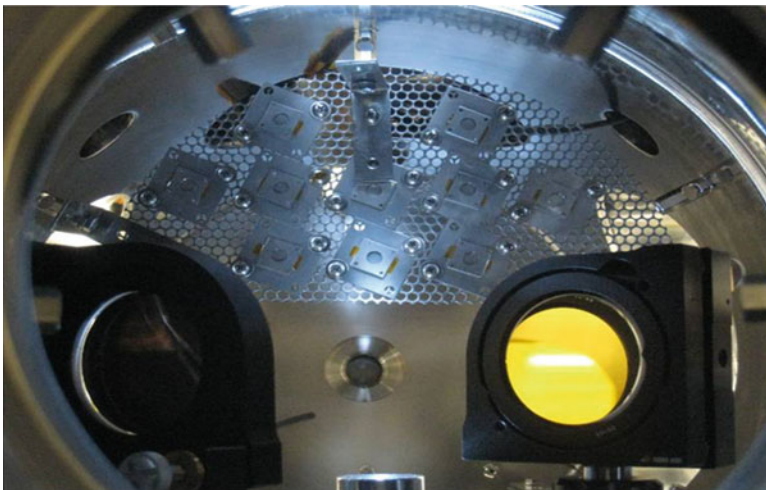
Fig. 6 The position of the net

Figure 7 shows the change in the virtual mass when the temperature of the QCM head is cycled between 13.5 and 16 °C. It can be calculated from this graph that a temperature change of 1° will change the flux by 1 % by.

The measurements of the flux and the mass changes by the QCM head are done at the same time. Each crystal on the net (Fig. 5) is given with a relative flux value that is based on assigning the flux 3.3×10^{14} atom/cm^2/shot a value of 100. The laser working frequencies to generate the atomic oxygen were selected as 1, 2 and 3 Hz.

Fig. 7 The influence of temperature
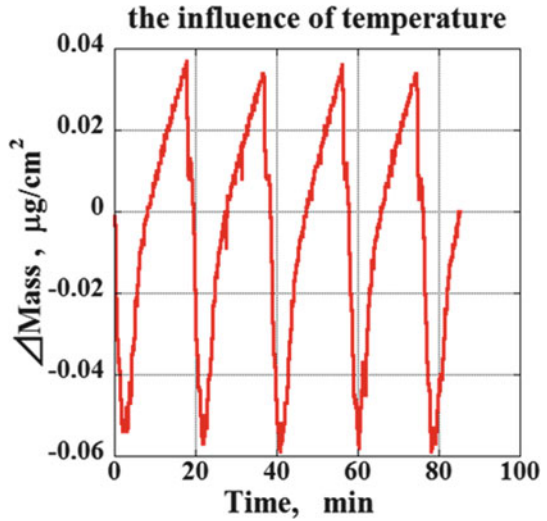
4 Results

4.1 Irradiation with a 3 Hz Repetition Rate

Table 1 presents the results of the AO flux measurements when using a 3 Hz laser repetition frequency. Figure 8 shows the two dimensional flux distribution over the sample holder. The relative values shown in Fig. 8 indicate the AO flux, as shown in Table 1.

4.2 Considerations

Table 2 shows the annual fluence of AO at the altitude of 400–800 km [3]. Min is the minimum solar activity in the case, Max is the maximum period and M is the middle. Table 3 shows the required time to simulate specific annual fluence of the atomic oxygen.

The condition in Table 2 can be simulated by the continuous irradiation from several days to several weeks.

Table 1 Flux distribution

QCM	Flux (atom/cm^2/shot)	Relation value
No. 1	3.96×10^{14}	120
No. 2	3.92×10^{14}	119
No. 3	3.77×10^{14}	114
No. 4	3.96×10^{14}	120
No. 5	2.66×10^{14}	81
No. 6	3.83×10^{14}	116
No. 7	3.87×10^{14}	117
No. 8	3.67×10^{14}	111
No. 9	3.77×10^{14}	114
No. 10	3.45×10^{14}	105
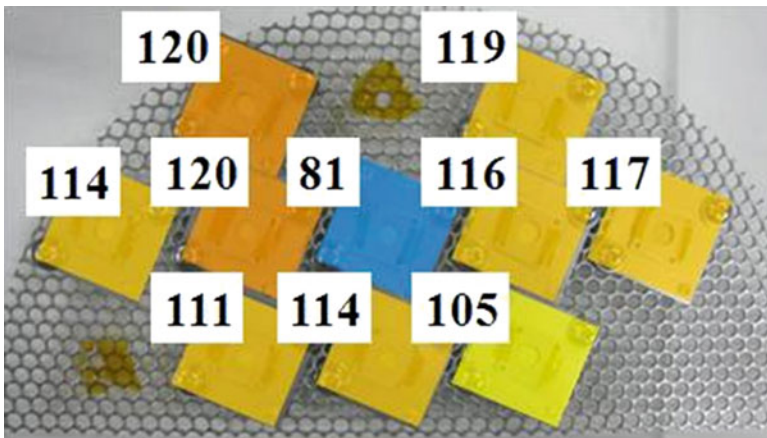
Fig. 8 The two dimensional distribution of AO flux (3 Hz)

Table 2 The annual AO fluence at different altitudes in LEO

(atom/cm^2)	400 km	500 km	600 km	700 km	800 km
1×10^{19}			Min		M
1×10^{20}		Min		M	Max
1×10^{21}	Min	M	Max		

Table 3 The calculated annual AO fluence and the time required to attain it

	1×10^{19} (atom/cm^2/year)	1×10^{20} (atom/cm^2/year)	1×10^{21} (atom/cm^2/year)
1 Hz	7 h	2 days 21 h	28 days 22 h
	1,251×	127×	13×
2 Hz	3.5 h	1 day 11 h	14 days 11 h
	2,502×	250×	25×
3 Hz	2.3 h	23 h	9 days 15 h
	3,809×	381×	38×

5 Conclusions

An experimental system that produces the atomic oxygen with a velocity of 8 km/s has been built. The atomic oxygen flux distribution inside the chamber is measured by using QCM. It is necessary to computerize this system in order to simulate the AO flux that irradiates continuously from several days to several weeks. It will be necessary to examine the change of flux by continuous irradiation in the future.

References

1. Gazaubon B, Paillous A, Siffre J, Thomas R (1996) Five-electron-volt atomic oxygen pulsed-beam characterization by quadrupolar mass spectrometry. J Spacecraft Rockets 33:870–876
2. Yokota K, Tagawa M (2007) Comparison of polyethylene and polyimide as a fluence monitor of atomic oxygen. J Spacecraft Rockets 44:434–438
3. Hastings D, Garrett H (2010) Spacecraft-environment interactions, Cambridge atmospheric and space science series. Cambridge University Press, Cambridge, pp 132–137

Author Index

Subject Index